Joachim R. R. Ritter
Ulrich R. Christensen
(Eds.)

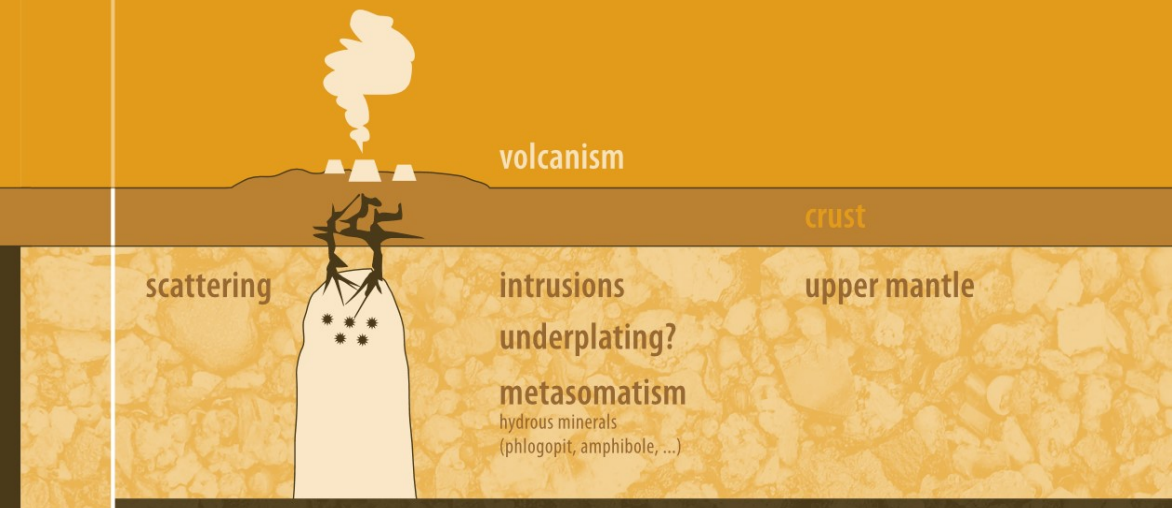

Mantle Plumes

A Multidisciplinary Approach

Springer

Joachim R. R. Ritter
Ulrich R. Christensen

Mantle Plumes

Joachim R. R. Ritter
Ulrich R. Christensen
(Editors)

Mantle Plumes

A Multidisciplinary Approach

With 157 Figures

Springer

PRIV.-DOZ. DR. JOACHIM R. R. RITTER
University of Karlsruhe
Geophysical Institute
Hertzstr. 16
76187 Karlsruhe
Germany

Email: Joachim.Ritter@gpi.uni-karlsruhe.de

PROF. DR. ULRICH R. CHRISTENSEN
Max-Planck Institute for Solar System Research
Max-Planck-Str. 2
37191 Katlenburg-Lindau
Germany

Email: Christensen@mps.mpg.de

Library of Congress Control Number: 2006937532

ISBN-13 978-3-540-68045 -1 Springer Berlin Heidelberg New York

Springer is a part of Springer Science+Business Media
springer.com

Cover design: deblik, Berlin
Typesetting: camera-ready by the authors
Production: Christine Adolph
Printing: Krips bv, Meppel
Binding: Stürtz AG, Würzburg

Printed on acid-free paper 30/2133/ca 5 4 3 2 1 0

Preface

The concept of mantle plumes, originally suggested by Morgan (1971), is widely but not unequivocally accepted as the cause for hotspot volcanism. Plumes are thought of as deep-rooted, approximately cylindrical regions of hot rising mantle rock with a typical diameter of 100-200 km. Pressure-release melting near the bottom of the lithosphere produces magmas that rise to the surface and lead, when the plate moves relative to the plume, to a chain of volcanic edifices whose age progresses with increasing distance from the plume. For a long time, the evidence for mantle plumes has been largely circumstantial. Laboratory and computer models of mantle convection show that under certain conditions plume-like structures can be found, and these simulations have been used to characterise their properties. Geodetic signals, such as topographic swells and associated geoid anomalies which surround the volcanic hotspots, support the plume hypothesis. They are best identified in an oceanic environment where the plume signal is usually less susceptible to be masked by effects of crustal or lithospheric heterogeneities. The isotopic and trace element composition of hotspot lavas differs from those of mid-oceanic ridge basalts which is interpreted as indication for a source reservoir different from average upper mantle rock. The idea of mantle plumes has gained widespread popularity in various disciplines of Earth science and has been used, sometimes perhaps excessively, to explain volcanic and other phenomena. In a number of cases the alleged plume nature has remained doubtful, for example when volcanism is sporadic or when a clear age progression is missing. This has led a few scientist to reject the plume concept entirely.

Direct imaging of mantle plumes by seismic tomography is a fairly recent achievement. Because plumes are comparatively thin structures, they are hard to detect in global tomographic models, although some progress has been made (Montelli et al. 2004). Convincing plume-like structures have been mapped in the upper mantle by dedicated regional seismic tomography experiments beneath a few hotspots. Because a sufficient aperture of the station network is needed, this has been restricted so far to subcontinental plumes and to Iceland for the lack of ocean-bottom seismometers. The limited aperture of regional seismic networks does not usually allow to track the plume into the lower mantle (if it extends in fact that deep), but observation of seismic phases, which are converted at mantle discontinuities (Li et al. 2003), can help to provide additional evidence on the plume structure.

A particular strength of the plume concept is that it provides a framework for explaining observational data from a broad range of geophysical, petrological, geological, geochemical and geodetic sources. In this spirit the present volume combines papers from all these disciplines. The book starts with a review of the geodynamical foundation of the plume hypothesis and proceeds with several case studies involving the major hotspots Hawaii and Iceland as well as minor volcanic regions, such as the French Massif Central. The volcanic Eifel region, Germany, has been the target of a concerted scientific effort in 1997-2003, with a large seis-

mic network as the core activity. The results strongly support a plume origin of the volcanism. As a consequence the Eifel plume, which before was a doubtful candidate, is one of the best characterised plumes in the world. Approximately half of the book deals with specific studies related to this upper mantle plume, which may well serve as the prototype of a moderately weak hotspot in a continental environment. The different contributions to the book show that the plume concept, which was invented 35 years ago to explain oceanic island chains in the Pacific, has found its firm place in the context of volcanic phenomena in different tectonic settings.

We like to thank all researchers who contributed to this book, especially the reviewers R. Allen, C. Ballentine, H. Downes, J. Evans, S. Funke, S. Gregersen, K. Haase, S. Husen, G. Ito, I. Kaneoka, S. Lebedev, M. Mai, J. Mechie, S. Niedermann, B. Meurers, P. Olson, T. Plenefisch, J. Plomerova, P. Sarda, H.-G. Stosch, M. van Camp, C. Weidle, G. Wörner and eight anonymous reviewers.

Britta Wawerzinek helped patiently with the preparation of the final page layout. At the end of this volume there is an appendix with 16 colour plates.

We dedicate this book to Dr. Günter Bock. Günter died in a tragic airplane crash while he was on his way to a meeting of the Eifel Plume Team in Luxembourg on 6th November 2002.

Joachim Ritter Ulrich Christensen

References

Li X, Kind R, Yuan X (2003) Seismic study of upper mantle and transition zone beneath hotspots. Phys Earth Planet Inter 136:79-92

Morgan WJ (1971) Convection plumes in the lower mantle. Nature 230:42-43

Montelli R, Nolet G, Dahlen FA, Masters G, Engdahl ER, Hung SH (2004) Finite-frequency tomography reveals a variety of plumes in the mantle. Science 303:338-343

Contents

Fluid Dynamics of Mantle Plumes

Neil Ribe[1], Anne Davaille[1], Ulrich Christensen[2]

[1] Institut de Physique du Globe, 4, Place Jussieu, 75252 Paris cédex 05, France,
[2] Max-Planck Institut für Sonnensystemforschung, Max-Planck-Strasse 2, 37191 Katlenburg-Lindau, Germany

1 Introduction

A 'hotspot' (Wilson 1963) is a long-term source of volcanism which is fixed relative to the plate overriding it. Common signatures of hotspots include a bathymetric swell and an associated gravity anomaly; basalt geochemistry different from normal mid-ocean ridge basalts; and volcanic chains with a clear age progression parallel to the plate motion, in some cases beginning with a voluminous flood basalt event (Morgan 1972). The total number of hotspots is controversial, but is probably around 40-50 (Richards et al. 1988; Sleep 1990) of which 8 or 9 are associated with flood basalts (Richards et al. 1989; Courtillot et al. 2003). Petrological (e.g. White and McKenzie 1995) and geophysical (e.g. Sleep 1990) studies suggest that hotspot material is 150-300 K hotter than the normal mantle, while flood basalts are associated with excess temperatures up to 400 K (e.g. Thompson and Gibson 2000).

Morgan (1971) was the first to propose that the characteristic surface signatures of hotspots were due to the rise and melting of hot plumes from deep in the mantle. Plumes, which we define here as localized hot upwellings, are ubiquitous in vigorously convecting fluids where they arise from thermal boundary layers, and are relatively well understood for simple laboratory systems. By contrast, our understanding of plumes in the Earth's mantle is still rudimentary, in large part because they are so difficult to observe. Recent advances in seismic imaging have improved this situation considerably, however. Surface-wave tomographic models have identified broad ($\approx$ 1000 km) ponds of slow material down to 200 km depth beneath many hotspots (e.g. Grand 2002; Shapiro and Ritzwoller 2002; Ritsema and Allen 2003; Debayle et al. 2005). Regional tomographic studies beneath Afar (Debayle et al. 2001), the Eifel (Ritter et al. 2001) and Iceland (see Ito et al. 2003) for references) image low-velocity anomalies down to the transition zone. Studies using converted phases (receiver functions) show thinner transition zones beneath Iceland and Hawaii, which may reflect the presence of a hot conduit (Nataf 2000, and refer-

ences therein). Finally, recent global tomographic studies (Zhao 2001; Montelli et al. 2004) have imaged cylindrical slow seismic P-wave velocity anomalies 300-500 km in diameter extending down to the core-mantle boundary beneath about 10 hotspots.

Yet despite recent advances, there is still no general consensus on the most important questions concerning plumes in the mantle: their depth of origin, their morphology, their longevity, even their existence. Much of the uncertainty is due to the fact that geophysical and geochemical observations at hotspots can often be explained by different 'plume' models, and even by models that do not involve plumes at all (e.g. Foulger and Natland 2003). Another difficulty is the inherently complicated dynamics of plumes in rheologically and chemically complex materials. Further confusion arises from the diversity of physical models in the literature: compositional vs. thermal buoyancy, continuous vs. "one-shot" buoyancy injection, boundary layer instability vs. point heat sources, etc.

This review aims to bring some order to this diversity for the benefit of nonspecialist readers. While several excellent reviews of various aspects of plumes exist (Whitehead 1988; Nataf 1991; Siggia 1994; Loper 1998; Schubert et al. 2001; Condie 2001; Jellinek and Manga 2004), none to our knowledge attempts a comprehensive overview of the literature from the point of view of fundamental fluid mechanics. Accordingly, the present review comprises three broad sections. Section 2 discusses the now-classic early work on plumes from point sources of buoyancy, which still dominates our image of what mantle plumes look like. Section 3 reviews work on plumes that arise as instabilities of thermal and thermochemical boundary layers. Finally, section 4 focusses on how plumes interact with the lithosphere. Limitations of space prevent us from discussing in detail a number of other interesting topics, such as the modulation of plume formation by large-scale mantle downwellings (Tan et al. 2002; Gonnermann et al. 2004; Lowman et al. 2004), the interaction of plumes with compositional boundaries and phase transitions (Kellogg 1991; Liu et al. 1991; Manga et al. 1993; Bercovici and Mahoney 1994; Nakakuki et al. 1994; Davies 1995; Schubert et al. 1995; Kumagai and Kurita 2000) and with each other (Kelly and Bercovici 1997; Manga 1997; Schaeffer and Manga 2001; Labrosse 2002; Schubert et al. 2004), and entrainment of compositionally dense material by thermal plumes (Olson 1984; Sleep 1988; Lister 1989; Davaille 1999a,b; Gonnermann et al. 2002; Davaille et al. 2002; Jellinek and Manga 2002, 2004; Schott et al. 2002; Namiki 2003; Zhong and Hager 2003).

2 Plumes from a point source of buoyancy

In the mantle, plumes are expected to develop as instabilities of thermal boundary layers (e.g. Parmentier et al. 1975; Loper and Stacey 1983). However, in vigorously convecting fluids such instabilities are transient and chaotic features whose local characteristics are difficult to quantify. Accordingly, many

of the early studies of mantle plumes focussed on the simpler case of an isolated laminar "starting plume" rising from a point source of buoyancy, a situation that is easily studied in the laboratory. Experiments performed using fluids with compositional (nondiffusing) buoyancy (Whitehead and Luther 1975; Olson and Singer 1985) and thermal buoyancy (Griffiths 1986a; Campbell and Griffiths 1990) led to what has become the "standard model" of a mantle plume: a large, bulbous "head" or "cavity" trailed by a narrow conduit (the "stem" or "tail") connecting it with its source (Fig. 1b). According to this model, the arrival of a plume head at the base of the lithosphere produces massive flood basalts, while the trailing conduit generates the subsequent volcanic track (Richards et al. 1989). The model successfully explains important features of several prominent hotspots, including the volume of the topographic swell (e.g. Davies 1988; Olson 1990; Sleep 1990) and the volume ratio between flood basalts and island chain volcanism (Olson and Singer 1985; Richards et al. 1989). Below we will address the question of whether long-lived cavity plumes can be generated from a thermal boundary layer heated over its entire area.

In the following, we discuss separately the cases of compositional and thermal buoyancy. The density and kinematic viscosity of the ambient ('mantle') fluid will be denoted by ρ_m and ν_m, respectively, and the corresponding properties of the plume fluid by ρ_p and ν_p. We set $\rho_m = \rho_p \equiv \rho$ everywhere except in the expression for the reduced gravity $g^\star = g(\rho_m - \rho_p)/\rho \equiv g\Delta\rho/\rho$. Mathematical expressions are written in terms of reduced gravity and kinematic viscosity for greater concision, while viscosity values for the mantle are given in terms of the more familiar dynamic viscosity $\mu \equiv \rho\nu$ (units Pa s). Finally, the rates of injection of volume and of thermal energy are denoted as Q and P, respectively.

2.1 Compositional buoyancy

Buoyant fluid that is steadily injected into an ambient fluid forms a quasi-spherical ball that grows until it is large enough to "lift off" from the injector (Fig. 1). A simple lift-off criterion was derived by Whitehead and Luther (1975). Ignoring for simplicity the effect of the boundary containing the injector, the sphere's rise velocity W is given by Stokes's law (Batchelor 1967)

$$W = \frac{g^\star a^2}{3\nu_m}\left(\frac{\nu_m/\nu_p + 1}{\nu_m/\nu_p + 3/2}\right) \equiv \frac{g^\star a^2}{3\nu_m} f(\gamma) \tag{1}$$

where a is the sphere's radius and $\gamma = \nu_m/\nu_p$. The sphere lifts off when W exceeds the rate of increase of the radius $da/dt = Q/4\pi a^2$, which occurs at a critical time t_{sep} and radius a_{sep} given by (Whitehead and Luther 1975)

$$t_{sep} = \left(\frac{4\pi}{3Q}\right)^{1/4}\left(\frac{\nu_m}{g^\star}\right)^{3/4}, \qquad a_{sep} = \left(\frac{3Q}{4\pi}\right)^{1/3} t_{sep}^{1/3} \tag{2}$$

where the factor f appearing in (1) has been neglected. By (2), both the time and radius of separation increase with increasing viscosity of the ambient fluid. For the large viscosities typical of the mantle, plume heads must be quite large ($a > 100$ km) to separate from their source (e.g. Whitehead and Luther 1975).

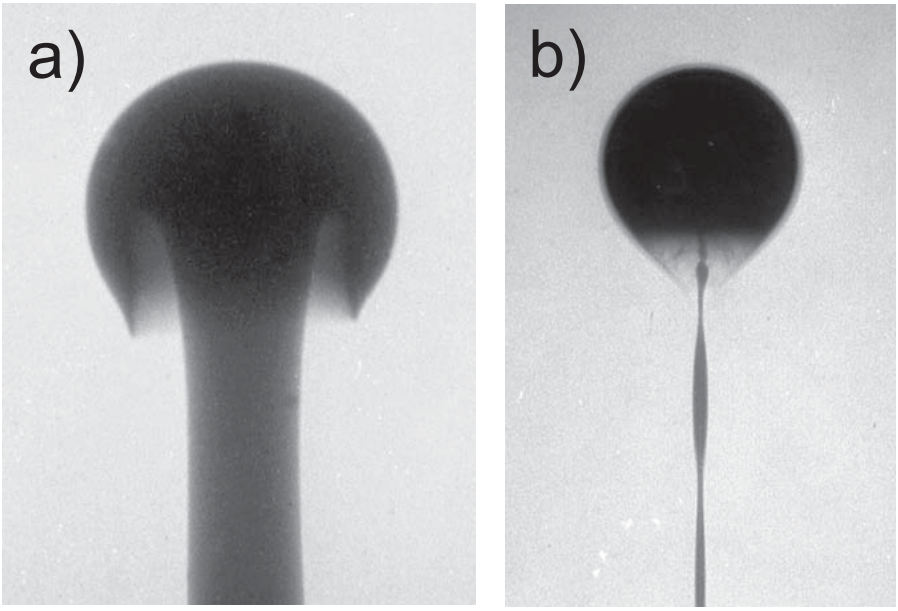

Fig. 1. Morphology of compositional starting plumes, from Olson and Singer (1985). (a) Diapiric plume, with viscosity comparable to that of its surroundings. (b) Cavity plume, much less viscous than its surroundings. Reproduced with permission from Cambridge University Press.

After liftoff, the morphology and dynamics of plumes depend strongly on the viscosity ratio $\gamma \equiv \nu_m/\nu_p$ (Whitehead and Luther 1975). When the injected fluid is more viscous ($\gamma \leq 1$) , the plume has roughly the shape of a cylinder (Fig. 1a) whose length $L(t)$ and radius $R(t)$ increase with time. Stokes's law (1) is not valid for such a geometry, which must instead be treated using slender body theory (e.g. Batchelor 1970). By solving numerically the coupled equations describing conservation of mass and the slender-body drag, Olson and Singer (1985) showed that an initial rapid increase of R and L is followed by a stage of slower growth where R is nearly constant and the velocity $W \equiv dL/dt$ of the plume tip is

$$W = \left(\frac{bg^\star Q}{\pi \nu_m} \ln \frac{L}{R} \right)^{1/2}, \tag{3}$$

where $b \approx 1.0$ is a constant determined by comparing the numerical solutions with experimental measurements. Note that W is nearly constant due to the slow variation of $\ln(L/R)$.

In the low-viscosity limit ($\gamma \gg 1$), the ascending plume is a "cavity plume" comprising a large head and a thin trailing conduit (Fig. 1b). The rate of change of volume of the head is just the injected flux Q less the flux required to build the (lengthening) stem, or

$$\frac{dV}{dt} = Q - \pi R_c^2 W \tag{4}$$

where $R_c \equiv (8\nu_p Q/\pi g^\star)^{1/4}$ is the conduit radius corresponding to pipe (Poiseuille) flow and W is the velocity of the head predicted by Stokes's law (1). For small times $t \ll 4(\pi\nu_m^6/g^{\star 3}Q\nu_p^3)^{1/4} \equiv \tau$, the second term on the right side of (4) is negligible, so $V \approx Qt$. Stokes's law (1) then implies $W \sim t^{2/3}$. For long times $t \gg \tau$, the velocity of the head becomes equal to the average upwelling velocity in the stem, and the head reaches a terminal velocity W_{term} and radius a_{term} (Whitehead and Luther 1975).

$$W_{term} = (g^\star Q/8\pi\nu_p)^{1/2}, \qquad a_{term} = (3W_{term}\nu_m/g^\star)^{1/2} \tag{5}$$

At intermediate times $t \sim \tau$ for which the volume of the stem has become significant but the head has not yet reached its terminal speed, the ascent speed is (Olson and Singer 1985)

$$W = 0.225(g^\star/\nu_m)^{4/5}Q^{3/5}t^{2/5}. \tag{6}$$

Because part of the injected flux Q is used to lengthen the stem, W increases less rapidly with time than it does ($W \sim t^{2/3}$) for $t \ll \tau$.

Compositionally buoyant cavity plumes can also entrain the denser ambient fluid through which they rise (Neavel and Johnson 1991; Kumagai 2002). Kumagai (2002) identified two distinct regimes: a 'vortex ring' regime for $\gamma \approx 10$ in which layers of entrained fluid form a scroll-like pattern inside the plume head, and a 'chaotic stirring' regime for $\gamma \geq 100$. Structures of the vortex ring type also occur in thermal starting plumes with temperature-dependent viscosity (Griffiths and Campbell 1990, Fig. 6a).

Interaction with large-scale flow

The interaction of compositional plumes with a large-scale ambient flow was first studied by Skilbeck and Whitehead (1978), who injected buoyant fluid into a shear flow generated by rotating the top surface of a tank containing another fluid. As the rising plume head is swept horizontally away from the source, the trailing conduit is tilted until it becomes gravitationally unstable at a tilt angle $\approx 30°$ from the vertical. The instability forms new, smaller cavity plumes whose spacing is independent of the volume flux Q (Whitehead 1982). Olson and Singer (1985) performed similar experiments by towing the

source at constant speed U at the bottom of a tank of motionless fluid (Fig. 2). The characteristic spacing λ and volume V of the new cavity plumes generated by the instability were found to scale as $\lambda \approx 12(\nu_m U/g^\star)^{1/2}$ and $V \approx 12(\nu_m/g^\star U)^{1/2}Q$, respectively, although these relationships break down for small (< 0.3) and large (> 10) values of the dimensionless parameter $(g^\star Q/\nu_m U^2)^{1/2}$. Skilbeck and Whitehead (1978) suggested that this instability might account for the discrete nature of volcanic island chains.

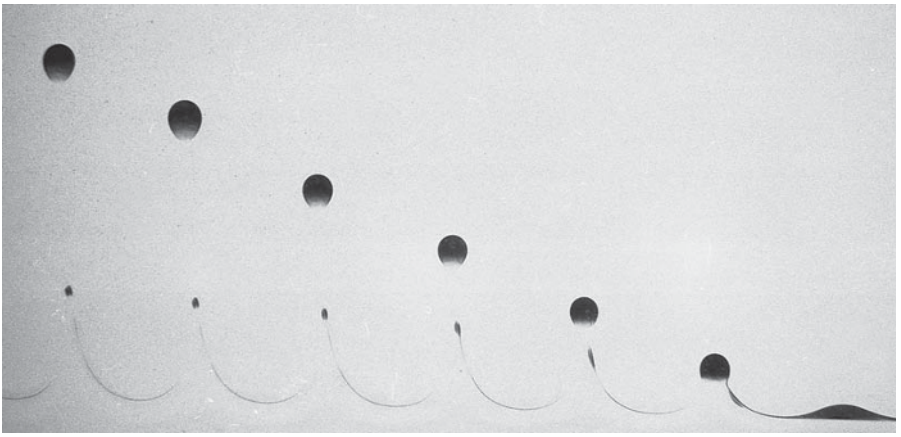

Fig. 2. Chain of cavity plumes behind a source of compositional buoyancy towed at constant speed, from Olson and Singer (1985). Reproduced with permission from Cambridge University Press.

Richards and Griffiths (1988) studied experimentally the interaction between a compositionally buoyant plume conduit and a large-scale shear flow, for low conduit tilt angles at which the instability documented by Skilbeck and Whitehead (1978) does not occur. They showed that the conduit's shape can be calculated by describing its motion as a vector sum of the shear velocity and a modified vertical Stokes velocity v_s for individual conduit elements. For a simple linear shear flow, the resulting steady-state shape is a parabola. In response to a sudden change in the shear flow, the lateral position $x(z)$ of such a conduit adjusts to a new steady-state position in a time z/v_s, where z is the height. Griffiths and Richards (1989) applied this theory to Hawaii, concluding that the sharpness of the bend in the Hawaiian-Emperor chain at 43 Ma implies that the deflection of the Hawaiian plume before the change in plate motion was < 200 km.

Solitary waves

The stem of a chemically buoyant plume can also support solitary waves, waves of large amplitude that propagate upwards without change in shape (Olson

and Christensen 1986; Scott et al. 1987; Whitehead and Helfrich 1988). In a frame travelling with the wave, the flow inside it exhibits recirculation along closed streamlines. Chemically distinct material can therefore be transported to the lithosphere with little contamination, at velocities $\approx$ 10 times that predicted by Stokes's law for a sphere of the same diameter (Olson and Christensen 1986). Subsequently, it was discovered that thermal plume stems could also support solitary waves (Schubert et al. 1989; Laudenbach and Christensen 2001; Fig. 3); in which case the wave will also be hotter than normal plume material. This could account for episodic magma production at weak hotspots and surges of activity at stronger hotspots (Laudenbach and Christensen 2001).

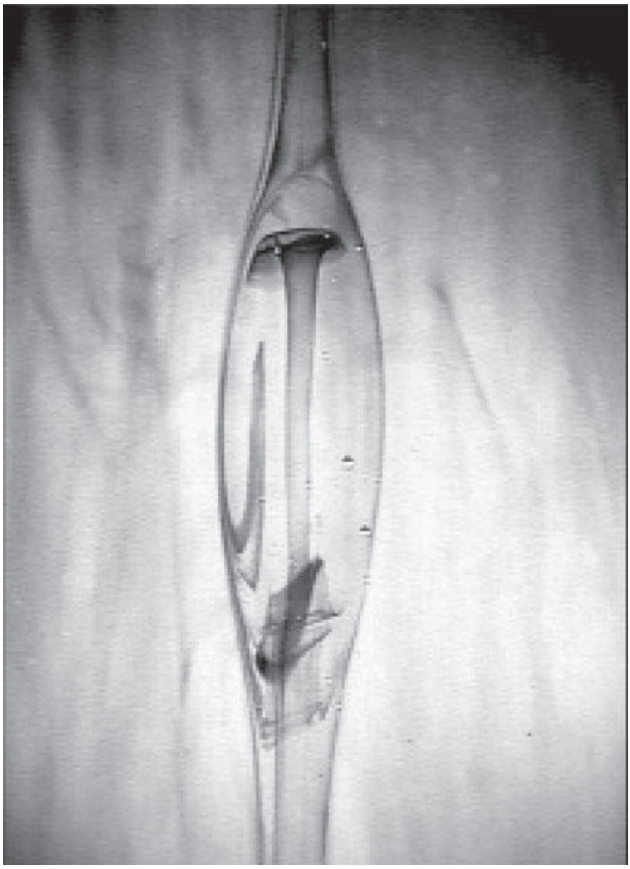

Fig. 3. Solitary wave ascending in a conduit formed by injecting hot fluid into a cooler ambient fluid (from Laudenbach and Christensen 2001). Reproduced with permission from Blackwell Publishing.

2.2 Thermal buoyancy

Because the viscosity of mantle material and of many experimental fluids decreases strongly with increasing temperature, thermal starting plumes generally are cavity plumes comprising a large head and a narrow stem. For clarity, we discuss first the dynamics of the plume stem; then of an isolated plume head ("thermal"); and finally the coupled dynamics of the head-stem system ("thermal starting plumes").

The stem

Fundamental to any discussion of the plume stem is an understanding of the structure of a steady plume above a point source of heat of strength P in a fluid with constant viscosity ν, thermal diffusivity κ, specific heat c_p, and thermal expansion coefficient α. The scaling laws for the vertical velocity W, the temperature anomaly ΔT, and the plume radius R are (Batchelor 1954)

$$W \sim \left(\frac{g\alpha P}{\pi\rho c_p \nu}\right)^{1/2}, \qquad \Delta T \sim \frac{P}{\kappa\rho c_p z}, \qquad R \sim \left(\frac{\rho c_p \nu\kappa^2}{g\alpha P}\right)^{1/4} z^{1/2}, \quad (7)$$

where z is the height above the point source. Physically, the scaling laws (7) reflect two distinct balances: between buoyancy and viscous resistance to shearing, and between advection and radial diffusion of heat. The ascent speed is constant, and the temperature anomaly decreases with height as z^{-1} due to thermal diffusion. The scalings (7) are valid to within multiplicative functions of the Prandtl number $Pr = \nu/\kappa$, which measures the ratio of momentum diffusivity ($\equiv$ viscosity) to thermal diffusivity. In the geologically relevant limit $Pr \gg 1$, the radial profile of vertical velocity is much wider than the radial profile of temperature, and the vertical velocity is nearly constant over the radius of the thermal anomaly (Fig. 4). Numerical results for finite Pr (e.g. Fuji 1963; Worster 1986) confirm the scalings (7), and analytical results for $Pr \gg 1$ have been derived by Worster (1986) and Vasquez et al. (1996).

The dynamics are very different when the viscosity depends strongly upon temperature, as is the case in the earth. Variable viscosity concentrates the upwelling in the hottest central part of the plume stem. Hence, even for $Pr \gg 1$, the thermal anomaly is wider than the radial velocity profile (Fig. 4), contrary to the constant-viscosity case. Olson et al. (1993) obtained an approximate solution of the boundary-layer equations for the steady flow above a point source of heat in a fluid whose viscosity depends on temperature as

$$\nu = \nu_m \exp\left(-\Gamma \frac{T - T_m}{\Delta T_0}\right), \quad (8)$$

where T_m is the temperature far from the plume and ΔT_0 is the temperature anomaly of the plume at its base. The upwelling velocity W on the axis and the temperature anomaly ΔT vary with height z as

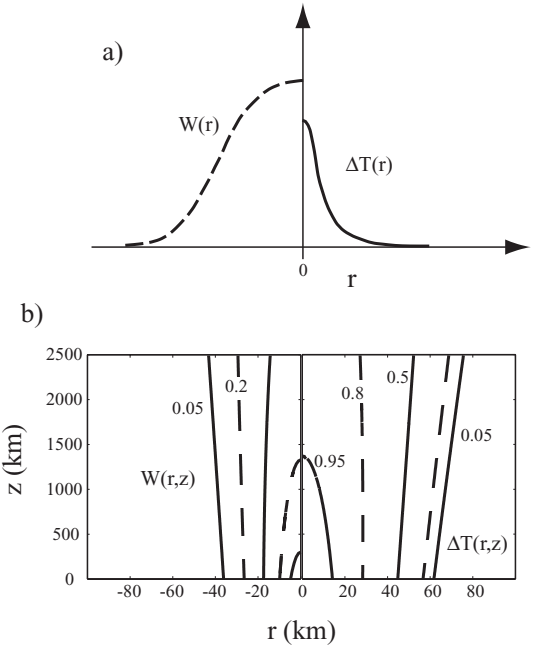

Fig. 4. Structure of steady plume stems above a point heat source at high Prandtl number. (a) Radial profiles of vertical velocity $W(r)$ and temperature anomaly $\Delta T(r)$ in a fluid with constant viscosity, at an arbitrary depth z (schematic). (b) Vertical velocity $W(r, z)$ and temperature anomaly $\Delta T(r, z)$ for a fluid with strongly temperature-dependent viscosity (Olson et al. 1993). W and ΔT are normalized by their maximum values on the axis $r = 0$.

$$W = \left(\frac{g\alpha P}{4\pi\rho c_p \nu_0(z)} \right)^{1/2}, \qquad \Delta T = \Delta T_0 \exp\left(\frac{-4\pi k \Delta T_0 z}{\Gamma P} \right), \tag{9}$$

where $\nu_0(z)$ is the viscosity on the plume centerline as a function of height z and k is the thermal conductivity. The expression (9) for W is identical to the constant-viscosity expression (7) except for the variability of the centerline viscosity $\nu_0(z)$. The temperature anomaly decreases exponentially with height, and the corresponding increase in viscosity causes the upwelling velocity W also to decrease with height. The radius δ_W of the upwelling region (the "conduit" proper) is smaller than the radius $\delta_T \sim [\ln(\nu_m/\nu_0)/2]^{1/2}\delta_W$ of the thermal halo (Fig. 4). For typical mantle parameter values, plumes with large viscosity variations (≥ 1000) have $\delta_W \sim 25 - 30$ km and $\delta_T \sim 60$ km, while plumes with low viscosity variations (≤ 100) are typically twice as broad.

Hauri et al. (1994) solved numerically the boundary-layer equations for a steady plume above a point heat source in a fluid with temperature- and stress-dependent viscosity, focussing on the amount of ambient material entrained into the plume by thermal diffusion. The fraction F_e of the mass flux at a given

height z that consists of entrained material is equal to the fractional decrease of the plume's excess temperature from its base to the height z. Hauri et al. (1994) find that F_e correlates negatively with the buoyancy flux $B \equiv \alpha P/c_p$ of the plume, such that $0.90 \geq F_e \geq 0.05$ for 100 kg s^{-1} $\leq B \leq$ 10000 kg s^{-1}.

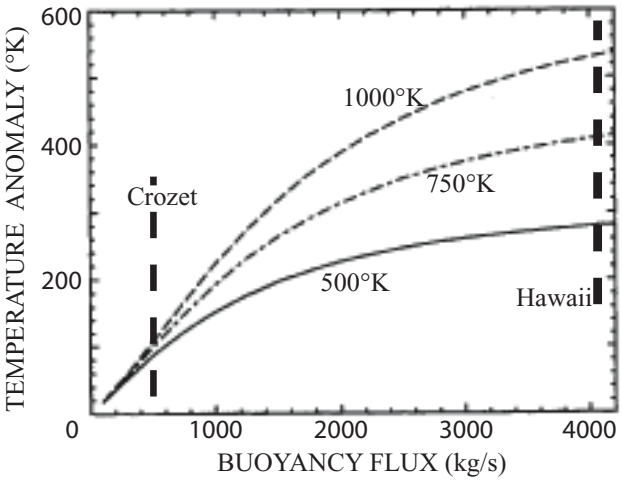

Fig. 5. Temperature anomaly beneath the lithosphere for a steady plume rising from the core-mantle boundary as a function of its buoyancy flux, for three values of the initial temperature anomaly at the boundary. Heavy dashed lines show estimated buoyancy fluxes for Crozet and Hawaii (adapted from Albers and Christensen 1996). Copyright 1996 by the American Geophysical Union. Reproduced by permission of the American Geophysical Union.

Albers and Christensen (1996) studied numerically a steady plume rising from a heat source in a mantle with realistic temperature-, pressure-, and stress-dependent viscosity, phase transitions, and compressibility, focussing on the conditions required for plumes to preserve sufficient excess temperature to melt beneath the lithosphere. They found that plume temperature in the upper mantle is mainly controlled by the buoyancy flux (Fig. 5). Plumes with $B < 1000$ kg s^{-1} (e.g., Crozet) would cool too much to melt beneath old lithosphere, and thus are unlikely to have come from the core-mantle boundary (CMB). On the other hand, plumes with fluxes comparable to the Hawaiian plume and arising from a thermal boundary layer at the CMB with a temperature jump $\approx$ 1000 K (Williams 1998) preserve sublithospheric temperature anomalies $\approx$ 500 K (Fig. 5), much greater than observed. This could indicate that the D'' layer at the CMB is compositionally stratified, which would prevent plumes from carrying the entire temperature anomaly (Farnetani 1997).

Thermals

If the source of buoyancy feeding a nascent plume head is suddenly turned off, the head will rise as an isolated "thermal" without a trailing conduit. Laboratory experiments (Griffiths 1986a) show that a thermal initally rises at constant speed through a distance comparable to its diameter, and then slows down while increasing in volume. The enlargement occurs because diffusion of heat warms a thin boundary layer of ambient fluid around the thermal, which then is advected back to the thermal's trailing edge and entrained. The total buoyancy of the thermal is therefore constant, and is proportional to the Rayleigh number $Ra = \alpha g \Delta T_0 V_0 / \kappa \nu_m$, where V_0 is the thermal's initial volume and ΔT_0 its initial temperature excess. The thermal's volume V and velocity W now have the self-similar forms (Griffiths 1986a)

$$V = \frac{\pi C_1^3}{6} Ra^{3/4} (\kappa t)^{3/2}, \qquad W = \frac{f}{2\pi C_1} Ra^{3/4} (\kappa t)^{-1/2}, \tag{10}$$

where f is defined by (1) and $C_1 \approx 1.0$ is a constant determined experimentally (Griffiths 1986a). Laboratory experiments using viscous oils (Griffiths 1986a) and corn syrup (Coulliette and Loper 1995) are consistent with (10). More qualitative laboratory experiments on thermals with variable amounts of compositional buoyancy were carried out by Griffiths (1986b).

Thermal starting plumes

A thermal starting plume is essentially an ascending thermal connected by a stem to a source of buoyancy. Accordingly, the plume head can grow in two ways: by the entrainment mechanism described in the previous subsection, and by supply of plume fluid through the stem. Unfortunately, no reliable scaling laws have yet been found to describe the evolution of the size and speed of the plume head in this case, and different studies of the problem are in conflict.

Griffiths and Campbell (1990) investigated experimentally the dynamics of starting thermal plumes by injecting hot glucose syrup with a temperature excess ΔT_0 into a cooler reservoir of the same fluid at a constant volumetric rate Q. The viscosity of the fluid depended strongly on temperature; let its value in the cooler reservoir be ν_m. Griffiths and Campbell (1990) proposed that the volume V of the plume head increases both by supply of injected hot fluid and by entrainment of cooler ambient fluid according to

$$\frac{dV}{dt} = Q + C_2 [\kappa g \alpha \Delta T_0 Q t / \nu_m]^{1/2} V^{1/3}, \tag{11}$$

where C_2 is an empirical entrainment constant. The cooling of the stem and the flux needed to lengthen it are implicitly neglected in (11).

The two terms on the right-hand side of (11) are comparable for times $t \approx (C_2^2 \nu_m / \kappa g \alpha \Delta T_0)^{3/5} Q^{1/5} \equiv \tau$. For small times $t \ll \tau$, entrainment is

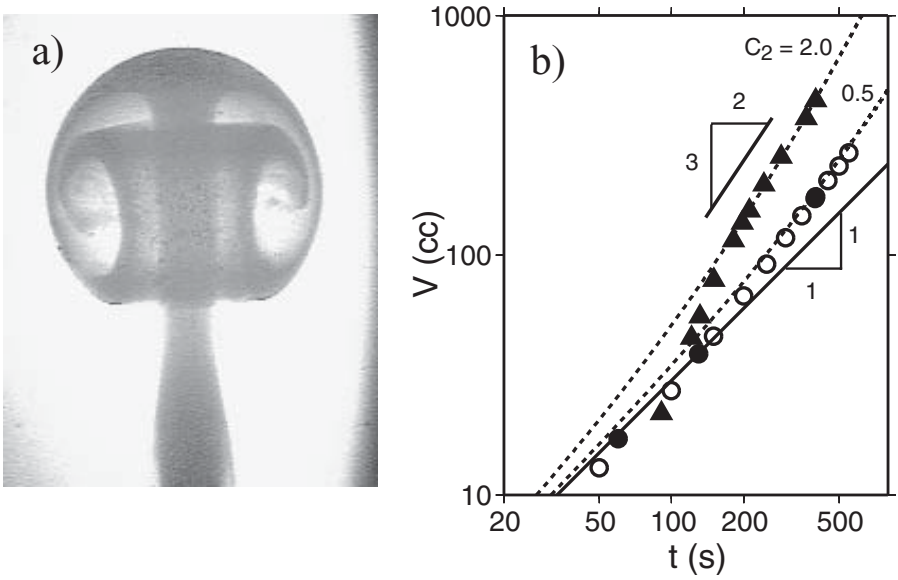

Fig. 6. (a) Starting thermal plume (photograph courtesy of N. Laudenbach). (b) Comparison of volumes of thermal starting plume heads measured experimentally by Griffiths and Campbell (1990) as functions of time with numerical predictions by Van Keken (1997). Filled circles: volumes for the experiment of figure 1 in Griffiths and Campbell (1990), as estimated by Van Keken (1997). Filled triangles: volumes for the experiment of figure 2 in Griffiths and Campbell (1990). Dashed lines: numerical solutions of (11) for $C_2 = 0.5$ and 2.0. Open circles: predictions of a full numerical simulation by Van Keken (1997). Solid line: $V = Qt$.

negligible, and $V = Qt$ as for a purely chemical plume. For large times $t \gg \tau$, the second (entrainment) term in (11) is dominant, implying

$$V = \left(\frac{4C_2}{9}\right)^{3/2} \beta \kappa^{3/4} t^{9/4}, \tag{12}$$

where $\beta = (g\alpha\Delta T_0 Q/\nu_m)^{3/4}$. The corresponding velocity of the head, calculated from Stokes' law for a relatively inviscid drop, is

$$W = \frac{1}{8}\left(\frac{6}{\pi}\right)^{2/3} C_2^{-1/2} \beta (\kappa t)^{1/4}, \tag{13}$$

On the basis of experiments with thermals, Griffiths and Campbell (1990) state that $1 \leq C_2 \leq 4$. Van Keken (1997) solved (11) numerically for different values of C_2 and compared the results with two experiments reported by Griffiths and Campbell (1990) in their figs. 1 and 2 (henceforth experiments E1 and E2). Van Keken's numerical solutions of (11) are indicated by dashed

lines in Fig. 6b, and the volumes observed experimentally by solid symbols. Experiment E1 agrees well with the numerical solution for $C_2 = 0.5$, while E2 is best fit by $C_2 = 2.0$ (although the agreement is poor for $t < 150$ s). Because experiments E1 and E2 were performed with the same nominal values of ΔT_0, Q, and ν_m, the differences between the observed volumes for $t > 120$ s may indicate a lack of reproducibility. Van Keken (1997) also performed a complete numerical simulation of the experiments, obtaining values of $V(t)$ (Fig. 6b, open circles) in excellent agreement with those observed in experiment E1. Neither the experiments nor the numerical simulation displays the asymptotic behavior $V \sim t^{9/4}$ predicted by (12), probably because the total time elapsed did not greatly exceed τ ($\tau = 70$-400 s for $0.5 \leq C_2 \leq 2.0$). For $t > 150$ s, the results of experiment E2 are better described by the law $V \sim t^{3/2}$ (10) for an isolated thermal (Fig. 6b).

Experiments on plumes produced by localized heating without fluid injection (Moses et al. 1993; Coulliette and Loper 1995; Kaminski and Jaupart 2003) show a different behavior: the head velocity increases rapidly for a short time and then attains a nearly constant value W_{term}. Fig. 7 shows isotherms (a-c) and profiles of vertical velocity on the axis (d) at different times for a thermal starting plume above a heater in a fluid with temperature-dependent viscosity. The lower portion (stem) of the plume quickly reaches a steady state, as shown by the similarity of the isotherms and velocity profiles for $t = 120$ s and 300 s in the height range 20 mm $\leq z \leq$ 70 mm. Along the axis, both the temperature and the vertical velocity decrease strongly with height, in qualitative agreement with the analytical solutions (9).

To explain the constancy of W_{term}, Coulliette and Loper (1995) proposed a modified version of Griffiths and Campbell (1990)'s model that accounted for incomplete entrainment of the hot thermal boundary layer surrounding the head. However, the resulting theory involves empirical constants whose values vary by factors of 2-5 among experiments. A possible cause of the difficulty may be the theory's neglect of the flux required to build the lengthening stem, which is important for compositional plumes (Whitehead and Luther 1975; Olson and Singer 1985).

Plumes generated by localized heat sources have also been studied in more complex and 'earthlike' configurations. Kellogg and King (1997) studied numerically the evolution of plumes in a spherical annulus of fluid with temperature-dependent viscosity. They found that the plume morphology depends strongly on the total viscosity contrast $\gamma \equiv \nu_m/\nu_p$, changing from 'diapiric' for $\gamma = 1$ to 'cavity' for $\gamma = 1000$, consistent with earlier results for compositionally buoyant plumes (Olson and Singer 1985; Fig. 1). Kerr and Mériaux (2004) carried out a comprehensive laboratory study of thermal plumes ascending in a shear flow in a fluid with temperature-dependent viscosity. Plumes initially rise with a constant velocity that is independent of the centerline viscosity ν_p. Subsequently, the ambient shear tilts the plume conduits, and in some cases significant cross-stream circulation and entrainment

into them is observed. However, the tilted conduits never develop gravitational instabilities of the kind observed on tilted compositional conduits (Fig. 2).

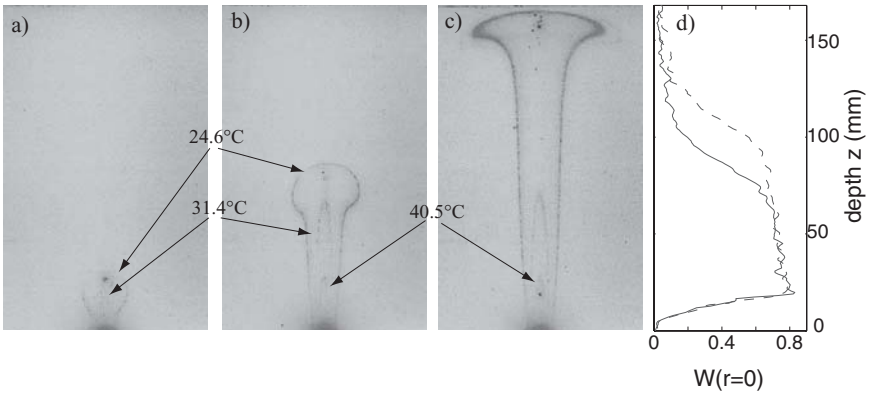

Fig. 7. Thermal starting plume above a heater ($P = 3$ W) in a sugar syrup with temperature-dependent viscosity, from Vatteville (2004). Viscosity varies by a factor of 20 between the heater (54° C) and the fluid far from the plume (20° C). (a)-(c): isotherms for the temperatures indicated, visualized using liquid crystals, at times $t = 60$ s (a), 120 s (b), and 300 s (c). (d): vertical velocity along the plume axis $r = 0$ as a function of height for $t = 120$ s (solid line) and 300 s (dashed line), measured using particle-image velocimetry (PIV).

2.3 Concluding remarks

The phenomenon of plumes from point sources of buoyancy comprises a large number of distinct cases: compositional vs. thermal buoyancy; steady vs. "one-shot" injection of buoyancy; injection of buoyancy with or without injection of mass; constant vs. variable viscosity. Faced with so many possibilities, investigators have naturally focussed on particular limiting or "intermediate asymptotic" (Barenblatt 1996) regimes for which simple power-law scalings can be found. Such laws typically express a balance between two dominant mechanisms (fluid supply and entrainment, advection and diffusion, etc.), and therefore provide valuable understanding of the essential physics. But their simplicity comes at the price of a limited range of validity, and makes it difficult to see how different laws are related to one another. What is needed are complete scaling laws that describe not only the intermediate asymptotic regimes, but also the transitions between them. Such laws are necessarily more complicated than simple power laws, and their determination requires a correspondingly greater numerical and/or experimental effort. Currently, no such laws exist even for relatively simple phenomena like isothermal, chemically

buoyant starting plumes with arbitrary viscosity contrasts, to say nothing of more complex cases such as unsteady thermal plumes. Complete scaling laws for phenomena like these would represent significant contributions to geophysics and to fluid mechanics generally.

3 Plumes as boundary layer instabilities

While plumes from point heat sources are conceptually useful, they are unlikely to represent fully the behavior of mantle plumes, which arise from instabilities of hot thermal boundary layers ('TBLs'). Earth's mantle is home to at least one TBL, the D'' layer at the core-mantle boundary, across which the temperature difference is at least 1000 K (Williams 1998). We begin by discussing the necessary conditions for plume formation in convecting fluids. We then consider one of the most commonly studied models for this process, that of plumes arising from the TBL that forms when an isothermal fluid layer is heated impulsively from below. Finally, we investigate the dynamics of plumes in fully developed convection, with a focus on certain crucial differences from the impulsive heating model.

3.1 Necessary conditions for plume formation

Hot thermal plumes are commonly observed in a layer of viscous fluid heated, even partially, from below (e.g. Sparrow et al. 1970; Krishnamurti 1970). The intensity of convection in a layer with thickness H, thermal expansion coefficient α, viscosity ν, and thermal diffusivity κ is determined by the global Rayleigh number

$$Ra = \frac{\alpha g \Delta T H^3}{\kappa \nu} \tag{14}$$

where ΔT is the temperature difference across the layer. Convection occurs when Ra exceeds a threshold $Ra_c \approx 1000$, the exact value of which depends on the boundary conditions (e.g. Chandrasekhar 1981). For isothermal and rigid boundaries, a regime diagram has been determined experimentally (Krishnamurti 1970; Weeraratne and Manga 1998). Just above Ra_c, the convective pattern is stationary, first as 2D rolls, then as 3D cells (e.g. hexagons). Around $Ra = 10^5$, the cell geometry becomes time-dependent. Above $Ra = 10^6$, well-defined cells no longer exist, and heat is transported by plumes that form as instabilities of the upper cold and lower hot thermal boundary layers. Fig. 8 shows the convective regime of a fluid layer as a function of its thickness and viscosity. Plumes can develop in an upper mantle of thickness 660 km only if its viscosity is lower than 10^{21} Pa s. For an average mantle viscosity of 10^{22} Pa s, plumes will be generated only if the layer thickness exceeds 2000 km. Convective motions originating at the CMB and extending across the whole mantle should therefore take the form of plumes.

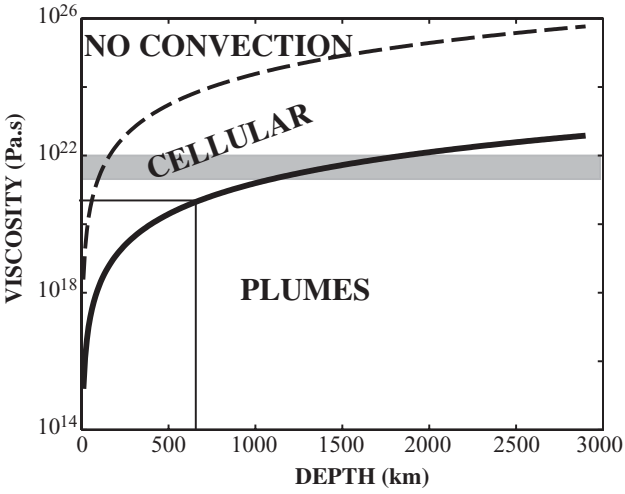

Fig. 8. Convective regime of a uniform fluid layer heated from below as a function of its thickness and viscosity. The grey bar shows the average viscosity of the whole mantle (e.g. Ricard et al. 1989), and the box at lower left delimits the conditions of the upper mantle. The calculation assumes $\kappa = 10^{-6}$ m^2 s^{-1}, $\alpha = 2 \times 10^{-5}$ K^{-1}, and $\Delta T = 3000$ K.

3.2 Starting thermal plumes due to impulsive bottom heating

In the most commonly studied configuration, an initially isothermal fluid layer is suddenly heated at time $t = 0$ by increasing the temperature of its lower boundary by an amount ΔT. Initially, the temperature in the TBL evolves by pure conduction following the standard "error function" profile $T = \Delta T \mathrm{erfc}(z/\delta)$, where $\delta = 2(\kappa t)^{1/2}$ is the thickness of the TBL and κ is the thermal diffusivity. In a fluid of constant viscosity ν, the stability of the TBL is controlled by the (time-varying) local Rayleigh number $Ra_{TBL} = g\alpha\Delta T\delta^3/\kappa\nu$, where g is the gravitational acceleration and α is the coefficient of thermal expansion. The TBL becomes unstable to small perturbations (incipient plumes) when Ra_{TBL} exceeds a critical value ≈ 1000 (Howard 1964).

Fig. 9 shows a laboratory experiment illustrating the evolution of convective instabilities in a fluid layer heated suddenly from below (Davaille and Vatteville 2005). The fluid's viscosity is temperature-dependent and varies by a factor of 15 across the TBL, but this variation is not sufficient to change the dynamics substantially relative to the constant-viscosity case. Initially, the TBL formed at the hot boundary grows by diffusion (Fig. 9a). When the local Rayleigh number Ra_{TBL} reaches the critical value, the TBL becomes unstable (Fig. 9b) and breaks up (Fig. 9c) to produce plumes (Fig. 9c-e). When a plume reaches the top boundary, it "ponds" there and spreads laterally (Fig.

9e). Once the hot TBL has been emptied, the plume stem begins to disappear from the bottom up (Fig. 9e), leaving only the cooling and shrinking sublithospheric pond. This last feature implies, for example, that the absence of a plume conduit in a tomographic image need not indicate the absence of a plume.

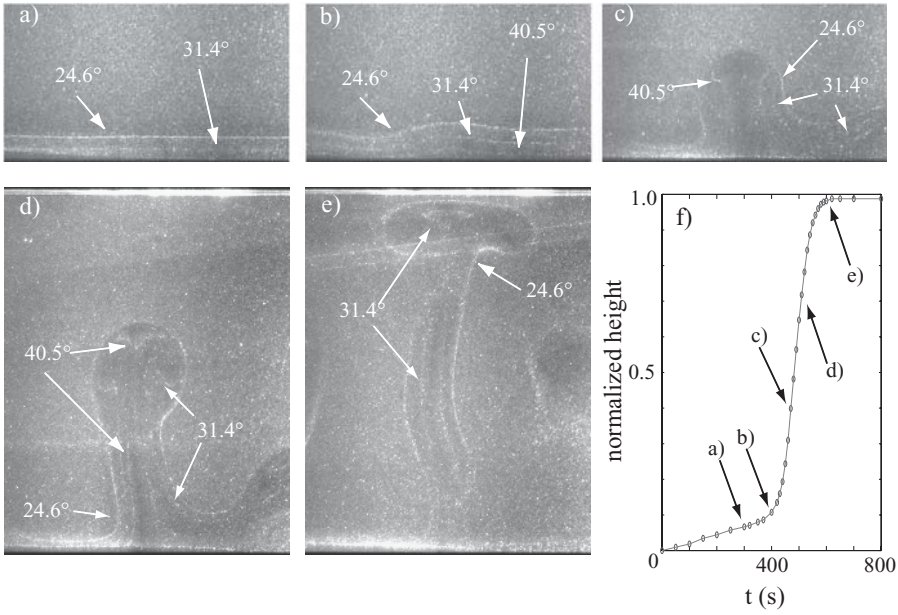

Fig. 9. Evolution of boundary layer instabilities in a layer of sugar syrup initially at temperature 21° C and suddenly heated from below to 53° C. Isotherms 24.6° C, 31.4° C, and 40.5° C, visualized using liquid crystals, are shown at times $t = 300$ s (a), 400 s (b), 460 s (c), 500 s (d), and 600 s (e). Continuous cooling of the plume from (c) to (e) is indicated by the progressive disappearance of the 40.5° C isotherm. Panel (f) shows the height (in units of the tank depth) of the 24.6° C isotherm as a function of time. Modified from Davaille and Vatteville (2005).

The dynamics of plume generation is more complex when the viscosity contrast γ across the TBL exceeds roughly 10^3. Two distinct stages can now be identified. Instability occurs initially as small-scale cellular convection confined to the low-viscosity "sublayer" of thickness $\delta_{sub} \equiv \delta / \ln \gamma$ near the hot surface $z = 0$ (Yuen and Peltier 1980; Loper and Eltayeb 1986; Thompson and Tackley 1998; Solomatov and Moresi 2002). In the second stage, the cells in the sublayer merge to form large incipient plumes which then ascend rapidly and drain the TBL (Christensen 1984; Olson et al. 1987; Thompson and Tackley 1998; Ke and Solomatov 2004). Ke and Solomatov (2004) showed that the growth rate of this second stage is independent of the sublayer viscosity and

depends only on the viscosity of the fluid above the TBL, as predicted by the theory of the Rayleigh-Taylor (gravitational) instability of a thin fluid layer beneath a half-space of fluid with a much higher viscosity (Whitehead and Luther 1975; Canright and Morris 1993).

The morphology of plumes generated by impulsive heating resembles qualitatively that of plumes from point sources of buoyancy, with a similar dependence on the total viscosity contrast γ. In the experiments of Fig. 9 with $\gamma = 15$, the plumes are close to the 'diapiric' limit and have poorly defined heads. In numerical simulations with $\gamma = 1300$, by contrast, Van Keken (1997) observed plumes with pronounced 'cavity' morphology and a strong 'scroll' structure within the head, similar to Fig. 6a. Non-Newtonian rheology generated even more complicated structures, such as detachment of the primary plume head and formation of a second one that ascends behind it (Van Keken 1997).

Farnetani and Richards (1995) used a numerical model of a plume issuing from a TBL to shed light on the controversial question of entrainment of ambient material into mantle plumes. Campbell and Griffiths (1990), reasoning from the large degrees of entrainment observed in thermal starting plumes (Fig. 6a), had earlier suggested that the geochemistry of flood basalts should reflect significant mixing of plume and ambient mantle material. This conclusion was contested by Farnetani and Richards (1995), who studied a more realistic model in which a plume arises from a TBL at the base of a mantle layer with temperature-dependent viscosity and phase transitions. Farnetani and Richards (1995) used a melting model to calculate representative isotopic and trace element ratios in melts extracted from the plume head. They found that the contribution of the entrained material was always small ($< 10\,\%$), and attributed this result to three principal causes: (1) entrained material is too cold to experience significant melting; (2) smooth variations of temperature inherited from the TBL decrease the entrainment rate; and (3) the mantle's finite depth does not allow a plume to ascend far enough for entrainment to become significant. Farnetani and Richards (1995) concluded that geochemical heterogeneity in flood basalts is either inherited from the TBL or due to lithospheric contamination. A similar conclusion was reached by Farnetani et al. (2002) using an extended version of the same model incorporating a chemically dense layer at the bottom of the TBL.

3.3 Plumes in fully developed convection

Plume generation in fully developed convection is a cyclic process in which the TBLs grow by thermal diffusion, become unstable, and then empty themselves rapidly into plumes, at which point the cycle begins again. The characteristic time scale τ_c for this process is the time required for the growing TBL to become unstable, and is (Howard 1964)

$$\tau_c = \frac{H^2}{\pi\kappa}\left(\frac{Ra_c}{Ra}\right)^{2/3}. \quad (15)$$

Because $Ra \sim H^3$ (14), τ_c is independent of the layer depth H. The scaling (15) is confirmed by laboratory experiments (e.g. Sparrow et al. 1970; Davaille and Jaupart 1993; Davaille 1999a; Manga et al. 2001). For the mantle, $\tau_c \approx 10$ Myr, 40 Myr and 200 Myr for dynamic viscosities $\mu_m = 10^{19}$ Pa s, 5×10^{20} Pa s, and 10^{22} Pa s, respectively. Such recurrence times are probably also upper bounds on plume lifetime (Davaille and Vatteville 2005). The corresponding values of the critical TBL thickness $\delta_c \equiv H(Ra_c/Ra)^{1/3}$ for the same viscosities are 31 km, 62 km and 140 km, respectively. Experiments show that the typical spacing between plumes is 3-6 δ_c (e.g. Sparrow et al. 1970; Tamai and Asaeda 1984; Asaeda and Watanabe 1989; Lemery et al. 2000; Davaille et al. 2002), which implies a plume spacing 100-840 km in the mantle. Detailed morphological studies show that the plumes are connected by a network of 'ridges' near the base of the layer (e.g. Houseman 1990; Christensen and Harder 1991; Tackley 1998; Trompert and Hansen 1998; Parmentier and Sotin 2000).

Once plumes are formed, they must be able to reach the surface to produce a hotspot. In classical Rayleigh-Bénard convection in a constant-viscosity fluid heated from below and cooled from above, hot (cold) plumes generally lose their identities before reaching the upper (lower) surface (Fig. 10a). There are two reasons for this. The first is that the rising hot (sinking cold) plumes tend to be disrupted by the sinking cold (rising hot) plumes they encounter. The disruption of hot plumes is enhanced by a dependence of viscosity on temperature, which makes hot plumes mechanically weaker than cold ones (Schaeffer and Manga 2001), and by internal heating, which decreases the strength of hot upwelllings relative to cold downwellings (Labrosse 2002). Second, plumes begin to interact after rising a distance comparable to their spacing, leading them to cluster or even to merge (Moses et al. 1993; Manga 1997; Xi et al. 2004). This can generate a large scale circulation with a wavelength comparable to the layer depth (e.g. Xi et al. 2004) that will also characterize the spacing of clusters of hot plumes that reach the top boundary.

In short, plumes in convecting homogeneous fluids are highly transient features, with little resemblance to the classical 'cavity plume' model (Fig. 1b). We thus have an apparent paradox: cavity plumes are favored by high viscosity contrasts ν_m/ν_p, yet are not observed in fully developed convection in fluids with strongly temperature-dependent viscosity (Nataf 1991). The resolution of this paradox is that most of the temperature drop in such a system occurs across a stagnant high-viscosity 'lid' at the top of the layer, leaving only a small temperature drop across the bottom TBL $\Delta T_{TBL} \approx 1.1\Delta T_{rheol}$ (Solomatov and Moresi 2000; Manga et al. 2001), where

$$\Delta T_{rheol} = \nu(T)\left[\frac{\partial\nu}{\partial T}(T)\right]^{-1} \quad (16)$$

is the rheological temperature scale (roughly the temperature change required to change the viscosity by a factor e). In the lowermost mantle, $\Delta T_{rheol} \approx 50 - 250$ K (Solomatov and Moresi 2002). Moreover, because the temperature anomaly carried by plumes rising from such a TBL is only about $0.6\Delta T_{TBL} \leq 150$ K (e.g. Farnetani 1997), the viscosity contrast between the plume and its surroundings will be even smaller than that across the TBL. Such small temperature and viscosity contrasts may be adequate to explain colder hotspots (e.g., Azores), but not ones as hot as Hawaii or ones that produce flood basalts.

In summary, the generation of cavity plumes in a fluid with temperature-dependent viscosity requires much larger temperature and viscosity contrasts across the lower TBL than typically exist under statistically steady-state conditions. Such large contrasts can be produced in a transient fashion by intense impulsive heating from below, which will produce large plumes with temperature anomalies $\approx 600 - 1000$ K. However, subsequent generations of instabilities from the TBL will be much smaller because the increasing average temperature of the fluid layer causes the viscosity contrast across the TBL to decrease as statistical steadiness is approached (e.g. Hansen and Yuen 2000). The inferred occurrence of large plume heads over the greater part of earth history therefore requires a more permanent mechanism to keep the temperature difference across the TBL large. Possibilities include an endothermic phase transition (Harder and Christensen 1996; Weinstein 1995) or a strong pressure-dependence of viscosity (Christensen 1985) just above the CMB, but there is no clear evidence for either (the recently discovered post-perovskite phase transition is apparently exothermic; Oganov and Ono 2004; Murakami et al. 2004). Another possibility is the influence of mobile tectonic plates and subduction, which rapidly transports cold material from the top of the layer to the bottom, thereby increasing ΔT_{TBL} (Lenardic and Kaula 1994; Jellinek et al. 2002). Yet a third possibility is the influence of chemical heterogeneity in the lowermost mantle, to which we now turn.

3.4 Thermochemical plumes

At least three things are necessary to explain the observed characteristics of hotspots: a large stable temperature difference across D''; generation of large plume heads with temperature anomalies not exceeding 500 K; and a way to "anchor" plume stems to generate long-lived volcanic tracks. One factor that can create all these conditions is compositional heterogeneity in the lowermost mantle. Such heterogeneity might be due to slab remnants (e.g. Olson and Kincaid 1991; Christensen and Hofmann 1994), delaminated continental material, relics of a primitive mantle (Gurnis and Davies 1986; Tackley 1998; Kellogg et al. 1999) enriched e.g. in iron (Javoy 1999), or chemical reactions with or infiltration from the core (e.g. Hansen and Yuen 1988). The potential importance of such heterogeneity has led many authors to study "thermochemical" convection in fluids whose density depends both on temperature

and composition. The following discussion focusses only on the morphology and dynamics of upwellings; for a review of thermochemical convection in general, see Davaille et al. (2003).

The most commonly studied situation comprises two superposed fluid layers of different composition, density, and viscosity. Let H_1 and H_2 denote the depths of the lower and upper layers, respectively, and ν_1 and $\nu_2 \equiv \gamma\nu_1$ the corresponding viscosities. In cases where the viscosity depends on temperature, ν_1 and ν_2 are taken to be the values at the mean temperature of the layer in question. Finally, the "Rayleigh number" Ra for the system is defined using (14) with $H = H_1 + H_2$, $\nu = \max(\nu_1, \nu_2)$, and ΔT equal to the total temperature difference across both layers.

The dynamics of a two-layer system are controlled by the interaction of compositional and thermal buoyancy, as measured by the ratio $B = \Delta\rho_X/\rho\alpha\Delta T$ of the stabilizing chemical density anomaly $\Delta\rho_X$ to the destabilizing thermal density anomaly $\rho\alpha\Delta T$ ("buoyancy ratio"; Olson 1984; Davaille 1999b), where α is the value of the thermal expansivity at the interface. For $B < 0.03$, chemical density heterogeneities are negligible and the system behaves as a single homogeneous fluid. For larger values of B and $Ra > 10^5$, two scales of convection coexist: compositionally homogeneous thermal plumes generated at the outer boundaries, and large-scale thermochemical instabilities that involve both fluids. The different regimes observed in laboratory experiments and numerical simulations are shown in Fig. 10 and described in more detail below.

Whole-layer regime and unstable doming

When B is less than a critical value $B_c \approx 0.4$ (the exact value depends weakly on the viscosity and depth ratios; Le Bars and Davaille 2002), the stable compositional stratification can be overcome by thermal buoyancy. The interface between the layers then becomes unstable, and convection occurs over the whole depth. An important characteristic of the interfacial instability is the "spouting" direction (Whitehead and Luther 1975), defined as the direction (up or down) in which finite-amplitude perturbations grow superexponentially to form dome-like structures (Fig. 10d, e). The theory of the Rayleigh-Taylor instability shows that spouting occurs in the direction of the layer with the lower "resistance" ν_i/H_i^3 (Ribe 1998). Thus the lower layer will spout into the upper one only if

$$H_1 < \frac{H_1 + H_2}{1 + \gamma^{1/3}}; \tag{17}$$

otherwise, spouting is downward (Le Bars and Davaille 2004a). Condition (17) implies, for example, that a less viscous layer will spout into a more viscous overlying mantle only if the former is much thinner.

As for the case of purely compositional plumes (Fig. 1), the morphology of thermochemical instabilities depends on the viscosity ratio $\nu_2/\nu_1 \equiv \gamma$. Suppose for definiteness that (17) is satisfied, so that spouting is upward. Then

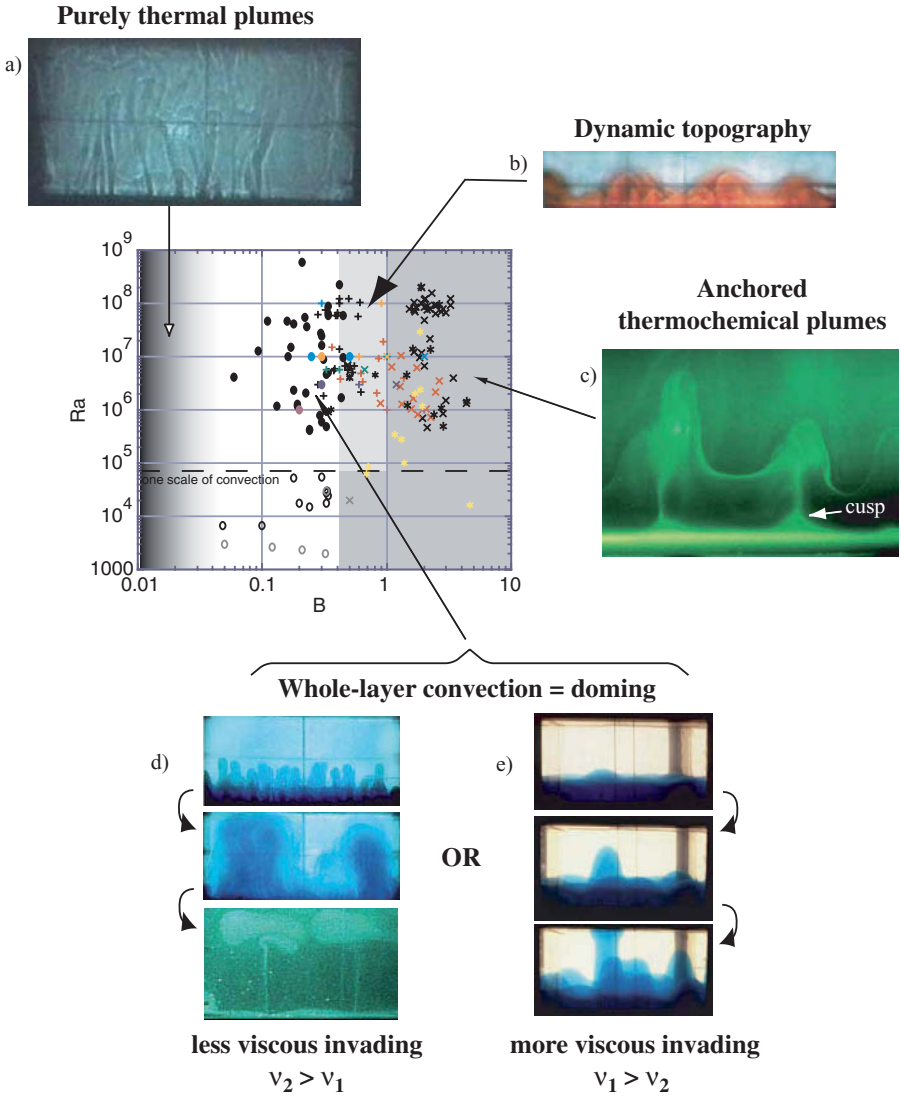

Fig. 10. Regimes of thermochemical convection as a function of Rayleigh number and buoyancy number. Black circles: whole-layer convection (open circles for experiments close to marginal stability). +: stratified convection and anchored plumes with a deformed interface (light shaded area). x: stratified convection with a flat interface (dark shaded area). ⋆: stratified convection with a non-convecting thinner layer. Laboratory experiments are shown in red (Richter and McKenzie 1981), dark blue (Olson and Kincaid 1991); yellow (Jellinek and Manga 2004) and black (Davaille 1999a,b; Davaille et al. 2002; Le Bars and Davaille 2002, 2004a). Numerical calculations are shown in grey (Schmeling 1988), light blue (Tackley 1998, 2002), brown (Kellogg et al. 1999; Montague and Kellogg 2000), purple (Hansen and Yuen 2000), green (Samuel and Farnetani 2003) and pink (McNamara and Zhong 2004a).

when the lower layer is more viscous ($\gamma < 1$), large cylindrical diapirs form (Fig. 10e), and secondary plumes can develop above them in the upper layer (Davaille 1999b). When $\gamma > 1$, by contrast, purely thermal instabilities first develop within the lower layer, and then merge to form large cavity plume heads (Fig. 10d). In both cases, if the lower layer is thin, the plumes empty it before they reach the upper boundary, and become disconnected from the lower boundary as in the purely thermal case (Fig. 9e). If the layer is thicker and/or $0.2 < B < B_c$, the plumes reach the upper boundary before disconnecting from the lower (Fig. 10e). They then begin to cool and lose their thermal buoyancy, and eventually collapse back to the bottom, whereupon the cycle begins again. When $\gamma > 5$ or $\gamma < 0.2$, each layer retains its identity over several pulsations. Since thermal buoyancy must overcome the stable compositional stratification before driving convection, the temperature anomaly θ carried by thermochemical instabilities is the slave of the compositional field (Le Bars and Davaille, 2004a) and is

$$\theta = (0.98 \pm 0.12)\frac{\Delta\rho_X}{\alpha\rho} \tag{18}$$

Le Bars and Davaille (2004a,b) give more details on the complexities of the whole layer regime.

According to (18), thermochemical instabilities with temperature anomalies 300-500 K can be produced at the base of the mantle by compositional density heterogeneities of 0.3-0.6%. If viscosity depends only on temperature, the plumes are then 10-3000 times less viscous than the bulk mantle (e.g. Solomatov and Moresi 2002), and should therefore have the form of cavity plumes. According to (17), the thickness of the dense less viscous layer from which they come must be less than 200-700 km. The diameter, wavelength and velocity of the plumes are mainly controlled by the more viscous upper layer since it retards motion over the whole depth (e.g. Whitehead and Luther 1975; Olson and Singer 1985; Herrick and Parmentier 1994). The scaling laws of Le Bars and Davaille (2004a,b) predict velocities ≈ 5 cm/yr, radius $\approx$ 500-1000 km, and spacing $\approx$ 2000-3500 km for cavity plumes at the base of the mantle.

Stratified regime: anchored hotspots, bumps and piles

For $B > B_c$, thermal buoyancy cannot overcome the stable compositional stratification. Convection remains stratified, and a TBL forms at the interface from which long-lived thermochemical plumes are generated (Fig. 10c). These plumes do not have a well-defined head, and the thermal anomaly they carry is weak, proportional to the temperature difference across the unstable part of the TBL above the interface (Christensen 1984; Farnetani 1997; Tackley 1998). These plumes entrain a thin filament (at most 5% of the total plume volume) of the denser bottom layer by viscous coupling and locally deform

the interface into cusps (Fig. 10c, Davaille 1999b). The interfacial topography serves in turn to anchor the plumes (Namiki and Kurita 1999; Davaille 1999a,b; Davaille et al. 2002; Jellinek and Manga 2002, 2004), which persist until the chemical stratification disappears through entrainment. Scaling laws based on laboratory experiments (Davaille et al. 2002; Gonnermann et al. 2002) suggest that plumes anchored in D'' could develop for $\Delta\rho_X > 0.6\%$, and that they could survive hundreds of millions of years, depending on the spatial extent and magnitude of the anchoring chemical heterogeneity. Such plumes could therefore produce much longer-lived hotspots than the transient plumes observed experimentally in isochemical convection (Fig. 9). However, plume longevity does not necessarily imply spatial fixity: plumes and their anchors can be advected by large-scale flow associated with strong downwellings such as subducting plates (Tan et al. 2002; Davaille et al. 2002; McNamara and Zhong 2004b).

When $B_c < B < 1$, thermal buoyancy is sufficient to maintain local thermochemical "bumps" on the interface (Fig. 10b), whose maximum height increases with increasing Ra and decreasing B (Le Bars and Davaille 2004a; McNamara and Zhong 2004a). If the lower layer is thin enough, it can break up and form stable "piles" (Tackley 1998, 2002).

More complicated morphologies can also arise. A "failed dome" occurs when most of the thermochemical dome falls back down, while the material of the upper layer, heated by thermal coupling, continues to rise and entrains a small amount of the lower denser layer (Fig. 11a; Kurita and Kumagai, personal communication 2004). Interaction of a thermochemical plume with a phase transition at 660 km depth also gives rise to complex dynamics (Farnetani and Samuel 2005), including ponding beneath the phase transition (Fig. 11b, panel e) and the penetration into the upper mantle of narrow filaments with temperature anomalies $\approx 100 - 150°$ C that could feed long-lived surface volcanism (Fig. 11b, panel f).

4 Interaction of plumes with the lithosphere

Because most of what we know about mantle plumes comes from the signatures produced by their interaction with the lithosphere, it is critical to understand the dynamics of this process. Most studies focus on one or the other of the two components (head and tail) of the classical "cavity plume" model. We begin by reviewing previous work on the (inherently time-dependent) dynamics of a starting plume head with a stationary lithosphere. We then turn to models for hotspot swells, which typically consider the interaction of a steady-state plume conduit with a moving lithosphere. Finally, we discuss the still more complicated case of interaction of mantle plumes with ocean ridges.

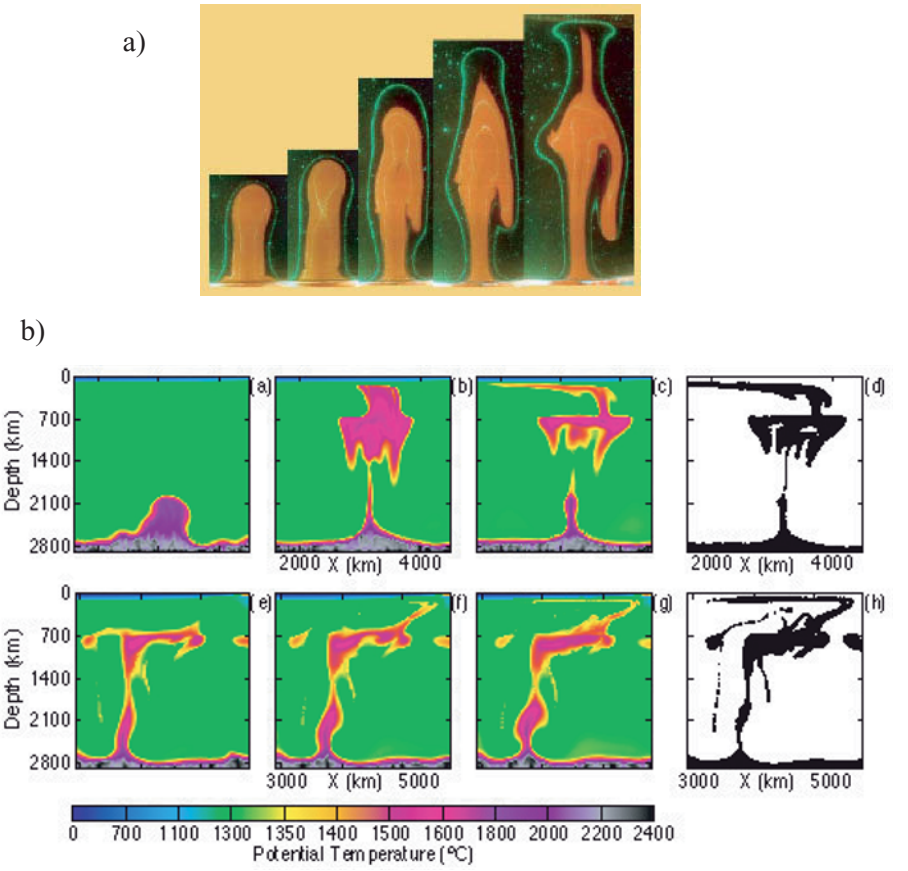

Fig. 11. Possible complex morphologies of thermochemical plumes. a) Laboratory experiment showing a "failed" dome. A thermochemical plume was generated by a flat heater with a constant power. Compositionally denser material (orange) was initially in a thin layer at the bottom of the tank. Green lines are isotherms (courtesy of K. Kurita). b) Numerical simulation of thermochemical plumes interacting with a phase transition at 660 km depth. Panels (d) and (h) show the distribution of active tracers. Modified from Farnetani and Samuel (2005).

4.1 Starting plumes

Olson and Nam (1986) performed laboratory experiments on the deformation of an initially spherical drop of buoyant low-viscosity fluid rising towards a high-viscosity boundary layer at the cooled free surface of a fluid with strongly temperature-dependent viscosity, and measured the amplitude of the surface topography as a function of time. The typical evolution was found to comprise a phase of relatively rapid uplift, followed by slower subsidence that corresponds to stagnation and lateral spreading of the drop below the cold

boundary layer. Griffiths and Campbell (1991) performed simpler experiments under isothermal conditions, and focussed on determining scaling laws for the drop's radius and the thickness of the "squeeze film" above it as functions of time. They also observed that the gravitationally unstable interface between the drop and the squeeze film eventually broke up via a Rayleigh-Taylor instability with a complex lateral planform dominated by short-wavelength ($\ll$ drop radius) upwellings and downwellings. Koch and Koch (1995) analyzed drop spreading below a free surface using a combination of numerical (boundary integral) and analytical methods. They identified three distinct asymptotic forms for the drop radius $R(t)$ as a function of time, depending on whether spreading of the drop is resisted primarily by normal stresses at the rim ($R \sim (t \ln t)^{1/5}$), shear stresses at the bottom ($R \sim t^{1/5}$), or stresses within the drop itself ($R \sim t^{1/2}$). Which of these regimes obtains depends on the relative values of the drop's aspect ratio (radius/thickness) and the viscosity contrast between the drop and its surroundings.

Models of starting plumes have also been constructed using more complex and earthlike rheological laws. Farnetani and Richards (1994) investigated a numerical model of an initially spherical drop rising towards the surface of a fluid whose viscosity depends strongly on pressure and (in some cases) temperature. The model predicts rapid uplift of the surface followed by slower subsidence (cf. Olson and Nam 1986), and melting rates that are consistent with the observed volumes and compositions of flood basalts. Moore et al. (1999) used a 3-D numerical model to study the interaction of an ascending thermal plume that impinges on cold, high-viscosity lithosphere at the surface of a fluid with strongly temperature-dependent viscosity. Small-scale, nonaxisymmetric convective instabilities were observed to occur in the boundary layer when the viscosity contrast between the plume and its surroundings exceeded a factor of about 10, leading to efficient thinning of the lithosphere. This is in contrast to earlier 2-D numerical experiments (Olson et al. 1988; Monnereau et al. 1993) which showed little lithospheric thinning.

Another factor that can influence strongly the sublithospheric distribution of starting plume material is lateral variations in lithospheric thickness. Sleep (1996, 1997, 2002) has pointed out that such thickness variations will cause the base of the lithosphere to act like an "upside-down drainage pattern" that guides the lateral flow of buoyant plume material. Ebinger and Sleep (1998) suggested that this effect can explain how the impact of a single large plume could have produced the complex distribution of Cenozoic volcanism in central/east Africa.

4.2 Models for hotspot swells

Detrick and Crough (1978) seem to have been the first to suggest that the large bathymetric swells associated with hotspots such as Hawaii are produced by thermomechanical interaction of a mantle plume with the lithosphere moving over it. According to this model, the plume heats and thins the lithosphere

above it, forming an inverted "trough" in the base of the lithosphere filled with hotter asthenospheric material. The density contrast between this material and the colder lithosphere to either side generates an Archimedean buoyancy force that supports the swell. The lithospheric thinning model successfully explains the low (0.004-0.005; Monnereau and Cazenave 1988) values of the geoid-topography ratio inferred for hotspot swells, which imply a depth of isostatic compensation within the normal (unthinned) lithosphere. However, the model cannot easily explain the great width ($\approx$ 1000 km) of many swells, or the rapid uplift of the swell in the direction of plate motion at hotspots such as Hawaii. These difficulties, together with the model's fundamentally static character, have led most geodynamicists to prefer an alternative "dynamic support" model in which the swell is maintained by hydrodynamic stresses applied to the base of the lithosphere by the plume. Sleep (1987) and Richards et al. (1988) proposed a kinematic model for this process in which the plume is envisioned as a pipe emptying into a low-viscosity asthenospheric channel of thickness d beneath a lithosphere moving at speed U in the direction x. The (two-dimensional) velocity in the channel was assumed to be the sum of a radial outflow from a vertical line source of strength $q \equiv Q/d$ per unit length and a uniform translation at the average speed $U/2$ of the shear flow induced by the plate motion, or

$$\boldsymbol{u} = \frac{q}{r}\boldsymbol{r} + \frac{U}{2}\boldsymbol{x}, \tag{19}$$

where $\boldsymbol{r}$ is a radial (horizontal) unit vector and r is the radial distance from the line source. Eqn. (19) implies that the plume fluid is separated from the surrounding asthenosphere by a roughly parabolic "stagnation streamline" which intersects the $x-$axis at a "stagnation point" $x = -2q/U$ upstream from the line source.

Olson (1990) proposed a more dynamically realistic model for hotspot swells (Fig. 12a), in which plume material with viscosity ν_p and buoyancy $g\Delta\rho$ is released at a constant volumetric rate Q from a fixed source beneath a plate moving at speed U. The buoyant fluid acts as a gravity current (Huppert 1982), spreading laterally against the base of the lithosphere in response to the lateral pressure gradients generated by the current's variable thickness. Because the current is thin relative to its lateral dimension, the flow within it is described by the equations of lubrication theory, which can be reduced to a single equation governing the layer thickness $S(x, y, t)$ as a function of the lateral coordinates and time. In the simplest version of the model, the spreading of the plume material is assumed to depend only on its own viscosity ν_p, and not on the viscosity ν_m of the ambient mantle; this assumption is valid when ν_m/ν_p does not greatly exceed the ratio of the layer's width to its thickness (Lister and Kerr 1989).

In steady state, the equation satisfied by S is (Olson 1990)

$$U\frac{\partial S}{\partial x} = \sigma\nabla_h^2 S^4 + Q\delta(x)\delta(y). \tag{20}$$

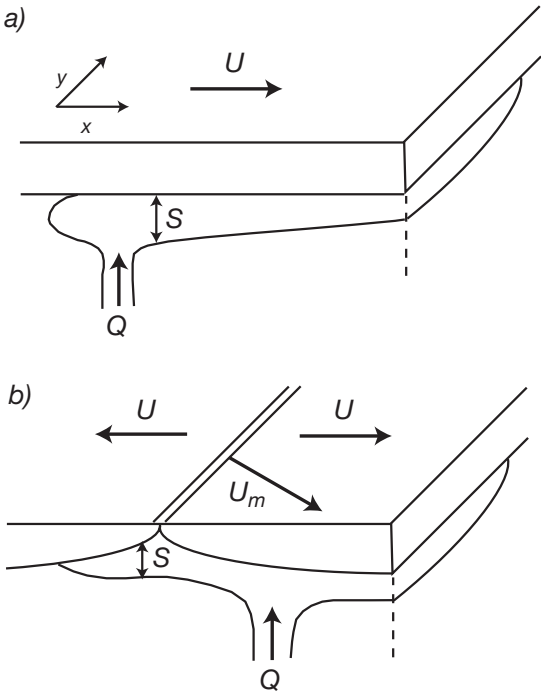

Fig. 12. (a) Thin-layer model for plume-plate interaction. Buoyant plume fluid is released at a volumetric rate Q from a source fixed beneath a plate moving at speed U. The plume fluid is advected downstream by the moving plate as it spreads laterally, forming a layer whose thickness $S(x, y)$ is much less than its lateral dimension. (b) Thin-layer model for plume-ridge interaction. The principle is similar to the plume-plate interaction model (a), except that the plume fluid is released near a mid-ocean ridge with half-spreading rate U that migrates at speed U_m relative to the plume.

where $\sigma = g^\star/48\nu_p$, ∇_h is the horizontal Laplacian operator, and δ is the Dirac function. Eqn. (20) shows that the shape and thickness of the layer is controlled by a balance of three factors: advection by the moving plate (first term), buoyancy-driven spreading at a rate proportional to the "spreadability" σ (second term); and the rate at which fluid is supplied by the plume stem at $(x, y) = (0, 0)$ (third term). A scaling analysis of (20) (Ribe and Christensen 1994) shows that the thickness and lateral extent L of the layer scale as

$$S \sim Q^{1/4}\sigma^{-1/4} \equiv S_0, \qquad L \sim Q^{3/4}\sigma^{1/4}U^{-1} \equiv L_0. \tag{21}$$

An analytical similarity solution of (20) valid far downstream from the plume stem ($x \gg L_0$) shows that the width of the layer is $y \sim L_0(x/L_0)^{1/5}$ (Ribe and Christensen 1994).

While the thin-layer model describes well the basic physics of plume-plate interaction, a more realistic model is required to predict the geophysical signatures of mantle plumes in detail. The most commonly used model (Ribe and Christensen 1994, 1999; Moore et al. 1998; Zhong and Watts 2002; Van Hunen and Zhong 2003) is similar to that shown in Fig. 12a, except that the plume is now generated by a circular temperature anomaly of amplitude ΔT at the bottom (depth ≈ 400 km) of a model box containing fluid whose viscosity depends on temperature and pressure. The cold, highly viscous fluid near the top of the box acts like a stiff "lithosphere" that moves quasi-rigidly. Some versions of the model (e.g. Ribe and Christensen 1999) also include an algorithm to calculate the degree and rate of partial melting in the plume and the distribution of the depleted residual material that results.

Fig. 13 shows the (potential) temperature in horizontal and vertical planes predicted by a numerical solution with parameters appropriate for the Hawaiian plume (Ribe and Christensen 1999). The hot plume fluid spreads beneath the lithosphere to form a thin layer, in accordance with the lubrication theory assumption. However, the dynamics of this layer are now more complex due to the effects of thermal buoyancy and variable viscosity. Moore et al. (1998) documented the existence of three distinct dynamical regimes in the layer, depending on the value of the ratio $\Delta T/\Delta T_{rheol} \equiv \beta$, where ΔT_{rheol} is the rheological temperature scale (16). For $\beta < 2$, the velocity and temperature vary smoothly across the layer. For $2 \leq \beta \leq 3$, the flow remains steady, but long, narrow convective structures aligned with the direction of plate motion appear. One of these is visible at $y \approx 225$ km in Fig. 13a; it corresponds to cold material from the lowermost lithosphere that becomes unstable and sinks into the mantle below. Finally, for $\beta > 3$, the flow in the layer becomes disordered and time-dependent.

The 3D convection model just described is sufficiently realistic that its predictions can be compared directly with geophysical observations. Most such work to date has focussed on Hawaii, the mantle plume with the largest and best-measured geophysical signatures. The model predicts well both the shape of the Hawaiian swell (Fig. 14), including its rapid uplift and subsequent slow subsidence with distance along the island chain. The cause of the rapid uplift is the "pileup" of plume fluid that can spread only a short distance upstream from the hotspot against the oncoming "wind" of the moving plate. The slow downstream subsidence reflects the decreasing thickness of the plume layer as it widens by gravitational spreading.

An important contribution to the topography of the swell is the buoyancy of the depleted residuum produced by partial melting. The magnitude of this effect ($\approx 0.7\%$ for 10% melting; Jordan 1997) led Phipps Morgan et al. (1995) to propose that the Hawaiian swell is compensated primarily by depletion buoyancy, rather than by thermal buoyancy. However, 3D convection models that include both types of buoyancy (Ribe and Christensen 1999) suggest that depletion buoyancy accounts for only about one-third of the swell topography, the rest being supported by thermal buoyancy. This is illustrated by the

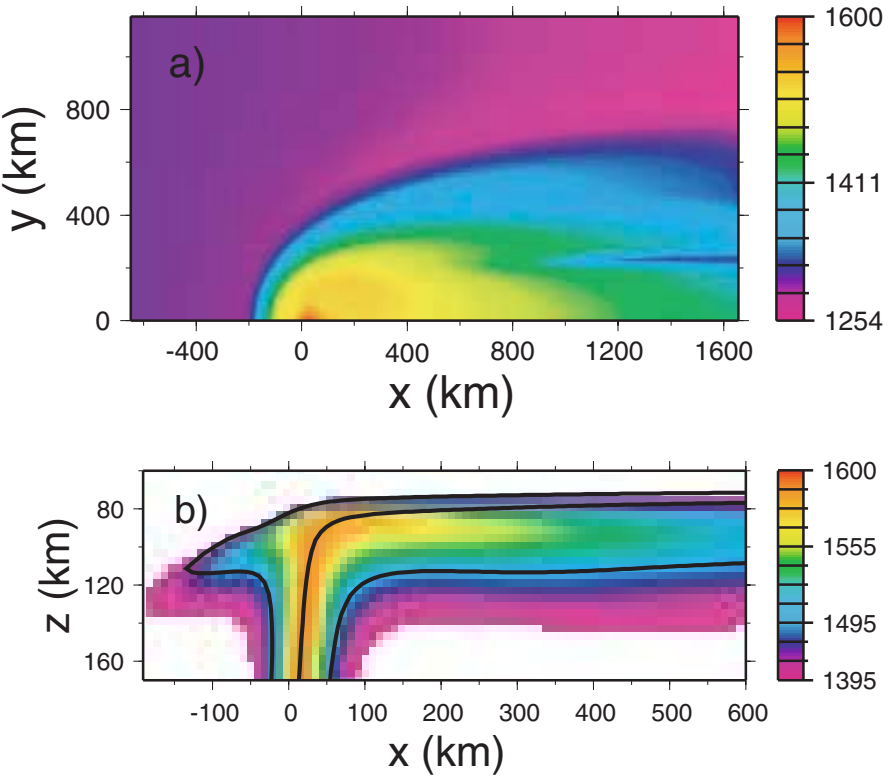

Fig. 13. Potential temperature (°C) for the reference Hawaiian plume model of Ribe and Christensen (1999). (a) horizontal plane at 110 km depth. $(x, y) = (0, 0)$ is the center of the plume stem at 400 km depth. (b) vertical plane containing the plume symmetry axis. Black lines are trajectories of unmelted plume material. Reproduced with permission from Elsevier.

dashed line in Fig. 14, which shows the axial topography predicted by the reference Hawaii model of Ribe and Christensen (1999) with depletion buoyancy neglected.

The success of the 3D model in predicting the swell topography makes it possible to constrain the values of key parameters of the Hawaiian plume via a formal inversion procedure (Ribe and Christensen 1999). The starting point is a set of analytical scaling laws, based on lubrication theory, for selected geophysical observables whose values are well determined by observations. Two such observables are the maximum uplift $H \sim 1350 \pm 100$ m of the swell and its half-width at the hotspot $W = 600 \pm 50$ km (Crough 1978; Wessel 1993). Their values as predicted by the 3D convection model are given accurately by the scaling laws

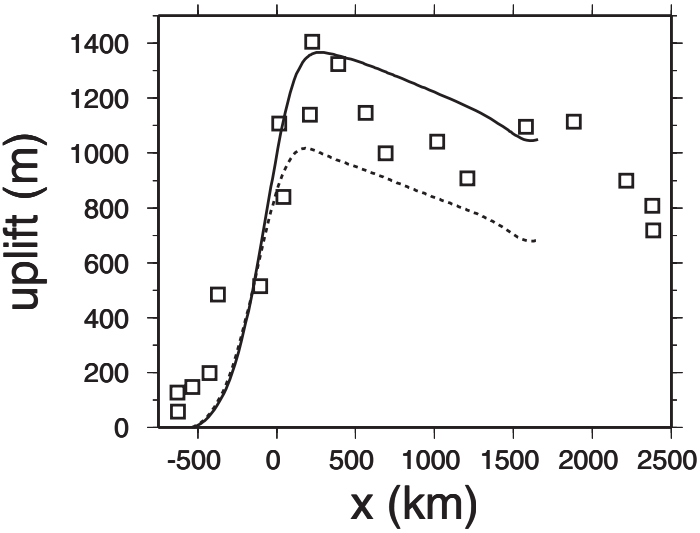

Fig. 14. Comparison of observed uplift along the axis of the Hawaiian swell (squares; Crough 1978) with predictions of the numerical model of Ribe and Christensen (1999) obtained with (solid line) and without (dashed line) melting-induced depletion buoyancy. Reproduced with permission from Elsevier.

$$H = \frac{\Delta\rho}{\rho_m - \rho_w} S_0 G(\Pi_b), \qquad W = 1.3 L_0 G(\Pi_b), \tag{22}$$

where ρ_2 is the density of seawater, $\Pi_b \equiv Q\sigma/U^2$ is the "buoyancy number", S_0 and L_0 are defined by (21), and the function G is determined by fitting the 3D model predictions. The analytical form of the scaling laws (22) allows them to be inverted numerically, thereby determining the range of plume parameters (buoyancy flux, excess temperature, etc.) that are compatible with the observed values of H and W. In this way Ribe and Christensen (1999) concluded that the minimum viscosity inside the plume is in the range $4 \times 10^{17} - 1.1 \times 10^{19}$ Pa s, and the buoyancy flux B in the range 2000-3300 kg s^{-1}. These values of B are smaller by a factor of 2-3 than values estimated in previous studies (Davies 1988; Sleep 1990) that did not account for the effects of depletion buoyancy and asthenospheric shear (Ribe and Christensen 1994), both of which reduce the thermal buoyancy flux required to produce a given uplift. Zhong and Watts (2002) applied a similar inversion procedure to a set of three observables comprising H, W, and the uplift rate measured at Lanai island, and concluded that the last of these required the excess temperature of the Hawaiian plume to exceed 400 K. However, this estimate would probably be lowered somewhat by the effect of depletion buoyancy, which was not included in Zhong and Watts' (2002) model. More recently, Van Hunen and Zhong (2003) used an extensive suite of 3-D numerical solutions to de-

velop alternative (not based on lubrication theory) scaling laws for H and W, and concluded that the swell topography is significantlly influenced by the ambient mantle viscosity ν_m. Laboratory experiments on thermal plumes spreading in a shear flow beneath a moving surface (Kerr and Mériaux 2004) also suggest that the lateral spreading is controlled by ν_m rather than by ν_p. The relative roles of the two viscosities in plume-plate interaction remains an open question that requires further investigation.

The interpretation of the gravity and geoid anomalies predicted by the 3D convection model is more complicated. The geoid/topography ratio (GTR) predicted by the model is typically around 0.008, much larger than the values $\approx$ 0.004-0.005 estimated for individual hotspot swells (Marks and Sandwell 1991; Monnereau and Cazenave 1988). In an attempt to resolve this paradox, Cserepes et al. (2000) extended the 3D convection model to include the flexural topography generated by volcanic loading of the lithosphere. They then applied to the synthetic topography and geoid data the same band-pass filter applied to the real data by Marks and Sandwell (1991). The GTR predicted by this extended model is in the range 0.004-0.005, in good agreement with previous estimates. The conclusion is that low values of the GTR inferred from observations reflect incomplete removal of (shallowly compensated) flexural topography by the filters, and that the "true" GTR of the swell itself is around 0.008.

We conclude this section by noting that recent seismic observations at Hawaii (Li et al. 2004) have shed new light on the origin of hotspot swells. Using S-to-P converted phases (receiver functions) originating at the base of the lithosphere, Li et al. (2004) showed that the lithospheric thickness decreases from 100–110 km beneath Big Island to 50–60 km beneath the island of Kauai, 500 km to the northwest. The width of the thinned region is about 300 km. These results suggest that the mode of support for the Hawaiian swell may be mixed, involving flow-induced dynamic stresses on the scale of the whole swell width ($\approx$ 1200 km) plus a substantial contribution from lithospheric thinning in the central portion (300 km wide). The fluid mechanics of this "dynamic thinning" model (Ribe 2004) remain to be investigated.

4.3 Plume-ridge interaction

Many oceanic hotspots lie on or near spreading ridges; well-known examples include the Iceland, Galapagos, and Azores hotspots. A variety of geophysical and geochemical observations indicate that the connection between these hotspots and their associated ridges is an active dynamical one. The evidence for such "plume-ridge interaction" (PRI) includes unusually aligned patterns of constructional volcanism near hotspots such as Galapagos and Reunion (Morgan 1978) and variations of bathymetry and basalt geochemistry along ridge segments near hotspots (e.g. Schilling 1985). The present review focusses on the strictly fluid dynamical aspects of PRI. Ito et al. (2003) give a

more extensive review that includes a substantial discussion of observational constraints.

The classic model for PRI, first proposed by Morgan (1978), envisages hotspots interacting with nearby ridges via a channel or "pipeline" in the asthenosphere. The plume and the ridge are here regarded as a "source-sink" pair, the former creating new asthenosphere by bringing material up from the deep mantle, the latter destroying it by converting it to lithosphere. In later versions of the model developed by Schilling and co-workers (e.g. Schilling 1985, 1991), the channel is supposed to be carved in the base of the lithosphere by the plume as the ridge migrates across and away from it. However, this "mantle plume source/migrating ridge sink" model is essentially kinematic, and does not explicitly consider the thermomechanical mechanisms whereby the channel is formed and maintained.

Starting in 1995, geodynamicists began to use dynamically self-consistent flow models to study PRI, both numerically and in the laboratory. The model most commonly used is simply a modified plume-plate interaction model with a new surface velocity boundary condition representing a ridge that spreads with half-rate U and migrates with velocity U_m relative to the plume (Fig. 12b). The plate-driven flow in the sublithospheric mantle is no longer a horizontal simple shear, as in the plume-plate model, but rather a "corner flow" with upwelling beneath the ridge.

The simplest case is that of a "ridge-centered" plume rising directly beneath a spreading ridge, Iceland being the main natural example. The model can be simplified even further by neglecting thermal diffusion, so that the diverging plates have zero thickness and the buoyancy of the plume fluid is purely chemical. Studies of this model using analog laboratory experiments (Feighner and Richards 1995), lubrication theory (Ribe et al. 1995), and 3-D numerical experiments with chemically buoyant tracer particles (Feighner et al. 1995) show that the plume head takes the form of a "bow-tie" in mapview (Fig. 15a). Physically, this shape reflects the competition between the gravitational spreading of the plume fluid and its advection away from the ridge by the diverging plates. The principal quantities of interest here are the thickness S of the plume head and its lateral extent ("waist width") W along the ridge axis. The scales for these quantities can be obtained from the lubrication theory equation that governs the steady thickness $S(x, y)$ of the plume head, which is (Ribe et al. 1995)

$$\frac{\partial}{\partial x}\psi(x, S) = \sigma\nabla_h^2 S^4 + Q\delta(x)\delta(y), \tag{23}$$

where $\psi(x, z)$ is the streamfunction that describes the corner flow driven by the diverging plates. By balancing the three terms in (23), one obtains (Ribe et al. 1995)

$$S \sim Q^{1/4}\sigma^{-1/4} = S_0, \quad W \sim Q^{1/2}U^{-1/2} = W_0, \tag{24}$$

The thickness scale S_0 is the same as that for the plume-plate model (21), but the scale W_0 is new, reflecting the fact that advection beneath a spreading ridge is dominantly vertical.

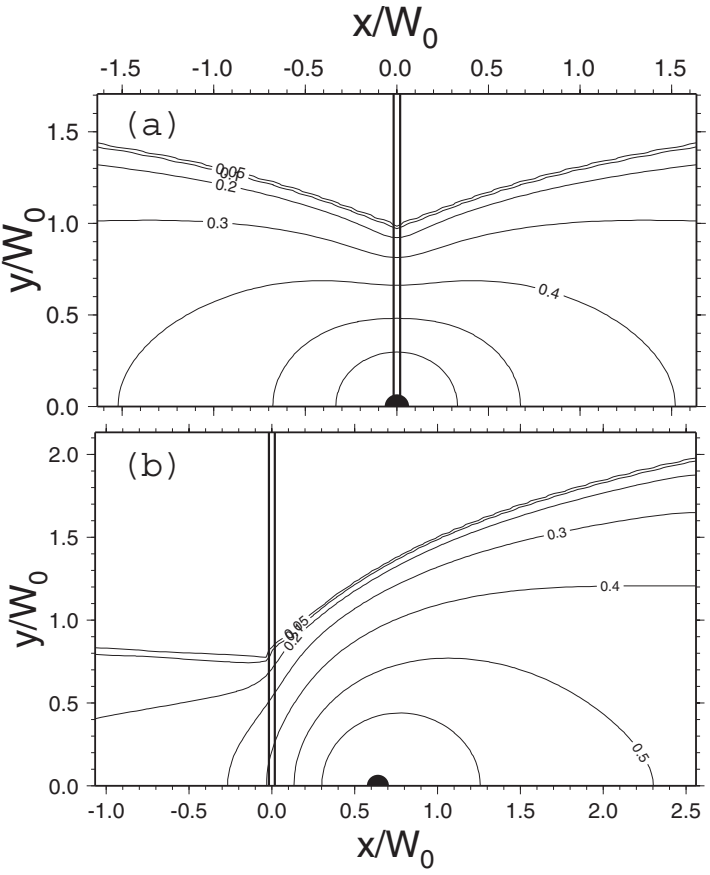

Fig. 15. Distribution of chemically buoyant plume predicted by a lubrication theory model for plume-ridge interaction (Ribe 1996); Fig. 12b) with buoyancy number $\Pi_b = 10$ and two values of the plume-ridge separation x_p. (a) Ridge-centered plume ($x_p = 0$). (b) Off-axis plume ($x_p = 0.64W_0$). In both cases, the finite thickness of the lithosphere has been neglected (channeling number $\Pi_c = 0$).

While the simple model just described is useful for understanding the essential fluid dynamics of ridge-centered plumes, the predicted "bow-tie" shape of the plume head is not very realistic because the model neglects the conductive thickening of the lithosphere away from the ridge. This thickening has two important effects. First, it generates a driving force for "upslope" flow

of the buoyant plume material toward the ridge along the sloping base of the lithosphere, in addition to the "self-spreading" force due to variations in the thickness of the plume head itself. In effect, the sloping bottom surfaces of the lithosphere to either side of the ridge acts like an inverted duct that tend to confine the plume fluid to a more or less narrow channel beneath and parallel to the ridge. However, the thickening of the lithosphere with distance from the ridge also causes it to act as a "sink" for plume material, which becomes part of the plate as it cools.

The effects of a thickening lithosphere are automatically included in 3-D models of ridge-centered thermal plumes in a fluid with strongly temperature-dependent viscosity (Ribe et al. 1995; Ito et al. 1996; Albers and Christensen 2001). These studies confirm that the lubrication scales (24) remain valid for this case, to within a weak additional dependence on the buoyancy number $\Pi_b = Q\sigma/U^2$. Albers and Christensen (2001) find

$$W \approx 2.13 W_0 \Pi_b^{0.069}. \tag{25}$$

By contrast, the thickening lithosphere has a strong effect on the aspect ratio A of the plume head, defined as the ratio of the ridge-parallel and ridge-normal dimensions of a given isothermal surface. Albers and Christensen (2001) find that

$$A \sim 2.5 \Pi_c^{0.36}, \quad \Pi_c = \sigma^{1/2} \kappa U^{-3/2}, \tag{26}$$

where the "channeling number" $\Pi_c \equiv [h(W_0)/S_0]^2$ is the (square of the) ratio of the lithospheric thickness $h(x) \equiv (\kappa U/x)^{1/2}$ at a distance $x = W_0$ from the ridge to the typical thickness S_0 of the plume head. Fig. 16 shows the distribution of the plume material calculated by Albers and Christensen (2001) for two values of Π_c, illustrating the strong channeling that occurs when $\Pi_c > 1$.

The channeling effect documented by Albers and Christensen (2001) is favored both by slow spreading rates and by low ($\mu_p \approx 10^{17}$ Pa s) plume viscosity. However, Ito et al. (1999) pointed out that the latter may not be realistic, as extraction of water from the mantle by partial melting can increase the viscosity of the residuum by 2-3 orders of magnitude (Hirth and Kohlstedt 1996). The 3-D numerical calculations of Ito et al. (1999) show that a dehydration-induced viscosity increase of this magnitude creates a "plug" of high-viscosity material directly beneath the ridge, within which the upwelling velocity is comparable to the plate spreading rate. The subsolidus plume material then spreads in the form of a broad pancake beneath the high-viscosity dehydrated layer, the base of which is effectively flat. This model can explain both the broad lateral extent of the topography anomaly around Iceland and the melting rates implied by the observed crustal thicknesses, unlike earlier models without dehydration strengthening (Ribe et al. 1995; Ito et al. 1996) that had to invoke melt migration over distances of several hundred km away from the plume. More recently, however, Ruedas et al. (2004) proposed a model that can explain the crustal thickness on Iceland without dehydration

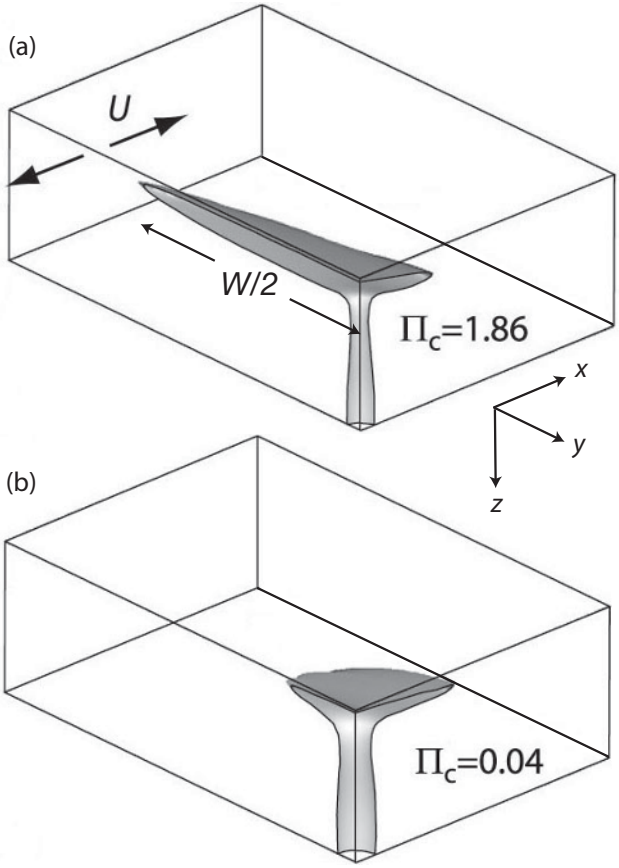

Fig. 16. Isothermal surfaces showing the distribution of hot material in a steady thermal plume rising beneath a spreading ridge, for two values of the channeling number Π_c (Eqn. 26). Modified from Albers and Christensen (2001). Reproduced with permission from Elsevier.

strengthening. At this point, it seems fair to say that melting processes beneath ridges are sufficiently complicated that any given observation can be explained by a variety of different models.

The nonsteady dynamics of ridge-centered plumes that result from a time-varying buoyancy flux have been studied numerically by Albers and Christensen (2001) and Ito (2001). The motivation for both studies is the "V-shaped" topographic ridges and gravity anomalies observed around the Reykjanes Ridge south of Iceland, which Vogt (1971) suggested were due to rapid channelized flow of plume material along the ridge away from the hotspot. Albers and Christensen (2001), using a model with a high channeling number $\Pi_c = 1.9$, showed that a pulse of excess buoyancy flux introduced at depth

travels up the plume stem and then along the ridge in both directions with a speed greatly exceeding the half-spreading rate. In Ito's (2001) model, by contrast, channelization is suppressed by a layer of high-viscosity dehydrated material, and pulses of plume material are dispersed radially away from the hotspot. In both models, the speed of ridge-parallel plume flow relative to the half-spreading rate is sufficient to account for the observed inclination of the V-shaped ridges relative to the Reykjanes ridge.

We move now from ridge-centered plumes to the next level of complexity: "off-axis" plumes located at some distance from a ridge. New dynamical questions now arise: how does the intensity of plume-ridge interaction (as measured e.g. by the waist width W) vary as a function of the plume-ridge separation x_p? What is the critical value of x_p beyond which interaction ceases? The first dynamical investigation of such questions was the analog laboratory study of Kincaid et al. (1995), who used a fluid with temperature-dependent viscosity to generate a lithosphere that thickened by conductive cooling as it moved away from a spreading ridge. Plume-ridge interaction was documented by observing particle trajectories and by measuring the temperature anomalies generated beneath the ridge by the hot plume. Based on the observed correlation between the temperature anomalies and the slope of the base of the model lithosphere, Kincaid et al. (1995) concluded that upslope flow was the critical factor responsible for the interaction. The lubrication theory solutions of Sleep (1996) also suggested that upslope flow could be important near ridges. However, more systematic studies based on lubrication theory Ribe (1996) and full 3-D modeling of thermal plumes (Ito et al. 1997) suggest that self-spreading is the primary cause of interaction, variations in lithospheric thickness playing a secondary role. Fig. 15b shows the shape of the plume head predicted by the lubrication theory model (Ribe 1996) for a plume located at a distance $x_p = 0.64W_0$ from a spreading ridge. Interaction between the two is indicated by the finite waist width W and the "leakage" of plume material across the ridge.

Both Ribe (1996) and Ito et al. (1997) find that the waist width progressively decreases as the plume-ridge separation x_p increases, eventually diminishing to zero when x_p reaches a critical value $(x_p)_{max} = C(\Pi_b, \Pi_c)W_0$, where C is a dimensionless function of Π_b and Π_c of order unity. Physically, $(x_p)_{max}$ is the distance which the buoyant plume material can spread "upstream" against the plate motion, which tends to advect the plume material away from the ridge. Examples of the variation of W as a function of x_p for a nonmigrating ridge is shown by the curves labelled $U_m/U = 0$ in Fig. 17. These curves are symmetric about the ridge because it does not matter which side of a (stationary) ridge the plume is on.

The dynamics of plume-ridge interaction become still more complicated when the ridge migrates relative to the plume, as is the case for nearly all real plume-ridge systems. For simplicity, we assume here that the migration velocity is parallel to the spreading velocity. The main effect of ridge migration is to break the across-ridge symmetry of the system, so that the dynamics now

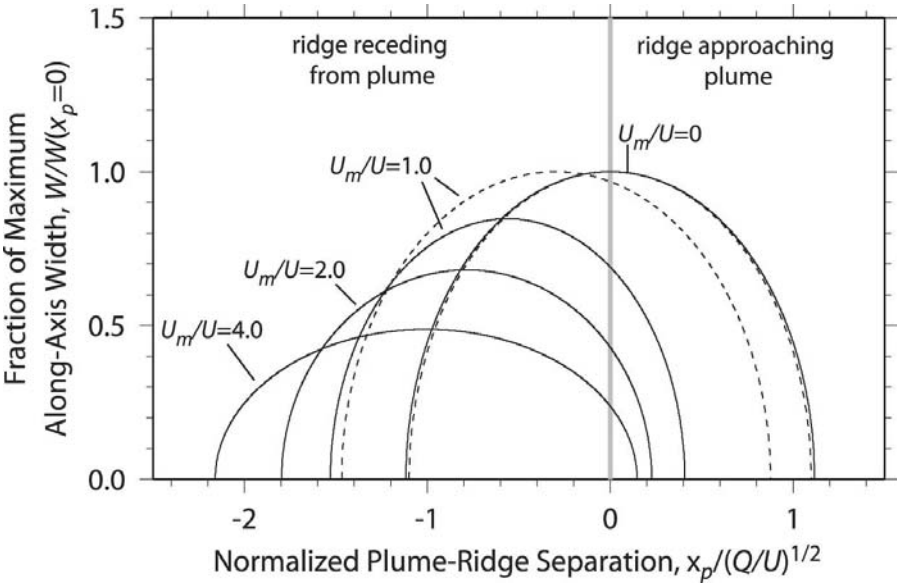

Fig. 17. Waist width W as a function of plume-ridge separation x_p, for $\Pi_b = 10$ and several values of the ridge migration speed U_m. The solid curves are the predictions of a lubrication theory model with channeling number $\Pi_c = 0$ (Ribe and Delattre 1998). The dashed curves are the predictions of the 3-D convection model of Ito et al. (1997). Figure adapted from Ito et al. (2003). Copyright 2003 by the American Geophysical Union. Reproduced by permission of the American Geophysical Union.

depend on whether the ridge is approaching or receding from the plume. This is because the velocity of the overriding plate relative to the plume is different in the two cases, being $U + U_m$ when the ridge approaches the plume and $U - U_m$ when it recedes from it. The "wind" that advects the plume material is therefore stronger in the former case, with the consequence that both the stagnation distance and the width of the plume head are smaller during the "approaching" stage than during the "receding" stage. Now the maximum plume-ridge interaction distance $(x_p)_{max}$ is proportional to the stagnation distance, and will therefore be greater in the latter case: plume-ridge interaction is stronger, and lasts longer, when the ridge is receding from the plume. This is illustrated in Fig. 17, which shows how the curves of waist width W as a function of plume-ridge separation x_p are shifted strongly toward the "receding" side as U_m increases. Moreover, the amplitude of the curves decreases as U_m increases, reflecting the fact that the width of the plume head as it approaches the ridge varies inversely with the "wind speed" $U + U_m$. However, this decrease was not seen in the 3-D convection model of Ito et al. (1997), for reasons that are not yet clear.

The investigations of plume-ridge interaction described above focus on the uppermost mantle, and treat the plume essentially as a source of buoyancy. An alternative approach (Kincaid et al. 1995; Jellinek et al. 2003) is to extend the boundaries of the model domain downward to include the thermal boundary layer from which the plumes originate. The question then becomes one of how a plume-dominated free convective flow interacts with a large-scale passive flow driven by plate motions. The most detailed study of this kind is that of Jellinek et al. (2003), who performed laboratory experiments using a fluid with temperature-dependent viscosity heated from below and driven at its surface by a ridge-like velocity boundary condition. They documented three different flow regimes, depending on the ratio V of the spreading rate to the typical plume rise velocity and the ratio γ of the interior viscosity to the viscosity of the hottest fluid. When $V \ll 1$ and $\gamma \geq 1$, the plume distribution is random and unaffected by the large-scale flow. The opposite extreme is represented by $V > 10$ and $\gamma > 100$, where plume formation is suppressed entirely and the large-scale flow carries all the heat flux. Interaction of the two flows occurs for intermediate values of V; established plume channels are now advected along the bottom boundary and focussed towards an upwelling beneath the ridge.

To conclude, we return to the hypothesis of Morgan (1978) and Schilling (1985) that off-axis plumes communicate with nearby ridges via a "channel" in the base of the lithosphere. Unlike ridge-parallel channels, whose origin is easy to understand dynamically (Albers and Christensen 2001), significant ridge-perpendicular channels have not been seen in any of the numerical or laboratory models discussed above. The existence of such channels thus remains an open question. Perhaps the observations that seem to suggest their existence can be explained by other means; or perhaps channels can be created by mechanisms not yet identified. One possibility that requires further study is the onset of small-scale convection in the asthenosphere, which might delay the thickening of the lithosphere between a hotspot and a ridge receding from it (Davaille and Lees 2004).

Acknowledgements

We thank P. Van Keken for providing the results of his numerical simulations of thermal starting plumes, and P. Olson and J. Dyon for assistance with the preparation of Figure 1. Cinzia Farnetani and Kei Kurita kindly made figures available prior to publication. Constructive reviews by G. Ito and an anonymous referee helped greatly to improve the manuscript. This is IPGP contribution number 2192.

References

Albers M, Christensen UR (1996) The excess temperature of plumes rising from the core-mantle boundary. Geophys Res Lett 23:3567–3570

Albers M, Christensen UR (2001) Channeling of plume flow beneath mid-ocean ridges. Earth Planet Sci Lett 187:207–220
Asaeda T, Watanabe K (1989) The mechanism of heat transport in thermal convection at high Rayleigh numbers. Phys Fluids A1:861–867
Barenblatt GI (1996) Scaling, self-similarity, and intermediate asymptotics. Cambridge University Press, Cambridge
Batchelor GK (1954) Heat convection and buoyancy effects in fluids. Q J R Met Soc 80:339–358
Batchelor GK (1967) An introduction to fluid dynamics. Cambridge University Press, Cambridge
Batchelor GK (1970) Slender-body theory for particles of arbitrary cross-section in Stokes flow. J Fluid Mech 44:419–440
Bercovici D, Mahoney J (1994) Double flood basalts and plume-head separation at the 660 km discontinuity. Science 266:1367–1369
Campbell IH, Griffiths RW (1990) Implications of mantle plume structure for the evolution of flood basalts. Earth Planet Sci Lett 99:79–93
Canright D, Morris S (1993) Buoyant instability of a viscous film over a passive fluid. J Fluid Mech 255:349–372
Chandrasekhar S (1981) Hydrodynamic and hydromagnetic stability, Dover, New York
Christensen U (1984) Instability in a hot boundary layer and initiation of thermochemical plumes. Ann Geophys 2:311–320
Christensen U (1985) Heat transport by variable viscosity convection II: Pressure influence, non-Newtonian rheology and decaying heat sources. Phys Earth Planet Int 37:183–205
Christensen UR, Harder H (1991) 3-D Convection with variable viscosity, Geophys J Int 104:213–226
Christensen UR, Hofmann AW (1994) Segregation of subducted oceanic crust in the convecting mantle, J. Geophys. Res 99:19867–19884
Condie KC (2001) Mantle plumes and their record in Earth history, Cambridge University Press, Cambridge
Coulliette DL, Loper DE (1995) Experimental, numerical and analytical models of mantle starting plumes. Phys Earth Planet Int 92:143–167
Courtillot V, Davaille A, Besse J, Stock J (2003) Three distinct types of hotspots in the Earth's mantle. Earth Planet Sci Lett 205:295–308
Crough ST (1978) Thermal origin of mid-plate hotspot swells. Geophys J R Astr Soc 55:451–469
Cserepes L, Christensen UR, Ribe NM (2000) Geoid height vs topography for a plume model of the Hawaiian swell. Earth Planet Sci Lett 178:29–38.
Davaille A, Jaupart C (1993) Transient high-Rayleigh number thermal convection with large viscosity variations, J. Fluid Mech 253:141–166
Davaille A (1999a) Two-layer thermal convection in miscible viscous fluids. J Fluid Mech 379:223–253
Davaille A (1999b) Simultaneous generation of hotspots and superswells by convection in a heterogeneous planetary mantle. Nature 402:756–760
Davaille A, Girard F, Le Bars M (2002) How to anchor plumes in a convecting mantle?, Earth Planet Sci Lett 203:62–634
Davaille A, Le Bars M, Carbonne C (2003) Thermal convection in a heterogeneous mantle, C R Acad Sci Géosciences, 335/1:141–156

Davaille A, Lees J (2004) Thermal modeling of subducted plates: tear and hotspot at the Kamchatka corner. Earth Planet Sci Lett 226:293–304

Davaille A, Vatteville J (2005) On the transient nature of mantle plumes. Geophys Res Lett 32: doi:10.1029/2005GL023029

Davies GF (1988) Ocean bathymetry and mantle convection, 1. Large-scale flow and hotspots. J Geophys Res 93:10467–10480

Davies GF (1995) Penetration of plates and plumes through the mantle transition zone. Earth Planet Sci Lett 133:507–516

Debayle E, Levêque J-J, Cara M (2001) Seismic evidence for a deeply rooted low-velocity anomaly in the upper mantle beneath the northeastern Afro/Arabian continent. Earth Planet Sci Lett 193:369–382

Debayle E, Kennett B, Priestley K (2005) Global azimuthal seismic anisotropy and the unique plate motion deformation of Australia. Nature 433:509–512

Detrick RS Crough ST (1978) Island subsidence, hot spots, and lithospheric thinning. J Geophys Res 83:1236–1244

Ebinger C, Sleep NH (1998) Cenozoic magmatism in central and east Africa resulting from impact of one large plume. Nature 395:788–791

Farnetani GC (1997) Excess temperature of mantle plumes: the role of chemical stratification across D''. Geophys Res Lett 24:1583–1586

Farnetani CG, Richards MA (1994) Numerical investigations of the mantle plume initiation model for flood basalt events. J Geophys Res 99:13813–13833

Farnetani CG, Richards MA (1995) Thermal entrainment and melting in mantle plumes. Earth Planet Sci Lett 136:251–267

Farnetani GC, Legras B, Tackley PJ (2002) Mixing and deformation in mantle plumes, Earth Planet Sci Lett 196: 1–15

Farnetani CG, Samuel H (2005) Beyond the thermal plume paradigm. Geophys Res Lett 32: doi:10.1029/2005GL022360

Feighner MA, Richards MA (1995) The fluid dynamics of plume-ridge and plume-plate interactions: An experimental investigation. Earth Planet Sci Lett 129:171–182

Feighner MA, Kellogg LH, Travis BJ (1995) Numerical modeling of chemically buoyant plumes at spreading ridges. Geophys Res Lett 22:715–718

Foulger GR, Natland JH (2003) Is hotspot volcanism a consequence of plate tectonics? Science 300:921–922

Fuji T (1963) Theory of the steady laminar natural convection above a horizontal line heat source and a point heat source. Int J Heat Mass Transfer 6:597–606

Gonnermann HM, Manga M, Jellinek AM (2002) Dynamics and longevity of an initially stratified mantle, Geophysical Research Letters 29: doi:10.1029/2002GL01485

Gonnermann HM, Jellinek AM, Richards MA, Manga M (2004) Modulation of mantle plumes and heat flow at the core mantle boundary by plate-scale flow: results from laboratory experiments. Earth Planet Sci Lett 226:53–67

Grand SP (2002) Mantle shear-wave tomography and the fate of subducted slabs. Phil Trans R Soc Lond A360:2475–2491

Griffiths RW (1986a) Thermals in extremely viscous fluids, including the effects of temperature-dependent viscosity. J Fluid Mech 166:115–138

Griffiths RW (1986b) The differing effects of compositional and thermal buoyancy on the evolution of mantle diapirs. Phys Earth Planet Int 43:261–273

Griffiths RW, Richards MA (1989) The adjustment of mantle plumes to changes in plate motion. Geophys Res Lett 16:437–440
Griffiths RW, Campbell IH (1990) Stirring and structure in mantle starting plumes. Earth Planet Sci Lett 99:66–78
Griffiths RW, Campbell IH (1991) Interaction of mante plume heads with the Earth's surface and the onset of small-scale convection. J Geophys Res 96:18295–18310
Gurnis M, Davies GF (1986) The effect of depth-dependent viscosity on convective mixing in the mantle and the possible survival of primitive mantle, Geophys Res Lett 13:541–544
Hansen U, Yuen DA (1988) Numerical simulations of thermo-chemical instabilities at the core-mantle boundary. Nature 33:237–240
Hansen U, Yuen DA (2000) Extended-Boussinesq thermal-chemical convection with moving heat sources and variable viscosity, Earth Planet Sci Lett 176:401–411
Harder H, Christensen UR (1996) A one-plume model of Martian mantle convection. Nature 380:507–509
Hauri EH, Whitehead JA, Hart SR (1994) Fluid dynamic and geochemical aspects of entrainment in mantle plumes. J Geophys Res 99:24275–24300
Herrick DL, Parmentier EM (1994) Episodic large-scale overturn of two-layer mantles in terrestrial planets. J Geophys Res 99:2053–2062.
Hirth G, Kohlstedt DL (1996) Water in the oceanic upper mantle: implications for rheology, melt extraction, and the evolution of the lithosphere. Earth Planet Sci Lett 144:93–108
Houseman GA (1990) The thermal structure of mantle plumes: axisymmetric or triple-junction?. Geophys J Int 102:25–43
Howard LN (1964) Convection at high Rayleigh number. In: H. Görtler (ed) Proc 11th intl congr applied mechanics, Springer, Berlin, pp 1109–1115
Huppert H (1982) The propagation of two-dimensional and axisymmetric viscous gravity currents over a rigid horizontal surface. J Fluid Mech 12:43–58
Ito G, Lin J, Gable CW (1996) Dynamics of mantle flow and melting at a ridge-centered hotspot: Iceland and the Mid-Atlantic Ridge. Earth Planet Sci Lett 144:53–74
Ito G, Lin J, Gable CW (1997) Interaction of mantle plumes and migrating mid-oceanic ridges: Implications for the Galapagos plume-ridge system. J Geophys Res 102:15403–15417
Ito G, Shen Y, Hirth G, Wolfe CJ (1999) Mantle flow, melting, and dehydration of the Iceland mantle plume. Earth Planet Sci Lett 165:81–96
Ito G (2001) Reykjanes 'V'-shaped ridges originating from a pulsing and dehydrating mantle plume. Nature 411:681–684
Ito G, Lin J, Graham D (2003) Observational and theoretical studies of the dynamics of mantle plume-mid-ocean ridge interaction. Rev Geophys 41: doi:10.1029/2002RG000117
Javoy M (1999) Chemical Earth models, C R Acad Sci 329:537–555
Jellinek AM, Manga M (2002) The influence of a chemical boundary layer on the fixity, spacing and lifetime of mantle plumes. Nature 41:760–763
Jellinek AM, Lenardic A, Manga M (2002) The influence of interior mantle temperature on the structure of plumes: Heads for Venus, Tails for the Earth. Geophys Res Lett 29: doi:10.1029/2001GL014624
Jellinek AM, Gonnermann HM, Richards MA (2003) Plume capture by divergent plate motions: Implications for the distribution of hotspots, geochemistry of mid-

ocean ridge basalts, and heat flux at the core-mantle boundary. Earth Planet Sci Lett 205:367–378
Jellinek AM, Manga M (2004) Links between long-lived hotspots, mantle plumes, D'', and plate tectonics. Rev Geophys 42: doi:10.1029/2003RG000144
Jordan TH (1979) Mineralogies, densities and seismic velocities of garnet lherzolites and their geophysical implications. In: Boyd FR, Meyer HOA (eds), The mantle sample: inclusions in kimberlites and other volcanics, vol. 2, Am Geophys Union, Washington, DC, pp 1–14
Kaminski E, Jaupart C (2003) Laminar starting plumes in high-Prandtl-number fluids, J Fluid Mech 478:287–298
Ke Y, Solomatov VS (2004) Plume formation in strongly temperature-dependent viscosity fluids over a very hot surface. Phys Fluids 16:1059–1063
Kellogg LH (1991) Interaction of plumes with a compositional boundary at 670 km. Geophys Res Lett 5:865–868
Kellogg LH, Hager BH, van der Hilst RD (1999) Compositional stratification in the deep mantle, Science 283:1881–1884
Kellogg LH, King SD (1997) The effect of temperature-dependent viscosity on the structure of new plumes in the mantle: Results of a finite element model in a spherical, axisymmetric shell. Earth Planet Sci Lett 148:13–26
Kelly A, Bercovici D (1997) The clustering of rising diapirs and plume heads. Geophys Res Lett 24:201–204
Kerr RC, Mériaux C (2004) Structure and dynamics of sheared mantle plumes. Geochem Geophys Geosyst 5: doi:10.1029/2004GC000749
Kincaid C, Ito G, Gable C (1995) Laboratory investigation of the interaction of off-axis mantle plumes and spreading centres. Nature 376:758–761
Koch DM, Koch DL (1995) Numerical and theoretical solutions for a drop spreading below a free fluid surface. J Fluid Mech 287:251–278.
Krishnamurti R (1970) On the transition to turbulent convection. J Fluid Mech 42:295–320
Kumagai I (2002) On the anatomy of mantle plumes: effect of the viscosity ratio on entrainment and stirring. Earth Planet Sci Lett 198:211–224
Kumagai I, Kurita K (2000) On the fate of mantle plumes at density interfaces. Earth Planet Sci Lett 179:63–71
Labrosse S (2002) Hotspots, mantle plumes and core heat loss. Earth Planet Sci Lett 199:147–156
Laudenbach N, Christensen UR (2001) An optical method for measuring temperature in laboratory models of mantle plumes. Geophys J Int 145:528–534
Le Bars M, Davaille A (2002) Stability of thermal convection in two superimposed miscible viscous fluids. J Fluid Mech 471:339–363
Le Bars M, Davaille A (2004a) Large interface deformation in two-layer thermal convection of miscible viscous fluids, J Fluid Mech 499:75–110
Le Bars M, Davaille A (2004b) Whole-layer convection in an heterogeneous planetary mantle. J Geophys Res 109: doi:10.1029/2003JB002617
Lemery C, Ricard Y, Sommeria J (2000) A model for the emergence of thermal plumes in Rayleigh-Bénard convection at infinite Prandtl number. J Fluid Mech 414:225–250
Lenardic A, Kaula WM (1994) Tectonic plates, D'' thermal structure and the nature of mantle plumes. J Geophys Res 99:15697–15708

Li X, Kind R, Yuan X, Wölbern I, Hanka W (2004) Rejuvenation of the lithosphere by the Hawaiian plume. Nature 427:827–829

Lister JR (1989) Selective withdrawal from a viscous two-layer system. J Fluid Mech 198:231–254

Lister JR, Kerr RC (1989) The propagation of two-dimensional and axisymmetric viscous gravity currents along a fluid interface. J Fluid Mech 203:215249

Liu M, Yuen DA, Zhao W, Honda S (1991) Development of diapiric structures in the upper mantle due to phase transitions. Science 252:1836–1839

Loper DE (1998) Mantle plumes and their effect on the Earth's surface: a review and synthesis, Dyn Atmos Oceans 27:35–54

Loper DE, Stacey FD (1983) The dynamical and thermal structure of deep mantle plumes. Phys Earth Planet Int 33:305–317

Loper DE, Eltayeb IA (1986) On the stability of the D'' layer. Geophys Astron Fluid Dyn 36:229–255

Lowman JP, King SD, Gable CW (2004) Steady plumes in viscously stratified, vigorously convecting, three-dimensional numerical mantle convection models with mobile plates, Geochem Geophys Geosyst 5: doi:10.1029/2003GC000583

Manga M (1997) Interactions between mantle diapirs. Geophys Res Lett 24:1871–1874

Manga M, Stone HA, O'Connell RJ (1993) The interaction of plume heads with compositional discontinuities in the Earth's mantle. J Geophys Res 98:19979–19990

Manga M, Weeraratne D, Morris SJS (2001) Boundary-layer thickness and instabilities in Bénard convection of a liquid with a temperature-dependent viscosity. Phys Fluids 13:802–805

Marks KM, Sandwell DT (1991) Analysis of geoid height versus topography for oceanic plateaus and swells using nonbiased linear regression. J Geophys Res 96:8045–8055

McNamara AK, Zhong S (2004a) Thermochemical structures within a spherical mantle : Superplumes or piles? J Geophys Res 109: doi:10.1029/2003JB002847

McNamara AK, Zhong S (2004b) The influence of thermochemical convection on the fixity of mantle plumes. Earth Planet Sci Lett 222:485–500

Monnereau M, Cazenave A (1988) Variation of the apparent compensation depth of hotspot swells with age of plate. Earth Planet Sci Lett 91:179–197

Monnereau M, Rabinowicz M, Arquis E (1993) Mechanical erosion and reheating of the lithosphere: A numerical model for hotspot swells. J Geophys Res 98:809–823

Montelli R, Nolet G, Dahlen FA, Masters G, Engdahl ER, Hung SH (2004) Finite-frequency tomography reveals a variety of plumes in the mantle. Science 303:338–343

Montague NL, Kellogg LH (2000) Numerical models of a dense layer at the base of the mantle and implications for the geodynamics of D''. J Geophys Res 105:11101–11114

Moore WB, Schubert G, Tackley P (1998) Three-dimensional simulations of plume-lithosphere interaction at the Hawaiian Swell. Science 279:1008–1011

Moore WB, Schubert G, Tackley P (1999) The role of rheology in lithospheric thinning by mantle plumes. Geophys Res Lett 26:1073–1076

Morgan WJ (1971) Convection plumes in the lower mantle. Nature 230:42–43

Morgan WJ (1972) Plate motions and deep mantle convection. Mem Geol Soc Am 132:7–22

Morgan WJ (1978) Rodriguez, Darwin, Amsterdam, ..., a second type of hotspot island. J Geophys Res 83:5355–5360

Moses E, Zocchi G, Libchaber A (1993) An experimental study of laminar plumes, J Fluid Mech 251:581–601

Murakami M, Hirose K, Sata N, Ohishi Y, Kawamura K (2004) Phase transition of $MgSiO_3$ perovskite in the deep lower mantle. Science 304:855–858

Nakakuki T, Sato H, Fujimoto H (1994) Interaction of the upwelling plume with a phase and chemical boundary at the 670 km discontinuity: Effects of temperature-dependent viscosity. Earth Planet Sci Lett 121:369–384

Namiki A (2003) Can the mantle entrain D''? J Geophys Res 108: doi:10.1029/2002JB002315

Namiki A, Kurita K (1999) The influence of boundary heterogeneity in experimental models of mantle convection. Geophys Res Lett 26:1929–1932

Nataf H-C (1991) Mantle convection, plates and hotspots. Tectonophysics 187:361–377

Nataf H-C (2000) Seismic imaging of mantle plumes. Ann Rev Earth Planet Sci 28:391–417

Neavel KE, Johnson AM (1991) Entrainment in compositionally buoyant plumes. Tectonophysics 200:1–15

Oganov AR, Ono S (2004) Theoretical and experimental evidence for a post-perovskite phase of MgSiO3 in Earth's D'' layer. Nature 430:445–448

Olson P (1984) An experimental approach to thermal convection in a two-layered mantle. J Geophys Res 89:11293–11301

Olson P (1990) Hot spots, swells and mantle plumes. In: Ryan MP (ed) Magma transport and storage. John Wiley and Sons, New York, pp 33–51

Olson P, Singer H (1985) Creeping plumes. J Fluid Mech 158:511–531

Olson P, Nam IS (1986) Formation of seafloor swells by mantle plumes. J Geophys Res 91:7181–7191

Olson P, Christensen UR (1986) Solitary wave propagation in a fluid conduit within a viscous matrix, J Geophys Res 91:6367–6374

Olson P, Schubert G, Anderson C (1987) Plume formation in the D'' layer and the roughness of the core-mantle boundary. Nature 327:409–413

Olson P, Schubert G, Anderson C, Goldman P (1988) Plume formation and lithosphere erosion: a comparison of laboratory and numerical experiments. J Geophys Res 93:15065–15084

Olson P, Kincaid C (1991) Experiments on the interaction of thermal convection and compositional layering at the base of the mantle. J Geophys Res 96:4347–4354

Olson P, Schubert G, Anderson C (1993) Structure of axisymmetric mantle plumes. J Geophys Res 98:6829–6844

Parmentier EM, Turcotte DL, Torrance KE (1975) Numerical experiments on the structure of mantle plumes. J Geophys Res 80:4417–4424

Parmentier EM, Sotin C (2000) Three-dimensional numerical experiments on thermal convection in a very viscous fluid: Implications for the dynamics of a thermal boundary layer at high Rayleigh number. Phys Fluids 12:609–617

Phipps Morgan J, Morgan WJ, Price E (1995) Hotspot melting generates both hotspot volcanism and a hotspot swell? J Geophys Res 100:8045–8062

Ribe NM (1996) The dynamics of plume-ridge interaction 2. Off-ridge plumes. J Geophys Res 101:16195–16204

Ribe NM (1998) Spouting and planform selection in the Rayleigh-Taylor instability of miscible viscous fluids. J Fluid Mech 234:315–336
Ribe NM (2004) Through thick and thin. Nature 427:793–795
Ribe NM, Christensen U (1994) Three-dimensional modeling of plume-lithosphere interaction. J Geophys Res 99:669–682
Ribe NM, Christensen UR, Theissing J (1995) The dynamics of plume-ridge interaction, 1: Ridge-centered plumes. Earth Planet Sci Lett 134:155–168
Ribe NM, Delattre WL (1998) The dynamics of plume-ridge interaction – III. The effects of ridge migration. Geophys J Int 133:511–518
Ribe NM, Christensen U (1999) The dynamical origin of Hawaiian volcanism. Earth Planet Sci Lett 171:517–531
Ricard Y, Vigny C, Froidevaux C (1989) Mantle heterogeneities, geoid, and plate motion : a Monte-Carlo inversion. J Geophys Res 94:13739–13754
Richards MA, Hager BH, Sleep NH (1988) Dynamically supported geoid highs over hotspots: Observation and theory. J Geophys Res 93:7690–7708
Richards MA, Griffiths RW (1988) Deflection of plumes by mantle shear flow : experimental results and a simple theory. Geophys J 94:367–376
Richards MA, Duncan RA, Courtillot VE (1989) Flood basalts and hot-spot tracks: Plume heads and tails. Science 246:103–107
Richter FM, McKenzie DP (1981) On some consequences and possible causes of layered convection. J Geophys Res 86:6133–6124
Ritsema J, Allen RM (2003) The elusive mantle plume. Earth Planet Sci Lett 207:1–12
Ritter JRR, Jordan M, Christensen UR, Achauer U (2001) A mantle plume below the Eifel volcanic fields, Germany. Earth Planet Sci Lett 186:7–14
Ruedas T, Schmeling H, Marquart G, Kreutzmann A, Junge A (2004) Temperature and melting of a ridge-centred plume with application to Iceland. Part I: Dynamics and crust production Geophys J Int 158:729–743
Samuel H, Farnetani CG (2003) Thermochemical convection and helium concentrations in mantle plumes. Earth Planet Sci Lett 207: 39–56
Schaeffer N, Manga M (2001) Interaction of rising and sinking mantle plumes, Geophys Res Lett 21:765–768
Schilling J-G (1985) Upper mantle heterogeneities and dynamics. Nature 314:62–57
Schilling J-G (1991) Fluxes and excess temperatures of mantle plumes infered from their interaction with migrating mid-ocean ridges. Nature 352:397–403
Schmeling H (1988) Numerical models of Rayleigh-Taylor instabilities superimposed upon convection. Bull Geol Inst Univ Uppsala 14:95–109
Schott B, Yuen DA, Braun A (2002) The influences of composition- and temperature-dependent rheology in thermal-chemical convection on entrainment of the D''-layer. Phys Earth Planet Int 146:139–145
Schubert G, Olson P, Anderson, Goldman P (1989) Solitary waves in mantle plumes. J Geophys Res 94:9523–9532
Schubert G, Anderson, Goldman P (1995) Mantle plume interaction with an endothermic phase change. J Geophys Res 100:8245–8256
Schubert G, Turcotte DL, Olson P (2001) Mantle convection in the Earth and planets, Cambridge University Press, Cambridge
Schubert G, Masters G, Olson P, Tackley P (2004) Superplumes or plume clusters? Phys Earth Planet Int 146:147–162

Scott DR, Stevenson DJ, Whitehead JA (1987) Observations of solitary waves in a viscously deformable pipe, Nature 319:759–761
Shapiro NM, Ritzwoller MH (2002) Monte-Carlo inversion for a global shear-velocity model of the crust and upper mantle. Geophys J Int 151:88–105
Siggia (1994) High Rayleigh number convection. Annu Rev Fluid Mech 26:137–168
Skilbeck JN, Whitehead JA (1978) Formation of discrete islands in linear islands chains. Nature 272:499–501
Sleep NH (1987) Lithospheric heating by mantle plumes. Geophys J R Astron Soc 91:1–11
Sleep NH (1988) Gradual entrainment of a chemical layer at the base of the mantle by overlying convection. Geophys J 95:437–447
Sleep NH (1990) Hotspots and mantle plumes: Some phenomenology. J Geophys Res 95:6715–6736
Sleep NH (1996) Lateral flow of hot plume material ponded at sublithospheric depths. J Geophys Res 101:28065–28083
Sleep NH (1997) Lateral flow and ponding of starting plume material. J Geophys Res 102:10001–10012
Sleep NH (2002) Local lithospheric relief associated with fracture zones and ponded plume material. Geochem Geophys Geosyst 3: doi:10.1029/2002GC000376
Solomatov VS, Moresi L (2000) Scaling of time-dependent stagnant lid convection: Application to small-scale convection on Earth and other terrestrial planets. J Geophys Res 105:21795–21817
Solomatov VS, Moresi L (2002) Small-scale convection in the D'' layer. J Geophys Res 107: doi:10.1029/2000JB000063
Sparrow EM, Husar RB, Goldstein RJ (1970) Observations and other characteristics of thermals. J Fluid Mech 41:793–800
Tackley PJ (1998) Three-dimensional simulations of mantle convection with a thermo-chemical basal boundary layer: D''? In: Gurnis M, Wysession M, Knittle E, Buffett B (eds) The core-mantle boundary region, Am Geophys Union, Washington DC, pp 231–253
Tackley PJ (2002) Strong heterogeneity caused by deep mantle layering, Geochem Geophys Geosyst 3: doi:10.1029/2001GC000167
Tamai N, Asaeda T (1984) Sheetlike plumes near a heated bottom plate at large Rayleigh number. J Geophys Res 89:727–734
Tan E, Gurnis M, Han L (2002) Slabs in the lower mantle and their modulation of plume formation. Geochem Geophys Geosyst. 3: doi:10.1029/2001GC000238
Thompson PF, Tackley PJ (1998) Generation of mega-plumes from the core-mantle boundary in a compressible mantle with temperature-dependent viscosity. Geophys Res Lett 25:1999–2002
Thompson RN, Gibson SA (2000) Transient high temperatures in mantle plume heads inferred from magnesian olivines in Phanerozoic picrites. Nature 407:502–505
Trompert RA, Hansen U (1998) On the Rayleigh number dependence of convection with a strongly temperature-dependent viscosity. Phys Fluids 10:351–360
Van Hunen J, Zhong S (2003) New insight in the Hawaiian plume swell dynamics from scaling laws. Geophys Res Lett 30: doi:10.1029/2003GL017646
Van Keken P (1997) Evolution of starting mantle plumes: a comparison between numerical and laboratory models. Earth Planet Sci Lett 148:1–11

Vasquez PA, Perez AT, Castellanos A (1996) Thermal and electrohydrodynamic plumes. A comparative study. Phys Fluids 8:2091–2096

Vatteville J (2004) Etude expérimentale des panaches : structure et evolution temporelle. Mémoire de DEA, ENS Lyon/IPG Paris

Vogt PR (1971) Asthenosphere motion recorded by the ocean floor south of Iceland. Earth Planet Sci Lett 13:153–160

Weeraratne D, Manga M (1998) Transitions in the style of mantle convection at high Rayleigh numbers. Earth Planet Sci Lett 160:563–568

Weinstein SA (1995) The effect of a deep mantle endothermic phase change on the sturcture of thermal convection in silicate planets. J Geophys Res 100:11719–11728

Weinstein SA, Olson PL (1989) The proximity of hotspots to convergent and divergent plate boundaries. Geophys Res Lett 16:433–436

Wessel P (1993) Observational constraints on models of the Hawaiian hot spot swell. J Geophys Res 98:16,095–16,104

White RS, McKenzie DP (1995) Mantle plumes and flood basalts. J Geophys Res 100:17543–17585

Whitehead JA, Luther DS (1975) Dynamics of laboratory diapir and plume models, J Geophys Res 80:705–717

Whitehead JA (1982) Instabilities of fluid conduits in a flowing Earth – are plates lubricated by the asthenosphere? Geophys J R Astron Soc 70:415–433

Whitehead JA (1988) Fluid models of geological hotspots. Ann Rev Fluid Mech 20:61–87

Whitehead JA, Helfrich KR (1988) Wave transport of deep mantle material. Nature 336:59–61

Williams Q (1998) The temperature contrast across D''. In: Gurnis M, Wysession M, Knittle E, Buffett B (eds) The core-mantle boundary region, Am Geophys Union, Washington DC, pp 73–81

Wilson TJ (1963) Evidence from islands on the spreading of the ocean floor. Can J Phys 41:863–868

Worster MG (1986) The axisymmetric laminar plume: asymptotic solution for large Prandtl number. Stud Appl Maths 75:139–152

Xi H-D, Lam S, Xia K-Q (2004) From laminar plumes to organized flows: the onset of large-scale circulation in turbulent thermal convection. J Fluid Mech 503:47–56

Yuen DA, Peltier WR (1980) Mantle plumes and the thermal stability of the D'' layer. Geophys Res Lett 7:625–628

Zhao D (2001) Seismic structure and origin of hotspots and mantle plumes. Earth Planet Sci Lett 192:251–265

Zhong S, Watts AB (2002) Constraints on the dynamics of mantle plumes from uplift of the Hawaiian Islands. Earth Planet Sci Lett 203:105–116

Zhong S, Hager BH (2003), Entrainment of a dense layer by thermal plumes. Geophys J Int. 154:666–676

Tracing the Hawaiian Mantle Plume by Converted Seismic Waves

Xiaohui Yuan, Xueqing Li, Ingo Wölbern and Rainer Kind

GeoForschungsZentrum Potsdam, Telegrafenberg, 14473 Potsdam, Germany

Abstract

Hotspots and seamount chains belong to the fundamental components of the global plate tectonics. The Hawaii-Emperor seamount chain is believed to have been created when the oceanic lithosphere continuously passed over a stationary mantle plume located under the Hawaiian islands. Hot buoyant material rises from great depth within a fixed narrow stem to the surface, penetrating the moving lithosphere and creating the volcanic seamounts and islands. We use teleseismic converted waves to look at the seismic velocity anomalies caused by the mantle plume from surface down to depths of the mantle transition zone. We applied the shear-wave (*S*) receiver function technique to map the thickness of the lithosphere. We found a gradual lithospheric thinning from the island of Hawaii (~100 km thickness) along the island chain to Kauai (~60 km thickness) with a width of about 300 km. In this zone our data favour the rejuvenation model, in which the plume returns the lithosphere to conditions close to the ocean ridge. The analysis of the *P*-to-*S* converted waves indicates an additional zone of very low *S*-wave velocity starting at a depth of 130-140 km beneath the central part of the island of Hawaii. We also see in the *P*-to-*S* conversions that the upper mantle transition zone is thinned by up to ~40 km to the southwest of the island of Hawaii. We interpret these observations as localized effects of the Hawaiian plume conduit in the asthenosphere and the mantle transition zone with an excess temperature of 300 °C. The large variation in the transition zone thickness suggests a lower mantle origin of the Hawaiian plume.

1 Introduction

The Hawaii-Emperor chain consists of approximately 100 volcanic islands, atolls, and seamounts extending ~6000 km northwest from the active volcanic island of Hawaii to the 75-80 Ma old Emperor seamounts near the Aleutian trench (Fig. 1). The younger southeastern part of the chain is situated on the Hawaiian swell, a ~1200 km broad, anomalously shallow region of the ocean floor, extending from the island of Hawaii to the Midway atoll (~2100 km long) and with a pronounced associated geoid anomaly. The maximum of both the topography and geoid anomaly occurs around the youngest island and both decrease to the northwest.

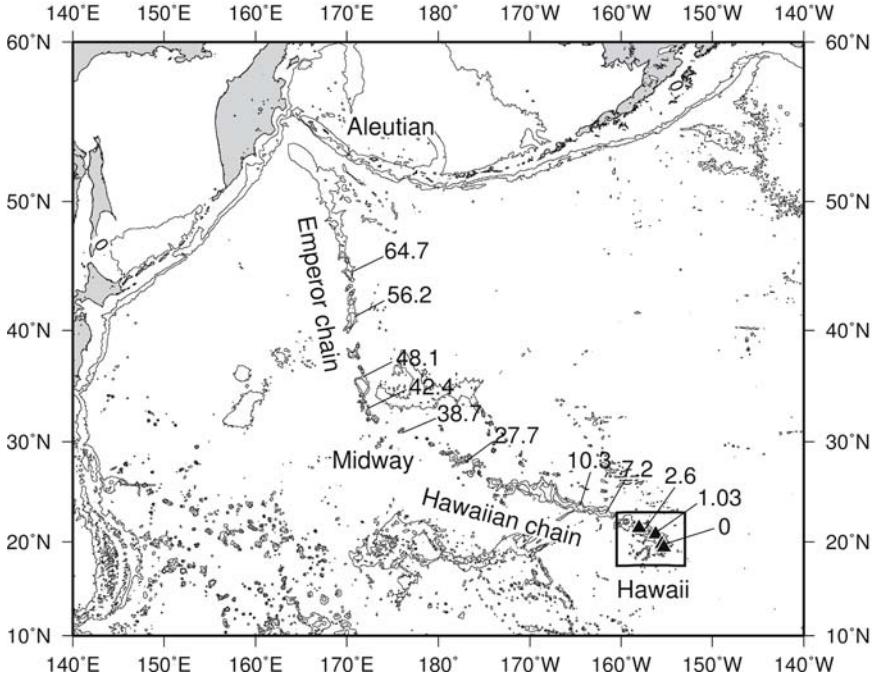

Fig. 1. Topographic map of the North Pacific showing the Hawaiian-Emperor volcanic chains. The numbers denote the ages of the seamounts in million years (Ma) and the islands along the chains (Raymound et al. 2000). Seismic stations used in this study are marked by triangles

The progressive decrease in age along the Hawaiian-Emperor volcanic chain is generally believed to result from the continuous motion of the Pacific lithosphere over a stationary mantle plume (Wilson 1963, Morgan 1971, Morgan et al. 1995). The Hawaiian plume is proposed to originate

from the lower mantle (Morgan 1971, Ji and Nataf 1998), or even from the core-mantle boundary (Russell et al. 1998). Hot material would rise from the root moving up within a narrow stem through the upper mantle. The radius of the plume conduit is thought to be thin, only 100-200 km, and the excess temperature within the plume is expected to be more than 200 °C (Nataf 2000). At shallow depth (<200 km), plume material may spread laterally over more than 1000 km, yielding a low velocity anomaly.

The plume hypothesis predicts several seismic features. In the mantle transition zone, a topographic anomaly of the 410 and 660 km discontinuities (the 410 and 660, respectively) may exist in the immediate vicinity of the upwelling plume column, with scales of a few hundred kilometres. The magnitude of the anomaly should be determined by the thermal nature of the phase boundaries and the excess temperature of the plume. For a 200 °C excess temperature the 410 would be depressed by ~15 km and the 660 would be uplifted by ~10 km (Bina and Helffrich 1994), resulting in a thinning of the transition zone by 20-30 km. The plume itself, consisting of thermally buoyant materials and the presence of a certain amount of melt, has lower seismic velocities than the surrounding mantle. In the upper mantle a 200 °C temperature increase will lower the *P*- and *S*- wave velocities (v_P, v_S) by 0.9-1.8% and 1.2-2.5%, respectively. In the lower mantle the correlation is weaker (0.5% and 1.0% for v_P and v_S, respectively) (Karato 1993). These velocity anomalies may possibly be directly detected with seismic means, such as tomography. The hot plume materials arising upon the base of the lithosphere may produce thermal and chemical reservoirs and viscous flow in the direction of plate motion, causing modification and reworking of the lithosphere. There are several hypotheses about the interaction of the plume with the lithosphere. The thickness and seismic velocity of the lithosphere may be observed by surface waves or seismic converted waves.

Although the existence of a thermal mantle plume beneath Hawaii is indicated by geochemical and gravity observations (Hofmann 1997, Watson and McKenzie 1991, Ribe and Christensen 1994), direct seismic observations are still rare. Most teleseismic tomography studies suffer from low resolution power (generally at ~1000 km) because of the scarcity of local seismic stations, especially ocean bottom seismometers (e.g., Grand 1994, Bijwaard et al. 1998). The global mapping of the mantle transition zone is not able to show the small-scale plume-related topography of the discontinuities (e.g., Flanagan and Shearer 1998). The absence of seismic observations led to a number of other alternatives to explain the origin of hotspots (e.g., Anderson 2000, Foulger and Natland 2003). Recently achieved improvements in resolution appear to have allowed seismology to image the deep root of the mantle plumes. In the lowermost mantle evidence has

been found showing that immediately above the core-mantle boundary southwest to Hawaii there exits a strong low shear-wave velocity anomaly with distinct anisotropic pattern over distances of only several hundred kilometres, indicating an origin of the Hawaiian plume (Russell et al. 1998). Teleseismic tomography with improved resolution observed a vertical channel of low velocity anomaly beneath Hawaii evidently continuing into the lower mantle (Montelli et al. 2004, Zhao 2004).

In the uppermost mantle, surface wave tomography shows a progressive thickening of the oceanic lithosphere towards the northwest beneath the central Pacific and a very pronounced anisotropic anomaly centred in the asthenosphere below Hawaii (Ekström and Dziewonski 1998, Ekström 2000). An average seismic structure of a 100 Ma old oceanic lithosphere was derived southwest of the islands of Oahu and Hawaii from preliminary data of surface wave dispersion with an array of ocean bottom seismometers, and a significant velocity reduction at asthenospheric depths closer than 300 km to the island chain was found (Laske et al. 1999). Regional teleseismic tomography using stations deployed on the islands (Wolfe et al. 2002) did not resolve a cylindrical plume conduit beneath the island of Hawaii because of the unsuitable distribution of stations and earthquakes. Instead, they found a secondary melting zone in the asthenosphere beneath Maui and Molokai. Lithospheric thickness is estimated to be ~70 km beneath the island of Oahu from converted body waves (Bock 1991), and 85-100 km from Rayleigh wave dispersion to the northwest of Oahu (Woods et al. 1991, Woods and Okal 1996) and between the islands of Hawaii and Oahu (Priestley and Tilmann 1999). This lithospheric thickness differs little from the thickness of 80-90 Ma undisturbed oceanic lithosphere (Nishimura and Forsyth 1988).

Seismic converted waves (with help of the receiver function method) provide a powerful and robust way to study the seismic discontinuities underneath the stations, which are caused directly or indirectly by the mantle plume. The receiver function method analysing *P*-to-*S* converted waves has been used for about 30 years (Burdick and Langston 1977). Recently a similar technique has been developed to analyse *S*-to-*P* converted waves (Farra and Vinnik 2000, Vinnik and Farra 2002). Therefore the two methods are named *P* and *S* receiver functions, respectively. Here we show the anomalies of the Hawaiian mantle plume with both methods.

2 Method and Data

We use *P* and *S* receiver function techniques to study crust and upper mantle discontinuities beneath the stations. Fig. 2 shows the ray paths of the *P*-to-*S* (*Ps*) and the *S*-to-*P* (*Sp*) converted waves along with the synthetic *P* and *S* receiver functions.

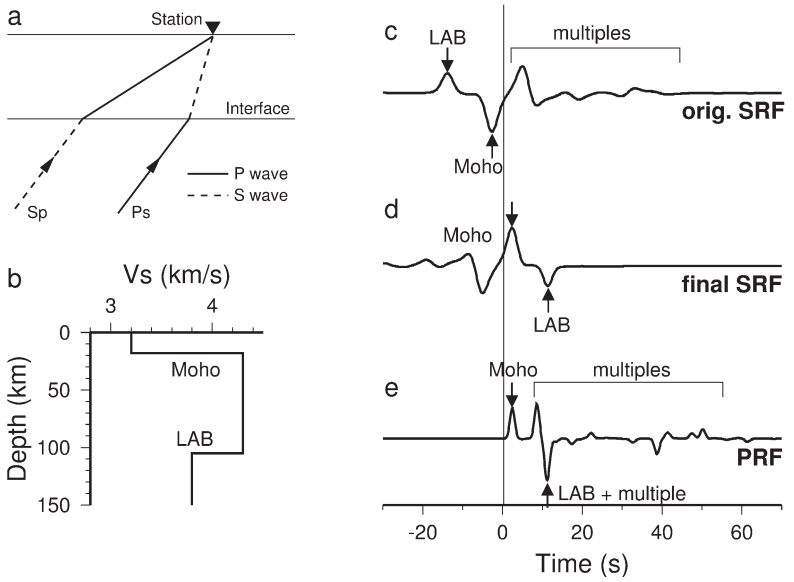

Fig. 2. (a) Sketch showing ray paths of teleseismic *P*-to-*S* (*Ps*) and *S*-to-*P* (*Sp*) converted waves below a station. Note that the piercing point of the *Sp*-wave is offset farther away from the station than that of the *Ps*-wave. (b) Velocity model for calculation of *P* and *S* receiver functions. The Moho and the lithosphere-asthenosphere boundary (LAB) are included in the model. (c) Synthetic *S* receiver function, in which the primary conversions arrive in front of the *S* (time zero) and the multiples are later than the *S*. (d) The final *S* receiver function after reversal of the amplitude polarity and the time axis from the *S* receiver function shown in (c). A moveout correction was also applied with a reference slowness of 6.4 s deg^{-1}. (e) Moveout corrected *P* receiver function calculated with model in (b)

The traditional receiver function method detects seismic discontinuities by identifying *P*-to-*SV* converted waves in the coda of *P*-waves. The converted *S*-wave travels more slowly to the stations than the originating *P*-wave does, and therefore, will be recorded after the direct *P*-wave in the *P*-wave train. The converted energy is usually weak (only several percent of the *P*-wave energy) and can be isolated from the *P*-wave with the help of data processing techniques (e.g., Yuan et al. 1997). We measure the differ-

ential time between the converted *S*- and the direct *P*-waves. Along with the primary conversions, multiple phases reverberating between the discontinuity and the Earth's surface can frequently be observed (see Fig. 2e). On one hand these multiples are useful in improving the constraint of crustal Poisson's ratio and thickness (Kind et al. 2002), on the other hand they interfere with the *Ps* conversions from the deeper lithosphere and asthenosphere.

While *P* receiver function analysis has become a routine method for studying the Moho and upper mantle boundaries, observations of *S*-to-*P* conversions are still much more rare. A *Sp* conversion is generated when an incoming *S*-wave penetrates a discontinuity beneath a seismic station. The *Sp* converted waves arrive at the station earlier than the main incoming *S*-waves. Usually *S*- and *SKS*-phases can be used for the *S* receiver functions. The *Sp* converted phases at a relatively shallow discontinuity such as the Moho and lithosphere-asthenosphere boundary are best identified at epicentral distances of 55-85°. For deeper discontinuities such as the mantle transition zone discontinuities, only earthquakes at greater distances can be used. The *Sp* conversions for earthquakes at shorter distances do not reach those depths. At distances larger than 85°, *SKS*-waves, which have much steeper incidence angles, can be used for the whole upper mantle structure.

The *S* receiver function analysis is practically identical to the *P* receiver function analysis. To separate the weak *Sp*-wave from the *S*-wave, we rotate the *Z*-, *N*- and *E*-components into the local *P*, *SV* and *SH* system. After deconvolving the *P*-component by the *SV*-component, we obtain the *S* receiver functions. The converted waves arrive earlier than the *S*-wave in the *S* receiver functions and later than the *P*-waves in the *P* receiver functions, whereas all the multiple reverberations appear later than the main reference phases in both the *P* and *S* receiver functions (see Fig. 2c-e). That means for the *S* receiver functions the primary conversions are separated from the multiples by the *S*-wave arrival, while in the *P* receiver functions they interfere with each other in the coda of *P*-waves. The coefficients of the *Sp* and *Ps* conversions have different signs. For an interface of increasing velocity with depth such as the Moho, the *Ps* has positive amplitude (Fig. 2e) whilst the *Sp* has negative amplitude (Fig. 2c). To make both datasets directly comparable, in the next step, we reversed the polarity of the *S* receiver function amplitudes as well as the time axis (Fig. 2d). In the resulting *P* and *S* receiver functions, positive amplitudes indicate velocity contrasts with velocity increasing downwards and vice verse. The time difference between the *Sp*- and *S*-wave can be measured in a single trace, if the data quality is good enough. Otherwise we use summation. The time difference depends on the ray parameter (distance moveout), which can be

corrected for by using a reference ray parameter and reference Earth model (moveout correction). To enable easy comparison of *Sp* and *Ps* times at a station, we applied the same reference slowness of 6.4 s deg^{-1} to both types of data. Times may be converted into the depth domain using a reference velocity model (e.g., the iasp91). For details see Yuan et al. (2006).

The ray paths and conversion (piercing) points of *P* and *S* receiver functions differ significantly (see Fig. 2a). Piercing points of *S* receiver functions occur much further away from the stations. *S* receiver functions are usually much noisier than *P* receiver functions, because *S*-waves are later arrivals. However, *Sp* data have the big advantage in that they are free of disturbing multiples. This advantage is very important for studying the lithosphere-asthenosphere boundary, since this boundary is almost invisible in *P* receiver functions due to crustal multiples arriving at nearly the same time (see Fig. 2b).

We used teleseismic *P*- and *S*-wave data of permanent seismic broadband stations KIP (GEOSCOPE) on Oahu, MAUI (GEOFON) on Maui and POHA (USGS) on the island of Hawaii, as well as the network of six temporary broadband stations (HIBSN) on the Island of Hawaii (Figs. 1 and 3) to look for a possible signature of the Hawaiian plume in *P*-to-*S* converted waves. HIBSN was operated jointly by the University of Cambridge and the US Geological Survey.

3 Observations

3.1 Topography of the mantle discontinuities - evidence for plume track in the mantle transition zone

The 410 and 660 km mantle discontinuities (short 410 and 660) can be comfortably observed with *P*-to-*S* converted waves. Synthetic calculations show that the *S*-to-*P* converted waves at the 410 and the 660 can only be observed at epicentral distances greater than 80 degrees (Yuan et al. 2006). In this distance range there is not much *S*-wave data available. Therefore we use *P* receiver functions to look at these discontinuities here. We compare the *P* receiver functions of stations KIP and HIBSN. An acausal 3-pole, 10-s low-pass filter was applied to the data to reduce the noise. Fig. 3 shows the individual receiver functions from station KIP (a) and HIBSN (b). They are moveout corrected for *Ps* at a slowness of 6.4 s deg^{-1} and sorted by back azimuth. On the top of each panel are the linear summations of *P* receiver functions for each station. Both the 410 and the 660 can be clearly seen in the summations as well as in the most individual traces (marked with *P410s* and *P660s*). At both stations the *P410s* arrives ~3 s

later (~47 s delay time) than predicted by the iasp91 model (~44 s). At station KIP the *P660s* is also delayed by ~2 s (at ~70 s). The thickness of the mantle transition zone can be estimated by the differential arrival times of the *P410s* and the *P660s*. The differential time at KIP is ~23 s, which is slightly less than the iasp91 value (24 s). In the summation trace of station HIBSN the *P660s* arrives at time of ~67 s. The differential time of the two discontinuities is ~20 s (~4 s less than the iasp91 value), giving an estimate of the transition zone thickness to be thinned by 30-40 km. In the individual trace display an uplift of the 660 can be obviously seen to the southwest backazimuth.

The simultaneous time delay of both the *P660s* and *P410s* phases observed at KIP could be interpreted with a low-velocity anomaly at shallow depth (less than 410 km) without changing the transition zone thickness. Modelling of melting parameter of the Hawaiian plume (Ribe and Christensen 1999) shows that due to the motion of the Pacific plate, the thermal anomaly could have a large extension along the axis of the swell to the northwest. Beneath KIP, which is about 600 km away from the assumed plume center around the island of Hawaii, the hot material (>1400 °C) could exist to a depth of more than 140 km and at 100 km depth. Its lateral extension could be more than 800 km across the swell. The hot material at shallow depths could reduce the v_P and v_S significantly, causing time delay for both the *P410s*- and *P660s*-phases. Assuming the mantle plume has a mushroom form, the lateral temperature anomaly at the transition zone depths will be limited in the immediate vicinity of the plume conduit. Outside this region, the depth of the transition zone discontinuities will not be influenced by the plume.

We interpret the thinning of the transition zone beneath HIBSN, probably mainly caused by uplift of the 660, with a high temperature anomaly in the transition zone associated with the presence of the mantle plume. The circle in Fig. 3c marks the piercing points at a depth of 660 km, where the largest 660 anomaly is found. Due to the lack of data right beneath and to the southeast of HIBSN, the radius of the plume is not well constrained. Within the circle the differential delay time of the *P660s* and *P410s* is averaged to be 3-5 s less than the global average. The corresponding 30-50 km thinning of the transition zone could be caused by a 200-350 °C higher temperature than the surrounding mantle. The differential times of *P660s* and *P410s* in the summation traces are 4 s smaller at HIBSN than at KIP, implying a temperature increase of about 300 °C within the transition zone beneath HIBSN. This temperature anomaly could be caused by the Hawaiian plume traversing the mantle transition zone. Similar observations have been made at other oceanic hotspots such as Iceland (Shen et al. 1998). However, by comparing the magnitudes of the maximum transition zone

thinning, the temperature anomaly beneath Hawaii is at least 100 °C higher than below Iceland at the same depth.

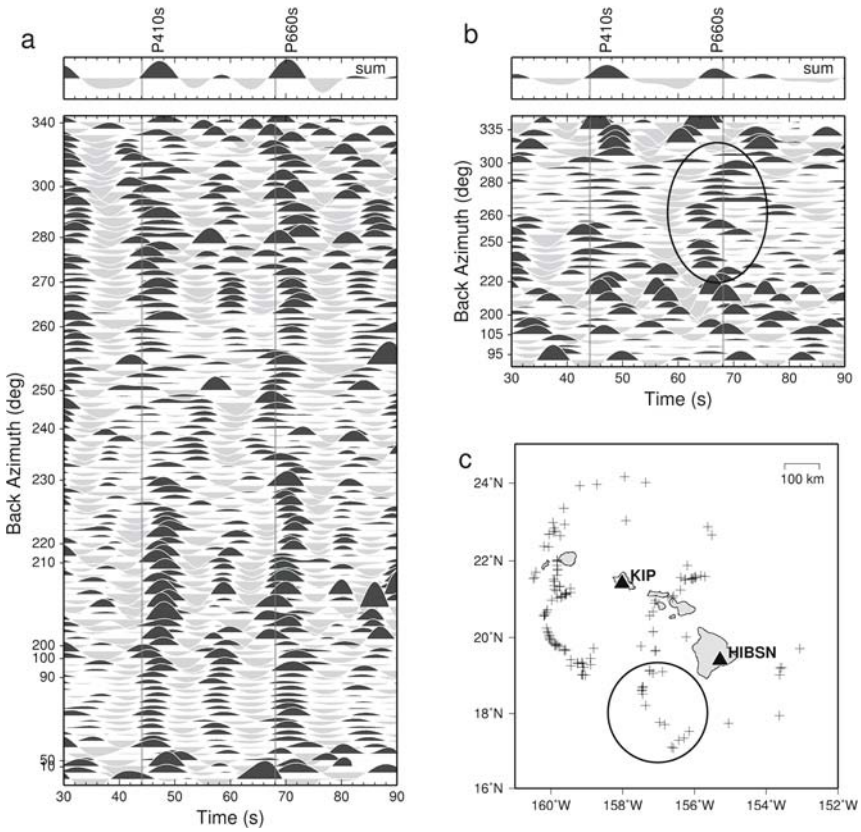

Fig. 3. *P* receiver functions of the KIP (a) and HIBSN (b) stations, sorted by back azimuth. The traces have been low-pass filtered with a corner frequency of 10 s and are shown in the time window of 30-90 s after the *P* arrival. Positive amplitudes are shaded in black, representing contrasts of increased velocity with depth. On the top of each panel is the summation trace for each station. The 410- and the 660-km discontinuities can be clearly seen and labelled. The grey thin lines mark the timings predicted by the iasp91 model. The piercing points at the depth of 660 km are plotted in (c). Circle marks the piercing points southwest of the island of Hawaii, where the 660-km discontinuity is obviously uplifted

3.2 A very low velocity zone in the asthenosphere - evidence for a plume conduit

We use a relatively higher frequency band (5-s low pass) of *P* receiver functions to look at the shallow mantle. Fig. 4 shows the stacked receiver functions of station KIP and HIBSN within a 35 s time window. At KIP the Moho phase is clearly seen at about 2.5 s and is followed by a negative phase at about 8 s. This negative phase can be interpreted as the boundary of lithosphere and asthenosphere at a depth of about 60 km, corresponding well to previous results (Bock 1991). However, as stated earlier, this phase can also be caused by crustal reverberations (see also Fig. 2e). Therefore we leave this problem of lithospheric thickness to the *S* receiver function in the next section, which is free of multiples. Waveforms of the receiver functions at HIBSN in the first 35 s delay time are different from those at KIP. At HIBSN, a significant negative phase appears at about 14 s, followed by a positive phase at ~18 s. The negative phase cannot possibly be caused by any crustal multiples, which are expected to arrive earlier (see supplementary information in Li et al. 2000). In Fig. 4c we calculated synthetic *P* receiver functions, showing that the suggested simple models fit the data fairly well. In order to see if it is possible to use *S* receiver function to better constrain this low-velocity layer (LVZ), we plotted the *Sp* piercing points and compared them with the *Ps* piercing points (see Fig. 7, for example). The *Sp* piercing points sample a much broader area. Unfortunately, the *S* receiver functions do not sample this LVZ. In this section we will concentrate our study to the *P* receiver functions.

The existence of a pronounced LVZ at depth more than 130 km is a robust observation of the *P* receiver functions at HIBSN, although the bottom of the LVZ could not be well constrained. A very low shear-wave velocity (less than 4 km s^{-1}) in the ultramafic mantle at depths larger than 100 km cannot be explained without the presence of significant partial melt, even if the effect of anelasticity on seismic velocity is considered (Sobolev et al. 1996) and the water content of olivine and pyroxene is assumed to be high (Karato and Jung 1998). This observed depth of the LVZ is consistent with the estimate of the depth and extent of the melt production region within the plume (~90-150 km depth) found by modelling the total melt production, residual depth anomaly, and geoid anomaly (Watson and McKenzie 1991). It also agrees with the depth of the deepest region of intensive partial melting below Hawaii (100-130 km) suggested by the investigation of the primary melt inclusions in olivine crystals (Sobolev and Nikogosian 1994). The deepest location of partial melting can be expected within the plume conduit where the temperature and water content of the minerals are highest. Therefore, the LVZ should indicate the central part of

the Hawaiian plume conduit. A few percent of partial melting is achieved below 130-140 km depth, and this, together with the high temperature and high water content of the plume material results in the observed very low shear-wave velocity.

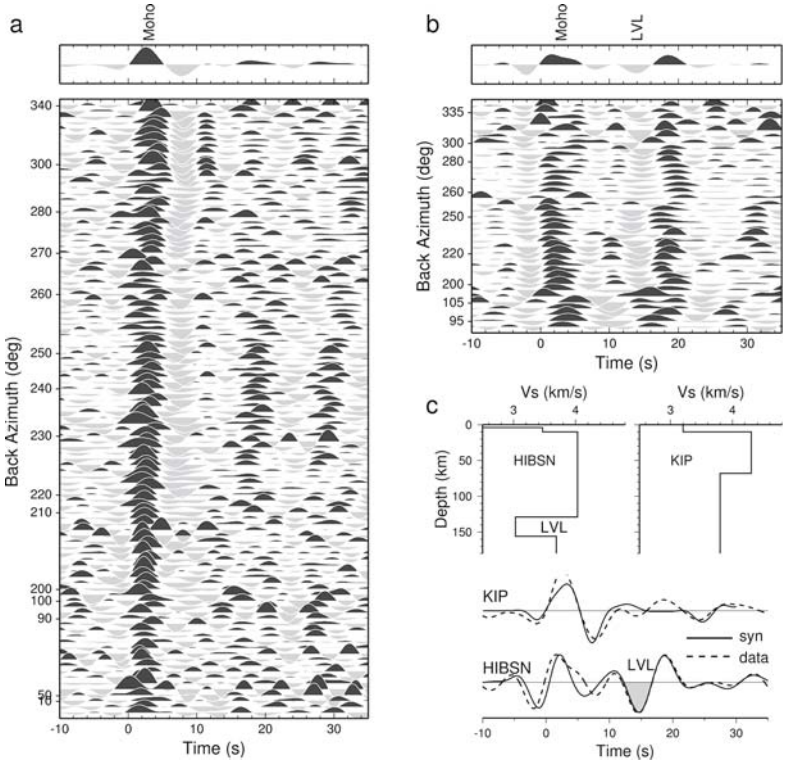

Fig. 4. The P receiver functions of the KIP (a) and HIBSN (b) stations, low-pass filtered with a corner frequency of 5 s, and sorted by back azimuth. (c) Synthetic *P* receiver functions calculated for simple models with a lithosphere thickness of 60 km below KIP and a low-velocity layer at 130 km depth below HIBSN

3.3 Variation in the lithosphere thickness - rejuvenation of the lithosphere by the mantle plume

The Hawaiian swell is a large area of anomalously shallow ocean floor with a pronounced geoid anomaly surrounding the Hawaiian chain (Ribe and Christensen 1994). Although there is a general agreement that the Hawaiian swell was created due to the thermomechanical processes related to plume-lithosphere interactions, various models have been proposed to explain the generating mechanism of the Hawaiian swell. The dynamic sup-

port model proposes that the swell is held up by dynamic pressure of the ascending mantle plume at the base of the lithosphere (Ribe and Christensen 1999, Sleep 1990). The thermal rejuvenation model holds that the oceanic lithosphere is heated from below when it passes the plume, causing lithospheric thinning that supports the isostatic uplift of the sea floor (Detrick and Crough 1978). In the underplating model the extracted basaltic melt of the plume material underplates the base of the lithosphere (Jordan 1979, Robinsen 1988, Morgan et al. 1995). The thickness of the lithosphere is a key parameter to choose among these models. Different models predict different thicknesses of the lithosphere. In the dynamic support model, the lithospheric thickness along the swell is relatively stable. The thermal rejuvenation model predicts a thinner lithosphere after passing the plume, while the underplating model predicts a thicker one.

The *S* receiver function method is suitable to study the discontinuities at depths of the lithosphere and asthenosphere. At these depths the *P* receiver functions are contaminated by the strong crustal multiples. Teleseismic *S*-waves have been selected for earthquakes with epicentral distances between 55° and 85° to calculate *S* receiver functions. Because only a few *SKS*-waves have been recorded, they are not included in this study. Fig. 5 shows the stacked *S* receiver functions for a section NW-SE along the island chain (Fig. 5b) and a section SW-NE perpendicular to it (Fig. 5c). The sections are formed by stacking individual traces with piercing points at 100 km depth with bins of 30 km and an overlapping of 10 km. Before summation, all traces have been corrected for their different epicentral distance or slowness with a reference slowness of 6.4 s deg^{-1}. A bandpass filter of 7-20 s was applied. We reversed the polarity of amplitudes and the time axis. A clear negative phase (labelled LAB), caused by velocity reduction downwards, is identified in Fig. 5b,c. Along the island chain (Fig. 5b) the LAB shallows to the northwest from the island of Hawaii (12 s/108 km) to Kauai (6 s/54 km). Perpendicular to the island chain on the SW-NE section (Fig. 5c), the lithosphere has the minimum thickness directly beneath the island chain (8 s/72 km), and it thins symmetrically on both sides to 108 km (12 s).

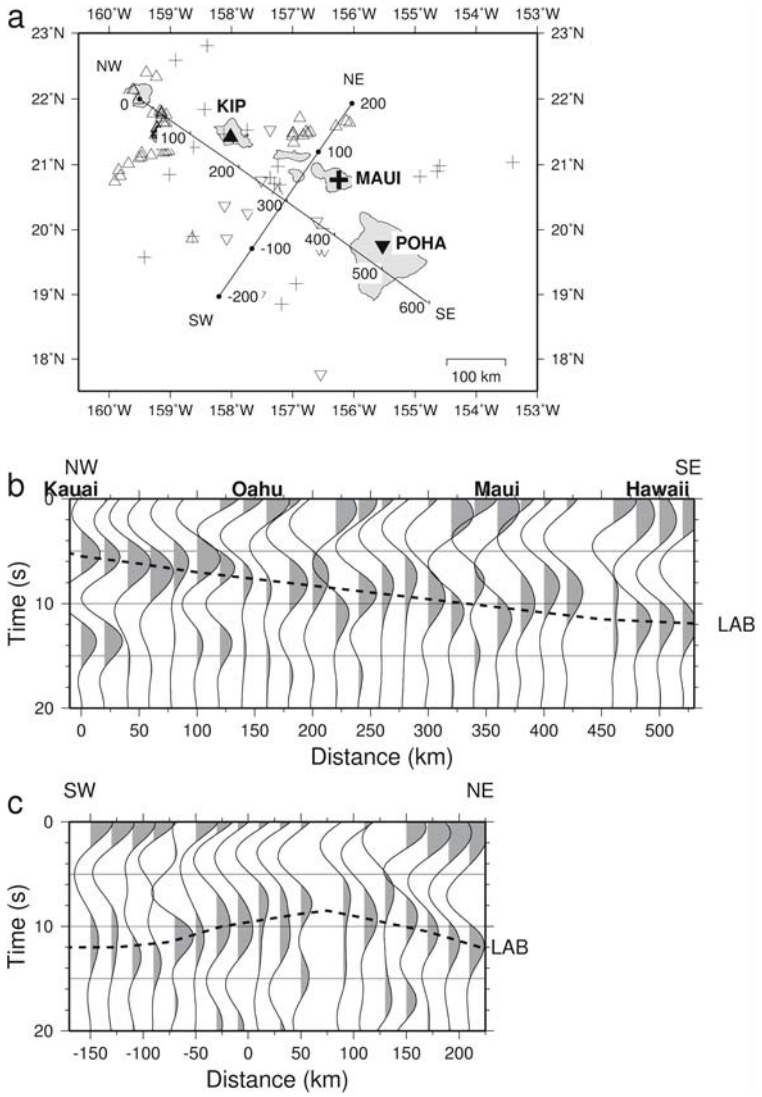

Fig. 5. (a) Piercing points of *S* receiver functions at 100 km depth (same symbols as stations). Two lines labeled NW-SE and SW-NE indicate the two sections, onto which the *S* receiver functions are projected. Section NW-SE is along the island chain (b) while section SW-NE is perpendicular to the chain (c) Zero time corresponds to the *S* arrival. Time scale is reversed. Moveout corrections are applied (reference slowness of 6.4 s deg^{-1}) before stacking. In section NW-SE (b) all *Sp* data are used that cover an up to 200 km broad sampling region at 100 km depth on each side of the section. In section SW-NE (c) only data southeast of KIP are used. A 7-20 s bandpass filter is applied to suppress the noise. LAB indicates the lithosphere-asthenosphere boundary

S receiver functions have also been stacked for each of the three stations (dashed lines in Fig. 6b). While stations KIP and POHA mainly sample the regions of elevated and not elevated LAB, respectively, MAUI samples a broader region with a dramatic change of the lithospheric thickness (see Fig. 5a). Therefore the LAB phase is smeared and unpronounced in the summation trace. We calculated synthetic *S* receiver function (solid lines in Fig. 6b) for models shown in Fig. 6a. The synthetic data match the observed *S* receiver functions reasonably well. The negative amplitudes labelled LAB can be reproduced using these models. Due to the strong remaining S-wave energy at time zero and the low-frequency content in the data, the crustal thickness could not be well constrained. Thus the crustal thickness in the models (~10 km beneath Oahu and ~20 km beneath Hawaii) should be ignored. Active-source seismic data have revealed a 12 km deep Moho in the study area (Zucca and Hill 1980, Lindwall 1988).

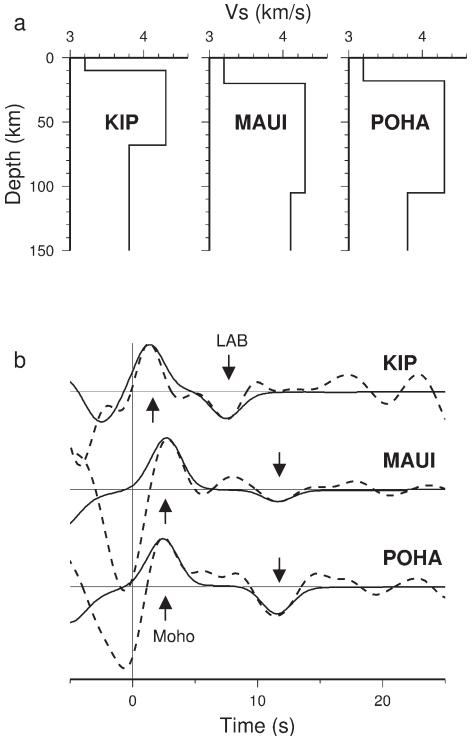

Fig. 6. Synthetic *S* receiver functions (solid line) calculated for models with different lithosphere thicknesses. The large amplitudes around zero time are amplitudes of *S*-waves projected onto the observed, stacked *S* receiver functions (dashed lines), resulted by imperfect coordinate rotation and should be ignored for the modelling

We compared the *S* receiver functions with conventional *P* receiver functions at the same stations and found good agreements. Moveout corrected *Sp* and *Ps* data of each station are stacked and shown in Fig. 7b. A closely correlated negative phase is marked in the *S* and *P* receiver function traces at each station and is interpreted as conversion from the lithosphere-asthenosphere boundary. Because of different locations of the piercing points (Fig. 7a) and interference with the crustal multiples in the *P* receiver functions, the marked phases are not completely identical.

The observation of a variation in lithospheric thickness along the island chain provides a new insight on plume-lithosphere interaction and the origin of the Hawaiian swell. While the Pacific plate is continually overriding the Hawaiian plume with a velocity of 7-8 cm y^{-1} (DeMets et al. 1990), the ascending plume material strikes the base of the lithosphere, spreads out laterally and forms a viscous flow mainly in the direction of plate motion. Hot plume material begins to undergo thermal convection and heats the lithosphere from below. A substantial amount of heat is trapped in the lower lithosphere. The increased temperature reduces the velocity of elastic waves, erodes and thins the lithosphere. In the vicinity of the present plume centre, only the lowest part of the lithosphere is heated and the lithospheric thickness does not change much with respect to that of a 90-100 Ma old oceanic plate (Priesley and Tilmann 1999). As time increases, more and more material of the lower part of the lithosphere is heated and the lithosphere-asthenosphere boundary becomes shallower. After 3-4 Ma of heating the thinnest lithosphere of 50-60 km is achieved beneath Oahu and Kauai which is about 400 km away from the current plume centre. Further away, at Midway, which passed the plume centre about 28 Ma ago, the lithosphere reaches a thermal balance and thickens again (Woods et al 1991, Woods and Okal 1996). Estimates of subsidence and paleolatitude histories derived from stratigraphic sequences of carbonate platforms of an ODP drilling leg also indicate a substantial amount of thermal resetting of the oceanic lithosphere (Larson et al. 1995). The amount of thermal age loss may be a function of the locations relative to the plume. We estimate that the Hawaiian plume has gradually reheated up to 50 km of the lower lithosphere within the last 3-4 Ma in an area of 500 x 300 km^2 along the island chain. Our data favours the rejuvenation model below the central part of the Hawaiian swell. However, because the lateral extent of the lithospheric thinning is significantly smaller than the extent of the Hawaiian topographic swell, a hybrid model combining the dynamic support model and the rejuvenation model is needed to explain the origin of the whole Hawaiian swell.

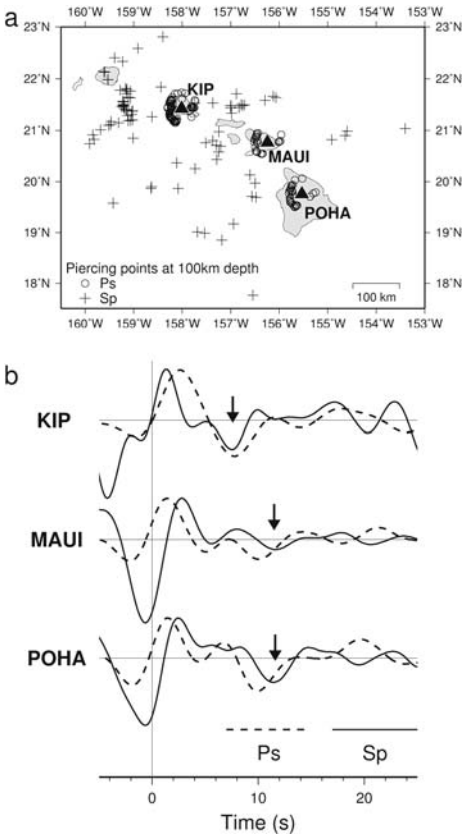

Fig. 7. Comparison of *P* (dashed lines) and *S* (solid lines) receiver functions at stations KIP, MAUI and POHA. Moveout corrections are made for a reference slowness of 6.4 s deg^{-1}. Time scale, as well as the polarity of amplitudes of the *S* receiver functions is reversed in order to be directly comparable with the *P* receiver functions. The *S* waves, as well as the multiple phases, appear at later time (prior to 0 s in this figure), and therefore do not interfere with the *Sp* conversions. Arrows mark the average time of conversion from the lithosphere-asthenosphere boundary. Both types of receiver functions agree reasonably well, considering the different locations of their piercing points and the contamination of the multiples on the *P* receiver functions

4 Conclusions

We have observed a number of features of the mantle plume in the upper mantle beneath Hawaii by using a combination of the *P* and *S* receiver function methods. The *P* receiver function is a powerful technique to study

the discontinuities in the crust, the uppermost mantle and the mantle transition zone. It is however less useful for the discontinuities at depths of the lithosphere and asthenosphere because of the interference with crustal multiples. The *S* receiver functions provide a suitable tool to study the boundary of the lithosphere and asthenosphere because they are free of multiples.

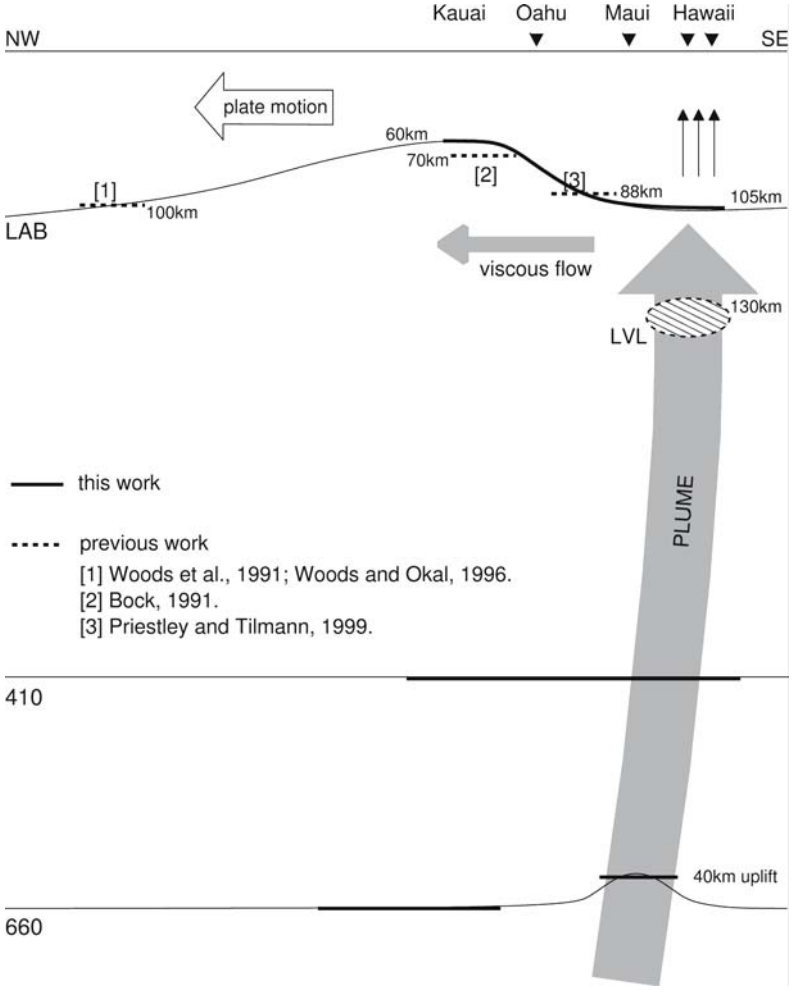

Fig. 8. Sketch summarizing available observations and possible interpretation of the Hawaiian mantle plume

Due to the relatively low passband of the *S*-waves they can not resolve a thin crustal thickness. The use of *S* receiver functions is also limited in studying transition zone discontinuities such as the 410 and the 660, be-

cause at these depths most of the teleseismic *S*-waves with smaller epicentral distances are over the critical angle to be converted into *P*-waves. Instead of *S*-waves, the *SKS*-waves with steeper incidence angles may be used.

In Fig. 8 we summarize our results. The seismic observations are plotted in thick lines. The thick solid lines summarize the results of Li et al. (2000, 2004). The thick dashed lines are previous observations. In the mantle transition zone, where the plume passes through, an uplift of the 660 km discontinuity by ~40 km can be derived from the *P* receiver functions. The uplift of the 660 is the main contribution to the thinning of the transition zone, associated with the hot mantle plume. Derived by the *S* receiver functions, the oceanic lithosphere can be seen to shallow gradually northwestwards along the island chain, suggesting a thermal rejuvenation of the lithosphere by the Hawaiian plume. Below the lithosphere an additional zone of very low velocity starting at a depth of 130-140 km beneath the central part of the island of Hawaii was observed in the *P* receiver functions and indicates a localized partial melting zone within the conduit of the plume.

Acknowledgements

The work is supported by the Deutsche Forschungsgemeinschaft and the GeoForschungsZentrum Potsdam. We thank Joachim Saul for his codes for calculation of synthetic *S* receiver functions and Neil McGlashan for carefully reading the manuscript. Waveform data are provided by GEOFON and IRIS data centres. We appreciate the comments of two anonymous reviewers.

References

Anderson DL (2000) Thermal state of the upper mantle: No role for mantle plumes. Geophys Res Lett 27:3623-3626.

Bijwaard H, Spakman W, Engdahl ER (1998) Closing the gap between regional and global travel time tomography. J Geophys Res 103:30055-30078.

Bina CR, Helffrich G (1994) Phase transition Clapeyron slopes and transition zone seismic discontinuity topography. J Geophys Res 99:15853-15860.

Bock G (1991) Long-period *S* to *P* converted waves and the onset of partial melting beneath Oahu, Hawaii. Geophys Res Lett 18:869-872.

Burdick LJ, Langston CA (1977) Modeling crust-structure though the use of converted phases in teleseismic body-waveforms. Bull Seism Soc Am 67:677-691.

DeMets C, Gordon G, Argus DF, Stein S (1990) Current plate motion. Geophys J Int 101:425-478.

Detrick RS, Crough ST (1978) Island subsidence, hot spots, and lithospheric thinning. J Geophys Res 83:1236-1244.

Ekström G (2000) Mapping the lithosphere and asthenosphere with surface waves: Lateral structure and anisotropy. In: Richards MA, Gordon RG and van der Hilst RD (eds) History and dynamics of global plate motions, AGU monograph, pp 239-255.

Ekström G, Dziewonski AM (1998) The unique anisotropy of the Pacific upper mantle. Nature 394:168-172.

Farra V, Vinnik L (2000) Upper mantle stratification by *P* and *S* receiver functions. Geophys J Int 141:699-712.

Flanagan MP, Shearer PM (1998) Global mapping of topography on transition zone velocity discontinuities by stacking *SS* precursors. J Geophys Res 103:2673-2692.

Foulger GR, Natland JH (2003) Is "hotspot" volcanism a consequence of plate tectonics? Science 300:921-922.

Grand SP (1994) Mantle shear structure beneath the Americas and surrounding oceans. J Geophys Res 99:11591-11621.

Hofmann AW (1997) Mantle geochemistry: the message from oceanic volcanism. Nature 385:219-229.

Ji Y, Nataf H-C (1998) Detection of mantle plumes in the lower mantle by diffraction tomography: Hawaii. Earth Planet Sci Lett 159:99-115.

Jordan TH (1979) Mineralogies, densities and seismic velocities of garnet lherzolites and their geophysical implications. In: Boyd FR and Meyer HOA (eds) The mantle sample: inclusions in kimberlites and other volcanics, Proc 2nd International Kimberlite Conference, AGU monograph, pp 1-14.

Karato S (1993) Importance of anelasticity in the interpretation of seismic tomography. Geophys Res Lett 20:1623-1626.

Karato S, Jung H (1998) Water, partial melting and the origin of the seismic low velocity and high attenuation zone in the upper mantle. Earth Planet Sci Lett 157:193-207.

Kind R, Yuan X, Saul J, Nelson D, Sobolev SV, Mechie J, Zhao W, Kosarev, G, Ni J, Achauer, U, Jiang M (2002) Seismic images of crust and upper mantle beneath Tibet: Evidence for Eurasian plate subduction. Science 298:1219-1221.

Larson R, Erba E, Nakanishi M, Bergersen DD, Lincoln JM (1995) Stratigraphic, vertical subsidence, and paleolatitude histories of leg 144 guyots. In Haggerty JA, Premoli Silva I, Rack F and McNutt MK (eds) Proc ODP, Sci Results, vol 144, College Station, TX, pp 915-933.

Laske G, Morgan JP, Orcutt JA (1999) First results from the Hawaiian SWELL pilot experiment. Geophys Res Lett 26:3397-3400.

Li X, Kind R, Priestley K, Sobolev SV, Tilmann F, Yuan X, Weber M (2000) Mapping the Hawaiian plume with converted seismic waves. Nature 405:938-941.

Li X, Kind R, Yuan X, Wölbern I, Hanka W (2004) Rejuvenation of the lithosphere by the Hawaiian plume. Nature 427:827-829.

Lindwall DA (1988) A Two-Dimensional Seismic Investigation of Crustal Structure Under the Hawaiian Islands Near Oahu and Kauai. J Geophys Res 93:12107-12122.

Montelli R, Nolet G, Dahlen FA, Masters G, Engdahl ER, Hung S-H (2004) Finite-frequency tomography reveals a variaty of plumes in the mantle. Science 303:338-343.

Morgan WJ (1971) Convective plumes in the lower mantle. Nature 230:42-43.

Morgan JP, Morgan WJ, Price E (1995) Hotspot melting generates both hotspot volcanism and a hotspot swell? J Geophys Res 100:8054-8062.

Nataf H-C (2000) Seismic Imaging of Mantle Plumes. Ann Rev Earth Planet Sci 28: 391-417.

Nishimura C, Forsyth D (1988) Rayleigh wave phase velocities in the Pacific with implications for azimuthal anisotropy and lateral heterogeneities. Geophys J Int 94:479-501.

Priestley K, Tilmann F (1999) Shear-wave structure of the lithosphere above the Hawaiian hot spot from two-station Rayleigh wave phase velocity measurements. Geophys Res Lett 26:1493-1496.

Raymond CA, Stock JM, Cande SC (2000) Fast Paloegene motion of the Pacific hotspots from revised global plate circuit constraints. In: Richards MA, Gordon RG and van der Hilst RD (eds) History and dynamics of global plate motions, AGU monograph, pp 359-375.

Ribe NM, Christensen UR (1994) Melt generation by plumes: a study of Hawaiian volcanism. J Geophys Res 99:669-682.

Ribe NM, Christensen UR (1999) The dynamical origin of the Hawaiian volcanism. Earth Planet Sci Lett 171:517-531.

Robinson EM (1988) The topographic and gravitational expression of density anomalies due to melt extraction in the uppermost oceanic mantle. Earth Planet Sci Lett 90:221-228.

Russel SA, Lay T, Garnero EJ (1998) Seismic evidence for small-scale dynamics in the lowermost mantle at the root of the Hawaiian hotspot. Nature 396:255-258.

Shen Y, Solomon SC, Bjarnason IT, Wolfe CJ (1998) Seismic evidence for a lower-mantle origin of the Iceland plume. Nature 395:62-65.

Sleep NH (1990) Hotspots and mantle plumes: Some phenomenology. J Geophys Res 95:6715-6736.

Sobolev AV, Nikogosian IK (1994) Petrology of long-lived mantle plume magmatism: Hawaii, Pacific and Reunion Island, Indian Ocean. Petrology 2:111-144.

Sobolev SV, Zeyen H, Stoll G, Werling F, Altherr R, Fuchs K (1996) Upper mantle temperatures from teleseismic tomography of French Massif Central including effects of composition, mineral reactions, anharmonicity, anelasticity and partial melt. Earth Planet Sci Lett 139:147-163.

Vinnik L, Farra V (2002) Subcratonic low-velocity layer and flood basalts. Geophys Res Lett 29:1049, 10.1029/2001GL014064.
Watson S, McKenzie DP (1991) Melt generation by plumes: a study of Hawaiian mechanism. J Petrol 32:501-537.
Wilson JT (1963) A possible origin of the Hawaiian island. Can J Phys 41:863-868.
Wolfe CJ, Solomon SC, Silver PG, VanDecar JC, Russo RM (2002) Inversion of body wave delay times for mantle structure beneath the Hawaiian islands: results from the PELENET experiment. Earth planet Sci Lett 198:129-145.
Woods MT, Okal EA (1996) Rayleigh-wave dispersion along the Hawaiian Swell: a test of lithospheric thinning by the thermal rejuvenation at a hotspot. Geophys J Int 125:325-339.
Woods MT, Lévêque J-J, Okal EA (1991) Two-station measurements of Rayleigh wave group velocity along the Hawai'ian swell. Geophys Res Lett 18:105-108.
Yuan X, Ni J, Kind R, Mechie J, Sandvol E (1997) Lithospheric and upper mantle structure of southern Tibet from a seismological passive source experiment. J Geophys Res 102:27491-27500.
Yuan X, Kind R, Li X, Wang R (2006) The *S* receiver functions: synthetics and data example. Geophy. J. Int. 165:555-564.
Zhao D (2004) Global tomograpic images of mantle plumes and subduction slabs: insight into deep Earth dynamics. Phys Earth Planet Inter 146:3-34.
Zucca JJ, Hill DP (1980) Crustal Structure of the Southeast Flank of Kilauea Volcano, Hawaii, From Seismic Refraction Measurements. Bull Seismol Soc Am 70:1149-1159

Iceland: The current picture of a ridge-centred mantle plume

Thomas Ruedas[1,2], Gabriele Marquart[3], and Harro Schmeling[1]

[1] Institute of Meteorology and Geophysics, J.W. Goethe University, Frankfurt am Main, Feldbergstr. 47, 60323 Frankfurt/M., Germany
[2] Dansk Lithosfærecenter/Geologisk Institut, Øster Voldgade 10, 1350 København K, Denmark, e-mail: tr@geol.ku.dk
[3] Space Research Organization Netherlands & University of Utrecht, Post box 80021, 3508 TA Utrecht, The Netherlands

Abstract

Currently the North Atlantic ridge is overriding the Iceland plume. Due to several ridge jumps the plume has been virtually ridge-centred since 20–25 Ma giving rise to extensive melting and crust formation. This review gives an overview over the results of the geophysical and, to minor extent, the geochemical research on the general structure of the Icelandic crust and the mantle beneath Iceland. In the first part, results mostly from topography/bathymetry, gravity, seismics/seismology, magnetotellurics, and geodynamical numerical modelling are summarised. They support the main conclusion that the Icelandic crust is up to ca. 40 km thick, whereby the lower crust and the uppermost mantle have an anomalously small density contrast and a gradual transition rather than a well-defined Moho. The interpretation of a good electrical conductor at 10–15 km depth as a molten layer is irreconcilable with a thick crust, so that alternative explanations have to be sought for this still enigmatic feature. In the second part, results from different branches of seismology, geochemistry, and numerical modelling on the Iceland plume are reviewed and discussed. For the upper mantle, combining seismological models, geodynamical models and crustal thickness data suggests that the plume has a radius of 100–120 km and an excess temperature of 150–200 K, while the structure of the plume head is less well known. The volume flux is likely to be 5–6 km^3/a, and numerical modelling indicates that water and its loss upon melting have a substantial impact on melt production and on the dynamics and distribution of segregating melt. Geochemical studies indicate that the plume source is quite heterogeneous and very probably contains material from the lower mantle. An origin of the plume somewhere in the lower

mantle is also supported by several seismological findings, but evidence is not unambiguous yet and has still to be improved.

1 Introduction

Mid-oceanic ridges and plumes are geodynamic key features of the earth which play prominent roles in igneous petrogenesis and crust formation. Mid-oceanic ridges evolve from rifts and are most fundamentally distinguished by their individual spreading velocities, which control several characteristics of their structure and melting style, but as a whole, they show a rather uniform crustal thickness of 6–7 km (e.g. White et al. 1992). For plumes, in contrast, the amount and style of melt generation and crustal production strongly depend on their own size and temperature, and the type of lithosphere they encounter when approaching the surface. A very particular situation arises, when a ridge and a plume merge, because the plume is now located under very thin lithosphere, which allows it to rise to very shallow depths and to maximise its capacity for melt production, without being oppressed by a thick lithospheric lid. The melt-producing potential of the ridge and of the plume are superimposed here.

The ridge-centred plume *par excellence* is presently the one beneath Iceland, a volcanic island created by the boost of volcanic activity since the coalescence of the Iceland plume and northern mid-Atlantic ridge southeast of Greenland some 20 Ma ago. In this paper, a review of results of different geophysical disciplines on the structure and processes in the earth's interior beneath Iceland is given, and an attempt is made to sketch a comprehensive, if preliminary, picture of the plume. In order to get the general picture, it concentrates on results dealing with the mantle and with crust–mantle interactions and interdependence.

2 The crust

In Iceland and the North Atlantic essentially three different types of oceanic crust exist: normal oceanic crust of average thickness (6–7 km) with transform fractures, generated at basically undisturbed mid-oceanic ridges (MOR); anomalous oceanic crust of increased thickness without fractures and a possibly non-orthogonal spreading direction relative to the MOR; and crust generated by the plume (White 1997). The second and the third type have several unusual features which, although intensively investigated, are not yet properly understood. One of the central controversial topics is the thickness of the Icelandic crust and the plume temperature. This involves also the question whether a layer between ca. 10–15 km and ca. 28–30 km with $v_P = 7 \ldots 7.4$ km/s is part of the crust or the top of a mantle with anomalously slow seismic velocities.

It is far beyond the scope of the following review to summarise and comment on all aspects of recent research on the Icelandic crust; most results on phenomena or structures restricted to the crust alone without broader relation to the mantle are omitted.

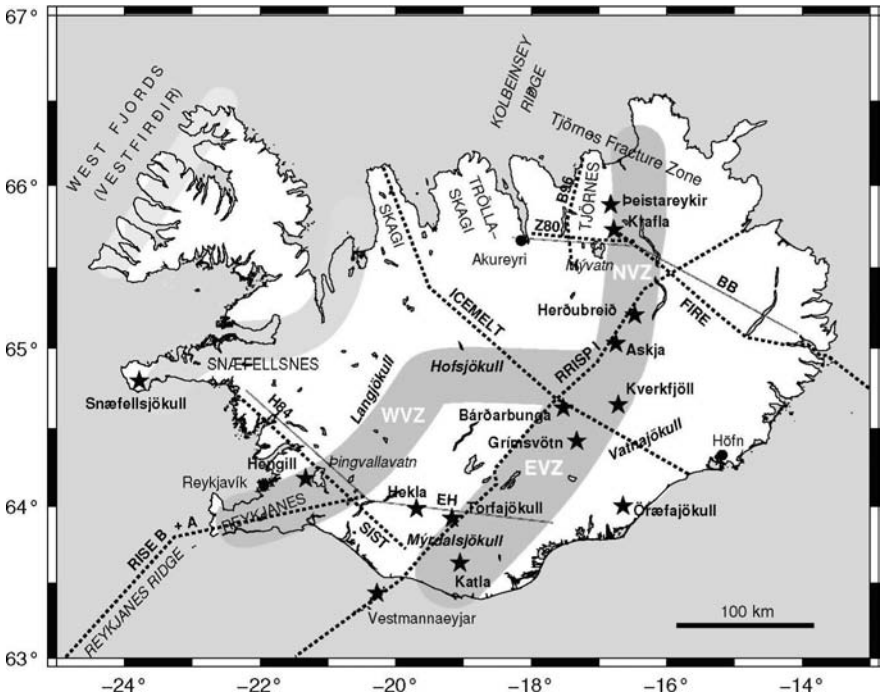

Fig. 1. Overview map of Iceland. Geophysical profiles shown: RRISP77 profile I (Gebrande et al. 1980), BB (Beblo and Björnsson 1980), Z80 (Zverev et al. 1980b), H84 (Hersir et al. 1984), EH (Eysteinsson and Hermance 1985), SIST (Bjarnason et al. 1993), FIRE (Staples et al. 1997), ICEMELT refraction (Darbyshire et al. 1998), B96 (Menke et al. 1998), RISE profiles A and B (Weir et al. 2001). Gray-shaded strips: neovolcanic zones (lighter gray: extinct); ⋆: major volcano; •: city; slanted bold text: glaciated area; dotted lines: seismic profiles; continuous lines: MT profiles.

2.1 Geotectonic evolution and present morphology

In the north Atlantic, the plume and the oceanic spreading centre have been interacting more or less since continental break-up in the late Palaeocene and early Eocene 58 Ma ago. Although it is commonly agreed that the plume has not always been located directly beneath the ridge, it is not yet clear whether the plume arrived under eastern or central Greenland (ca. 62–64 Ma ago) before rifting in the east started. But there seems to be consensus that rifting

preceded plume-related volcanism in western Greenland (Skogseid et al. 1992, Larsen et al. 1992, Chalmers et al. 1995, White 1997, Scarrow et al. 2000) and that the subsequent massive volcanism and final break-up in the east were due to the melting of the plume, which preferentially took place at "thinspots" of the lithosphere. However, the exact position of the plume during late Cretaceous/early Tertiary time is still controversial: while Lawver and Müller (1994) and Torsvik et al. (2001) located it beneath the southeastern or central part of the Greenland craton during initial break-up and beneath the Greenland–Iceland Ridge at 37 Ma, White and McKenzie (1989) positioned it beneath the Scoresby Sound area and at the spreading centre, respectively. As Clift et al. (1995) point out, the Lawver and Müller (1994) model, which they favour, can explain better the anomalously slow subsidence shortly after rifting observed in several ODP borehole cores, while the White and McKenzie (1989) model accounts more readily for the thickened crust of the Iceland–Faeroe ridge. An initial position under central Greenland is also in better agreement with the appearance of picrites and flood basalts in western Greenland at about the same time, which was probably caused by splitting resp. redirecting of the plume upwelling by the lithospheric keel of the Greenlandic craton (e.g. Larsen et al. 1992, Riisager and Abrahamsen 1999, Nielsen et al. 2002); as an alternative to the notion of a young plume, it has been proposed that the Iceland plume is much older and was already the cause for the basalts of Ellesmere Island, northern Greenland, and the Alpha Ridge in the Arctic (e.g. Forsyth et al. 1986). The eruption rate during the generation of the flood basalts in the North Atlantic Igneous Province has been estimated as more than $1\,\mathrm{km}^3/\mathrm{a}$, compared to 0.023–$0.038\,\mathrm{km}^3/\mathrm{a}$ for Iceland today (Richards et al. 1989). The total volume of the volcanics amounts to $6.6 \cdot 10^6\,\mathrm{km}^3$ distributed over an area of $1.3 \cdot 10^6\,\mathrm{km}^2$ (Condie 2001).

The style of interaction between the plume and the lithosphere depends on their relative movement and controls the tectonic evolution of Iceland. Since the early formation of Iceland more than 20 Ma ago, there is evidence for still ongoing eastward jumps of the ridge from now extinct rifts in northwestern Iceland (activity ceased 15 Ma ago) and on Snæfellsnes to the still active Western Volcanic Zone (WVZ) 7–9 Ma ago (Hardarson et al. 1997), and to the present Northern and Eastern Volcanic Zones (NVZ, EVZ). The EVZ began to form ca. 3 Ma ago. The link to the North Atlantic ridge system is accommodated by the Tjörnes Fracture Zone (TFZ) in the north, an analogue of the common oceanic transform fault, but broader than most of them, and the "bookshelf"-type faults of the South Iceland Transfer Zone (figure 1). Similar shifts have happened 3–7 Ma years ago from a rift on the Skagi peninsula to the present NVZ and from the ~ 20 Ma-old western fjords to Skagi earlier (Sæmundsson 1979). Hardarson et al. (1997) estimate one rift zone cycle to last about 12 Ma, including activity overlap during relocations.

On a topographic/bathymetric map of Iceland and the North Atlantic (figure 2), the different types of oceanic crust are easily visible: normal oceanic

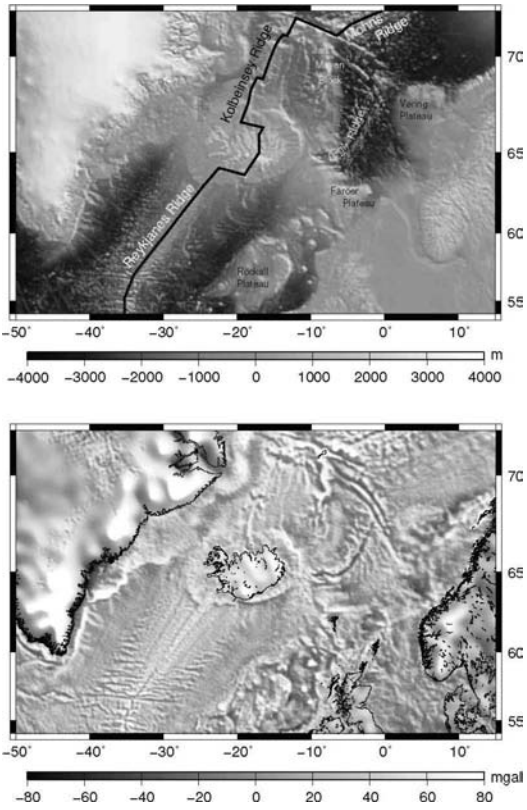

Fig. 2. Topography and bathymetry from GTOPO30 (top), and free-air gravity from Sandwell and Smith (1997) (bottom) of Iceland and its surroundings; the colour scale for gravity is clipped at ±80 mgal. *The colour version of this figure is displayed on colour plate 1.*

crust is present south of the Reykjanes Ridge, beyond ca. 58° N, and in principle also to the north of Iceland at the Kolbeinsey Ridge; the Reykjanes Ridge itself features anomalous oceanic crust characterised by V-shaped structures, increased crustal thickness, a weak relief, the almost complete absence of transform faults, and an axial high instead of the usual median valley (Appelgate and Shor 1994, Weir et al. 2001). White (1997) explained these features by anomalously high crustal temperatures, which precludes brittle rheology normally resulting in the formation of the central graben. Iceland itself forms the top of a roughly circular rise with a maximum topography of ca. 2.8 km above the surrounding seafloor lying in the centre of a positive geoid anomaly with an amplitude of $\gtrsim 30$ m with respect to the hydrostatic reference earth; note that the Icelandic geoid anomaly reaches a value of around 70 m if taken relative to the geodetic reference ellipsoid. The topographic high extends into the NW–SE-striking Greenland–Iceland–Faeroe Ridge created by feeding of hot material from the plume into the spreading centre when the plume itself was still off the MOR (Vink 1984). Seismic, topographic, and bathymetric data suggest that the crust of Iceland and the oceanic aseismic ridge has a much greater thickness than normal oceanic crust (White 1997, also see

sect. 2.2); for instance, seismic profiles shot between the Faeroe Islands and Iceland yield 25–33 km for the aseismic ridge (Richardson et al. 1998, Smallwood et al. 1999). Regional geoid–topography ratios are often used to infer the depth extent of density anomalies. Values for the Iceland area are around 1.5 m/km, which is rather low compared with other thermal swells, probably due to a strong contribution of the Airy-compensated shelf (Sandwell and MacKenzie 1989, Marquart 1991). A more detailed investigation of the regional geoid taking into account the thermal structure of the lithosphere revealed a ratio of ~ 7 m/km, which requires a compensation depth below the base of the lithosphere and is hence most probably due to dynamic support by the Iceland plume (Marquart 1991). Analysis of the admittance, i.e. the spectral ratio of geoid and topography, also indicated that Iceland and the western Faeroe Plateau are supported by a deep, sublithospheric anomaly (Heller and Marquart 2002).

It is a striking feature of Iceland that the formation of anomalous crust is much more pronounced to its south than to its north. The Kolbeinsey ridge has an unusually shallow bathymetry as well, but the crust north of the TFZ basically resembles normal oceanic crust both structurally and geochemically (see section 3.2). Due to the influence of the plume the crust of the Reykjanes Ridge has a significantly greater thickness than normal oceanic crust (8.4–11 km), and decays to the normal value over a distance of ca. 1000 km from the plume centre (Smallwood et al. 1995, Weir et al. 2001). The formation of the southward-pointing V-shaped ridges is often explained by temporal variations of this influence which result in low-viscosity pulses from the plume with a period of 5–10 Ma, flowing along the ridge axis (e.g. Vogt 1971, 1976, see section 3.3) and producing excess crust. Furthermore it accounts for the fact that these V-shaped ridges are visible only in bathymetric and gravity (figure 2), but not in magnetic anomalies. White et al. (1995) and White (1997) estimated the temperature anomaly of the plume-affected mantle beneath the ridge to 30–50 K on the grounds of the observed excess thickness of about 2 km caused by the increase in melt production. Jones et al. (2002) determined an along-ridge propagation velocity of the pulses of 20–25 cm/a for distances $\lesssim 700$ km and of 10–15 cm/a beyond from bathymetric, short-wavelength gravity, and magnetic data. They could also extract a weaker pulsing with a period of only 2–3 Ma from their data and also reported northward-pointing V-shaped structures from the area between the Kolbeinsey Ridge and Jan Mayen, although these are smaller and much more blurred. – This view of course implies that the pulses are controlled by the plume and caused by some variability in its flux or temperature. As an alternative, however, it is possible that the relative movement of the plume and the overriding lithosphere, which has a particular thermal structure and underwent several rift relocations, is responsible for the variability in crust formation expressed by the V-shaped ridges (Hardarson et al. 1997). These authors note that the age of the troughs between the three most pronounced V-ridges (15 and 5 Ma, respectively) coincides approximately with the time

of rift relocations. It is still a matter of debate whether rift relocations and pulses are initiated by the plume or whether the varying productivity is just a response of the melting mantle to the changing lithospheric conditions.

2.2 Seismics and gravimetry

Several seismic profiles have been shot in different parts of Iceland since the early 1960s. Data interpretation, however, especially for early experiments has been ambiguous, giving rise to the controversy whether the Icelandic crust is thin or thick. Pálmason (1971) defined a layer model in analogy to the oceanic crust with an upper crust of 3–6 km thickness, characterised by strong $v_{P,S}$ gradients due to the successive closure of fractures. Larger thicknesses usually correspond to higher age (Flóvenz and Gunnarsson 1991). Angenheister et al. (1980) and Gebrande et al. (1980) interpreted data observed along profile 1 of the RRISP77 experiment (see figure 1) and defined a shallow reflector at about 10 km depth as the Moho and the layer beneath, down to 30 km, as mantle with anomalous low velocities due to the presence of partial melt (see also table 1). Zverev et al. (1980a,b) investigated larger parts of the crust outside the neovolcanic zone (figure 1, line Z80) and reported evidence for crustal structure down to ~ 20 km. Although Gebrande et al. (1980) did not ignore the possibility of other explanations such as gabbroic material, they preferred the thin-crust model in view of the magnetotelluric measurements, which image a good conductor at that depth (Beblo and Björnsson 1980, see sect. 2.3). A reinterpretation of the RRISP77 dataset by Menke et al. (1996) resulted in a crustal thickness of 20–30 km. Moreover, the previously observed high attenuation was attributed to local factors, whereas the lower crust as a whole was found to be much less attenuating.

In the southwest of Iceland the SIST crustal tomography experiment Bjarnason et al. (1993) (see figure 1) confirms the finding of earlier experiments that the Icelandic crust is structurally similar to oceanic crust, although thicker (see table 1). At a depth of 20–24 km (base of layer 3), there is a strong, slightly westward-dipping reflector interpreted as the Moho. From the velocities measured directly above and below this reflector, Bjarnason et al. (1993) infer that it lies in unmolten rock, probably gabbro at temperatures of only 600–900 °C. More recently, the RISE profile along the axes of the Reykjanes Peninsula and Ridge and oblique to the ridge (Weir et al. 2001, see fig. 1) has extended the image of the southwestern Icelandic crust away from the plume. Combined seismic refraction and gravity models from the RISE profiles confirm the presence of a thickened, but solid crust gradually approaching values typical of normal oceanic crust southward.

The FIRE profile (Staples et al. 1997), a partly marine reflection/refraction profile from the Faeroe Islands to Krafla in northeastern Iceland (see figure 1), basically shows that the northeastern Icelandic crust is similar to the southwestern. A low-velocity upper crust with a steep velocity gradient is separated from a very thick lower crust with a weak-to-moderate veloc-

Table 1. Representative P-wave velocities and depths to bottom (z_{bot}) of the crustal levels for the crust models of Pálmason (1971) and Flóvenz (1980), the RRISP77 profile I (Gebrande et al. 1980), SIST (Bjarnason et al. 1993), FIRE (Staples et al. 1997), the ICEMELT refraction profile (Darbyshire et al. 1998, 2000), RISE profiles A and B (Weir et al. 2001) and for receiver functions of individual stations throughout Iceland from the HOTSPOT campaign (Schlindwein 2006, Du and Foulger 1999, 2001, Du et al. 2002); in the receiver function values, the first rows for each crust segment are from Schlindwein (2006), the second rows are calculated from v_S using $v_P/v_S = 1.7$. The mantle v_P of 7.7 km/s from SIST is an apparent velocity. The RISE values are for zero-age crust, with smaller values applying to the ridge profile.

layer	v_P (km/s)	z_{bot} (km)
"Layer model" after Pálmason (1971)		
upper crust (layer 0–2)	2.75–5.08	0–2.5
lower crust (layer 3)	6.5	≤ 6.2
mantle (layer 4)	7.2	–
RRISP77		
upper crust	≤ 6.5	~ 5
lower crust	6.5–6.9	10–15
anomalous mantle	7–7.4	30
SIST		
upper crust (layer 2A)	3.5	0.7–3
middle crust (layers 2B,C)	5–6.5	3–7
lower crust (layer 3, "4")	6.5–7.2	20–24
mantle	7.6–7.7	–
FIRE		
upper crust	3–6.2	4
transition		6
lower crust	6.5–7.35	19–35
mantle	$> 7.9 \ldots 8$	–
ICEMELT		
upper crust	3.2–6.3...6.7	2–11 (av. 5)
middle crust	6.6–6.9	9–12
lower crust	$> 6.9 \ldots 7.4$	19–41
RISE		
upper crust	≤ 6.8	4.5–7.3
lower crust	6.5–7.2	11–21
HOTSPOT receiver functions		
upper crust	$< 7 \ldots 7.2$	6–14
	< 6.5	6.5–11
lower crust	7.2–7.4	20–42
	6.5–7.2	20–40

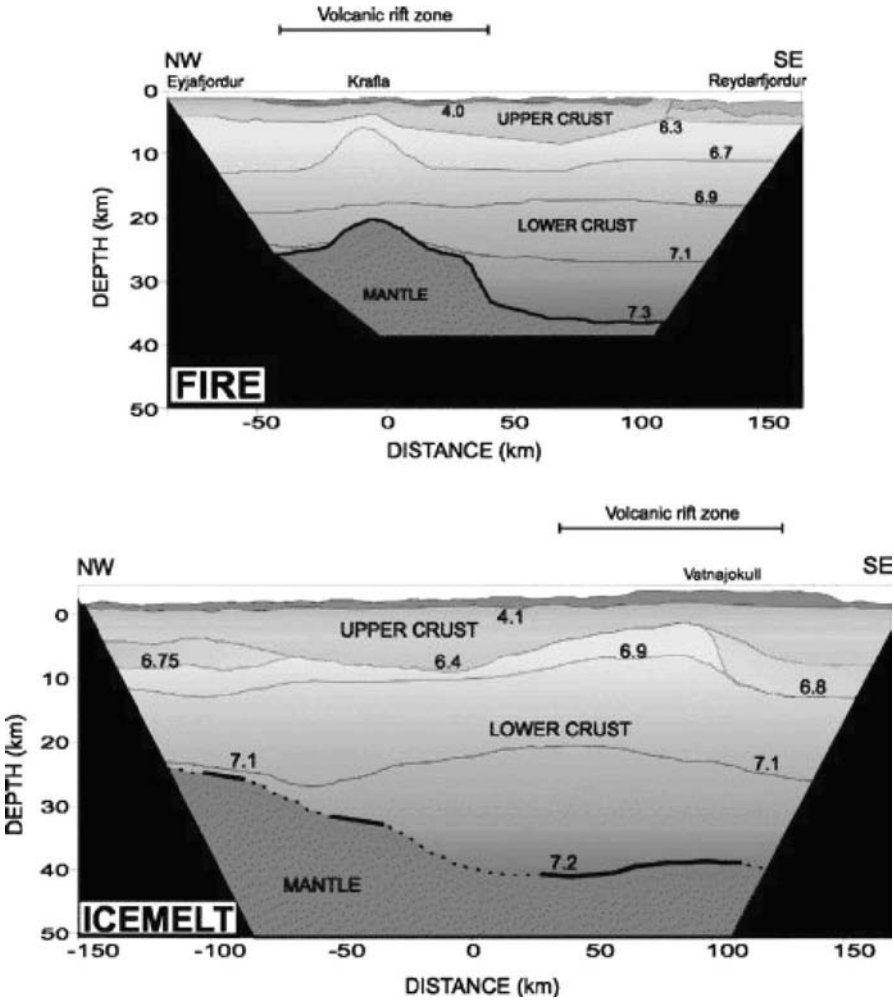

Fig. 3. Top: crustal model for the NVZ from FIRE (Staples et al. 1997); bottom: crustal model for the ICEMELT refraction line across central Iceland (Darbyshire et al. 1998). Note that only disjoint segments of the Moho are imaged. (Reprinted with permission from Darbyshire, F. A., Bjarnason, I. Þ., White, R. S., Flóvenz, Ó. G.: Crustal structure above the Iceland mantle plume imaged by the ICEMELT refraction profile; Geophys. J. Int. 135(3), 1131–1149, 1998 © Blackwell.)

ity increase by a transition layer of 2–4 km thickness (figure 3, upper part). Similar to the SIST profile, the high lower crust velocities are ascribed to either gabbro or an olivine-rich residue from which a tholeiitic melt has separated; this notion is also in qualitative agreement with petrological models of magma evolution at hotspots and v_P estimates derived from them (Farnetani et al. 1996). The strong reflector interpreted as the Moho dips away from the

neovolcanic zone with a steep angle of ca. 30°: Moho depths below the NVZ lie around 19 km, but reach 35 km under eastern Iceland (Staples et al. 1997) and 25–31 km below the west flank of the NVZ (Menke et al. 1998) (profile B96 in figure 1). In particular, a pronounced shallowing of the Moho and a strong updoming of the lower crust are observed beneath Krafla (Brandsdóttir et al. 1997, Menke et al. 1998). Staples et al. (1997) conclude that the temperature at the base of the crust is less than 800 °C, because otherwise such a strong Moho topography could not persist long enough to fit the observations; they presume that it is not a stationary feature anyway and relate it to thickening due to extrusive flows and variations in plume activity and melt productivity, maybe modulated by the jumps of the spreading centre. Poisson's ratios of 0.26–0.27 have been derived for the lower crust, also indicating that it is cold, solid, and essentially free of melt (Menke et al. 1998, Staples et al. 1997).

Along a third refraction profile, which has been shot as part of the ICEMELT experiment (Darbyshire et al. 1998, see fig. 1), a crustal thickness of 25–30 km for the northwestern half of the profile and of 38–40 km beneath central Iceland and Vatnajökull was inferred. Beneath Vatnajökull the lower crust forms a root with a maximum v_P of 7.2 km/s (figure 3, lower part) which shows that melt production by the plume and underplating exceeds crustal thinning by the rifting process (Darbyshire et al. 1998).

The thick crustal root of Iceland leads to a minimum in the Bouguer anomaly of more than −40 mgal (Fedorova et al. 2005) and would normally be expected to cause high topography, which is though not observed (Menke 1999). Under the assumption that the topography is locally isostatically compensated and that thickness variations are restricted to the lower crust, one can attempt to determine the densities of the lower crust and uppermost mantle under Iceland. Menke (1999) estimated for the lower crust $\varrho_{lc} = 3060 \pm 50\,kg/m^3$, and for the density jump across the Moho $89 \pm 12\,kg/m^3$, leading to a mantle density as low as $\varrho_m = 3150 \pm 60\,kg/m^3$. He stated that even the combined effects of thermal expansion, depletion, and entrainment of basaltic material into the uppermost mantle can hardly account for such a low mantle density. It should be kept in mind that not all density anomalies in the crust and mantle beneath Iceland may contribute isostatically to the observed topography, but may in parts be dynamically compensated by viscous or elastic stresses in the asthenosphere or lithosphere. Other authors found somewhat larger $\Delta\varrho_{m-lc}$ jumps of 103, 130 ± 30 and $154\,kg/m^3$, respectively (Fedorova et al. 2005, Allen et al. 2002b, Kaban et al. 2002), whereby the density contrast varies regionally: while for instance East Iceland, the West Fjords and especially the Greenland–Iceland Ridge have a higher density contrast, the contrary is true for the extinct Skagi–Snæfellsnes rift (Fedorova et al. 2005). Staples et al. (1997) get low ϱ_m values only for the NVZ, while outside they estimate $\varrho_m = 3240\,kg/m^3$ and high densities in the lowermost crust. Thus, it seems plausible to consider a mantle with only slightly reduced density in the plume in combination with a thick, unusually dense crust. For such a model setup Guðmundsson (2003)

concluded, based on crustal thickness, topography, and gravity information, that the density of the plume mantle is reduced by only up to $20\,\mathrm{kg/m^3}$ relative to normal mantle, but that the density contrast between the lower crust of Iceland and the adjacent ridges (with $\varrho_{\mathrm{lc}} = 2980\,\mathrm{kg/m^3}$) could be as high as $140 \ldots 170\,\mathrm{kg/m^3}$. This would also result in the low density contrast needed to reconcile a thick crust and the rather low topography. He argues that the enhancement of melting and its deeper onset due to high temperatures and the effect of water would enrich the crust in olivine and raise the Fe content of crustal minerals, both of which increase the density. Furthermore, the plume source might contain more iron than normal mantle (see section 3.2), and a phase transition from plagioclase to garnet in the thickest parts of the crust could also contribute to the inferred density.

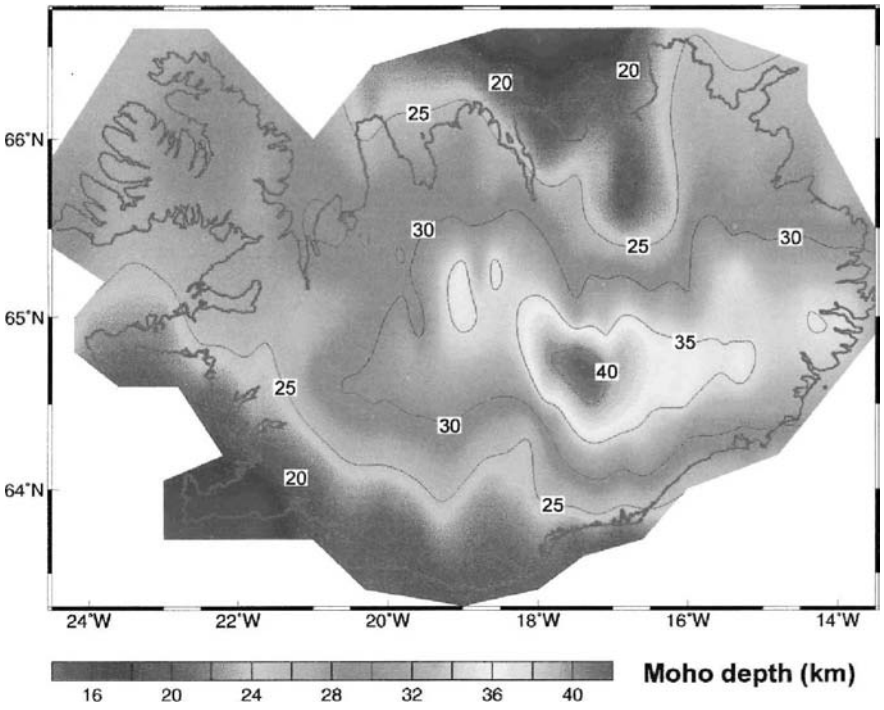

Fig. 4. Map of the Mohorovičić discontinuity of Iceland. (Reprinted from Earth Planet. Sci. Lett. 181(3), Darbyshire, F. A., White, R. S., Priestley, K. F.: Structure of the crust and uppermost mantle of Iceland from a combined seismic and gravity study, pp. 409–428, © (2000), with permission from Elsevier.) *The colour version of this figure is displayed on colour plate 2.*

In an attempt to construct a Moho map, Darbyshire et al. (2000) (figure 4) summarised the available information from seismics and modelled it together

with Bouguer gravity data (Eysteinsson and Gunnarsson 1995). According to this map, a maximum crustal thickness of 40–41 km is reached beneath Vatnajökull, but Moho depths of more than 25 ... 30 km are ubiquitous between the northwestern peninsula and the eastern coast. The thinnest crust is located beneath southern Iceland, reaching a minimum of about 16 km under Reykjanes and the NVZ. As a whole, this Moho map provides a useful picture of the crustal thickness of Iceland, although it must be kept in mind that for some areas the database is sparse and often restricted to gravity and that Moho depth is only known at short segments along the seismic profiles. Their gravity modelling demonstrated the need of a cylindrical low-density body in the uppermost mantle, but they did not investigate the effect of a plume head, although its existence is likely according to mantle dynamical models and surface wave studies (Allen et al. 2002a). Allen et al. (2002b), Kaban et al. (2002), and Fedorova et al. (2005) also published Moho maps of Iceland which differ locally in several places by up to ca. 5 km, but the general picture emerging from the maps is quite consistent. An interesting new feature in the map by Fedorova et al. (2005) is the presence of thickened crust off the East Icelandic coast, which is thought to be related to a continental splinter of Greenlandic provenance, similar to what has been proposed for the Jan Mayen microcontinent by Bott (1985); surface wave observations indicate that the lithosphere in that region is also substantially thicker than under the rest of Iceland (e.g. Bjarnason and Sacks 2002).

In the crustal structure model by Kaban et al. (2002) also a thin elastic lithosphere of not more than 6 km thickness is included and temperatures below are estimated to lie between 650 and 950 °C, and they argued for a thick transition zone between crust and mantle consisting of a mixture of mafic and ultramafic rocks. Additional hints for the temperature structure of the Icelandic crust are obtained from calculated v_P/v_S ratios (Allen et al. 2002b), which do not show evidence for extensive presence of partial melt beneath 15 km depth. The absence of melt is also supported by $Q_P = 200 \ldots 300$ and $Q_S = 150 \ldots 600$ found for mid- to lower-crustal depths in central and southwestern Iceland, indicating temperatures between 700 and 775 °C if gabbroic material is assumed (Menke and Levin 1994, Menke et al. 1995).

The depth distribution of earthquake hypocentres is a further important indicator for the thermal structure, because rupture is associated with brittle behaviour and correspondingly low temperatures. Several evaluations of hypocentre depths of Icelandic earthquakes show that there are hardly any quakes at depths greater than ca. 12 km within a distance of ca. 100 km from the volcanic zones and that the maximum depth of hypocentres increases in older crust (e.g. Stefánsson et al. 1993, Rögnvaldsson et al. 1998, Tryggvason et al. 2002). Tryggvason et al. (2002) estimated the temperature at this depth to lie between 580 and 750 °C on the basis of borehole heat flow measurements. This is also supported by models of the viscosity structure beneath the Krafla region, which give best results for an elastic plate of not

more than 12 km and a lower crust viscosity of about $3 \cdot 10^{19}$ Pa s (Pollitz and Sacks 1996).

Recently, the stations of the HOTSPOT network have been used to derive $v_{P,S}(z)$ profiles from the inversion of receiver functions and surface waves (Du and Foulger 1999, 2001, Du et al. 2002, Schlindwein 2006). A common feature is a strong positive velocity gradient in the upper few kilometres corresponding to the upper crust, nearly constant velocities in the lower crust, and sometimes another positive gradient at the crust–mantle transition. In several cases, however, the boundary between upper and lower crust is not sharp, and the Moho, which is found at depths of 20–33 km below older crust and up to 40 km in the junction of the neovolcanic zones, is also frequently smeared over a certain depth interval. These values agree generally with those e.g. from seismic refraction surveys. Du and Foulger (2001) note that in general the upper crust thins and the lower crust thickens towards the rifting zones. At various sites in western and northern Iceland, a slight low-velocity zone (LVZ) is present in the lower crust (Du and Foulger 2001, Du et al. 2002, Schlindwein 2006).

The comprehensive receiver function study of Schlindwein (2006), including 28 HOTSPOT stations from all parts of Iceland, reveals the apparent absence of a contiguous, sharp Moho below Iceland and rather indicates a gradational change from crust to mantle velocities in many places, also pointing toward a broad transition zone from crust to mantle. A similar conclusion was drawn by Fedorova et al. (2005) in their study of seismic, gravity, and topography data.

2.3 Electromagnetics

Interpretations of electromagnetic deep sounding experiments in Iceland (Beblo and Björnsson 1980, Thayer et al. 1981, Hersir et al. 1984, Eysteinsson and Hermance 1985) revealed a well-conducting layer between a depth of roughly 8 to 20 km, found everywhere except in the old crust in northeastern Iceland. Beblo and Björnsson (1980) interpreted short-period data from two profiles in northeastern Iceland (one across the NVZ and the adjacent Tertiary areas (line BB in figure 1) and one following the RRISP77 profile I), and discovered a 5–10 km thick well-conducting layer with a resistivity ρ of only 15 Ω m between two more resistive layers with about 100 Ω m. In the rift zone the top of the good conductor is as shallow as 10 km, but dives to about 20 km at greater distances from the NVZ. The high-ρ layer with 70–100 Ω m beneath it reaches down to at least 100 km, indicating a small geothermal gradient.

Thayer et al. (1981) studied the Krafla–Mývatn area and localised the good conductor ($\Delta h \leq 4$ km, $\rho \leq 10\,\Omega$ m) at a depth of 8 to 15 km. In these early studies this well-conducting layer was interpreted as the partly molten uppermost mantle or mantle–crust transition zone. Beblo and Björnsson (1980) concluded from comparison with laboratory data from partially

molten basalt and ultramafites that the low resistivity is due to temperatures of 1000–1100 °C, at which a basaltic partial melt with a melt fraction $\varphi \leq 0.1$ would be present. Thayer et al. (1981) also provided estimates for the melt fraction at $z > 15$ km and found low values (for interconnected channels) of 1.7–3.3% for the depth range between 15 and 30 km, and of 1.2–2.5% below, indicating low porosities throughout the melting region of the plume.

This interpretation of crustal structure based on electromagnetic studies is in striking contrast to the new seismic and seismological observations of a thick, relatively cold crust down to more than 20 km. As an alternative to the shallow-melt model, enrichment of low-grade metamorphic minerals with high conductivities such as zeolites in the lower crust has been proposed (e.g. Smallwood et al. 1998); further long-term cooling would explain why the high-conductivity layer descends to greater depths with increasing distance from the spreading centre.

As an additional observation to derive crustal structure and temperature the geochemical composition and eruption temperature of lavas can be used. For central Iceland, Breddam (2002) derived eruption temperatures of up to 1240 °C and initial crystallisation pressures and temperatures of 1–1.5 GPa and 1270 °C, respectively, which gives a rough estimate of 30–45 km for the lithospheric thickness above the plume centre. For the NVZ, Nicholson and Latin (1992) determined a crustal thickness of ca. 22 km for the Krafla region, which is in fair agreement with the findings from the FIRE experiment (Staples et al. 1997, Brandsdóttir et al. 1997) and an independent geochemical study by Maclennan et al. (2001b). In this latter investigation, however, the observed range of crystallisation pressures and temperatures (0.3–1 GPa and 1160–1350 °C) indicated that crust formation does not only take place at shallow magma chambers but happens over a large depth range from 10 km down into the uppermost mantle at 30 km.

2.4 Geodynamical modelling

A first attempt to numerically model the evolution and structure of the Icelandic crust as produced by a spreading ridge dates back to Pálmason (1973, 1980). Pálmason (1980) developed a two-dimensional kinematic model of the crust to investigate the relation between the widths of the lava deposition and strain zones in the axial area and the dip angle and deposition rate of the Tertiary basalt pile. His models suggest that the width of the volcanic zone ($\sim$ 40–125 km) and the spreading rate have not changed significantly in the last 10–15 Ma. This finding, however, does not constrain the total magma production rate, which might have varied through time, including the possibility of plume pulses. From his match of the dipping angle of basaltic layers he assessed that the visible part of the Tertiary extrusives was emplaced outside the innermost 50 km of the volcanic zone. The fraction of dikes in the upper crust and the sharpness of the transition to the intrusive lower crust

is controlled by the ratio of the widths of the crustal strain zone and of the lava deposition zone and by the amount of strain taken up by normal faults.

Menke and Sparks (1995) followed a more comprehensive approach including the region of melt generation in the uppermost mantle. In their model the crust formed from it in a 160 km deep two-dimensional FD model. The results from their preferred model with a shallow, rather narrow accretion zone show that the combined action of upwelling and spreading is not strong enough to produce a hot crust, especially if hydrothermal cooling in the upper crust is accounted for; models with a broader accretion zone or vertically uniform dike injection lead to reduced downwelling or a hotter crust, respectively, but cannot explain observations equally well. In particular, the preferred model does not yield a large, shallow layer of partial melt. Of course, the inclusion of hydrothermal cooling by assuming a higher thermal conductivity in the active zone is not very well constrained, and it is unclear if values such as a five- or eightfold increase as used for oceanic crust are equally appropriate for the subaerial crust.

Crustal thicknesses are also the result of some mantle convection models of the Iceland plume (Ribe et al. 1995, Ito et al. 1996, 1999, Ruedas et al. 2004, Ruedas 2004, 2006). Details of crustal structure cannot be resolved by such models, as crust formation is only modelled in a simplified way. Melt is extracted from the melting regions of the plume and ridge within ridge-perpendicular planes, accumulated on top of the model within an accretion zone at the spreading axis and transported laterally away from the ridge as new crust according to the plate motion. While the proper choice of the width of the accretion zone and of the deformation zone (i.e. the zone in which the plate velocity is not reached yet) is critical for the thickness of the crust at the very ridge axis, crustal thicknesses outside these zones are hardly affected by these parameters. As an example, figure 5 shows the crustal thickness of a mantle convection model for the Iceland plume with melt extraction of Ruedas et al. (2004) with a plume with 136 K excess temperature and a melt extraction threshold of 1 % after 21 Ma of model time. For comparison, the length and colour scales are similar to those of the observed crustal thickness map (figure 4). Clearly the maximum of the Icelandic crust is broader and thins away from the NVZ which may be due to viscous crustal relaxation (Buck 1996). Furthermore, the models by Ito et al. (1999) and Ruedas (2006) show that stiffening of the plume head by dehydration broadens the melting zone in the plume and accordingly the shape of the accreted crust. Such models demonstrate the importance of observed crustal thicknesses as constraints for the melt production rate and the mantle dynamics below Iceland and will be further addressed in section 3.3. Nonetheless, it is worth noting that the nature of the Icelandic quasi-Moho has implications for constraining melt production: if that transitional zone in the lowermost crust turns out to contain some mantle material, the total amount of melt required to match "crustal" thicknesses is smaller, as pointed out by Foulger et al. (2005); in this case, the plume could have a lower temperature excess and upwelling rate.

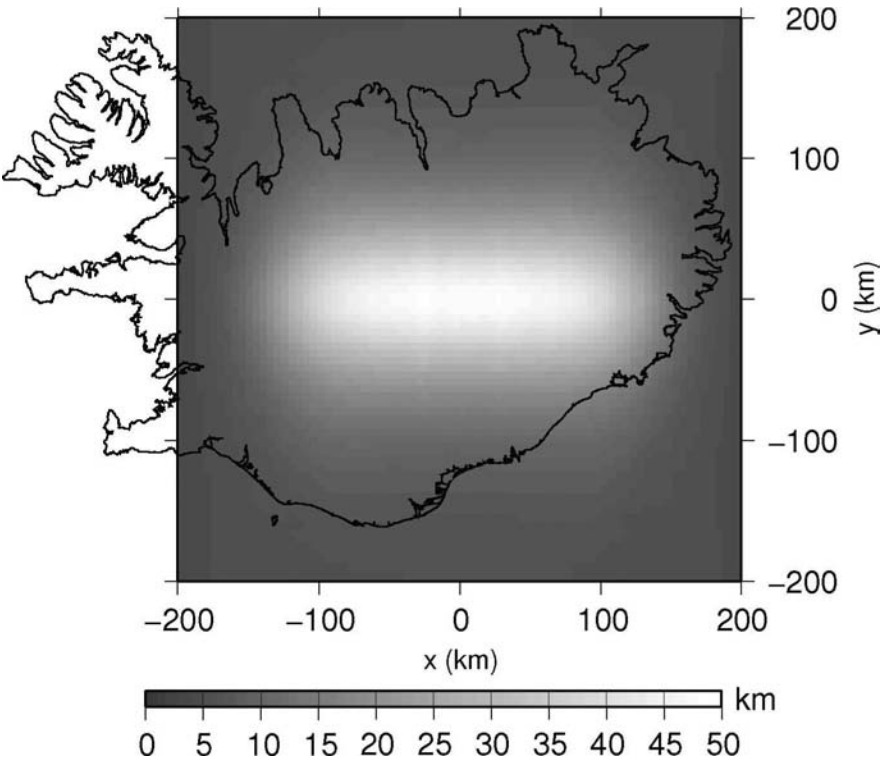

Fig. 5. Calculated crustal thickness (in km) of a convection model of the Iceland plume with 136 K plume excess temperature and 1 % melt extraction threshold (Ruedas et al. 2004) at 21 Ma model time. The ridge axis is located at $x = 800$ km, and is 60 km wide; plate drift has not yet transported crust further than about 210 km from it. *The colour version of this figure is displayed on colour plate 2.*

2.5 Synopsis

The series of large field experiments conducted since the early 1990s has contributed much to the clarification of the picture of the Icelandic crust and led to a preference for a model of a rather thick, cool crust; crustal thickness estimates from modelling of mantle melting also tend to larger values. This notion is most strongly supported by the results of seismological investigations of several kinds; in particular, the results of the RRISP77 campaign, which had stimulated the discussion in the first place, turned out to allow for a thick-crust interpretation as well, and much of the controversy was probably due to a too narrowed view on those results. The results summarised in table 1 suggest that the thickness of the crust ranges from about 20 km beneath some parts of the neovolcanic zones to about 40 km at the plume centre and in the older Tertiary regions of eastern Iceland.

Nonetheless, seismological and gravity studies, which even resulted in Moho maps, also put some restrictions on this seemingly neat and simple solution. It remains a fact that the Moho is not clearly seen in many places and that the lowermost layer of the thick crust seems to have some unusual properties (e.g. Schlindwein 2006, Kaban et al. 2002, Fedorova et al. 2005), which suggests that it does not consist of usual gabbroic lower-crust material, but that it partly has a transitional character. For this reason, several workers have pointed out that there is no classical sharp Moho throughout Iceland, but that there is a crust–mantle transition zone with a thickness of some kilometres; a receiver function study of Pacific oceanic islands by Leahy and Park (2005) suggests that a blurred Moho is a common feature of oceanic islands, and they propose a tripartite model of normal oceanic crust between an extrusive top and an underplated bottom as a general overall structure. Thus, Moho maps of Iceland, while useful, have to be taken *cum grano salis*, and the clarification of the fine structure and the lithology of the lowermost crust remains an issue.

The strongest contradiction to the thick-crust model still comes from magnetotelluric measurements, which had already strongly influenced the interpretation of the RRISP77 data. Given the ambiguities of the method, e.g. the problem to distinguish between a moderately good conductor of considerable thickness and a very thin high-conductivity layer, and in view of the variety of results from other methods, it seems, however, necessary to consider alternatives to the usually invoked layer of partial melt like the presence of certain metamorphic phases with greater effort. The special character of the Icelandic crust might make it difficult to develop such explanations, because analogies from continental crust, where a similar good conductor is observed, have to be made with care.

3 The mantle beneath Iceland

In this section we review several studies concerning the questions whether the Iceland plume is hot and narrow or broad and cool, how heterogeneous the plume is and whether the plume emerges from the core–mantle boundary (CMB) or from the bottom of the transition zone. Some key variables of the plume from several studies are listed in table 2 to highlight the large range of results. However, when comparing T anomaly or radius estimates from field observations with those from numerical models, one should bear in mind that the authors frequently do not make clear for which depth their temperature estimate is valid. This is important, since the temperature contrast may well vary at different depths due to conductive cooling upon ascent and enthalpic cooling during melting.

Table 2. Preferred values of some characteristic variables of the Iceland plume in the upper mantle from different published field observations, numerical models, and laboratory experiments.

T anomaly, ΔT_P, K	75	numerical	Ito et al. (1996), broad
	93	numerical	Ribe et al. (1995)
	100	numerical	Keen and Boutilier (2000); initial plume head
	100–200	seismics/numerical	Nielsen et al. (2002); initial plume head
	135–150	numerical	Ruedas et al. (2004), Kreutzmann et al. (2004)
	140	lab/numerical	Feighner et al. (1995)
	$\gtrsim 150$	P–S differential times	Shen et al. (1998, 2002)
	162–184	chemistry	Putirka (2005) (ΔT_{pot})
	170	numerical	Ito et al. (1996), narrow
	180	numerical	Ito et al. (1999)
	< 200	regional tomography	Foulger et al. (2001)
	~ 200	regional tomography	Wolfe et al. (1997)
	~ 200	seismics	Smallwood et al. (1999)
	200–300	global tomography	Bijwaard and Spakman (1999)
	~ 250	chemistry	Nicholson and Latin (1992)
	250–350	regional tomography	Hung et al. (2004)
	263	analytical/chemistry	Schilling (1991)
	$\lesssim 300$	seismology	Allen et al. (1999)
radius, r_P, km	40	numerical	Albers and Christensen (2001)
	50	He isotopes	Breddam et al. (2000)
	60	numerical	Ito et al. (1996), narrow
	60–100	seismology	Allen et al. (2002a)
	100	numerical	Ito et al. (1999), Ito (2001)
	100	seismology	Bjarnason et al. (1996), Allen et al. (1999)
	100	regional tomography	Tryggvason et al. (1983)
	≥ 100	global tomography	Montelli et al. (2004)
	100–125	regional tomography	Foulger et al. (2001)

	125–150	regional tomography	Hung et al. (2004)
	≤ 150	regional tomography	Wolfe et al. (1997)
	~ 150	chemistry/analytical	Maclennan et al. (2001a)
	< 200	P–S differential times	Shen et al. (1998)
	≤ 250	global tomography	Bijwaard and Spakman (1999)
	≥ 300	numerical	Ito et al. (1996), broad, Ribe et al. (1995)
volume flux, q, km^3/a	0.7884	analytical	Ribe and Delattre (1998), case 2
	1.26	analytical/numerical	Steinberger (2000)
	1.43	analytical/chemistry	Schilling (1991), best estimate
	2.1	numerical	Ito et al. (1996), narrow
	2.2	gravity/bathymetry	Ito and Lin (1995)
	2.23	analytical	after Sleep (1990); incl. Jan Mayen, see sect. 3.3
	2.5	seismology	Allen et al. (2002a)
	4.94	laboratory/numerical	Feighner et al. (1995)
	6.08	numerical	Ribe et al. (1995)
	6.1	numerical	Ito (2001), average
	6.4	numerical	Ito et al. (1999)
	12	numerical	Ito et al. (1996), broad
waist width, y_{P0}, km	850	laboratory	Feighner and Richards (1995)
	870	numerical	Ito et al. (1996), narrow
	900	numerical	Feighner et al. (1995)
	923	analytical/chemistry	Schilling (1991)
	1620	numerical	Ito et al. (1999)
	2300	numerical	Ito et al. (1996), broad

3.1 Seismology

Tomography and surface waves observations

Seismic tomography has been commonly used to image the deep structure of the Iceland mantle plume. The first mantle tomographic image was based on teleseismic data from a permanent seismic network, and although coverage was poor in some regions, a clear P-wave anomaly of 2 to more than 3 % in some parts was detected down to 375 km depth (Tryggvason et al. 1983). From the data of the ICEMELT experiment (Bjarnason et al. 1996), Wolfe et al. (1997) derived a P- and S-wave velocity anomaly model for the upper mantle between 100 and 400 km depth (figure 6) displaying an approximately circular and vertically continuous structure centred beneath the junction of the three neovolcanic zones and Vatnajökull, with a maximum P-wave anomaly of about −2 % and a S-wave anomaly of about −4 %. Both anomalies have basically similar shapes, although the S-wave anomaly extends a bit more northward and has a second maximum at 100–125 km depth under central Iceland, which might be related to incipient melting of the plume or effects causing seismic anisotropy. As an upper bound to the radius of the plume, Wolfe et al. (1997) suggest 150 km; they estimate the excess temperature to be ca. 200 K.

The HOTSPOT experiment (e.g. Allen et al. 1999, 2002a, Foulger et al. 2001) provided an even larger dataset and resulted in new tomographic images which show a strong low-velocity anomaly beneath Iceland, reaching down to at least 450 km. It essentially confirmed the ICEMELT estimates for r_P and ΔT_P, as well as the location of the plume centre, but indicated slightly larger velocity reductions. It is worth noting, however, that these radius and velocity anomaly amplitude estimates turn out to represent rather an upper bound on the size and a lower bound on the velocity reduction, if the finiteness of seismic wavelengths is accounted for (Allen and Tromp 2005, also see below); in this case, $50\,\mathrm{km} \lesssim r_\mathrm{P} \lesssim 100\,\mathrm{km}$, whereby the velocity anomalies can exceed −10 % for a very narrow plume. An interesting feature is the N–S asymmetry of the plume head, which was resolved most clearly in the study of Allen et al. (2002a), which included Love waves and used the crust model of Allen et al. (2002b) to remove the crustal signal. According to Foulger et al. (2001) a branch of the plume is visible beneath the Reykjanes Ridge, which is also discernible in the global tomography by Zhao (2001), and the plume head is apparently sharply bounded in the north at the position of the TFZ. Another remarkable feature is a zone in the uppermost mantle ($z < 100\,\mathrm{km}$) above the main melting region, where the v_S anomaly is 2 % *weaker* than in the outer parts of the plume head; such a fast relative anomaly has also been imaged by Li and Detrick (2003b) at depths greater than 90 km with Rayleigh waves. Allen et al. (2002a) suggested that this is due to particularly high degrees of depletion, but in this case it would not affect this whole depth range, because the onset of major melting seems to lie not much deeper than about 100 km (Shen and Forsyth 1995), so that the depletion effect is ex-

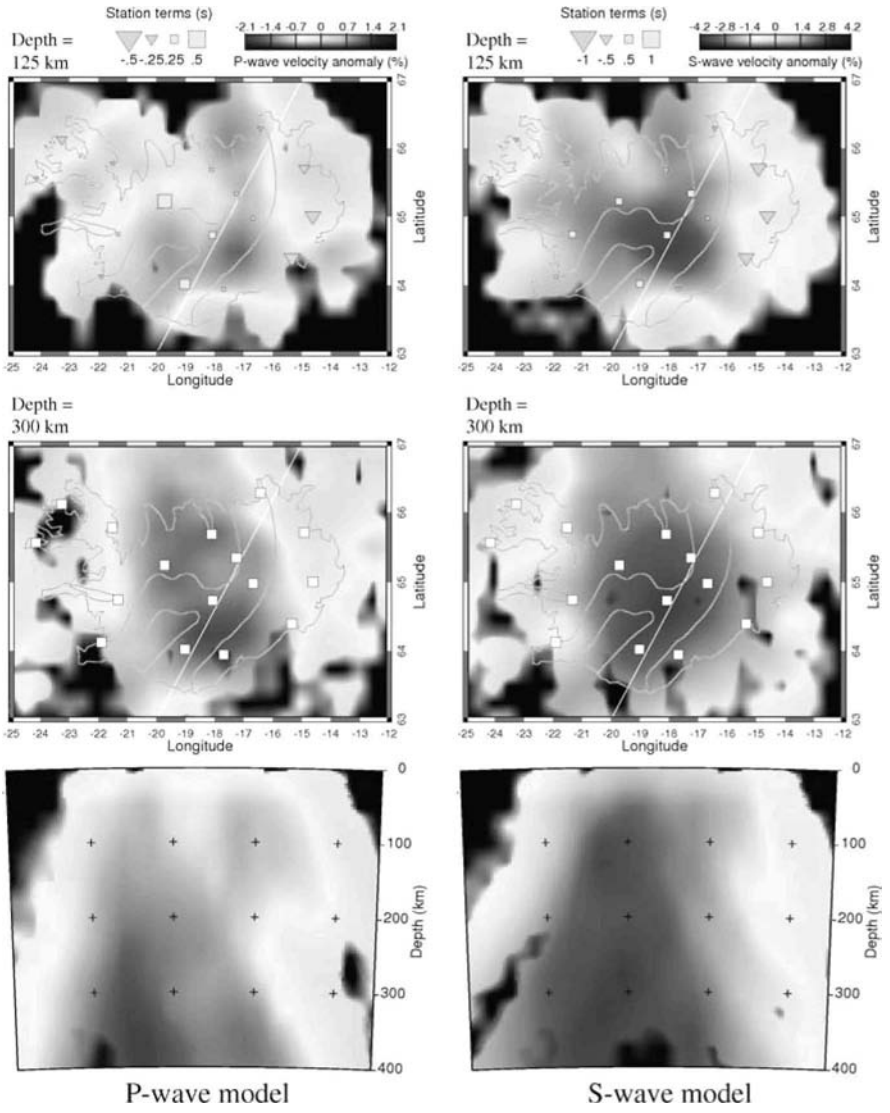

Fig. 6. Horizontal and vertical cross sections of the P-wave (left) and S-wave (right) seismic velocity anomaly models of the ICEMELT experiment. (Reprinted from Wolfe, C. J., Bjarnason, I. Þ., VanDecar, J.C., Solomon, S.C.: Seismic structure of the Iceland mantle plume, Nature 385(5727), pp. 245–247, © 1997, with permission from Nature Publishing Group.) *The colour version of this figure is displayed on colour plate 3.*

pected at shallower depth; besides it supports the notion of fast and efficient melt extraction, as the effect of melt on velocities does not seem to play a major role here. Li and Detrick (2003b) suggested an effect related to radial anisotropy as an alternative explanation.

The temperature estimate of Wolfe et al. (1997) did not take into account quantitatively the influence of melt, water content, anelasticity and anisotropy on wave velocities, which would lead to a lower excess temperature. On the other hand, they remark that wavefront healing by rays diffracted around the plume could have faked shorter traveltimes and thus have masked a larger ΔT_P value. This is generally confirmed by modelling the contributions of attenuation and diffraction to the observed traveltime delay of the HOTSPOT data with independent methods, where a maximum S-velocity anomaly of $-12\,\%$ was derived for the best-fit model plume with $r_\mathrm{P} = 100\,\mathrm{km}$ (Allen et al. 1999).

Unfortunately, Allen et al. (1999) cannot constrain the magnitude of the temperature anomaly very well, so their estimate of $\Delta T_\mathrm{P} \lesssim 300\,\mathrm{K}$ must be regarded as a very soft upper bound. However, a recent study by Hung et al. (2004), which improved regional tomographic images of Iceland substantially by accounting for the finite wavelength of seismic waves, found the P- and S-wave anomalies to be 2–3 and 1.6–2.3 times larger, respectively, than in the older studies, i.e. $-3.5\,\%$ and $-6.2\,\%$, respectively, between 200 and 400 km; assuming the same, purely thermal relation as previous studies, ΔT_P would then be 250–350 K, but alternatively, they suggest that very deep melts could contribute to the effect. – In the interpretation of the HOTSPOT data, the effects of depletion and anisotropy were not taken into account quantitatively either due to the poor constraints on their effect on the velocities and the limited knowledge of the orientation of the dominant flow field. However, Foulger et al. (2001) remark that their observed $v_\mathrm{P}/v_\mathrm{S}$ ratios cannot be explained by the thermal effect alone, but require additionally the presence of a few tenths of a percent of partial melt at depths between 100 and 300 km; while the deeper bound might still be in agreement with hydrous damp melting, the shallower is probably an overestimate due to the limited resolution in the uppermost mantle, because partial melts are to be expected at shallower depths as well.

Although the ICEMELT and HOTSPOT data resulted in quite impressive images of the plume, it should be kept in mind that the inversion procedure for regional data might broaden anomalous regions (Wolfe et al. 1997), produce downward smearing effects so that a broad shallow structure could hardly be distinguished from a narrow deep one (Keller et al. 2000), and has poor resolution in the uppermost mantle due to insufficient cross-overs of steep incident teleseismic rays. Therefore a possible broad, spread-out plume head ($z \lesssim 100\,\mathrm{km}$) could not be expected to be revealed by this type of tomography, and neither could a detailed image of the melting region. As ray density is very low beneath 400–450 km, structures at the depth of the transition zone cannot be resolved either, although depth resolution is greater and

better in finite-frequency tomography than in ray tomography (Hung et al. 2004). Furthermore, the small aperture of the ICEMELT geometry raises the question if the outermost imaged parts are indeed unaffected mantle valid as a reference or if the tomographic image rather shows the innermost part of a much broader anomaly (Keller et al. 2000). The solution for this problem would be to establish a much larger network including marine stations.

Li and Detrick (2001) analysed ICEMELT and HOTSPOT surface wave traveltimes and amplitudes to gain information about the depths too great for controlled-source seismics and too shallow for the regional tomography and found evidence for the presence of melt in the crust and the upper mantle, especially beneath the rift zones. On a larger scale, and with a much lower resolution than body waves, Rayleigh and Love waves show group velocity reductions between ca. 5 and 9 % for periods between 100 and 150 s beneath Iceland, which also indicates the presence of a strong anomaly in the upper mantle (Levshin et al. 2001). A similar study by Pilidou et al. (2005) using SV-waves confirms the existence of a large anomaly 4–7 % slower than PREM above 200 km; it is 1600 km along-ridge, reaching Jan Mayen in the north, and 600 km across, and presumably marks the size of the entire plume head.

Global seismic tomography plays a key role in the determination of the deep structure of plumes, but compared with regional seismic tomography, it has a much smaller resolution, which is critical when it comes to mapping of rather thin structures like plume conduits. Bijwaard and Spakman (1999) and Zhao (2001) published P-wave models spanning the whole depth range of the mantle beneath the northern Atlantic, which display a twisted and tilted anomaly of varying amplitude starting at the CMB roughly beneath the southern tip of Greenland. The Bijwaard and Spakman (1999) model is very broad and has only very small values close to the CMB, but it rises to −0.5 % for most of the lower mantle and develops a complex, widely spread structure with connections to low-velocity anomalies as distant as beneath central Europe (figure 7). The Zhao (2001) model is quite similar but has weaker anomalies in the depth range between 2000 and 1400 km. Above 1000 km both models show a broad −0.5 % region, and in the upper mantle, the anomaly is significantly stronger. Beside the plume-related anomaly, the model of Bijwaard and Spakman (1999) shows a low velocity anomaly in the upper mantle extending beneath Greenland, which was also found in an upper-mantle tomographic study by Zhang and Tanimoto (1993). In the model of Zhao (2001), the cold, fast Greenland craton reaches deeper, and there is only a small slow patch in the uppermost lower mantle beneath it. In the tomographic S-wave model of Grand (2002), the central North Atlantic anomaly shows lateral extensions parallel to the ridge direction down to ca. 350 km and becomes more circular below, with the centre remaining under Iceland or being displaced only slightly to the southwest. Its amplitude decays to some −0.7 to −0.8 % to the bottom of the transition zone and stays on that value to ca. 1150 km, whereby the anomaly becomes wider. At depths between 1150 and ca. 1800 km, the anomaly widens towards northwestern Eu-

rope, which is seen in a similar style by Bijwaard and Spakman (1999), while only a very weak signal remains under Iceland itself. The anomaly remains at very low amplitudes almost down to the CMB directly under Iceland.

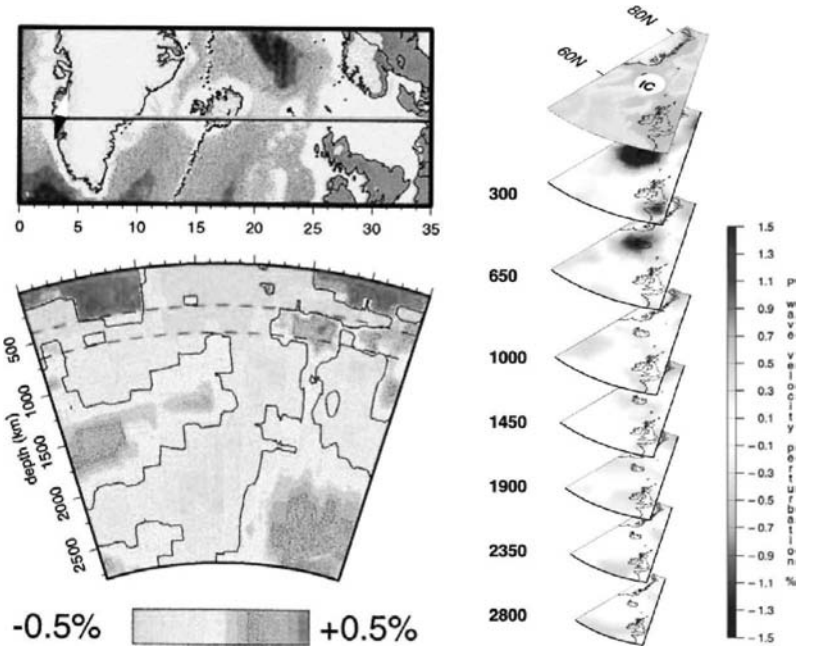

Fig. 7. Global P-wave seismic tomography images of the mantle beneath Iceland. Left: Roughly ridge-perpendicular vertical cross-section (slightly modified, reprinted from Earth Planet. Sci. Lett. 166(3–4), Bijwaard, H., Spakman, W.: Tomographic evidence for a narrow whole mantle plume below Iceland, pp. 121–126, © (1999) with permission from Elsevier). Right: horizontal cross-sections (reprinted with permission from Montelli, R., Nolet, G., Dahlen, F. A., Masters, G., Engdahl, E. R., Hung, S.-H.: Finite-frequency tomography reveals a variety of plumes in the mantle; Science 303(5656), 338–343 © 2004 AAAS). Note that the colour scales are clipped at $\pm 0.5\,\%$ in the left image and at $\pm 1.5\,\%$ in the right image. *The colour version of this figure is displayed on colour plate 4.*

A relatively narrow, significant low-velocity structure in the upper mantle beneath Iceland underlain by a weaker, at best diffuse anomaly in the lower mantle is confirmed by other global tomographic models (e.g. Grand 1994, Ritsema et al. 1999, Mégnin and Romanowicz 2000), although these images do not always show a contiguous structure for the whole depth range of the mantle, which might be due to the different and rather coarse resolution of the models. An attempt by Pritchard et al. (2000) to pinpoint the anomaly in the mid-mantle indicates a structure with a radius of no more than 125 km and $\Delta v_P \leq -1.5\,\%$ some 1500 km beneath the Iceland–Faeroe Ridge, but the

authors remark that the result is ambiguous, because only raypaths from a very limited azimuth range could be used. The position of the source region of the plume beneath Iceland at the CMB is corroborated by the detection of an ultra-low-velocity zone with a diameter of ca. 250 km by Helmberger et al. (1998). This is well in agreement with radius estimates for the plume of Bijwaard and Spakman (1999), who estimated a radius ≤ 250 km for the upper and 200–350 km for the lower mantle. A more precise assessment is not possible due to the limited resolution, but it is basically in agreement with the results from regional tomographic studies, as is the temperature estimate of 200–300 K, assuming entirely thermal effects.

Although estimates of plume radii based on global tomography models are quite moderate, it should be pointed out that in most tomography models a large background reduction in seismic wave speed is seen (figure 7), filling large parts of the upper mantle in the North Atlantic around Iceland. This large scale anomaly is presumably directly related to the large geoid high in this region (Marquart and Schmeling 2004).

A methodical progress was recently made by Montelli et al. (2004), who performed P-wave tomography taking into account the finiteness of seismic wavelengths for the long-period parts of their data. Their Iceland model shows a strong signal in the upper mantle, which greatly decays to only -0.2 or -0.3 % in the lower mantle (figure 7), leading them to propose a root depth of at most 1000 km for the Iceland plume. They suggest that the Iceland plume is confined to the upper mantle, and its image is deepened and broadened due to downward leakage and lateral smearing. While their resolution tests (Montelli et al. 2004, online supplement) confirm that a 800 km broad, hot, purely upper-mantle anomaly can leak downward several hundred kilometres, they also show that a whole-mantle plume narrower by up to 400 km would reproduce the observed data quite well, especially if one assumes a lower excess temperature than their 300 K. In their observed data, the anomaly can be tracked down consistently with Bijwaard and Spakman (1999) and Zhao (2001) to at least 1900 km, but it is unclear to which of the low-velocity regions in the north Atlantic area it could be related below that level. More recent S-wave tomography (Montelli et al. 2005) gives a clearer picture of a plume stem reaching down to the lowermost mantle, although the amplitude of the anomaly varies.

Altogether, it can be stated that an anomaly amplitude of at most 0.5 %, as observed in the lower mantle, does yield some indication for the existence of a whole-mantle plume. However, the weakness of the signal in the lower mantle in global tomography models has provoked doubts about a lower-mantle origin of the Iceland plume among some authors (e.g. Foulger et al. 2001, Foulger and Pearson 2001).

Anisotropy

Recent anisotropy studies (Bjarnason et al. 2002, Li and Detrick 2003a, Xue and Allen 2005) show the remarkable result that the S-wave anisotropy distribution partly reflects roughly the plate geometry and that neither a spreading-parallel nor a radial pattern, which could be assigned to the plume, are obvious from the data. The traveltime difference observed by Bjarnason et al. (2002) and Xue and Allen (2005) between the fast and the slow S phase is larger in the east than in the west and corresponds to a 100–200 km thick anisotropic layer in the east. Bjarnason et al. (2002) find the divide between the anisotropy domains to be located up to 100 km to the west of the NVZ and EVZ, which is interpreted as a manifestation of former locations of the spreading centre still conserved due to the sluggishness of crystal reorientation. The observed anisotropy can be explained by the shear of the diverging plates relative to a roughly NNW-directed flow with a velocity of ca. 3 cm/a. Furthermore, Li and Detrick (2003a) find a flip in the orientation of Rayleigh-wave anisotropy beneath western Iceland at a depth of about 50 km: above that level, the anisotropy indicates mantle flow parallel to the fossil spreading direction, whereas below it is ridge-parallel (roughly, NE–SW), suggesting plume head channelling and/or the effect of vertical melt films; beneath central Iceland, anisotropy at $z < 50$ km is weak and indicates that buoyant upwelling controls the orientation of crystals. At depths greater than 100 km, the N–S orientation observed in S-waves dominates. Xue and Allen (2005), who used a larger dataset than the earlier studies, found some differences between their splitting directions in western Iceland and those of Bjarnason et al. (2002) and Li and Detrick (2003a). They find stronger evidence for a ridge-parallel flow than Li and Detrick (2003a), although locally they rather interpret the pattern as directed towards the adjacent ends of the Kolbeinsey and Reykjanes Ridges, respectively, somewhat reminiscent of flow from an off-axis plume to a MOR. Similar to Bjarnason et al. (2002), they identify a single layer as the cause for the anisotropy. – A similar ridge-parallel, deep-reaching shear wave anisotropy pattern at parts of the East Greenland margin can be interpreted as ridge-parallel flow of plume material at earlier stages of the evolution of the Atlantic (Ücisik et al. 2005), highlighting the temporal persistence of this feature, but this view is not the only possible one. These authors also assumed a single layer in the upper mantle as the source of the anisotropy; the splitting times they find are of about the same magnitude as those of the studies on Iceland itself.

By contrast, surface wave anisotropy studies at the Reykjanes Ridge (Gaherty 2001) indicate that small-scale convection in the melting zone induces a mostly vertical orientation of olivine $\mathfrak{a}$ axes at $z < 100$ km, which is frozen in when the material moves outward and results in increasing anisotropy, whereas at greater depth the usual horizontal fabric of passive spreading of older lithosphere is observed. Gaherty (2001) interprets this as buoyancy-driven thermal convection due to the influence of the nearby hotspot. On

a larger scale, Pilidou et al. (2005) found the fast direction of horizontally travelling SV-waves to be parallel to the spreading direction of the plates at Reykjanes, while it flips to roughly N–S orientation near Iceland. These authors also found a decrease of anisotropy from some 5 % at 75 km to zero at 350 km.

Receiver function analysis and controlled-source experiments

Another method to gain information about the depth of origin of the plume is an analysis of travel-time differences of P–S conversions from the discontinuities at 410 km and 660 km. Since the presence of a thermal anomaly crossing the transition zone of the mantle narrows the stability fields of the olivine polymorphs, the difference of the arrival times of P–S conversions from these boundaries is reduced. The ICEMELT and HOTSPOT data have been used for this type of study, and a narrowing of the transition zone relative to IASP91 was indeed observed beneath Iceland (Shen et al. 1998, 2002). The effect was strongest in a region ca. 1° south of the junction of the volcanic zones, reaching a thinning by about 20 km. A possible extension of the anomaly further to the south is suggested by the fact that its observed maximum is at the southernmost border of the covered area and is also supported by the tilt of the stem imaged by Pilidou et al. (2005), although it must be kept in mind that the resolution of their model is already coarse at that depth. No significant deviation of the position of the discontinuities relative to IASP91 was found outside the region ascribed to the plume, suggesting that the plume indeed is rather narrow (and that an adequate reference was used in the ICEMELT tomography). It also indicates that the plume originates from the lower mantle and not from a hypothetical thermal boundary layer at the transition zone. Furthermore, Shen et al. (2003) found a close spatial relation of the stem position in the upper mantle to a discontinuity of very limited horizontal extent at 1050 km depth; a similar feature has been observed beneath Hawaii, which suggests that it is peculiar to hotspot locations and argues in favour of a lower-mantle origin of plumes. Shen et al. (1998, 2002) estimated that the plume excess temperature at the depth level of the transition zone is at least 140–150 K and its radius at most 200 km. It is possible that the pv → mj transition, which occurs at approximately the same depth, but has a positive Clapeyron slope, partly compensates the effect of the pv → rw transition (Hirose 2002). As Shen et al. (2002) did not take into account the former in their calculation of the excess temperature, their estimate should be regarded as a lower bound, and the plume might actually be hotter than 1800 °C at the bottom of the upper mantle. – The use of receiver functions for tracking the plume through the transition zone has also been criticised by Keller et al. (2000) who could not observe the thinning effect at several other hotspots and claim that it is thus not hard evidence for a lower-mantle origin of the plume.

Using receiver functions from HOTSPOT registrations, Schlindwein (2006) found a low-velocity zone in the uppermost mantle beneath most of Iceland, except the West Fjords and east Iceland, which increases in strength and shallows towards the youngest parts of the island and ends abruptly at the east margin of the NVZ. She interpreted this LVZ as asthenosphere, and the difference between its top and the depth of the Moho may serve as a constraint on the thickness of the unmolten lithospheric lid, which would hence reach a maximum thickness of 8–10 km.

Under favourable circumstances diving rays on the long refraction profiles (described in section 2.2) also probed the uppermost mantle. From the SIST data, Bjarnason et al. (1993) estimated a mantle P-wave velocity of 7.6–7.7 km/s, based on observed apparent velocities occasionally as high as 7.74 km/s. For the mantle beneath northeastern Iceland, the FIRE data suggest 7.9 km/s under the NVZ and 8.1–8.3 km/s under the adjacent Tertiary areas; the corresponding estimates for the mantle temperature are $\sim 1500\,^{\circ}\mathrm{C}$ under the neovolcanic zone and $\sim 800\,^{\circ}\mathrm{C}$ in the lithospheric mantle (Staples et al. 1997).

3.2 Geochemistry

Geochemical sources of the Iceland plume

On Iceland itself, one expects that the volcanism is characterised geochemically by contributions from the plume and from the normal oceanic asthenosphere; however, it is still subject to controversy whether the common MORB source really contributes to Icelandic volcanism and how many non-MORB sources are involved. There is agreement about a chemically heterogenous plume, but some workers postulate a major contribution from a depleted MORB source in addition to two other reservoirs like HIMU or EM-1 (Hanan and Schilling 1997, Hanan et al. 2000, Stracke et al. 2003), whereas others find the influence of MORB on Iceland to be small (e.g. Thirlwall et al. 2004) and regard the significant depleted component as a non-MORB one e.g. from the lower mantle. An old MORB-like mantle source which rests on the 660 km discontinuity might though have been picked up by the ascending plume and carried upward without mixing, but rather as a "sheath" (Thirlwall 1995, Fitton et al. 1997, Hardarson et al. 1997, Kempton et al. 2000, Fitton et al. 2003), which would influence more remote parts down the ridges (e.g. Murton et al. 2002, see fig. 8); the latter view has been supported by numerical models by Farnetani et al. (2002). – Yet other workers prefer two-source models with a MORB-source (Mertz and Haase 1997) or another common north Atlantic endmember (Ellam and Stuart 2000) together with a second, possibly regionally varying endmember or two different types of sources derived from more local studies (e.g. Nicholson and Latin 1992, Breddam 2002). Nicholson and Latin (1992) explain the compositional variability by imperfect mixing of melt from different depths, the deepest originating from about 140 km, from

which they deduce a plume potential temperature of 1580 °C; in a more recent study, Putirka (2005) arrived even at a T_{pot} of 1637 °C on the basis of Mg and Fe contents in olivine. – It should be mentioned that in addition to source heterogeneity, which might exist at such a small scale as 10–20 km (Furman et al. 1995), crustal contamination enhances the chemical variability of lavas, but the view that all variability is due to this mechanism (Óskarsson et al. 1985) has been countered by many investigations which regard the crustal contribution as minor (e.g. Meyer et al. 1985, Hémond et al. 1993).

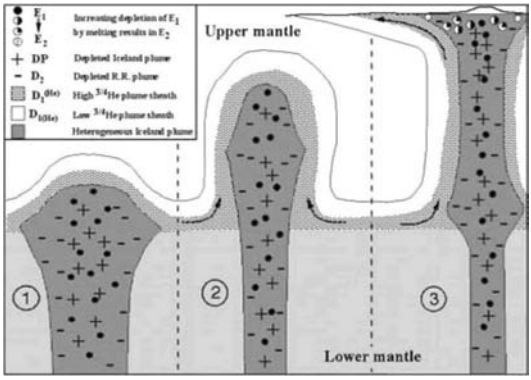

Fig. 8. Schematic geochemical structure of the Iceland plume and its evolution. (From Murton, B. J., Taylor, R. N., Thirlwall, M. F.: Plume-ridge interaction: a geochemical perspective from the Reykjanes Ridge; J. Petrol., 2002, vol. 43(11), pp. 1987–2012, by permission of Oxford University Press.)

A frequently found signature in many studies is that of recycled oceanic lithosphere, to which both the crust and the lithospheric mantle contribute (Chauvel and Hémond 2000, Skovgaard et al. 2001, Breddam 2002, Peate et al. 2003, Kent et al. 2004), and it has been proposed as a candidate for the depleted non-MORB mantle source on the grounds of its low $\delta^{18}O$ (e.g. Skovgaard et al. 2001, Macpherson et al. 2005) and high $^{40}Ar/^{36}Ar$ ratio (Burnard and Harrison 2005). However, opinions seem to differ on whether the entire composition can be explained by upper-mantle sources (Chauvel and Hémond 2000) or whether certain undegassed lower-mantle components (e.g. FOZO) are also required (Stecher et al. 1999, Hilton et al. 1999, Breddam 2002). Importantly, recycling of old oceanic lithosphere involves the presence of some eclogite from its crustal section in the plume. Geochemical evidence for this has in fact been found in rocks from the whole lifespan of the plume, for instance as a requirement of an Fe-rich source component (e.g. Scarrow et al. 2000, Korenaga and Kelemen 2000) or on the basis of lead isotope geochemistry (e.g. Thirlwall et al. 2004); the latter study supports an Iapetus origin of what once has been MORB, but considering Nd/Sm, it comes to the conclusion that it has a different origin than the more depleted sources. Recently, Foulger et al. (2005) have used the evidence for eclogite to propose a model for Iceland which discards the plume altogether and explains the whole anomaly in terms of remelting of old subducted crust.

Breddam et al. (2000) could show a strong correlation between the plateau-like maximum of the ^{3}He anomaly and the seismic velocity and Bouguer gravity anomaly observed on Iceland (figure 9), and deduce a width of not much more than 100 km for the plume conduit; recently, Macpherson et al. (2005) could show with a larger dataset that the central Icelandic maximum is actually not plateau-like, but rather interspersed with ^{3}He/^{4}He at the MORB level, which can be interpreted as a sign of small-scale heterogeneity in the mantle. This low value for r_P (see table 2) might rather reflect the width of the damp melting zone, which is probably narrower than what would be considered as "the plume" with regard to the thermal or seismic anomaly. As they note, He is degassing from the source already during the initial hydrous melting stage due to its strong incompatibility before the plume has undergone significant lateral spreading or the melting-induced increase in viscosity has occurred; this could explain why the correlation with the geophysical signals from the plume stem is strongest for He. However, a certain fraction of the He is transported with the material of the spreading plume head, which indicates that the viscosity increase due to dehydration which causes it (see section 3.3) is notable below the dry solidus already. – Although a correlation between the plume and He is obvious, none of the mentioned studies yields a proof for an origin of the ^{3}He from the lower mantle. Similarly, an unusually high, primordial ratio of ^{22}Ne/^{21}Ne in some samples from Reykjanes and central Iceland has also been interpreted as possible evidence for a small undegassed lower-mantle component in the plume source (Dixon et al. 2000, Moreira et al. 2001), but a corresponding solar ratio of ^{3}He/^{4}He was not observed in those samples.

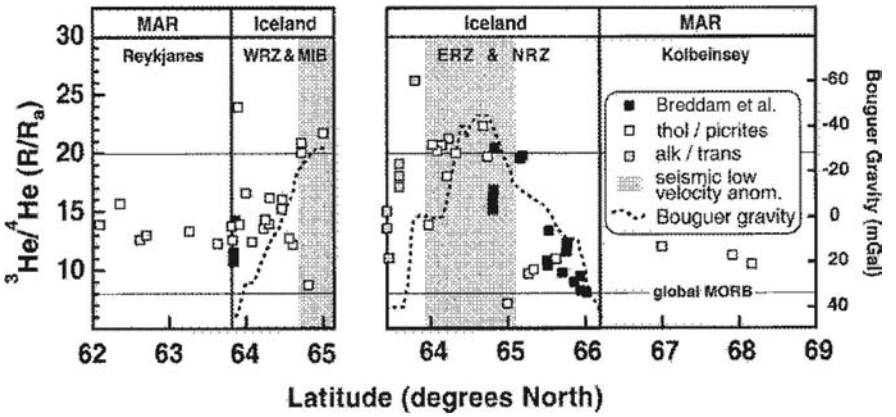

Fig. 9. Along-ridge positions of the ^{3}He/^{4}He, Bouguer, and seismic velocity anomalies (slightly modified, reprinted from Earth Planet. Sci. Lett. 176(1), Breddam, K., Kurz, M. D., Storey, M.: Mapping out the conduit of the Iceland mantle plume with helium isotopes, pp. 45–55, © (2000) with permission from Elsevier).

An issue of special interest with regard to melting, rheology and several geophysical observables is the water content of the mantle and the question whether the plume has a water content different from that of normal mantle. Recent investigations of basalt samples from the northern Atlantic (Jamtveit et al. 2001), and especially from along the Reykjanes Ridge and Iceland itself (Nichols et al. 2002) yield evidence that indeed the plume source has water concentrations of more than 300 ppm, probably as much as 620–920 ppm; they remark that there is considerable variability among the samples from Iceland. Compared with this the source of MORB at the southern Reykjanes Ridge has a value of only 165 ppm, which agrees well with independent estimates for the normal upper mantle (Wood 1995, Saal et al. 2002). The boundary between both sample sets is about 650 km from the plume centre, thereby providing another constraint for the influence of the plume.

The mixing ratios of the three components of Hanan and Schilling (1997) vary spatially and also have not been constant over time: mixing proportions resp. their ratios vs. eruption time show a decrease of the "enriched component (e)" contributions from 15 to 9 Ma and a pronounced pulse of the dominant most radiogenic plume component (p) between 6 and 10 Ma, peaking at 7.5–8 Ma and coinciding with a boost of volcanic activity. This observation is in agreement with other evidence for temporal variations in magmatism over the past 70 Ma with a periodicity of 3–8 Ma as recorded in several seamounts (e.g. O'Connor et al. 2000), in the V-shaped structures of the Reykjanes Ridge, and concluded from crustal thickness estimates (Allen et al. 2002b).

Altogether, the geochemical results are quite diverse and partly contradictory, but well-established key results include the existence of considerable heterogeneity of the mantle sources, in particular the presence of a source derived from recycled oceanic crust, and an increased water content in the mantle beneath Iceland.

Reykjanes and Kolbeinsey Ridges

The geochemical footprint of the plume extends along the Reykjanes Ridge (Schilling 1973), as visible in rare-earth element (REE), Pb, and ^{3}He anomalies, which seem to correlate well with e.g. the thermal anomaly over more than 1500 km (Taylor et al. 1997). They claim that the plume actually contaminates a very large part of the North Atlantic asthenosphere and that the geochemical trends along the ridge can be explained best by mixing of MORB and plume melts in continuously varying proportions. However, the combined crustal thickness and geochemistry model of Maclennan et al. (2001a) suggests that the region where melting is immediately affected by the upwelling of the plume is limited to a ~150 km-radius zone beneath central Iceland and does not reach to the Þeistareykir volcano in the NVZ.

The presumed along-ridge flow of plume material can be expected to provide a radial, if distorted, geochemical cross-section through the plume. In particular, material from the above mentioned sheath (Fitton et al. 1997,

Kempton et al. 2000) does not enter the central part of the plume and is thus most likely to produce melts in ridge sections somewhat remote from Iceland (figure 8). A detailed analysis of the chemical abundances and Nd–Sr–He isotopes of a large set of samples from several hundred kilometres of the Reykjanes Ridge by Murton et al. (2002) displays not only the typical along-ridge gradients in several geochemical observables, but exposes also a chemical variability which lets these authors propose a total of six different sources of melt in Iceland and its surroundings, two of which are related with the sheath. In agreement with the link between certain sources and certain parts of the plume, not all of these sources are found everywhere in the region, some are restricted to Iceland, whereas others only occur on the ridge; Thirlwall et al. (2004) conclude from their Pb isotope study that locally on Iceland, mixing processes are essentially binary.

As mentioned in section 2.1, the north–south asymmetry of the Icelandic crust is one of the most prominent tectonic characteristics and suggests that a corresponding asymmetry exists in the plume–MOR interaction, at least on the shallowest level, where the mantle melts. While a fairly gradual transition from the OIB-type, diverse Icelandic signature to MORB can be observed along the Reykjanes Ridge, the situation at the Kolbeinsey ridge is less clear. Mertz et al. (1991) did not find plume–MORB mixing trends north of the TFZ especially in the Pb signature and defined the TFZ as a geochemical boundary; Mertz and Haase (1997) argued that MORB source mixes with different enriched end-members, of which the southern is present in the plume. In contrast, newer studies with a larger dataset yielded indication for influence of the plume north of Iceland, e.g. elevated $^3He/^4He$ (Taylor et al. 1997, Botz et al. 1999, Schilling et al. 1999, Chauvel and Hémond 2000). In a synoptical investigation of Pb, Nd, Sr, and He systematics, Schilling et al. (1999) emphasise the importance of He for the assessment of the influence of the Iceland plume and declare the Spar Fracture Zone, which is located halfway between Iceland and Jan Mayen resp. ca. 300 km north of the TFZ, as the approximate boundary, although the high-$^3He/^4He$ signature of Iceland extends even further northward. Similarly, Blichert-Toft et al. (2005) find a smooth transition through the TFZ for one of their source components, but the general picture they develop of the northern Atlantic is one of three geochemical domains with boundaries at Iceland and Jan Mayen, respectively; they suggest that the northern and the southern part of the plume sample and transport different sources. The weak signature of V-structures in the crust as far north as the northern Kolbeinsey Ridge and Jan Mayen (Jones et al. 2002) (see section 2.1) and the synchronism of plume pulses on Iceland and planform anomalies around the Kolbeinsey Ridge (Abelson and Agnon 2001) would also support the arguments of an influence of the Iceland plume on the ridge in the north.

Upwelling velocities from geochemical modelling

A main characteristic of a plume and also a key number to constrain numerical experiments is its material flux. On the basis of REE and isotope geochemistry, topography data, mass balance considerations (White 1997), and ^{238}U–^{230}Th disequilibria (Elliott 1997), the magnitude of active upwelling beneath Iceland was found to be rather moderate, and certainly much smaller than in Hawaii. White (1997) conjectures that much of the plume material is readily integrated into the diverging oceanic plates and follows its motion. From crustal thickness measurements and REE concentrations the active upwelling was estimated to be 2–4 times (Allen et al. 2002a, Holbrook et al. 2001) or even up to ten times (Maclennan et al. 2001a) larger than the mass flux due to rifting; higher values (5–20 cm/a in the centre) are also supported by newer ^{238}U–^{230}Th data (Kokfelt et al. 2003). The variations between these models can be attributable to different assumptions, e.g. concerning the potential temperature, melting entropy, or the depth for which the estimate holds, but the significant common conclusion is the importance of active flow for explaining the anomalies found beneath Iceland. In the study by Sleep (1990), a volume flux of 2.23 km^3/a is given[4], which corresponds to a maximum upwelling velocity of about 4.6 cm/a, if one uses $r_P = 125$ km and assumes that the r_P values in table 2 represent the radius at which the anomaly has decayed to $1/e$ of its maximum. Schilling (1991) estimated a flux of 1.43 km^3/a, which would correspond to a maximum upwelling at about 3 cm/a for the same r_P. It should be noted that his high estimate of $\Delta T = 263$ K is not necessarily correct, because the flux can also be produced in part by chemical buoyancy, which he did not take into account in his model.

3.3 Geodynamic modelling

Ridge–plume interaction models

In the 1990s, a number of numerical experiments has been conducted on the interaction of plumes and ridges, many of them with special emphasis on Iceland. In general, they have matched some of the field observations while contradicting others.

Feighner and Richards (1995) and Feighner et al. (1995) studied in laboratory and numerical experiments the ascent of chemical plumes beneath a spreading ridge and observed the development of a tight lacing of the plume

[4] In the paper of Sleep (1990), actually a buoyancy flux of 1400 kg/s is given; this buoyancy flux is transformed to a volume flux estimate using $\alpha = 3 \cdot 10^{-5}$ 1/K, $\varrho_0 = 3300$ kg/m^3, $\Delta T = 200$ K and assuming a Gaussian flux distribution for better comparison. It should be noted that this estimate includes the possible flux of the weak plume postulated as the cause for the Jan Mayen hotspot. On the other hand, it is still questionable whether Jan Mayen is really the surface expression of a plume; e.g. it is far from being ranked primary in the Courtillot et al. (2003) compilation, because there is only little safe information.

head which they called a waist. By applying their results for the shape of a steady-state plume head to the Iceland plume, they came to the conclusion that it has now, i.e. after 60 Ma, become stationary, judging from the comparison of the observed extent of the geochemical anomaly with their results of 850 and 900 km, respectively, for the plume's waist width. Although it is possible that the Iceland plume has reached a quasi-stationary state now, their results are not straightforwardly applicable to Iceland, since they neglected the relative motion of plume and ridge and also implied a constant melt production which is in contradiction with the observation of V-shaped surface features and findings from geochemistry. Furthermore they assumed a (nearly) isoviscous rheology with $\eta_0 = 10^{21}$ Pa s and it is difficult to assess if thermal weakening and dehydration stiffening make this an acceptable approximation to the rheology of the upper, say, 150 km beneath Iceland.

Ribe et al. (1995) also studied numerically a ridge-centred plume and used their model to estimate the dynamic and total topography of the Iceland plume and favour a cool, broad, and slow plume ($\Delta T = 93$ K, $r_P > 300$ km, $v_{zP} \approx 2$ cm/a; see table 2). Such a plume scenario is in contradiction to geochemical results (cf. section 3.2), but in the Ribe et al. (1995) model a narrow, hot plume would produce far too much melt. It must be noted, however, that they assumed ideal fractional melting, did not account for possible redistribution of melt by migration before extraction, and assumed a rather low mantle potential temperature T_{pot} of only 1324 °C, so that it is not clear if their melt production results are appropriate, although their values for normal oceanic crust are realistic.

Ito et al. (1996) made a similar investigation, but assumed a slightly higher T_{pot} of 1350 °C and included some effects related to melt dynamics, in particular buoyancy contributions from depletion and melt retention, although they did not explicitly model melt migration. Nonetheless, their observations are basically consistent with those of Ribe et al. (1995) in that their cool, broad plume ($\Delta T = 75$ K, $r_P = 300$ km) fits better the observed values of crustal thickness, topography, and gravity, while their hot, narrow plume ($\Delta T = 170$ K, $r_P = 60$ km) can better explain estimates of total crustal production rates, geochemical anomalies and the seismic tomography from ICEMELT. They find that the depletion and melt retention and the damping effect of latent heat on temperature are secondary effects compared with thermal buoyancy and tend to cancel out. Thus, the effect of melting on large-scale convection would be minor, as far as depletion, melt retention and latent heat are concerned, but its influence on dynamical topography, the mantle gravity signal or P-wave traveltimes is significant, especially for the hot, narrow plume. Both Ribe et al. (1995) and Ito et al. (1996) fail to reproduce channelling of plume material into the ridge, because the viscosity ranges accurately tractable with their methods do not allow for sufficiently large viscosity contrasts. However, Ito et al. (1996) note that their estimates for total excess crust production by a hot plume, which agree well with obser-

vations, suggest that along-axis melt generation is significantly higher than in their model.

A new attempt to shed light on the properties of the plume was made by Ruedas et al. (2004). They combined convection models with plumes of different temperature and with different amounts of retained melt with an explicit model of melt generation and segregation in the melting zone of the ridge and plume after Schmeling (2000). Based on a melting parameterisation of Hirschmann (2000) they calculated the thickness of the generated crust as described in section 2.4 and used it to constrain temperature and retained melt within the plume. The difference of the approach of Ruedas et al. (2004) with the earlier models lies primarily in the more complete energy equation used, which also included phase transitions in the deep upper mantle, in the more detailed treatment of melt dynamics and the special consideration given to the retained melt fraction. Figure 10 shows the maximum total thickness of the generated crust for different excess temperatures and retained melt fractions assuming anhydrous melting and temperature- and depth-dependent viscosity. As both the degree of melting and the upwelling velocity increase with the plume temperature, the total crustal thickness is a strongly non-linear function of the excess temperature. In order to produce a normal oceanic crust, the retained melt has to be as low as 1 % or less, and a potential temperature of 1410 °C is required. Given the observed crustal thickness as discussed in section 2.3, excess temperatures of 100–150 K at 200 km depth are required, which correspond to upwelling velocities decreasing from more than 10 cm/yr near the bottom of the melting zone (>100 km) to 1 cm/yr near the top of the melting zone. As a result, melting rates are an order of magnitude higher in the deepest part of the melting zone compared to the shallow melting region. Such a strong decrease of upwelling related melt production has also been found by Maclennan et al. (2001b) who inverted REE concentrations of central Icelandic basalts. Figure 10 also indicates that rather less than more than 1 % melt is retained in the mantle, in agreement with general geochemical findings, because otherwise the crust at normal ridge ($\Delta T_P = 0$ K) would be substantially thinner than observed.

Models with dehydration melting

A major progress which removes several problems with the hot, narrow plume was made by Ito et al. (1999) by introducing the effect of dehydration on viscosity. They found that the viscosity increase by loss of water to deep low-degree melts, which they assume to be of about two orders of magnitude, largely suppresses active buoyant upwelling, leading to a significantly lower melt production rate and upwelling in the melting zone controlled by the spreading rate of the plates. Modelling of incompatible element concentrations indicates an enriched source, but still does not match the field evidence for gradual mixing of plume and MORB source by along-axis melt migration. Melting is restricted to $z > 40$ km in these models by assumptions about

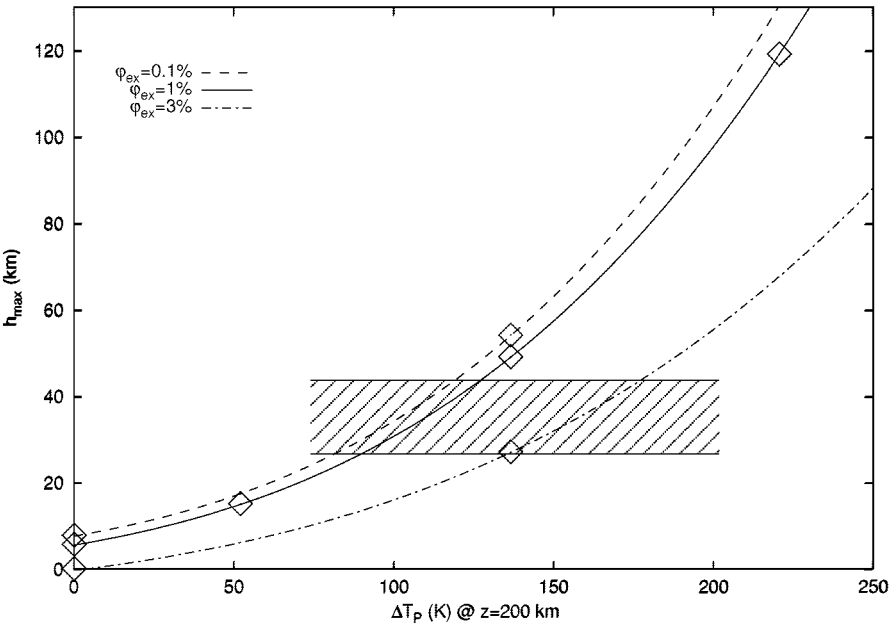

Fig. 10. Maximum steady-state crustal thickness as a function of $\Delta T_{\mathrm{P}}(z = 200\,\mathrm{km})$ and maximum retained melt fraction, φ_{ex}, for a background mantle T_{pot} of 1410 °C; the diamonds represent the steady-state h_{max} values from the numerical models of Ruedas et al. (2004), the hatched area indicates observed crustal thicknesses. The curves should not be used for extrapolation much beyond the ΔT_{P} range shown, because limiting effects such as clinopyroxene exhaustion are expected at very high ΔT_{P}. (Modified after, and reprinted with permission from, Ruedas, T., Schmeling, H., Marquart, G., Kreutzmann, A., Junge, A.: Temperature and melting of a ridge-centered plume with application to Iceland. Part I: Dynamics and crust production. Geophys. J. Int. 158(2), 729–743, 2004 © Blackwell.)

hydrothermal cooling at the ridge and application of a criterion for the exhaustion of clinopyroxene as a switch for the suppression of further melting. It is actually possible that Ito et al. (1999) underestimate the effect of water and melting dehydration, because they do not assume an elevated water content for the plume (see section 3.2). However, a contradiction to dehydration stiffening is obtained by viscosity estimates from postglacial rebound measurements (e.g. Sigmundsson 1991) and postseismic/postdiking deformation observations (Pollitz and Sacks 1996), because both indicate values of $3 \cdot 10^{18}$–10^{19} Pa s for the uppermost mantle beneath Iceland. Apart from the influence of non-Newtonian behaviour, Ito et al. (1999) proposed as an explanation that estimates from rebound models are essentially sensitive to the structure of the uppermost mantle, which can be controlled significantly by accumulated or retained melt, while its effect on larger-scale mantle convection would be marginal. – Recent models with a water-rich plume in a

hydrous background mantle by Ruedas (2004, 2006) confirm the damping effect of dehydration stiffening on melt production found by Ito et al. (1999) and suggest that for water concentrations as those found in the Iceland region (cf. section 3.2), the plume must be ca. 200 K hotter than the background in the mid-upper mantle. These models also reproduce the shape of the anomalous crust, especially its along-ridge extent, better than models without the effect of water. It is interesting to note that the plume excess temperatures of the hot, hydrous models of Ito et al. (1999) and Ruedas (2004) agree well with the estimate of 162–184 K for the difference in potential temperatures derived from geochemical investigations by Putirka (2005); that study also supports the assumption of a rather hot background mantle.

Predicting geophysical observables

Mantle convection models of plumes allow the calculation of fields of physical quantities such as temperature, depletion, and porosity. Using rock physics relations these fields have been used to predict geophysical observables such as seismic anomalies, electrical conductivities and magnetotelluric response functions (Kreutzmann et al. 2004, Ruedas 2006). Taking the dynamical models of Ruedas et al. (2004) with varying excess temperatures and retained melt fractions Kreutzmann et al. (2004) predicted seismic anomalies characterised by two low velocity zones. Such a double low velocity zone, which has also been obtained in hydrous plume models of Ruedas (2006), is in agreement with seismic surface wave inversions by I. Bjarnason (see the dash-dotted curve in figure 11, and Kreutzmann et al. 2004, for references). While the deeper anomaly may be attributed to enhanced water content and/or the onset of melting, the shallower one results from high temperatures associated with the elevated plume head compared to a cooler reference lithosphere. The best agreement with seismic observations could be obtained with a plume of about 135 K excess temperature at 200 km depth, 1 % retained melt and some additional water within the plume stem. As figure 11 indicates, a hydrous plume stem may cause stronger seismic anomalies than those of traditional tomography. If, however, the recent results from finite-frequency tomography (Montelli et al. 2004, Hung et al. 2004, cf. sect. 3.1) prove right, or the effect of wave front healing has underestimated the seismic anomalies so far (cf. section 3.1), the anomalies from the convection models can be brought in closer agreement with observations. The MT transfer functions calculated from the electrical conductivities by Kreutzmann et al. (2004) revealed that at realistic melt contents, there is hardly a possibility to separate the plume signal from the ridge at the periods of currently available observations. In fact, at low retained melt fractions Kreutzmann et al. (2004) show that for electrical conductivity the effect of depletion may overcompensate the effect of the well-conducting melt. Even more importantly, the hydrous models of Ruedas (2006) suggest that upon dehydration melting the deep part of the melting region of the plume may become electrically less conductive than the

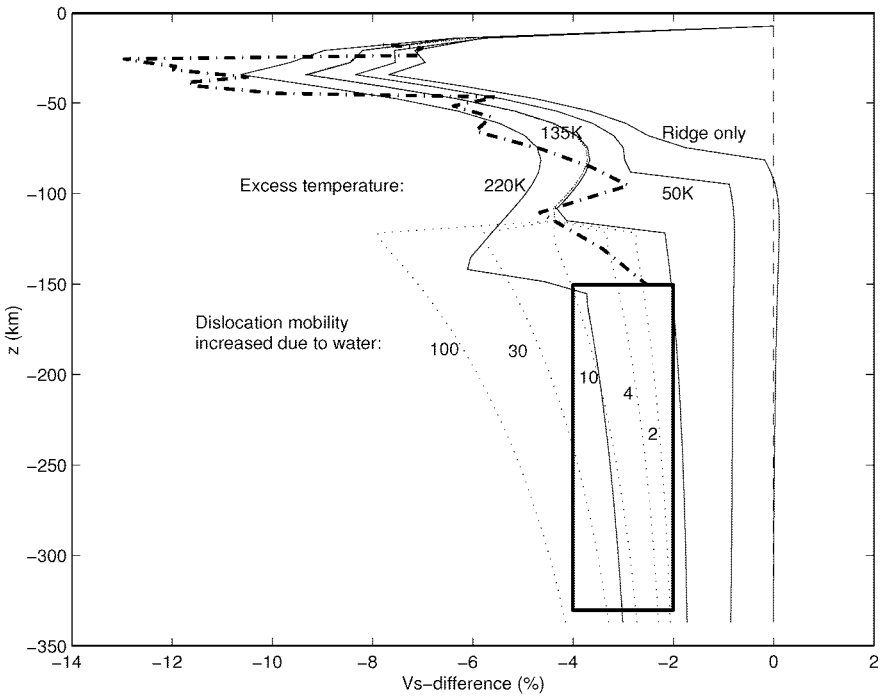

Fig. 11. Comparison of modelled depth profiles of $\delta v_S/v_S$ in % at the plume centre for dynamic plume models with different excess temperatures and the normal ridge with seismological observations. Dash-dotted curve results from surface wave inversions in central Iceland, the rectangle gives the range of seismic tomography studies. The dotted curves show the effect of water, amplifying the velocity anomaly by increasing the mobility of dislocations. (Reprinted with permission from Kreutzmann, A., Schmeling, H., Junge, A., Ruedas, T., Marquart, G., Bjarnason, I. Þ.: Temperature and melting of a ridge-centered plume with application to Iceland. Part II: Predictions for electromagnetic and seismic observables. Geophys. J. Int. 159(3), 1097–1111, 2004 © Blackwell.)

ambient mantle, and only the deep, hydrous, and still unmolten part of the plume stem might give a strong conductivity anomaly. Given the small plume stem radii as summarised in table 2, the detection of plumes by MT methods thus remains a challenge.

Gravity and mantle flow model for the North Atlantic

A different approach compared to the idealised plume models discussed above has been applied by Marquart and Schmeling (2004), who converted the tomography model of Bijwaard and Spakman (1999) (see figure 7 left) to temperature (figure 12 left) assuming a depth-dependent thermal expansivity. By scaling a temperature and depth-dependent mantle viscosity they fitted

gravity and geoid to observations for wavelengths < 4000 km. While in the Bijwaard and Spakman (1999) tomography model the strongest seismic velocity reduction in this region exists at around 80 km depth beneath Iceland, in deeper parts of the upper mantle the anomaly is not situated directly beneath Iceland, but to the west of it and below the Kolbeinsey ridge, and scales to an excess temperature of 150 to 200 °C (figure 12). In the deeper mantle a broad anomalous region rises from west to east (as can be seen in figure 7) and scales to about the same excess temperature as in the upper mantle (figure 12). Based on this temperature field and the resulting dynamic flow field Marquart et al. (2006) obtained a large-scale upwelling in the upper mantle situated NW of Iceland and along the Kolbeinsey Ridge (figure 12 right), which leads to a dynamic topography between 200 and 400 m. This flow model is to some extent in agreement with studies on azimuthal anisotropy in the North Atlantic (Levshin et al. 2001) and can also explain the geochemical gradient along the Reykjanes Ridge and the very shallow bathymetry and thick but geochemically uniform crust along the entire Kolbeinsey Ridge.

Creation of V-shaped ocean topography pattern

A very special feature of the Iceland plume never reproduced by stationary plumes are the V-shaped patterns of the Reykjanes Ridge (see section 2.1). It has repeatedly been suggested that they were generated by pulsations of the plume and a concomitant enhancement of the injection of plume material into the ridge (Vogt 1971, 1976). Albers and Christensen (2001) have succeeded in producing a very similar structure in numerical models with large viscosity contrasts between plume and lithosphere and low spreading rates. Yale and Phipps Morgan (1998) had already observed in models with a thermal and compositional lithosphere including a narrow asthenospheric channel beneath the ridge that excess flux from a plume would be strongly focused and yield a dynamic topography in good agreement with observations if the plume is hot and narrow. However, the model of Albers and Christensen (2001) results in a very narrow ($r_P \approx 40$ km), hot plume stem with a very low viscosity ($< 10^{17}$ Pa s), which seems to contradict seismic tomography models and estimates of viscosity and crust generation, whereas a broader plume would have too large a buoyancy flux (cf. table 2). – As an alternative, Ito (2001) proposes an extension of the model of Ito et al. (1999) with a plume of varying radius, but constant maximum ΔT and moderate viscosity contrast. The radius variations of the plume bring ring-like pulses of abnormally hot material towards the edge of the lithosphere, where they spread radially, conserving the higher temperatures preferentially in the along-axis portions while conductive cooling damps them below older lithosphere. The propagating pulse generates a V-shaped crustal thickness and gravity anomaly; this mechanism only works if dehydration-enhanced viscosity is included in the model. Ito (2001) points out that in spite of the flow velocity decrease predicted for radially spreading pulses, the curvature of the V-shaped structures

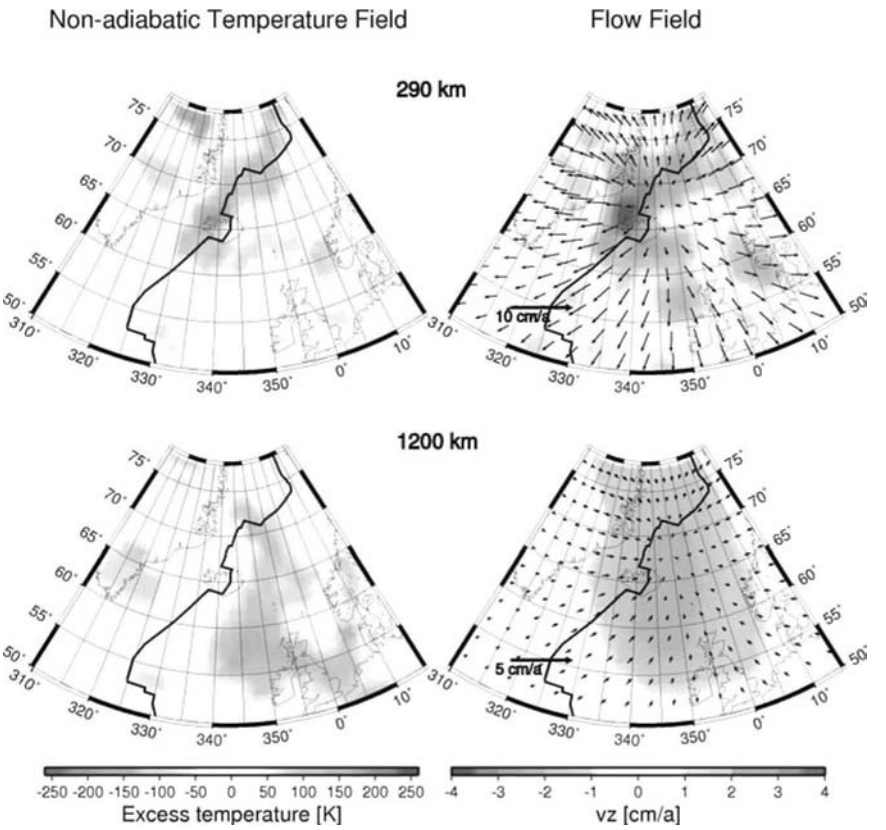

Fig. 12. Non-adiabatic temperature field in the mantle below the North Atlantic based on the Bijwaard and Spakman (1999) tomography model at 290 and 1200 km depth (left) and resulting mantle flow field (right). *The colour version of this figure is displayed on colour plate 4.*

is only weak, so that the patterns appear almost as linear as pulses of along-axis injections would be. Recent surface wave investigations by Dunn et al. (2005) support a broad, deep rather than a shallower, narrowly channelled plume flow beneath the Reykjanes Ridge. – A different mechanism leading to V-shaped patterns, not controlled by temporal variations of the plume, was recently found by Rabinowicz and Briais (2002) in three-dimensional models of a system including a hotspot and segmented ridges which can adopt their position to the current stress field of the lithosphere. This model features a complicated polyhedral pattern of convection cells and small-scale convection rolls perpendicular to the ridge which results in significant along-axis variations in temperature and crustal thickness as well as in the formation of transform faults. A superimposed along-ridge large-scale convection current

leads to a corresponding drift of the local anomalies beneath the spreading plates, resulting in a V-shaped structure.

Alternatives to the plume model

As mentioned in previous sections, some authors doubt the validity of the plume concept and propose alternative models which try to explain the observations with causes in the upper mantle alone. For instance, King and Anderson (1995) suggest that the North Atlantic Igneous Province was not caused by a plume head, but rather by convection driven by the strong lateral temperature contrast between the old Greenland craton and the rifted lithosphere. More recently, Foulger and Anderson (2005) and Foulger et al. (2005) proposed that the chemical anomalies and the excess melt production in the Iceland region can be explained by a chunk of oceanic lithosphere which got trapped in the final stage of the closure of the Iapetus ocean and was too young and hot at the time to subduct fully. These authors estimate the fraction of old oceanic crust in the mantle source of the Icelandic crust to be a few tens of percent, whose gabbroic part would be molten to 60–80%. However, it remains unclear if eclogite can be dynamically and chemically stable over the long time since the closure of Iapetus more than 410 Ma ago. Furthermore, extensive melting of such a large fraction of the mantle is difficult to imagine without an additional heat source, because the consumption of latent heat, which is already significant in the lower-degree melting in a purely peridotitic plume head, would probably preclude the suggested high melting degrees (e.g. Phipps Morgan 2001). At this stage, these ideas also still lack support from numerical models.

3.4 Synopsis

The combined efforts of seismological surveys, geochemistry, and numerical modelling have led to a clearer picture of the Iceland plume, especially as far as the upper mantle is concerned. The characterisation of the plume in the lower mantle has at least evolved so far that Iceland is viewed by many authors as one of the best-established examples for a plume which originates somewhere in the lower mantle. Nonetheless, the number and depth of origin of geochemically distinct sources and especially the depth of the plume's root remain unresolved.

Seismic tomography and convection models have converged in the last years towards a model of a rather hot and moderately narrow plume in the upper mantle, which leads to a significant amount of active upwelling. The values in table 2 suggest that the maximum temperature anomaly at a depth of about 200–300 km lies between 150 and 200 K and that the radius of the plume is 100–150 km. The extreme r_P values from geochemistry and global tomography are less reliable due to the lack of resolution of these methods, and it is remarkable that some of the chemical ΔT_P estimates tend to higher

values than those of other methods. This could be due to insufficient consideration of source heterogeneity, e.g. contributed by an eclogitic component, but it is also possible that the simplifications in $\Delta v_{P,S}$–ΔT_P conversion, the limited resolution in seismological models, and the numerical limitations of convection models fail to reproduce a very narrow plume core with significantly higher temperature and lower viscosity. Possible deficiencies of the numerical models to reproduce the flow field of the plume accurately are also indicated by the large discrepancy between volume flux estimates. It should be noted however, that the more realistic models including the dynamical effect of dehydration (Ito et al. 1999, Ruedas 2004) suggest that a relatively large volume flux is necessary to reproduce crustal thicknesses and volumes in a hydrous model and avoid plume temperatures significantly above current estimates. The effect of dehydration also implies to some extent that the flow of plume material along the ridge is rather broad and deep than narrow and shallow; nonetheless, it is reasonable to assume that due to the temperature effect, some focusing does take place near the ridge, although it might not be as strong as in the models by Albers and Christensen (2001).

Assessing the seismological findings for the Iceland plume, one can state that all tomographic studies agree about a pronounced anomaly in the upper mantle. Especially the regional tomography models of the ICEMELT and HOTSPOT data provide a detailed structure of the upper 400 km of the mantle, but they cannot image beneath a depth of 400–450 km. All global tomography models yield some evidence of a low-velocity anomaly in the lower mantle, but the resolved structures diversify the more the deeper mantle levels are considered, and they cannot always be regarded as contiguous.

In principle, the poorer visibility is also at least qualitatively expected from mineral physics, because the anharmonic variation of seismic velocities with temperature depends strongly on thermal expansivity for a given composition, and the thermal expansivity of transition-zone and lower-mantle minerals is considerably smaller than that of upper-mantle minerals under the respective p–T conditions.

The presence of a gap in the LVZ in the mid-mantle beneath Iceland as seen in some tomographic models (see section 3.1) is thus not necessarily evidence against the CMB origin of the plume either, because the plume conduit thins or its seismic contrast weakens, possibly to a size or value beyond seismic resolution. It might even be possible that the conduit disrupts or the plume source is exhausted and the lack of a deep root indicates that the rest of the tail is now ascending.

If the plume stems from the lower mantle, one would expect this to be expressed in its geochemical signature. Obviously, the mantle beneath Iceland and its surroundings is quite heterogeneous, and especially analyses of noble gases provide strong evidence that there is a contribution from the lower mantle, although it seems that this contribution is not dominating. Another important result is that old recycled oceanic lithosphere – probably both the crustal and the mantle component – are significant sources of Icelandic

melts. It would be interesting if evidence for recycled old lithosphere can also be derived from other than geochemical data. One could speculate that the weak high-velocity zone visible in some global tomography models in the transition zone or at the top of the lower mantle near Iceland is a candidate for such an old slab. Furthermore, if indeed only a part of the plume actually is from the lower mantle and if this core plume is wrapped by a sheath of e.g. compositionally distinct upper-mantle material at the base of the transition zone, this could also be part of the explanation for the marked change in the tomographic images of the plume across the 660 km-discontinuity. In contrast, it is still debated if depleted mantle sources on Iceland are identical with the MORB source. Along the Reykjanes and Kolbeinsey Ridges, gradients are observed in several geochemical markers. They are a manifestation of the decreasing influence of the plume with distance due to mixing with other mantle sources, but could also partially represent a horizontal cross-section through the spreading plume head with different parts of a sheath previously wrapped around the ascending plume producing varying melts at different distances from the axis, as proposed e.g. by Murton et al. (2002) (also see figure 8).

Recently, Ritsema and Allen (2003) made clear, that the question of the depth of origin of the Iceland plume cannot be decided on the basis of seismological data at the present stage. They demonstrated that a regional network with an aperture of more than 1000 km and dense (50–100 km) station spacing would be necessary to track the anomaly down into the lower mantle, and claimed that preliminary evidence for a deeper origin from global tomography and receiver function analysis would justify a larger regional investigation.

Acknowledgements

We thank Vera Schlindwein for giving us access to an early version of her manuscript on receiver functions of Iceland. Fruitful discussions with Wolf Jacoby are highly appreciated. Abigail Barker gave some helpful explanations of geochemical issues. The map plots of figures 1, 2 and 12 have been made with the GMT mapping software (Wessel and Smith 1998). Cecily Wolfe kindly provided a high-resolution version of figure 6. This study was partly supported by research grants Schm 872/6-1 and Schm 872/6-2 of the Deutsche Forschungsgemeinschaft and by The Danish National Research Foundation to TR.

References

Abelson M, Agnon A (2001) Hot spot activity and plume pulses recorded by geometry of spreading axes. Earth Planet Sci Lett 189(1–2):31–47

Albers M, Christensen UR (2001) Channeling of plume flow beneath mid-ocean ridges. Earth Planet Sci Lett 187:207–220

Allen RM, Nolet G, Morgan WJ, Vogfjörd K, Bergsson BH, Erlendsson P, Foulger GR, Jakobsdóttir S, Julian BR, Pritchard M, Ragnarsson S, Stefánsson R (1999) The thin hot plume beneath Iceland. Geophys J Int 137(1):51–63

Allen RM, Nolet G, Morgan WJ, Vogfjörd K, Bergsson BH, Erlendsson P, Foulger GR, Jakobsdóttir S, Julian BR, Pritchard M, Ragnarsson S, Stefánsson R (2002a) Imaging the mantle beneath Iceland using integrated seismological techniques. J Geophys Res 107(B12):2325. doi: 10.1029/2001JB000595

Allen RM, Nolet G, Morgan WJ, Vogfjörd K, Nettles M, Ekström G, Bergsson BH, Erlendsson P, Foulger GR, Jakobsdóttir S, Julian BR, Pritchard M, Ragnarsson S, Stefánsson R (2002b) Plume driven plumbing and crustal formation in Iceland. J Geophys Res 107(B8):2163. doi: 10.1029/2001JB000584

Allen RM, Tromp J (2005) Resolution of regional seismic models: Squeezing the Iceland anomaly. Geophys J Int 161(2):373–386

Angenheister G, Gebrande H, Miller H, RRISP Working Group (1980) Reykjanes Ridge Iceland Seismic Experiment (RRISP 77). J Geophys 47:228–238

Appelgate B, Shor AN (1994) The northern mid-Atlantic and Reykjanes Ridges: spreading center morphology between 55°50'N and 63°00'N. J Geophys Res 99(B9):17935–17956

Beblo M, Björnsson A (1980) A model of electrical resistivity beneath NE-Iceland, correlation with temperature. J Geophys 47:184–190

Bijwaard H, Spakman W (1999) Tomographic evidence for a narrow whole mantle plume below Iceland. Earth Planet Sci Lett 166:121–126

Bjarnason IÞ, Menke W, Flóvenz ÓC, Caress D (1993) Tomographic image of the mid-Atlantic plate boundary in southwestern Iceland. J Geophys Res 98:6607–6622

Bjarnason IÞ, Sacks IS (2002) The plume, lithosphere and asthenosphere of Iceland. In: Geophys. Res. Abstr., vol 4. EGS, Nice

Bjarnason IÞ, Silver PG, Rümpker G, Solomon SC (2002) Shear-wave splitting across the Iceland hotspot: Results from the ICEMELT experiment. J Geophys Res 107(B12):2382. doi:10.1029/2001JB000916

Bjarnason IÞ, Wolfe CJ, Solomon SC, Guðmundsson G (1996) Initial results from the ICEMELT experiment: Body-wave delay times and shear-wave splitting across Iceland. Geophys Res Lett 23(5):459–462. Correction in Geophys Res Lett 23(8):903 (1996)

Blichert-Toft J, Agranier A, Andres M, Kingsley R, Schilling JG, Albarède F (2005) Geochemical segmentation of the Mid-Atlantic Ridge north of Iceland and ridge-hot spot interaction in the North Atlantic. Geochem Geophys Geosyst 6(1). doi:10.1029/2004GC000788

Bott MHP (1985) Plate tectonic evolution of the Icelandic transverse ridge and adjacent regions. J Geophys Res 90(B12):9953–9960

Botz R, Winckler G, Bayer R, Schmitt M, et al. (1999) Origin of trace gases in submarine hydrothermal vents of the Kolbeinsey Ridge, north Iceland. Earth Planet Sci Lett 171(1):83–93

Brandsdóttir B, Menke W, Einarsson P, White RS, Staples RK (1997) Färoe-Iceland Ridge Experiment — 2. Crustal structure of the Krafla central volcano. J Geophys Res 102(B4):7867–7886

Breddam K (2002) Kistufell: Primitive melt from the Iceland mantle plume. J Petrol 43(2):345–373

Breddam K, Kurz MD, Storey M (2000) Mapping out the conduit of the Iceland mantle plume with helium isotopes. Earth Planet Sci Lett 176:45–55

Buck WR (1996) Shallow redistribution of crust produced by mantle plumes at mid-ocean ridges. In: Þorkelsson B (ed) Abstracts, p 117. European Seismological Commission, Veðurstofa Íslands (Icelandic Meteorological Office), Ministry for Environment, University of Iceland, Reykjavík

Burnard P, Harrison D (2005) Argon isotope constraints on modification of oxygen isotopes in Iceland Basalts by surficial processes. Chem Geol 216(1–2):143–156

Chalmers JA, Larson LM, Pedersen AK (1995) Widespread Palaeocene volcanism around the northern North Atlantic and Labrador Sea: evidence for a large, hot, early plume head. J Geol Soc Lond 152:965–969

Chauvel C, Hémond C (2000) Melting of a complete section of recycled oceanic crust: Trace element and Pb isotope evidence from Iceland. Geochem Geophys Geosyst 1. doi:1999GC000002

Clift PD, Turner J, Ocean Drilling Program Leg 152 Scientific Party (1995) Dynamic support by the Icelandic plume and vertical tectonics of the northeast Atlantic continental margins. J Geophys Res 100(B12):24473–24486

Condie KC (2001) Mantle Plumes and Their Record in Earth History. Cambridge University Press

Courtillot V, Davaille A, Besse J, Stock J (2003) Three distinct types of hotspots in the Earth's mantle. Earth Planet Sci Lett 205(3–4):295–308

Darbyshire FA, Bjarnason IÞ, White RS, Flóvenz ÓG (1998) Crustal structure above the Iceland mantle plume imaged by the ICEMELT refraction profile. Geophys J Int 135(3):1131–1149

Darbyshire FA, White RS, Priestley KF (2000) Structure of the crust and uppermost mantle of Iceland from a combined seismic and gravity study. Earth Planet Sci Lett 181:409–428

Dixon ET, Honda M, McDougall I, Campbell IH, Sigurdsson I (2000) Preservation of near-solar neon isotopic ratios in Icelandic basalts. Earth Planet Sci Lett 180(3–4):309–324

Du Z, Foulger GR (2001) Variation in the crustal structure across central Iceland. Geophys J Int 145(1):246–264

Du ZJ, Foulger GR (1999) The crustal structure beneath the northwest fjords, Iceland, from receiver functions and surface waves. Geophys J Int 139(2):419–432

Du ZJ, Foulger GR, Julian BR, Allen RM, Nolet G, Morgan WJ, Bergsson BH, Erlendsson P, Jakobsdóttir S, Ragnarsson S, Stefánsson R, Vogfjörd K (2002) Crustal structure beneath western and eastern Iceland from surface waves and receiver functions. Geophys J Int 149(2):349–363

Dunn R, Delorey A, Gaherty J (2005) Surface wave investigation of the effect of the Icelandic hotspot on the upper mantle beneath the Reykjanes Ridge. In: Geophys. Res. Abstr., vol 7, p 05978

Ellam RM, Stuart FM (2000) The sub-lithospheric source of north Atlantic basalts: evidence for, and significance of, a common end-member. J Petrol 41(7):919–932

Elliott T (1997) Fractionation of U and Th during mantle melting: a reprise. Chem Geol 139:165–183

Eysteinsson H, Gunnarsson K (1995) Maps of gravity, bathymetry and magnetics for Iceland and surroundings. Tech Rep OS-95055/JHD-07, Orkustofnun

Eysteinsson H, Hermance JF (1985) Magnetotelluric measurements across the Eastern Neovolcanic Zone in south Iceland. J Geophys Res 90(B12):10093–10103

Farnetani CG, Legras B, Tackley PJ (2002) Mixing and deformations in mantle plumes. Earth Planet Sci Lett 196(1–2):1–15

Farnetani CG, Richards MA, Ghiorso MS (1996) Petrological models of magma evolution and deep crustal structure beneath hotspots and flood basalt provinces. Earth Planet Sci Lett 143(1–4):81–94

Fedorova T, Jacoby WR, Wallner H (2005) Crust-mantle transition and Moho model for Iceland and surroundings from seismic, topography and gravity data. Tectonophys 396(3–4):119–140

Feighner MA, Kellogg LH, Travis BJ (1995) Numerical modeling of chemically buoyant mantle plumes at spreading ridges. Geophys Res Lett 22(6):715–718

Feighner MA, Richards MA (1995) The fluid dynamics of plume-ridge and plume-plate interactions: An experimental investigation. Earth Planet Sci Lett 129:171–182

Fitton JG, Saunders AD, Kempton PD, Hardarson BS (2003) Does depleted mantle form an intrinsic part of the Iceland plume? Geochem Geophys Geosyst 4(3):1032. doi:10.1029/2002GC000424

Fitton JG, Saunders AD, Norry MJ, Hardarson BS, Taylor RN (1997) Thermal and chemical structure of the Iceland plume. Earth Planet Sci Lett 153:197–208

Flóvenz ÓG (1980) Seismic structure of the Icelandic crust above layer three and the relation between body wave velocity and the alteration of the basaltic crust. J Geophys 47:211–220

Flóvenz ÓG, Gunnarsson K (1991) Seismic crustal structure in Iceland and surrounding area. Tectonophys 189:1–17

Forsyth DA, Morel-a l'Huisser P, Asudeth I, Green AG (1986) Alpha Ridge and Iceland – products of the same plume? J Geodyn 6:197–214

Foulger GR, Anderson DL (2005) A cool model for the Iceland hotspot. J Volc Geotherm Res 141(1–2):1–22

Foulger GR, Natland JH, Anderson DL (2005) A source for Icelandic magmas in remelted Iapetus crust. J Volc Geotherm Res 141(1–2):23–44

Foulger GR, Pearson DG (2001) Is Iceland underlain by a plume in the lower mantle? Seismology and helium isotopes. Geophys J Int 145(3):F1–F5

Foulger GR, Pritchard MJ, Julian JR, Evans BR, Allen RM, Nolet G, Morgan WJ, Bergsson BH, Erlendsson P, Jakobsdóttir S, Ragnarsson S, Stefánsson R, Vogfjörd K (2001) Seismic tomography shows that upwelling beneath Iceland is confined to the upper mantle. Geophys J Int 146(2):504–530

Furman T, Frey F, Park KH (1995) The scale of source heterogeneity beneath the eastern neovolcanic zone, Iceland. J Geol Soc Lond 152:997–1002

Gaherty JB (2001) Seismic evidence for hotspot-induced buoyant flow beneath the Reykjanes Ridge. Science 293:1645–1647

Gebrande H, Miller H, Einarsson P (1980) Seismic structure of Iceland along RRISP-Profile I. J Geophys 47:239–249

Grand SP (1994) Mantle shear structure beneath the Americas and surrounding oceans. J Geophys Res 99(B6):11591–11622

Grand SP (2002) Mantle shear-wave tomography and the fate of subducted slabs. Phil Trans R Soc Lond A360(1800):2475–2491

GTOPO30 (1996) GTOPO30 (Global 30 Arc-Second Elevation Data Set). Dataset, U.S. Geological Survey, EROS Data Center, Sioux Falls, South Dakota. `http://lpdaac.usgs.gov:80/gtopo30/gtopo30.html`

Guðmundsson Ó (2003) The dense root of the Icelandic crust. Earth Planet Sci Lett 206:427–440

Hanan BB, Blichert-Toft J, Kingsley R, Schilling JG (2000) Depleted Iceland mantle plume geochemical signature: Artifact of multicomponent mixing? Geochem Geophys Geosyst 1. doi:1999GC000009

Hanan BB, Schilling JG (1997) The dynamic evolution of the Iceland mantle plume: the lead isotope perspective. Earth Planet Sci Lett 151:43–60

Hardarson BS, Fitton JG, Ellam RM, Pringle MS (1997) Rift relocation — a geochemical and geochronological investigation of a palaeo-rift in northwest Iceland. Earth Planet Sci Lett 153:181–196

Heller DA, Marquart G (2002) An admittance study of the Reykjanes Ridge and elevated plateaux between the Charlie-Gibbs and Senja fracture zones. Geophys J Int 148(1):65–76

Helmberger DV, Wen L, Ding X (1998) Seismic evidence that the source of the Iceland hotspot lies at the core–mantle boundary. Nature 396:251–255

Hémond C, Arndt NT, Lichtenstein U, Hofmann AW, Óskarsson N, Steinthorsson S (1993) The heterogeneous Iceland plume: Nd-Sr-O isotopes and trace element constraints. J Geophys Res 98:15833–15850

Hersir GP, Björnsson A, Pedersen LB (1984) Magnetotelluric survey across the active spreading zone in southwest Iceland. J Volc Geotherm Res 20:253–265

Hilton DR, Grönvold K, Macpherson CG, Castillo PR (1999) Extreme $^3He/^4He$ ratios in northwest Iceland: constraining the common component in mantle plumes. Earth Planet Sci Lett 173:53–60

Hirose K (2002) Phase transitions in pyrolitic mantle around 670-km depth: Implications for upwelling of plumes from the lower mantle. J Geophys Res 107(B4):10.1029/2001JB000597

Hirschmann MM (2000) Mantle solidus: Experimental constraints and the effects of peridotite composition. Geochem Geophys Geosyst 1. doi: 2000GC000070

Holbrook W S Larsen HC, Korenaga J, Dahl-Jensen T, Reid ID, Kelemen PB, Hopper JR, Kent GM, Lizarralde D, Bernstein S, Detrick RS (2001) Mantle thermal structure and active upwelling during continental breakup in the North Atlantic. Earth Planet Sci Lett 190(3–4):251–266

Hung SH, Shen Y, Chiao LY (2004) Imaging seismic velocity structure beneath the Iceland hot spot: A finite frequency approach. J Geophys Res 109(B8). doi:10.1029/2003JB002889

Ito G (2001) Reykjanes 'V'-shaped ridges originating from a pulsing and dehydrating plume. Nature 411:681–684

Ito G, Lin J (1995) Oceanic spreading center–hotspot interactions — constraints from along-isochron bathymetric and gravity anomalies. Geology 23(7):657–660

Ito G, Lin J, Gable CW (1996) Dynamics of mantle flow and melting at a ridge-centered hotspot: Iceland and the mid-Atlantic ridge. Earth Planet Sci Lett 144:53–74

Ito G, Shen Y, Hirth G, Wolfe CJ (1999) Mantle flow, melting and dehydration of the Iceland mantle plume. Earth Planet Sci Lett 165:81–96

Jamtveit B, Brooker R, Brooks K, Melchior Larsen L, Pedersen T (2001) The water content of olivines from the North Atlantic Volcanic Province. Earth Planet Sci Lett 186:401–415

Jones SM, White N, Maclennan J (2002) V-shaped ridges around Iceland: Implications for spatial and temporal patterns. Geochem Geophys Geosyst 3(10):1059. doi:10.1029/2001GC000361

Kaban MK, Flóvenz O, Pálmason G (2002) Nature of the crust-mantle transition zone and the thermal state of the upper mantle beneath Iceland from gravity modeling. Geophys J Int 149(2):281–299

Keen CE, Boutilier RR (2000) Interaction of rifting and hot horizontal plume sheets at volcanic margins. J Geophys Res 105(B6):13375–13387

Keller WR, Anderson DL, Clayton RW (2000) Resolution of tomographic models of the mantle beneath Iceland. Geophys Res Lett 27(24):3993–3996

Kempton PD, Fitton JG, Saunders AD, Nowell GM, Taylor RN, Hardarson BS, Pearson G (2000) The Iceland plume in space and time: a Sr–Nd–Pb–Hf study of the North Atlantic rifted margin. Earth Planet Sci Lett 177(3–4):255–271

Kent AJR, Stolper EM, Francis D, Woodhead J, Frei R, Eiler J (2004) Mantle heterogeneity during the formation of the North Atlantic Igneous Province: Constraints from trace element and Sr-Nd-Os-O isotope systematics of Baffin Island picrites. Geochem Geophys Geosyst 5(11). doi: 10.1029/2004GC000743

King SD, Anderson DL (1995) An alternative mechanism of flood basalt formation. Earth Planet Sci Lett 136:269–279

Kokfelt TF, Hoernle K, Hauff F (2003) Upwelling and melting of the Iceland plume from radial variation of ^{238}U–^{230}Th disequilibria in postglacial volcanic rocks. Earth Planet Sci Lett 214(1–2):167–186. Erratum in Earth Planet Sci Lett 217(1–2):219–220

Korenaga J, Kelemen PB (2000) Major element heterogeneity in the mantle source of the North Atlantic igneous province. Earth Planet Sci Lett 184(1):251–268

Kreutzmann A, Schmeling H, Junge A, Ruedas T, Marquart G, Bjarnason IÞ (2004) Temperature and melting of a ridge-centered plume with application to Iceland. Part II: Predictions for electromagnetic and seismic observables. Geophys J Int 159(3):1097–1111. doi:10.1111/j.1365-246X.2004.02397.x

Larsen LM, Pedersen AK, Pedersen GK, Piasecki S (1992) Timing and duration of Early Tertiary volcanism in the North Atlantic: new evidence from West Greenland. In: Storey BC, Alabaster T, Pankhurst RJ (eds) Magmatism and the Causes of Continental Break-up, pp 321–333. No 68 in Geological Society Special Publication, The Geological Society, London

Lawver LA, Müller RD (1994) Iceland hotspot track. Geology 22:311–314

Leahy GM, Park J (2005) Hunting for oceanic island Moho. Geophys J Int 160(3):1020–1026

Levshin AL, Ritzwoller MH, Barmin MP, Villaseñor A, Padgett CA (2001) New constraints on the arctic crust and uppermost mantle: surface wave group velocities, P_n, and S_n. Phys Earth Planet Int 123(2–4):185–204

Li A, Detrick RS (2001) Rayleigh wave constraints on shear wave velocities beneath Iceland. In: EOS Trans. AGU, vol 82, pp T32C–03

Li A, Detrick RS (2003a) Azimuthal anisotropy and phase velocity beneath Iceland: implication for plume-ridge interaction. Earth Planet Sci Lett 214(1–2):153–165. Correction in Earth Planet Sci Lett 218(1–2):241 (2004)

Li A, Detrick RS (2003b) Structure of crust and upper mantle beneath Iceland from Rayleigh wave tomography. In: EOS Trans. AGU, vol 84, pp V12B–0593

Maclennan J, McKenzie D, Grönvold K (2001a) Plume-driven upwelling under central Iceland. Earth Planet Sci Lett 194(1–2):67–82

Maclennan J, McKenzie D, Grönvold K, Slater L (2001b) Crustal accretion under northern Iceland. Earth Planet Sci Lett 191(3–4):295–310

Macpherson CG, Hilton DR, Day JMD, Lowry D, Grönvold K (2005) High-$^3He/^4He$, depleted mantle and low-$\delta^{18}O$, recycled oceanic lithosphere in the source of central Iceland magmatism. Earth Planet Sci Lett 233(3–4):411–427

Marquart G (1991) Interpretation of geoid anomalies around the Iceland hotspot. Geophys J Int 106:149–160

Marquart G, Schmeling H (2004) A dynamic model for the N-Atlantic based on gravity and tomography data. Geophys J Int 159(1):40–52

Marquart G, Schmeling H, Čadek O (2006) Dynamic models for flow and seismic anisotropy in the North-Atlantic and comparison with observations. Geochem Geophys Geosyst In revision

Mégnin C, Romanowicz B (2000) The three-dimensional shear velocity structure of the mantle from the inversion of body, surface and higher-mode waveforms. Geophys J Int 143(3):709–728

Menke W (1999) Crustal isostasy indicates anomalous densities beneath Iceland. Geophys Res Lett 26(9):1215–1218

Menke W, Brandsdóttir B, Einarsson P, Bjarnason IÞ (1996) Reinterpretation of the RRISP-77 Iceland shear-wave profiles. Geophys J Int 126:166–172

Menke W, Levin V (1994) Cold crust in a hot spot. Geophys Res Lett 21(18):1967–1970

Menke W, Levin V, Sethi R (1995) Seismic attenuation in the crust at the mid-Atlantic plate boundary in south-west Iceland. Geophys J Int 122:175–182

Menke W, Sparks D (1995) Crustal accretion model for Iceland predicts 'cold' crust. Geophys Res Lett 22(13):1673–1676

Menke W, West M, Brandsdóttir B, Sparks D (1998) Compressional and shear velocity structure of the lithosphere in northern Iceland. Bull Seis Soc Am 88(6):1561–1571

Mertz DF, Devey CW, Todt W, Stoffers P, Hofmann AW (1991) Sr-Nd-Pb isotope evidence against plume–asthenosphere mixing north of Iceland. Earth Planet Sci Lett 107:243–255

Mertz DF, Haase KM (1997) The radiogenic isotope composition of the high-latitude North-Atlantic mantle. Geology 25(5):411–414

Meyer PS, Sigurdsson H, Schilling JG (1985) Petrological and geochemical variations along Iceland's Neovolcanic zones. J Geophys Res 90(B12):10043–10072

Montelli R, Nolet G, Dahlen FA (2005) Deep plumes in the mantle: geometry and dynamics. In: Geophys. Res. Abstr., vol 7, p 02473

Montelli R, Nolet G, Dahlen FA, Masters G, Engdahl ER, Hung SH (2004) Finite-frequency tomography reveals a variety of plumes in the mantle. Science 303(5656):338–343. Supporting online material at `http://www.sciencemag.org/cgi/content/full/1092485/DC1`

Moreira M, Breddam K, Curtice J, Kurz MD (2001) Solar neon in the Icelandic mantle: new evidence for an undegassed lower mantle. Earth Planet Sci Lett 185(1–2):15–23

Murton BJ, Taylor RN, Thirlwall MF (2002) Plume-ridge interaction: a geochemical perspective from the Reykjanes Ridge. J Petrol 43(11):1987–2012

Nichols ARL, Carroll MR, Höskuldsson Á (2002) Is the Iceland hot spot also wet? Evidence from the water contents of undegassed submarine and subglacial pillow basalts. Earth Planet Sci Lett 202(1):77–87

Nicholson H, Latin D (1992) Olivine tholeiites from Krafla, Iceland: Evidence for variations in melt fraction within a plume. J Petrol 33(5):1105–1124

Nielsen TK, Larsen HC, Hopper JR (2002) Contrasting rifted margin styles south of Greenland: implications for mantle plume dynamics. Earth Planet Sci Lett 200(3–4):271–286

O'Connor JM, Stoffers P, Wijbrans JR, Shannon PM, Morrissey T (2000) Evidence from episodic seamount volcanism for pulsing of the Iceland plume in the past 70 Myr. Nature 408:954–958

Óskarsson N, Steinþorsson S, Sigvaldason GE (1985) Iceland geochemical anomaly: origin, volcanotectonics, chemical fractionation and isotope evolution of the crust. J Geophys Res 90(B12):10011–10025

Peate DW, Baker JA, Blichert-Toft J, Hilton DR, Storey M, Kent AJR, Brooks CK, Hansen H, Pedersen AK, Duncan RA (2003) The Prinsen af Wales Bjerge formation lavas, East Greenland: the transition from tholeiitic to alkalic magmatism during palaeogene continental break-up. J Petrol 44(2):279–304

Phipps Morgan J (2001) Thermodynamics of pressure release melting of a veined plum pudding mantle. Geochem Geophys Geosyst 2. doi: 2000GC000049

Pilidou S, Priestley K, Debayle E, Guðmundsson Ó (2005) Rayleigh wave tomography in the North Atlantic: high resolution images of the Iceland, Azores and Eifel mantle plumes. Lithos 79(3–4):453–474

Pollitz FF, Sacks IS (1996) Viscosity structure beneath northeast Iceland. J Geophys Res 101(B8):17771–17793

Pritchard MJ, Foulger GR, Julian BR, Fyen J (2000) Constraints on a plume in the mid-mantle beneath the Iceland region from seismic array data. Geophys J Int 143(1):119–128

Putirka KD (2005) Mantle potential temperatures at Hawaii, Iceland, and the mid-ocean ridge system, as inferred from olivine phenocrysts: Evidence for thermally driven mantle plumes. Geochem Geophys Geosyst 6(5):Q05L08. doi:10.1029/2005GC000915

Pálmason G (1971) Crustal Structure of Iceland from Explosion Seismology. 1st edn. Soc. Sci. Iceland, Reykjavík

Pálmason G (1973) Kinematics and heat flow in a volcanic rift zone, with application to Iceland. Geophys J R astr Soc 33:451–481

Pálmason G (1980) A continuum model of crustal generation in Iceland; Kinematic aspects. J Geophys 47:7–18

Rabinowicz M, Briais A (2002) Temporal variations of the segmentation of slow to intermediate spreading mid-ocean ridges 2. A three-dimensional model in terms of lithosphere accretion and convection within the partially molten mantle beneath the ridge axis. J Geophys Res 107(B6). doi: 10.1029/2001JB000343

Ribe NM, Christensen UR, Theißing J (1995) The dynamics of plume-ridge interaction, 1: Ridge-centered plumes. Earth Planet Sci Lett 134:155–168

Ribe NM, Delattre WL (1998) The dynamics of plume-ridge interaction — III. The effects of ridge migration. Geophys J Int 133(3):511–518

Richards MA, Duncan RA, Courtillot VE (1989) Flood basalts and hot-spot tracks: Plume heads and tails. Science 246:103–107

Richardson KR, Smallwood JR, White RS, Snyder DB, Maguire PKH (1998) Crustal structure beneath the Faroe Islands and the Faroe–Iceland Ridge. Tectonophys 300:159–180

Riisager P, Abrahamsen N (1999) Magnetostratigraphy of Palaeocene basalts from the Vaigat Formation of West Greenland. Geophys J Int 137(3):774–782

Ritsema J, Allen RM (2003) The elusive mantle plume. Earth Planet Sci Lett 207(1–4):1–12

Ritsema J, van Heijst HJ, Woodhouse JH (1999) Complex shear wave velocity structure imaged beneath Africa and Iceland. Science 286:1925–1928

Rögnvaldsson ST, Guðmundsson Á, Slunga R (1998) Seismotectonic analysis of the Tjörnes Fracture Zone, an active transform fault in north Iceland. J Geophys Res 103(B12):30117–30129

Ruedas T (2004) Convection and Melting Processes in a Mantle Plume under a Spreading Ridge, with Application to the Iceland Plume. PhD thesis, J.W. Goethe University Frankfurt am Main. Logos Verlag Berlin

Ruedas T (2006) Dynamics, crustal thicknesses, seismic anomalies, and electrical conductivities in dry and hydrous ridge-centered plumes. Phys Earth Planet Int 155(1–2):16–41

Ruedas T, Schmeling H, Marquart G, Kreutzmann A, Junge A (2004) Temperature and melting of a ridge-centered plume with application to Iceland. Part I: Dynamics and crust production. Geophys J Int 158(2):729–743. doi:10.1111/j.1365-246X.2004.02311.x

Saal AE, Hauri EH, Langmuir CH, Perfit MR (2002) Vapour undersaturation in primitive mid-ocean-ridge basalt and the volatile content of Earth's upper mantle. Nature 419:451–455

Sæmundsson K (1979) Outline of the geology of Iceland. Jökull 29:7–28

Sandwell DT, MacKenzie KR (1989) Geoid height versus topography for oceanic plateaus and swells. J Geophys Res 94(B6):7403–7418

Sandwell DT, Smith WHF (1997) Marine gravity anomaly from Geosat and ERS-1 satellite altimetry. J Geophys Res 102(B5):10039–10054

Scarrow JH, Curran JM, Kerr AC (2000) Major element records of variable plume involvement in the north Atlantic province tertiary flood basalts. J Petrol 41(7):1155–1176

Schilling JG (1973) Iceland mantle plume: Geochemical study of Reykjanes ridge. Nature 242:565–571

Schilling JG (1991) Fluxes and excess temperatures of mantle plumes inferred from their interaction with migrating mid-ocean ridges. Nature 352:397–403

Schilling JG, Kingsley R, Fontignie D, Poreda R, Xue S (1999) Dispersion of the Jan Mayen and Iceland mantle plumes in the Arctic: A He–Pb–Nd–Sr isotope tracer study of basalts from the Kolbeinsey, Mohns, and Knipovich Ridges. J Geophys Res 104(B5):10543–10569

Schlindwein V (2006) On the use of teleseismic receiver functions for studying the crustal structure of Iceland. Geophys J Int 164(3):551–568

Schmeling H (2000) Partial melting and melt segregation in a convecting mantle. In: Bagdassarov N, Laporte D, Thompson AB (eds) Physics and Chemistry of Partially Molten Rocks, pp 141–178. Kluwer Academic Publishers

Shen Y, Forsyth DW (1995) Geochemical constraints on the initial and final depths of melting beneath mid-ocean ridges. J Geophys Res 100(B2):2211–2237

Shen Y, Solomon SC, Bjarnason IÞ, Nolet G, Morgan WJ, Allen RM, Vogfjörd K, Jakobsdóttir S, Stefánsson R, Julian BR, Foulger GR (2002) Seismic evidence for a tilted mantle plume and north-south mantle flow beneath Iceland. Earth Planet Sci Lett 197(3–4):261–272

Shen Y, Solomon SC, Bjarnason IÞ, Wolfe CJ (1998) Seismic evidence for a lower mantle origin of the Iceland plume. Nature 395:62–65

Shen Y, Wolfe CJ, Solomon SC (2003) Seismological evidence for a mid-mantle discontinuity beneath Hawaii and Iceland. Earth Planet Sci Lett 214(1–2):143–151

Sigmundsson F (1991) Post-glacial rebound and asthenosphere viscosity in Iceland. Geophys Res Lett 18(6):1131–1134

Skogseid J, Pedersen T, Eldholm O, Larsen BT (1992) Tectonism and magmatism during NE Atlantic continental break-up: the Vøring Margin. In: Storey BC, Alabaster T, Pankhurst RJ (eds) Magmatism and the Causes of Continental Break-up, pp 305–320. No 68 in Geological Society Special Publication, The Geological Society, London

Skovgaard AC, Storey M, Baker J, Blusztajn J, Hart SR (2001) Osmium–oxygen isotopic evidence for a recycled and strongly depleted component in the Iceland mantle plume. Earth Planet Sci Lett 194(1–2):259–275

Sleep NH (1990) Hotspots and mantle plumes: Some phenomenology. J Geophys Res 95(B5):6715–6736

Smallwood JR, Staples RK, Richardson KR, White RS, the FIRE Working Group (1999) Crust generated above the Iceland mantle plume: From continental rift to oceanic spreading center. J Geophys Res 104(B10):22885–22902

Smallwood JR, White RS, Minshull TA (1995) Sea-floor spreading in the presence of the Iceland Plume: the structure of the Reykjanes Ridge at 61° 40' N. J Geol Soc Lond 152:1023–1029

Smallwood JR, White RS, Staples RK (1998) Deep crustal reflectors under Reydarfjörður, eastern Iceland: crustal accretion above the Iceland mantle plume. Geophys J Int 134(1):277–290

Staples RK, White RS, Brandsdóttir B, Menke W, Maguire PKH, McBride JH (1997) Färoe-Iceland Ridge Experiment, 1, Crustal structure of northeastern Iceland. J Geophys Res 102(B4):7849–7866

Stecher O, Carlson RW, Gunnarsson B (1999) Torfajökull: a radiogenic end-member of the Iceland Pb-isotopic array. Earth Planet Sci Lett 165(1):117–127

Stefánsson R, Böðvarsson P, Slunga R, Einarsson P, Jakobsdóttir S, Bungum H, Gregersen S, Havskov J, Hjelme J, Korhonen H (1993) Earthquake prediction research in the South Iceland Seismic Zone and the SIL project. Bull Seis Soc Am 83:696–716

Steinberger B (2000) Plumes in a convecting mantle: Models and observations for individual hotspots. J Geophys Res 105(B5):11127–11152

Stracke A, Zindler A, Salters VJM, McKenzie D, Blichert-Toft J, Albarède F, Grönvold K (2003) Theistareykir revisited. Geochem Geophys Geosyst 4(2):8507. doi:10.1029/2001GC000201

Taylor RN, Thirlwall MF, Murton BJ, Hilton DR, Gee MAM (1997) Isotopic constraints on the influence of the Icelandic plume. Earth Planet Sci Lett 148:E1–E8. Express Letter

Thayer RE, Björnsson A, Álvarez L, Hermance JF (1981) Magma genesis and crustal spreading in the northern neovolcanic zone of Iceland: telluric-magnetotelluric constraints. Geophys J R astr Soc 65:423–442

Thirlwall MF (1995) Generation of the Pb isotopic characteristics of the Iceland plume. J Geol Soc Lond 152:991–996

Thirlwall MF, Gee MAM, Taylor RN, Murton BJ (2004) Mantle components in Iceland and adjacent ridges investigated using double-spike Pb isotope ratios. Geochim Cosmochim Acta 68(2):361–386. Correction in Geochim Cosmochim Acta 69(21):5139–5140 (2005)

Torsvik TH, Mosar J, Eide EA (2001) Cretaceous–Tertiary geodynamics: a North Atlantic exercise. Geophys J Int 146(3):850–866

Tryggvason A, Rögnvaldsson SÞ, Flóvenz ÓG (2002) Three-dimensional imaging of the P- and S-wave velocity structure and earthquake locations beneath Southwest Iceland. Geophys J Int 151(3):848–866

Tryggvason K, Husebye E, Stefánsson R (1983) Seismic image of the hypothesized Icelandic hot spot. Tectonophysics 100:97–118

Ücisik N, Guðmundsson Ó, Priestley K, Larsen TB (2005) Seismic anisotropy beneath east Greenland revealed by shear wave splitting. Geophys Res Lett 32(8):L08315. doi:10.1029/2004GL021875

Vink GE (1984) A hotspot model for Iceland and the Vøring plateau. J Geophys Res 89(B12):9949–9959

Vogt PR (1971) Asthenospheric motion recorded by the ocean floor south of Iceland. Earth Planet Sci Lett 13:155–160

Vogt PR (1976) Plumes, sub-axial pipe flow, and topography along the mid-oceanic ridge. Earth Planet Sci Lett 29:309–325

Weir NRW, White RS, Brandsdóttir B, Einarsson P, Shimamura H, Shiobara H, RISE Fieldwork Team (2001) Crustal structure of the northern Reykjanes Ridge and Reykjanes Peninsula, southwest Iceland. J Geophys Res 106(B4):6347–6368

Wessel P, Smith WHF (1998) New, improved version of the Generic Mapping Tools released. EOS Transactions, AGU 79:579

White RS (1997) Rift-plume interactions in the North Atlantic. Phil Trans Roy Soc Lond A 355(1723):319–339

White RS, Bown JW, Smallwood JR (1995) The temperature of the Iceland plume and origin of outward-propagating V-shaped ridges. J Geol Soc Lond 152:1039–1045

White RS, McKenzie DP (1989) Magmatism at rift zones: The generation of volcanic continental margins and flood basalts. J Geophys Res 94(B6):7685–7729

White RS, McKenzie DP, O'Nions RK (1992) Oceanic crustal thickness from seismic measurements and rare earth element inversions. J Geophys Res 97(B13):19683–19715

Wolfe CJ, Bjarnason IÞ, VanDecar JC, Solomon SC (1997) Seismic structure of the Iceland mantle plume. Nature 385(5727):245–247

Wood BJ (1995) The effect of H_2O on the 410-kilometer seismic discontinuity. Science 268:75–76

Xue M, Allen RM (2005) Asthenospheric channelling of the Icelandic upwelling: Evidence from seismic anisotropy. Earth Planet Sci Lett 235(1–2):167–182

Yale MM, Phipps Morgan J (1998) Asthenosphere flow model of hotspot-ridge interactions: a comparison of Iceland and Kerguelen. Earth Planet Sci Lett 161:45–56

Zhang YS, Tanimoto T (1993) High-resolution global upper mantle structure and plate tectonics. J Geophys Res 98(B6):9793–9823

Zhao D (2001) Seismic structure and origin of hotspots and mantle plumes. Earth Planet Sci Lett 192(3):251–265

Zverev SM, Litvinenko IV, Pálmason G, Yaroshevskaya GA, Osokin NN (1980a) A seismic crustal study of the axial rift zone in Southwest Iceland. J Geophys 47(1–3):202–210

Zverev SM, Litvinenko IV, Pálmason G, Yaroshevskaya GA, Osokin NN, Akhmetjev MA (1980b) A seismic study of the rift zone in Northern Iceland. J Geophys 47(1–3):191–201

Combined Gas-geochemical and Receiver Function Studies of the Vogtland/NW Bohemia Intraplate Mantle Degassing Field, Central Europe

Horst Kämpf[1], Wolfram H. Geissler[1] and Karin Bräuer[2]

[1]GeoForschungsZentrum Potsdam, Germany
[2]Umweltforschungszentrum Leipzig-Halle, Germany

1 Introduction

The study area – the western part of the Eger (Ohře) Rift (Fig. 1) – belongs to the European Cenozoic rift system (ECRIS) (Ziegler 1992, Prodehl et al. 1995, Dezes et al. 2004). This system of graben structures and intraplate volcanic fields spreads over a distance of some 1100 km from the Mediterranean to the North Sea coast, including the French Massif Central, the Upper Rhine Graben, the Eifel, the North Hessian Depression, the Vogelsberg, and the Eger Rift (Fig. 1, inset map). There are different models to explain the widespread rifting and associated volcanism in the foreland of the Alpine orogen. Most of them are related to the effects of Alpine collision (e.g. Ziegler 1992). However, there also exist ideas of a mantle plume or several small mantle plumes (mantle fingers) as the source of the magmatic activity (e.g., Granet et al. 1995, Goes et al. 1999).

Indications for reduced seismic velocities in the upper mantle beneath the western Eger Rift were found in previous studies (e.g., Raikes and Bonjer 1983, Faber et al. 1986, Plomerová and Babuška 1988, Passier and Snieder 1996, Plomerová et al. 1998, Babuška and Plomerová 2001). However, a teleseismic study of the western part of the Bohemian Massif comparable to that in the French Massif Central (Granet et al. 1995) and the Eifel area/Rhenish Massif, Germany (Ritter et al. 2001, Keyser et al. 2002) is still in progress (Babuška et al. 2003).

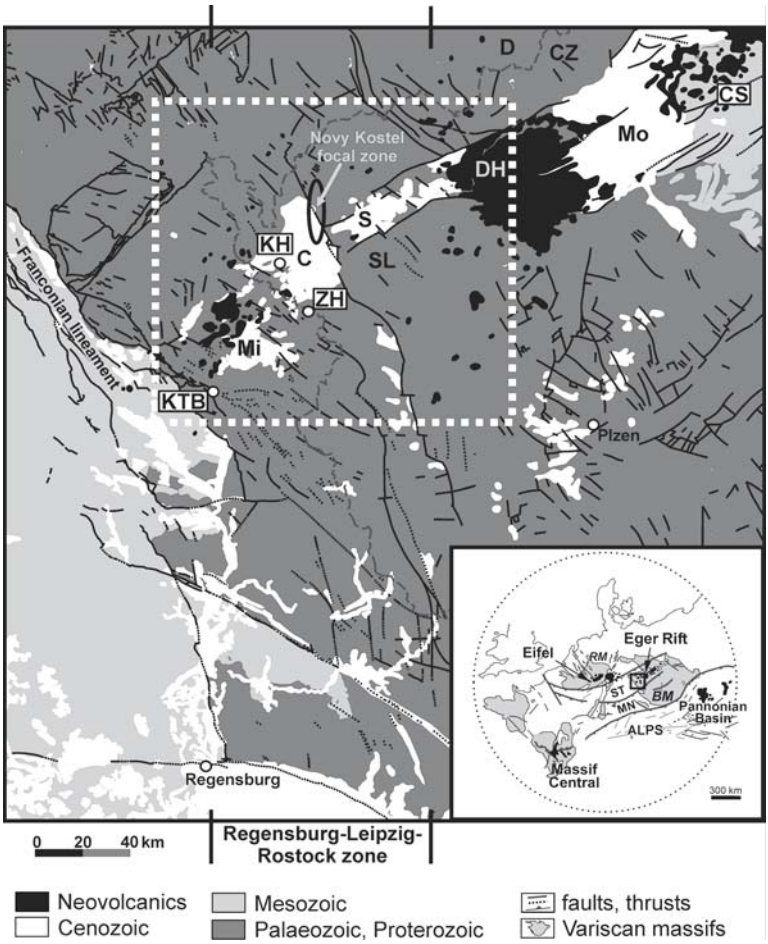

Fig. 1. Distribution of Tertiary–Quaternary volcanic fields and sedimentary basins in the western part of the Bohemian Massif (after Bayerisches Geologisches Landesamt 1998, Bankwitz et al. 2003a). The WSW–ENE striking line of sedimentary basins *Mi* (Mitterteich Basin), *C* (Cheb Basin), *S* (Sokolov Basin), and *Mo* (Most Basin), as well as the volcanic fields *DH* (Doupovske hory Mts.) and *CS* (České Středohoří) mark the Eger (Ohře) Graben. *KTB*, superdeep borehole of the German Continental Deep Drilling Programme KTB; *ZH*, Železná hůrka volcano; *KH*, Komorní hůrka volcano, both Quaternary; *SL*, Slavkovský Les. The ellipse at the northeastern corner of the Cheb Basin marks the Nový Kostel focal zone (earthquake swarm seismoactive region). Since 1985/86 more than 90% of the total seismic energy has been released in this zone (Fischer and Horálek 2003). The box marks the working area (western Eger Rift). Inset map: Location of the study area within western and central European volcanic provinces (after Wilson and Downes 1991). *RM*, Rhenish Massif; *BM*, Bohemian Massif; *ST*, Saxothuringian; *MN*, Moldanubian

The isotope (He and C) compositions of CO_2-rich gas emanations of mineral springs and mofettes from the French Massif Central (Matthews et al. 1987, Aeschbach-Hertig et al. 1999), the East and West Eifel volcanic fields/Germany (Giggenbach et al. 1991, Griesshaber et al. 1992, Aeschbach-Hertig et al. 1996) and the western Eger Rift/Czech–German border region (Weinlich et al. 1999, 2003, Geissler et al. 2005) give evidence for the ascent of gases originating from fluid reservoirs in the European subcontinental mantle (ESCM).

The results of fluid mapping at the surface (gas composition, gas flow, isotope ratios) in continental rift environments and of teleseismic tomography are not completely compatible. Whereas tomography studies can commonly resolve upper mantle structure in depths greater than 100 km, fluid mapping is mainly directed to depths less than 70 km. The focus of our research is the subcrustal depth-range (ca. 25 to 60 km) beneath the western Eger Rift (cf. Geissler et al. 2005).

The lithosphere of the Bohemian Massif was profoundly affected by several geotectonic cycles (rifting, subduction, collision) during the last two Ga. The Avalonian–Cadomian/Panafrican evolution of terranes accreted in the Variscan belt of central Europe shows several subduction events and island arc settings (660 to 540 Ma), obduction, intensive magmatism and crustal extension (540 to 530 Ma), and rifting/ocean basin formation (490 to 440) Ma (Linnemann et al. 2000). The area under investigation is situated in the transition zone between two Variscan structural units, the Saxothuringian (ST) in the north and the Teplá-Barrandian/Moldanubian (MN) in the south (Fig. 1, inset map). These structural units are composed of magmatic and multiphase deformed metamorphic rocks, which are partly covered by sediments of Palaeozoic, Mesozoic and Cenozoic age. At the Upper Cretaceous–Tertiary boundary, an approximately 50 km wide and 300 km long ENE–WSW striking continental rift evolved in the area of the Palaeozoic suture. Ulrych and Pivec (1997), Ulrych et al. (2003), and Wilson and Downes (1991, 1992) described the role of the Cretaceous/Tertiary tectono-magmatic events in this region and their influence on crustal and mantle properties. The following discussion is focused on the most recently active processes in the western part of the Eger Rift: further formation of the Cheb Basin, CO_2 emanations, Quaternary alkaline volcanic activity, neotectonic uplift in the Slavkovský Les area, and earthquake swarm activity (Fig. 1).

Table 1. Compiled results of gas mapping (gas fluxes, gas compositions, isotope (C, He) ratios) according to Weinlich et al. (1999): locations numbers 1–22, 24–45, 47–74, Weinlich et al. (2003): loc. numbers 75–90, and Geissler et al. (2005): loc. numbers 23, 46, 91–102. The gas composition (air corrected) was calculated from Ar contents assuming dissolved air composition. The He isotope ratios were expressed as air-corrected R/R_a values, where R_a is the atmospheric ratio 1.39 x 10^{-6}. sf. Water, surface water; n.a., not analysed; a.c., air contaminated.

Locality	name	sampling date	location number	GPS Coordinates (WGS 84) [°N]	[°E]
Geilsdorf	Neumühle, well	28.04.1992	1	50.421	12.048
Schönbrunn	mine, 453m (Bad)	28.04.1992	2	50.419	12.106
Ebersbach	gas spurts in pond	04.10.1993	3	50.364	12.175
Bad Elster	Marienquelle I	28.04.1992	4	50.287	12.248
Bad Elster	Marienquelle III	28.04.1992	5	50.287	12.248
Bad Elster	Moritzquelle	27.04.1992	6	50.280	12.239
Bad Elster	Sprudel I	24.04.1992	7	50.279	12.238
Bad Elster	Sprudel II	23.04.1992	8	50.275	12.242
Bad Elster	Sprudel III	23.04.1992	9	50.275	12.246
Bad Elster	Sprudel IV	20.10.1992	10	50.272	12.245
Doubrava		05.06.1992	11	50.260	12.240
Dolni Paseky	Kyselka	25.04.1992	12	50.236	12.236
Bad Brambach	Schillerquelle	21.11.1985	13	50.222	12.298
Bad Brambach	Eisenquelle	27.04.1992	14	50.222	12.299
Bad Brambach	Untere Grenzquelle	29.04.1992	15	50.221	12.294
Bad Brambach	Obere Grenzquelle	29.04.1992	16	50.220	12.293
Hennebach		05.05.1993	17	50.245	12.356
Plesná	Smrčina	04.05.1993	18	50.226	12.370
Schönberg	Säuerling	04.05.1993	19	50.176	12.333
Františkovy Lazně	Kostelní	06.05.1993	20	50.116	12.352
Kopanina		05.05.1993	21	50.206	12.458
Dolní Častkov	mofettes	04.05.1993	22	50.167	12.497
Vackovec	mofette Bublák center	08.12.2003	23	50.143	12.454
Hartoušov	mofettes	05.05.1993	24	50.132	12.464
Devin	mofettes	05.05.1993	25	50.160	12.428
Soos	mofettes	05.05.1993	26	50.150	12.403
Soos	Cisařský pramen	05.05.1993	27	50.148	12.403
Soos	Vera	05.05.1992	28	50.150	12.399
Mýtina	Kyselký hamr	07.05.1993	29	50.015	12.465
Brtná	village	06.05.1993	30	50.009	12.528
Brtná	viaduct	19.04.1994	31	50.012	12.529
Poustka		06.05.1993	32	50.000	12.546
Podlesi	Radionka	07.05.1993	33	50.050	12.566
Jedlová		06.06.1992	34	49.973	12.589
Panský vrch	Štolni kyselka	07.05.1993	35	49.944	12.646

Table 1. (cont.)

Gas flux (free gas) [dm^3h^{-1}]	Gas/water ratio [dm^3dm^{-3}]	CO_2 [vol.%]	N_2 [vol.%]	He [vol.%]	CH_4 [vol.%]	$^{13}C_{CO2}$ [‰]	R/R_a
0.10	0.10	0.03	97.82	2.02	0.152	–17.8	0.18
98.5	0.00001	0.7	98.08	0.77	0.454	–17.4	0.71
2.0	sf. water	28.05	71.94	traces	0.0077	–9.1	n.a.
6.0	0.156	97.44	2.52	0.0285	0.0116	–5.6	1.61
0.10	0.00020	62	37.77	0.188	0.0374	–6.0	n.a.
34.0	0.085	97.34	2.62	0.016	0.016	–5.2	n.a.
0.10	pumped	58.04	41.73	0.185	0.0382	–5.0	1.67
-	pumped	95.24	4.72	0.012	0.0277	–4.6	n.a.
1.00	pumped	95.33	4.56	0.0373	0.0714	–4.3	n.a.
0.10	pumped	99.69	0.31	0.0025	0.001	–5.0	2.08
0.40	0.0025	93.72	6.21	0.0363	0.0317	–5.9	1.27
2.8	0.039	99.89	0.06	0.032	0.0199	–5.7	1.66
88	1.170	99.08	0.92	0.0014	0.0022	–4.1	n.a.
20	0.092	99.16	0.84	0.00013	0.0007	–4.3	1.94
0.05	pumped	73.89	25.78	0 .153	0.184	–5.9	1.93
0.10	pumped	98.18	1.78	0.0198	0.0146	–5.9	2.3
0.03	0.001	82.59	16.68	0.17	0.555	–6.6	2.34
144	0.29	99.97	0.032	0.00012	0.0003	–3.0	1.7
7.0	0.20	99.99	0.014	traces	0.00009	–4.4	1.83
>2500	>0.25	99.75	0.248	0.0022	0.0023	–3.9	2.16
0.60	0.0083	85.36	13.6	0.0856	0.945	–2.4	4.3
4000	mofettes	99.21	0.78	0.006	0.0014	–1.9	2.58
28,050	mofettes	99.96	0.034	0.0019	0.00024	–2.0	5.89
6000	mofettes	99.94	0.062	0.0022	0.0004	–2.1	2.38
760	mofettes	99.92	0.08	0.0015	0.0033	–1.8	n.a.
21,130	mofettes	99.99	0.003	0.00087	0.0001	–2.9	n.a.
7610	3.02	99.99	0.009	0.00009	0.0002	–3.6	3.43
6540		>99.9				–2.4	n.a.
402	1.39	99.99	0.01	0.000046	0.0001	–4.2	3.45
123	3.42	99.97	0.029	0.000035	0.0002	–3.8	n.a.
404	5.61	99.96	0.035	0.00017	0.0031	–4.2	2.41
167	0.31	95.91	4.03	0.0251	0.034	–3.3	2.29
11.0	0.15	99.66	0.34	0.00043	0.00002	–5.4	a.c.
36.0	0.11	98.99	0.97	0.018	0.021	–6.3	1.82
10.4	0.03	87.54	12.28	0.027	0.16	–2.9	2.41

Table 1. (cont.)

Locality	name	sampling date	location number	GPS Coordinates (WGS 84) [°N]	[°E]
Skelné hutě		07.05.1993	36	49.924	12.652
Tachov	Mineralka	09.06.1992	37	49.795	12.650
Prameny	Prameny kyselka	08.05.1993	38	50.047	12.727
Prameny	mofette	28.04.1994	39	50.045	12.724
Nová Ves		30.09.1993	40	50.071	12.779
Louka	Grünska kyselka	08.05.1993	41	50.067	12.788
Mariánské Lazně	Farská kyselka	10.05.1993	42	50.015	12.724
Mariánské Lazně	Smard`och (mofettes)	30.09.1993	43	50.013	12.717
Mariánské Lazně	Křížový pramen III	20.04.1994	44	49.977	12.704
Mariánské Lazně	Ferdinand	20.04.1994	45	49.962	12.707
Mariánské Lazně	Mariiny (mofettes)	14.05.2003	46	49.976	12.709
Mariánské Lazně	Vličí	05.10.1993	47	49.970	12.678
Podhorní Vrch	Sirňák (mofettes)	30.09.1993	48	49.978	12.788
Horká	Martinov	10.05.1993	49	49.939	12.759
Chotenov	Koňský pramen	07.06.1992	50	49.933	12.739
Dolní Kramolín	Ilsano	10.05.1993	51	49.913	12.754
Michalovy Hory	Čiperka	07.06.1992	52	49.912	12.785
Čihaná	well H–3	08.05.1993	53	50.013	12.799
Čihaná	Kyselka	25.11.1993	54	50.012	12.799
Hoštěc		09.05.1993	55	49.990	12.829
Otrocin		08.05.1993	56	50.017	12.894
Poseč		18.04.1994	57	50.021	12.923
Dobrá Voda		02.10.1993	58	49.987	12.949
Běranovka		10.05.1993	59	49.938	12.835
Pěkovice		03.10.1993	60	49.928	12.871
Křepkovice		27.04.1994	61	49.931	12.878
Nezdice		03.10.1993	62	49.944	12.906
Zahrádka		09.05.1993	63	49.942	12.910
Hanov		02.10.1993	64	49.912	12.884
Zhořec		11.05.1993	65	49.905	12.897
Úterý	Reiterbergerův pramen	02.10.1993	66	49.947	12.975
Křivce		09.05.1993	67	49.936	12.972
Konstatinovy Lázně	Prusíkuv pramen	04.10.1993	68	49.881	12.977
Poloučany	Kozi	02.10.1993	69	49.889	13.013
Kokašice	Lučni	01.10.1993	70	49.878	12.955
Břetislav	Čeliv creek	27.04.1994	71	49.875	12.965
Břetislav	Kyselka	01.10.1993	72	49.874	12.966
Břetislav	Studánka Lásky	11.05.1993	73	49.863	12.972
Horske Domsky	Tripisty	11.05.1993	74	49.824	13.069
Maiersreuth	well M5	06.04.1995	75	49.986	12.415
Neualbenreuth	well E1	06.04.1995	76	49.975	12.439
Kondrau	Diepholdt spring	06.04.1995	77	49.998	12.290

Table 1. (cont.)

Gas flux (free gas) [dm^3h^{-1}]	Gas/water ratio [dm^3dm^{-3}]	CO_2 [vol.%]	N_2 [vol.%]	He [vol.%]	CH_4 [vol.%]	$^{13}C_{CO2}$ [‰]	R/R_a
84.4	0.21	90.49	9.46	0.019	0.0503	–5.3	1.97
60.0	pumped	99.9	0.081	0.0015	0.0192	–3.3	1.81
11.2	0.014	99.84	0.15	0.000093	0.0039	–3.1	n.a.
800	mofette	99.85	0.14	0.0043	0.0071	–2.0	n.a.
>8000	mofette	99.9	0.079	0.0013	0.0215	–2.1	4.6
0.10	pumped	96.22	3.73	0.0151	0.0317	–5.4	4.46
149	0.128	99.99	0	0.00013	0.0062	–2.8	3.94
5200	mofettes	99.98	0.016	0.00062	0.0018	–2.3	3.51
135.6	1.88	99.96	0.034	0.000036	0.0009	–3.9	a.c.
8240	5.72	99.97	0.026	0.000004	n.n.	–4.0	a.c.
87,000	mofettes	99.91	0.091	0.00181	0.00104	–2.7	4.6
11.5	0.063	99.99	0	0.0011	0.0005	–3.8	n.a.
3800	mofettes	99.85	0.11	0.027	0.027	–2.4	3.34
6.3	0.07	99.55	0.44	traces	0.0098	–3.5	n.a.
4.1	0.024	94.28	5.6	0.0044	0.119	–4.0	3.27
164.4	0.51	98.16	1.79	0.0005	0.0505	–2.6	2.63
396	0.60	99.98	0.022	0.00032	0.0023	–4.1	3.32
1300	2.92	99.74	0.24	0.0033	0.0137	–2.7	1.69
772	n.a.	99.76	0.23	0.0033	0.0099	–2.8	n.a.
210	pumped	99.96	0.036	0.000056	0.0012	–3.8	4.09
72	0.25	99.97	0.025	traces	0.0006	–4.6	4.08
0.50	n.a.	87.16	12.41	0.0612	0.348	–3.9	n.a.
1.20	n.a.	90.15	9.75	0.061	0.0404	–4.9	2.4
7.1	0.02	99.99	0	0.00027	0.014	–3.8	2.56
1.0	n.a.	99.82	0.16	0.0016	0.0148	–4.1	n.a.
3.6	0.02	96.71	3.04	0.0203	0.233	–2.9	2.34
5.6	0.02	99.96	0	0.0019	0.0405	–3.9	n.a.
50.8	0.18	96.57	3.24	0.0467	0.142	–3.5	n.a.
24.0	0.12	99.94	0	0.0015	0.06	–4.7	n.a.
10.2	sf. water	98.5	1.42	0.0204	0.059	–2.8	2.39
1.7	0.006	77.08	22.69	0.105	0.124	–4.6	n.a.
10.5	0.025	74.87	24.58	0.199	0.28	–4.2	1.78
2130	pumped	99.97	0.019	0.00068	0.012	–3.6	2.82
0.04	0.0005	95.12	3.94	0.025	0.901	–7.4	n.a.
48	0.44	99.98	0.018	0.000043	0.002	–3.1	2.73
430	sf. water	99.96	0.037	0.00005	0.0018	–3.6	n.a.
6.5	0.04	96.76	3.19	0.0032	0.0406	–2.5	2.8
12.0	0.28	99.5	0	0.0078	0.484	–5.5	1.9
0.03	n.a.	66.99	32.88	0.126	0.0024	–6.9	1.31
23.8	0.032	51.3	47.41	0.237	0.055	–8.8	2.19
235	0.10	65.31	33.77	0.194	0.038	–8.2	2.54
2650		94.14	5.72	0.04	0.015	–5.4	n.a.

Table 1. (cont.)

Locality	name	sampling date	location number	GPS Coordinates (WGS 84) [°N]	[°E]
Kondrau	Gerwigquelle	04.04.1995	78	50.000	12.287
Großschlattengrün	Reichel pond	03.04.1995	81	49.971	12.155
Wiesau	Neue Otto spring	03.04.1995	82	49.913	12.165
Hohenberg	Carolinen Spring	05.04.1995	84	50.095	12.230
Kothigenbibersbach	Kothigenbibersbach	05.04.1995	85	50,080	12.155
Bad Alexandersbad	Luisen spring	06.04.1995	86	50.017	12.020
Schönwald	Sophien spring	04.04.1995	87	50.217	12.105
Hölle	Höllensprudel II	30.09.1996	88	50.367	11.691
Bad Steben	Wiesenquelle	30.09.1996	89	50.365	11.635
Langenau	Max Marien spring	30.09.1996	90	50.330	11.557
Nova Ves	mine N. Ves II (nr. 2)	12.03.2001	91	50.177	12.410
Vackovec	mofette Bublák north	12.03.2001	92	50.146	12.450
Karlovy Vary	well BJ 35+36+37	08.10.2001	93	50.223	12.884
Karlovy Vary	Dorotka	08.10.2001	94	50.218	12.889
Karlovy Vary	Sadovy	08.10.2001	95	50.228	12.879
Korunní	Kyselka (well BJ–22)	09.10.2001	96	50.340	13.071
Klášterec nad Ohří	Euzenie	09.10.2001	97	50.378	13.170
Louny	drill hole	09.10.2001	98	50.348	13.804
Bilina	Bilinska kyselka	10.10.2001	99	50.543	13.757
Bravany u Loun	well BV–5	10.10.2001	100	50.403	13.721
Sokolov	mine Jiři (well OV–70)	12.10.2001	101	50.212	12.679
U Mostku (Brück)		12.05.2003	102	50.174	12.444

The Cheb Basin, which is located in the centre of the area under investigation, is a small intracontinental basin, and was formed during the Late Tertiary as a result of the reactivation of earlier Hercynian faults present within the basement. The basin developed at the intersection of the ENE-trending Eger Graben (early Tertiary) and the NW-trending pre-Neogene Mariánské Lázně fault. This fault system forms the eastern boundary of the basin and is marked by a 50 to 100 m high escarpment that can be traced along strike, for over 100 km (Bankwitz et al. 2003b).

The region under investigation is known as the most interesting European earthquake swarm region. This type of seismicity is characterised by the occurrence of thousands of small and intermediate magnitude swarm earthquakes ($M_L < 5$). Recently, earthquake swarms have been interpreted as a common feature of volcanic regions and mid-ocean rifts (Hill 1977, Sigmundsson et al. 1997, Hill and Prejean 2005). Swarms in intraplate regions without active volcanism are unusual (Špičák and Horálek 2001).

Table 1. (cont.)

Gas flux (free gas) [dm^3h^{-1}]	Gas/water ratio [dm^3dm^{-3}]	CO_2 [vol.%]	N_2 [vol.%]	He [vol.%]	CH_4 [vol.%]	$^{13}C_{CO2}$ [‰]	R/R_a
1320		41.87	56.47	0.212	0.26	–6.3	2.37
1.5		78.85	14.42	0.029	0.418	–0.6	n.a.
1017	0.743	99.12	0.83	0.004	0.023	–3.6	2.91
638	0.545	99.22	0.75	0.002	0.005	–3.1	n.a.
2.1	0.011	50.26	48.73	0.124	0.05	–6.1	3.39
320	0.242	98.64	1.26	0.005	0.046	–3.3	3.52
4.4	0.129	74.05	24.72	0.199	0.021	–4.5	n.a.
1584	0.186	86.00	13.6	0.045	0.01	–7.5	n.a.
3759	0.74	71.5	27.84	0.127	0.139	–7.2	n.a.
1.0	0.002	97.35	2.54	0.005	0.007	–7.4	n.a.
n.a.	n.a.	99.94	0.055	0.0011	0.00033	–2.1	6.1
n.a.	n.a.	99.95	0.044	0.0021	0.00027	–1.7	5.7
n.a.	n.a.	n.a.	n.a.	n.a.	n.a.	–3.7	2.1
n.a.	n.a.	97.51	2.43	0.0236	0.03737	–3.0	2.4
n.a.	n.a.	99.56	0.43	traces	0.00085	–4.6	n.a.
n.a.	n.a.	n.a.	n.a.	n.a.	n.a.	–3.5	2.4
n.a.	n.a.	99.80	0.20	traces	0.00348	–5.1	1.5
n.a.	n.a.	96.79	2.58	0.0099	0.62008	–10.4	1.8
n.a.	n.a.	n.a.	n.a.	n.a.	n.a.	–8.3	1.4
n.a.	n.a.	96.71	3.13	0.0463	0.11295	–5.8	1.8
n.a.	n.a.	99.06	0.29	0.0045	0.64363	–4.6	1.9
n.a.	n.a.	97.25	2.72	0.0213	0.00871	–0.8	5.2

The youngest known volcanic activity in the area occurred about 0.5 to 0.3 Ma (Wagner et al. 2002, Geissler et al. 2004). The most significant earthquake activity is located in the Nový Kostel focal zone (50.24°N, 12.44°E; Fig. 1; Bankwitz et al. 2003a, Fischer and Horálek 2003), where the 1985/86 and 2000 intensive swarms and the December 1994, January 1997, and February 2004 swarms took place. Source mechanisms with significant non-double-couple components indicate tensile earthquakes, which could be caused by a high pore-fluid pressure (Špičák and Horálek 2001, Vavryčuk 2002, Hainzl and Ogata 2005). Parotidis et al. (2003) and Bräuer et al. (2005a) hypothesize that ascending magmatic fluids trigger activity of small and intermediate magnitude swarm earth-quakes by causing pore-pressure perturbations that change the effective stresses.

2 Gas flux, composition and isotope (C, He) ratios of free gases from mineral springs and mofettes

The procedure of gas flux measurement as well as techniques for analysing the chemical composition and the carbon and helium isotope compositions have been described by Weinlich et al. (1998, 1999). The compositions and flow rates of gas emanations, and the isotope (C, He) ratios of CO_2 and He of 102 mineral springs and dry gas vents (mofettes) in the western Eger Rift and its surrounding have been analysed (Table 1). The studies have resulted in the identification of three gas escape centres, which may be distinguished based on their CO_2 fluxes: (1) Františkovy Lázně/Cheb Basin (≈90 $m^3\ h^{-1}$), (2) Mariánské Lázně and its surroundings and in southeastern direction up to Konstantinovy Lázně (≈156 $m^3\ h^{-1}$) and (3) Karlovy Vary (≈356 $m^3\ h^{-1}$). The escaping CO_2 of the three gas escape centres amounts to a minimum of 610 $m^3\ h^{-1}$ or 2.4×10^8 mol a^{-1} of free CO_2 gas. Including the CO_2 dissolved or fixed as HCO_3^-, the entire CO_2 flux approaches 930 $m^3\ h^{-1}$ or 3.6×10^8 mol a^{-1}. Although the highest gas fluxes are measured in the Spa Karlovy Vary, the dimension of this degassing centre is smaller compared to Františkovy Lázně/Cheb Basin and Mariánské Lázně (Fig. 2b). The enormous gas fluxes in the escape centres are explained assuming fault-bounded degassing channels (Weinlich et al. 1998, 1999, 2003).

Fig. 2. (next page) **a)** Distribution pattern of the gas composition (air corrected) from selected locations (see Table 1) in the Vogtland, NW Bohemia and the Oberpfalz area plotted into topographic map (GTOPO30 from USGS EROS DATA Center). The CO_2 concentration is expressed by the degree of the grey filling. The numbers near the columns correspond to sampling locations (see Table 1). *ML*, Mariánské Lázně; *KTB*, location of the German Continental Deep Drilling Boreholes (KTB). The broken line marks the area with CO_2 concentrations higher than 99 vol.% CO_2 at the surface. **b)** Distribution of the isotope ratios from the same locations as in a) (except for location 3, where the $^3He/^4He$ ratio was not determined) plotted into topographic map (GTOPO30 from USGS EROS DATA Center). The black sectors correspond to the percentage of MORB-Type He and the numbers are $\delta^{13}C$ values (‰). Grey circular areas mark the gas escape centres. Carbon isotope values marked by an asterisk (e.g. –2.1*) denote mofettes (see Table 1)

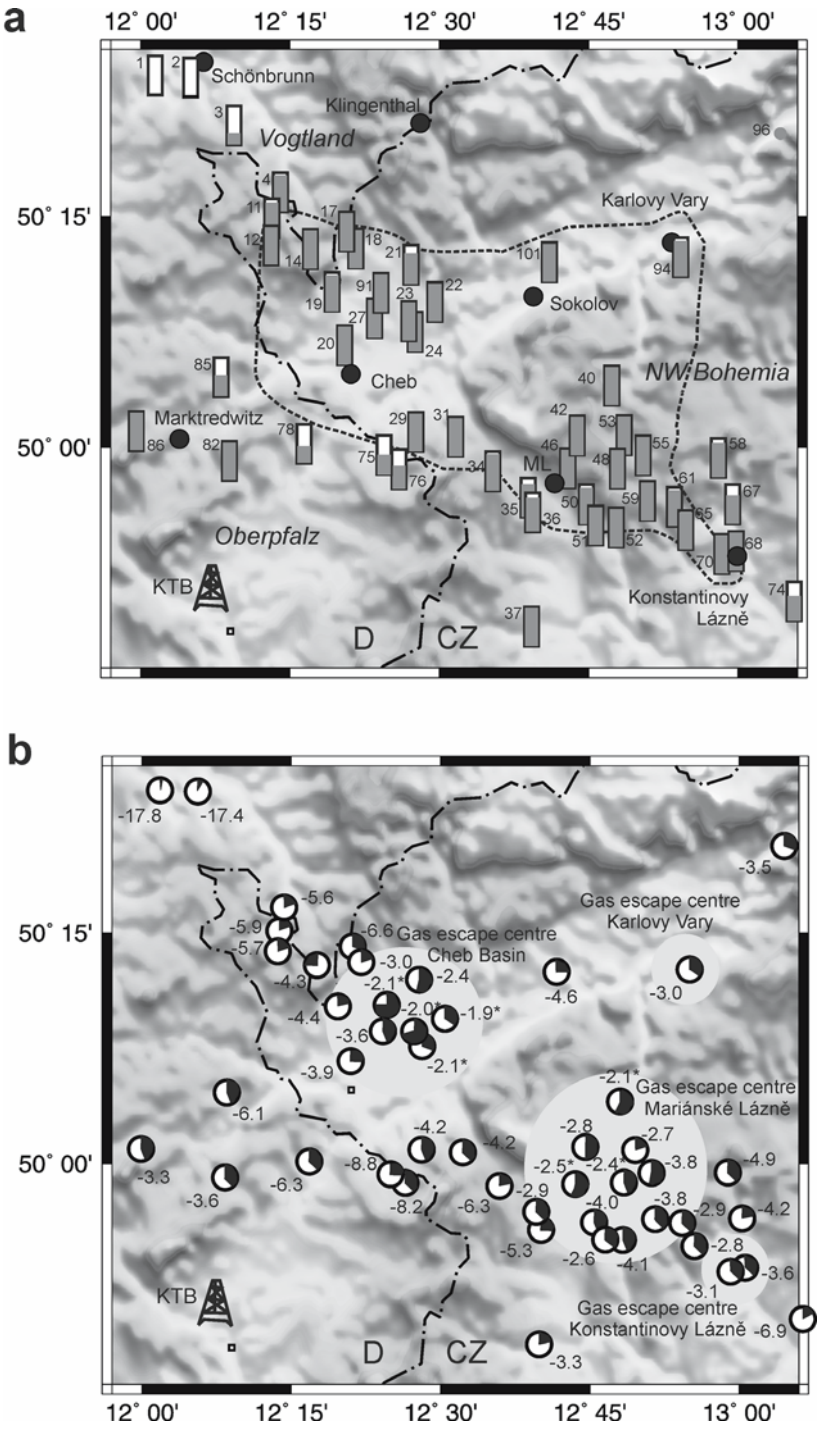
a
12° 00'
12° 15'
12° 30'
12° 45'
13° 00'
50° 15'
50° 00'
Schönbrunn
Klingenthal
Vogtland
Karlovy Vary
Sokolov
Cheb
NW Bohemia
Marktredwitz
ML
Oberpfalz
KTB
D
CZ
Konstantinovy Lázně
b
Gas escape centre Karlovy Vary
Gas escape centre Cheb Basin
Gas escape centre Mariánské Lázně
Gas escape centre Konstantinovy Lázně
KTB
D
CZ

The gas of all gas escape centres consists of nearly pure CO_2 (Fig. 2a) with $\delta^{13}C$ values between –2 ‰ and –4 ‰ and contains a high percentage of upper mantle derived helium (R/R_a between ~ 2.4 and ~ 6.1), (Fig. 2b, Table 1). The highest $\delta^{13}C$ values of CO_2 with –1.8 ‰ to –2.9 ‰ occur in the mofettes. With increasing distance from the gas escape centres, gas fluxes and CO_2 contents decrease, whereas the N_2, He and partly CH_4 contents rise (Fig. 2a, Table 1). The sampling points to the east of Karlovy Vary (mostly outside of region shown in Fig. 2) show gas geochemical signatures as observed at the periphery of the other degassing centres (Table 1, locations 96 to 100).

Not only the gas composition, but also the isotopic (C, He) signatures change between degassing centres and periphery. Proceeding away from the gas escape centres, both $\delta^{13}C$ values and $^3He/^4He$ ratios decrease. For instance, in the Vogtland area northwest of the degassing centre Cheb Basin, there is evidence of only isotopically light CO_2 with $\delta^{13}C$ values between –17.8 and –17.4 ‰ and R/R_a values between 0.18 and 0.71 at locations Neumühle (location 1) and Schönbrunn fluorite mine (location 2), respectively. These R/R_a values are relatively small, but are still well above the range of typical crustal *He* (R/R_a <0.1)! (Fig. 2b, Table 1).

Whereas all degassing centres are characterised by the same range of $\delta^{13}C$ values, their $^3He/^4He$ ratios differ. The highest $^3He/^4He$ ratios were found in the degassing centre Cheb Basin with $^3He/^4He$ up to 6.1 (R/R_a). The R/R_a values in the surrounding of Mariánské Lázně are up to 4.6, whereas in Karlovy Vary only $^3He/^4He$ ratios of ~ 2.4 (R/R_a) were found. Polyak et al. (1985) analysed gas from the Vřidlo mineral spring in Karlovy Vary and obtained an R/R_a value of 2.6 in good agreement with our results.

3 Geophysical “mapping” of the lithosphere and the upper mantle using receiver functions

The receiver function method is now a practicable tool to study and map seismic discontinuities both on a regional as well as on a local scale (Vinnik 1977, Langston 1979, Zandt et al. 1995, Kind et al. 2000). The fundamentals of the method used are described by Kind et al. (1995) and Yuan et al. (1997). The processed receiver functions provide images of the crust and upper mantle similar to steep angle reflection images of the crust, however with lower seismic frequencies since earthquakes are utilized as seismic sources.

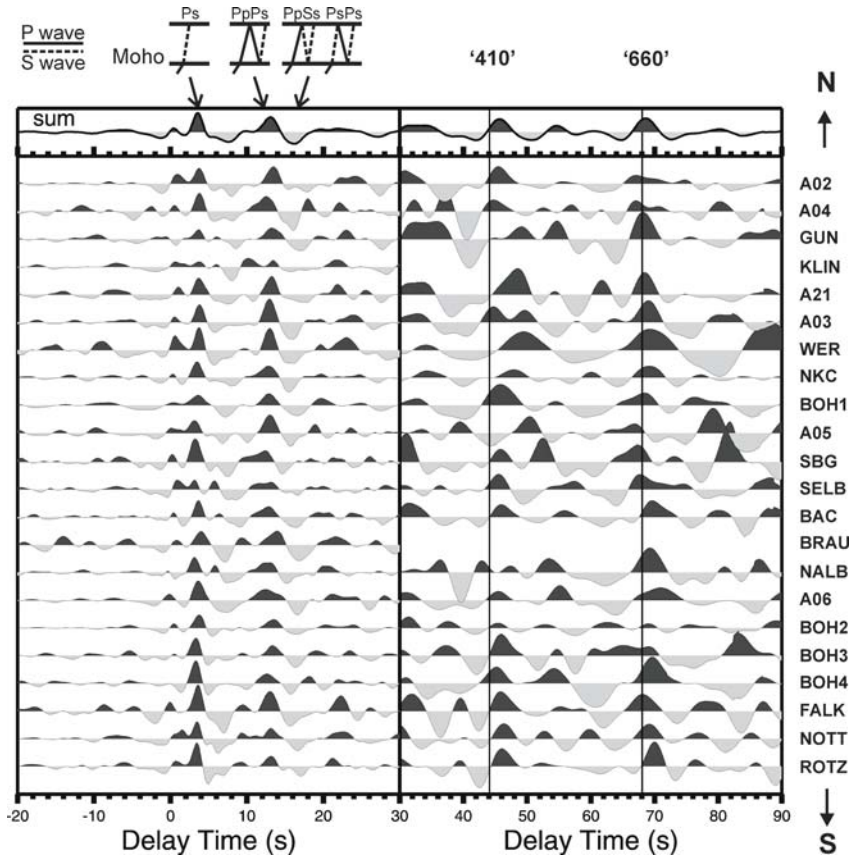

Fig. 3. Stacked receiver functions for seismological stations within the study area. Traces were high-pass filtered (corner period 12 seconds) between –20 and 30 seconds delay time and low-pass filtered between 30 and 90 seconds delay (corner period 5 seconds). The converted phases from the Moho, the 410 km and 660 km seismic discontinuities are marked in the stack trace

Multiple reflections and conversions between the base of the crust and the surface of the Earth occur and must be considered (Fig. 3). For calculations of move-out corrections and Moho piercing point locations we used the iasp91 velocity model (Kennett and Engdahl 1991). Generally, strong conversions from the Moho can be observed with positive polarity between 3 and 4 seconds delay time and their multiple phases between 12 and 16 seconds delay time (Fig.3).

Table 2. Seismological station parameters, *Ps* delay time of conversion (t_{ps}) from the Moho and the upper mantle discontinuities at 410 km and 660 km depth, and number of stacked traces (n).

Station	Longitude [°E]	Latitude [°N]	Elevation [m]	Institution	Recording period
NKC	12.448	50.233	564	IG CAS	2000 – 2003
BOH1[1)]	12.754	50.187	420	GFZ/SZGRF	1997 – 2001
BOH2[1)]	12.874	49.967	660	GFZ/SZGRF	1997 – 1998
BOH3	12.760	49.920	610	GFZ/SZGRF	1997 – 1998
BOH4	12.651	49.872	540	GFZ/SZGRF	1997 – 1998
NOTT	12.122	49.811	490	KTB/Munich	1995
FALK	12.225	49.861	465	KTB/Munich	1995
ROTZ	12.208	49.768	430	KTB/Munich	1995
A02	12.159	50.487	414	GFZ/SZGRF	1995 – 1996
A03	12.364	50.294	610	GFZ/SZGRF	1995 – 1996
A04	12.568	50.424	900	GFZ/SZGRF	1995 – 1996
A05	12.104	50.187	670	GFZ/SZGRF	1995 – 1996
A06	12.119	49.980	635	GFZ/SZGRF	1995 – 1996
A21	12.056	50.312	530	GFZ/SZGRF	1995 – 1996
WER	12.376	50.287	670	GFZ/SZGRF	1999 – 2000
GUN	12.332	50.364	660	GFZ/SZGRF	1999 – 2000
KLIN	12.462	50.358	640	GFZ/SZGRF	1999 – 2001
SELB	12.179	50.154	580	GFZ/SZGRF	1999 – 2001
NALB	12.461	49.981	640	GFZ/SZGRF	2000 – 2001
BAC	12.840	50.086	530	GFZ/SZGRF	2000 – 2001
SBG	12.305	50.182	595	GFZ/SZGRF	1998 – 2001
BRAU	12.087	50.082	600?	GFZ/SZGRF	1998 – 1999
LAC	12.625	50.051	838	IG CAS	1997 – 1998
P02	12.396	50.319	670	Potsdam/GFZ	2000
P04	12.300	50.188	765	Potsdam/GFZ	2000
P06	12.253	50.240	580	Potsdam/GFZ	2000
P10	12.298	50.225	580	Potsdam/GFZ	2000
P11	12.331	50.270	610	Potsdam/GFZ	2000
P12	12.472	50.411	890	Potsdam/GFZ	2000

[1)] GÜRALP-40T seismometers were provided by the Dublin Institute for Advanced Studies (DIAS)

Moho *Ps* delay times (Table 2) can be translated directly into Moho depth, if one assumes a constant average *P*-wave velocity (v_P) of 6.3 km/s and a v_p/v_s ratio of 1.73 and multiplies the observed delay times by a value of 8.3 km/s. As it is obvious from Table 2, most stations show delay times of about 3.6 to 3.8 s (about 30 to 32 km depth).

Table 2. (cont.)

Seismometer	Moho t_{ps}[s]	410 t_{ps}[s]	660 t_{ps}[s]	n
STS-2	3.4	47.9	69.2	89
GÜRALP-40T / MARK L-4-3D / TSJ-10	3.6	45.8	68.5	30/13
GÜRALP-40T	3.8	45.3	68.6	36
MARK L-4-3D	3.3	45.9	69.1	15
MARK L-4-3D	3.3	45.2	69.6	21
STS-2	3.5	46.3	69.2	43
STS-2	3.6	45.8	68.1	12
STS-2	3.5	46.0	70.0	18
GÜRALP-3T	3.8	45.5	67.1	29
GÜRALP-3T	3.8	49.6	69.0	27
STS-2	3.8	(44.7)	(67.1)	9
GÜRALP-3T / MARK L-4-3D	3.4	(50.4)	(66.9)	22
GÜRALP-3T	3.6	45.5	71.0	28
GÜRALP-3T	3.7	48.5	68.5	19
MARK L-4-3D	3.8	(49.5)	(69.2)	10/5
MARK L-4-3D / TSJ-10	3.7	(49.1)	(68.2)	14/7
MARK L-4-3D	3.8	-	-	21
MARK L-4-3D / TSJ-10	3.1	45.5	67.7	18/14
MARK L-4-3D / STS2 / TSJ-10	3.1	47.4	69.3	17
TSJ-10	3.7	45.9	69.6	21
TSJ-10	3.2	45.8	67.4	5/4
MARK L-4-3D	4.0	-	-	7
Stack trace:	3.6	45.7	68.6	412
SM3	3.5	-	-	44
LE-3D/5s / MARK L-4-3D	3.7	-	-	3
LE-3D/5s / MARK L-4-3D	3.3	-	-	6
LE-3D/5s / MARK L-4-3D	2.9	-	-	9
LE-3D/5s / MARK L-4-3D	3.1	-	-	3
LE-3D/5s / MARK L-4-3D	3.5	-	-	7
LE-3D/5s / MARK L-4-3D	3.8	-	-	8

However, beneath the Cheb Basin the converted phases from the Moho arrive already 3.0 to 3.3 s after the *P*-wave (25 to 27 km depth). Later Moho arrivals (4.3 to 4.5 s delay time, 36 to 37 km depth) were observed at stations WET and KHC south of the study area within the Bohemian Massif (Geissler et al. 2005). At a few stations (e.g., SELB, BOH1, KLIN) reduced Moho conversion amplitudes were observed. They can be explained by strong lateral variations of pieces of a sharp Moho or a broad

velocity gradient zone between 25 and 32 km depth. Because reduced Moho conversion amplitudes are observed at single stations, we favour the latter explanation.

Intracrustal phases occur within 2 seconds delay time, which are most probably caused by strong velocity gradients within the uppermost crystalline crust (Málek et al. 2001, Hemmann et al. 2003). Receiver function modelling showed that relatively smooth crustal seismic velocity models can explain most of the observed data whereas complex *P*-wave models (mainly from reflection seismic studies) with more than one high or low velocity layer in the crust do not explain the observed receiver functions (see Fig. 6 in Geissler et al. 2005).

Further conversions are observed at about 6 s delay time beneath several stations in the region where earthquake swarms occur as well as CO_2 escapes at the surface (e.g., stations NALB and SELB in Fig. 3). Stacking the single traces with moveout corrections for primary and multiple phases implies that the observed "6 s phase" might be a primary conversion, that means that it could have its origin in about 50 to 60 km depth. However, the moveout differences are very small and are within the resolution limits. Signals from 410 and 660 km discontinuities are delayed by up to 2 seconds compared to theoretical delay times calculated from the iasp91 earth model (Fig. 3, Table 2), possibly indicating reduced seismic velocities in the upper mantle (above 410 km) relative to the standard earth model iasp91.

The uncertainty of *Ps* delay time measurements is in the range of ±0.1 to ±0.2 s for Moho conversions assuming constant crustal seismic velocities, which results in a depth uncertainty of about ±1.5 to ±2 km for Moho depths. Generally, variations in the background velocity model may influence the depth estimations from *Ps* delay times. We assumed an average crustal *P*-wave velocity of 6.3 km/s and a v_p/v_s ratio of 1.73. Variations of the *P*-wave velocity of ±0.2 km/s would result in ±2 km depth uncertainty, however, up to now no information on small-scale average crustal *P*-wave velocity fluctuations is available. The uncertainty for the single station measurements of delay times from the transition zone discontinuities (410 and 660) might be in the range of less than ±1 s. A broader discussion of resolution and possible uncertainties of the method can be found in Geissler et al. (2005).

To search for the lateral distribution of the "6 s phase" (Fig. 4), we divided the study area in several boxes and applied a common conversion point method (Fig. 4a, b). The size and distribution of the boxes was chosen after several tests including stacking within back-azimuth windows at single stations. A more regular grid was not possible due to the inhomogeneous station distribution.

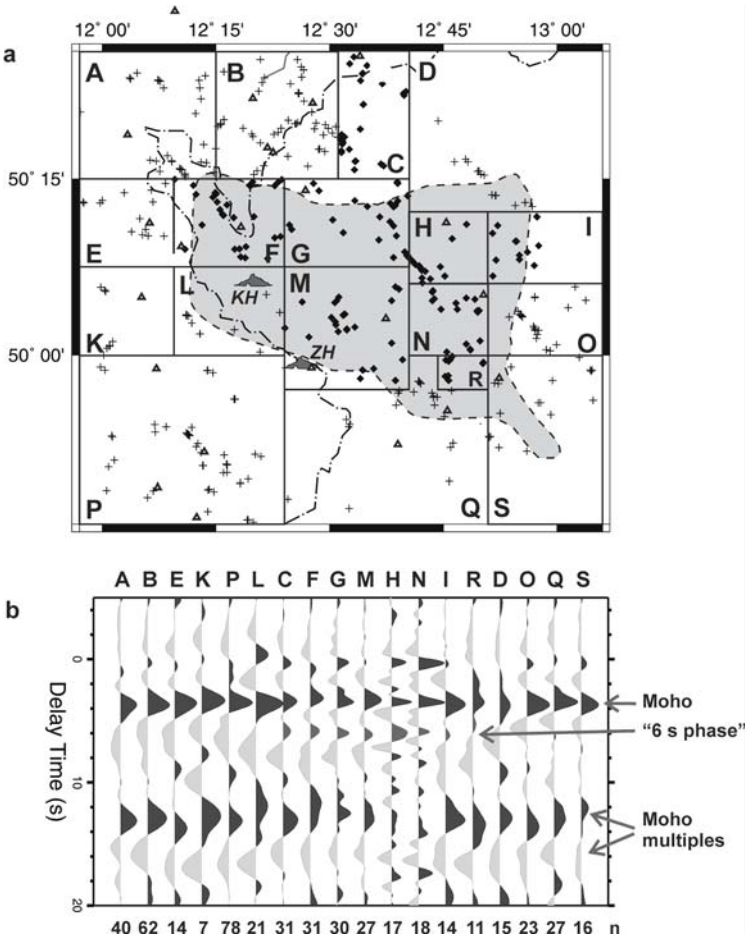

Fig. 4. a) Mapping of the "6 s phase" in relation to the distribution of mantle derived fluids at surface. Piercing points of the "6 s phase" at 50 km depth were mapped. Single receiver function traces with piercing points in the specific boxes were stacked (common conversion points). Crosses mark boxes where no "6 s phase" was observed in the stack trace, whereas diamonds mark boxes with a "6 s phase" in the stack trace (see b). The light-grey area marks the region of nearly pure CO_2 escape (>99 vol.% CO_2) at the surface; see also Fig. 2a. Triangles mark locations of stations, data of which is shown in Fig. 3. *ZH*, Železná hůrka volcano; *KH*, Komorní hůrka volcano (both Quaternary). **b)** Stack traces for common conversion points (boxes) in a). Primary and multiple conversions from the Moho and the "6 s phase" are marked. An updoming of the Moho in the regions with the "6 s phase" is visible, especially in the Moho multiples

4 Discussion

4.1 Origin and sources of the CO_2-dominated free gases from mineral springs and mofettes

CO_2 is the carrier phase for mantle-derived fluids. The combination of carbon and helium isotope ratios is a useful tool to evaluate the origin of fluids. The $\delta^{13}C$ values of the CO_2-rich locations lie within the range of mantle-derived CO_2 (Cartigny et al. 1998), although the mofette gas is partly enriched in ^{13}C in comparison to typical MORB samples. Isotope fractionation due to CO_2–water interaction may explain the lower $\delta^{13}C$ values of most mineral springs in comparison to the mofette $\delta^{13}C$ values as well as the enriched $\delta^{13}C$ values of same low mineralised springs with extremely low gas/water ratios (Weinlich et al. 1999). The lower $\delta^{13}C$ values at the CO_2-rich mineral springs can be explained by isotope fractionation due to formation of HCO_3^- in groundwater, assuming that the gas stems from the same magmatic reservoir that supplies the adjacent mofettes. At low mineralised springs marked by low pH values (< 4.3) no HCO_3^- can be formed. In combination with extremely low gas/water ratios, the isotope fractionation by formation of dissolved CO_2 may result in $\delta^{13}C$ values enriched in ^{13}C up to 1.3 ‰ (see Table 1). The much lower $\delta^{13}C$ values of the nitrogen-dominated free gas of the thermal water escapes Schönbrunn and Neumühle (Table 1, locations 1, 2) may reflect an organic carbon source. As the $^3He/^4He$ ratios imply some mantle He contribution to the gas phase at these locations, too, we assume that the CO_2 represents a mixture of organic and mantle-derived components.

Fig. 5. (next page) **a)** $CO_2/^3He$ ratios vs. CO_2 concentrations of the area under investigation. The MORB $CO_2/^3He$ range is based on data of Marty and Zimmermann (1999), and the ESCM range is defined by data from the Massif Central (Matthews et al. 1987) and the East Eifel, Laacher See mofette field (Giggenbach et al. 1991, Aeschbach-Hertig et al.1996), two other areas that belong to the European Cenozoic rift system. The error bars are smaller than the plotted symbols. **b)** $^3He/^4He$ (R/R_a) vs. $CO_2/^3He$ ratios for our sampling locations. The MORB range (Marty and Zimmermann 1999) as well as literature data from the French Massif Central (Matthews et al. 1987) and the East Eifel, Laacher See mofette field (Giggenbach et al. 1991, Aeschbach-Hertig et al. 1996) are also plotted. The error bars are smaller than the plotted symbols

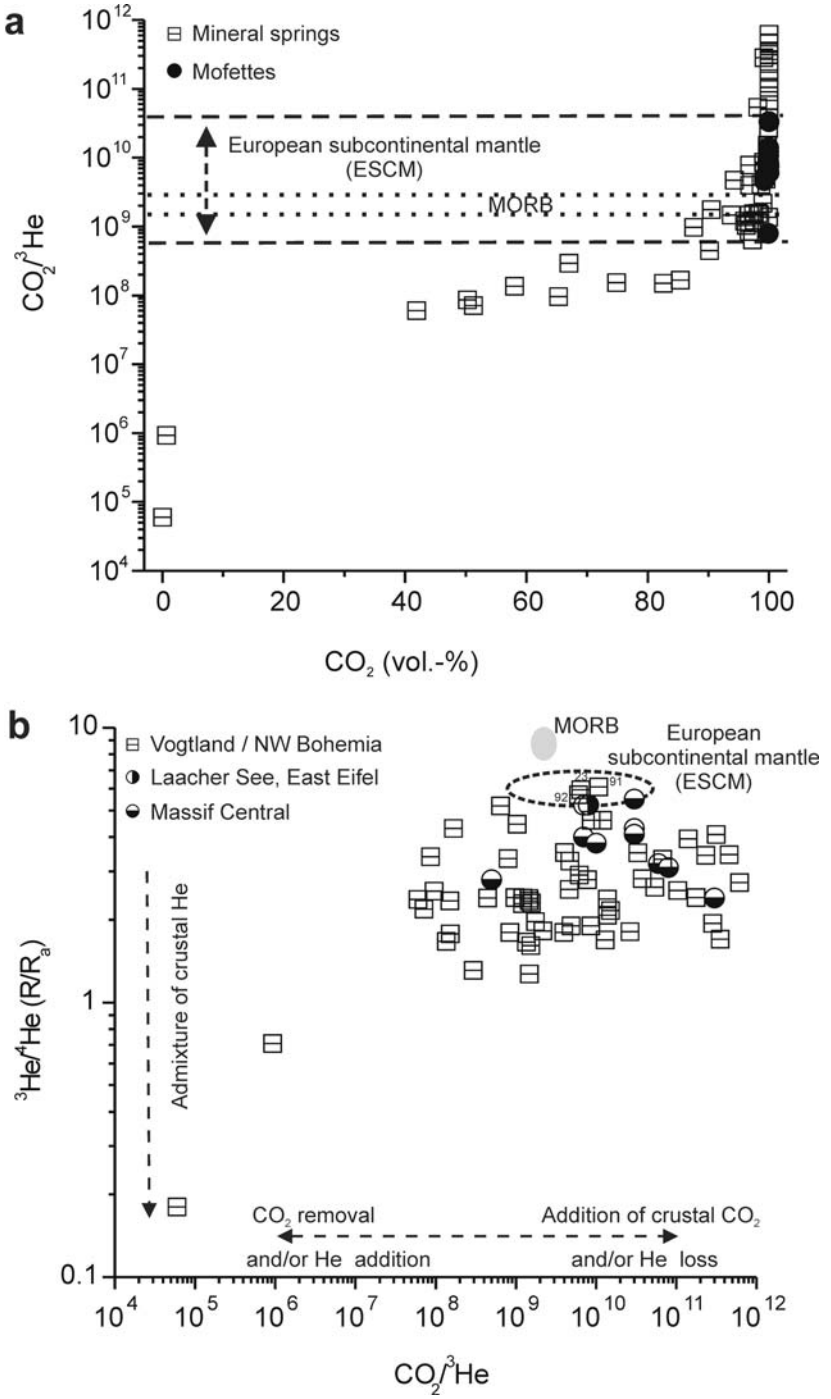
a
Mineral springs
Mofettes
European subcontinental mantle (ESCM)
MORB
CO2/3He
CO2 (vol.-%)
b
Vogtland / NW Bohemia
Laacher See, East Eifel
Massif Central
MORB
European subcontinental mantle (ESCM)
Admixture of crustal He
CO2 removal and/or He addition
Addition of crustal CO2 and/or He loss
3He/4He (R/Ra)
CO2/3He

Due to the fact that the interpretation of $\delta^{13}C$ values alone does not allow a clear identification of the origin of CO_2, the $CO_2/^3He$ ratios are often consulted for this purpose. Figure 5a shows the relationship between the $CO_2/^3He$ and CO_2 concentration of the free gases of the area under investigation. It is obvious that only a few of our samples are directly consistent with the MORB range (Marty and Zimmermann 1999), but most data, in particular the mofette data, fall into the ESCM range, derived from gas data of the French Massif Central and the Eifel area (Matthews et al. 1987, Giggenbach et al. 1991; Aeschbach-Hertig et al. 1996). $CO_2/^3He$ ratios smaller than the ESCM range were found at the periphery of the degassing centres and may be explained by loss of CO_2 during the migration away from degassing channels and distribution at shallow levels.

The He isotope ratios are used to distinguish between crustal and upper mantle-derived components. Figure 5b shows the $^3He/^4He$ ratios in relation to the $CO_2/^3He$ ratios. The $^3He/^4He$ ratios of our area under investigation are far from ratios of typical sedimentary basins (Sherwood Lollar et al. 1997) or natural gas fields in central Europe (Elliot at al. 1993, Ballentine et al. 1996). In a natural gas reservoir (the west Texas Permian basin), Ballentine et al. (2001) found linear correlations between $^3He/^4He$ ratios and CO_2 contents as well as between $CO_2/^3He$ ratios and CO_2 contents. Assuming a $\delta^{13}C_{CO2}$ fractionation of 2 ‰ (Mattey 1991) between the CO_2 dissolved in the magma and the gas phase, they simulated the evolution of the gas phase in relation to a degassing magma body and showed that both $CO_2/^3He$ and $\delta^{13}C_{CO2}$ decrease with increasing CO_2 extraction. In other words, at the beginning of the degassing process the most ^{13}C-rich CO_2 is released and the highest $CO_2/^3He$ ratios are observed. In this sense the higher than MORB-typical $\delta^{13}C$ values of the mofettes may indicate a beginning magma degassing process.

On the other hand, Ballentine (1997) studied mantle He/Ne ratios in well gases from continental settings around the world and showed that He/Ne fractionation in the gas phase of a mantle melt is controlled by the gas/melt volume ratio. The smaller the gas/melt ratio, the smaller is the He fraction in the gas phase. Ballentine (1997) was able to explain the well gas data by clearly smaller gas/melt ratios in subcontinental environments compared to mid-ocean ridge environments, leading to a more pronounced He/Ne fractionation in continental settings. Similar to He/Ne, the $CO_2/^3He$ and $^{13}C/^{12}C$ ratios will be maximally fractionated for the lowest gas/melt ratios. In this sense, the higher-than-MORB $CO_2/^3He$ and $\delta^{13}C$ of the mofettes need not really be related to a very early stage of magma degassing, but may just represent the special situation of particularly low gas/melt ratios in a continental rift zone.

In Figure 5b, the $^{3}He/^{4}He$ ratios are plotted versus $CO_2/^{3}He$ along with literature data from the Massif Central and the East Eifel (Laacher See mofette field), two other areas that belong to the European Cenozoic rift system (Fig. 1, inset map). The $CO_2/^{3}He$ ratios that are lower than the ESCM signature may represent preferential loss of magmatic CO_2 (Sherwood Lollar et al. 1997) and/or addition of crustal derived helium (Bräuer et al. 2004). The $CO_2/^{3}He$ ratios higher than the ESCM range are more difficult to understand. In principle, this signature could either reflect an admixture of crustal carbon or preferential loss of He from the mantle-derived fluid. However, an admixture of crustal CO_2 is unlikely because no carbonate reservoir is known in the investigation area, except for small isolated carbonate depositions in the Cheb Basin (Buzek et al. 1996), and in addition an admixture of carbonate-derived CO_2 should be reflected by a ^{13}C-enriched isotope composition at these mineral springs, which is not observed.

Because the rate of He diffusion is relatively low in basaltic melts or carbon-oxygen-hydrogen fluids, He has to be supported on its way through the crust and CO_2 is assumed to be the carrier fluid (Ballentine et al. 2001). Mantle-derived fluid and water (e.g. groundwater) meet only in the uppermost crust. During migration away from the degassing channels and distribution in shallow levels, fluids lose helium more readily than CO_2 (e.g. Snyder et al. 2001).

Detailed isotope studies at the Eisenquelle mineral spring, Bad Brambach (Table 1, loc. no. 14) have resulted in the observation that both the $^{20}Ne/^{36}Ar$ and N_2/Ar ratios are lower than expected for dissolution equilibrium at 10 °C (Bräuer et al. 2004). Following the different solubility $He<Ne<N_2<Ar<<CO_2$ (Handbook of Chemistry and Physics 1995/96) in water, this may indicate that an efficient stripping process has affected the fluid, resulting in an increased $CO_2/^{3}He$ ratio. However, the gas phase derived from that stripping process would have increased $^{20}Ne/^{36}Ar$ and N_2/Ar and decreased $CO_2/^{3}He$ ratios, contrary to observations at Bad Brambach. The stripping process must therefore take place somewhere along the fluid transport path between the degassing magma body and the gas discharge at the surface, due to the different surroundings of the migration path ways.

At the relevant mineral springs, a second gas phase depleted in He, Ne and N_2 is then extracted from the residue left behind by stripping. Such a stripping process has been proposed earlier to explain increased $CO_2/^{3}He$ ratios in volcanic systems (e.g. Matthews et al. 1987; van Soest et al. 1998; Snyder et al. 2001).

High resolution monitoring studies at the Bublák mofette marked by the highest gas flux rate in the Cheb Basin have resulted in the estimation of a

CO_2 transport velocity of >400 m/day for the upper crust (Bräuer et al. 2003, 2004). The $^3He/^4He$ ratio of about 6 R_a from the free gas phase of the Bublák mofette is in agreement with the results of noble gas analyses of two xenoliths from the Quaternary volcano Železná hůrka located at the southwest boundary of the Eger Rift (Bräuer et al. 2004) and covers the ESCM range given by Dunai and Porcelli (2002). The high gas flux and the high transport velocity in combination with the $^3He/^4He$ ratio of about 6 R_a indicate that the Bublák gas is directly derived from a presently active magma reservoir in the upper mantle beneath the Cheb Basin. In other words, the $\delta^{13}C$ value and the $^3He/^4He$ ratio of the Bublák mofette may characterize the magma reservoir that supplies the mofette.

4.2 Origin of the "6 s phase"

We now discuss results from teleseismic receiver function analysis of the data from temporary and permanent seismic stations (Geissler et al. 2005) together with the results from the Czech and German reflection seismic studies (Tomek et al. 1997, Behr et al. 1994, DEKORP Res. Group 1988). Geissler et al. (2005) performed forward modelling to test simple *S*-wave velocity (v_S) models that can explain the observed "6 s phase". As it is obvious from this modelling, models with single velocity anomalies in the crust or uppermost mantle could explain the observation. We favour the model with a converter in the uppermost mantle (Figure 10e in Geissler et al. 2005), because there are also indications for a local seismic discontinuity in 56 km depth from the reflection seismic profile 9HR (MR_3 in Tomek et al. 1997, plate 13; boxes H+N in Fig. 4a). Further local upper mantle reflections were observed by Tomek et al. (1997, plate 13) at subcrustal depths of 35 km (MR_1) and 42 km (MR_2, box R in Fig. 4a) beneath the degassing area. Also reflector M_1 at about 32 km depth might be from the upper mantle. According to Tomek (personal communication), it is not possible to interpret the polarities of these reflections.

Seismic discontinuities in the lithospheric upper mantle were found in various tectonic settings worldwide (cf., Hales 1969, Ginzburg et al. 1979, Keller et al. 1994, Bostock 1999, Ascencio et al. 2003, Rost and Williams 2003). There are also a wide variety of possible explanations for these discontinuities, including the spinel-to-garnet lherzolite transition, compositional differences due to differentiation processes or the presence of partial melt, anisotropic layers with preferred orientation of olivine crystals, and relic subduction zones (eglogites).

In Figure 4a we plotted the piercing points of the analysed rays at 50 km depth together with the results of the gas mapping at the surface (Fig. 2a).

Interpreting the "6 s phase" as being of uppermost mantle origin, the distribution of diamonds in Figure 4a outline more or less areas with relatively reduced seismic velocities in the uppermost mantle above a seismic converter, according to Geissler et al. (2005). If the "6 s phase" is associated with upper mantle structure, then the average velocity reduction in the uppermost mantle above the converter might be up to 8% (v_p/v_s = 1.79) or 5% for v_p and 11.5% for v_s (v_p/v_s = 1.92), respectively, relative to a "normal" upper mantle *P*-wave velocity of 8.0 km/s (v_p/v_s = 1.79). This could indicate the presence of 3 to 5% melt or fluids in the uppermost mantle (Faul et al. 1994). However, also water-bearing minerals (phlogopite, amphibole) can lower the seismic velocities in the uppermost mantle significantly, as it was already discussed by Glahn et al. (1992) for the Urach volcanic field (S Germany), and could explain at least some percent of the assumed seismic velocity reduction. The higher seismic velocities beneath the discontinuity might represent normal upper mantle rocks or slightly depleted rocks (harzburgites/dunites) in the source region of alkaline magmas.

The "6 s phase" is present also to the North and Northeast of the CO_2 degassing at the surface (boxes C and G, Fig. 4a). The Nový Kostel and Klingenthal focal zones (Neunhöfer and Meier 2004) are located in this area. This observation seems to be in good accordance to the hypothesis of the existence of permeability barriers in the seismogenic zones of that area. The lack of CO_2 exhalations around Nový Kostel and northwards could be explained by rock units above the hypocenters that act as permeability barriers and capping the hydraulic system. In consequence, the permeability barriers might prevent the mantle-derived fluids from vertical ascent and force its lateral distribution (Bräuer et al 2003).

O'Reilly and Griffin (1985) explained a sharp seismic velocity increase in the uppermost mantle beneath south-eastern Australia with the spinel lherzolite–garnet lherzolite transition, which might be a relatively sharp transition over a pressure interval of only about 2 kbar (6 km), according to Webb and Wood (1986). However, up to now no garnet-bearing upper mantle xenoliths are reported from the Eger Rift area and the spinel stability field may be expanded down to about 90 km (Franz et al. 1997, Medaris et al. 1999). Therefore, it is questionable if the spinel–garnet transition would be the best explanation for the observed seismic discontinuity in the study area.

For interpretation of the origin of the "6 s phase" we combined the results of the mapped fluid characteristics from the Vogtland and NW Bohemia with receiver function results of the lithosphere in the same area. The geophysical image and the fluid research identify the actual situation of active crust/mantle interaction processes. A broad velocity gradient-

zone between the crust and upper mantle was modelled by Geissler et al. (2005) to explain the reduced amplitudes of Moho conversions that are observed at some stations (e.g. SELB, BOHA 1, KLIN). This velocity gradient zone in the area of CO_2 degassing could be caused by a magmatic overprinting of a former sharp Moho discontinuity as it can still be observed in the surroundings (Figs. 4, 6). Also the high reflectivity observed in deep seismic measurements (Trappe and Wever 1990, Bleibinhaus et al. 2003) could be related to small magmatic intrusions into the lower crust. The positions of the degassing centres at the surface with isotopic signatures of the European subcontinental mantle ($^3He/^4He$ ratios up to 6.1 R_a), as well as the positions of the Quaternary scoria cones of Komorní hůrka and Železná hůrka overlap with the positions of the local converters/reflectors in the depth of approximately 50 to 60 km (Fig. 6) (this study, Tomek et al. 1997). We propose that CO_2 degasses from presently active magma/fluid reservoirs within a highly metasomatic mantle between 27 and about 50 km and migrates vertically through the uppermost mantle and the crust to the surface using deep-reaching faults. Local reflectors just beneath the Moho as observed in reflection seismic profiling (Tomek et al. 1997) might be related to such still active reservoirs. According to Thomas (1992), the CO_2 release from the melt may start between 30 and 21 km depth.

5 Model of the asthenosphere–lithosphere interaction

The receiver function study and gas-geochemical and isotope fingerprints made it possible to find a link for mantle–crust interaction processes at different depths (Fig. 6) based on the following summarized results:

Asthenospheric up-welling beneath the western Eger Rift area is indicated by different seismic studies (Raikes and Bonjer 1983, Faber et al. 1986, Plomerová and Babuška 1988, Passier and Snieder 1996, Plomerová et al. 1998), but a possibly existing small-scale mantle plume has not yet been imaged by seismic tomography. An isolated subcrustal seismic converter/reflector exists at a depth of approximately 50 to 60 km (this study, Tomek et al. 1997), which can be interpreted as the base of a zone of a highly metasomatic mantle infiltrated from presently active melt (magma/fluid reservoirs).

In the same area a local scale Moho updoming from about 31 km at the rim to 27 km depth in the centre (NNW–SSE extension of 40 km) was observed (Geissler et al. 2005). Local observations of weak or absent Moho conversions (this study) point to a transition zone rather than a sharp ve-

locity contrast at the crust–mantle boundary beneath parts of the western Eger Rift. Increased reflectivity in the lower crust northeast of the KTB and beneath the Vogtland (Trappe and Wever 1990, Behr et al. 1994, Bleibinhaus et al. 2003) can be interpreted as low angle shear zones partly filled with fluids and/or small magmatic intrusions (sills/dikes) or partial melting (cf., Matthews 1986, Wever and Meissner 1987, Vanderhaege and Teyssier 1997). A decreased thickness of the seismogenic (brittle) upper crust can be inferred from the spatial distribution of repeatedly occurring earthquake swarms (Horálek et al. 2000), and is interpreted as a rheological effect based on interaction with CO_2-dominated fluids. Finally, CO_2-dominated emanations of upper mantle derived origin exist, distributed over an area of approximately 1500 km^2 at the surface (Weinlich et al. 1999, 2003). The gas characteristics of the samples cover the ESCM range in the $^3He/^4He$ (R/R_a) vs. $CO_2/^3He$ plot (this study). All features together indicate a systematic mantle–crust coupling by presently active magmatic processes beneath the western Cheb Basin.

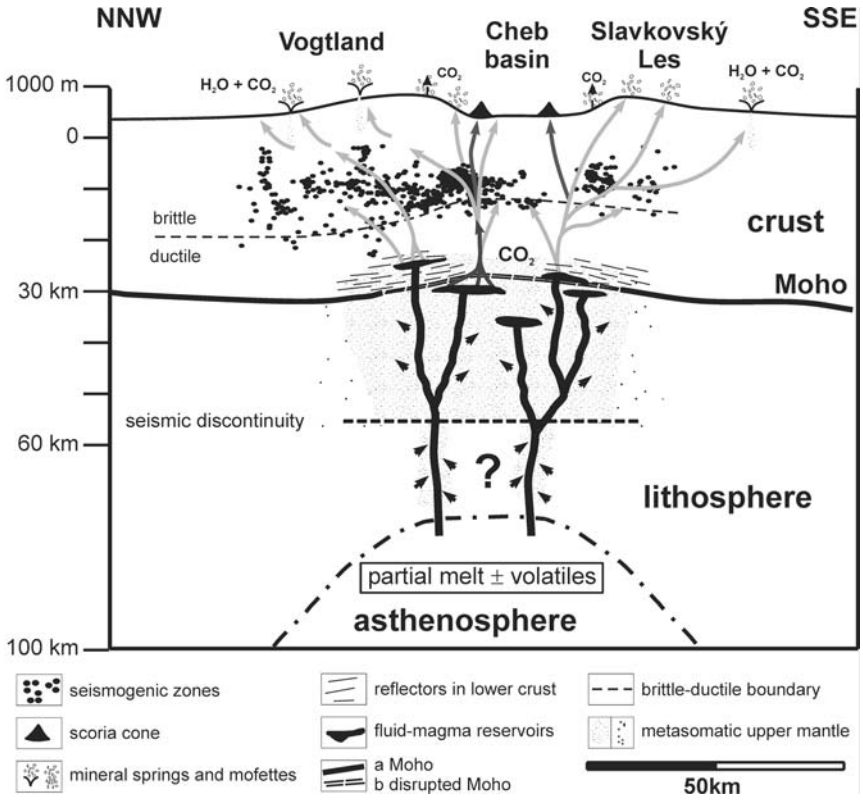

Fig. 6. (previous page) Cartoon illustrating the asthenosphere–lithosphere interaction in the NW Bohemia/Vogtland region, according to Geissler et al. (2005). In this figure the results of former studies (Trappe and Wever 1990, Babuška and Plomerová 2001, Weinlich et al. 1999, 2003, Horálek et al. 2000, Bräuer et al. 2003) are compiled with new results (Geissler et al. 2005). Black channels mark uprising CO_2 dissolved in melts; grey channels mark the CO_2-fluid transport through the crust. The NW Bohemia/Vogtland earthquake swarm activity in the Nový Kostel focal zone (Fig. 1) is primarily induced by a presently active magmatic intrusion from the uppermost mantle into the lower crust beneath the Cheb Basin and related ascending CO_2-dominated fluids (Bräuer et al. 2005a,b)

Geophysical results from the French Massif Central and the Eifel area (Germany) proved individual active asthenospheric mantle fingers (plumes) beneath these areas. Both regions and also the western Eger Rift are marked by the occurrence of degassing fields of upper mantle derived fluids with nearly the same isotope (C, He) characteristic but far from the plume signature of Ocean Island Basalt (OIB).

Acknowledgements

We would like to thank J. Tesař for measuring the gas composition. For fluid sampling assistance in the Czech Republic we have to thank T. Pačes (Czech Geological Survey), T. Vylita (SPLZAK, Karlovy Vary) and H. Voborníková (HPV Prague). Technical assistance was provided by R. Meinert, N. Kadlec, E. Schnabel and W. Staedter. We would like to thank S. Niedermann (GFZ Potsdam) and J. Sültenfuß (University Bremen) for supplementary $^3He/^4He$ measurements.

We thank our colleagues K. Klinge and T. Plenefisch (SZGRF Erlangen), R. Kind (GFZ Potsdam), and M. Brunner (University of Jena) for making temporary seismic measurements in the Vogtland/NW Bohemia area possible and for discussion. Data and stations were provided by E. Schmedes (University of Munich), F. Krüger and F. Scherbaum (University of Potsdam), B. Jacob (DIAS Dublin), A. Boušková, J. Horálek, J. Zedník (all IG CAS Prague) and V. Nehybka (IPE Brno). This research has been supported by the Studienstiftung des Deutschen Volkes, the GeoForschungsZentrum Potsdam (GFZ), the Geophysical Instrument Pool of GFZ, the GEOFON network of GFZ, the Bundesanstalt für Geowissenschaften und Rohstoffe (Seismologisches Zentralobservatorium Gräfenberg), the Deutsche Forschungsgemeinschaft and the European Community.

References

Aeschbach-Hertig W, Kipfer R, Hofer M, Imboden DM, Wieler R, Signier P (1996) Quantification of gas fluxes from the subcontinental mantle: The example of Laacher See, a maar lake in Germany. Geochim Cosmochim Acta 60:31-41

Aeschbach-Hertig W, Hofer M, Kipfer R, Imboden DM, Wieler R (1999) Accumulation of mantle gases in a permanently stratified volcanic lake (Lac Pavin, France). Geochim Cosmochim Acta 63:3357-3372

Ascencio E, Knapp JH, Owens TJ, Helffrich G (2003) Mapping fine-scale heterogeneities within the continental mantle lithosphere beneath Scotland: Combining active- and passive-source seismology. Geology 31(6):477-480

Babuška V, Plomerová J (2001) Subcrustal lithosphere around the Saxothuringian-Moldanubian Suture Zone – a model derived from anisotropy of seismic wave velocities. Tectonophysics 332:185-199

Babuška V, Plomerová J, BOHEMA working group (2003) Seismic Experiment Searches for Active Magmatic Source in Deep Lithosphere, Central Europe. EOS Transactions, 84(40):409, 416-417

Bankwitz P, Schneider G, Kämpf H, Bankwitz E (2003a) Structural characteristics of epicentral areas in Central Europe: Study case Cheb Basin (Czech Republic). J Geodyn 35:5-32

Bankwitz P, Bankwitz E, Bräuer K, Kämpf H, Störr M (2003b) Deformation structures in Plio- and Pleistocene sediments (NW Bohemia, Central Europe). In: van Rensbergen P, Hillis RR, Maltman AJ, Morley CK (eds) Subsurface Sediment Mobilization, Spec Publ Geol Soc London 206:73-93

Ballentine CJ, O'Nions RK, Coleman ML (1996) A Magnus opus: Helium, neon, and argon isotopes in a North Sea oilfield. Geochim Cosmochim Acta 60:831-849

Ballentine C.J. (1997) Resolving the mantle He/Ne and crustal $^{21}Ne/^{22}Ne$ in well gases. Earth Planet Sci Lett 152:233-249

Ballentine CJ, Schoell M, Coleman D, Cain BA (2001) 300-Myr-old magmatic CO_2 in natural gas reservoirs of the west Texas Permian basin. Nature 409:327-331

Bayerisches Geologisches Landesamt (1998) Geologie von Bayern. CD-ROM, Bayerisches Geologisches Landesamt, München

Behr HJ, Dürbaum HJ, Bankwitz P (eds) (1994) Crustal structure of the Saxothuringian Zone: Results of the deep seismic profile MVE-90 (East). Z geol Wiss 22(6):647-769

Bleibinhaus F, Stich D, Simon M, Gebrande H (2003) New results from amplitude preserving prestack depth migration of the Münchberg/Vogtland segment of the MVE deep seismic survey. J Geodyn 35:33-43

Bostock MG (1999) Seismic imaging of lithospheric discontinuities and continental evolution. Lithos 48:1-16

Bräuer K, Kämpf H, Strauch G, Weise SM (2003) Isotopic evidence ($^3He/^4He$, $^{13}C_{CO2}$) of fluid triggered intraplate seismicity. J Geophys Res 108: 2070; doi: 10.1029/2002JB002077

Bräuer K, Kämpf H, Niedermann S, Strauch G, Weise SM (2004) Evidence for A nitrogen flux directly derived from the European subcontinental mantle in the western Eger Rift, Central Europe. Geochim Cosmochim Acta 68:4935-4947

Bräuer K, Kämpf H, Niedermann S, Strauch G (2005a) Evidence for ascending upper mantle-derived melt beneath the Cheb basin, central Europe. Geophys Res Lett 32: L08303, doi:10.1029/2004GL022205

Bräuer K, Kämpf H, Niedermann S, Strauch G (2005b) Correction to "Evidence for ascending upper mantle-derived melt beneath the Cheb basin, central Europe". Geophys Res Lett 32: L18304, doi:10.1029/2005GL024344

Buzek C, Holy F, Kvacek Z (1996) Early Miocene flora of the Cypris shale (Western Bohemia). Acta Musei Nat Prague, B, Hist Naturalis 52:1-72

Cartigny P, Harris JW, Phillips D, Giraud M, Javoy M (1998) Subduction-related diamonds? – The evidence for a mantle-derived origin from coupled $\delta^{13}C$ – $\delta^{15}N$ determinations. Chem Geol 147:147-159

Dezes P, Schmid SM, Ziegler PA (2004) Evolution of the European Cenozoic Rift System: interaction of the Alpine and Pyrenean orogens with their foreland lithosphere. Tectonophysics 389:1-33

DEKORP Research Group (1988) Results of the DEKORP 4/KTB Oberpfalz deep seismic reflection investigations. J Geophys 62:69-101

Dunai TJ, Porcelli D (2002) Storage and Transport of Noble Gases in the Subcontinental Lithosphere. Rev Mineral Geochem 47:371-409

Elliot T., Ballentine C.J., O'Nions R.K., Ricchiuto T. (1993) carbon, helium neon and argon isotopes in a Po Basin (northern Italy) natural gas field. Chem Geol 106:429-440

Faber S, Plomerová J, Babuška V (1986) Deep-seated lateral variations beneath the GRF array inferred from mislocation patterns and P residuals. J Geophys 60:139-148

Faul UH, Toomey DR, Waff HS (1994) Intergranular basaltic melt is distributed in thin, elongated inclusions. Geoph Res Lett 21(1):29-32

Fischer T, Horálek J (2003) Space-time distribution of earthquake swarms in the principal focal zone of the NW-Bohemian/Vogtland seismoactive region: period 1985–2001. J Geodyn 35:125-144

Franz L, Seifert W, Kramer W (1997) Thermal evolution of the mantle underneath the Mid-German Crystalline Rise: Evidence from mantle xenoliths from the Rhön area (Central Germany). Mineralogy and Petrology 61:1-25

Geissler WH, Kämpf H, Bankwitz P, Bankwitz E (2004) Das quartäre Tephra-Tuff-Vorkommen von Mýtina (Südrand des westlichen Eger-Grabens/ Tschechische Republik): Indikationen für Ausbruchs- und Deformationsprozesse. Z Geol Wiss 32(1):31-54

Geissler WH, Kämpf H, Kind R, Bräuer, K., Klinge K, Plenefisch T, Horálek J, Zednik J, Nehybka V (2005) Seismic structure and location of a CO_2 source in the upper mantle of the western Eger Rift, Central Europe. Tectonics 24: TC5001, doi: 10.10292004TC001672

Giggenbach WF, Sano Y, Schmincke HU (1991) CO_2-rich gases from Lakes Nyos and Monoun, Cameroon; Laacher See, Germany; Dieng, Indonesia, and Mt. Gambier, Australia – variations on a common theme. J Volcan Geotherm Res 45: 311-323

Ginzburg A, Makris J, Fuchs K, Perathoner B, Prodehl C (1979) Detailed structure of the crust and upper mantle along the Jordan-Dead Sea Rift. J Geophys Res 84:5605-5612

Glahn A, Sachs PM, Achauer U (1992) A teleseismic and petrologic study of the crust and upper mantle beneath the geothermal anomaly Urach/SW-Germany. Phys Earth Planet Interior 69:176-206

Goes S, Spakman W, Bijwaard H (1999) A Lower Mantle Source for Central European Volcanism. Science 286:1928-1930

Granet M, Wilson M, Achauer U (1995) Imaging a mantle plume beneath the Massif Central (France). Earth Planet Sci Lett 136: 281-296

Griesshaber E, O´Nions RK, Oxburgh ER (1992) Helium and carbon isotope systematics in crustal fluids from the Eifel, the Rhine Graben and Black Forest, F.R.G. Chem Geol 99:213-235

Hainzl S, Ogata Y (2005) Detecting fluid signals in seismicity data through statistical earthquake modelling. J Geophys Res 110: B05S07, doi:1029/2004JB003247

Handbook of Chemistry and Physics (ed. D.R. Lide), 76th edn 1995-1996, CRC Press LLC, Boca Raton

Hales AL (1969) A seismic discontinuity in the lithosphere. Earth Planet Sci Lett 7:44-46

Hemmann A, Meier T, Jentzsch G, Ziegert A (2003) Similarity of waveforms and relative relocation of the earthquake swarm 1997/98 near Werdau. J Geodyn 35:191-208

Hill DP (1977) A model for earthquake swarms. J Geophys Res 82: 1347-1352

Hill DP, Prejean S (2005) Magmatic unrest beneath Mammoth Mountains, California. J Volcanol Geotherm Res 146:257-283

Horálek J, Fischer T, Boušková A, Jedlička P (2000) Western Bohemia/Vogtland region in the light of the WEBNET network. Studia geoph et geod 44(2):107-125

Keller GR, Mechie J, Braile LW, Mooney WD, Prodehl C (1994) Seismic structure of the uppermost mantle beneath the Kenya rift. In: Prodehl C., Keller GR, Khan MA (eds) Crustal and Upper Mantle Structure of the Kenya Rift. Tectonophysics 236:210-216

Kennett BLN, Engdahl ER (1991) Traveltimes for global earthquake location and phase identification. Geophys J Int 105:429-465

Keyser M, Ritter JRR, Jordan M (2002) 3D shear-wave velocity structure of the Eifel plume, Germany. Earth Planet Sci Lett 203:59-82

Kind R, Kosarev GL, Petersen NV (1995) Receiver functions at the Stations of the German Regional Seismic Network (GRSN). Geophys J Int 121:191-202

Kind R, Sobolev SV, Yuan X, Li X, Gossler J, Kosarev G, (2000) Analysis of major global tectonic structures using *P*-to-*S* converted seismic wave. In: Boschi E, Ekström G, Morelli A (eds) Problems in Geophysics for the New Millen-

nium. Istituto Nazionale di Geofisica e Vulcanologia, Editrice Compositori, Bologna, pp 141-150

Langston CA (1979) Structure Under Mount Rainier, Washington, Inferred From Teleseismic Body Waves. J Geophys Res 84(B9):4749-4762

Linnemann U, Gehmlich M, Tichomirova M, Buschmann B, Nasdala L, Jonas P, Lützner H, Bombach K (2000) From Cadomian subduction to Early Paleozoic rifting: the evolution of Saxo-Thuringia at the margin of Gondwana in the light of single zircon geochronology and basin development (central European Variscides, Germany). In: Franke W, Haak V, Oncken O, Tanner D (eds) Orogenic Processes: Quantification and Modelling in the Variscan Belt. Spec Publ Geol Soc London 179:131-153

Málek J, Broz M, Fischer T, Horálek J, Hrubcova P, Janský J, Novotny O, Ruzek B (2001) Seismic measurements along short profiles in western Bohemia during the Celebration 2000 experiment. Acta Montana IRSM AS CR, Series A 18(121):15-28

Marty B, Zimmermann L (1999) Volatiles (He, C, N, Ar) in mid-ocean ridge basalts: Assessment of shallow-level fractionation and characterization of source composition. Geochim Cosmochim Acta 63:3619-3633

Mattey DP (1991) Carbon-dioxide solubility and carbon isotope fractionation in basaltic melt. Geochim Cosmochim Acta 55:3467-3473

Matthews DH (1986) Seismic reflections from lower crust around Britain. In: Dawson J, Carswell D, Hall J, Wedepohl K (eds) The Nature of the Lower Continental Crust. Blackwell, Oxford, pp 11-21

Matthews A, Fouillac C, Hill R, O'Nions RK, Oxburgh ER (1987) Mantle-derived volatiles in the continental crust: the Massif Central of France. Earth Planet Sci Lett 85:117-128

Medaris LG, Wang HF, Fournelle JH, Zimmer JH, Jelinek E (1999) A cautionary tale of spinel peridotite thermobarometry: an example from xenoliths of Kozakov volcano, Czech Republic. Geolines 9:92-96.

Neunhöfer H, Meier T (2004) Seismicity in the Vogtland/Western Bohemia earthquake region between 1962 and 1998. Studia geoph et geod 48:539-562

O'Reilly SY, Griffin WL (1985) A xenolith-derived geotherm for southeastern Australia and its geophysical implications. Tectonophysics 111:41-63

Parotidis M, Rothert E, Shapiro SA (2003) Pore-pressure diffusion: A possible triggering mechanism for the earthquake swarms 2000 in Vogtland/NW-Bohemia, central Europe. Geoph Res Lett 30(20): 2075, doi:10.1029/2003GL018110

Passier ML, Snieder RK (1996) Correlation between shear wave upper mantle structure and tectonic surface expressions: Application to central and southern Germany. J Geophys Res 101:25,293-25,304

Plomerová J, Babuška V (1988) Lithospheric thickness in the contact zone of the Moldanubicum and Saxothuringicum in central Europe. Phys Earth Planet Int 51:159-165

Plomerová J, Babuška V, Sileny J, Horálek J (1998) Seismic Anisotropy and Velocity Variations in the Mantle beneath the Saxothuringicum-Moldanubicum Contact in Central Europe. Pure appl geophys 151:365-394

Polyak BG, Prasolov EM, Čermák V, Verkhovskiy AB (1985) Isotopic composition of noble gases in geothermal fluids of the Krušne Hory Mts., Czechoslovakia, and the nature of the local geothermal anomaly. Geochim Cosmochim Acta 49:695-699

Prodehl C, Müller S, Haak V (1995) The European Cenozoic rift system, In: Olsen KH (ed) Continental rifts: evolution, structure, tectonics. Developments in Geotectonics 25:133-212, Elsevier

Raikes S, Bonjer K-P (1983) In: Fuchs K, von Gehlen K, Mälzer H, Murawski H, Semmel A (eds) Plateau uplift, the Rhenish shield - a case history. Springer-Verlag, Berlin, pp 315-331

Ritter JRR, Jordan M, Christensen UR, Achauer U (2001) A mantle plume below the Eifel volcanic fields, Germany. Earth Planet Sci Lett 186:7-14

Rost S, Williams Q (2003) Seismic detection of sublithospheric plume head residue beneath the Pitcairn hot-spot chain. Earth Planet Sci Lett 209:71-83

Sherwood Lollar B, Ballentine CJ, O´Nions RK (1997) The fate of mantle derived carbon in a continental sedimentary basin: Integration of C/He relationships and stable isotope signatures. Geochim Cosmochim Acta 61:2295-2307

Sigmundsson F, Einarsson S, Rognvaldsson T, Foulger GR, Hodgkinson KM, Thorbergsson G (1997) The 1994-1995 seismicity and deformation at the Hengill triple junction, Iceland: Triggering of earthquakes by minor magma injection in a zone of horizontal shear stress. J Geophys Res 102:15,151-15,161

Snyder G, Poreda R, Hunt A, Fehn U (2001) Regional variations in volatile composition: Isotopic evidence for carbonate recycling in the Central American volcanic arc. Geochem Geophys Geosyst 2, 10, doi:10.1029/ 2001GC000163

Špičák A, Horálek J (2001) Possible role of fluids in the process of earthquake swarm generation in the West Bohemia/Vogtland seismoactive region. Tectonophysics 336:151-161

Thomas R (1992) Results of investigations on melt inclusions in various magmatic rocks from the northern border of the Bohemian Massif. In: Kukal Z (ed) Proceedings of the 1st International Conference on the Bohemian Massif, Prague, Czechoslovakia, Sept. 26-Oct. 3, 1988, Czech Geological Surv Prague, pp 298-306

Tomek Č, Dvořáková V, Vrána S (1997) Geological interpretation of the 9HR and 503M seismic profiles in Western Bohemia. In: Vrána S Štědrá V (eds) Geological model of Western Bohemia related to the KTB borehole in Germany. J Geol Sci, Geology 47. Praha, pp 43-50

Trappe H, Wever T (1990) Seismic evidence of increased tectonothermal activity near the Oberpfalz deep continental drilling location (SE Germany). Geologische Rundschau 79(3):649-658

Ulrych J, Pivec E (1997) Age-related Contrasting Alkaline Volcanic Series in North Bohemia. Chem Erde 57:311-336

Ulrych J, Lloyd FE, Balogh K (2003) Age Relations and Geochemical Constraints of Cenozoic Alkaline Volcanic Series in W Bohemia: A Review. Geolines 15:168-180

van Soest MC, Hilton DR, Kreulen R (1998) Tracing crustal and slab contributions to arc magmatism in the Lesser Antilles island arc using helium and carbon relationships in geothermal fields. Geochim Cosmochim Acta 62:3323-3335

Vanderhaege O, Teyssier C (1997) Formation of the Shuswap metamorphic complex during late-orogenic collapse of the Canadian Cordillera: Role of ductile thinning and partial melting of the mid- to lower crust. Geodynamica Acta 10:41-58

Vavryčuk V (2002) Non-double-couple earthquakes of 1997 January in West Bohemia, Czech Republic: Evidence for tensile faulting. Geophys J Int 149:364-373

Vinnik LP (1977) Detection of waves converted from *P* to *SV* in the mantle. Phys Earth Planet Inter 15:39-45

Wagner GA, Gögen K, Jonckheere R, Wagner I, Woda C (2002) Dating of Quaternary volcanoes Komorní Hůrka (Kammerbühl) and Železná Hůrka (Eisenbühl), Czech Republic, by TL, ESR, alpha-recoil and fission track chronometry. Z geol Wiss 30(3):191-200

Webb SA, Wood BJ (1986) Spinel-pyroxene-garnet relationships and their dependence on Cr/Al ratio. Contrib Mineral Petrol 92:471-480

Weinlich FH, Tesař J, Weise SM, Bräuer K, Kämpf H (1998) Gas flux distribution in mineral springs and tectonic structure in the western Eger Rift. J Czech Geol Soc 43:91-110

Weinlich FH, Bräuer K, Kämpf H, Strauch G, Tesař J, Weise SM (1999) An active subcontinental mantle volatile system in the western Eger Rift, Central Europe: Gas flux, isotopic (He, C, and N) and compositional fingerprints. Geochim Cosmochim Acta 63:3653-3671

Weinlich FH, Bräuer K, Kämpf H, Strauch G, Tesař J, Weise SM (2003) Gas Flux and Tectonic Structure in the Western Eger Rift, Karlovy Vary – Oberpfalz and Oberfranken, Bavaria. Geolines 15:181-187

Wever T, Meissner R (1987) About the nature of reflections from the lower continental crust. Ann Geophys 5B:349-352

Wilson M, Downes H (1991) Tertiary–Quaternary Extension-Related Alkaline Magmatism in Western and Central Europe. J Petrology 32:811-849

Wilson M, Downes H (1992) Mafic alkaline magmatism associated with the European Cenozoic rift system. Tectonophysics 208:173-182

Yuan X, Ni J, Kind R, Mechie J, Sandvol E (1997) Lithospheric and upper mantle structure of southern Tibet from a seismological passive source experiment. J Geophys Res 102(B12):27,491-27,500

Zandt G, Myers SC, Wallace TC (1995) Crust and mantle structure across the Basin and Range-Colorado Plateau boundary at 37°N latitude and implications for Cenozoic extensional mechanism. J Geophys Res 100(B6):10,529-10,548

Ziegler PA (1992) European Cenozoic rift system. Tectonophysics 208:91-111

Crustal and Upper Mantle Structure of the French Massif Central Plume

Andreas Barth[1], Michael Jordan[2] and Joachim R.R. Ritter[1]

[1]Geophysical Institute, University of Karlsruhe, Hertzstr. 16, 76187 Karlsruhe, Germany
[2]Department of Geology and Geophysics, University of Utah, 135 South 1460 East, Salt Lake City, Utah 84112, USA

Abstract

The Cenozoic volcanism in the French Massif Central region is fed by an upper mantle plume, which was revealed by teleseismic tomography about 10 years ago. This contribution reviews earlier studies and applies a new method to image the crust and upper mantle in the region. Since teleseismic tomography alone has only moderate ability to resolve crustal structures, we perform an integrated study by a joint teleseismic-gravimetric inversion to investigate the gross crustal imprints of the Massif Central. We use a 3-dimensional joint inversion code, which allows a variable model parameterisation, and 3D ray tracing to perform an iterative inversion. Travel time residuals are corrected for Moho topography and sedimentary influences to avoid mapping of known crustal structure into the mantle.

Our study finds a prominent low-velocity structure in the upper mantle, which is interpreted as the thermal signature of the Massif Central plume. With a modelled diameter of about 100-120 km it reaches down to at least 330 km depth. The average determined seismic *P*-wave velocity contrast is -0.6% to -1.0% in the shallow asthenospheric mantle and deeper upper mantle. We found two low-velocity channels in the crustal layer beneath the Cantal/Monte Dore and south of the Devès volcanic fields. A zone of mainly high density and increased seismic velocity is determined in the crust south of the Limagne Graben between the two volcanic fields. Furthermore the Massif Central is characterised by increased seismic scattering in the lithosphere as found by studying the teleseismic *P*-wave coda. We interpret the detected high-velocity/high-density body and the lithospheric scatterers as cooled magmatic intrusions, produced during the Cenozoic volcanism.

1 Introduction

Geophysical and geochemical research has been performed in the French Massif Central (Fig. 1) to study the structure and geodynamic implications of the underlying mantle plume. This contribution combines seismological and gravimetric observations for a joint inversion to image the crustal and upper mantle structures and to interpret their geodynamical implications.

The French Massif Central is part of the European Variscan mountain belt (Matte 1986). In the Paleocene (65-35 Ma) a first volcanic stage took place, followed by a phase of rifting as part of the European Cenozoic Rift

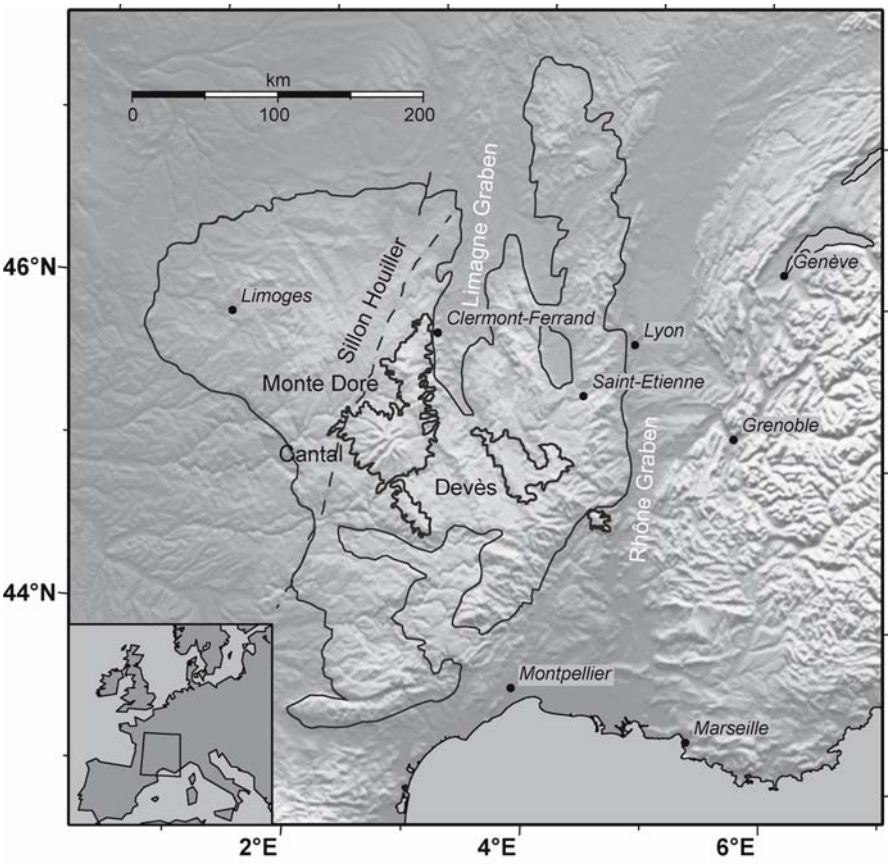

Fig. 1. The French Massif Central region. The thick outlines indicate Neogene volcanic areas, the thinner line represents the Variscan basement of the Massif Central

System during the Oligocene (26-24 Ma). In the Massif Central the main rift is the Limagne Graben in its northern part. A second volcanic stage began in the early Miocene (20 Ma) with latest activity about 6 ka BC (Brousse et al. 1969, Miallier et al. 2004).

To study the origin of the volcanism and the deep structure of the Massif Central a teleseismic tomography project was conducted in 1991/92 by running a temporary station network (Fig. 2) in the central Massif Central region (Granet et al. 1995a). The teleseismic *P*-wave tomography revealed a low-velocity zone in the upper mantle beneath the Massif Central down to at least 180 km depth, which was interpreted as a small mantle plume. Later studies estimated its depth to at least 250-270 km (Granet et al. 1995b, Piromallo and Morelli 2003), with a seismic *P*-wave velocity contrast of -2% to -2.5% at 100-270 km depth. In the lithosphere two vertical low-velocity channels were detected which coincide with the location of the volcanic complexes of Cantal/Mont Dore and Devès (Granet et al. 1995a). Taking into account the prominent Bouguer gravity low in Massif Central region, it was concluded that no or only a small amount of melt is needed to explain the negative seismic velocity anomaly in the mantle (Granet et al. 1995a).

Sobolev et al. (1997b) showed that the detected velocity perturbation could be explained nearly entirely by temperature. In their model the excess temperature of the plume is 150-200°C relative to the average potential temperature of the upper mantle. Their temperature model was used as an input for a dynamic convection model. The resulting topography and geoid agreed well with observations in the region of interest (Sobolev et al. 1997a). Ritter (2005) estimated the buoyancy flux of the plume using the above excess temperature, a plume radius of 60-75 km, non-linear viscosity and a Poiseulle flow law. This calculation resulted in a buoyancy flux of 0.09-0.7 Mg/s, what is about ten times more than the flux of the Eifel plume under the Rhenish Massif (Ritter 2005).

According to Werling and Altherr (1997) the petrologic analysis of equilibrated xenoliths gives a steady-state geotherme of about 90 mWm^{-2}. They found a thinned lithosphere of about 70-80 km thickness beneath the Massif Central. Dèzes et al. (2004) assume that thermal thinning of the lithosphere occured since the middle Miocene (14 Ma), when increased volcanic activity took place in the southern Massif Central. After Sobolev et al. (1997b) the main lithospheric thinning occurs beneath the volcanic fields in NW-SE direction, which was determined by Müller et al. (1997) as the orientation of maximum horizontal compressional stress. Using this stress-field deduced from earthquake focal mechanisms, geological indica-

tors, borehole breakouts, overcoring and hydraulic fracturing data, they argued that first-order stress orientations would be the same in the crust and the subcrustal lithosphere beneath the Massif Central.

Recent mantle xenolith studies found geochemical differences in samples from the northern Massif Central, dominated by the Limagne-Graben structure, and the southern part with the large Cantal volcanic area (Fig. 1): Lenoir et al. (2000) analysed trace elements of peridotites and found older and more refracted samples in the region north of 45.5°N than in the area south of it. Downes et al. (2003) combined these results with isotopic data

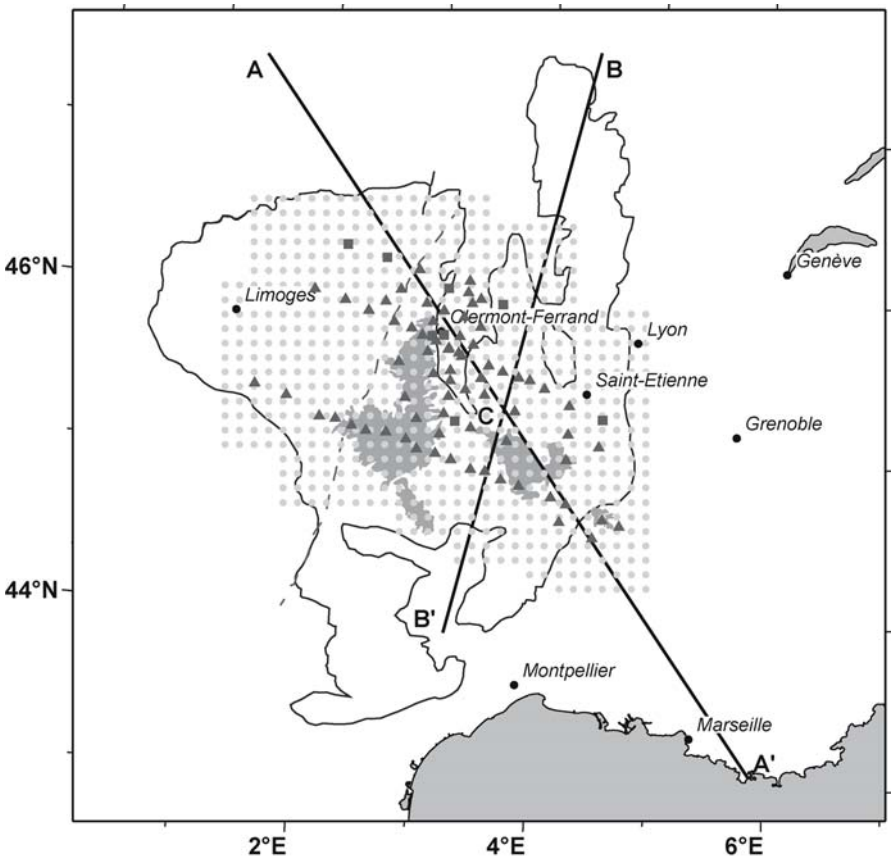

Fig. 2. Location map of seismic station distribution, showing the mobile Massif Central network (triangles, Granet et al. 1995a) and permanent stations (squares). The two lines indicate the positions of the cross-sections in *Fig. 11, 12*. The grey dots indicate the resampled linear grid of the Bouguer data. Grey-shaded regions indicate Neogene volcanic areas

and confirmed the differences between the two regimes. Lenoir et al (2000) assigned the consolidation of the two different lithospheric domains to the Variscan orogeny and suggested an asthenospheric channelling effect along the two lithospheric blocks. Thus upwelling asthenosphere in the South follows the lithospheric suture zone, which acts as a mechanical boundary.

Granet et al. (1998), however, identified two other regions by a seismic shear-wave splitting study. They distinguish the region east of the Sillon Houiller fault zone and the region west of it by different anisotropic patterns. In the East they determined the fast polarisation direction φ of the shear-waves to be roughly parallel ($\varphi \approx$ N100°E) to the lithospheric low-velocity zone found by Granet et al. (1995b) and related this polarisation direction to magmatic flow during periods of volcanic activity. In the West they detected φ parallel to the Sillon Houiller ($\varphi \approx$ N30°E). This division was explained by a stable lithospheric regime in the West and a heterogeneous, reworked lithosphere beneath the Neogene volcanic areas in the East.

To study the lithosphere-asthenosphere system of the Massif Central we derive a detailed tomographic model. We use a new imaging technique with the same teleseismic recordings used by Granet et al. (1995a,b) and additional crustal travel time corrections (Barth 2002) as well as gravity data. We review analyses of coda phases, which estimate the distribution of small-scale structures in the lithosphere that cannot be resolved by teleseismic tomography. The integrated structural model is then interpreted together with recent geophysical and geochemical models.

2 Joint inversion of travel time residuals and gravity data

Based on the teleseismic waveforms recorded by the mobile stations of the Massif Central project 1991/92 (Granet et al. 1995a) and additional permanent stations plus a Bouguer gravity dataset (Fig. 2), a new inversion model is obtained using the JI-3D method (Jordan 2003). Compared to previously published models our joint inversion uses gravity and travel time data, a variable model parameterisation, individual a priori station corrections for crustal structure, 3D ray tracing, an iterative quasi non-linear approach and 3D resolution tests. This approach gains a deeper and better resolved model than previously available.

2.1 Inversion routine and starting model

JI-3D (Joint Inversion in 3 Dimensions) is an inversion method that simultaneously determines 3D density and seismic velocity perturbations from Bouguer gravity and seismic travel time delays. The model parameterisation consisting of blocks and nodes is adapted to the observed seismic ray distribution. The blocks explicitly define the volume that contributes to the determination of an individual model parameter (Fig. 3). Since the ray density is often highest below the centre of the station network and back azimuths are best distributed there, model blocks there have a smaller size

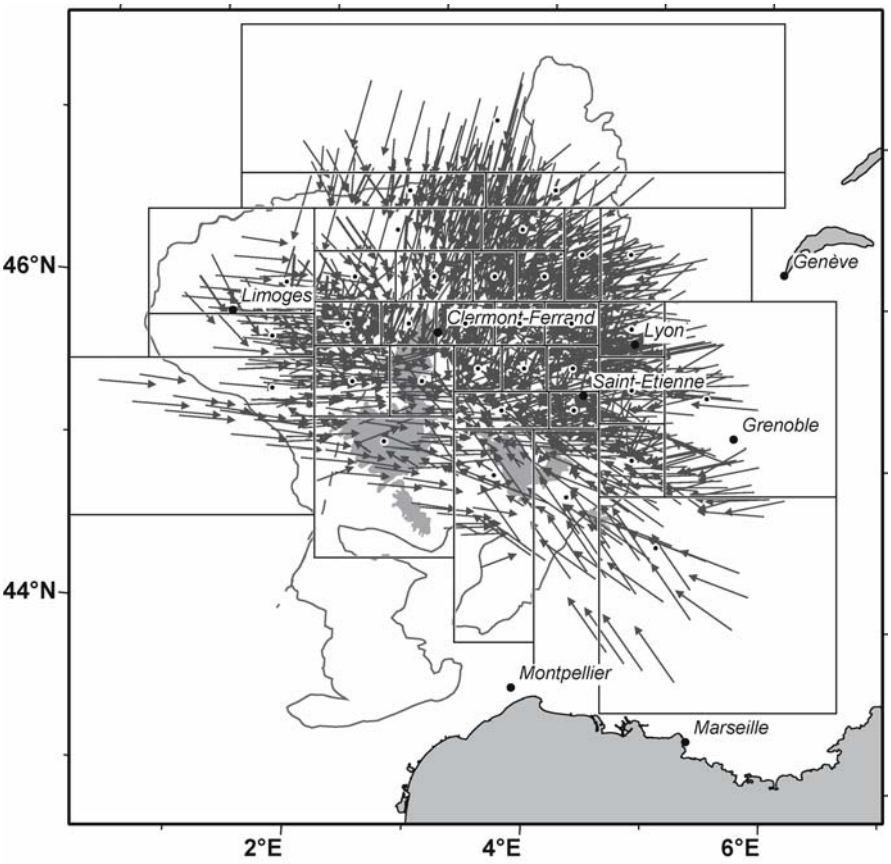

Fig. 3. Parameterisation and ray distribution of model layer five (178 km to 252 km depth). Arrows are projections of incoming teleseismic rays within the layer. Dots indicate the nodes of the surrounding blocks and correspond to the spatial centre of data information density

than model blocks at the edges. The parameterisation is designed so that all model parameters are equally well resolved, which leads to stable and more unique results without oscillations and only minimum vertical smearing. The actual velocity parameter is assigned to a node at the centre of information of each model block, where ray density is highest. This allows exact control over the resolution properties and avoids artificial velocity jumps at the block boundaries. 3D ray tracing is performed iteratively through the updated velocity model and is based on Steck and Prothero (1991). Using the Bayes algorithm after Zeyen and Achauer (1997), JI-3D minimises iteratively the following four quantities and conditions (see Eq. 1):

1. the difference $\Delta\vec{d}$ between the observed data vector and the synthetic data vector predicted by the current inversion model (including travel time residuals and Bouguer anomalies),
2. the difference between the velocity model parameters $\Delta\vec{v}$ and those predicted by the density model parameters $\Delta\rho$ and the correlation between variations of velocity and density parameters in matrix $\boldsymbol{B}$,
3. the difference $\Delta\vec{p}$ between the parameters of the initial model and the current model (including velocity and density perturbations),
4. the difference $\Delta\vec{p}_{dens}$ between modelled densities in adjacent density blocks weighted with distance $\Delta\boldsymbol{R}$.

While points 1 and 2 represent the physical imaging process, 3 and 4 are used to obtain further numerical stability. Thus the summed object function to be minimised is:

$$\begin{aligned}\left[\Delta\vec{d}^{\,T}\boldsymbol{C}_{\boldsymbol{d}}^{-1}\Delta\vec{d}\right] + \left[\left(\Delta\vec{v}-\boldsymbol{B}\Delta\rho\right)^{T}\boldsymbol{C}_{\boldsymbol{B}}^{-1}\left(\Delta\vec{v}-\boldsymbol{B}\Delta\rho\right)\right] + \\ \left[\Delta\vec{p}^{\,T}\boldsymbol{C}_{\boldsymbol{p}}^{-1}\Delta\vec{p}\right] + \left[\left(\Delta\vec{p}_{dens}/\Delta\boldsymbol{R}\right)^{T}\boldsymbol{C}_{\boldsymbol{S}}^{-1}\left(\Delta\vec{p}_{dens}/\Delta\boldsymbol{R}\right)\right] \rightarrow min.\end{aligned} \tag{1}$$

The inversion process depends highly on the a priori variances that are contained in the following covariance matrices (Jordan 2003): The data covariance matrix $\boldsymbol{C_d}$, the coupling covariance matrix $\boldsymbol{C_B}$, the model covariance matrix $\boldsymbol{C_p}$ and the smoothing covariance matrix $\boldsymbol{C_S}$.

$\boldsymbol{C_d}$ contains weighted errors for the travel time residuals and gravity data as a priori variances. The different influence of seismic and gravimetric data is considered by an additional constant factor. The a priori variances in matrices $\boldsymbol{C_p}$, $\boldsymbol{C_B}$ and $\boldsymbol{C_S}$ are determined through a trade-off process to achieve high variance reductions at moderate model lengths.

Due to the unfavourable ray distribution at crustal depths teleseismic inversion tends to map upper mantle heterogeneities into the little constrained crust. Therefore, we choose to include short-wavelength gravity data to improve the near surface resolution of our study. To integrate both data sets we employ an empirical law for the density-velocity relation that was formulated by Birch (1961):

$$B = dv/d\rho = 3 \cdot 10^{-3} \, \frac{km}{s} \Big/ \frac{kg}{m^3} . \tag{2}$$

A similar relation was also found by Christensen and Mooney (1995). The variance of the coupling B between velocity and density parameters is chosen so that the velocity and density model are effectively coupled without forcing identical anomalies.

Our inversion model consists of seven layers (Table 1). The uppermost layer includes topography and a priori known crustal station effects. The deepest layer has to be considered as possibly contaminated with structure projected from below the model. Therefore we only interpret layers two to six at a maximum depth of 330 km, where vertical smearing effects from adjacent layers are negligible.

Table 1 Structure of the model used for the inversion

Layer [number]	Depth [km]	Background velocity [km/s]	Inversion mode
1	-2-0	5.80	none, fixed
2	0-35	6.50	teleseismic-gravimetric
3	35-106	8.04	teleseismic
4	106-178	8.11	teleseismic
5	178-252	8.32	teleseismic
6	252-329	8.60	teleseismic
7	329-410	9.03	teleseismic

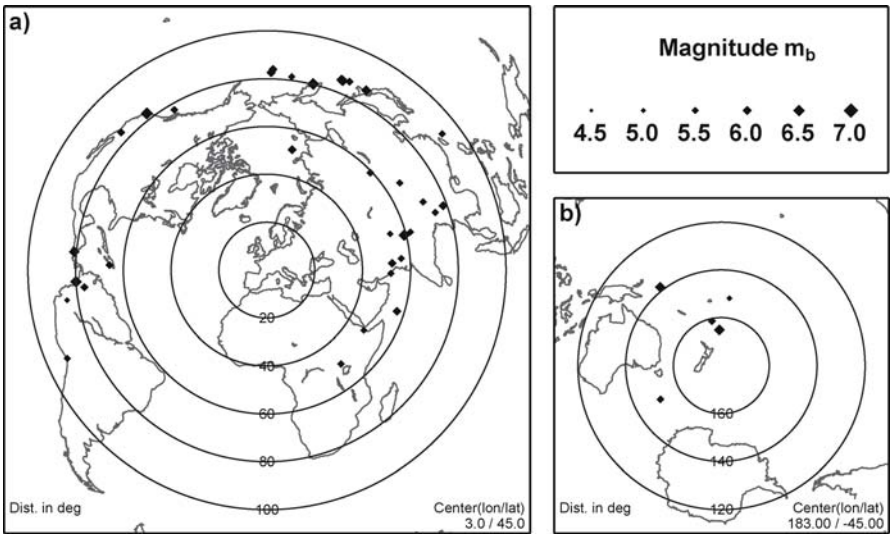

Fig. 4. Event distribution used for the teleseismic tomography. Circles indicate distance in degrees from the centre of the network. **a)** shows 38 epicentres which provided *P*-phases as first arrivals, **b)** 6 events with *PKP*-phases. Hypocentre locations were taken from Engdahl et al. (1998)

2.2 Data selection

Both datasets, gravity and travel times, are significantly affected by crustal anomalies. Mainly sediments and the Moho topography have a distinct influence on the data (Waldhauser et al. 1998), but are known in the region from numerous previous studies (references in Barth 2002). We use a priori constraints of the crustal structure to avoid artefacts in the otherwise underconstraint crustal layer. To have two consistent datasets for the joint inversion, the data are additionally reduced to sea level: The gravity data are reduced to Bouguer anomalies (excluding topographic effects); the teleseismic travel times are corrected for the travel time of the rays from sea level to actual station elevation. As background velocity model we use iasp91 (Kennett and Engdahl 1991).

Travel times

We determined 1457 arrival times from 44 earthquakes recorded during the teleseismic field experiment from October 1991 until April 1992 (Granet et al. 1995a) to have a consistent dataset and quantitative error estimates as a priori data variances for the Bayes inversion. The event distri-

bution is shown in Fig. 4. The azimuthal coverage is good apart from a gap at SSW-backazimuthal direction.

We correct the picked arrival times for known crustal deviations relative to the iasp91 model. These deviations include variations in sediment thickness, station elevation and Moho topography, and are used to determine individual 1D velocity models for each station site. We then correct the respective crustal residuals according to their theoretical angle of ray incidence (Barth 2002, Martin et al. 2005). In general we find negative correction terms in the whole region due to the elevated Moho (~30 km depth, Zeyen et al. 1997) relative to the iasp91 Moho (35 km depth). The positive correction terms mainly occur in the Rhône- (Southeast) and the Limagne-Graben (North) due to the low-seismic velocity of the sediments. Most correction terms vary between -0.1 s and +0.1, large enough to be important for a seismic inversion (Fig. 5).

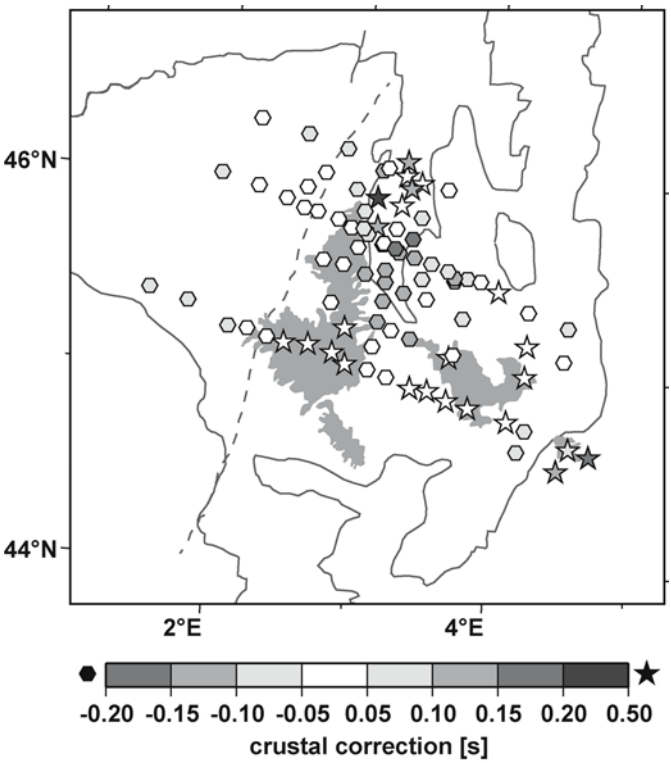

Fig. 5. Crustal corrections for travel times for each seismic station. Stars indicate positive values (later arrival time than iasp91), hexagons indicate negative values (earlier arrival time)

Following Evans and Achauer (1993) we normalised the corrected residuals by subtracting the average residual of each event separately. The resulting relative residuals (in the following just called residuals) are free of first order effects from outside the model (source uncertainties and source-side heterogeneities). The average residuals for each station (Fig. 6) are negative in the North of the station network. In the South and South-

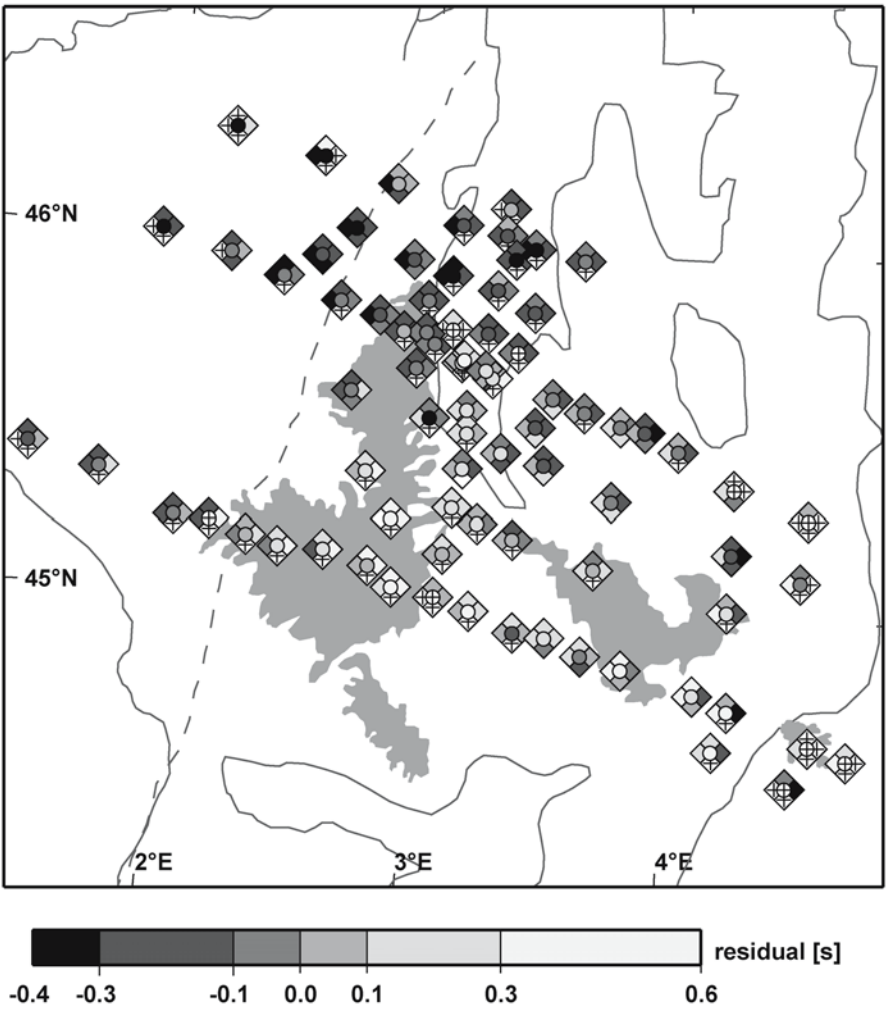

Fig. 6. 5-segment plot of relative residuals for each seismic station. The four outer segments represent the average relative residual for rays with an incidence from N, S, E and W. Accordingly, the central segment represent the relative residuals of vertically incident core phases. A cross marks segments containing no data

east the average residuals are positive indicating a broad low-velocity anomaly at depth. The maximum residuals are found in the southern part of the Limagne Graben and further south. The maximum contrast between the main anomaly and the residuals in the surrounding region is about 0.4 s for near-vertical ray incidence. Stations in the East show positive residuals for rays incident from the West, which limits the eastern extension of the plume. Similarly, stations in the West have positive delays for rays from the East (Fig. 6).

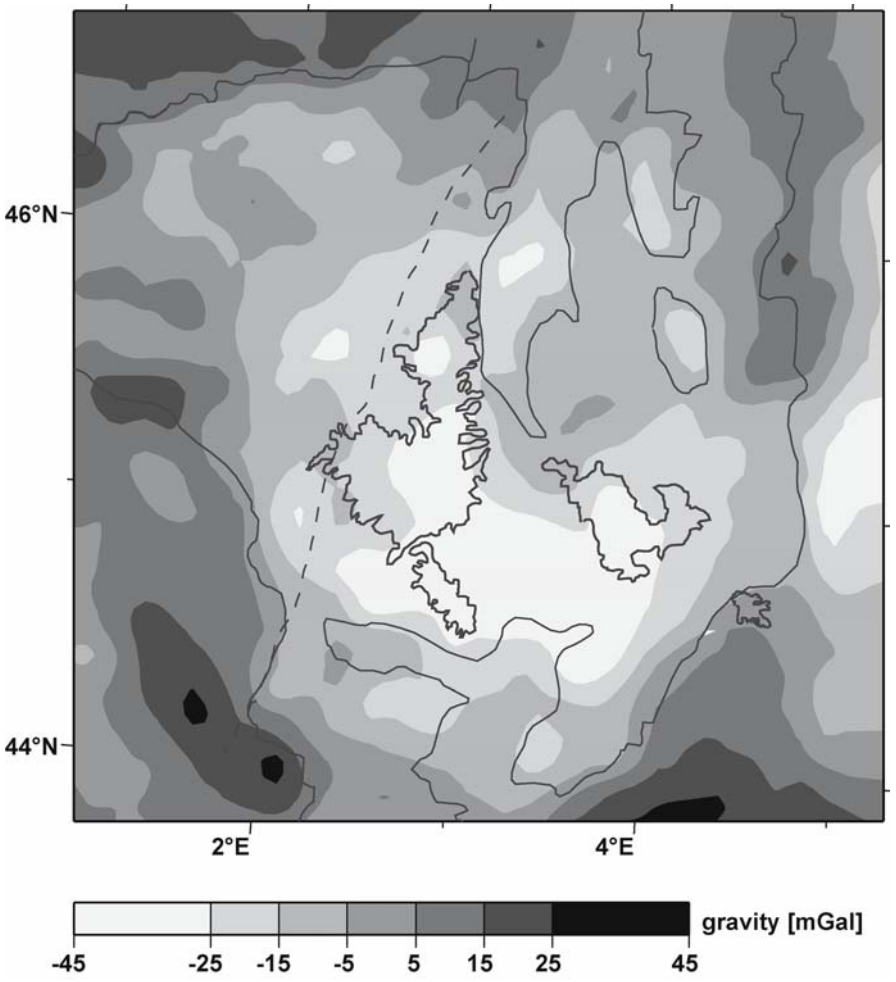

Fig. 7. Interpolated basic input Bouguer gravity data

Gravity

Figure 7 shows the basic dataset of Bouguer anomalies interpolated by splining from a regular 5'×5' (≈ 10 km×10 km) grid. The data was provided by the Bureau de Recherches Géologique et Minière (BRGM, Orléans). The influence of the Alpine orogenic root in the East (negative anomaly starting at 5°E and 45°N in Fig. 7) and the continental margin in the Southeast (positive anomaly starting at 4°E and 44°N in Fig. 7) occur at the edges of the area of interest and are excluded from the final dataset

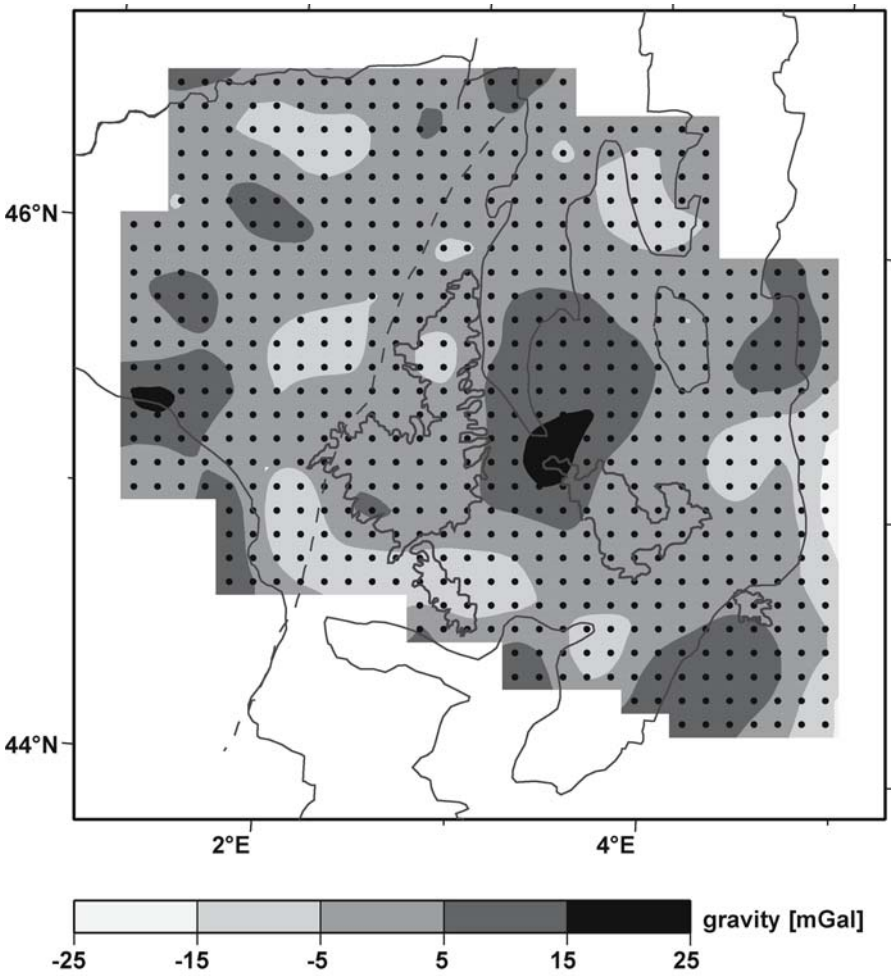

Fig. 8. Gridded gravity data used for the joint inversion. Grid spacing is 10 km

(Fig. 8). The dominant signal, in Fig. 7 is a negative Bouguer gravity anomaly in the centre of the study region. It results from the mantle plume below the Massif Central, which is a zone of increased temperature causing reduced density (Sobolev et al. 1997b). This basic dataset is corrected for the crustal influences described above and for the gravity signal of the Alpine orogenic root and the continental margin (Bauer 1995). Since teleseismic resolution is high in the mantle, we include additional gravity constraints only in the crust, where ray incidence is mostly vertical and thus resolution is low. So we perform the joint teleseismic-gravimetric inversion only in the crustal layer, and reduce the corrected Bouguer signal to effects that primarily result from the crustal layer by spatial filtering (Fig. 8).

Density anomalies at a certain depth cause Bouguer anomalies with a minimum horizontal extent of three to four times the depth (in case of a cylindrical body, see Ritter et al., this volume). Accordingly low-pass wavelength filtering is used to remove gravity anomalies from large mantle heterogeneities. To keep the crustal anomalies in our data, we set the wavelength for the maximum gravity signal to l40 km (four times the crustal layer depth of 35 km, see Table 1). Very small-scale density anomalies cannot be resolved, because the model parameterisation in the crustal layer is too coarse. So a high-pass wavelength filter with a minimum wavelength of 60 km is used in addition. The remaining crustal gravity signal (resampled to a 10 km×10 km grid, Fig. 8) is free of the major negative anomaly of the original input dataset (Fig. 7), which thus is assigned to greater depth. Beside several second-order effects, the resulting dataset shows a positive Bouguer anomaly of about 20 mGal in the central part of the area. As we will discuss in Sect. 4 this anomaly can be assigned to a high-density body, which possibly results from cooled magma intrusions.

2.3 Modelling results

After five iterations the joint inversion converges to a 31.8% variance reduction for the velocity model and 14.3% for the density model. Further iterations do not improve the variance reduction. According to Jordan (2003), these low-variance reductions are due to the large model block sizes especially at the edges of the deep layers (Fig. 3). Since the inversion results in a homogeneous velocity for each block, heterogeneities inside a block cannot be modelled. Thus, on one hand large block sizes are necessary in deep layers to achieve a uniform resolution and consequently a uni-

formly constrained model and on the other hand they are the reason for low-variance reductions.

The modelling results after the final iteration are shown as horizontal (Fig. 9 and 10) and vertical cross-sections (A-C-A' and B-C-B' in Fig. 11, for location see Fig. 2) through the model. *P*-wave velocity perturbations are given in percent deviation from the starting model (Table 1). These sections show a continuous low-velocity anomaly (LVA) of about 100-120 km diameter. In the crustal layer the LVA (-0.5% to -0.7% velocity contrast with respect to the surrounding) is split in two parts and coincides spatially with the Cantal/Monte Dore and Devès volcanic complexes (Fig. 10a). In the mantle layers the LVA broadens with a partly increased velocity contrast of up to -0.8% (Fig. 10b-f). As previous authors we interpret the LVA as a mantle plume. In the northwestern part relatively increased velocities are found in our model. A high-density body (density amplitude +0.5%) is revealed in Fig. 9, resulting from the positive gravity

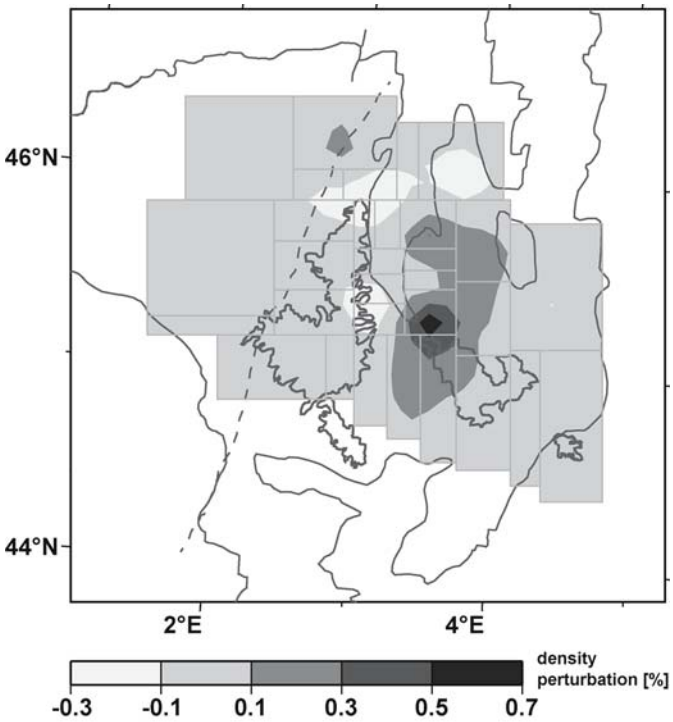

Fig. 9. Horizontal cross-section of the crustal density model at 0 km to 35 km depth (layer two of the inversion model). See *Fig. 10* for the velocity model

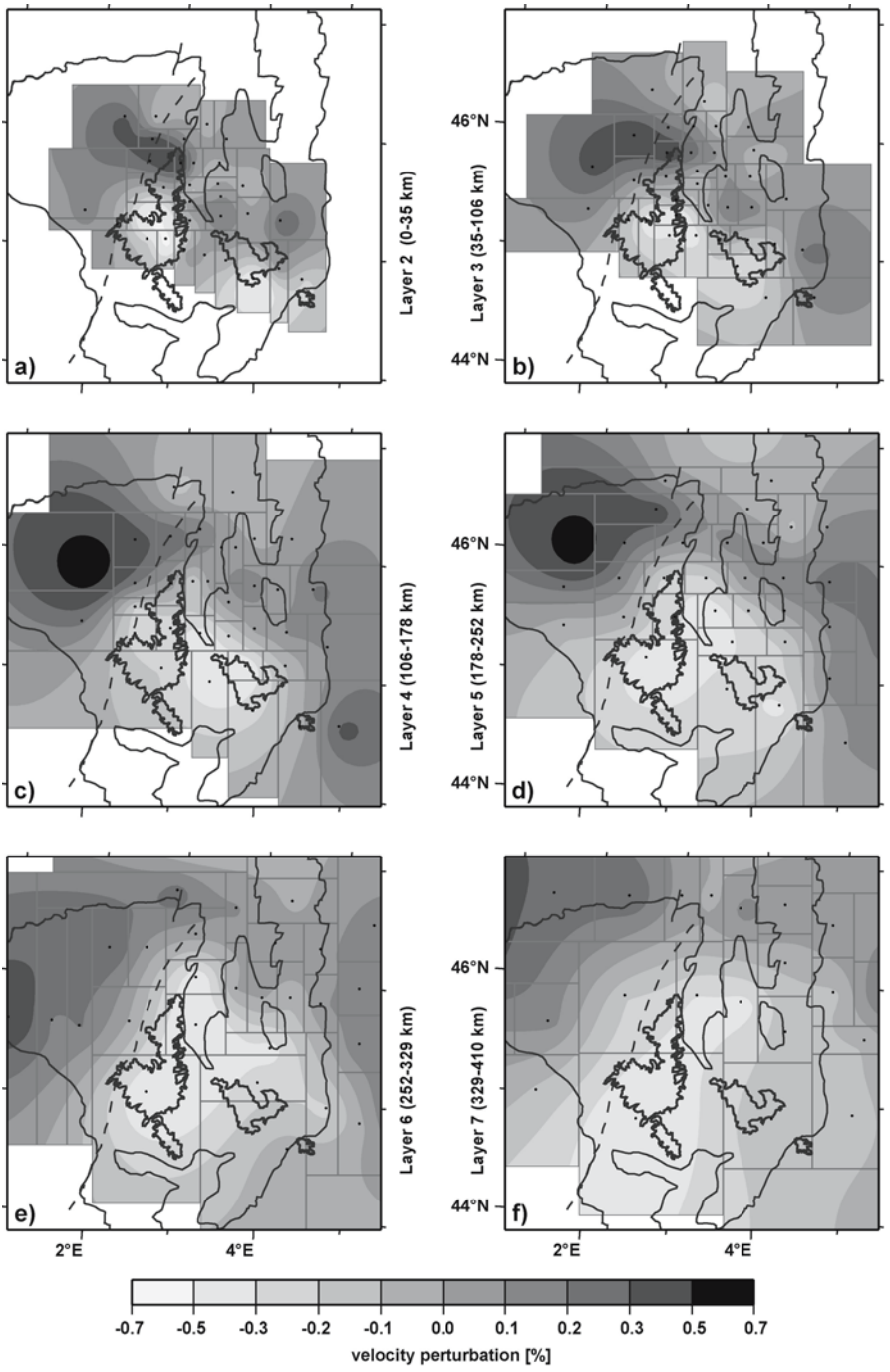
a)
Layer 2 (0-35 km)
b)
Layer 3 (35-106 km)
c)
Layer 4 (106-178 km)
d)
Layer 5 (178-252 km)
e)
Layer 6 (252-329 km)
f)
Layer 7 (329-410 km)
46°N
44°N
2°E
4°E
-0.7 -0.5 -0.3 -0.2 -0.1 0.0 0.1 0.2 0.3 0.5 0.7
velocity perturbation [%]

Fig. 10 (previous page & colour plate 5). Horizontal cross-section through the inversion model (layers 2-7). Shown are *P*-wave velocity perturbations with respect to the background model (compare Table 1). See *Fig. 9* for the crustal density model

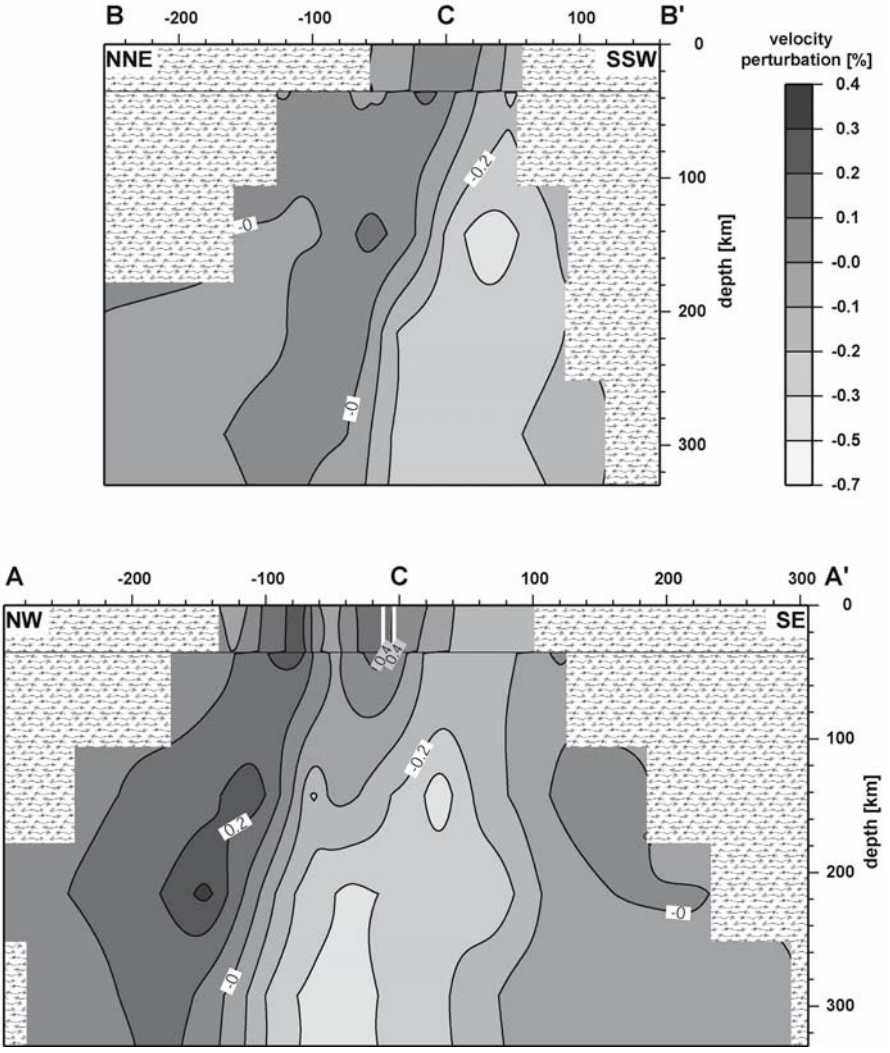

Fig. 11. Cross-section through the *P*-wave model after the final iteration, using the observed data. Section positions are indicated in *Fig. 2*. Distance is given in kilometres. Beside the velocity perturbation the position of the crustal density anomaly is displayed by two white contour lines (0.4% perturbation anomaly), just NW of the crossing point (*C*)

data input (Fig. 8). This high-density body coincides with a small high-velocity anomaly at the southern end of the Limagne Graben (Fig. 10a) that was already detected by Granet et al. (1995a, 1995b) and Gehrig (2004). The mantle LVA continues downwards into the deepest resolvable model layer (330 km depth, Fig. 10f and 11) and may even reach the 410 km discontinuity (top of the mantle transition zone), however a plume origin from the mantle transition zone cannot be fully resolved with our dataset.

2.4 Resolution

To test the reliability of velocity and density structures in the model resolution tests are performed. Additionally, the model resolution matrix $\boldsymbol{R}$ is analysed. Most main-diagonal elements of $\boldsymbol{R}$ are between 0.7 and 1 and the off-diagonal elements are quite small (generally well below 0.1), indicating a well-behaved inversion and not too much coupling (smearing) between the model parameters.

One reconstruction test (Fig. 12) shows the resolution of the vertical sections in Fig. 11. As input anomaly we choose a plume-like low-velocity anomaly (dashed lines in Fig. 12). To calculate a synthetic data set we use the same 3D ray geometry as for the real data and the same Bouguer gravity grid. The input model structure consists of a low-velocity zone reaching from beneath the Moho down to the base of the model at 410 km depth. The amplitude of the *P*-wave velocity contrast is -1.2% within a 60 km radius and it decreases linearly to 0% at a radius of 110 km. Accordingly a high-velocity zone combined with a high-density body is placed in the crustal layer. It has an inner radius of 20 km with a maximum velocity amplitude of +1.4% (density +1%) and an outer radius of 35 km.

After forward calculating synthetic travel time residuals and gravity data Gaussian noise (standard deviation: 0.1 s for the travel time residuals and 1 mGal for the Bouguer data) is added. These noise amplitudes are similar to the uncertainties in the observed data.

The result of the iterative joint inversion using the synthetic dataset (Fig. 12) resolves the shape of the synthetic plume-like input structure especially in the deeper layers very well. The influence of the crustal high-velocity/high-density structure however bends the plume in the upper mantle layer three (35 km to 106 km depth, see Table 1) to the South. A smearing of the plume structure into the crustal layer could not be avoided. The average recovered velocity contrast is about -0.9% (or 75% of the input anomaly). This demonstrates the problem of resolution of shallow structure and indicates an underestimation of recovered anomalies, what was

also found in other studies (see also Keyser et al. 2002). The resolved density contrast is about 0.4% and it is slightly shifted compared to its original location. The perturbation amplitudes of velocity and density are underestimated. This is consistent with synthetic tests that reveal that JI-3D tends to underestimate velocity contrasts (Jordan 2003, Keyser et al. 2002).

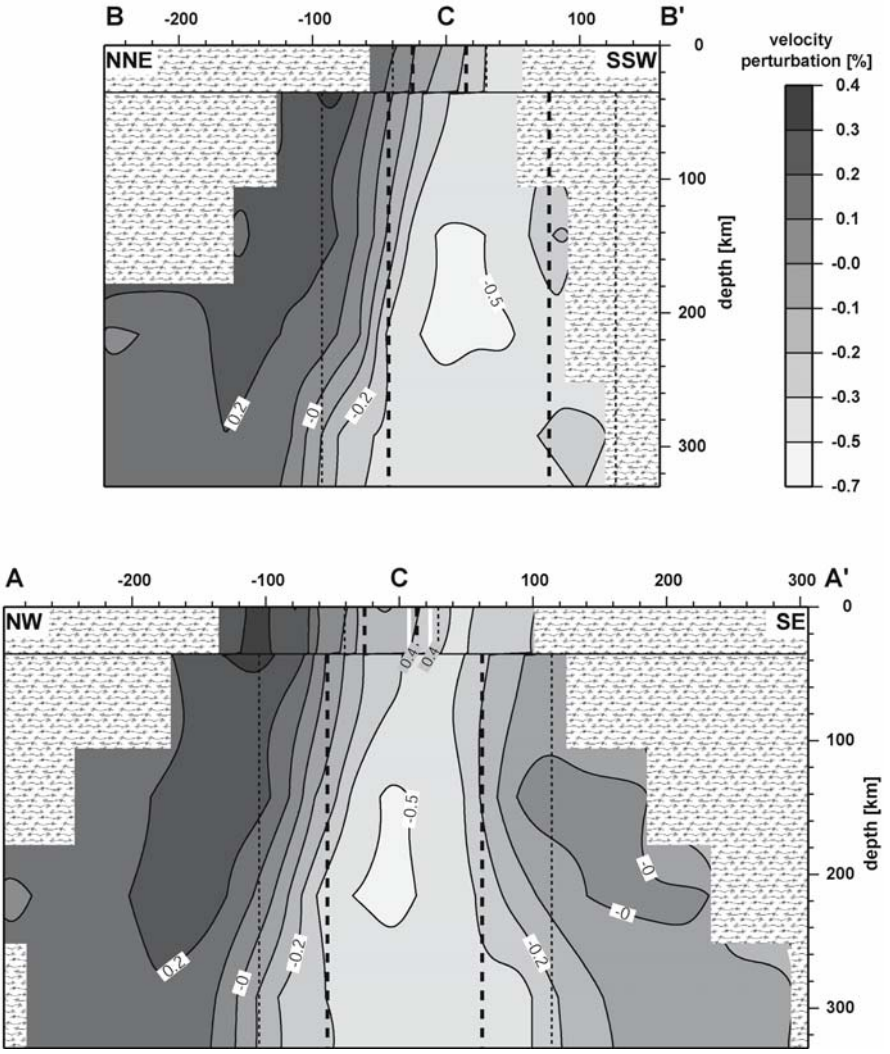

Fig. 12. According *Fig. 11*, but using synthetic data for a resolution test. The data is calculated using a cylindrical plume, with constant amplitude within the thick dashed lines, decreasing to 0% perturbation at the thin dashed lines. For details see text

3 Scattering at small-scale structures

The teleseismic tomography in the Massif Central can resolve only structures larger than about 20 km. However, small-scale heterogeneities (< 10 km) in the lithosphere were detected by analysing the *P*-wave coda of teleseismic recordings (Ritter et al. 1997, 1998, Ritter and Rothert 2000, Hock et al. 2004). These studies are reviewed in the following. As data waveforms of 13 intermediate-depth events were selected (Fig. 13), which occurred mostly at more than 100 km depth (a complete list is given in Ritter and Rothert 2000). The recording stations were the mobile stations from the Massif Central 1991/92 project and seven stations of the permanent Auvergne network of the University of Clermont-Ferrand (Fig. 2).

Ritter et al. (1997) report about high frequency (2-4 Hz dominant frequency) scattered phases in the teleseismic coda, which are most probably generated at heterogeneities in the lower crust. Pronounced lower crustal heterogeneity was also discovered by Novak (1993) while studying the coda phases along two seismic refractions lines across the Limagne Graben. Both studies inferred that lower crustal heterogeneities of about 0.2-2 km diameter (a) with velocity fluctuations (σ) of a few percent could explain the observed scattered seismic phases. The teleseismic waveforms

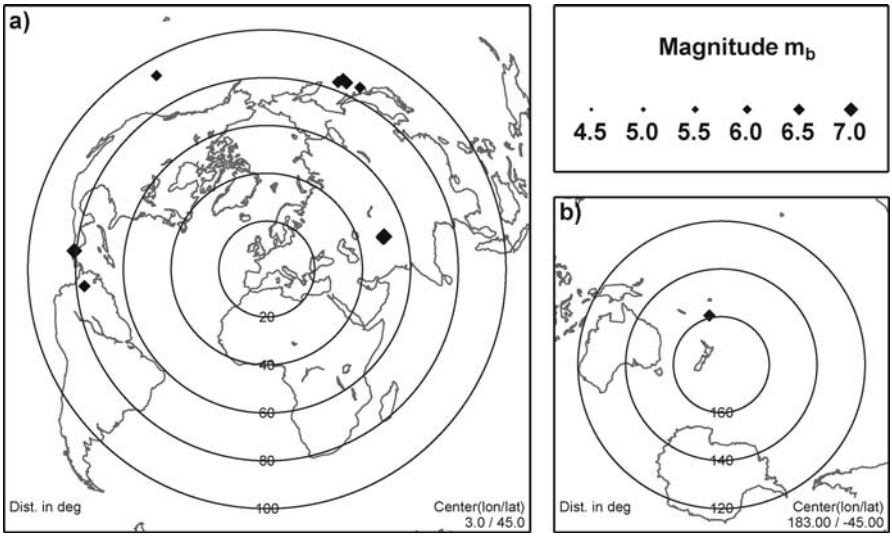

Fig. 13. Distribution of intermediate-depth earthquakes used for the scattering analysis of the *P*-wave coda. **a)** 12 epicentres with direct *P*-phases, **b)** one epicentre with first arrival *PKP*-phase

were later studied with more sophisticated methods: For the teleseismic fluctuation wavefield method (TFWM) the scattered arrivals at a seismic station are separated from the mean (coherent) wavefield (Ritter et al. 1998). A data example is shown in Fig. 14 with STACK as mean wavefield and with residual seismograms (RES) containing the separated scattered phases of four stations. The ratio of the mean wavefield and the scattering intensities can be used to statistically describe the heterogeneity of the medium through which the wavefield propagated (for details see Ritter et al. 1998). As the TFWM cannot resolve the thickness of the scattering layer, only two optional models are given: scattering in the crust and in the whole lithosphere.

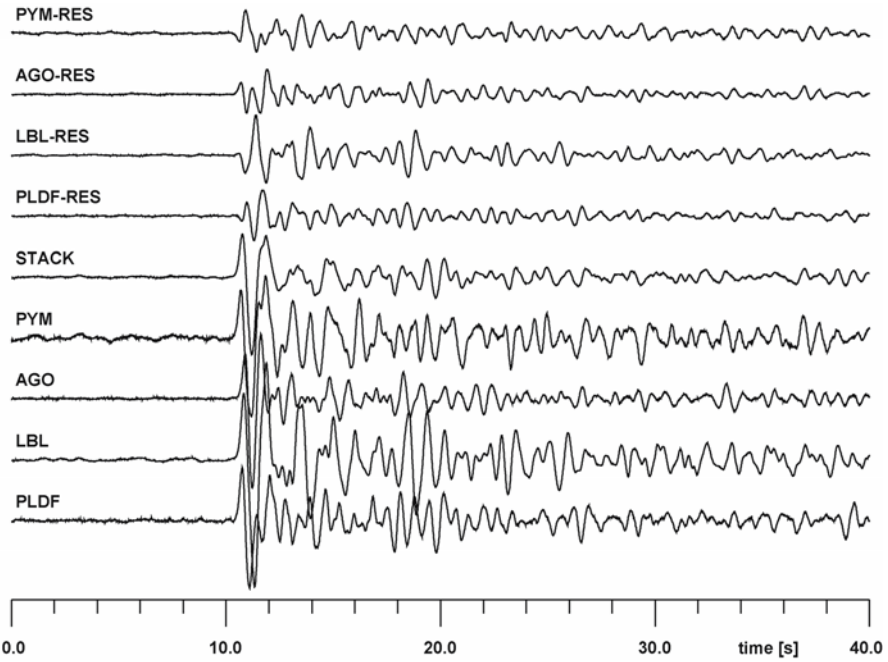

Fig. 14. Data example for the scattering analysis with the same amplitude scaling for all traces. The teleseismic waveforms were recorded by the permanent Auvergne network of the University of Clermont-Ferrand at the stations PLDF, LBL, AGO and PYM (lower four traces). The source is a 228 km deep Hindu Kush earthquake (*mb* 6.0) on 21st March 1998. These recordings are stacked with the measured slowness (7.9 s/°) and backazimuth (73.6°). Scattered signals are recovered by determination of residual seismograms at the individual stations (upper four traces)

Ritter and Rothert (2000) used the events from Fig. 13 and determined a random medium with Gaussian or exponential distribution of the scatterers underneath the Massif Central with the following properties: If scattering occurs preferably in the crust, then 1 km < a < 3 km with 4% < σ < 10%. Increased scattering in the lithospheric mantle would be compatible with a > 5 km and $\sigma \approx$ 1-3%. The simulation of the teleseismic coda envelopes with the energy flux method after Korn (1997) gained a model with a 20-30 km thick scattering layer, which implies strong scattering preferentially in the crust. These heterogeneities are characterised by 1.5 km < a < 5 km (strongly depending on the assumed correlation function, Gaussian or exponential) with 3.5% < σ < 4.5% (Hock et al. 2004).

Compared to 11 other regions in Europe (e.g. Baltic Shield, North Germany, Frankonian Jura) the TFWM revealed that the most intense scattering occurs in the Eifel and Massif Central regions (Hock et al. 2004) which can be explained by magmatic intrusions related to the mantle plume activity (Ritter and Rothert 2000). Solidified gabbroic intrusions, for instance, in a mafic granulite lower crust have a 3-5% velocity contrast relative to the host rocks. Thus cooled magma chambers and dykes with dense cumulates in the lower and upper crust are regarded as strong seismic heterogeneities below the volcanic fields of the Massif Central.

4 Discussion and Interpretation

The applied joint inversion of seismic travel times and Bouguer gravity produces a stable result that can resolve a structure such as an upper mantle plume. Vertical smearing of the velocity structure affects partly crustal regions, but the mantle is well-resolved. The inversion result of a synthetic seismic low-velocity mantle plume (Fig. 12) shows a similar shape as the plume structure revealed by the observed data (Fig. 11). However, the amplitudes of *P*-wave velocity perturbations are underestimated. Likewise the density anomaly in the crustal layer (Fig. 9) is likely to be stronger than the modelled +0.5% contrast.

The resolved upper mantle plume structure is estimated to have an average diameter of about 100-120 km. The velocity contrast relative to the surrounding upper mantle ranges between -0.5% and -0.8% and the depth from about 35 km down to least 330 km. The top of the upper mantle plume is not well resolved (within layer three, 35 km to 106 km depth, see Fig. 10b) and depends mainly on the parameterisation of the model grid. However, an asthenospheric upwelling to 60-80 km is assumed in the region (Werling and Altherr 1997). A forward calculation of near-vertical

teleseismic rays through the low-velocity structure in Fig. 10 results in a maximum contrast of travel time residuals between the main anomaly and the surrounding region of about 0.3 s for a near vertical incidence. Compared to the maximum observed travel time residuals (see Sect. 2.2), this value confirms the underestimation of the velocity contrast as found by the synthetic modelling. Hence we assume a *P*-wave velocity (v_p) reduction between 0.6% and 1.0% inside the plume that can better explain the observed contrast in relative residuals up to 0.4 s. This velocity contrast corresponds to a temperature (T) increase of 100-150°C using available v_p-T relations which take into account inharmonic and inelastic effects in upper mantle material (e.g. Goes et al. 2004, Ritter 2005). For this temperature range and a diameter of 100 km the buoyancy flux of the Massif Central plume can be estimated to 0.09-0.2 Mg/s (Ritter 2005).

The Massif Central plume clearly reaches the bottom of our model (Fig. 10f and 11). This leads to the hypothesis for an even deeper source possibly in the mantle transition zone as determined for the Eifel plume (Ritter, this volume).

The Massif Central plume is situated below the southern part of the Limagne Graben and further to the South underneath the volcanic fields of Cantal/Monte Dore and Devès. At 35-106 km depth (Fig. 10b) the northern transition between low- and high-velocity perturbations is roughly along a line at 45.5°N. This supports the hypothesis of an East-West striking lithospheric block boundary as suggested by Lenoir et al. (2000) based on geochemical analyses of mantle xenoliths. The western end (~2.5°E) of the LVA seems to be confined by a downward extension of the Sillon Houllier fault, which may act as another mechanical boundary for the asthenospheric upwelling. The change in fast directions of *SKS*-splitting observations also identifies the Sillon Houllier as a possible deep-reaching structural element (Granet et al. 1998).

The joint inversion of travel time and gravity data in the crustal layer results in a zone of increased velocity combined with a high-density body beneath the southern Limagne Graben. A crustal high-velocity zone was revealed in the region with crustal seismic tomography by Gehrig (2004). In the same region the scattering analysis (see Sect. 3) finds increased seismic scattering compared to other regions in Europe. We interpret these modelling results as cooled magmatic intrusions which remained in the crust while magma penetrated from the plume to the surface. These intrusions and the Cenozoic volcanic fields are thus the uppermost imprints of the Massif Central mantle plume.

Acknowledgements

We thank M. Mai and C. Weidle for their critical and constructive remarks and J. Mathar for testing appropriate bandpass filters for the gravity data. The seismic waveforms were provided by the Massif Central project 1991/92 (Granet et al. 1995a), Geoscope (Paris) and RéNaSS (Strasbourg). Gravity data was provided by the Bureau de Recherches Géologique et Minière (BRGM, Orléans). Seismic processing was done using SeismicHandler (Stammler 1993). The figures were made using GMT (Wessel and Smith 1998).

References

Barth A (2002) P-Wellen-Tomographie des oberen Mantels und der Übergangszone unter Eifel und Zentralmassiv. Diploma thesis, Institute of Geophysics, University of Göttingen (in German)

Bauer C (1995) 3D Schweremodellierung krustaler Strukturen im französischen Zentralmassiv unter Einbeziehung seismischer und geologischer Informationen. Diploma thesis, Geophysical lnstitute, University of Karlsruhe (in German)

Birch F (1961) The velocity of compressional waves in rocks to 10 kilobars. J Geophys Res 66:2199-2224

Brousse R, Delibrias G, Labeyrie J, Rudel A (1969) Eléments de chronologie des eruptions de la Chaîne des Puys. Bull Soc géol France 8:223-245

Christensen NI, Mooney WD (1995) Seismic velocity structure and composition of the continental crust; a global view. J Geophys Res 100:9761-9788

Dèzes P, Schmid SM, Ziegler PA (2004) Evolution of the European Cenozoic Rift System: interaction of the Alpine and Pyrenean orogens with their foreland lithosphere. Tectonophysics 389:1-33

Downes H, Reichow MK, Mason PRD, Beard AD, Thirlwall MF (2003) Mantle domains in the lithosphere beneath the French Massif Central: trace element and isotopic evidence from mantle clinopyroxenes. Chem Geol 200:71-87, doi: 10.1016/S0009-2541(03)00126-8

Engdahl ER, van der Hilst R, Buland R (1998) Global teleseismic earthquake relocation with improved travel times and procedures for depth determination. Bull Seism Soc Am 88:722-743

Evans JR, Achauer U (1993) Teleseismic velocity tomography using the ACH method: theory and application to continental-scale studies. In: Iyer HM, Hirahara K (eds) Seismic Tomography: Theory and Practice. Chapman and Hall, London, pp 319-360

Hock S, Korn M, Ritter JRR, Rothert E (2004) Mapping random lithospheric heterogeneities in northern and central Europe. Geophys J Int 157:251-264, doi: 10.1111/j.1365-246X.2004.02191.x

Gehrig M (2004) 3-D-Geschwindigkeitsstruktur der Oberkruste unter dem Limagne-Graben (Französisches Zentralmassiv). Diploma thesis, Geophysical Institute, University of Karlsruhe (in German)

Goes S, Cammarano F, Hansen U (2004) Synthetic seismic signal of thermal mantle plumes. Earth Planet Sci Lett 218:403-419

Granet M, Stoll G, Dorel J, Achauer U, Poupinet G, Fuchs K (1995a) Massif Central (France): new constraints on the geodynamical evolution from teleseismic tomography. Geophys J Int 121:33-48

Granet M, Wilson M, Achauer U (1995b) Imaging a mantle plume beneath the French Massif Central. Earth Planet Sci Lett 136:281-296

Granet M, Glahn A, Achauer U (1998) Anisotropic Measurements in the Rhinegraben Area and the French Massif Central: Geodynamic Implications. Pure appl geophys 151:333-364

Jordan M (2003) JI-3D - A new approach to high resolution regional seismic tomography: Theory and applications. PhD thesis, University of Göttingen

Kennett BLN, Engdahl ER (1991) Traveltimes for global earthquake location and phase identification. Geophys J Int 105:429-465

Keyser M, Ritter JRR, Jordan M (2002) 3D shear wave velocity structure of the Eifel plume, Germany. Earth Planet Sci Lett 203:59-82

Korn M (1993) Determination of site-dependent scattering Q from *P*-wave coda analysis with an energy-flux model. Geophys J Int 113:54-72

Korn M (1997) Modelling the teleseismic *P* coda envelope: depth dependent scattering and deterministic structure. Phys Earth Planet Inter 104:23-36

Lenoir X, Garrido CJ, Bodinier J-L, and Dautria J-M (2000) Contrasting lithospheric mantle domains beneath the Massif Central (France) revealed by geochemistry of peridotite xenoliths. Earth Planet Sci Lett 181:359-375

Novak O (1993) Integrierte geophysikalisch-petrologische Interpretation des obersten Mantels und der unteren Kruste im Bereich des südlichen Limagnegrabens (Frankreich). Diploma thesis, Geophysical Institute, University of Karlsruhe (in German)

Martin M, Ritter JRR and the CALIXTO working group (2005) High-resolution teleseismic body wave tomography beneath SE-Romania - I.: Implications for three-dimensional versus one-dimensional crustal correction strategies with a new crustal velocity model, Geophys J Int 162:448-460

Matte P (1986) Tectonics and plate tectonics model for the Variscan belt of Europe. Tectonophysics 126:329-374

Miallier D, Michon L, Évin J, Pilleyre T, Sanzelle S, and Vernet G (2004) Volcans de la chaîne des Puys (Massif central, France) : point sur la chronologie Vasset–Kilian–Pariou–Chopine. C R Geoscience 336:1345-1353

Müller B, Wehrle V, Zeyen H, Fuchs K (1997) Short-scale variations of tectonic regimes in the western European stress province north of the Alps and Pyrenees. Tectonophysics 275:199-219

Piromallo C, Morelli A (2003) *P* wave tomography of the mantle under the Alpine-Mediterranean area. J Geophys Res 108:2065, doi: 10.1029/2002JB001757

Ritter JRR (2005) Small-scale mantle plumes: Imaging and geodynamic aspects. In: Wenzel F (ed) Perspectives in Modern Seismology, Lecture Notes in Earth Sciences 105. Springer Verlag, Heidelberg, 69-94

Ritter JRR The seismic signature of the Eifel plume. This volume

Ritter JRR, Rothert E (2000) Variations of the lithospheric seismic scattering strength below the Massif Central, France and the Frankonian Jura, SE Germany. Tectonophysics 328:297-305

Ritter JRR, Mai PM, Stoll G, Fuchs K (1997) Scattering of teleseismic waves in the lower crust: observations in the Massif Central, France. Phys Earth Planet Int 104:127-146

Ritter JRR, Shapiro SA, Schechinger B (1998) Scattering parameters in the lithosphere below the Massif Central, France, from teleseismic *P*-wavefield records. Geophys J Int 134:187-198

Ritter JRR, Mathar JP, Jordan M, Gabriel G Gravity anomalies and the Eifel plume in the western Rhenish Massif. This volume

Sobolev SV, Babeyko AY, Christensen U, Granet M (1997a) Temperature and dynamics of the upper mantle beneath the French Massif Central. In: Fuchs K (ed) Upper mantle heterogeneities from active and passive seismology. Kluwer Academic Publishers, Dodrecht Boston London, pp 269-275

Sobolev SV, Zeyen H, Granet M, Achauer U, Bauer C, Werling F, Altherr R, Fuchs K (1997b) Upper mantle temperatures and lithosphere-asthenosphere system beneath the French Massif Central constrained by seismic, gravity, petrologic and thermal observations. Tectonophysics 275:143-164

Stammler K (1993) SeismicHandler: programmable multichannel data handler for interactive and automatic processing of seismological analyses. Comp Geosci 19:135-140

Steck L, Prothero W (1991) A 3-D raytracer for teleseismic body-wave arrival times. Bull Seism Soc Am 81:1332-1339

Waldhauser F, Kissling E, Ansorge J, Mueller St (1998) Three-dimensional interface modelling with two-dimensional seismic data: the Alpine crust-mantle boundary. Geophys J Int 135:264-278

Werling F, Altherr R (1997) Thermal evolution of the lithosphere beneath the French Massif Central as deduced from geothermobarometry on mantle xenoliths. Tectonophysics 275:99-141

Wessel P, Smith WHF (1998) New, improved version of Generic Mapping Tools released. EOS Trans AGU 79:579 pp

Zeyen H, Achauer U (1997) Joint inversion of teleseismic delay times and gravity anomaly data for regional structures. In: Fuchs K (ed) Upper mantle heterogeneities from active and passive seismology. Kluwer Academic Publishers, Dodrecht Boston London, pp 155-169

Zeyen H, Novak O, Landes M, Prodehl C, Driad L, Hirn A (1997) Refraction-seismic investigation of the northern Massif Central (France). In: Fuchs K, Altherr R, Müller B, Prodehl C (eds) Stress and stress release in the lithosphere. Tectonophysics, 275:99-117

Geodynamic Setting of the Tertiary Hocheifel Volcanism (Germany), Part I: $^{40}Ar/^{39}Ar$ geochronology

Zuzana Fekiacova[1,2], Dieter F. Mertz[1,3] and Paul R. Renne[3,4]

[1] Johannes Gutenberg-Universität, Institut für Geowissenschaften, Becher-Weg 21, 55099 Mainz, Germany
[2] Now at: Max Planck-Institut für Chemie, Abteilung Geochemie, Becher-Weg 27, 55128 Mainz, Germany
[3] Berkeley Geochronology Center, 2455 Ridge Road, Berkeley, California 94709, U.S.A.
[4] Department of Earth and Planetary Science, University of California, Berkeley, California 94720, U.S.A.

Abstract

The Eifel volcanism is part of the Cenozoic Central European Volcanic Province and is located close to the Rhine Graben which has been formed by rifting and subsidence since the Eocene. Whereas the Quaternary volcanism of the Eifel appears to be genetically related to mantle plume activity, the cause of the Tertiary volcanism of the Hocheifel volcanic field is less clear. Here, we present geochronological evidence for the geotectonic setting of the Tertiary Eifel volcanism based on $^{40}Ar/^{39}Ar$ dating of 27 samples from 25 volcanic occurrences. Included are samples from the northern Upper Rhine Graben in order to evaluate a possible relationship between Hocheifel volcanism and Rhine Graben taphrogenesis.

The geological relevance of the age data used for the geological discussion is indicated by plateau-type age spectra and tested by inverse isochron calculations. For the Hocheifel, two periods of activity at ca. 44 to 39 Ma and 37 to 35 Ma were inferred. Both age groups are represented by

basanites as well as by more differentiated rocks and there is no clear relation between age and chemical composition. The time span dated for the northernmost Upper Rhine Graben volcanism is 59 to 47 Ma indicating foiditic to basanitic activity up to ca. 15 m.y. prior to the onset of rifting and subsidence.

The Hocheifel volcanic activity is interpreted to represent the propagation of the pre-rift volcanism of the northern Upper Rhine Graben to the NW because the Hocheifel activity closely follows in time pre-rifting northern Upper Rhine Graben volcanism and the older period of Hocheifel activity shows propagation of younger volcanism to the north. In addition, the Hocheifel tectonic pattern derived from the time - space relation of volcanism corresponds to stress field conditions identical to those of the Upper Rhine Graben at the time of Hocheifel volcanic activity. Magma generation therefore appears to be related to decompression by extension during Middle to Upper Eocene. However, in contrast to the northern Upper Rhine Graben with graben formation subsequent to pre-rifting volcanism, no relevant rifting or subsidence occurred in the Hocheifel. The taphrogenetic evolution in between the Upper and Lower Rhine Graben regions was suspended in an early stage.

1 Introduction

The Hocheifel volcanic field is located in the Hercynian Rhenish Massif in Germany (Fig. 1) and consists of about 300 Tertiary eruptive centres (e.g. Huckenholz 1983). To the East and West of the Hocheifel, the Quaternary Eifel volcanic fields border. The Eifel volcanism represents the westernmost site of the Central European Volcanic Province (CEVP), a generally W-E striking volcanic belt of Cenozoic age extending from West Germany to Poland.

The geodynamic setting of the Tertiary Hocheifel volcanism is not clear. The Eifel together with neighbouring volcanic fields are located close to a Tertiary rift system (Fig. 1). Therefore, on one hand magma generation by decompressional melting related to lithospheric extension has been suggested (e.g. Wilson and Downes 1991; Ziegler 1992). On the other hand, there is seismological (e.g. Ritter et al. 2001) combined with isotopic evidence (e.g. Hoernle et al. 1995) that at least in part CEVP volcanism is related to mantle plume activity. The setting of the Eifel volcanism is so far unique within the CEVP as there is Tertiary and recent volcanic activity at more or less the same site. Thus, the evolution of volcanism can be evaluated using different time frames.

Aim of this contribution is to decipher the geodynamic setting of the Tertiary Hocheifel volcanism by geochronological, geochemical and isotope data. We present evidence from $^{40}Ar/^{39}Ar$ dating (Part I) as well as from major and trace element concentrations and Sr, Nd, Pb isotope ratios (Part II, Fekiacova et al., this volume).

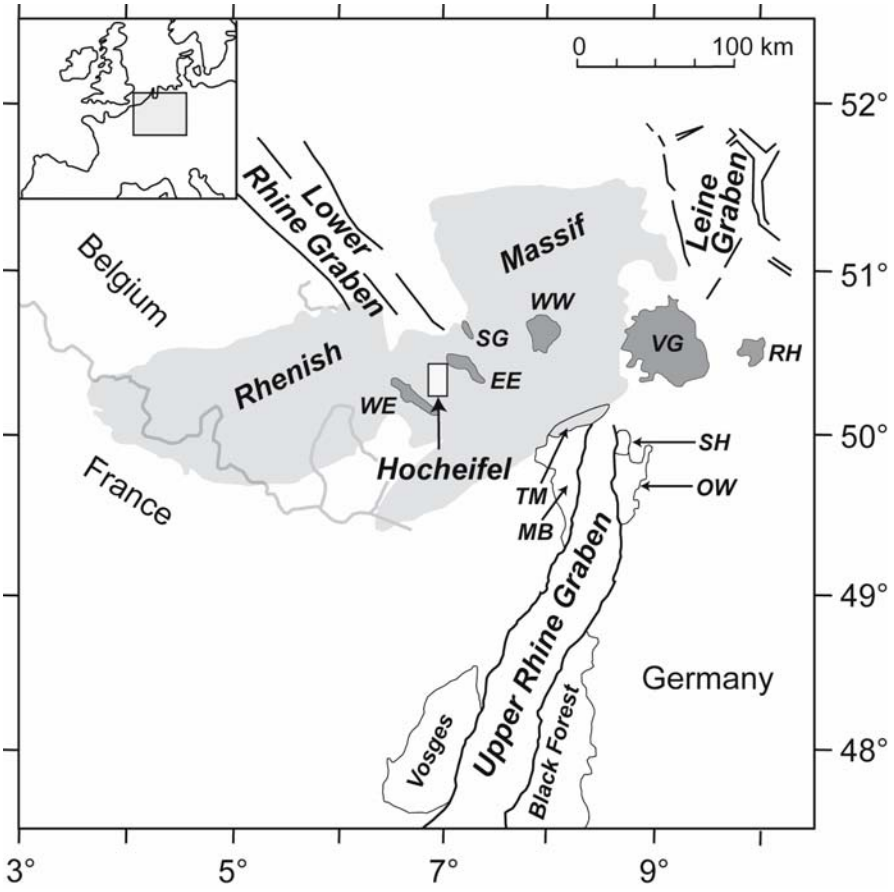

Fig. 1. Tectonic setting of Cenozoic volcanic fields (*WE*=West Eifel, *EE*=East Eifel, *WW*=Westerwald, *VG*=Vogelsberg, *RH*=Rhön, *SG*=Siebengebirge) and relation to the Tertiary Upper Rhine Graben - Lower Rhine Graben - Leine Graben rift system. Inset "Hocheifel" refers to the maps in Figs. 2 and 4. The northwestern and northeastern flanks of the northern Upper Rhine Graben are formed by the geological units of Mainz Basin (*MB*), Taunus Mountains (*TM*), Sprendlingen Horst (*SH*) and Odenwald (*OW*)

2 Geological setting and sampling

The Tertiary Hocheifel volcanic field together with the neighbouring volcanic fields of Siebengebirge, Westerwald, Vogelsberg and Rhön (Fig. 1) represent the western part of the Cenozoic CEVP. These volcanic fields developed close to an extensive Central and West European Cenozoic rift system which originated in the Alpine foreland and is interpreted as a result of tensional reactivation of originally Late Hercynian fractures (Ziegler 1992). The Hocheifel is situated northwest of a triple junction-type constellation comprising the Upper Rhine Graben, Lower Rhine Graben and Leine Graben (Fig. 1). In addition to the Hocheifel volcanic rocks, we collected samples from the northern Upper Rhine Graben flanks in order to evaluate a possible relationship between Hocheifel volcanism and Rhine Graben taphrogenesis during the Tertiary. Table 1 lists the grid coordinates of the Hocheifel and Rheingraben sampling locations.

The Hocheifel volcanism spreads over ~1000 km^2 in between the Quaternary West and East Eifel volcanic fields and produced mostly more primitive alkali basaltic rocks and to a minor extend differentiated lavas. A systematic compositional zoning within the Tertiary Hocheifel field has been suggested with the most differentiated lavas erupting in the centre and the less differentiated lavas mostly occurring in the outer region (Huckenholz 1983). The Hocheifel lavas mostly intruded weakly metamorphosed Devonian and Carboniferous sediments of the Hercynian Rhenish Massif. Major tectonic elements of parts of the Hocheifel area were mapped by, e.g., Fuchs (1974). Figure 2 shows that NE striking host rock syncline and anticline structures are cut by N striking cross faults. These faults are interpreted as being of late Hercynian age with later reactivation since locally Tertiary intrusions are regarded to have used the faults as pathways (e.g. Fuchs 1974). The basaltic to trachytic samples taken for our Hocheifel study cover the entire range of chemical compositions known from this region. Also, various geographic areas were sampled with emphasis on the centre of the Hocheifel field with major volcanic activity around the village of Kelberg. This sampling pattern is shown in Fig. 2. Information on the geology of several of these occurrences as well as on their petrography and geochemistry are given in Huckenholz and Büchel (1988) together with further references.

Foiditic to basanitic rocks were taken from three geological units forming the northernmost Upper Rhine Graben flanks (Fig. 1): Taunus Mountains (weakly metamorphic rocks of the Hercynian Rhenish Massif), Sprendlingen Horst (Palaeozoic metamorphic and magmatic basement with Rotliegend sediment cover) and Mainz Basin (Tertiary sediments).

Negendank (1969) describes occurrences and petrography of Tertiary volcanic rocks of the northern Upper Rhine Graben.

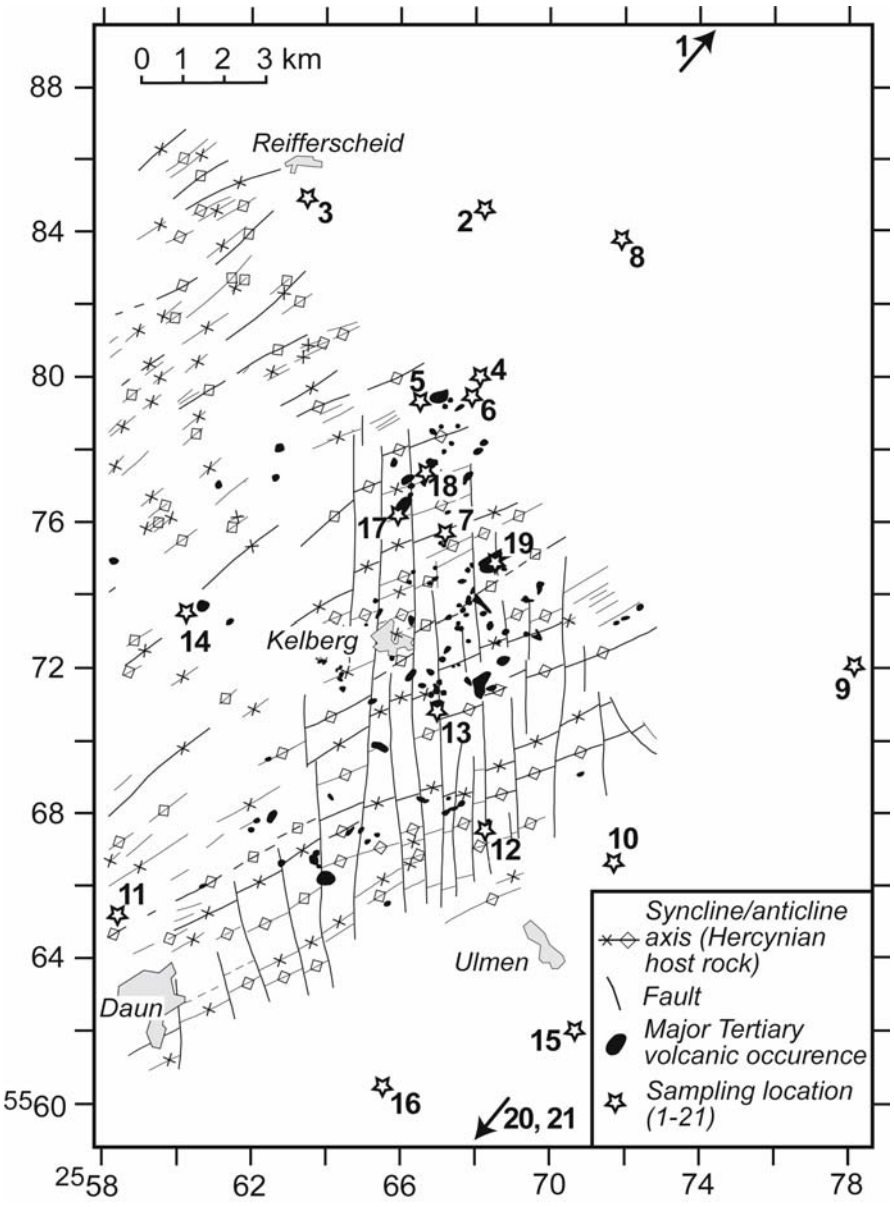

Fig. 2. Hocheifel sampling locations. Tectonic elements are taken from the geological map of Fuchs (1974). For geographic orientation the villages of Reifferscheid, Kelberg, Ulmen and Daun are shown

3 Sample preparation and analytical method

For sample preparation fresh hand specimen were selected by petrographic criteria. Altered domains manifested by olivine phenocrysts with iddingsite rims and fracture fillings were removed. 2-3 kg fresh rock material of each sample was crushed into pieces <5 mm using a hydraulic press and aliquots were prepared. Further crushing and sieving yield different grain size fractions in the range <1mm. They were rinsed with water and dried down in an oven at a temperature of ca. 60 °C. The fractions 250-355 μm and 355-500 μm were used for $^{40}Ar/^{39}Ar$ dating. For producing magnetic ground mass and phenocryst (sanidine, plagioclase, amphibole) dating separates an isodynamic Frantz magnetic separator was used. We checked each of our ground mass separates through binocular microscope hand picking in order to ensure that there is no contamination by xenolithic material. Microprobe analyses on selected ground mass separates show that plagioclase, containing some mol-% orthoclase, generally represents a significant component.

$^{40}Ar/^{39}Ar$ analysis samples were loaded in wells in Al disks (Renne et al. 1998) and irradiated in the cadmium shielded port (CLICIT) at the Triga reactor at University of Oregon and analysed at the Berkeley Geochronology Center. Values of *J* (a measure of fast neutron fluence) were determined from the mean of 12 single-crystal laser fusion analyses of co-irradiated Fish Canyon sanidine based on an age of 28.02 Ma (Renne et al. 1998). Corrections for interfering nucleogenic isotopes of Ar were determined from analyses of irradiated CaF_2 and a synthetic K-bearing glass using the values given by Renne (1995). The samples were baked out at ca. 200 °C for about 12 hours prior to analysis and heated incrementally with a CO_2 laser with an integrator lens by up to 24 degassing steps for each sample. Extraction line operation, including sample heating, is fully automated. Blanks for the extraction line were measured and blank correction was applied as described by Sharp et al. (1996). Reactive components, such as H_2O, CO_2, CO, and N_2, were removed from the sample gas using SAES GP-50 Zr-Al getters operated at 400˚C. The purified gas was analysed using a Mass Analyser Products 215-50 gas source mass spectrometer, configured for a resolution of 450. Mass discrimination was determined from repeated analyses of air Ar using an on-line pipette, yielding a mean value of 1.0058 ± 0.0012/a.m.u. during the course of this study. The decay constants and isotopic ratios used are those given by Steiger and Jäger (1977). Uncertainties for ages are given at the 2σ level and include errors arising from irradiation and Ar analysis but do not include errors in decay constants, the age of the standard, or isotopic abundances of K.

4 Results

The $^{40}Ar/^{39}Ar$ incremental heating technique dating results on volcanic rocks from 19 Hocheifel occurrences and 6 occurrences of the northern Upper Rhine Graben are presented in a file which can be requested from the authors. Figures 3a-d show the corresponding age spectra. Principally, there are three types of age spectra: 1) flat spectra forming age plateau matching the criteria given by Fleck et al. (1977), 2) flat spectra forming age plateau with step ages scattering slightly more than allowed by the Fleck et al. (1977) definition, 3) discordant spectra.

Type 1 age spectra are represented by mineral as well as ground mass separates. Figure 3a indicates the type 1 minerals comprising trachyte from Reimerath (sanidine plateau age = 40.1±0.3 Ma), basanite from Vogelsherdchen (sanidine/plagioclase plateau age = 35.2±0.3 Ma) as well as latites from Quiddelbach and Bocksberg (amphibole plateau ages = 37.0±0.3 and 39.7±0.3 Ma, respectively). Figure 3b indicates the type 1 ground masses comprising basanites from Hoch-Bermel, Staufskopf, Bad Neuenahrer Berg, Hohe Acht, Kopp, Nürburg, Rabenkopf, Stetteritz and Forstberg (plateau ages = 35.9±0.3, 37.0±0.3, 35.2±0.3, 36.3±0.3, 35.9±0.3, 35.0±0.3 Ma, 58.7±0.4 Ma, 48.7±0.2Ma and 47.2±0.3 Ma, respectively), hawaiite from Steimelskopf (plateau age = 37.5±0.3 Ma) and latite from Quiddelbach (plateau age = 37.0±0.3 Ma). Plateau and integrated ages of the mineral separates are identical within analytical error in each case. The ground mass separates also yield identical plateau and integrated ages or show minor deviation up to ca. 4 %. A duplicate analysis on the Reimerath trachyte (Fig. 3a) yields identical sanidine plateau ages of 40.1±0.3 Ma for separates #33239-01 and #33239-02, respectively, indicating that our results are reproducible and thus analytically significant. Also, amphibole and ground mass separates prepared from the Quiddelbach latite yield identical plateau ages of 37.0±0.3 and 37.1±0.3 Ma, respectively. This concordance in addition shows that mineral as well as ground mass plateau ages can be regarded as geologically meaningful.

Type 2 age spectra (Fig. 3c) are represented by ground masses comprising basalt from Scharfer Kopf (forced plateau age = 37.0±0.9 Ma) and basanites from Reifferscheid, Nollenbachtal, Steineberger Ley, Kastelberg and Forst (forced plateau ages = 39.0±0.6, 41.9±0.9, 35.2±0.5, 37.3±0.7 Ma and 50.6±0.5 Ma, respectively). „Forced“ means that the plateau ages are calculated accepting 3σ instead of 2σ for the confidence interval of the $^{40}Ar_{rad}/^{39}Ar_K$ ratios of the plateau steps. Forced plateau ages and integrated ages are identical within analytical errors given, except for the Steineberger Ley, Kastelberg and Forst basanites with a maximum deviation up to

ca. 7 %. In most cases, the forced plateau is related to high-temperature degassing steps, which are correlated with relatively low Cl/K and high Ca/K ratios (Fig. 3c). This indicates that during high-temperature degassing most probably Ar from groundmass plagioclase is released predominantly. In contrast, the forced plateau of the Kastelberg and Steineberger Ley basanites are related to low-temperature or medium-temperature degassing, respectively, comprising step ages with relatively low Ca/K ratios. The Ar released most likely preferentially comes from groundmass nepheline (high Cl/K) in case of Kastelberg and from groundmass K-feldpar (low Cl/K) in case of Steineberger Ley. Since volcanic feldspars as well as nepheline are regarded as suitable Ar chronometer, we consider the outlined relation between degassing temperature, step age and geochemical composition as additional evidence that the forced plateau ages are geologically meaningful. Type 2 age spectrum shapes indicate minor disturbances of the Ar isotope system, however, we suggest that these disturbances do not affect the determination of the geological age significantly. We conclude that the forced plateau age is the best available estimate for the age of these lavas.

Type 3 age spectra (Fig. 3d) are represented by ground masses comprising basanites from Barsberg, Rote Heck, Hörkopf and Steinbuckel (integrated ages = 33.8±0.3 Ma, 35.8±0.3 Ma, 54.5±0.3 Ma and 47.3±0.2 Ma, respectively). The shapes of the spectra reflect relevent disturbances of the Ar isotope system most likely largely caused by Ar redistribution related to recoil effects during neutron irradiation. Assuming that there is no ^{39}Ar loss caused by recoil, the integrated ages can be regarded as a good approximation to the geological age. However, such an estimate does not consider that there could in addition be geologically caused disturbances of the Ar isotope system, e.g., Ar loss by alteration. Because of these uncertainties we do not include the type 3 age spectra in the geological discussion.

All samples were evaluated by inverse isochron calculations. In each case, the calculated isochrons define trapped $^{40}Ar/^{36}Ar$ ratios identical within analytical errors with or lower than the atmospheric ratio of 295.5. Since no initial $^{40}Ar/^{36}Ar$ ratio >295.5 was detected, we conclude that no excess Ar is related to the samples measured. Summarising, we interpret the plateau and forced plateau ages to represent geologically meaningful ages of the lavas dated.

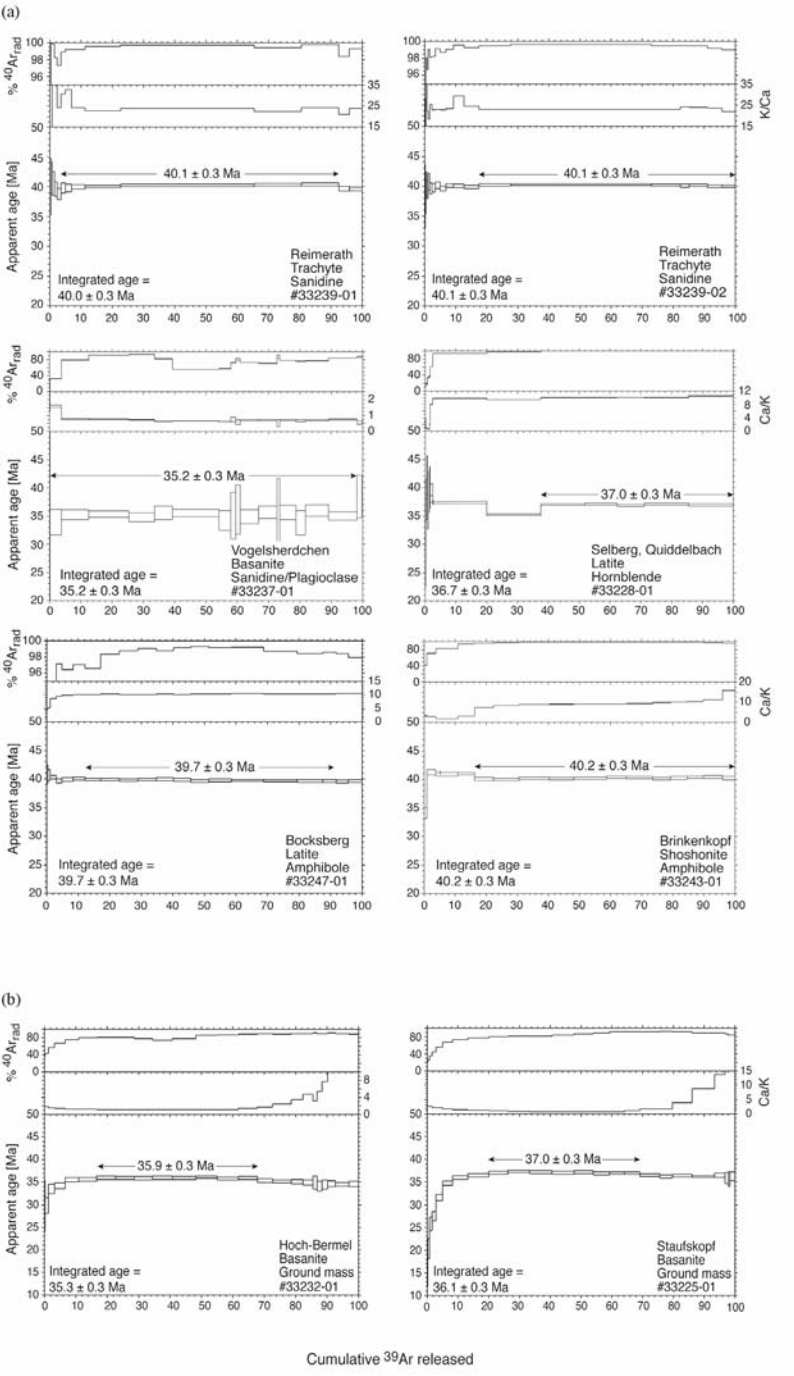
(a)
% 40Arrad
Apparent age [Ma]
K/Ca
Ca/K
40.1 ± 0.3 Ma
Integrated age = 40.0 ± 0.3 Ma
Reimerath Trachyte Sanidine #33239-01
Integrated age = 40.1 ± 0.3 Ma
Reimerath Trachyte Sanidine #33239-02
35.2 ± 0.3 Ma
Integrated age = 35.2 ± 0.3 Ma
Vogelsherdchen Basanite Sanidine/Plagioclase #33237-01
37.0 ± 0.3 Ma
Integrated age = 36.7 ± 0.3 Ma
Selberg, Quiddelbach Latite Hornblende #33228-01
39.7 ± 0.3 Ma
Integrated age = 39.7 ± 0.3 Ma
Bocksberg Latite Amphibole #33247-01
40.2 ± 0.3 Ma
Integrated age = 40.2 ± 0.3 Ma
Brinkenkopf Shoshonite Amphibole #33243-01
(b)
35.9 ± 0.3 Ma
Integrated age = 35.3 ± 0.3 Ma
Hoch-Bermel Basanite Ground mass #33232-01
37.0 ± 0.3 Ma
Integrated age = 36.1 ± 0.3 Ma
Staufskopf Basanite Ground mass #33225-01
Cumulative 39Ar released

(b) cont.

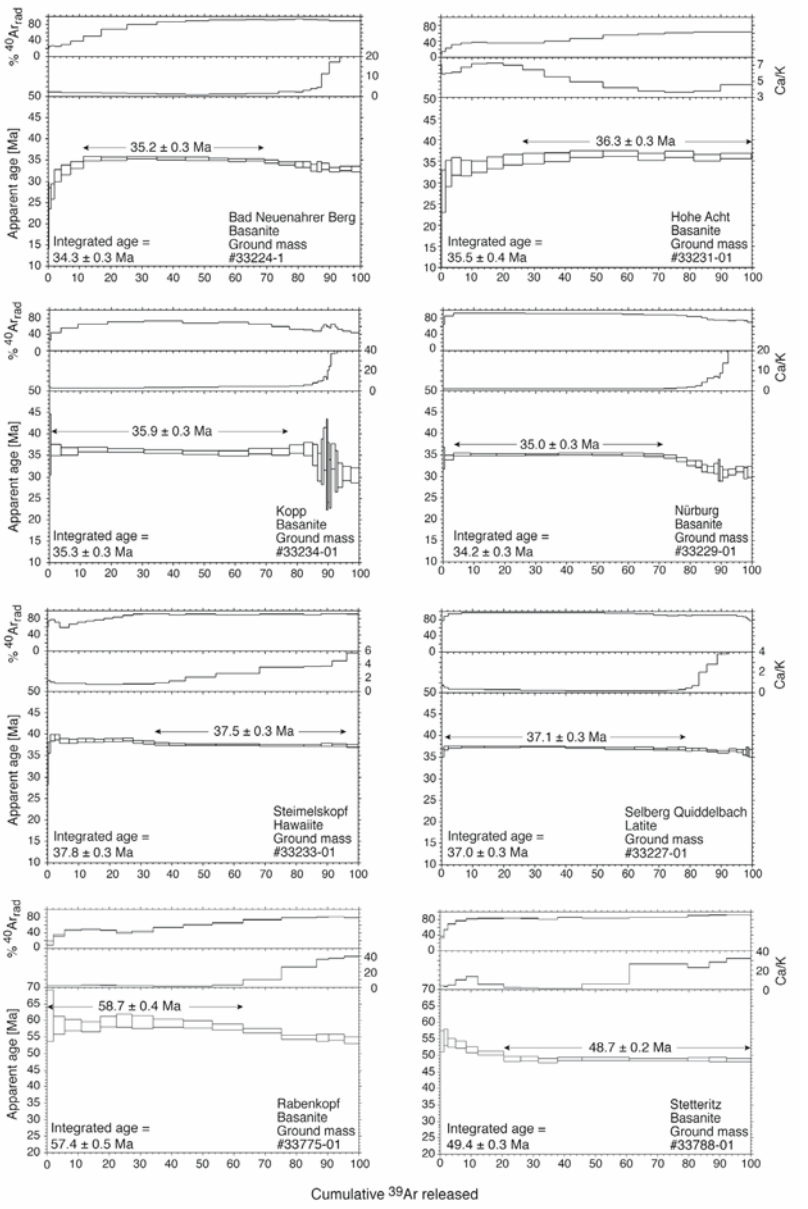
% 40Arrad
Apparent age [Ma]
Ca/K
35.2 ± 0.3 Ma
Integrated age = 34.3 ± 0.3 Ma
Bad Neuenahrer Berg
Basanite
Ground mass
#33224-1
36.3 ± 0.3 Ma
Integrated age = 35.5 ± 0.4 Ma
Hohe Acht
Basanite
Ground mass
#33231-01
35.9 ± 0.3 Ma
Integrated age = 35.3 ± 0.3 Ma
Kopp
Basanite
Ground mass
#33234-01
35.0 ± 0.3 Ma
Integrated age = 34.2 ± 0.3 Ma
Nürburg
Basanite
Ground mass
#33229-01
37.5 ± 0.3 Ma
Integrated age = 37.8 ± 0.3 Ma
Steimelskopf
Hawaiite
Ground mass
#33233-01
37.1 ± 0.3 Ma
Integrated age = 37.0 ± 0.3 Ma
Selberg Quiddelbach
Latite
Ground mass
#33227-01
58.7 ± 0.4 Ma
Integrated age = 57.4 ± 0.5 Ma
Rabenkopf
Basanite
Ground mass
#33775-01
48.7 ± 0.2 Ma
Integrated age = 49.4 ± 0.3 Ma
Stetteritz
Basanite
Ground mass
#33788-01
Cumulative 39Ar released

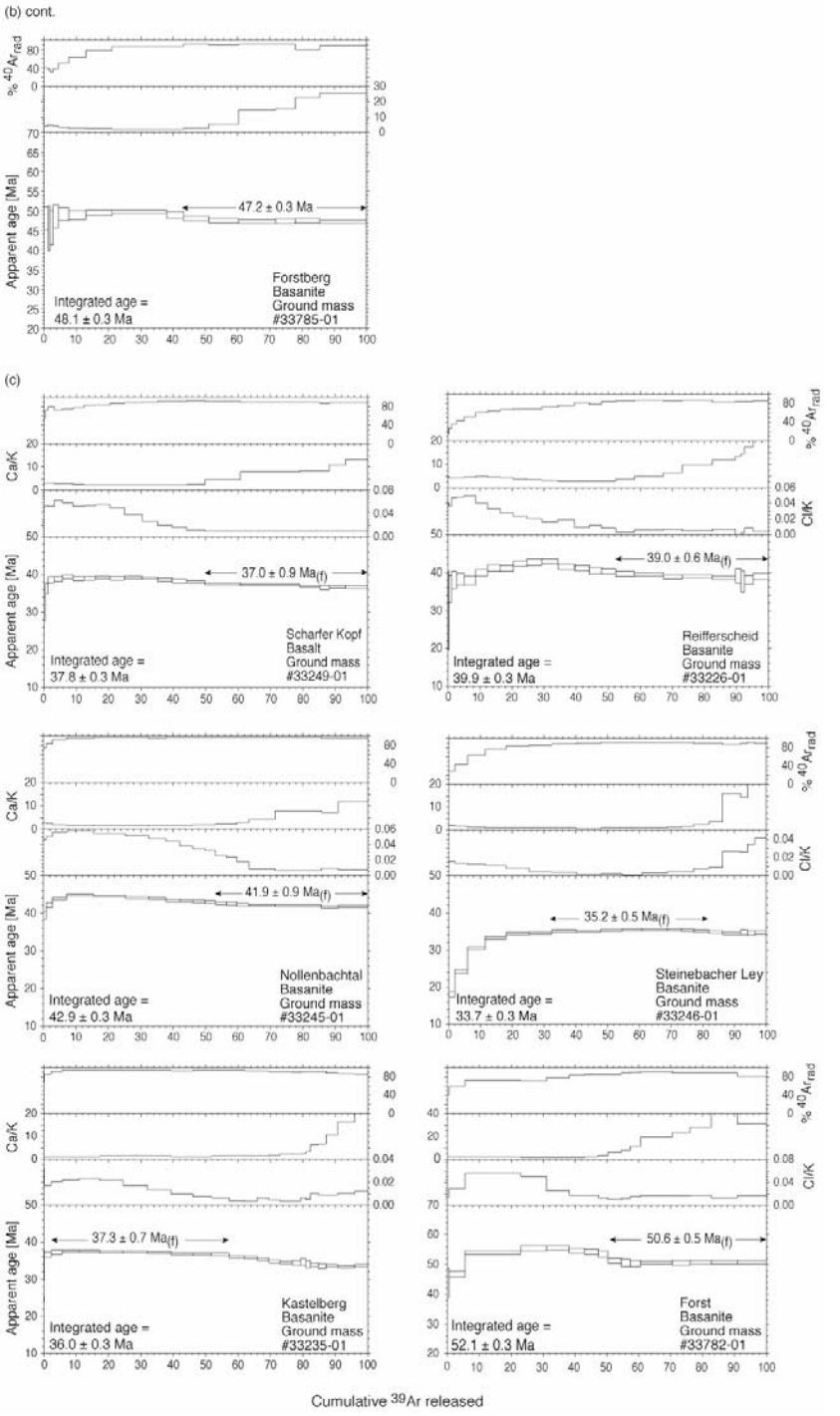
(b) cont.
% 40Arrad
Apparent age [Ma]
47.2 ± 0.3 Ma
Integrated age = 48.1 ± 0.3 Ma
Forstberg Basanite Ground mass #33785-01
(c)
Ca/K
Cl/K
37.0 ± 0.9 Ma(f)
Integrated age = 37.8 ± 0.3 Ma
Scharfer Kopf Basalt Ground mass #33249-01
39.0 ± 0.6 Ma(f)
Integrated age = 39.9 ± 0.3 Ma
Reifferscheid Basanite Ground mass #33226-01
41.9 ± 0.9 Ma(f)
Integrated age = 42.9 ± 0.3 Ma
Nollenbachtal Basanite Ground mass #33245-01
35.2 ± 0.5 Ma(f)
Integrated age = 33.7 ± 0.3 Ma
Steinebacher Ley Basanite Ground mass #33246-01
37.3 ± 0.7 Ma(f)
Integrated age = 36.0 ± 0.3 Ma
Kastelberg Basanite Ground mass #33235-01
50.6 ± 0.5 Ma(f)
Integrated age = 52.1 ± 0.3 Ma
Forst Basanite Ground mass #33782-01
Cumulative 39Ar released

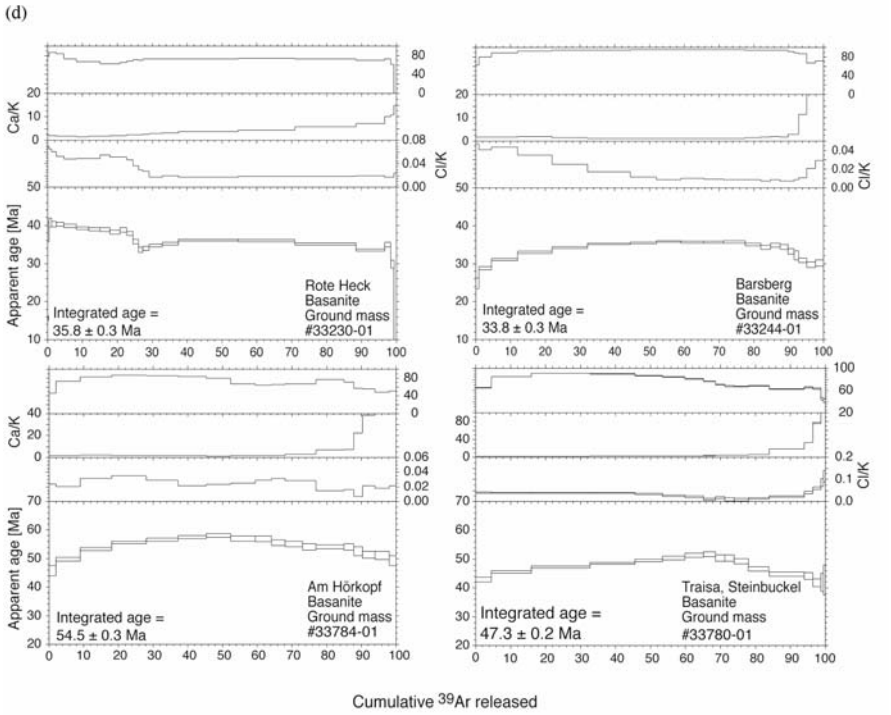

Fig. 3. $^{40}Ar/^{39}Ar$ age spectra showing incremental heating results on mineral plateau (a), ground mass plateau (b), ground mass forced plateau (c) and disturbed spectra (d). Subscript f in (c) indicates forced plateau

5 Discussion

5.1 Comparison with conventional K-Ar ages

Several of the occurrences we measured by the $^{40}Ar/^{39}Ar$ incremental heating technique were dated previously using the conventional K-Ar method (Cantarel and Lippolt 1977; Horn et al. 1972; Lippolt and Fuhrmann 1980; Müller-Sohnius et al. 1989). Table 1 compares the $^{40}Ar/^{39}Ar$ plateau ages regarded to be geologically significant with conventional K-Ar ages on total rock, mineral or mineral mixture separates. Eight out of 14 occurrences show either up to ca. 20 % younger or up to ca. 7 % older conventional K-Ar total rock ages compared to $^{40}Ar/^{39}Ar$ groundmass, amphibole or sanidine plateau ages. This discrepancy can be explained by Ar loss or excess Ar related to the younger or the older K-Ar total rock separates, respectively. For the Hocheifel volcanic rocks, Horn and Müller-Sohnius

(1988) showed significant disturbances in their K-Ar system. Lippolt et al. (1976) have argued that Tertiary total rocks from Sprendlingen Horst and Odenwald (Northern Upper Rhine Graben) volcanic occurrences are effected by Ar loss, because they yield up to 20 % younger K-Ar ages than separates of minerals regarded to be Ar retentive and therefore suitable for K-Ar dating. Also, excess Ar contamination is a known feature of phonolitic, foiditic and alkaline volcanic rocks from the Quarternary Eifel (e.g. Fuhrmann and Lippolt 1986; 1987) or from Tertiary fields (Rittmann and Lippolt 1998) of the western CEVP. Generally, our data confirm the results of, e.g., Lippolt et al. (1976). Therefore, we conclude that total rock conventional K-Ar ages published from CEVP volcanic fields represent a good approach to the geological age. However, they are not necessarily useful for high-precision geochronology purposes.

Six occurences show identical conventional total rock K-Ar and $^{40}Ar/^{39}Ar$ plateau ages considering analytical errors. In these cases, the total rocks contain negligible rock or mineral components with insufficient Ar retentivity or with excess Ar. As an example, the total rock separate from the location Reimerath represents a trachytic composition and the Ar measured on the total rock most likely almost exclusively originates from sanidine. This leads to a concordance between the $^{40}Ar/^{39}Ar$ sanidine plateau age and the K-Ar total rock age of 40.1±0.3 and 40.1±1.1 Ma, respectively.

For the sample locations Kastelberg and Steineberger Ley the K-Ar ages on feldspar and nepheline mineral mixture separates are up to ca. 15 % higher than the corresponding $^{40}Ar/^{39}Ar$ groundmass plateau.

In contrast to these feldspar/nepheline separates all K-Ar ages on amphiboles are identical with the $^{40}Ar/^{39}Ar$ plateau ages within analytical error. Based on the age concordance, we consider the K-Ar amphibole ages to be geologically significant, and we therefore use the published data (Müller-Sohnius et al. 1989) in our geological discussion.

The samples showing disturbed $^{40}Ar/^{39}Ar$ age spectra yield integrated $^{40}Ar/^{39}Ar$ ages up to 28 % older than the corresponding conventional K-Ar total rock ages (locations Barsberg, Am Hörkopf, Traisa). Since the inverse isochron calculations give no indication of excess Ar and assuming that the age spectrum disturbances are mainly caused by Ar isotope redistribution from recoil, the conventional K-Ar total rock ages appear to be affected by Ar loss. However, it is also possible that net loss of ^{39}Ar from the system by recoil has occurred, in which case the integrated $^{40}Ar/^{39}Ar$ ages would be spuriously old.

Table 1. Sampling data and TAS classification on samples from the Hocheifel and the Northern Upper Rhine Graben as well as a comparison of $^{40}Ar/^{39}Ar$ ages of this work regarded to be geologically significant with previously published conventional K-Ar ages.

Sample #	Sample location Topographic map 1: 25000, grid coordinates	TAS[1)]	Suggested age [Ma] This work	Previous K-Ar ages [Ma]
Hocheifel				
1	Bad Neuenahrer Berg (hill top) 5408 Bad Neuenahr-Ahrweiler, 25 80 64/56 00 05	Basanite	35.2±0.3 gm	34±2 tr (3)
2	Staufskopf (hill top in Näßbachtal) 5607 Adenau, 25 68 30/55 84 69	Basanite	37.0±0.3 gm	
3	Reifferscheid (quarry at Alte Burg) 5607 Adenau, 25 63 48/55 84 90	Basanite	39.0±0.6 gm	39.3±0.8 amph (4)
4	Vogelsherdchen (quarry Bruchtal) 5607 Adenau, 25 68 08/55 79 88	Basanite	35.2±0.3 san/plag	35.5±1.3 tr (4)
5	Quiddelbach (Selberg, quarry at street) 5607 Adenau, 25 66 63/55 79 30	Latite	37.0±0.3 amph	29.5±0.8 tr (2), 36.6±0.7 amph (4)
6	Nürburg (castle hill, small quarry) 5607 Adenau, 25 67 90/55 79 45	Basanite	35.0±0.3 gm	33.0±1.0 tr (2), 31.9±1.1/32.3±1.1 tr (4)
7	Rote Heck (hill top) 5607 Adenau, 25 67 08/55 7555	Basalt	[2)]	
8	Hohe Acht (at the top, view point) 5608 Virneburg, 25 71 90/55 83 85	Basanite	36.3±0.3 gm	37.3±1.1 tr (2)
9	Hoch-Bermel (quarry, south wall) 5708 Kaisersesch, 25 78 13/55 72 13	Basanite	35.9±0.3 gm	32.3±1.2 tr (4)
10	Steimelskopf (hill top) 5708 Kaisersesch, 25 71 70/55 66 75	Hawaiite	37.5±0.3 gm	39.4±1.4 tr (4)

Table 1. (cont.)

Sample #	Sample location Topographic map 1: 25000, grid coordinates	TAS[1)]	Suggested age [Ma] This work	Previous K-Ar ages [Ma]
11	Kopp (small hill top E of road Daun – Dockweiler) 5706 Hillesheim, 25 58 40/55 65 20	Basanite	35.9±0.3 gm	
12	Kastelberg (small quarry, west flank of hill top) 5707 Kelberg, 25 68 20/55 67 50	Basanite	37.3±0.7 gm	40.3±0.8 neph/plag/kf (4)
13	Brinkenkopf (quarry SW of Brinkenkopf) 5707 Kelberg, 25 66 96/55 70 82	Shoshonite	40.2±0.3 amph	40.4±0.8 tr (2), 39.0±0.9 amph (4)
14	Barsberg (little hill top E of Bongard) 5707 Kelberg, 25 60 40/55 73 55	Basanite	[2)]	26.7±1.0 tr (4)
15	Nollenbachtal (cliff close to Auderath mill) 5807 Gillenfeld, 25 70 60/55 61 88	Basanite	41.9±0.9 gm	37.5±1.4 tr (4)
16	Steineberger Ley (boulders at hill top slope) 5807 Gillenfeld, 25 65 60/55 60 53	Basanite	35.2±0.5 gm	41.5±0.8 plag/kf (4)
17	Bocksberg (SE of Nürburgring racing course) 5607 Adenau, 25 65 95/55 76 30	Latite	39.7±0.3 amph	41.9±1.1 tr (2)
18	Scharfer Kopf (at Nürburgring racing course) 5607 Adenau, 25 66 65/55 77 43	Basalt	37.0±0.9 gm	
19	Reimerath (quarry) 5607 Adenau, 25 68 50/55 74 83	Trachyte	40.1±0.3 san	40.1±1.1 tr (2)
20[3)]	Hillscheid (occurrence at upper hill top slope) 5806 Daun, 25 58 75/55 54 26	Basanite	43.7±0.2 gm	
21[3)]	Eckfeld maar (drill core at 64.7m) 5806 Daun, 25 58 50/55 53 35	Basanite	44.3±0.4 gm	

Table 1. (cont.)

Sample #	Sample location Topographic map 1: 25000, grid coordinates	TAS[1)]	Suggested age [Ma] This work	Previous K-Ar ages [Ma]
Northern Upper Rhine Graben				
22	Rabenkopf (quarry at NW flank of hill top) Taunus Mountains 5913 Presberg, 34 27 66/55 45 72	Basanite	58.7±0.4 gm	
23	Am Hörkopf (quarry at hill top) Taunus Mountains 5913 Presberg, 34 24 53/55 44 92	Basanite	[2)]	40.4±1.6 tr (1)
24	Forst (quarry ca. 1.5 km W of Forst) Mainz Basin 6514 Bad Dürkheim, 34 39 55/54 76 80	Basanite	50.6±0.5 gm	52.4±2.0 tr (1)
25	Stetteritz (construction site at Stetteritzer Ring #36) Sprendlingen Horst 6118 Darmstadt-Ost (Roßdorf), 34 85 42/55 25 10	Foidite	48.7±0.2 gm	43.5±1.7 tr (1)
26	Traisa (Steinbuckel, quarry N of Ramstadter Straße) Sprendlingen Horst 6118 Darmstadt-Ost (Roßdorf), 34 79 40/55 23 36	Basanite	[2)]	34.0±1.4 tr (1)
27	Forstberg (small quarry at W flank of hill top) Sprendlingen Horst 6119 Groß-Umstadt, 34 79 40/55 19 50	Basanite	47.2±0.3 gm	44.4±1.8 tr (1)

[1)] Data used for TAS classification are from Fekiacova et al. (part II of this contribution, this volume)

[2)] Samples without age indication do not yield geologically significant $^{40}Ar/^{39}Ar$ ages based on disturbed age spectra.

[3)] $^{40}Ar/^{39}Ar$ age from Mertz et al. (2000)

amph = amphibole, *gm* = ground mass (magnetic), *kf* = *K*-feldspar, *neph* = nepheline, *plag* = plagioclase, *tr* = total rock.

(1) Horn et al. (1972), (2) Cantarel and Lippolt (1977), (3) Lippolt and Fuhrmann (1980), (4) Müller-Sohnius et al. (1989). Data from references (1), (2), (3) are recalculated to IUGS constants, renormalised to an age of standard LP6 = 128.9 Ma and rounded.

5.2 Hocheifel age distribution and relation to tectonics

The evaluation of the Tertiary Hocheifel volcanism is based on 22 age determinations, comprising the $^{40}Ar/^{39}Ar$ ages presented in Table 1, and 4 conventional K-Ar amphibole ages from Müller-Sohnius et al. (1989). There is a younger age group ranging from 35.0 to 37.5 Ma and an older broader age group ranging from 39.0 to 44.3 Ma which shows a maximum of volcanic activity at ca. 40 Ma. As outlined in part II of our contribution (Fekiacova et al., this volume) this distinction is also supported by the isotope pattern since volcanic rocks of each age group show coherent isotope compositions which, however, differ significantly from group to group.

On the basis of the time scale of Berggren et al. (1995) with the boundary Middle Eocene/Upper Eocene defined at 37 Ma most of the volcanic activity of the younger phase is of Upper Eocene age, whereas the older phase is of Middle Eocene age. However, since our data set represents a random test, volcanism younger than Eocene can not definitively ruled out for the Tertiary Hocheifel.

No clear relation between age and chemical composition can be derived, confirming the results of Müller-Sohnius (1993). Both age groups are represented by less differentiated basanites as well as by more differentiated rocks (hawaiite, shoshonite, latite, trachyte). However, basanites are the youngest rocks with a maximum of volcanic activity at 35 to 36 Ma, whereas the more differentiated rocks show maxima at ca. 37 Ma and 40 Ma.

The volcanism represented by the older age group generally appears to become younger from south to north (Fig. 4a). Volcanic activity propagated from occurrences Eckfeld and Hillscheid at ca. 44 Ma via Nollenbachtal at ca. 42 Ma and Darscheid, Brinkenkopf as well as Reimerath at ca. 40 Ma to Nürburg as well as Reifferscheid at ca. 39 Ma, resulting in a hypothetic average propagation velocity of ca. 7 mm/a. For the distribution of the volcanism of the younger age group no systematic pattern with geography can be identified (Fig. 4b). Müller-Sohnius (1993) concluded on the basis of a comprehensive set of conventional K-Ar data that the entire Hocheifel volcanism was stationary throughout its eruptive history. Defining tectonic lineaments by connecting occurrences with identical ages indicate discrete pathways for magma ascent active during phases at ca. 40, 39, 38-36 and 35 Ma (Fig. 4c). These lineaments form a pattern which corresponds to the stress field derived for the Upper Rhine Graben for the time span ca. 40-35 Ma (e.g. Schumacher 2002) with NNE-SSW compression and ESE-WNW extension. In this case, the ESE striking lineaments represent transform zones between NNE striking extension zones. The N-S faults mapped by Fuchs (1974) appear to be steep dextral strike-slip faults.

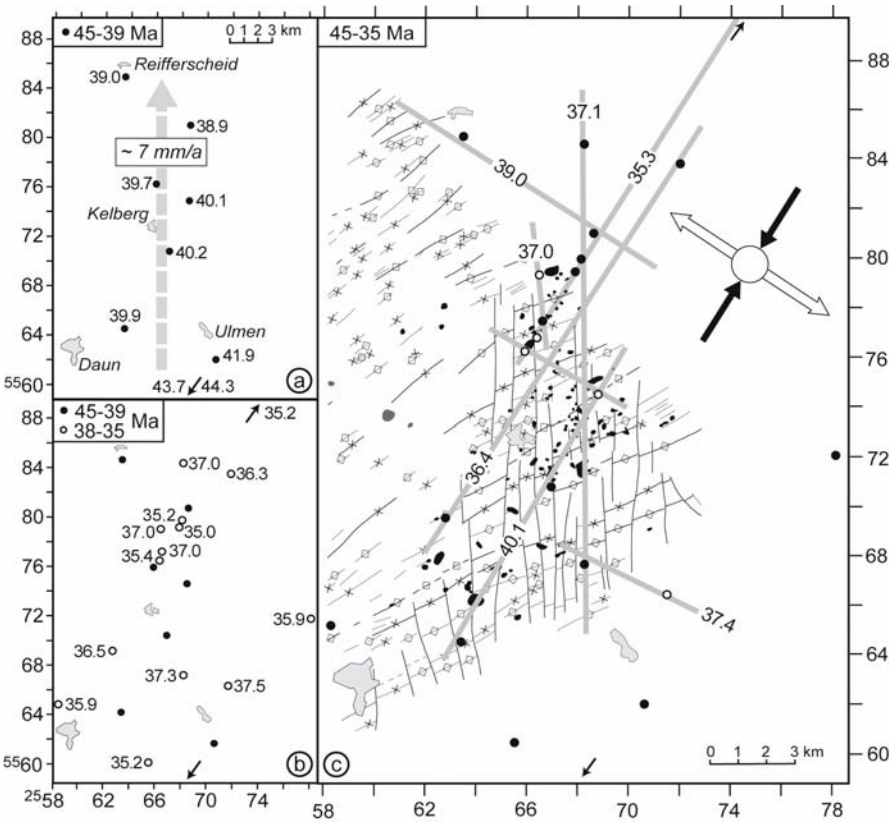

Fig. 4. Hocheifel volcanic pulses based on $^{40}Ar/^{39}Ar$ ages of this work together with conventional K-Ar ages on amphibole from literature and their spatial distribution. (a) shows an older phase of activity, (b) the older together with a younger phase of activity and (c) the relation between space - time distribution of volcanism and regional tectonic pattern. Filled and open arrows of stress field symbol in (c) represent directions of compression and extension, respectively. Grey lines are tectonic lineaments derived from the distribution of contemporaneous volcanic activity, indicating distinct pathways for magma ascent at discrete times of magma production

5.3 Relation to Upper Rhine Graben Taphrogenesis

The volcanic rocks measured from the northern Upper Rhine Graben (47-59 Ma, early Middle Eocene to middle Upper Palaeocene) are older than those from the Hocheifel. Initial Upper Rhine Graben rifting and starting subsidence is derived from composition and succession of lacustrine sediments from the basis of the Rhine Graben trough (e.g. Sittler 1969) for the

time since middle to late Middle Eocene (< ca. 45 Ma). Therefore, for the northern Upper Rhine Graben region (Sprendlingen Horst, Taunus Mountains, Mainz Basin) the volcanism occurred prior to the onset of rifting. This is also supported by conventional K-Ar dating results (e.g. Horn et al. 1972). The Hocheifel volcanism follows in time the pre-rifting volcanism of the northern Upper Rhine Graben, and the older Hocheifel volcanic phase shows propagation of younger volcanism to the north. Also, the Hocheifel tectonic pattern derived from the time - space relation of the volcanism corresponds to the stress field of the Upper Rhine Graben at that time. These indications suggest that in terms of geodynamic setting the Hocheifel volcanism is the northwestern propagation of the pre-rifting volcanism of the northern Upper Rhine Graben. However, in contrast to the Upper Rhine Graben, no relevant rifting or subsidence subsequent to volcanic activity occurred in the Hocheifel field.

5.4 Relation to neighbouring Tertiary volcanism

For the neighbouring western part CEVP volcanic fields to the NE or E (Siebengebirge, Westerwald, Vogelsberg, Rhön) of the Hocheifel (Fig. 1), several of the available geochronological data are conventional total rock K-Ar ages. These ages are of limited use for high-precision geochronology as outlined above, however, together with published conventional mineral K-Ar ages and some available $^{40}Ar/^{39}Ar$ ages, enable a useful preliminary conclusion. Siebengebirge, Westerwald and Rhön major volcanic activity occurred to a large extent contemporaneously within the Upper Oligocene to Lower Miocene at ca. 28-17 Ma, although there are also subordinate phases of activity in the Westerwald and Rhön considerably younger (Lippolt and Todt 1978; Todt and Lippolt 1980; Lippolt 1982). The Vogelsberg (Bogaard and Wörner 2003) and Main trap (Fuhrmann and Lippolt 1987) volcanism follows closely at about 17-15 Ma. The overlap in time for volcanic activity of Siebengebirge, Westerwald and Rhön could indicate similar tectonic setting and cause of volcanism. Since the Hocheifel activity is older, its inferred geodynamic setting could be different from that of the younger neighbouring CEVP fields.

6 Conclusions

The geological relevance of the $^{40}Ar/^{39}Ar$ age data used for the geological discussion is indicated by plateau-type age spectra as well as inverse

isochron calculations showing that there are no age-significant disturbances of the Ar isotope system.

Two periods of activity of Hocheifel volcanism from ca. 44 to 39 Ma and ca. 37 to 35 Ma are inferred. There is no relation between age and chemical composition. Both age groups are represented by less as well as more differentiated rocks. However, basanites are the youngest rocks with a maximum of volcanic activity at 35 to 36 Ma, whereas the more differentiated rocks show maxima at ca. 37 Ma and 40 Ma, respectively.

The northern Upper Rhine Graben area samples yield a period of foiditic to basanitic volcanism from 59 to 47 Ma, i.e., basic activity started at least ca. 15 m.y. prior to initial rifting and onset of subsidence derived from Rhine Graben trough sedimentation.

In terms of geodynamic setting, the Hocheifel activity appears to represent the northwestern propagation of the pre-rifting volcanism of the northern Upper Rhine Graben based on the following indications: a) The Hocheifel volcanism closely follows in time the pre-rifting volcanism of the northern Upper Rhine Graben, b) the older period of Hocheifel activity appears to become younger to the north, c) the Hocheifel tectonic pattern derived from the time - space relation of the volcanism corresponds to stress field conditions identical to those of the Upper Rhine Graben at the time of Hocheifel volcanic activity.

Thus, a plausible cause for the generation of the Hocheifel magmas could be decompression related to Middle to Upper Eocene extension processes. In contrast to the Upper and Lower Rhine Graben no relevant rifting or subsidence occurred subsequent to volcanic activity, indicating that the taphrogenetic evolution in between the Upper and Lower Rhine Graben regions was suspended in an early stage.

Acknowledgements

We thank I. van der Zander for support with sampling. Helpful reviews by G. Woerner and an anonymous referee are highly appreciated. This project was funded by the German Research Foundation (DFG, Bonn) via grant Me 1155/4-1 to D.F.M. and by the Landessammlung für Naturkunde Rheinland-Pfalz/Naturhistorisches Museum at Mainz, Germany.

References

Berggren WA, Kent DV, Swisher CC, Aubry MP (1995) A revised geochronology and chronostratigraphy. In: Berggren WA et al (eds) Geochronology, time scales, and global stratigraphic correlation. SEPM special publication 54, pp 129-212

Bogaard PJF, Wörner G (2003) Petrogenesis of basanitic to tholeiitic volcanic rocks from the Miocene Vogelsberg, Central Germany. J Petrol 44:569-602

Cantarel P, Lippolt HJ (1977) Alter und Abfolge des Vulkanismus der Hocheifel. N Jb Geol Paläont Mh 10:600-612

Fleck RJ, Sutter JF, Elliot DH (1977) Interpretation of discordant $^{40}Ar/^{39}Ar$ age-spectra of Mesozoic tholeiites from Antarctica. Geochim Cosmochim Acta 41:15-32

Fuchs G (1974) Das Unterdevon am Ostrand der Eifeler Nordsüd-Zone. Beitr Naturkund Forsch Südwestdeutschl Beih 3:3-163

Fuhrmann U, Lippolt HJ (1986) Excess argon and dating of Quaternary Eifel volcanism. II. Phonolithic and foiditic rocks near Rieden. N Jb Geol Paläont Abh 172(1):1-19

Fuhrmann U, Lippolt HJ (1987) Excess argon and dating of Quaternary Eifel volcanism: III. Alkali basaltic rocks of the Central West Eifel/FR Germany. N Jb Geol Paläont Mh 4:213-236

Hoernle K, Zhang YS, Graham D (1995) Seismic and geochemical evidence for large-scale mantle upwelling beneath the eastern Atlantic and western and central Europe. Nature 374:34-39

Horn P, Lippolt HJ, Todt W (1972) Kalium-Argon-Alterbestimmungen an tertiären Vulkaniten des Oberrheingrabens I. Gesamtgesteinsalter. Eclog geol Helv 65(1):131-156

Horn P, Müller-Sohnius D (1988) A differential etching and magnetic separation approach to whole-rock potassium-argon dating of basaltic rocks. Geochem J 22:115-128

Huckenholz HG (1983) Tertiary volcanism of the Hocheifel area. In: Fuchs K, von Gehlen K, Mälzer H, Murawski H, Semmel A (eds) Plateau Uplift, The Rhenish Shield - A case history, Springer, Berlin etc, pp 121-128

Huckenholz HG, Büchel G (1988) Tertiärer Vulkanismus der Hocheifel. Fortschr Miner 66:43-82

Lippolt HJ (1982) K/Ar age determinations and the correlation of Tertiary volcanic activity in Central Europe. Geol Jb D52:113-135

Lippolt HJ (1983) Distribution of volcanic activity in space and time. In: Fuchs K, von Gehlen K, Mälzer H, Murawski H, Semmel A (eds) Plateau Uplift, The Rhenish Shield - A case history, Springer, Berlin etc, pp 112-120

Lippolt HJ, Fuhrmann U (1980) Vulkanismus der Nordeifel: Datierung von Gang- und Schlotbasalten. Aufschluß 31:540-547

Lippolt HJ, Todt W (1978) Isotopische Alterbestimmungen an Vulkaniten des Westerwaldes. N Jb Geol Paläont Mh 6:332-352

Lippolt HJ, Horn P, Todt W (1976) Kalium-Argon-Alter von Mineralien und Einschlüssen der Basalt-Vorkommen Katzenbuckel und Roßberg. N Jb Miner Abh 127(3):242-260

Mertz DF, Swisher CC, Franzen JL, Neuffer FO, Lutz H (2000) Numerical dating of the Eckfeld maar fossil site, Eifel, Germany: a calibration mark for the Eocene time scale. Naturwiss. 87:270-274

Müller-Sohnius D (1993) Variation on a 36-Ma-old theme: length, intensity and rhythm of volcanism. A record from the Hocheifel (Germany). J Volc Geotherm Res 55:261-270

Müller-Sohnius D, Horn P, Huckenholz HG (1989) Kalium-Argon-Datierungen an tertiären Vulkaniten der Hocheifel. Chem Erde 49:119-136

Negendank J (1969) Beschreibung einiger tertiärer Alkali-Basalte im nördlichen Oberrheingraben. Notizbl Hess Landesamt Bodenforsch 97:283-295

Renne PR (1995) Excess ^{40}Ar in biotite and hornblende from the Norils'k 1 intrusion: Implications for the age of the Siberian Traps. Earth Planet Sci Lett 131:165-176

Renne PR, Swisher CC, Deino AL, Karner DB, Owens TL, DePaolo DJ (1998) Intercalibration of standards, absolute ages and uncertainites in ^{40}Ar/^{39}Ar dating. Chem Geol 145:117-152

Ritter JRR, Jordan M, Christensen UR, Achauer U (2001) A mantle plume below the Eifel volcanic fields, Germany. Earth Planet Sci Lett 186:7-14

Rittmann U, Lippolt HJ (1998) Evidence for distortion of Tertiary K/Ar ages by excess argon - example given by three alkali olivine basalts from Nothern Hesse, Germany. Eur J. Mineral 10:95-110

Schumacher ME (2002) Upper Rhine Graben: Role of preexisting structures during rift evolution. Tectonics 21(1):1-17

Sharp WD, Turrin BD, Renne PR, Lanphere MA (1996) ^{40}Ar/^{39}Ar and K/Ar dating of lavas from the Hilo 1-km core hole, Hawaii Scientific Drilling Project. J Geophys Res B101(5):11,607-11,616

Sittler C (1969) The sedimentary trough of the Rhine Graben. Tectonophysics 8:543-560

Steiger RH, Jäger E (1977) Subcommission on geochronology: Convention on the use of decay constants in geo- and cosmochronology. Earth Planet Sci Lett 36:359-3692

Todt W, Lippolt HJ (1980) K-Ar age determinations on Tertiary volcanic rocks: V. Siebengebirge und Siebengebirgs-Graben. J Geophys 48:8-23

Wilson M, Downes H (1991) Tertiary-Quaternary extension related alkaline magmatism in Western and Central Europe. J Petrol 32:811-849

Ziegler PA (1992) European Cenozoic rift system. Tectonophysics 208:91-111

Geodynamic Setting of the Tertiary Hocheifel Volcanism (Germany), Part II: Geochemistry and Sr, Nd and Pb Isotopic Compositions

Zuzana Fekiacova[1,2], Dieter F. Mertz[1] and Albrecht W. Hofmann[2]

[1] Johannes Gutenberg-Universität, Institut für Geowissenschaften, Becher-Weg 21, 55099 Mainz, Germany
[2] Max Planck-Institut für Chemie, Abteilung Geochemie, Becher-Weg 27, 55128 Mainz, Germany

Abstract

Major and trace element as well as isotopic compositions on 26 volcanic rocks from the Tertiary Hocheifel volcanic field and for comparison from Upper Rhine Graben occurrences (western Central European Volcanic Province) were measured in order to provide geochemical evidence for the geodynamic setting of the Tertiary Eifel volcanism. Except for a few differentiated lavas there are mainly basanitic compositions. These rocks were produced by low degree partial melting of a previously metasomatized garnet peridotite source at pressures and temperatures corresponding to depths of about 75 to 90 km. In contrast to the differentiated lavas, most of the basanites are not significantly affected by crustal contamination. In the Hocheifel, the crustally contaminated basanites and the differentiated lavas form an older age group (ca. 44-39 Ma). In contrast, the basanites not affected by crustal contamination belong to a younger age group (ca. 37-35 Ma) indicating a change in the petrogenetic style of evolution with time. Low-radiogenic Sr together with high-radiogenic Nd and Pb of the Hocheifel lavas show isotope characteristics similar to LVC (Low Velocity Composition) or FOZO (Focal Zone) mantle sources. Since FOZO is con-

sidered to be a common component in the entire mantle, a contribution from the deep mantle can be neither confirmed nor excluded. Plate reconstruction modelling indicates that the Hocheifel volcanic field at its time of activity ca. 40 m.y. ago was located ~1000 km southwest relative to its recent position, and therefore a relation to a mantle-stationary Quaternary Eifel plume is not plausible. Integrating evidence from geochronology, geochemistry, isotopic compositions and plate reconstruction, we conclude that the Tertiary Hocheifel volcanism is not genetically related to a mantle plume but is caused by Middle to Upper Eocene pre-rift extensional decompression related to the Rhine Graben taphrogenetic evolution.

1 Introduction, geological setting, sampling

The Hocheifel represents the westernmost Tertiary volcanic field of the Central European Volcanic Province (CEVP). The geodynamic setting of the Hocheifel volcanic field is controversially discussed. Plausible hypotheses for explaining the cause of Hocheifel volcanism are magma generation by rift-related lithospheric extension or plume activity. These hypotheses are outlined in more detail in part I of our contribution (Fekiacova et al., this volume) together with the geological setting of the Hocheifel volcanism as well as the data sampling. In part I we present evidence on the geodynamic setting of the Hocheifel volcanism from $^{40}Ar/^{39}Ar$ geochronology. In part II (this paper) we provide additional evidence by major and trace elements as well as Sr, Nd and Pb isotope ratios.

2 Analytical methods

For element and isotope analyses powder aliquots of total rocks from 20 Hocheifel and for comparison from 6 Upper Rhine Graben volcanic occurrences were prepared.

Major elements were determined by M. Thirlwall (London University XRF facility at Royal Holloway) using a Philips PW1480 XRF spectrometer. Concentrations were determined on glass discs prepared from sample powder. Ignition at 1100°C provides the loss on ignition (LOI). Major element 2σ are about 0.15, 0.10, 0.10, 0.05, 0.10, 0.10, 0.01, 0.01, 0.005 and 0.005 wt.% for Si, Al, Fe, Mg, Ca, Na, K, Ti, Mn and P, respectively. The accuracy is estimated to be similar to the 2σ based on the conformity of standard results to recommended values and on isotope dilution studies (Thirlwall et al. 2000).

Trace elements were analyzed at the Max Planck Institute for Chemistry, Mainz, by laser ablation inductively-coupled plasma mass spectrometry using a Finnigan Element 2 equipped with a Merchantek 213 nm laser. Sample powders were melted into glass beads using iridium strips without any flux agent. BHVO-1 and BHVO-2 standards were melted using the same procedure as for samples for controlling the glass preparation procedure. In order to avoid oxidation and evaporation of elements, melting occurred in a closed system under argon atmosphere. Additional standards NIST 612, KL2 and T1 glasses (Jochum et al. 2000) were analyzed contemporaneously with the samples. The average relative standard deviations based on repeated measurements of the standard materials range from 2 to 10%.

Strontium, Nd and Pb isotopic compositions were measured at the Max Planck Institute using a Finnigan MAT 261 thermal ionisation mass spectrometer. The sample powders were dissolved in a mixture of concentrated HF and HNO_3. Strontium and the REE (Rare Earth Elements) were separated using a cation exchange column (BioRad AG 50x80, 100 - 200 mesh, column volume = 5 ml**)** with 2.5N HCl as eluent. Neodymium was then separated from the other REE by reversed-phase chromatography on HDEHP (di(2-ethylhexyl) phosphoric acid) coated Teflon columns (column volume = 2 ml) with 0.18N HCl as eluent. The total blank contributions in each case were < 0.01% for Sr and Nd, respectively, and are considered to be not significant. The measured values are normalized to the standard NIST SRM 987 of $^{87}Sr/^{86}Sr = 0.71025$ and to the La Jolla standard of $^{143}Nd/^{144}Nd = 0.51186$. Lead was separated using an anion exchange resin (AG 1X8, 100-200 mesh, column volume =100 µl) with a HBr and HNO_3 mixture as eluent (e.g. Lugmair and Galer 1992). Lead isotopic compositions were measured using the triple spike technique (Galer 1999) in order to correct for instrumental mass fractionation. The measured values were referenced to the NIST SRM 981 Pb standard. The total Pb blanks ranged from 12 to 17 pg contributing < 0.2% to the sample Pb which was typically 10 to 20 ng.

3 Results

3.1 Major and trace elements

Major and trace element concentrations are reported in Table 1. Included are also analyses for the standards BHVO-1 and BHVO-2. Based on the TAS classification (Fig. 1a) of LeMaitre et al. (1989) the majority of our

Table 1. Major (wt.%) and trace element (ppm) concentrations of Hocheifel and Upper Rhine Graben lavas

Hocheifel							
Location *	Bad Neuenahrer Berg	Staufskopf	Reifferscheid	Vogelsherdchen	Quiddelbach	Nürburg	Rote Heck
Sample #	1	2	3	4	5	6	7
SiO_2	41.68	44.59	42.48	43.61	56.31	41.48	45.53
Al_2O_3	13.89	14.41	14.89	14.58	20.71	13.95	13.93
FeO	8.13	7.52	9.09	8.52	2.63	9.13	7.90
Fe_2O_3	2.26	2.09	2.53	2.37	1.95	2.54	2.19
MgO	11.55	10.59	10.10	10.22	1.56	9.78	9.27
CaO	12.68	12.47	12.01	11.63	5.21	12.88	12.13
Na_2O	3.98	2.27	3.16	3.69	5.82	3.60	3.65
K_2O	1.16	2.12	0.95	1.05	4.10	1.38	1.23
TiO_2	2.39	2.15	3.05	2.28	0.94	2.55	2.20
MnO	0.20	0.20	0.18	0.20	0.19	0.21	0.19
P_2O_5	0.82	0.48	0.51	0.66	0.19	1.07	0.72
Total	98.74	98.89	98.95	98.81	99.62	98.58	98.94
Mg# **	67	67	61	63	39	60	63
TAS	basanite	basanite	basanite	basanite	latite	basanite	basalt
Cs	0.55	0.55	0.65	0.39	1.30	0.63	0.22
Rb	26.24	52.44	33.96	18.56	115.00	36.03	23.69
Ba	716.40	679.57	471.22	622.87	977.00	641.44	653.81
Th	8.69	7.68	5.56	7.11	19.50	11.02	8.72
U	2.24	2.00	1.46	1.70	4.80	2.81	2.28
Nb	91.25	79.07	65.83	80.33	120.00	104.96	83.32
Ta	4.97	4.36	3.97	4.17	5.46	6.49	4.41
La	71.71	62.58	44.87	75.47	87.60	89.22	76.73
Ce	126.89	108.24	87.03	133.83	126.00	159.63	134.73
Pb	2.91	3.41	3.29	3.36	5.00	3.42	2.81
Pr	13.53	11.80	10.45	14.06	11.10	17.83	15.18
Sr	982.48	983.79	717.77	1127.55	635.00	1024.63	1179.72
Nd	52.15	43.30	41.44	51.41	32.50	65.42	55.75
Sm	9.04	7.62	7.86	8.62	4.89	11.21	9.41
Hf	4.69	5.32	5.01	4.81	9.80	5.48	4.96
Zr	207.64	234.35	195.75	218.91	514.00	235.07	215.01
Eu	2.79	2.41	2.43	2.68	1.47	3.42	2.80
Gd	7.66	6.67	6.91	7.16	3.43	9.48	7.92
Tb	1.10	0.95	0.97	1.04	0.59	1.29	1.10
Dy	6.01	5.24	5.32	5.50	3.52	6.88	5.93
Ho	1.09	0.96	0.95	0.95	0.71	1.20	1.03
Y	27.59	24.89	24.06	24.21	21.70	31.26	27.96
Er	2.72	2.60	2.48	2.56	2.28	3.15	2.75
Tm	0.37	0.35	0.32	0.33	0.36	0.41	0.36
Yb	2.40	2.33	2.04	2.16	2.49	2.57	2.19
Lu	0.34	0.35	0.29	0.31	0.39	0.36	0.32

Table 1. (cont.)

Hocheifel							
Location *	Hohe Acht	Hoch-Bermel	Steimelskopf	Kopp	Kastelberg	Brinkenkopf	Barsberg
Sample #	8	9	10	11	12	13	14
SiO_2	42.86	42.87	47.60	42.27	41.06	51.09	41.90
Al_2O_3	13.11	14.73	15.31	13.02	13.82	17.51	14.24
FeO	7.97	7.85	6.10	8.65	9.20	5.37	8.39
Fe_2O_3	2.21	2.18	2.91	2.40	2.56	3.22	2.33
MgO	14.69	11.65	8.82	13.75	11.60	3.82	11.18
CaO	11.80	11.86	9.60	11.64	12.44	8.05	12.17
Na_2O	2.92	3.37	4.36	3.29	3.16	4.20	3.55
K_2O	0.60	1.30	1.97	0.61	1.31	2.78	1.48
TiO_2	2.26	2.48	1.77	2.34	2.74	2.06	2.59
MnO	0.17	0.19	0.18	0.21	0.19	0.22	0.21
P_2O_5	0.38	0.55	0.47	0.64	0.60	0.65	0.62
Total	98.96	99.03	99.08	98.82	98.68	98.97	98.66
Mg# **	72	68	64	69	64	45	65
TAS	basanite	basanite	hawaiite	basanite	basanite	shoshonite	basanite
Cs	0.72	0.77	1.05	0.66	0.32	2.60	0.54
Rb	33.97	50.08	58.37	54.75	26.85	94.00	43.86
Ba	393.33	553.04	647.24	556.97	447.14	762.00	622.00
Th	4.52	8.08	9.51	7.64	4.57	12.80	8.14
U	1.16	2.01	2.58	1.90	1.20	4.06	1.95
Nb	55.24	94.67	93.06	86.58	64.15	97.70	96.24
Ta	3.34	5.16	4.88	5.33	3.92	6.15	5.60
La	34.53	53.93	63.08	55.97	38.62	81.10	67.75
Ce	67.09	101.06	107.66	102.44	77.80	151.00	122.04
Pb	2.09	2.97	4.58	2.57	1.52	7.00	2.46
Pr	7.87	11.55	11.40	11.84	9.40	16.70	13.88
Sr	552.99	768.61	812.51	687.82	627.98	684.00	928.05
Nd	31.15	44.50	40.54	46.15	37.27	57.60	52.09
Sm	6.18	8.09	6.95	8.18	7.18	10.10	8.89
Hf	3.99	5.43	5.13	5.45	4.15	7.70	5.65
Zr	156.05	216.19	258.52	227.73	153.26	343.00	240.82
Eu	1.93	2.56	2.16	2.51	2.30	3.08	2.77
Gd	5.60	7.13	5.86	7.33	6.16	7.98	7.98
Tb	0.81	1.01	0.84	1.03	0.88	1.26	1.13
Dy	4.50	5.56	4.58	5.71	4.79	6.44	6.11
Ho	0.79	0.98	0.84	1.02	0.86	1.18	1.09
Y	20.62	25.85	22.64	27.43	21.21	33.20	29.21
Er	2.10	2.62	2.28	2.71	2.29	3.35	2.93
Tm	0.28	0.35	0.31	0.36	0.30	0.47	0.38
Yb	1.75	2.22	2.08	2.21	1.89	2.87	2.41
Lu	0.25	0.31	0.30	0.32	0.26	0.42	0.34

Table 1. (cont.)

Hocheifel						
Location *	Nollenbachtal	Steine-berger Ley	Bocksberg	Scharfer Kopf	Reimerath	Hillscheid
Sample #	15	16	17	18	19	20
SiO_2	43.53	41.57	56.87	45.36	66.74	43.69
Al_2O_3	13.78	13.45	17.49	13.75	17.49	14.34
FeO	9.92	2.29	3.89	8.65	1.57	8.59
Fe_2O_3	2.76	8.25	2.88	2.40	1.75	2.39
MgO	9.18	11.77	2.12	10.77	0.45	11.10
CaO	12.36	13.02	5.62	10.98	1.28	11.48
Na_2O	2.64	3.46	4.94	3.00	4.84	3.28
K_2O	1.10	1.34	3.22	1.01	4.52	0.86
TiO_2	2.47	2.36	1.50	2.18	0.69	2.51
MnO	0.30	0.21	0.18	0.19	0.10	0.18
P_2O_5	0.56	0.986	0.57	0.55	0.20	0.49
Total	98.59	98.70	99.27	98.84	99.62	98.90
Mg# **	57	67	37	64	20	65
TAS	basanite	basanite	latite	basalt	trachyte	basanite
Cs	12.76	0.84	1.40	0.39	2.90	0.69
Rb	23.47	96.70	123.00	23.76	180.00	39.41
Ba	600.89	914.60	801.00	436.40	656.00	565.78
Th	7.19	13.02	15.60	5.41	27.60	5.86
U	2.01	3.20	4.79	1.37	6.17	1.36
Nb	55.94	130.16	101.00	60.10	102.00	73.62
Ta	3.33	6.39	6.65	3.40	6.32	4.33
La	55.96	95.40	83.50	48.03	88.70	47.98
Ce	95.22	161.84	156.00	92.54	138.00	86.24
Pb	3.23	3.15	10.00	3.46	11.00	2.38
Pr	10.59	17.73	17.10	10.25	12.90	9.96
Sr	828.68	1362.51	621.00	756.82	309.00	806.67
Nd	41.33	64.40	57.80	40.44	38.70	38.77
Sm	7.85	10.61	10.00	7.33	6.08	7.17
Hf	4.63	5.24	9.70	4.44	8.60	4.61
Zr	181.77	268.24	439.00	179.69	368.00	196.36
Eu	2.37	3.16	2.84	2.34	1.61	2.22
Gd	7.24	8.95	7.66	6.76	4.00	6.65
Tb	1.00	1.22	1.20	0.97	0.67	0.93
Dy	5.48	6.43	6.34	5.11	3.87	5.05
Ho	1.00	1.13	1.15	0.93	0.76	0.91
Y	25.75	31.97	33.20	24.13	21.90	24.85
Er	2.66	2.93	3.27	2.39	2.34	2.41
Tm	0.34	0.39	0.47	0.31	0.36	0.31
Yb	2.13	2.39	2.97	1.93	2.41	2.00
Lu	0.31	0.34	0.43	0.28	0.39	0.29

Table 1. (cont.)

Upper Rhine Graben								
Location *	Rabenkopf	Am Hörkopf	Forst	Stetteritz	Steinbuckel	Forstberg		
Sample #	21	22	23	24	25	26	BHVO-1	BHVO-2
SiO_2	41.27	42.02	42.22	40.37	44.50	43.12	n.d.	n.d.
Al_2O_3	12.60	11.50	12.66	12.39	13.22	12.86		
FeO	9.52	9.10	8.51	8.13	8.24	8.64		
Fe_2O_3	2.65	2.53	2.36	2.26	2.29	2.40		
MgO	12.64	14.23	12.90	11.62	11.46	11.64		
CaO	12.52	11.36	12.53	15.74	11.84	12.47		
Na_2O	2.54	3.03	3.04	2.55	2.42	3.68		
K_2O	0.87	1.03	0.69	1.16	1.36	0.79		
TiO_2	2.83	2.50	2.37	2.39	1.99	2.20		
MnO	0.21	0.20	0.18	0.20	0.20	0.20		
P_2O_5	0.71	0.61	0.60	1.10	0.77	0.82		
Total	98.35	98.10	98.07	97.90	98.29	98.81		
Mg# **	65	69	68	67	67	66		
TAS	basanite	basanite	basanite	foidite	basanite	basanite	basalt	basalt
Cs	0.74	0.88	15.69	3.01	1.76	0.58	0.10	0.09
Rb	31.10	30.43	30.37	29.94	38.25	43.25	10.00	9.51
Ba	616.57	554.85	682.54	1097.3	745.75	748.83	139.41	134.70
Th	7.49	6.13	6.24	13.40	9.13	7.76	1.41	1.30
U	1.93	1.57	1.44	3.15	2.76	2.42	0.46	0.44
Nb	89.67	80.66	84.11	122.79	82.79	99.89	20.22	20.09
Ta	5.49	4.60	5.16	6.39	4.89	5.54	1.35	1.25
La	61.75	52.13	48.69	105.53	72.57	63.51	16.95	16.23
Ce	116.06	98.55	90.01	169.84	121.68	111.38	40.38	39.69
Pb	2.21	3.01	2.14	1.18	4.30	2.59	1.93	1.39
Pr	13.66	12.19	10.62	18.63	13.52	12.70	5.76	5.51
Sr	940.80	842.31	812.88	1075.2	1185.28	883.44	419.26	397.52
Nd	53.20	47.88	41.83	70.72	50.56	50.31	26.69	25.36
Sm	9.55	8.21	7.65	11.70	8.85	8.56	6.64	6.20
Hf	6.36	5.41	4.96	5.53	4.87	5.14	4.99	4.51
Zr	266.32	229.92	208.05	259.57	222.88	231.72	188.86	170.69
Eu	2.95	2.48	2.39	3.41	2.67	2.62	2.23	2.16
Gd	8.45	7.24	6.83	9.70	7.62	7.54	6.91	6.31
Tb	1.12	0.96	0.93	1.30	1.03	1.03	1.05	0.95
Dy	5.77	4.86	5.02	6.75	5.61	5.29	5.97	5.35
Ho	1.01	0.81	0.87	1.16	0.99	0.92	1.06	0.94
Y	27.37	21.85	23.01	31.25	26.97	24.93	27.98	25.18
Er	2.58	2.03	2.23	2.93	2.58	2.40	2.80	2.53
Tm	0.33	0.25	0.29	0.37	0.33	0.30	0.36	0.33
Yb	2.04	1.54	1.79	2.29	2.12	1.90	2.24	2.03
Lu	0.29	0.21	0.26	0.33	0.30	0.27	0.32	0.28

* Grid coordinates for sampling locations are given in part I of this contribution (Fekiacova et al., this volume); ** Mg# = 100 x $Mg^{2+}/(Mg^{2+} + Fe^{2+})$. FeO and Fe_2O_3 were calculated from Fe_2O_3(total) using the coefficients of Middlemost (1989). *BHVO-1* and *BHVO-2* are the standards melted and analyzed together with the samples. Trace elements of samples # 5, 13, 17 and 19 were analyzed by Activation Laboratories (ACTLABS), Canada. *n.d.* = not determined.

Hocheifel sample suite is represented by 13 basanites which together with two basalts are termed “undifferentiated group” (i.e. samples with SiO_2 < 47.5 wt.%) herein for brevity. A “differentiated group” (i.e. samples with SiO_2 > 47.5 wt.%) of five Hocheifel lavas are of hawaiitic, shoshonitic, latitic and trachytic compositions. The Upper Rhine Graben lavas are represented by 5 basanites and a single foidite.

Figure 1b-i shows the major element oxide variations of the Hocheifel and Upper Rhine Graben lavas. In addition, data from the neighbouring Westerwald (Haase et al. 2004), Vogelsberg (Bogaard and Wörner 2003) as well as Quaternary West and East Eifel volcanic fields (Mertes and Schmincke 1985) are shown for comparison. TiO_2 (2.15 - 3.1 wt.%), Fe_2O_3 (10.45 - 13.78 wt.%) and CaO (10.98 - 13.02 wt.%) concentrations of the undifferentiated and differentiated Hocheifel lavas generally decrease with

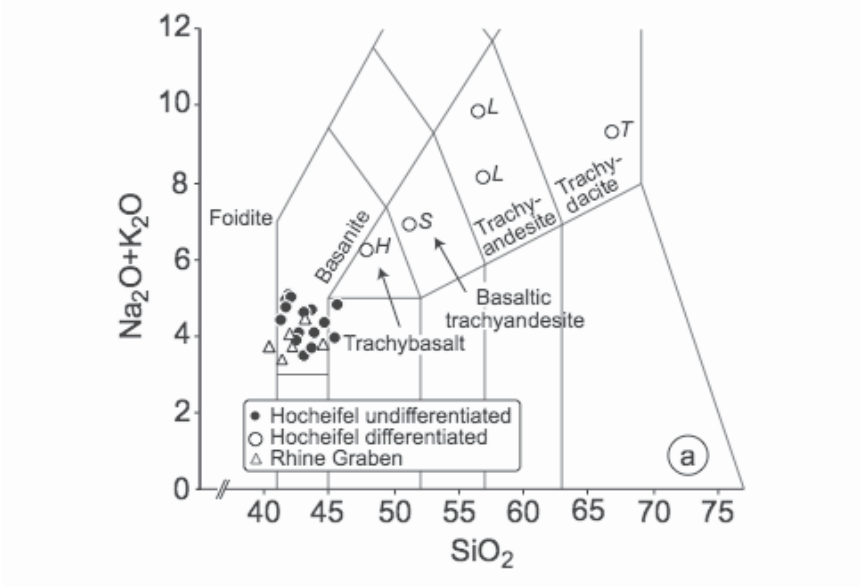

Fig. 1. Total alkali vs. silica (TAS) classification of Hocheifel and Upper Rhine Graben volcanic rocks (a) and comparison of their major element compositions with data from neighbouring volcanic fields using Harker-type diagrams (b-i next page, top). Concentrations in wt.%. See text for data references. *T* - trachyte, *L* - latite, *S* – shoshonite, *H* – hawaiite

Fig. 2. (next page, bottom) Chondrite-normalized Rare Earth Element (REE) patterns of Hocheifel undifferentiated (blue) and differentiated (red) as well as Upper Rhine Graben (green) volcanic rocks. Numbering corresponds to sample numbers in Table 1. C1 chondrite data used for normalization are from Evensen et al. (1978)

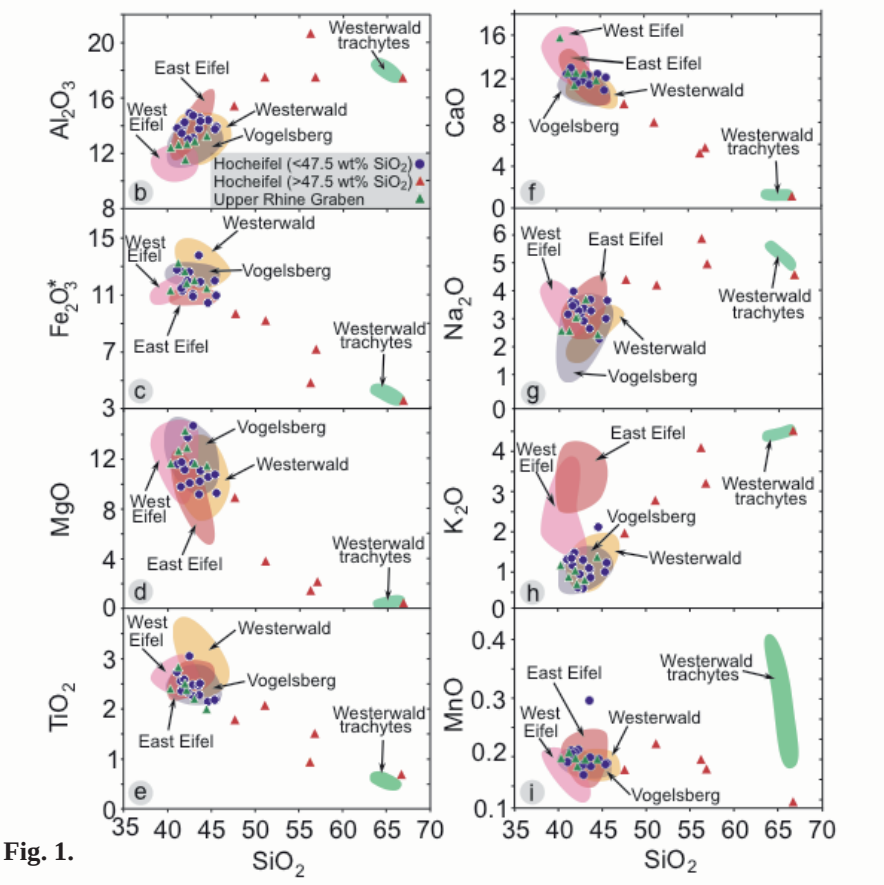
Al2O3
Fe2O3*
MgO
TiO2
CaO
Na2O
K2O
MnO
SiO2
SiO2
Westerwald trachytes
East Eifel
West Eifel
Westerwald
Vogelsberg
Hocheifel (<47.5 wt% SiO2)
Hocheifel (>47.5 wt% SiO2)
Upper Rhine Graben
b
c
d
e
f
g
h
i

Fig. 1.

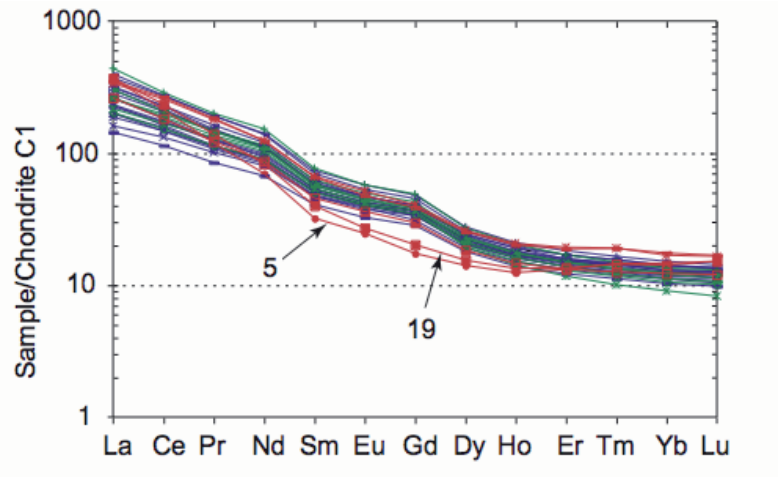
Sample/Chondrite C1
1000
100
10
1
5
19
La Ce Pr Nd Sm Eu Gd Dy Ho Er Tm Yb Lu

Fig. 2.

increasing SiO_2. The undifferentiated Hocheifel lavas have similar concentrations as the Tertiary Westerwald and Vogelsberg basanites and alkali basalts, although the Westerwald samples show higher Fe_2O_3 (up to 14.51 wt.%) and TiO_2 (up to 3.71 wt.%) concentrations. Also, there is a general overlap of the Quaternary East Eifel and undifferentiated Hocheifel data fields, except for K_2O which is substantially higher and MgO which is partly lower in the Quaternary East Eifel. In contrast, the West Eifel differs significantly from the Hocheifel and there is little or no overlap in the data fields of SiO_2 vs. Al_2O_3, Fe_2O_3, CaO, Na_2O, K_2O and MnO, respectively. The major element compositions of the Upper Rhine Graben resemble the undifferentiated Hocheifel with the exception of Al_2O_3 which is lower in the Upper Rhine Graben volcanic rocks.

The Hocheifel and Upper Rhine Graben volcanic rocks have similar subparallel chondrite-normalized REE patterns (Fig. 2). The light Rare Earth Elements (LREE) are enriched relative to the middle REE (MREE) and heavy REE (HREE). Chondrite-normalized $(La/Sm)_n$ and $(La/Lu)_n$ ratios range from 3.4 to 11.3 and from 14.7 to 33.8, respectively. Two differentiated Hocheifel samples (#19 trachyte from Reimerath and #5 latite from Quiddelbach) show concave REE patterns, with MREE lower compared to the other samples.

Also, the Hocheifel and Upper Rhine Graben volcanic rocks have similar primitive mantle-normalized patterns (Fig. 3). For the undifferentiated Hocheifel and Upper Rhine Graben, highly incompatible elements, e.g., Rb, Ba, Th or U are up to ca. 60 times enriched relative to less incompatible elements such as Yb or Lu. Cs concentrations vary more compared to the other elements, but this feature is most likely a result of alteration. There are negative Pb, K and Ti anomalies with $(Pb/*Pb)_N \sim 0.3$, $(K/*K)_N \sim 0.4$ and $(Ti/*Ti)_N \sim 0.4$ (the superscripted symbol "*" indicates the hypothetical concentration of the corresponding element calculated by interpolation between the two neighbouring elements on the abscissa). In addition to the K, Pb and Ti anomalies of the undifferentiated group, the differentiated Hocheifel samples show negative Ba anomalies. This anomaly is more pronounced in the most differentiated samples. In contrast, the Pb anomalies are least pronounced in the most differentiated samples. Figure 3b shows that almost all Hocheifel and Upper Rhine Graben lavas have primitive mantle-normalized trace element patterns similar to those of ocean island basalts (Weaver 1991; Hofmann 1997) with highly incompatible elements up to 100 times enriched compared to the primitive upper mantle. Also, Tertiary undifferentiated Hocheifel and Quaternary West and East Eifel lavas generally have similar shapes of the primitive mantle-normalized trace element patterns.

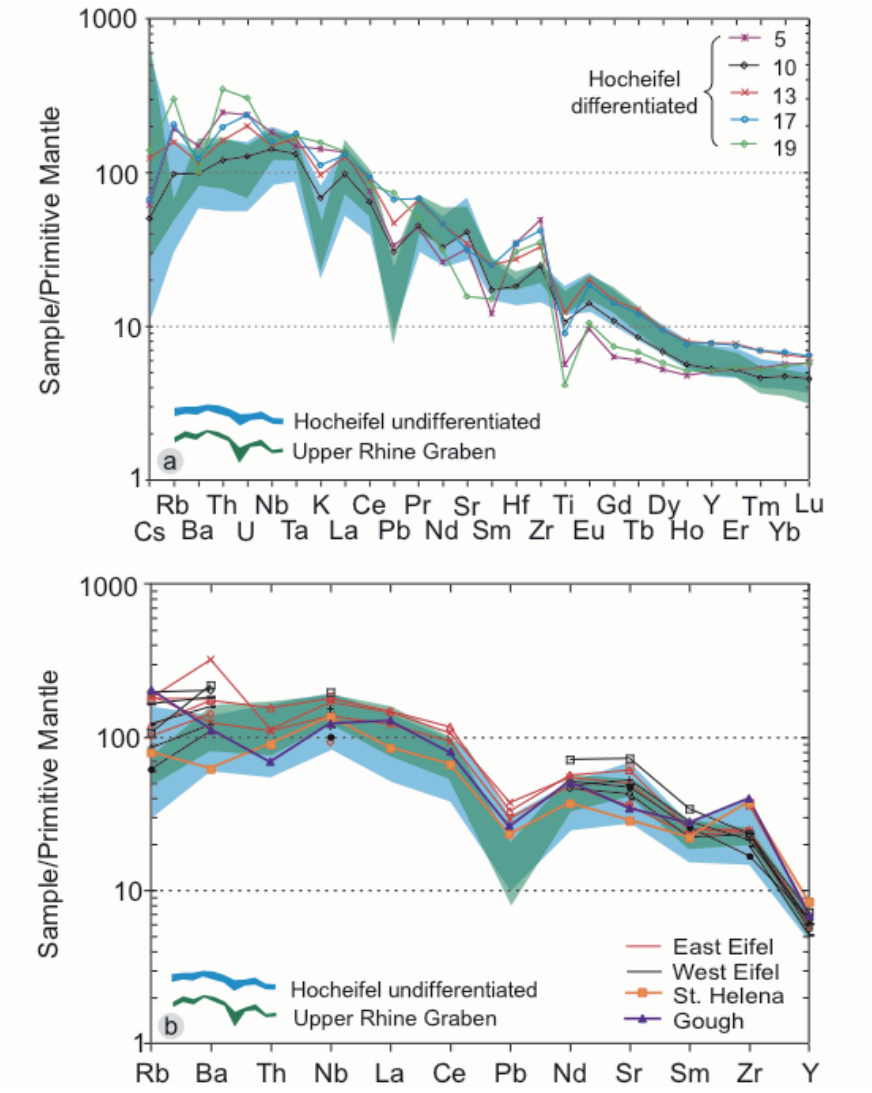

Fig. 3. (a) Primitive mantle-normalized trace element patterns of Hocheifel undifferentiated (blue) and differentiated (various colours) as well as Upper Rhine Graben (green) volcanic rocks. Numbering corresponds to sample numbers in Table 1. (b) Comparison with average St. Helena and Gough ocean island basalts (GEOROC database; http://georoc.mpch-mainz.gwdg.de) and Quaternary East and West Eifel volcanic rocks. Primitive mantle data used for normalization are from McDonough and Sun (1995)

3.2 Sr, Nd and Pb isotopic compositions

Table 2 presents the measured Sr, Nd and Pb isotopic compositions of the Hocheifel lavas as well as initial ratios calculated based on $^{40}Ar/^{39}Ar$ age data (Fekiacova et al., this volume). The initial ratios range from 0.70320 to 0.70449 for $^{87}Sr/^{86}Sr$, 0.51268 to 0.51288 for $^{143}Nd/^{144}Nd$, 19.524 to 19.776 for $^{206}Pb/^{204}Pb$, 15.618 to 15.649 for $^{207}Pb/^{204}Pb$ and 39.301 to 39.609 for $^{208}Pb/^{204}Pb$ and are shown in Fig. 4 together with data from the Quaternary Eifel volcanic fields and Eifel crustal xenolith. In the discussion below the initial isotope ratios of the Hocheifel volcanic rocks are used exclusively.

The differentiated Hocheifel lavas have higher $^{87}Sr/^{86}Sr$ ratios, except for one sample, and three out of five differentiated lavas show lower $^{143}Nd/^{144}Nd$ ratios compared to the undifferentiated samples (Fig. 4a). On the basis of $^{40}Ar/^{39}Ar$ geochronology, Hocheifel lavas form two age groups, an older (ca. 44-39 Ma) and a younger (ca. 37-35 Ma), referred to as “Hocheifel old” and “Hocheifel young”, respectively. There is a relationship between initial isotopic composition and age of the Hocheifel volcanic activity. The older age group is represented by samples with more radiogenic Sr and generally less radiogenic Nd compared to the younger age group. Whereas the younger Hocheifel lavas have relatively constant $^{87}Sr/^{86}Sr$ at ~ 0.70332 and vary only in $^{143}Nd/^{144}Nd$ ratios, the Sr and Nd isotopic initial compositions of the older lavas are negatively correlated. The younger age group has one outlier which is a differentiated rock with relatively radiogenic Sr. The Tertiary Hocheifel Sr and Nd initial isotopic compositions are different from those of the Quaternary West and East Eifel lavas, except of two West Eifel samples. Generally, at a given $^{143}Nd/^{144}Nd$ ratio, Quaternary lavas have more radiogenic Sr than Tertiary lavas. The samples of the older Hocheifel age group and the West Eifel form linear arrays which converge in the East Eifel data field.

In $^{208}Pb/^{204}Pb$ vs. $^{206}Pb/^{204}Pb$ space (Fig. 4b) the Hocheifel lavas and the West and East Eifel form linear, rather subparallel trends. Whereas the West and East Eifel data fields overlap, the Hocheifel data form a distinct field. At a given $^{206}Pb/^{204}Pb$, the Hocheifel have lower $^{208}Pb/^{204}Pb$ ratios compared to the Quaternary Eifel lavas indicating a higher time-integrated Th/U ratio in the Quaternary source. In $^{207}Pb/^{204}Pb$ vs. $^{206}Pb/^{204}Pb$ space (Fig. 4c) the Hocheifel samples also form a data field distinct from that of the Quaternary samples. At a given $^{207}Pb/^{204}Pb$, the Tertiary lavas are more radiogenic in $^{206}Pb/^{204}Pb$ than the Quaternary lavas.

Table 2. Sr, Nd and Pb isotopic compositions of Hocheifel lavas

Sample #	$^{86}Sr/^{87}Sr_m$ ±2σ	$^{86}Sr/^{87}Sr_i$	$^{143}Nd/^{144}Nd_m$ ±2σ	$^{143}Nd/^{144}Nd_i$
1	0.703357	0.70332	0.512877	0.51285
	0.000015		0.000006	
2	0.703383	0.70330	0.512803	0.51278
	0.000011		0.000028	
3	0.703651	0.70357	0.512821	0.51279
	0.000011		0.000009	
4	0.703307	0.70328	0.512879	0.51286
	0.000015		0.000006	
5	0.704022	0.70375	0.512867	0.51284
	0.000012		0.000006	
6	0.703357	0.70331	0.512865	0.51284
	0.000013		0.000008	
7	0.703465	0.70344	0.512837	0.51281
	0.000014		0.000006	
8	0.703378	0.70329	0.512813	0.51278
	0.000010		0.000007	
9	0.703364	0.70327	0.512858	0.51283
	0.000010		0.000007	
10	0.703405	0.70329	0.512870	0.51284
	0.000016		0.000006	
11	0.703360	0.70324	0.512888	0.51286
	0.000009		0.000007	
12	0.703269	0.70320	0.512911	0.51288
	0.000011		0.000015	
13	0.704167	0.70394	0.512780	0.51275
	0.000013		0.000012	
14	0.703391			
	0.000014			
15	0.703808	0.70376	0.512791	0.51276
	0.000013		0.000016	
16	0.703366	0.70326		
	0.000014			
17	0.704548	0.70423	0.512705	0.51268
	0.000010		0.000025	
18	0.703429	0.70338		
	0.000014			
19	0.705453	0.70449	0.512709	0.51268
	0.000010		0.000009	
20	0.704109	0.70402	0.512816	0.51278
	0.000010		0.000009	

Table 2. (cont.)

Sample #	$^{206}Pb/^{204}Pb_m$ ±2σ	$^{206}Pb/^{204}Pb_i$	$^{207}Pb/^{204}Pb_m$ ±2σ	$^{207}Pb/^{204}Pb_i$	$^{208}Pb/^{204}Pb_m$ ±2σ	$^{208}Pb/^{204}Pb_i$
1						
2						
3	19.9439	19.776	15.6567	15.649	39.8194	39.609
	0.0009		0.0010		0.0030	
4						
5						
6						
7	19.8083	19.524	15.6483	15.635	39.6810	39.324
	0.0008		0.0008		0.0027	
8						
9	19.9893	19.753	15.6338	15.623	39.7509	39.440
	0.0008		0.0008		0.0023	
10						
11						
12	19.8842	19.599	15.6310	15.618	39.7434	39.386
	0.0010		0.0011		0.0035	
13	19.7977	19.572	15.6573	15.647	39.5353	39.301
	0.0008		0.0008		0.0025	
14						
15	19.9057	19.653	15.6588	15.647	39.6523	39.354
	0.0006		0.0006		0.0021	
16						
17						
18						
19						
20						

Subscript "*m*" = measured ratio, subscript "*i*" = calculated initial ratio; Sr, Nd and Pb isotopic compositions were referenced to NBS 987, La Jolla and NBS 981 standards, respectively. Repeated measurements of standards during this study yielded the following ratios ± 2σ: $^{87}Sr/^{86}Sr$ = 0.710230 ± 0.000029 (n = 10), $^{143}Nd/^{144}Nd$ = 0.5118807 ± 0.000036 (n = 15), $^{206}Pb/^{204}Pb$ = 16.9402 ± 0.0030, $^{207}Pb/^{204}Pb$ = 15.4968 ± 0.0029 and $^{208}Pb/^{204}Pb$ = 36.7231 ± 0.0099 (n = 65).

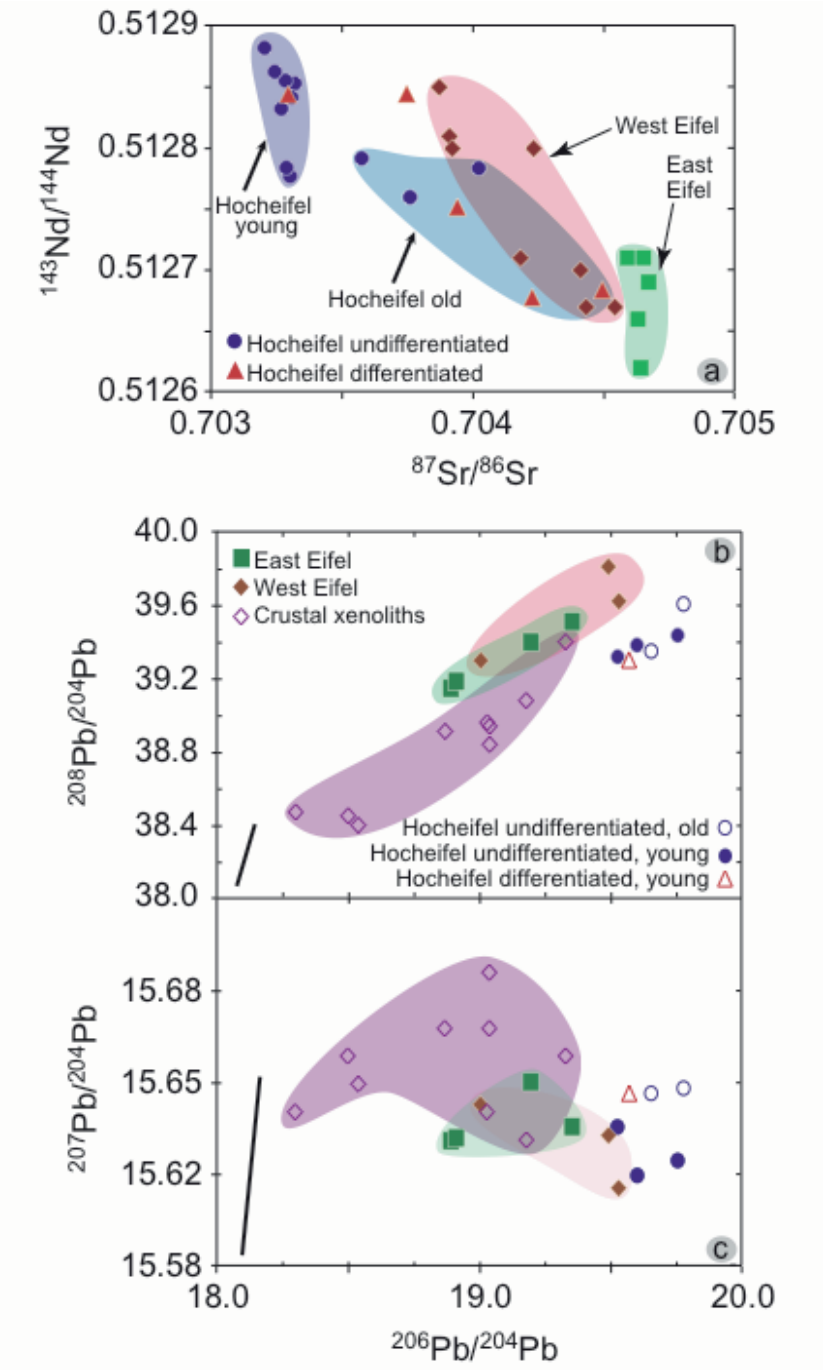
0.5129
0.5128
0.5127
0.5126
143Nd/144Nd
Hocheifel young
Hocheifel old
West Eifel
East Eifel
Hocheifel undifferentiated
Hocheifel differentiated
a
0.703
0.704
0.705
87Sr/86Sr
40.0
39.6
39.2
38.8
38.4
38.0
208Pb/204Pb
East Eifel
West Eifel
Crustal xenoliths
b
Hocheifel undifferentiated, old
Hocheifel undifferentiated, young
Hocheifel differentiated, young
15.68
15.65
15.62
15.58
207Pb/204Pb
c
18.0
19.0
20.0
206Pb/204Pb

Fig. 4. (previous page) Sr, Nd (a) and Pb (b, c) initial isotopic compositions of Tertiary Hocheifel volcanic rocks compared to lavas from the Quaternary East and West Eifel volcanic fields (Wörner et al. 1986; Wedepohl et al. 1994) and to Eifel crustal xenoliths (see Fig. 5 for references). Symbol size corresponds to 2σ analytical error. Black lines in Pb isotope spaces indicate the effects of instrumental mass fractionation of 0.5 ‰ per atomic mass unit. Previously published Pb isotope data on volcanic rocks from Cenozoic CEVP volcanic fields were obtained by conventional thermal-ionisation mass spectrometry. However, these conventional Pb data could be affected by instrumental fractionation. The true Pb isotope composition of any sample lies along a line plotted through the measured composition with similar length as and parallel to the instrumental mass fractionation trajectory represented by the black lines. In contrast, the Pb isotope data on the Hocheifel lavas presented in this paper are measured using the triple spike technique (see analytical methods) which allows to correct instrumental mass fractionation appropriately. Therefore, a comparison with previously published data could be biased by interlaboratory differences caused by insufficiently corrected instrumental mass fractionation effects

4 Discussion

4.1 Crustal contamination

Tertiary Hocheifel and Upper Rhine Graben volcanic rocks erupted through continental lithosphere which is ~50-60 km thick beneath the Rhenish Massif (Babuška and Plomerová 1992; Goes et al. 2000). Therefore, these rocks could potentially be contaminated by crustal material, and we evaluate this question in the following. While the lower crust beneath the Rhenish Massif is composed of mafic and felsic granulites (Stosch and Lugmair 1984, 1986; Rudnick and Goldstein 1990), the upper crust consists of Paleozoic sediments and volcanic rocks (e.g. Mengel et al. 1991). Green-core clinopyroxenes from Quaternary Eifel basanites and picrites show that these magmas have stagnated in the lower crust (Duda and Schmincke 1985; Sachs and Hansteen 2000). We have considered the geochemical and isotopic characteristics of the lower and upper crust to evaluate possible crustal contamination.

Positive Pb and negative Nb anomalies in normalized trace element patterns are geochemical tracers typical of continental crust and most island arc lavas, whereas complementary negative Pb and positive Nb anomalies are characteristic of nearly all ocean island basalts (OIB) and mid-ocean ridge basalts (MORB) as outlined by Hofmann et al. (1986) and Hofmann (1997). These authors showed that the compatibilities (or bulk partition coefficients) of Nb and Pb are similar to those of U and Ce, respectively,

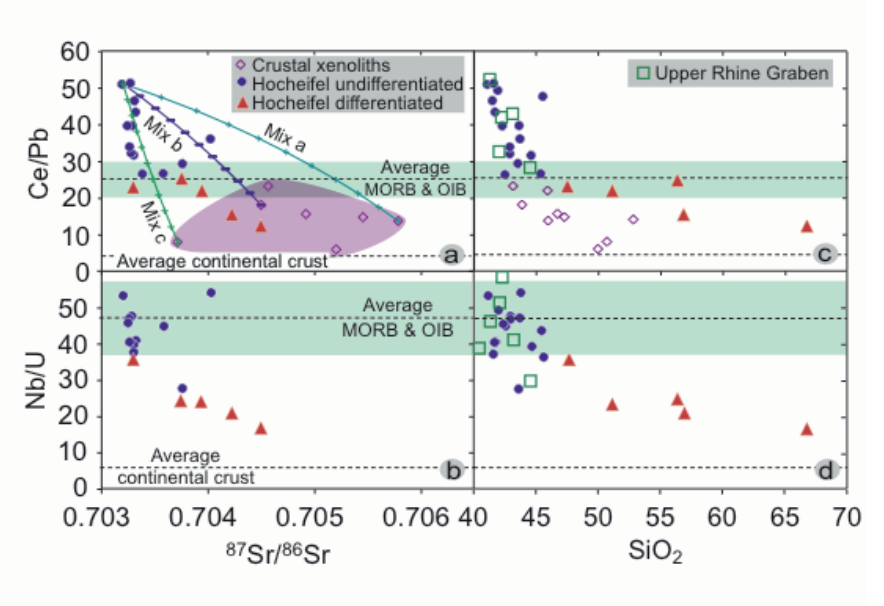
Crustal xenoliths
Hocheifel undifferentiated
Hocheifel differentiated
Upper Rhine Graben
Mix a
Mix b
Mix c
Average MORB & OIB
Average continental crust
Ce/Pb
Nb/U
a
b
c
d
$^{87}Sr/^{86}Sr$
SiO_2

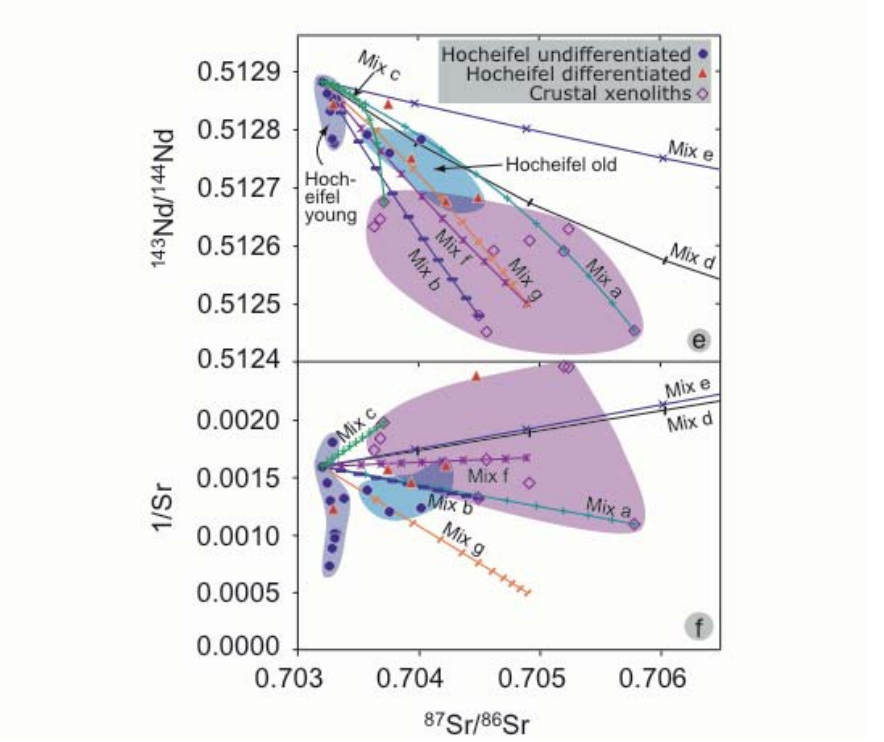
Hocheifel undifferentiated
Hocheifel differentiated
Crustal xenoliths
Mix c
Mix e
Mix d
Hocheifel old
Hoch-
eifel
young
Mix f
Mix b
Mix g
Mix a
$^{143}Nd/^{144}Nd$
1/Sr
e
f
$^{87}Sr/^{86}Sr$

Fig. 5. (previous page) Ce/Pb and Nb/U vs. $^{87}Sr/^{86}Sr$ (a, b) and SiO_2 concentrations (c, d) as well as $^{87}Sr/^{86}Sr$ vs. $^{143}Nd/^{144}Nd$ (e) and 1/Sr (f) of Hocheifel or Upper Rhine Graben volcanic rocks compared to average values of oceanic basalts and continental crust and Eifel crustal xenoliths. Data for the lower crustal granulites are from Stosch and Lugmair (1984), Loock et al. (1990), Rudnick and Goldstein (1990) and for the average continental crust and oceanic basalts from Rudnick and Gao (2003) and Hofmann et al. (1986), respectively. Lines in (a), (e) and (f) labeled "*Mix a*" to "*Mix e*" represent mixing curves between an undifferentiated Hocheifel sample and different types of possible crustal contaminants from the Eifel area: *Mix a, b, c* - lower crustal xenoliths (Stosch and Lugmair 1984), *Mix d* - upper crust (Devonian), *Mix e* - metamorphic basement (mica schist), *Mix f* - lower crustal granulite, *Mix g* - partial melt of lower crustal granulite (all Wörner et al. 1985). There are differing numbers of plotted samples because of incomplete geochemical data sets or unusual values which appear analytically not significant. Ticks of mixing curves indicate 10% mixing steps

during OIB/MORB-type mantle melting. Such mantle-derived melts typically have ratios of Nb/U ≈ 47 and Ce/Pb ≈ 25, which are much higher than typical (continental) crustal ratios of Nb/U ≈ 10 and Ce/Pb ≈ 4. These parameters can therefore be used as tracers of crustal contamination. The undifferentiated Hocheifel samples with low SiO_2 contents have low $^{87}Sr/^{86}Sr$ ratios but high Nb/U and Ce/Pb ratios similar to the "canonical" values of OIB and MORB (Hofmann et al. 1986) highlighted in Fig. 5. In contrast, the high-SiO_2 samples have high $^{87}Sr/^{86}Sr$ and low Nb/U and Ce/Pb ratios indicating significant crustal contamination. Figure 5 shows mixing calculations for several models of crustal contamination involving various lower-crustal xenoliths (Mix a, b, c; Stosch and Lugmair 1984), and estimates of local upper and lower crust (Wörner et al. 1985). The results show that the older group of Hocheifel lavas appears to have been contaminated by lower crustal material, with no involvement of upper crustal rocks. In contrast, the chemical and isotopic trends of the younger group of Hocheifel lavas (and by comparison also the Rhine Graben samples) have not been affected by significant crustal contamination.

4.2 Melting conditions

Most of the undifferentiated Hocheifel and Upper Rhine Graben lavas have geochemical and isotopic characteristics distinct from those of the continental crust indicating that they were formed by melting of a mantle source. We can estimate depth and melting conditions using the silica content and major element oxide ratios as for example CaO/Al_2O_3, CaO/TiO_2 and Al_2O_3/TiO_2 (Herzberg 1992). Experimental results of Kushiro (1996)

show that melting of a garnet lherzolite at about 25-30 kbar and 1425-1500°C can produce silica under-saturated (< 45%) magmas. The experimentally produced melts have CaO/Al_2O_3, CaO/TiO_2 and Al_2O_3/TiO_2 ratios similar to those of Hocheifel and Upper Rhine Graben lavas (Fig. 6). Thus, the Hocheifel and Upper Rhine Graben lavas appear to originate from melting of a garnet-bearing source at temperatures of ~1425–1500 °C and pressures of ~25-30 kbar, corresponding to a depth of about 75-90 km.

4.3 Melting model

The Hocheifel undifferentiated lavas show isotope compositions indicating derivation from a depleted magma source. However, melting of a depleted mantle does not produce trace element characteristics similar to those of the Hocheifel and Upper Rhine Graben lavas (Fig. 7a). The Hocheifel magma-source is more enriched than depleted mantle.

A first-order estimate of the source composition can be obtained by the simplifying assumption that the undifferentiated lavas represent simple equilibrium melts from a uniform source and by applying the inversion method outlined by Hofmann and Feigenson (1983). A plot of normalized La/Yb vs. La shows two separate strongly linear correlations for the Hocheifel and the Upper Rhine Graben lavas (Fig. 8a). In contrast, the La/Yb ratios are not correlated with Sr (or Nd, not shown) isotope ratios (Fig. 8b), indicating that the differences in LREE enrichment are not primarily caused by different source compositions but by differences in the degree of melting. In other words, although the isotopic differences clearly indicate source heterogeneity, the chemical heterogeneity in the source(s), e.g. La/Yb source ratios, is more likely reflected by the scatter than by the systematics (slope and intercept) of the correlation.

Fig. 6. (next page, top) Experimental results of Kushiro (1996) on melting of a garnet peridotite at high pressures and temperatures for major element oxide ratios. Green-coloured field corresponds to a pressure of 25 kbar and to temperatures of 1425-1500 °C, light orange-coloured field corresponds to a pressure of 30 kbar and to temperatures of 1460-1500 °C. Olive-coloured range represents overlap between both fields

Fig. 7. (n. p., bottom) Primitive mantle-normalized results of trace element modelling of Hocheifel and Upper Rhine Graben mantle sources. (a) Partial melting of average depleted mantle, taken from Salters and Stracke (2004). Percentages represent degrees of partial melting. (b) Melting of an enriched source generated by a 90:10 mixture (orange) of depleted mantle (blue) and a FOZO melt (pink). FOZO melt (sample RVV-360A) is taken from Lassiter et al. (2003). Modelling parameter, data sources and estimation procedure are described in the Appendix

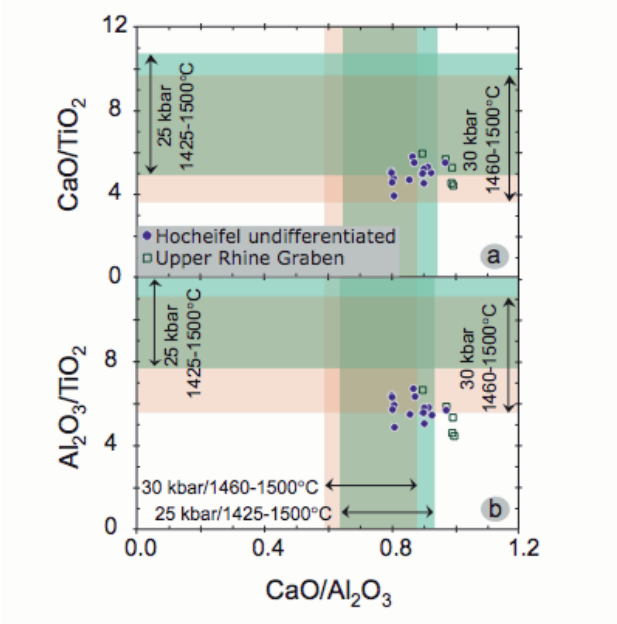
CaO/TiO2
Al2O3/TiO2
CaO/Al2O3
25 kbar
1425-1500°C
30 kbar
1460-1500°C
Hocheifel undifferentiated
Upper Rhine Graben
30 kbar/1460-1500°C
25 kbar/1425-1500°C
a
b

Fig. 6.

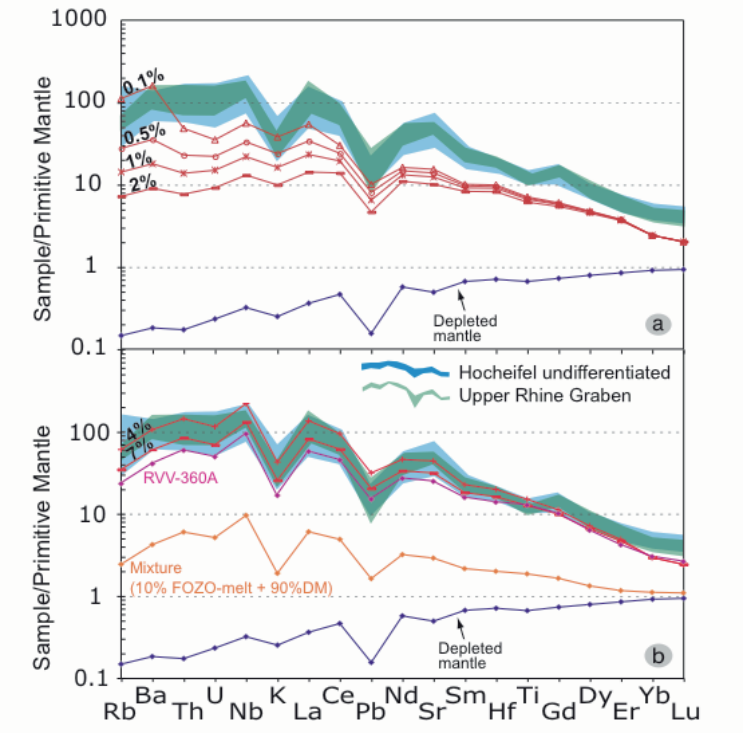
Sample/Primitive Mantle
0.1%
0.5%
1%
2%
Depleted mantle
Hocheifel undifferentiated
Upper Rhine Graben
RVV-360A
Mixture
(10% FOZO-melt + 90%DM)
Rb Ba Th U Nb K La Ce Pb Nd Sr Sm Hf Ti Gd Dy Er Yb Lu
a
b

Fig. 7.

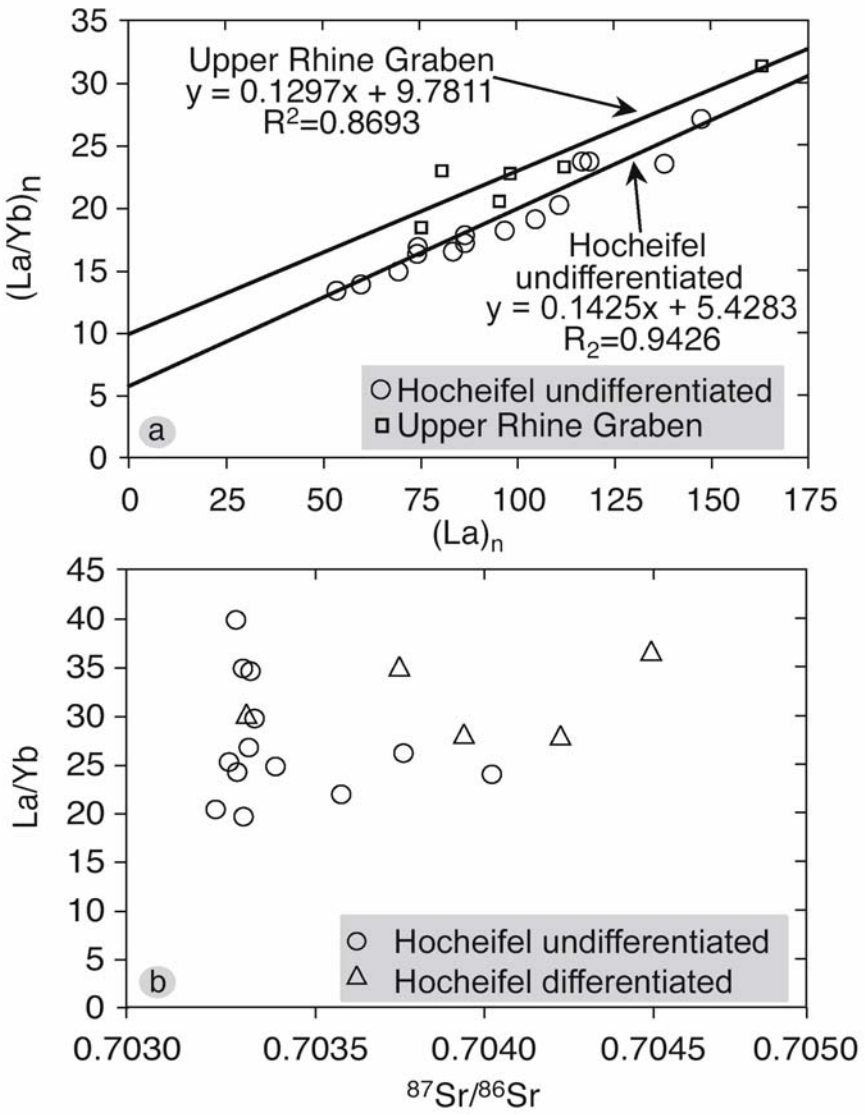

Fig. 8. Primitive mantle-normalized La/Yb vs La (a) of Hocheifel and Upper Rhine Graben undifferentiated lavas and calculated linear regressions. Primitive mantle values for normalization are from McDonough and Sun (1995). La/Yb vs. $^{87}Sr/^{86}Sr$ of Hocheifel undifferentiated and differentiated lavas (b)

The y-axis intercepts of the correlation lines can be used to infer minimum values for the $(La/Yb)_n$ ratios of the mantle source(s). If the partition coefficients remain constant as a function of melt fraction, then the rele-

vant equation for a series of melts formed from uniform sources by different degrees of equilibrium partial melting is (as given by e.g. Hofmann and Feigenson 1983)

$$\frac{C^{La}}{C^{Yb}} = \frac{D_0^{Yb} - \frac{\left(1-P^{Yb}\right)}{\left(1-P^{La}\right)} \cdot D_0^{La}}{C_0^{Yb}} \cdot C^{La} + \frac{\left(1-P^{Yb}\right)}{\left(1-P^{La}\right)} \cdot \frac{C_0^{La}}{C_0^{Yb}}$$

where C and C_0 are the concentrations in the melts and the source, respectively. D_0 and P are the bulk mineral-melt partition coefficients as defined by Shaw (1970), namely the sum of the mineral/melt coefficients weighted by the mineral proportions of the unmelted source (D_0) and of the proportions in which these phases enter the melt (P). In a C_{La}/C_{Yb} versus C_{La} plot, the intercept I is

$$I = \frac{\left(1-P^{Yb}\right)}{\left(1-P^{La}\right)} \cdot \frac{C_0^{La}}{C_0^{Yb}}$$

and

$$\frac{C_0^{La}}{C_0^{Yb}} = \frac{\left(1-P^{La}\right)}{\left(1-P^{Yb}\right)} \times I$$

corresponds to the minimum possible La/Yb ratio of the source, as long as $P^{Yb} \geq P^{La}$, as it is the case for mantle peridotite sources. The intercept of $(La/Yb)_n \approx 5$ therefore points to a strongly LREE enriched source with $(La/Yb)_n \geq 5$. However, such an enriched source would rapidly evolve isotopically and would not be a long-lasting feature. In general, metasomatic models are well suited to reconcile source compositions characterized by trace element enrichment coupled with isotopic depletion. Because of the isotopic similarity of the Hocheifel lavas with FOZO compositions as shown later, we develop a metasomatic model based on the chemical composition of observed FOZO lavas.

We can estimate compositions of an enriched source using the trace element concentrations of Raivavae lavas, which show FOZO-type characteristics (Stracke et al. 2005). We assume that a Raivavae-melt, rather than erupting directly at the surface, impregnates a depleted mantle at the base of the lithosphere and thus generates an enriched, young source. Mixing of 10% of a FOZO-melt (sample RVV 360A; Lassiter et al. 2003) and 90% of depleted mantle produces an enriched source with $(La/Yb)_n \sim 5$. The isotopic composition of this enriched, mixed source will be dominated by the FOZO melt, rather than the depleted mantle. Melting of this enriched

source at 4-7% produces trace element characteristics similar to those of the Hocheifel and Upper Rhine Graben lavas (Fig. 7b). The heavy REE (HREE) concentrations are lower in the modelled melts than in the Hocheifel and Upper Rhine Graben lavas. The higher HREE values of the Hocheifel and Upper Rhine Graben lavas may simply reflect the effect of fractional crystallization, which modifies the composition of the (modelled) primary partial melts.

It has been previously suggested that negative K and Ti anomalies can result from melting of an amphibole-bearing source (e.g. Späth et al. 2001). However, melting of an amphibole-bearing source produces features which are not present in the Hocheifel lavas, for example significant negative Ba anomalies (not shown). Also, if the negative K anomaly is caused by a residual K-phase, the bulk partition coefficient of K should be higher than those of the most highly incompatible elements. This buffering effect by a K-phase should result in a lower variability of K compared to these other elements (Hofmann 1988). However, the variability plot in Figure 9 shows that this is not the case. Therefore, we conclude that the negative K anomaly must be a source feature rather than being caused by partial melting effects with residual K-phases.

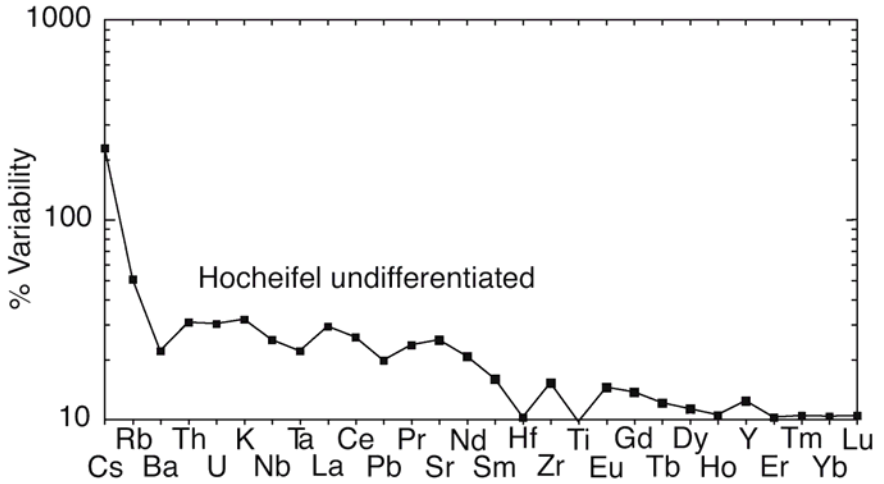

Fig. 9. Variability plot of element concentrations of undifferentiated Hocheifel lavas. Variability is defined as percent relative standard deviation (RSD): 100 x σ/average value

4.4 Relation to the Quaternary Eifel plume

Seismic tomography revealed the presence of a low *P*-wave velocity anomaly below the Quaternary West and East Eifel volcanic fields (Ritter et al. 2000, Ritter et al. 2001, Ritter this volume). This anomaly extends to at least 400 km depth, is attributed to an excess temperature of about 150-200 K and is interpreted to represent a mantle plume causing the Quaternary Eifel volcanism. In order to evaluate whether the Tertiary Hocheifel lavas contain such a mantle plume component, we compare the Hocheifel isotope compositions of the crustally not contaminated samples with those of the Quaternary Eifel samples. Figure 4a shows that at a given $^{143}Nd/^{144}Nd$ the Hocheifel lavas are less radiogenic in $^{87}Sr/^{86}Sr$. In Pb isotope spaces (Fig. 4b, c), at a given $^{208}Pb/^{204}Pb$ and $^{207}Pb/^{204}Pb$, the Hocheifel is more radiogenic in $^{206}Pb/^{204}Pb$ compared to the Quaternary Eifel lavas. Also, the Hocheifel and the Quaternary Eifel form subparallel trends in a $^{208}Pb/^{204}Pb$ vs. $^{206}Pb/^{204}Pb$ diagram (Fig. 4b). Thus, although lavas from both, Tertiary and Quaternary volcanic fields show similar trace element patterns (Fig. 3), the isotope compositions indicate that the Quaternary and Tertiary Eifel volcanism tap distinct sources. However, we know several well-established mantle plumes with internal isotopic heterogeneity (e.g. Abouchami et al. 2005). Thus differences in isotope patterns alone do not furnish sufficient evidence to rule out that the Tertiary Hocheifel lavas are plume-type precursors of the Quaternary Eifel plume.

4.5 Mantle source

Figure 5 presents isotopic and elemental evidence that the undifferentiated and differentiated lavas of the older phase of Hocheifel activity are contaminated by crustal material. Therefore, these samples are not suitable for characterization of source components and we focus on the uncontaminated younger phase of volcanism. In $^{87}Sr/^{86}Sr$ vs. $^{143}Nd/^{144}Nd$ space, contaminated and uncontaminated samples can clearly be distinguished (Fig. 5e). In Pb isotope space, we cannot make this distinction because of incomplete data set and a general similarity in Pb isotope compositions (Fig. 4b, c). In all Sr, Nd and Pb isotope diagrams (Fig. 10a-c) the lavas of the younger phase overlap with or plot close to the fields of FOZO (FOcal ZOne), HIMU (high-μ) and LVC (Low Velocity Composition). FOZO was initially introduced by Hart et al. (1992) who suggested that it represents a widespread lower mantle component. However, it was recently redefined by Stracke et al. (2005) as a component occurring in the entire mantle. HIMU refers to a mantle component characterized by high time-integrated

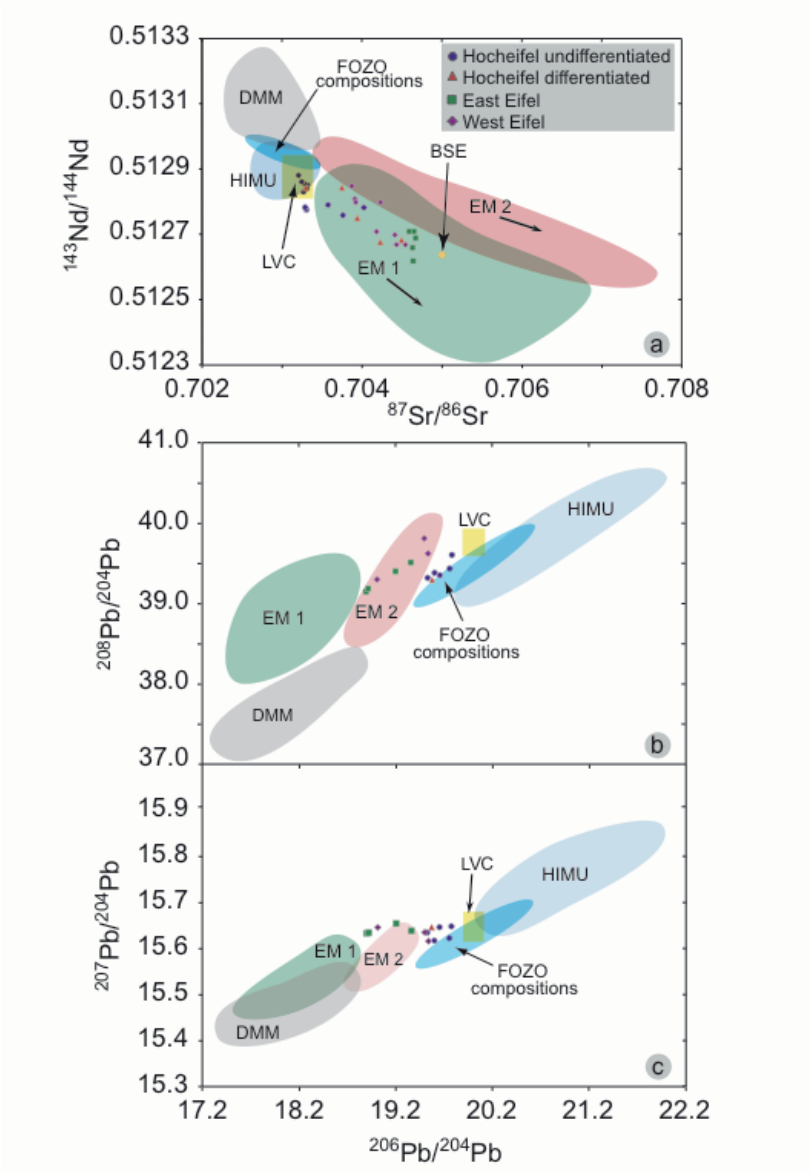

Fig. 10. Sr vs. Nd (a) and Pb vs. Pb (b, c) isotope compositions of the Hocheifel lavas compared to global mantle reservoirs. Data for *FOZO* (Focal Zone) and *LVC* (Low Velocity Component) are from Stracke et al. (2005) and Hoernle et al. (1995), respectively, for *DMM* (Depleted MORB Mantle), *EM1* (Enriched Mantle 1), *EM2* (Enriched mantle 2), *HIMU* (High $^{238}U/^{204}Pb$) reservoirs from GEOROC (http://georoc.mpch-mainz.gwdg.de) and PeTB (http://earthref.org/GERM) databases, and for *BSE* (Bulk Silicate Earth) from Evensen et al. (1978)

$^{238}U/^{204}Pb$ ratios (Zindler and Hart 1986). LVC was described by Hoernle et al. (1995) as an upper mantle reservoir with HIMU-type characteristics which is ubiquitous beneath eastern Atlantic, Central Europe and the western Mediterranean. However, Stracke et al. (2005) showed that it closely resembles the (redefined) FOZO component, but differs significantly from a "real" HIMU as originally defined from basalts of St. Helena and the Cook-Austral Islands. In terms of Pb isotope compositions the Hocheifel lavas resemble more FOZO-LVC rather than HIMU. Also, if the Hocheifel data array in $^{208}Pb/^{204}Pb$ vs. $^{206}Pb/^{204}Pb$ space is interpreted to result from mixing, the subparallel arrangement of HIMU and Hocheifel array excludes HIMU involvement. We therefore conclude that the Hocheifel volcanic rocks most likely originate from a FOZO or LVC-type source. Since this mantle component may also be common in the upper mantle, this conclusion cannot be used to argue either for or against a plume origin of the Hocheifel volcanism.

4.6 Plate reconstruction

Evidence whether the Eocene Hocheifel volcanism is genetically related to the Quaternary Eifel plume or not can be derived from plate reconstruction modelling. In the Eifel, Quaternary and Eocene volcanism occur at similar geographic locations, at about 50.5°N latitude and 7°E longitude. In order to estimate the geographic position of the Eifel at the time of the Eocene volcanic activity at about 40 Ma we modelled the movement of the Eurasian plate using the UNAVCO Plate Motion Calculator (http://sps.unavco.org/dxdt/model). Most of the tested models (e.g. GSRM v1.2, REVEL 2000, APKIM2000.0, ITRF2000, NUVEL 1A) yield consistent results indicating that the Eurasian plate moves with a speed of 23.7 to 25.8 mm/yr and an azimuth between 49.9° and 53.9° clockwise from north, i.e., towards the northeast. Provided that there were no significant changes in speed and azimuth of the Eurasian plate over the last ~40 m.y., the Eifel was located ca. 950-1050 km southwest from its recent position. Thus, considering a mantle-stationary Eifel plume, the Eocene Hocheifel activity cannot represent the Eifel plume precursor volcanism. The projected paleo-location of the Hocheifel at ~40 Ma approximately coincides with the present-day location of the recent mantle plume beneath the French Massif Central (Downes 1984; Granet et al. 1995, Barth et al. this volume) which is situated about 1000 km south to the Eifel. The isotope data on Massif Central (Chauvel et al. 1984; Downes 1984; Briot et al. 1991) overlap with Hocheifel lavas in Pb isotope spaces, however, this is not the case in the $^{87}Sr/^{86}Sr$ vs. $^{143}Nd/^{144}Nd$ diagram (not shown). Since

there is no consistent isotopic overlap, a genetic relation between the Massif Central plume and the Hocheifel sources cannot be confirmed.

5 Conclusions

The Tertiary Hocheifel and Upper Rhine Graben samples represent relatively undifferentiated (basanite, basalt) and to a lesser extent differentiated (hawaiite, shoshonite, latite, trachyte) compositions. The magmas were produced by partial melting of a garnet peridotite source at pressures and temperatures corresponding to depths of about 75 to 90 km.

Primitive mantle-normalized trace element patterns of the undifferentiated samples show negative Pb, K and Ti and positive Nb-Ta anomalies. The Nb-Ta and Pb anomalies are typical of OIB and MORB. The negative K anomaly is likely to be a source property rather than being caused by melting in the presence of residual amphibole.

The differentiated and a few basanitic magmas have been affected by crustal contamination, whereas the majority of the basanitic/basaltic magmas do not show significant influence from crustal material. All the crustally contaminated Hocheifel undifferentiated lavas belong to the older age group of Hocheifel volcanism. In contrast, the younger age group is represented by undifferentiated magmas not contaminated by crustal material, thus indicating a change in petrogenetic regime with time.

Trace element modelling indicates that the Hocheifel and Upper Rhine Graben basanites and basalts were produced by low degree melting (4-7%) of a LREE-enriched source, which may have been produced by infiltration of a FOZO-type melt into a depleted mantle region such as the base of the lithosphere.

Sr, Nd and Pb isotope compositions suggest that the source of the Hocheifel magmas has LVC (Low Velocity Composition) or FOZO (Focal Zone) characteristics. However, this information cannot be used to argue either for or against a plume origin.

Plate reconstruction modelling shows that the Hocheifel volcanic field at its time of activity ca. 40 m.y. ago was located ~1000 km southwest relative to its recent position. Therefore, the Hocheifel volcanism cannot be related to the Quaternary Eifel plume, and the interpretation of the Hocheifel volcanism as precursor activity of the recent plume is not plausible.

Integrating evidence from geochronology, geochemistry, isotope compositions and plate reconstruction, we suggest that the Tertiary Hocheifel volcanism is caused by pre-rift extensional decompression related to Rhine

Graben taphrogenetic processes during the Middle to Upper Eocene. In the Eifel, the spatial coincidence of Tertiary taphrogenesis-related and Quaternary plume-related volcanism may therefore be coincidental.

Acknowledgements

We thank M. Thirlwall (London) for measuring the XRF data, K.-P. Jochum and B. Stoll for helping with LA-ICP-MS analyses, W. Abouchami and S.J.G. Galer (all Mainz) for help with lab work and Pb data reduction. K. Haase (Kiel) provided a thorough and constructive review. P. Koppenhöfer helped with drawing the figures. This project was funded by the Deutsche Forschungsgemeinschaft (DFG, Bonn) via grant Me 1155/4-1 to D.F.M. and by the Landessammlung für Naturkunde Rheinland-Pfalz/Naturhistorisches Museum at Mainz, Germany.

References

Abouchami W, Hofmann AW, Galer SJG, Frey FA, Eisele J, Feigenson M (2005) Lead isotopes reveal bilateral asymmetry and vertical continuity in the Hawaiian mantle plume. Nature 434:851-856

Babuška V, Plomerová J (1992) The lithosphere in central Europe - seismological and petrological aspects. Tectonophysics 207:141-163

Bogaard PJF, Wörner G (2003) Petrogenesis of basanitic to tholeiitic volcanic rocks from the Miocene Vogelsberg, Central Germany. J Petrol 44(3):569-602

Briot D, Cantagrel JM, Dupuy C, Harmon RS (1991) Geochemical evolution in crustal magma reservoirs: Trace element and Sr-Nd-O isotopic variations in two continental intraplate series at Monts Dore, Massif Central, France. Chem Geol 89:281-303

Chauvel C, Jahn B (1984) Nd-Sr isotopes and REE geochemistry of alkali basalts from the Massif Central, France. Geochim Cosmochim Acta 48:93-110

Downes H (1984) Sr and Nd isotope geochemistry of coexisting alkaline magma series, Cantal, Massif Central, France, Earth Planet Sci Lett 69:321-334

Duda Q, Schmincke HU (1985) Polybaric differentiation of alkali basaltic magmas: evidence from green-core clinopyroxenes. Contrib Mineral Petrol 91:340-353

Evensen NM, Hamilton PJ, O'Nions RK (1978) Rare-earth abundances in chondritic meteorites. Geochim Cosmochim Acta 42:119-1212

Galer SJG (1999) Optimal double and triple spiking for high precision lead isotopic measurements. Chem Geol 157:255-274

Goes S, Govers R, Vacher P (2000) Shallow mantle temperatures under Europe from *P*- and *S*-wave tomography. J Geophys Res 105:11153-11169

Granet M, Wilson M, Achauer U (1995) Imaging a mantle plume beneath the French Massif Central, Earth Planet.Sci Lett 136:281-296

Haase KM, Goldschmidt B, Garbe-Schönberg CD (2004) Petrogenesis of Tertiary continental intraplate lavas from the Westerwald region, Germany. J Petrol. 45(5):883-905

Hart S, Hauri E, Oschmann LA, Whitehead JA (1992) Mantle plumes and entrainment: isotopic evidence. Science 256:517-520

Herzberg C (1992) Depth and degree of melting of komatiites. J Geophys Res 97: 4521-4540

Hoernle K, Zhang YS, Graham D (1995) Seismic and geochemical evidence for large-scale mantle upwelling beneath the eastern Atlantic and western and central Europe. Nature 374:34-39

Hofmann AW (1988) Chemical differentiation of the Earth: the relationship between mantle, continental crust and oceanic crust. Earth Planet Sci Lett 90:297-314

Hofmann AW (1997) Mantle geochemistry: the message from oceanic volcanism. Nature 385:219-229

Hofmann AW, Feigenson MD (1983) Case studies on the origin of basalt I. Theory and reassessment of Grenada basalts. Contrib Mineral Petrol 84:382-389

Hofmann AW, Jochum KP, Seufert M, White MW (1986) Nb and Pb in oceanic basalts: new constraints on mantle evolution. Earth Planet Sci Lett 79:33-45

Jochum KP, Hofmann AW, Ito E, Seufert HM, White WM (1983) K, U and Th in mid-ocean ridge basalt glasses and heat production, K/U and Rb in the mantle. Nature 306:431-436

Jochum KP, Dingwell DB, Rocholl A, Stoll B, Hofmann AW (2000) The preparation and preliminary characterisation of eight geological MPI-DING reference glasses for in-situ microanalyses. Geostand Newslett 24(1):87-133

Kushiro I (1996) Partial melting of a fertile mantle peridotite at high pressures: An experimental study using aggregates of diamond. In: Earth Processes: Reading the Isotopic Code, American Geophysical Union, Monograph 95:109-122

Lassiter JC, Blichert-Toft J, Hauri EH, Barsczus HG (2003) Isotope and trace element variations in lavas from Raivavae and Rapa, Cook-Austral islands; constraints on the nature of HIMU- and EM-mantle and the origin of mid-plate volcanism in French Polynesia. Chem Geol 202:115-138

Le Maitre RW, Bateman A, Dudek A et al. (1989) A classification of igneous rocks and glossary of terms. Blackwell, Oxford etc.

Loock G, Stosch HG, Seck HA (1990) Granulite facies lower crustal xenoliths from the Eifel, West Germany: petrological and geochemical aspects. Contrib Mineral Petrol 105:25-41

Lugmair GW, Galer SJG (1992) Age and isotopic relationship among the angrites Lewis Cliff 86010 and Angora dos Reis. Geochim Cosmochim Acta 56:1673-1694

McDonough WF, Sun SS (1995) The composition of the Earth. Chem Geol 120:223-253

Mengel K, Sachs PM, Stosch HG, Wörner G, Loock G (1991) Crustal xenoliths from Cenozoic volcanic fields of Western Germany: Implications for structure and composition of the crust. Tectonophysics 195:271-289

Mertes H, Schmincke HU (1985) Mafic potassic lavas of the Quaternary West Eifel field (Western Germany) I. Major and trace elements. Contrib Mineral Petrol 89:330-345

Middlemost E (1989) Iron oxidation ratios, norms and the classification of volcanic rocks. Chem Geol 77:19-26

Ritter JRR, Achauer U, Christensen UR and the Eifel Plume Team (2000) The teleseismic tomography experiment in the Eifel region, Central Europe: design and first results. Seism Res Lett 71: 437-443

Ritter JRR, Jordan M, Christensen UR, Achauer U (2001) A mantle plume below the Eifel volcanic fields, Germany. Earth and Planet Sci Lett 186:7-14

Rudnick RL, Gao S (2003) Composition of the continental crust. In: Rudnick RL (ed) The crust, Treatise on Geochemistry, vol 3, Elsevier, pp 1-64

Rudnick RL, Goldstein SL (1990) The Pb isotopic compositions of lower crustal xenoliths and the evolution of lower crustal Pb. Earth Planet Sci Lett 98:192-207

Sachs PM, Hansteen TH (2000) Pleistocene underplating and metasomatism of the lower continental crust: a xenolith study. J Petrol 41:331-356

Salters VJM, Stracke A (2004) Composition of the depleted mantle. Geochem Geophys Geosyst 5(5), Q05004, DOI:10.1029/2003GC000597

Shaw DM (1970) Trace element fractionation during anatexis. Geochim Cosmochim Acta 34:237-243

Späth A, Le Roex AP, Opiyo-Akech N (2001) Plume-lithosphere interaction and the origin of continental rift-related alkaline volcanism-the Chyulu Hills Volcanic Province, Southern Kenya. J Petrol 42(4):765-787

Stosch HG, Lugmair GW (1984) Evolution of the lower continental crust: granulite facies xenoliths from the Eifel, West Germany. Nature 311:368-370

Stosch HG, Lugmair GW (1986) Trace element and Sr and Nd isotope geochemistry of peridotite xenoliths from the Eifel (West Germany) and their bearing on the evolution of the subcontinental lithosphere. Earth Planet Sci Lett 80:281-298

Stracke A, Hofmann AW, Hart SR (2005) FOZO, HIMU and the rest of the mantle zoo. Geochem Geophys Geosyst 6(5), Q05007, DOI:10.1029/2004GC000824

Thirlwall MF, Singer BS, Marriner GF (2000) ^{40}Ar-^{39}Ar ages and geochemistry of the basaltic shield stage of Tenerife, Canary Islands, Spain. J Volcanol Geotherm Res 103:247-297

Weaver BL (1991) Trace element evidence for the origin of ocean-island basalts. Geology 19:123-126

Wedepohl KH, Gohn E, Hartmann G (1994) Cenozoic alkali basaltic magmas of western Germany and their products of differentiation. Contrib Mineral Petrol 115:253-278

Wörner G, Staudingel H, Zindler A (1985) Isotopic constraints on open system evolution of the Laacher See magma chamber (Eifel, W-Germany). Earth Planet Sci Lett 75:37-49

Wörner G, Zindler A, Staudingel H, Schmincke HU (1986) Sr, Nd, and Pb isotope geochemistry of Tertiary and Quaternary alkaline volcanics from West Germany. Earth Planet Sci Lett 79:107-119

Zindler A, Hart S (1986) Chemical geodynamics. Ann Rev Earth Planet Sci 14:493-571

Appendix: Modelling parameter used for melt modelling in section 4.3

Partition coefficients and source compositions

	D_{Gt}	D_{Cpx}	D_{Opx}	D_{Ol}	Bulk D_0	Bulk P	Depleted mantle	RVV-360A
Rb	0.0002	0.0004	0.0002	0.0003	0.00032	0.00047	0.088	14
Ba	0.00007	0.0004	0.000006	0.000005	0.00014	0.00053	1.2	270
Th	0.009	0.00566	0.002	0.00005	0.00256	0.00761	0.0137	4.71
U	0.028	0.0113	0.002	0.00038	0.00560	0.01748	0.0047	1.01
Nb	0.015	0.01	0.004	0.0005	0.00474	0.01312	0.21	62
K					0.00560	0.01748	60	4067.49
La	0.0007	0.015	0.004	0.0005	0.00572	0.01781	0.234	37.4
Ce	0.017	0.038	0.004	0.0005	0.01436	0.05006	0.772	76.1
Pb					0.01436	0.05006	0.0232	2.28
Nd	0.064	0.0884	0.012	0.00042	0.03444	0.11827	0.713	33.9
Sr	0.0007	0.091	0.0007	0.00004	0.03105	0.11896	9.8	497
Sm	0.23	0.1509	0.02	0.0011	0.06499	0.21783	0.27	6.47
Hf	0.4	0.14	0.024	0.0011	0.07010	0.22370	0.199	3.95
Ti	0.6	0.14	0.086	0.015	0.09243	0.22001	798	15467.1
Gd	1.2	0.16	0.065	0.0011	0.12018	0.33381	0.395	5.51
Dy	2	0.17	0.065	0.0027	0.16443	0.45099	0.531	4.29
Er	3	0.18	0.065	0.013	0.22329	0.59460	0.371	1.86
Yb	5.5	0.25	0.08	0.02	0.37700	1.00430	0.401	1.35
Lu	7	0.276	0.12	0.02	0.46404	1.21376	0.063	0.18

Mineral modes				
Source	0.05	0.34	0.08	0.53
Partial melt	0.13	1.31	-0.49	0.05

The equation of Shaw (1970) for non-modal batch melting was used:
$C_L/C_0 = 1/(D_0+F*(1-P))$
where
C_L = trace element concentration in the extracted melt
C_0 = trace element concentration in the solid
F = degree of melting
D_0 = bulk partition coefficient for the minerals in the original solid ($D_i=x_1*D^i_1+x_2*D^i_2+\ldots$)
D^i_1 = mineral/melt partition coefficient for element i and mineral 1 ($x_1+x_2+\ldots=1$)
P = bulk partition coefficient for the minerals entering the melt ($P=p_1*D^i_1+p_2*D^i_2+\ldots$)
p_1 = fraction of the mineral 1 entering the melt

Model parameters (partition coefficients, mineral modes of source and partial melt, composition of depleted mantle) are from Salters and Stracke (2004), with exception of the partition coefficients for Pb and K. It has been suggested that Pb behaves similarly to Ce (Hofmann et al. 1986) and K similarly to U (Jochum et al. 1983) during melting processes. Therefore, for Pb and K we used the bulk partition coefficients of Ce and U, respectively. Data on FOZO-type lavas (Raivavae) are from Lassiter et al. (2003). We used the composition of sample RVV 360A which rather than erupting at the surface infiltrates the depleted mantle region at the base of the lithosphere. 10% of this melt are added to 90% depleted peridotite to generate the enriched, mixed source. Melt fractions of 4 to 7% of this source produce trace element characteristics similar to those of the Hocheifel and Upper Rhine Graben lavas (Fig. 7b). The composition of the primitive mantle is from McDonough and Sun (1995).

The Quaternary Volcanic Fields of the East and West Eifel (Germany)

Hans-Ulrich Schmincke

Lisch 2a, 24326 Ascheberg, hschmincke@ifm-geomar.de

Abstract

The two Quaternary volcanic fields in the Eifel region of Germany (West Eifel Volcanic Field - WEVF; East Eifel Volcanic Field - EEVF) resemble each other in their temporal, spatial, structural and compositional evolution but also differ significantly in several parameters. Most volcanoes in both fields erupted foiditic potassic (K_2O/Na_2O >1) lavas with phenocrystic phlogopite and microlitic leucite being mineralogically most diagnostic as are the corresponding major and trace element characteristics. Volcanoes are dominantly scoria cones, of which about half erupted lava flows, and maars, their formation being partly governed by magma-water interaction. Phreatomagmatic eruptive activity reflecting variable degrees of magma/water mixing occurred during the growth of many scoria cones especially during the initial growth stage.

Volcanic activity in the WEVF started slowly less than 700 ka ago after the Rhenish shield had begun an accelerated phase of uplift with highly silica-undersaturated foiditic magmas near Ormont at the border with Belgium in the NW and peaked in the central part of the field between ca. 600 and 450 ka. Following a subsequent lull in activity, volcanism migrated to the SE, the frequency of volcano formation increasing during the past <100 ka, the youngest eruption having occurred at 11 ka. Most lavas are mafic with rare intermediate and local small highly evolved centers in the eastern central part of the field. Magma fractionation at high pressure, such as near the crust/mantle boundary, is reflected in common green-core cli-

nopyroxene phenocrysts in many types of lavas - in both fields - and high temperature overprinting, partial melting and metasomatism of lower/middle crustal granulites. Very mafic and much less silica-undersaturated sodic olivine nephelinites and relatively LILE-poor sodic basanites with groundmass plagioclase, both being distinctly less isotopically enriched than the foidites, erupted in the southeastern WEVF during the past <50 ka side-by-side with foidites.

Distinct suites of ultramafic xenoliths, each with many variants, are recognized: (1) depleted and enriched peridotites (lherzolites, dunites, harzburgites and wehrlites) comprising several groups (highly deformed porphyroclastic xenoliths in the periphery and high-temperature recrystallized anhydrous types and metasomatized types near the center) and (2) cumulate-textured hornblendites, glimmerites and pyroxenites. The fact that clastic maar deposits are especially rich in peridotite and other ultramafic xenoliths is explained by xenolith-rich mafic volatile-rich magmas rising from greater depth coupled with high expulsion speeds during phreatomagmatic explosions. The near-absence of peridotite xenoliths and the abundance of clinopyroxene-, phlogopite- and amphibole-rich ultramafic cumulates containing remnants of peridotites in maar deposits in the southeastern part of the WEVF is probably due to more efficient filtering and dissolution of mantle peridotite fragments in subcrustal to lower crustal magma reservoirs in which the cumulates formed.

Volcanic activity in the EEVF started about 460 ka ago or slightly earlier. As in the WEVF, early activity in the western part of the EEVF is dominated by mafic foiditic lava compositions. A prominent phonolitic complex in its center (Rieden, ca. 430-360 ka) is represented by intrusions, domes, ignimbrites, and widespread fallout tephra. A younger eastern subfield beginning with the partly trachytic highly evolved phonolitic Wehr crater complex at about 215 ka ago was followed soon by the emplacement of potassic basanitic to tephritic scoria cones chiefly in the Neuwied tectonic basin. Volcanism extended east as far as Rhine River and south to close to the Moselle. Most EEVF basanite volcanoes formed ca. 215-190 ka ago. These lavas differ from the young sodic basanites in the WEVF by higher concentrations of Al, K, Ba, Rb and lower concentrations of Fe, Na, P, Sr, LREE, Zr/Nb ratios exceeding 3 for a given Mg#. The EEVF basanites are also less mafic and commonly evolved to early-erupted tephrite, volcanic edifices being generally larger than those in the WEVF. Volcanic activity was minor until 12,900 years BP when the phonolitic Laacher See Volcano (LSV) erupted >6 km^3 magma, mostly during a few days, resulting in a Plinian fallout tephra layer recognized from southern Sweden to northern Italy. This is the most important very late Pleistocene stratigraphic marker bed in Central Europe. The partially evacuated

strongly zoned reservoir was located ca. 5-8 km beneath the surface. The eruption, like many scoria cones in both fields, started phreatomagmatically. Rhine River was dammed during the eruption by massive tephra accumulation, forming a 20 m deep lake. The uncontrolled rupture of the tephra dam generated flood waves recognizable in deposits at least as far north as Bonn. The sulfur-rich LSV magma coupled with eruption columns at least 25 km high probably impacted climate significantly in the northern hemisphere.

The degree of melting based on CaO/Al_2O_3 ratios is lowest in the melilite nephelinites that abound in the WEVF but are rare in the EEVF (resembling EM 1) and highest for the basanites in both fields, possibly also reflected in their higher eruptive volume and more common differentiation to intermediate lavas. At least three compositionally distinct mantle domains can be distinguished from each other in the Eifel fields based on available radiogenic Sr-, Nd-, and Pb- ratios of mafic lavas and many incompatible element concentrations and ratios. The dominant foidites in both fields and especially the potassic EEVF basanites are the most radiogenic magmas compared to other Cenozoic volcanic fields in central Europe. These magmas may have been derived from the base of the metasomatized lithosphere. The spatial overlap of the highly alkalic Quaternary magmas, erupted during the early/main stages in both fields, with the southern part of the Eocene Hocheifel field suggests that the geologically young metasomatism that may have affected the base of the lithosphere could have largely resulted from Tertiary magmatic activity. The lack of indicators for metasomatism in the much more widespread Tertiary Eifel lavas is difficult to explain otherwise. The much less radiogenic young basanites and even less radiogenic olivine nephelinites of the WEVF fall close to the broad field of Tertiary lavas in central Europe and may have been derived from a similar possibly asthenospheric mantle source.

In the WEVF, a foiditic magma source was reactivated during the past ca. 100 ka or less. Simultaneously, magmas from a new compositional mantle domain supplied sodic basanites and olivine nephelinites to the surface during the past about 50 ka erupting in the southeastern part of the field side-by-side with foiditic lavas. The two compositionally distinct but spatially adjacent melting domains were probably stacked vertically. In the EEVF, the compositional mantle domain supplying foiditic magmas to the surface terminated between about 350 and 215 ka ago, after which time compositionally different less foiditic but more potassic and enriched basanites and minor tephrites erupted in the eastern subfield, locally evolving to voluminous phonolite. The youngest volcano in the Eifel, Ulmener Maar of extremely LILE-enriched intermediate composition, formed about 11,000 a BP, 2000 years after LSV erupted.

Mantle source regions beneath the fields are chemically distinct on different scales, larger domains differing in isotopic and smaller-scale domains in trace element ratios. Compositionally contrasting, but closely spaced, compositional domains in the mantle a few km across – representing heterogeneous compositions within, and/or differential rise of portions of, a mantle diapir - were activated successively with time or even released magma nearly simultaneously. A prominent example is the practically synchronous eruption of the ol-nephelinitic Mosenberg center followed immediately by the nearby melilite nephelinitic Meerfelder Maar, the largest in the Eifel. An example on a larger scale is the juxtaposition of the leucitite and plagioclase-free phonolitic Rieden and the adjacent Wehr-Laacher See basanite/plagioclase-bearing phonolite systems.

Volcano field analysis shows that magma mass eruption rates increased toward the center of both fields, coupled with an increasing degree of differentiation. The central parts of the fields show the highest erupted volumes and the highest flux of magmatic gases. These and other parameters are interpreted to mirror the central part of one or more magma collection zones in the upper mantle/Moho at least 30 (EEVF) to 50 km (WEVF) in length resulting in magma focusing in the center of both fields. Fields are dominantly oriented NW-SE, reflecting lithosphere cracking in response to the present lithospheric SW-NE-oriented tensional stress field north of the Alps which however was probably strongly enhanced by the similarly-oriented Paleozoic stress field. Cracks acting as magma pathways thus formed most easily perpendicular to the minimum compressional principal stress (σ_3) in a NW-SE direction with σ_1 (the maximum compressional principal stress) being vertical. Magma collection zones underlying both fields probably extended significantly laterally beyond the surface area of the volcanic fields because the most mafic magmas were erupted in the periphery of the fields. Magmas generated beyond the surface fields may have only risen as far as the crust/mantle transition zone in view of the abundant evidence for high-pressure fractionation at and below the crust/mantle boundary as well as surface degassing extending beyond the fields. Lithosphere cracking extended to the southeast during a lull in activity in the WEVF (between ca. 450-100 ka) as reflected in a migration of melt supply and surface volcanic activity. Migration of surface volcanism in the EEVF from W to ESE also occurred during a pause in surface volcanism between 350 and 215 ka and was associated with activation of a compositionally distinct melting domain. Both fields developed on either side, and in the hinge zones, of the area of maximum Quaternary uplift, magmas in the WEVF and western EEVF rising in uplifted parts of the Rhenish Massif while the eastern EEVF lavas erupted in the downfaulted Neuwied basin, part of the Rhine Rift structure.

Major Paleozoic structural discontinuities in both fields such as the Eifel N-S graben zone in the western and the Siegen thrust in the eastern field, and Tertiary faults in the Neuwied Basin, appear to have caused deviations in dike orientations and regionally significant boundaries in magma composition and xenolith suites. This suggests that some upper crustal fractures (zones of weakness) extend significantly downward into the lithosphere.

The total mass of magma supplied to the base of the crust and crustal reservoirs (estimated to have been between 300 and 500 km^3) – and possibly rates of magma risen from the melting anomalies – was probably higher in the EEVF than in the WEVF. This is indicated by the volume of parent magmas that have to be postulated to generate the relatively voluminous highly evolved phonolite centers and possibly also by the much higher CO_2-flux in the EEVF provided present flux rates are representative. Magma supply to the crust – and possibly magma production – was strongly focused beneath several centers in the EEVF contrasting with more diffuse magma-leaking in the WEVF, a more typical intraplate volcanic field. It is uncertain, however, whether magma focusing in the EEVF was entirely due to higher magma supply from the mantle – possibly resulting from higher degrees of partial melting – or to lower rates of lithosphere extension allowing for higher crack and dike coalescence (Takada 1994) and thus magma focusing. Volcanic activity in the Eifel is presently dormant but not extinct judging from the past temporal pattern of eruptions. Future volcanoes are likely to grow in the southeastern part of both Eifel fields.

The absence of a shear-wave anomaly between 170 and 240 km in the seismic low velocity anomaly in the mantle (Eifel Plume) may be due to separation of an upper diapir ("blob") providing thermal energy and melt to the basal lithosphere. The upper part (30-140 km) of the seismic low velocity anomaly in the mantle has a diameter of more than 100 km and thus extends significantly beyond both volcanic fields. This upper part may correspond to the magma migration or collection zone culminating between about 37 and 30 km below the surface where the crust-mantle boundary is not sharply defined and may be the site of voluminous magma underplating. The shapes, sizes, directions and volcano concentrations of both fields do not mirror the subcircular shape of the anomaly. Provided the present mantle anomaly (plume) represents the deep mantle roots to the Quaternary volcanism, two smaller dimensions of spatially and compositionally distinct ascending "magma supply fingers" are evident. The smaller ones are a few km across and have life times on the order of several 100 ka. Two or more of these make up a volcanic field, a deep plume source (mantle diapir) spawning one or more surface field.

1 Introduction

The study of volcanoes on the Earth's surface has been important in the development of speculations and models on the physical and chemical nature and history of melting anomalies in the mantle. The source regions of the silicate melts, a small portion of which once generated and repeatedly accumulated and stored on its way up, ultimately feed the tiny dimples on the surface called volcanoes. Without volcanoes, there would be no research money to investigate the location and nature of their ultimate source. In fact, concentrations of numerous volcanoes in volcanic fields, areas commonly called ***hot spots***, are the ultimate motivation to delineate the source area(s) of melt generation in the mantle by employing a variety of geophysical methods, an endeavor characterizing the majority of papers in this volume. Nevertheless, as this review will show, straightforward correlation of tomographically-based mantle anomalies to the location, size and shape of the volcanic fields, as well as temporal and spatial migration of volcanism and activation of distinct mantle domains is impossible at present.

Research highlights on the Quaternary Eifel volcanic fields during the past nearly 50 years include: the information mantle peridotite xenoliths provide on the structure and evolution of the source areas of magmas erupted; metasomatic overprinting of mantle peridotite; polybaric magma evolution; the importance of magma-water interaction – and not merely by CO_2 explosions – in triggering and governing eruptions; the evolution of strongly compositionally zoned highly evolved magma columns (Laacher See Volcano) and the complexity of Plinian eruptive and depositional mechanisms; inferences on magma source and magma collection areas derived from volcano field analysis.

The nature and history of lithospheric and asthenospheric mantle domains from which the magmas feeding the volcanoes are likely to have been generated are also inferred using methods quite different from geophysical ones. Three examples in this volume focus on the mineralogical and chemical nature of mantle xenoliths carried to the surface by the rising magmas and the composition of noble gases in constituent minerals of such nodules of deep-seated origin and in gases escaping on the surface (Witt-Eickschen this volume, Trieloff and Altherr this volume).

In this overview, I will summarize the results of volcanological, petrological and geochemical studies of the Quaternary Eifel volcanic fields in the 1980ies and 1990ies with new results coming forth to the present. This synthesis helps to put some constraints both in space and time on the location and nature of the deep-seated anomalies in the mantle from

which the volcanoes were fed. This method of ***volcano field analysis*** is completely independent of those employed in geophysical studies or detailed analysis of mantle xenoliths. A combination of results derived from the different approaches should, however, lead to a fuller and more coherent model of mantle melting anomalies and their surface expression.

I begin with the general setting of the Eifel volcanic fields, followed by a brief resume of both fields, a discussion of the main types of volcanoes, their structure, eruptive mechanisms and relative abundance in both fields. Subsequent sections summarize the main compositional groups of lavas erupted and stages of magma differentiation. This is followed by a discussion of the main results of volcano field analysis. The question whether or not volcanic activity is extinct in the Eifel will be treated at the end of the report.

To keep the paper at reasonable length, references are kept to a minimum, much of the literature prior to 1990 having been summarized in earlier reviews of the Quaternary Eifel fields (Schmincke 1982, Schmincke et al. 1983, 1990) from which some of the present information is taken. The synthesis volume of 6 years of interdisciplinary studies in the Rhenish Shield (Fuchs et al. 1983) is the foundation for many aspects discussed in this review. Papers published after 1990 will be given preference in the list of references. The present paper has been abbreviated from a more fully illustrated review that also contains maps of all localities mentioned in the text as well as numerous color photographs illustrating field relationships (Schmincke 2006).

2 General setting of the Quaternary Eifel volcanic fields

Most geologically young Central European Volcanic Fields (CEVF) developed during the Tertiary between about 45 and 10 million years with a peak in the Miocene (20-15 Ma) and minor Pliocene volcanism following, and accompanying, Eocene to Miocene rifting of the Rhine graben and uplift of the Rhenish Shield and other Paleozoic blocks (Figs. 1, 2).

Some volcanic fields such as at Cheb (Northern Bohemia, Czech Republic), Auvergne in central France, southern France and the West and East Eifel (Germany) also developed in the Quaternary. However, the total number of these younger volcanoes and thus the Quaternary magma eruption- and probably magma production- rates are of much smaller volume compared to the more prolific Tertiary volcanism. Wilson and Downes (1992, 2006) provide detailed up-to-date summaries of Tertiary to Quarternary volcanism in continental Europe and the Mediterranean area. The

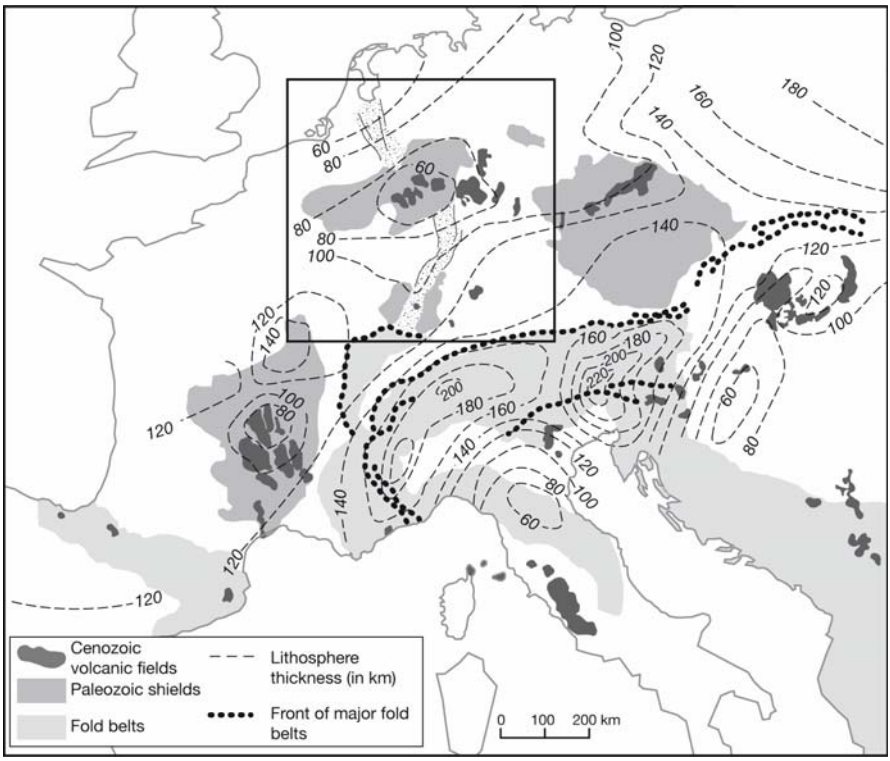

Fig. 1. Cartoon of Cenozoic volcanic fields in the three major uplifted Paleozoic blocks in Central Europe. Dashed line shows depth to lithosphere after Babuška and Plumerová (1992). Box shows enlarged portion (Fig. 2). Modified from Schmincke (1982)

CEVF can be related to two major tectonic domains: some volcanic areas (for example Westerwald, Rhön, Eifel, Auvergne) grew on uplifted and in part still rising huge Paleozoic blocks (Figs. 1,2). Uplifted river terraces on the Rhine River and its tributaries provide clear evidence that this process is continuing (Meyer and Stets 1998, this volume). Some volcanic centers are located in rift zones that cut or border uplifted blocks but activity has been most voluminous on the blocks themselves. Examples of rift-related volcanic fields include the Eger Rift, Upper Rhine Rift, which continues in the Leine Graben (Lower Hessian Depression) northeast of Frankfurt, with the Kaiserstuhl in the south and, east of Frankfurt, the Vogelsberg massif, the most prominent volcanic structure in Central Europe (Bogaard and Wörner 2003). A major difference between most of the large Tertiary and the relatively small-volume Quaternary volcanic fields is the dominance of alkali basalts and basanites and, in some, tholeiites, in the Tertiary,

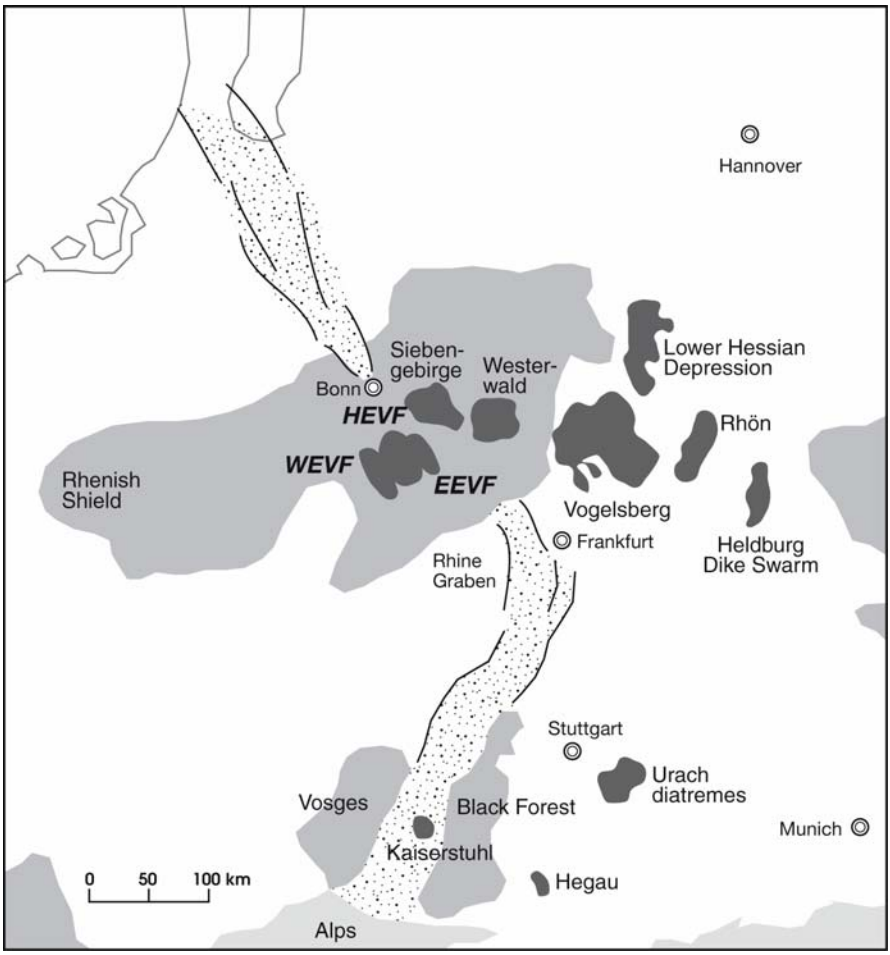

Fig. 2. Enlargement of part of figure 1, showing Cenozoic volcanic fields on the uplifted Rhenish shield and in adjacent areas. The area of the Eocene Hocheifel Volcanic Field (HEVF) overlaps that of the Quaternary East and West Eifel Volcanic Fields (WEVF and EEVF). Modified from Schmincke (1982)

contrasting with highly alkalic and silica-undersaturated magmas in the younger fields. Nevertheless, Tertiary melilite-rich lavas dominate in the Swabian Urach province (e.g. Keller et al. 1990; Wilson et al. 1995) and nephelinite lavas were erupted late in the evolution of some areas such as the Rhön (Jung and Hoernes 2000) and also the Hessian Depression (Kramm and Wedepohl 1990) and Tertiary Hocheifel (Huckenholz 1983; Fekiacova et al. (a) this volume). The spatial and temporal relationship be-

tween the arc of Western to Central European volcanic fields and the Alpine deformation front are discussed at the end of the paper.

2.1 Regional setting

The Eifel volcanic fields are situated on top of the Rhenish shield, a large lithospheric block that has experienced several periods of uplift during the past 40 million years and is still rising in some areas (Fuchs et al. 1983). The onset of volcanic activity in the western central part of the Rhenish Massif (West Eifel Volcanic Field (WEVF)) at ca. 700 ka and in the central part (East Eifel Volcanic Field (EEVF)) at ca. 460 ka closely follows accelerated rates of uplift beginning about 0.8 Ma ago (Meyer and Stets 1998; this volume).

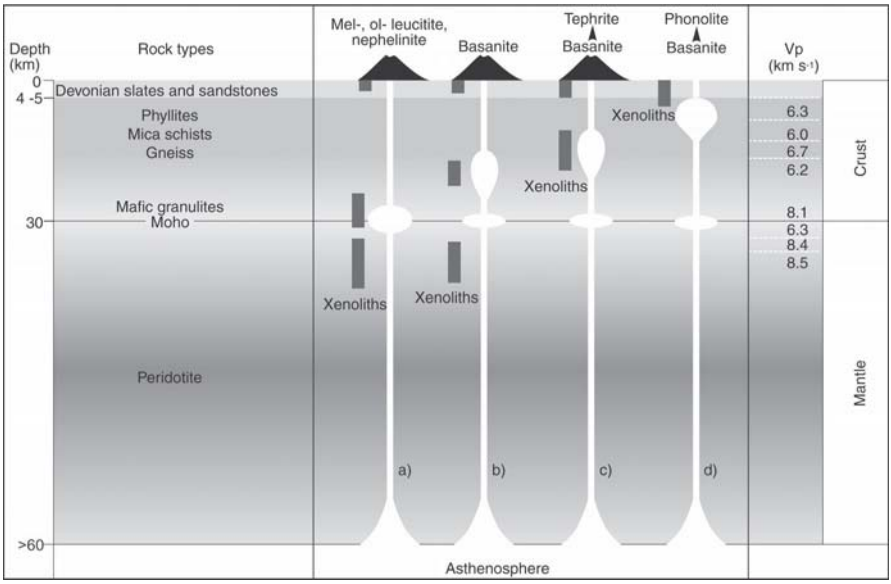

Fig. 3. Cartoon of crustal section beneath the Quaternary Eifel volcanic fields showing four different types of volcanic systems and hypothetical position of magma reservoirs at several levels. The position of magma reservoirs have been inferred from different types of xenoliths, thermobarometry of phenocrysts, microthermometry of fluid inclusions in minerals and other criteria. (a) volcanoes of primitive composition with magma reservoirs along the crust-mantle-boundary; (b, c) scoria cones with intermediate to mafic zoned lavas and magma reservoirs in the middle crust; (d) highly evolved, mostly phonolitic volcanoes such as Laacher See Volcano. Seismic velocities from Mechie et al. (1983) and Prodehl et al. (1992). Modified from Schmincke (1982)

The upper 4-6 km of the pre-Tertiary basement beneath both WEVF and EEVF consist of Lower Devonian sandstones, slates and graywackes, mostly Siegen, Hunsrück and Ems formations (Meyer 1986) (Fig. 3).

Middle Devonian limestones and Lower Mesozoic Buntsandstein occur in structural depressions in the eastern central part of the WEVF (Eifel NSZ), a structural lineament that is also mirrored in fissure directions and xenolith types (see below). In the EEVF, the Neuwied tectonic basin subsided by some 350 m, beginning in the Eocene and culminating during the Oligocene/Miocene, some faults being still active at present. The basin extends from just east of Laacher See to the Sayner Sprung, a major NW-SE fault with 200 m offset east of the Rhine River, separating the Neuwied Basin from the Westerwald to the east. Dominant fault directions in the basin are NW-SE and NE-SW. The most pronounced Paleozoic suture in the EEVF, the steeply dipping 120 km-long Siegen thrust crossing the EEVF just east of Laacher See, strikes roughly NE-SW (Meyer and Stets 1981). This thrust also marks the approximate boundary between an older western (Rieden) and younger eastern (Wehr/Laacher See) subfield of the EEVF. The possible influence of these structural basement discontinuities on fracture directions acting as magma pathways is discussed below.

Crustal xenoliths abound in many volcanoes, especially in maars and phreatic/phreatomagmatic phases in scoria cones and evolved volcanic complexes. Much information on crustal lithology and stratigraphy has been gained from detailed studies of such xenoliths, especially by comparing xenolith densities with detailed seismic refraction data (see below) (e.g. Wörner et al. 1982; Mechie et al. 1983; Grapes 1986; Mengel et al. 1991; Sachs and Hansteen 2000). Of special interest is the striking density distribution in the boundary zone between crust and mantle beneath both volcanic fields (Mechie et al. 1983; Prodehl et al. 1992, 1995). Beneath the Westerwald east of Rhine River, an area once covered by Tertiary volcanoes (Haase et al. 2004), and the EEVF, a 1 km thick high velocity layer occurs at ca. 30 km, underlain by an inversion zone with 7 km/s and a gradual transition to 8 km/s below 37 km (Fig. 3). This high velocity layer is missing beneath the WEVF and the adjoining Ardennes mountains. In these regions, a velocity of 8 km/s is reached at 37 km and the Moho is marked by distinct velocity gradients several kilometers thick.

3 The Quaternary Volcanic Fields of the Eifel

The Quaternary Eifel volcanic fields (Fig. 4) are dominated by scoria cones and maars and are typical intraplate volcanic fields except for their

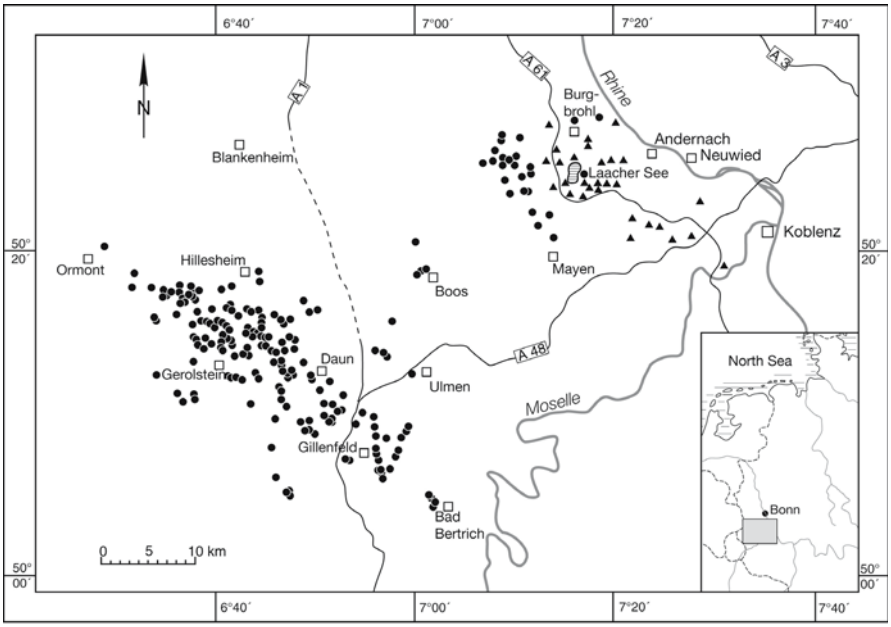

Fig. 4. Major eruptive centers of the Quaternary West and East Eifel volcanic fields. The younger centers of the EEVF (< 0.215 Ma) are shown by triangles (eastern subfield). Modified from Schmincke (1982)

unusual K-rich dominantly nephelinitic-leucititic-basanitic compositions. Few intraplate volcanic areas on Earth are better exposed, allowing detailed studies of the internal structure and evolution of scoria cones.

3.1 The West Eifel Volcanic Field (WEVF)

The WEVF field (600 km^2) is about 50 km long and extends from Ormont, at the border with Belgium in the northwest, to Bad Bertrich at the Moselle river in the southeast. The field is defined by about 240 volcanoes, 66 % scoria cones, half with lava flows and 30 % maars (Mertes 1983; Büchel and Mertes 1982), the total amount of magma erupted being about 1.7 km^3. Scoria/agglutinate cones and maar volcanoes (this is the type locality for maars) are most common, more than 50 % of the centers having erupted lava flows, some up to 7 km long (Wartgesberg). The larger WEVF differs from the EEVF field by having more mafic and silica-undersaturated magmas, a greater abundance and larger size of peridotite xenoliths and the restriction of highly differentiated magmas to two small localities in the eastern center of the field. Available age data and paleoclimatic and geo-

morphic criteria (Lippolt 1983; Büchel and Lorenz 1982; Mertes and Schmincke 1983; Fuhrmann and Lippolt 1987; Schnepp and Hradetzky 1994; Zolitschka et al. 1995) indicate that probably all volcanoes erupted between ca. 700 and ca. 11 ka. Volcanic activity may have peaked between ca. 550 and 450 ka, followed by a lull in activity between ca. 450 and 100 ka and a subsequent increase in volcano formation (see below).

Among the ca. 30 maars, those of greatest volcanological, petrological and touristic interest are the "Dauner maar group" (Schalkenmehrener Maar, Weinfelder Maar, also called Totenmaar, and the Gemündener Maar in the southeast), the Meerfelder Maar in the west, and, in the southern part of the volcanic field, the especially well-preserved Pulvermaar, whose infilling lake is 74 m (!) deep. Unfortunately, the tephra rings surrounding the maars are very poorly exposed today, with the exception of the Meerfelder Maar and a pit in the Pulvermaar deposits.

3.2 East Eifel Volcanic Field (EEVF)

The EEVF (about 30-35 km in length, 10-20 km wide, 400 km^2) consists of about 100 volcanoes, ca. 80 % scoria cones (Fig. 5), rare maars, tephra rings and some lava flows as well as several larger phonolitic volcanic complexes (Kempenich, Rieden, Wehr, Laacher See). The volcanological, petrographic and chemical variability is much greater than in the WEVF as is the volume of individual scoria cones. The EEVF can be subdivided temporally, spatially, tectonically, morphologically and geochemically into an old poorly-exposed field west of Laacher See (Rieden subfield) and a younger one (the Laacher See area proper including the Wehr center to the west) to the east. Both subfields are oriented NW-SE although several scoria cone groups in the center of the Neuwied basin are arranged roughly E-W. The younger subfield occupies the central area of the Neuwied tectonic basin west of Rhine River.

Four relatively well-defined eruptive periods can be distinguished from each other in the EEVF (Schmincke et al. 1983; Viereck 1984; Bogaard and Schmincke 1988, 1990; Schmincke et al. 1990; Bogaard (pers. comm.)), preceded by one or more older fallout tephra layers (ca. 460 ka old) whose eruptive centers are uncertain but maybe located in the WEVF (Bogaard pers. comm.).

I. The oldest poorly exposed and poorly studied peripheral Kempenich center in the NW consists of (olivine) (melilite) nephelinite mafic volcanoes and several moderately to highly evolved leucite phonolite necks (about 450 to 500 ka).

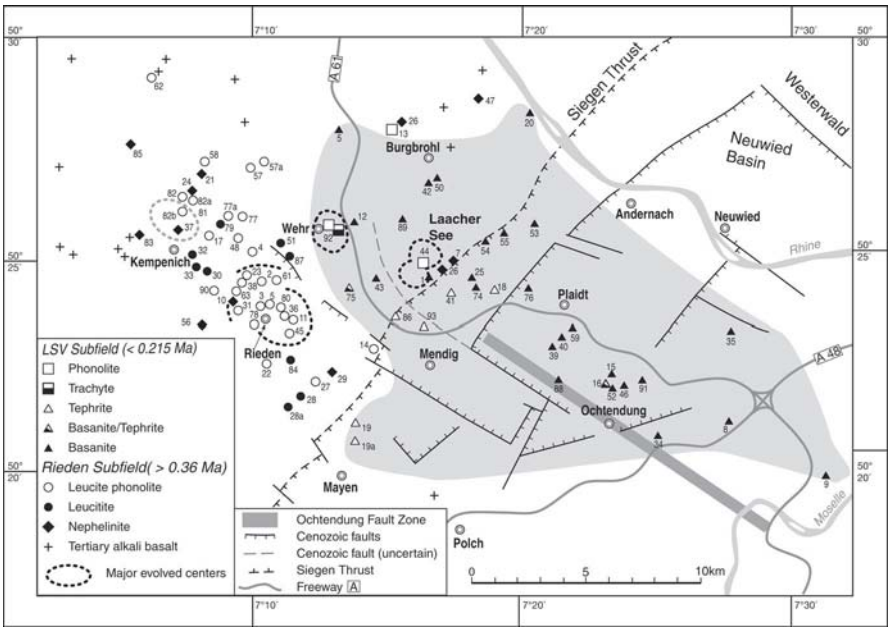

Fig. 5. Distribution of volcanoes and Cenozoic faults in the East Eifel Volcanic Field. The four main phonolitic evolved centers are Kempenich (tentative), Rieden, Wehr and Laacher See. Younger LSV subfield is shaded disregarding 2 foiditic volcanoes NE of LSV. The main tectonic features are the Paleozoic Siegen Thrust and the Cenozoic normal faults (after Meyer (1986) and Ahorner (1983)) bounding and within Neuwied Basin. Numbers refer to single eruptive centers listed in Schmincke (2006). The seismically active Ochtendung Fault Zone (Ahorner 1983) is paralleled by a graben (dashed line) formed during eruption of Laacher See Volcano. Modified from Duda and Schmincke (1978) and Bednarz et al. (1983)

II. The better-exposed and well-documented second oldest phase in the western subfield is the Riedener volcanic complex (ca. 5 km^3 DRE (dense rock equivalent), ca. 430 to 360 ka) in the topographically higher area around the town of Rieden (Viereck 1984). A caldera basin up to 2.5 km in diameter is filled mainly by plagioclase-free, in part garnet-bearing leucite-phonolite ignimbrite deposits, exogenous and endogenous domes, fallout tephra, some regionally widespread, and thick lake sediments. The peripheral centers are mainly mafic to intermediate leucitite scoria cones and lava flows of similar age as the main complex.

III. The southeastern subfield of the EEVF (younger than ca. 215 ka) is dominated by basanite-tephrite volcanic centers and two highly evolved complexes (Fig. 5). The phonolite/trachyte complex of the Wehrer Kessel and the phonolitic volcano of the Laacher See are located in the western

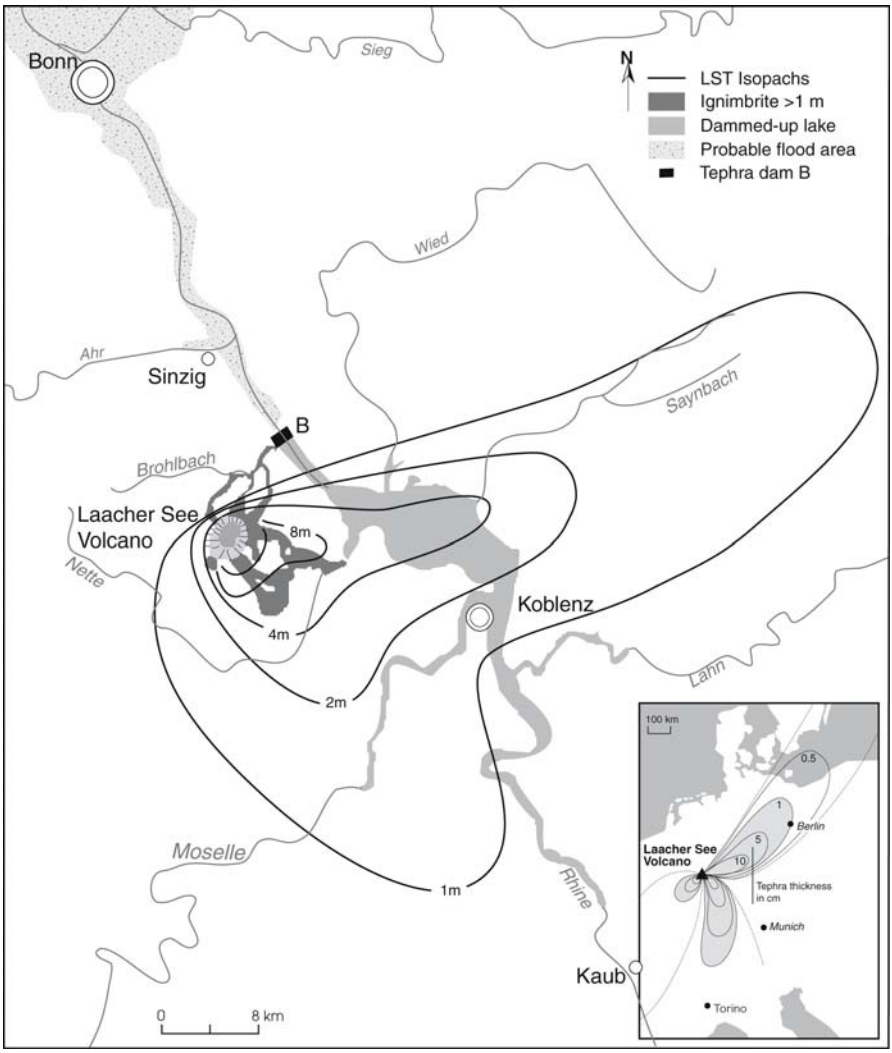

Fig. 6. Distribution of Laacher See Tephra lobes in central Europe (inset) and in the proximal area across the Rhine River. Ignimbrite deposits are shown in some radial valleys (Brohltal and Nettetal). Dammed-up lake generated during the late phase of the eruption. Temporary tephra dam formed at the mouth of Brohlbach where pyroclastic flows channeled within Brohltal valley entered the Rhine River (B). Modified from Park and Schmincke (1997)

part of the southeastern subfield in a topographically higher area. The plagioclase-bearing phonolitic to minor trachytic Wehr volcano erupted twice, its major (older) eruption being $^{40}Ar/^{39}Ar$ laser-dated as 215 ± 4 ka BP ("Hüttenberg tephra") (Bogaard et al. 1989). This very precisely dated

event is a critical one because this tephra layer directly underlies many basanitic and tephritic scoria cones of the eastern subfield. Most of these formed <30 ka after the Wehr eruption between 215 and 190 ka, but most mafic eruptive centers are located well east of the Wehrer Kessel in the central part of the tectonically subsided Neuwied basin. Two minor phonolite eruptions occurred at ca. 150 ka at Wehrer Kessel (Glees Tephra, GT) and at ca. 116 ka from Dümpelmaar (DMT). At least one major tephrite center (Niedermendig cone and lava flow) and a few tephritic volcanoes, some producing widespread subplinian tephritic fallout lapilli layers, developed at this stage.

IV. Laacher See Volcano (LSV), the youngest and best documented phonolite center (Figs. 5, 6), erupted at 12.9 ka BP as shown by warve studies and ^{14}C dating (Brauer et al. 1999; Litt et al. 2003) matched by single crystal $^{40}Ar/^{39}Ar$ dating (Bogaard 1995) and U-Th disequilibria (Bourdon et al. 1994). The magma volume erupted (>6.3 km^3), dominantly fallout tephra deposits, exceeds that of all mafic volcanoes erupted in both Eifel fields together implying that a large volume of mafic parent magma must have been present beneath erupted Laacher See phonolite magma (see below). However, only extremely small volumes of basanite lapilli were erupted, mixed with phonolite, during the terminal stage of the eruption (Wörner and Wright 1984). This is powerful evidence that the volume of primitive mafic magmas generated in the melting anomaly and emplaced into the crust is very much larger than the small volume fraction that was successful in making it to the surface.

4 Volcanic constructs and fragmentation and eruptive mechanisms

Several contrasting endmember types of volcanic constructs in the Quaternary Eifel volcanic fields differ from each other chemically and mineralogically, in their petrogenesis and, therefore, also in the volume, morphology, height, structure and rock type. Mafic magmas occur chiefly as scoria (cinder) cones, agglutinate cones, tephra cones (rings), widespread (sub-Plinian) fallout layers, maars and lava flows. The much larger phonolitic complexes show intrusive rocks (where strongly eroded) and local extrusive domes (Rieden) but are dominated by widespread volcaniclastic deposits (ignimbrites, Plinian fallout tephra fans and voluminous reworked volcaniclastics).

4.1 Mafic volcanoes

By far the most common type of volcano in the Eifel is the mafic to rarely intermediate scoria cone. Scoria (cinder) cones, the most typical volcanic landforms of continental intraplate volcanic fields, are generally accepted to grow within a few weeks to months. Because of such short eruptive periods, they are often called monogenetic volcanoes. This term is difficult to apply in the Quaternary Eifel volcanic fields, however, because the good exposures in many quarries show that many extremely well-exposed cones consist of several different volcanic phases of both, pyroclastic, phreatic and phreatomagmatic activity belying their simple external shape. These phases contrasting in eruptive mechanism and commonly also in composition may be separated from each other in some by one or more soil zones, evidence for vegetation and other signs of major interruption lasting thousands to tens of thousands of years. The term monogenetic should thus not be taken too literally and does not apply everywhere. It should be understood in terms of a construction period that is short compared to the hundred thousands or even millions of years that characterize large stratocones or huge ocean island volcanoes.

Scoria cones and maars can occur as isolated edifices, larger volcanic complexes reflecting migration of activity along a fracture but recording one major eruption, in clusters of closely spaced individual centers, generally of the same composition and as multi-stage volcanoes. Multi-stage scoria cones and clusters are of some interest with respect to the longevity of magma flux. Fissures beneath some scoria cones, facilitated by rejuvenated old fractures, possibly remained hot long enough to provide convenient preheated routes to facilitate repeated rise of new magma batches. A corollary is that many if not most attempts of very small-volume magma batches to erupt on the surface of the Earth remain unsuccessful; the rising magma freezes during ascent through a cold crust (or in the upper mantle). The densest cluster of volcanoes is the scoria cone (and maar) ring surrounding Laacher See basin, the eruptive site of the large LSV eruption (see below).

4.2 The initial stage of scoria cones

Extensive quarrying of many scoria cones in the Eifel has allowed study of the entire evolution of a cone from the initial to the terminal stage. Nearly all scoria cones begin with an initial hydroclastic stage, represented by an initial maar and/or tephra ring phase. Obviously, magma may rise along fractures that are also the sites of groundwater circulation (Lorenz 1973)

since the upper basement rocks in the Eifel (Devonian sandstones and slates) have nearly no porosity. Increasing magma flux rate and/or dwindling water supply caused a transition to pyroclastic eruptions leading to the formation of agglutinate/scoria cones. Minor to moderate interaction of magma and water is common throughout much of the evolution of many cones as reflected in well-bedded deposits, poor vesiculation of juvenile clasts and variable amounts of country rock fragments, a classic example being Herchenberg volcano (Bednarz and Schmincke 1990).

4.3 Scoria-agglutinate cone facies and growth stages

Primitive alkaline mafic magmas are typical of the Eifel scoria cones and their lava flows. Compositional zonation is common. An instructive example is the young basanitic scoria cone/lava flow/maar complex at Wartgesberg that demonstrates that even the most homogeneous and primitive WEVF volcanoes are compositionally zoned. The initial tephra deposit is slightly evolved (MgO 9.4 wt%, Cr 362 ppm, Ni 140 ppm) while the terminal subplinian tephra is significantly more mafic (MgO 13.67 wt%, Cr 520 ppm, Ni 298 ppm) but similar to the bulk of the volcano scoria and major lava flow. This ubiquitous type of differentiation which we have found in practically all larger scoria cone complexes studied in the EEVF must have taken place probably at low pressure in middle to upper crustal reservoirs. The total volume erupted in a single scoria cone generally is $<<0.1$ km^3. All scoria cones have been modified by several glacial and interglacial climatic periods. The crater depression is recognizable in some volcanoes but most craters are largely filled and covered by clastic crater deposits (see below). Many scoria cones consist of several nested craters, evidence that the main eruptive center migrated repeatedly during the course of an eruption and several conduits were active simultaneously at times, commonly along linear fissures.

Two main facies types can be distinguished in a well-exposed scoria cone: crater facies and wall facies. The crater facies is separated from the wall facies mostly by semicircular faults or funnel-shaped surfaces along which large blocks subsided. The central part of a crater with a diameter of ca. 50-100 m continues downward. These deeper levels are exposed in the older Tertiary volcanic conduits e.g. of the Hocheifel or Westerwald. The initial deposits of many scoria cones result from magma-water interaction and mostly decrease rapidly within 100 to 200 m of the crater wall, thus representing in effect a tephra ring or initial maar. The lower crater facies consists of erupted stringers of lava that were so hot in the immediate surroundings of a circular or fissure-like conduit during deposition that they

have been welded together to form a compact rock called agglutinate. In some quarries, blocks of agglutinates remain in the center because they are difficult to quarry. The last major filling of a crater directly beneath the morphological depression characteristically consists dominantly of round bombs up to 50 cm in diameter.

Three different types of deposits commonly mark the terminal stages of a scoria cone. Renewed encounter of magma/groundwater may generate well-bedded deposits that reflect late-stage magma-water interaction. Also, especially in the EEVF, widespread lapilli fallout deposits up to several meters thick that can extend much farther than the actual scoria cone, commonly of more mafic composition, form during the waning stage of a scoria cone evolution. Lava-filled fissures may form compact dikes in the lower part of a quarry. Clastic crater deposits often preserve several hundred thousand years of volcanic and nonvolcanic sedimentation and erosion. In the East Eifel, bone fragments and tools record human activity in the area which dates back at least 200,000 years (Bosinski 1992).

The wall facies consists of coarse-grained scoria breccias that may be moderately welded close to the crater rim but become increasingly less welded and uncompacted and finer grained distally. The matrix between these breccias is made up increasingly towards the top of a scoria cone of deposits that formed during destabilization of the upper part of the wall facies and represent basically reworked deposits formed during mature stages of cone growth.

4.4 Maars, tephra rings, and tephra cones

The Eifel maars - a major tourist attraction - are the type locality for a characteristic type of volcano: a more or less circular crater in the basement, some filled with water, up to 1.7 km in diameter, surrounded by a low wall of tephra, dominated by fragments of country rock. The difference between maars and tuff rings, as defined by Lorenz (1973), is that maars are craters excavated in the preexisting land surface while tephra rings are constructed on top. Tephra rings also contain a much higher proportion of juvenile clasts, often moderately to highly vesicular and generally altered by groundwater into palagonite.

Maars and the related tephra rings have similar volumes and size (diameter). Tephra deposits of the low, flat tephra rings surrounding maar craters differ from scoria cones by the absence of cinder and lava spatter deposited hot, by their smaller grain size and good bedding. Essential clasts are commonly angular, studded with country rock fragments (greatly compromising bulk chemical analyses) and few vesicles. Tephra rings con-

tain especially abundant country rock fragments (up to and exceeding 90 vol%) with individual fragments reaching diameters exceeding 2 m.

The traditional explanation for maars held that they are gas explosion funnels resulting from CO_2-rich magmas, the highly alkalic – and therefore CO_2-rich – Eifel magmas having been thought to represent a suitable candidate. Detailed studies during the past few decades have provided convincing evidence for a different explanation (e.g. Lorenz 1973; Schmincke 1977b) that is here modified, however. On one hand, the vesicularity of juvenile tephra particles in hydroclastic deposits such as those of initial hyaloclastite tephra rings at the base of scoria cones, is much too low to reflect fragmentation of the magma by expansion of a magmatic gas phase. The angular glassy particles show that quenching by water is the rule having exerted stresses on the magma that provide for thorough fragmentation by thermal shock. The very large pressures that can be calculated from the huge size of ejected blocks cannot be explained by accumulation of magmatic gases. Moreover, the tephra has been deposited in a cold and moist to wet state. Poor sorting and cross bedding are excellent evidence for lateral ground transport by base surges. All these data leave little doubt for the common interaction of magma and water. Nevertheless, the high ascent rates of the very alkalic Eifel magmas may have facilitated magma-water encounter and variable interaction and mixing (Schmincke 1977 b). This interpretation is here re-emphasized for several reasons. Volcanic lapilli and ash-sized fragments in several maar deposits (e.g. of the four most famous maars Dreiser Weiher, Meerfelder Maar, Pulvermaar and Ulmener Maar) are neither glassy nor angular nor nonvesicular. Slightly vesicular, tachylitic, composite (such as those at Herchenberg, Bednarz and Schmincke 1990), round to ovoid ash and lapilli shapes (pellets) similar to those in melilitite tuffs (e.g. Keller et al. 1990) are common. All these textural features suggest that pyroclastic processes played a major role in the fragmentation, agglutination and final clast formation of these low-viscosity and volatile-rich melts, the pelletal shape being conditioned by surface tension. Nevertheless, magma-water interaction likely played a major role as well as reflected in the dominance of lithic fragments in the deposits, intense mixing of comminuted country rock and magma and cauliflower-shaped dense lapilli and bombs choked with small chips of slate and sandstone. Since up to 90 % or more by volume of the particles in many maar deposits are represented by lithoclasts, dominantly Devonian slates and sandstones, the real magma volume erupted in many maars at the surface is quite trivial. This could mean that the rising magma at these sites may never have been able to reach the surface had it not contacted groundwater with ensuing steam explosions that shattered the roof and propelled the mixture to the surface.

4.5 Lava flows

Approximately half of the scoria cones have erupted lava flows, commonly emitted late during an eruption. These flows are mostly <4 km (rarely as much as 7 km) long. Examples of large flows are the Hochsimmer lava in the EEVF and, in the WEVF, the young basanitic Wartgesberg lava, olivine nephelinite Mosenberg lava and thick intensely mined foidite flow at Kalem. The famous leucititic and tephritic lava flows at Mayen and Mendig in the EEVF have been mined at a minor scale since prehistoric and more intensely since Roman times. Millstones made of these lavas were exported into many countries during the past few hundred years. Mining has resumed during the past two decades e.g. for ornamental material for churches such as Cologne cathedral. The suitability of these lavas is mainly due to their evenly distributed high porosity (about 25 vol% in the famous Niedermendiger Lava) and advanced groundmass crystallization, mechanical properties that facilitate sawing and prevent flaking.

4.6 Laacher See Volcano

The very late Quaternary Plinian eruption of phonolitic Laacher See Volcano (LSV) at 12,900 a BP, the youngest of three major phonolitic volcanic complexes in the EEVF, is one of the major prehistoric Plinian eruptions of highly evolved magma in central and southern Europe (Fig. 6). Certain patterns, such as complex feedback mechanisms of external and internal forcing factors determined the course of the eruption. In particular, the initial and terminal hydroclastic stages, now known to be typical of many Plinian and other types of eruptions, were first recognized at Laacher See. The eruption was characterized by the progressive emptying and explosive degassing of a phonolitic magma column (>6.3 km^3 of magma) strongly zoned with respect to mineralogy, chemical composition, volatile concentration, physical properties and types of wall rock xenoliths and juvenile cumulates. The Laacher See volcano has been – and is being - studied in much detail during the past 35 years (e.g. Wörner and Schmincke 1984 a, b; Wörner et al. 1985; Wörner and Wright 1984; Bogaard and Schmincke 1985 a, b; Freundt and Schmincke 1986; Harms and Schmincke 2000; Harms et al. 2004), major results having been summarized in Schmincke et al. (1990, 2000) and Schmincke (2004).

An initial phreatic to phreatomagmatic phase was followed by the first of two major plinian stages, resulting in widespread pumice lapilli and ash lobes throughout central Europe. SW-NE-directions of the main fallout lobes are interpreted to be the result of the main tropopause wind direction

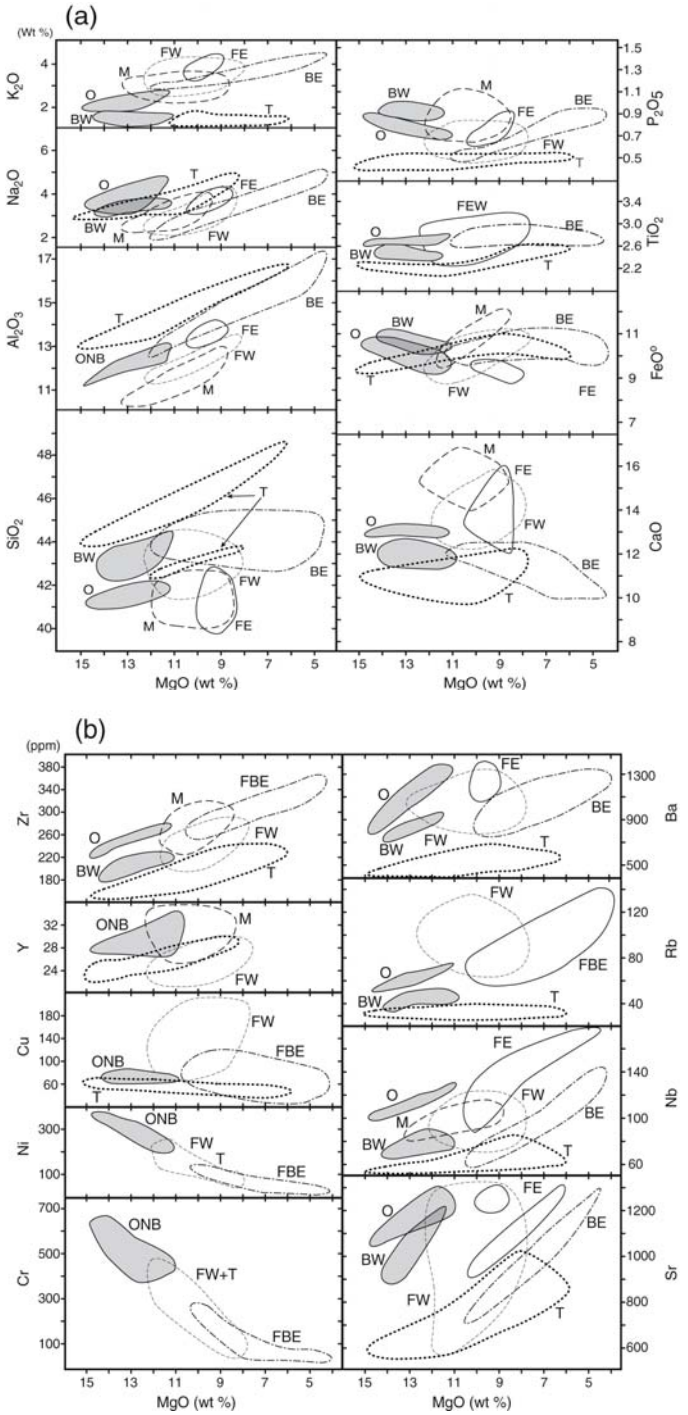
(a)
(Wt %)
K2O
Na2O
Al2O3
SiO2
P2O5
TiO2
FeO°
CaO
FW
FE
M
O
BW
T
BE
ONB
FEW
MgO (wt %)
(b)
(ppm)
Zr
Y
Cu
Ni
Cr
Ba
Rb
Nb
Sr
FBE
FW+T

Fig. 7. (previous page) Major and trace element concentrations vs MgO of volcanic rocks of the WEVF and EEVF. FeO^0 = total iron. Compositional fields are drawn for distinct compositional groups that are shown separately where appropriate. Abbreviations: WEVF: *O* = olivine nephelinites, *BW* = basanites, *ONB* where of similar composition. *M*= melilite nephelinites (shown as separate field where appropriate, otherwise included in *FW*, *FW* = leucitites and nephelinites. EEVF: *BE* = basanites, *FE*= foidites, combined (*FBE*) where appropriate. Some trace element concentrations are not available for all rocks. The *O* and *BW* (*ONB*) fields are shaded for clarity. Compositional fields of Eocene rocks (HEVF) are shown for comparison. See text for discussion. Modified from Schmincke (1982)

identical to present-day directions. Migration of the eruptive focus to the northern part of the Laacher See basin was accompanied by unsteady eruptive patterns and influx of water into the collapsed conduit system. Most pyroclastic density currents formed during this phase of complex crater relocation. A second main oscillating Plinian phase was followed by dominantly phreatomagmatic eruptions of gray, crystal-rich tephra (Upper Laacher See Tephra) during the terminal phreatomagmatic stage forming spectacular proximal high energy surge and chute-and-pool deposits.

The main phase of LSV probably lasted at most a few days judging from the duration of similar Plinian historic eruptions and other types of evidence such as likely mass eruption rates. During the eruption a huge lake had formed behind a natural tephra dam, accumulated in a canyon of the Rhine River, and was catastrophically drained following collapse. Slow deposition of fine-grained ash during the very terminal phase was interrupted by at least one phase of gully erosion and generation of debris flows. The eruption had a significant impact on climate owing to large masses of stratospheric aerosols on account of the sulfur-rich magma composition (see below).

5 Magmas of the Quaternary Eifel volcanic fields

5.1 Magma suites

Most mafic Quaternary Eifel magmas are potassic with K_2O slightly exceeding Na_2O (Fig. 7).

Rocks are phyric to highly phyric, total phenocrysts ranging up to 30 %. Phenocrysts in the mafic lavas are dominated by clinopyroxene (Ti-augite) with generally <5 % olivine, phlogopite and titanomagnetite (Figs. 8, 9).

Amphibole, apatite, titanite and, in some rocks, hauyne appear as liquidus phases in the intermediate rocks, with phenocrystic plagioclase, sanidine, hauyne, nosean, leucite and phlogopite/biotite being restricted to

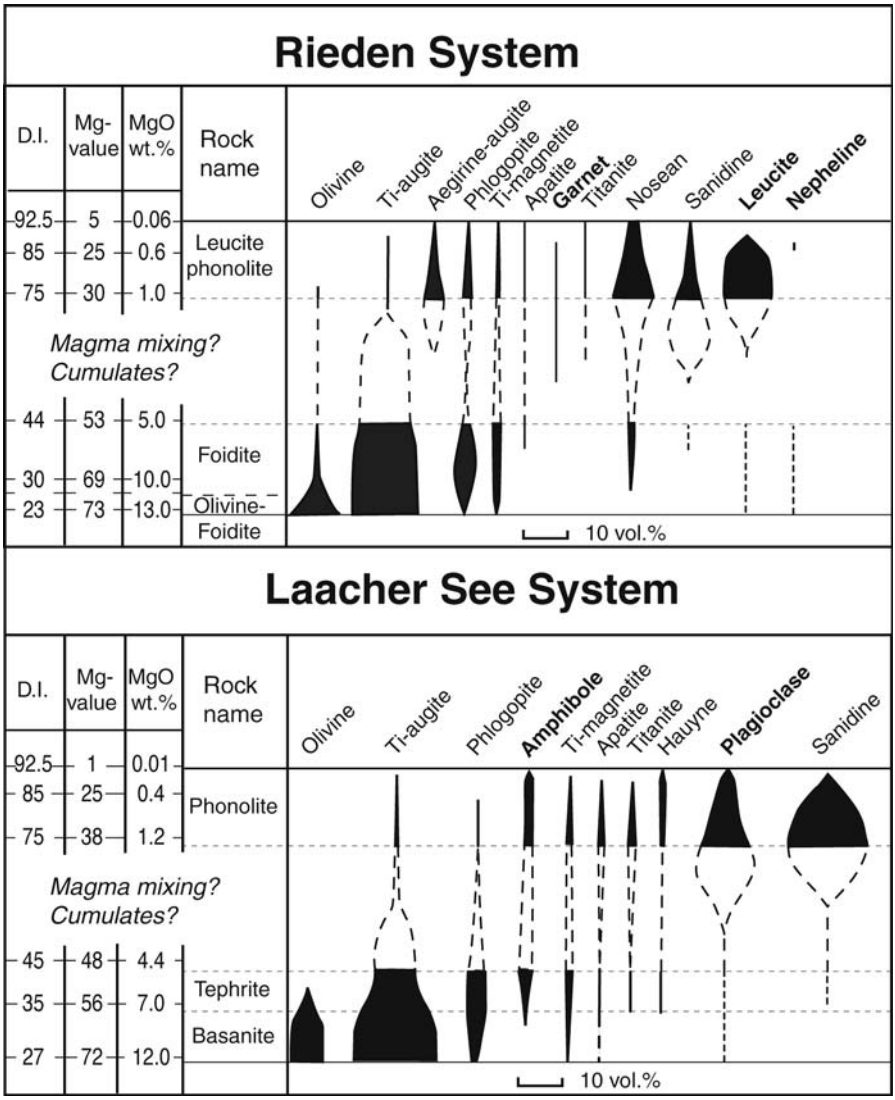

Fig. 8. Change in modal phenocryst mineralogy with rock composition in Rieden and Laacher See systems (EEVF). *D.I.* = Thornton-Tuttle differentiation index. Characteristic mineral phases (garnet, leucite and nepheline for the Rieden rocks and amphibole and plagioclase for the Wehr/LSV rocks) are shown in bold. Modified from Duda and Schmincke (1978) and Bednarz et al. (1983)

the phonolitic and rare trachytic (Wehr) magmas, the latter lacking feldspathoids (Fig. 8). Calcite phenocrysts occur in at least one phonolite. Groundmass phases in the mafic rocks include variable amounts of leucite

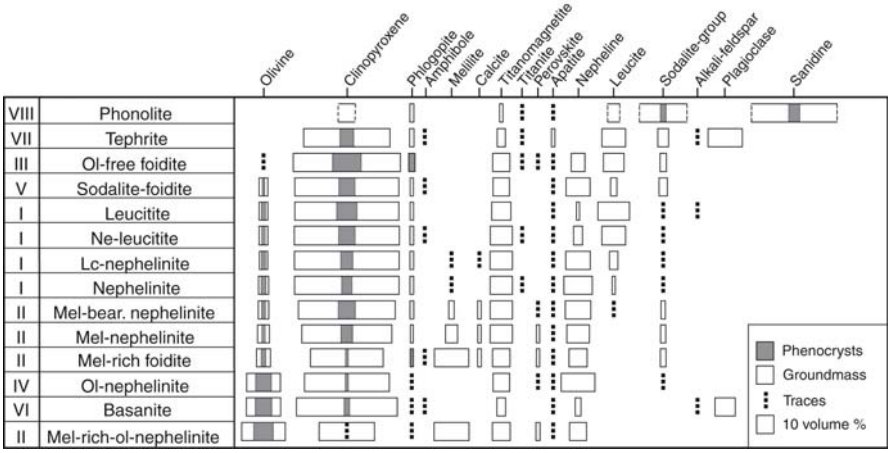

Fig. 9. Change in modal phenocryst mineralogy with rock composition in lavas from the WEVF. Modified from Mertes and Schmincke (1985)

and nepheline – in some alkali feldspar - in foiditic lavas, and plagioclase in basanites.

The primitive volcanic rocks are grouped into two major suites that show moderate geochemical, spatial and temporal coherency, some comprising a range in composition from primitive to highly evolved (Schmincke 1982; Mertes and Schmincke 1985; Duda and Schmincke 1978, 1985). A highly enriched leucitite- (melilite)-nephelinite suite (F) dominates in the WEVF. Two ol-rich very mafic sodic suites are restricted to the younger WEVF (basanite (B) and olivine nephelinite (ON)). The basanite-tephrite suite in the EEVF is strongly potassic and moderately mafic, eruptive centers outnumbering the mafic foidites in the EEVF. The suites are referred to below as FW (west), FE (east), ONB (west) and BE (east) (Fig. 7). The leucitite-nephelinite and melilite nephelinite fields are shown separately in Fig. 7.

5.2 FW Suite

Most FW nephelinites, leucitites and melilite nephelinites show high K_2O (mostly 2.5-4 wt%) and related elements (Rb, Ba, LREE) as well as high MgO and Ca and low Al concentrations, MgO ranging from 7 to 14 wt% (mean Mg values: 61-67). Rocks of intermediate to highly evolved composition are rare (only five volcanoes). Chemically, and, in part, petrographically two major distinct subgroups occur. For example, melilite nephelinites are characterized by very high CaO (up to 16.5 wt%) and Nb, by

higher P, Fe and CO_2, and by slightly lower Al, Si and K concentrations compared to the leucitites and nephelinites. They also show Na_2O/K_2O >1 and primary carbonate, as based on groundmass textures and the almost exclusive restriction to melilite nephelinites – also in the EEVF - possibly due to unmixing of a carbonatitic liquid. Rare carbonate in the groundmass of coeval lavas of other compositions shows textural evidence of secondary alteration.

5.3 FE Suite

Leucitites, nephelinites and melilite nephelinites and their derivative magmas make up the older western subfield in the EEVF, the leucitites grouped around the centrally located Rieden eruptive center, the nephelinites more around, and east, of the Kempenich complex phonolite volcanoes. The mafic magmas can be further subdivided according to differences in major (Na, Ti, Fe) and trace (Sr, Nb, Rb, Ba) element concentrations. The suite as a whole chemically resembles the FW magmas of the WEVF except for significantly higher Al_2O_3 (>12.5 wt%) with little overlap with the WEVF magmas (<13.5 wt%). Trace element compositions are similar to the FW suite except for the much higher Sr, Ba and Nb contents in some or all of the Hochstein/Herchenberg/Leilenkopf magmas. A few volcanoes in the EEVF (e.g. Sulzbusch) show Na_2O/K_2O >1.

5.4 ONB (ON and BW) Suites

About 11 % of the WEVF volcanoes form two young (<0.05 ? Ma) chemically distinct suites of sodic lavas (Na_2O/K_2O >1) comprising groundmass plagioclase-bearing olivine-rich basanites and olivine nephelinites. Their similarity lies in their mafic character, relatively low K_2O, young age and spatial concentration in the southeastern to eastern part of the field. Olivine (both phenocrysts and xenocrysts) in these rocks greatly exceeds cpx, Cr-spinel xenocrysts being common. All rocks are very mafic with high Cr, Ni, Co and MgO concentrations >11 % (mean Mg-values 71-72) but are slightly enriched in large-ion lithophile (LIL) elements. They represent the most primitive suite of all Quaternary Eifel magmas and approximate primary magmas. However, the interpretation of the high Cr, Ni and Mg concentrations is complicated by the fact that xenocrystic nodule debris (xenocrysts of ol, opx and spinel) is common in the olivine nephelinites. The ONB lavas are distinguished chemically from the FW suite by lower Ba, Rb, Ca, Nb and Zr among the trace elements, and K and Ca among the

major elements. However, their P, Sr and Y contents are among the highest in the WEVF lavas (Figs. 10, 11).

The olivine nephelinites are slightly more enriched than the basanites, e.g. by having K_2O concentrations close to 2 wt% (compared to 1.5 to 1.8 for the BW rocks) and also CaO/Al_2O_3 >1 suggesting lower degrees of partial melting (Fig. 10). The basanite eruptive centers which define the extreme eastern/southeastern margin of the field are compositionally (including their enriched isotope ratios, see below) closest among the Quaternary magmas to the Tertiary alkali basalt and thus to an asthenospheric source.

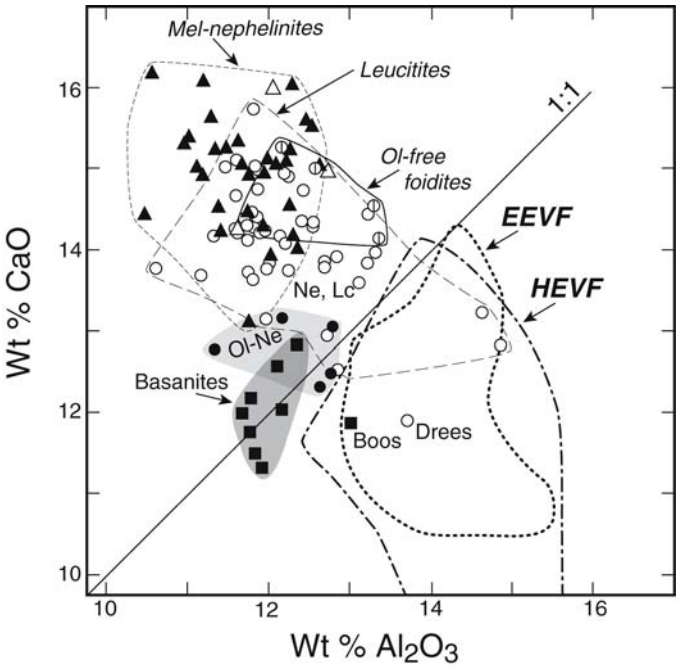

Fig. 10. CaO versus Al_2O_3 for primitive and moderately evolved WEVF lavas. Two localities outside the main compositional fields are shown separately (Boos, Drees). Fields for the Quaternary EEVF and the Eocene HEVF lavas are shown for comparison. For rock symbols see Fig. 14. Modified from Mertes and Schmincke (1985)

5.5 BE Suite

Most younger (<0.2 Ma) volcanoes in the EEVF represent a basanite-tephrite-phonolite suite in the eastern subfield west, east and south of Laacher See, overlapping spatially only slightly with the FE suite of the

older western subfield. The basanite magmas can be clearly distinguished from the older nephelinite/leucitites by their higher SiO_2, and in part, FeO and lower Na_2O, P_2O_5, CaO, Nb, Sr, Ba, Cu, and, in part TiO_2. Al_2O_3 concentrations are similar between the suites except for the Leilenkopf and Hochsimmer lavas (lower Al_2O_3-concentrations). The primitive BE magmas differ from those of the BW suite by being distinctly less mafic, MgO mostly <10.2 wt % and never exceeding 11 %, the lower limit for the BW magmas. On the other hand, the Na_2O- concentrations of the basanites are only slightly lower and overlap those of the BW magmas (2.3-3.1 wt % BE, 2.8-3.1 BW) while their K_2O-concentrations are about twice as high (2.9-3.4 wt% BE versus 1.5-1.8 wt% BW) with Rb and Ba also correspondingly higher. Other significant differences comprise P_2O_5 concentrations (0.5-0.7 wt% BE, 0.7-1.0 wt% for BW), higher Zr/Nb ratios (3.3-4.1 BE, 2.6-3.2 BW) CaO/Al_2O_3 ratios (0.83-0.91 BE, 0.88-1.0 BW) and distinctly lower P_2O_5 (0.5-0.7 wt% BE, 0.7-1.1 wt% BW) and lower Sr concentrations.

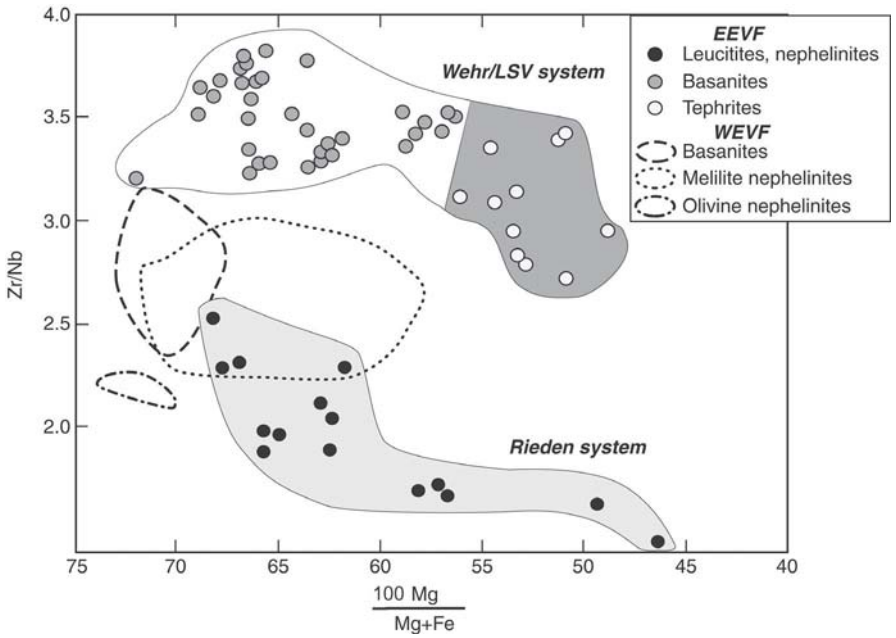

Fig. 11. Zr/Nb versus Mg# for EEVF and WEVF mafic to intermediate volcanic rocks. There is no compositional overlap between the older Rieden and younger Laacher See Volcano compositional subfields

5.6 Ulmen magma

The magma composition of the youngest volcano in the Eifel, the Ulmener Maar, at the southeastern margin but slightly outside the main WEVF, is of special interest because of the very young age of the volcano (11 ka BP, Zolitschka et al. 1995). Minor juvenile clasts are found as small grayish slightly vesicular commonly composite lapilli in the strongly carbonate-cemented phreatomagmatic deposits that consist to >90 volume % of Devonian lithoclasts. With 6.3 wt% MgO and an Mg# of 65, this lava is at the boundary between primitive and differentiated magma compositions. The very low Cr (76 ppm) and Ni (48 ppm) concentrations indicate that the magma underwent massive olivine and clinopyroxene fractionation. The lava (41 wt% SiO_2) has the highest concentrations of Na_2O, P_2O_5 and incompatible elements such as Ba, Rb, Sr, Zr and all LILE elements of any Quaternary lava of similar Mg# so far analyzed. Its Ce (284 ppm) and La (178 ppm) concentrations are unmatched by any Eifel lava so far analyzed. This extreme composition is most easily explained as having been derived from a mafic magma generated by very low degrees of partial melting. Some of the phreatomagmatic deposits are strongly cemented by carbonate, most likely of primary origin in analogy with volcaniclastic rocks of similar composition (e.g. Herchenberg, Bednarz and Schmincke 1990) where the cementing carbonate has been analyzed. Interestingly, the Ulmen volcano is not only close to the area of highest regional uplift (Kelberger Hoch) but it is also surrounded by the remnants of a cluster of Tertiary volcanoes and thus possibly a strongly metasomatized lithosphere (see below).

5.7 Differences between primitive magmas

The primitive magmas of the Eifel suites reflect both variable degrees of partial melting as well as derivation from different types of mantle compounded by small-scale compositionally contrasting mantle domains. Significant crustal contamination is ruled out as a mechanism for having significantly affected these highly silica-undersaturated Sr- and Nd-rich mafic magmas based e.g. on radiogenic isotope ratios (Wörner et al. 1986).

Fractionation of clino- and/or orthopyroxene, olivine and spinel at both high and intermediate pressure has undoubtedly occurred as shown by the chemical differences below. The clearly observed differences in K, Na, Al, Si, Cr, P and, to a lesser degree, in Ti and Fe at similar Mg^- values, trace element concentrations and ratios and radiogenic isotopes, however, are inexplicable in terms of any combination of fractionating phases.

There are consistent and significant differences in the EEVF between the younger BE (high (3.55 ± 0.3) Zr/Nb ratios) and older Rieden suite magmas (2.20 ± 0.3), Zr/Nb ratios for rocks having similar Sr and Nd isotope ratios (Fig. 11). The WEVF basanites show the highest (2.9 ± 0.3) and the olivine nephelinites the lowest (2.2 ± 0.1) Zr/Nb ratio in that field. Interestingly, when compared at similar MgO concentrations, high CaO/Al_2O_3 ratios correlate negatively with Zr/Nb ratios. In other words, accessory Zr-bearing phases are preferentially retained in the source area relative to Nb-phases at low degrees of melting. Thus, mantle source regions beneath the fields are chemically distinct on different scales, larger domains differing in isotopic and smaller-scale domains in trace element ratios.

The Tertiary basalts (analyses in Duda and Schmincke 1978; Mertes and Schmincke 1985; Huckenholz 1983; Huckenholz and Büchel 1985; Fekiacova et al. this volume and unpubl data) contrast strongly in nearly all major and incompatible trace elements with all Quaternary lavas at comparable MgO concentrations (Fig. 7). The Tertiary basalts show higher SiO_2, Al_2O_3, Y and Zn concentrations. At a given Mg#, they are distinctly lower in TiO_2, CaO, K_2O, Zr, Nb, Ba, Rb, Ce, La, and V and show higher concentrations in Al_2O_3, Na_2O, Y and Zn. The small but distinctive group of ONB suite lavas resemble the Tertiary lavas most closely but maintain the distinct Quaternary magmatic character as shown by low Al_2O_3, relatively high CaO and higher concentrations of several incompatible elements.

The striking difference in LILE concentrations between the strongly silica-undersaturated Quaternary foidites (Fig. 7) and the Eocene Hocheifel basalts cannot be interpreted entirely in terms of lower degree of partial melting of the young lavas. Significant decoupling of trace and minor elements, commonly regarded as reflecting metasomatic enrichment in the mantle, are evident between the Quaternary and many other alkalic provinces as well as between different Quaternary Eifel magma groups. For example, most Quaternary Eifel magmas are not especially enriched in Ti, P and Y compared to alkali basalts in general, while they show unusually strong enrichment in Nb, Rb, Ba and K. The higher Ba, Rb, Nb, Zr and K concentrations in the FW and ON suite, compared to the BW magmas, are not correlated with P_2O_5 concentrations. In fact, the "less enriched" BW magmas have the highest P contents. Derivation from compositionally heterogeneous mantle sources is likely but difficult to quantify at this stage.

Among the major elements, Al concentrations strongly contrast with the LILE concentrations, the Tertiary alkali basalts showing the highest and the melilite nephelinites the lowest Al concentrations. This feature, coupled with the very high Ca concentrations, steep REE patterns, constant

concentration levels in Y, Sc, Yb, Lu and high La/Y ratios (exceeding 37) is most easily explained if garnet was a residual phase during low degrees of partial melting producing the F-suite magmas. The fact that garnet has not been found in xenoliths in the Eifel is not considered significant because the area of melt generation is likely located below the zone of rapid uprise in which mantle fragments become first incorporated in the magma prior to temporary or permanent storage in magma reservoirs.

The suggestion of at least two strongly contrasting mantle source reservoirs is supported by differences in $^{87}Sr/^{86}Sr$ and $^{143}Nd/^{144}Nd$-isotope ratios (Wörner et al. 1986, note that in table 1 and figure 2 of Wörner et al. samples 382, 393 and 350 (Tertiary basalts) are listed together with Quaternary rocks of the EEVF). Based on the limited number of rocks analyzed, three major groups of radiogenic isotope ratios can be distinguished from each other among the Quaternary lavas, largely correlating with K-enrichment. The least enriched ONB-suite magmas show the lowest $^{87}Sr/^{86}Sr$ (<0.70392) and the highest $^{143}Nd/^{144}Nd$ ratios (>0.51280) and $^{206}Pb/^{204}Pb$ ratios (19.490), all being very similar to those in many Tertiary basalts of regionally adjacent fields (Wörner et al. 1986; Fekiacova et al. this volume). These ratios are closest to the Low Velocity Component (LVC) (Hoernle et al. 1995) or European Asthenospheric Reservoir (EAR) (Cebria and Wilson 1995) and most closely resemble OIB. The ON lavas are slightly less isotopically enriched than the basanites. The WEVF foidites are less radiogenic than those in the EEVF, with the younger BE suite – the most potassic Eifel magmas – representing the most enriched Eifel magmas ($^{87}Sr/^{86}Sr$ >0.7046; $^{143}Nd/^{144}Nd$ <0.51271) and also compared to other CEVF magmas. The isotope ratios of the WEVF foidites and the EEVF magmas fall into the EM-1-type mantle field in Sr-Nd space (enriched lithosphere), that may represent recycled lithosphere with some mantle being on a binary mixing line with the less radiogenic BW magmas, a topic discussed more fully elsewhere (e.g. Kempton et al. 1988; Wilson and Downes 2006).

The BW suite magmas were derived from a mantle source similar to that producing the Tertiary Hocheifel magmas except for the higher P, Zr, Y, Ba and Sr-concentrations in the young Westeifel magmas.

6 Xenoliths

6.1 Ultramafic xenoliths

Two broad groups of ultramafic xenoliths are found in many Eifel volcanoes: (a) peridotites of many different types and (b) pyroxenites,

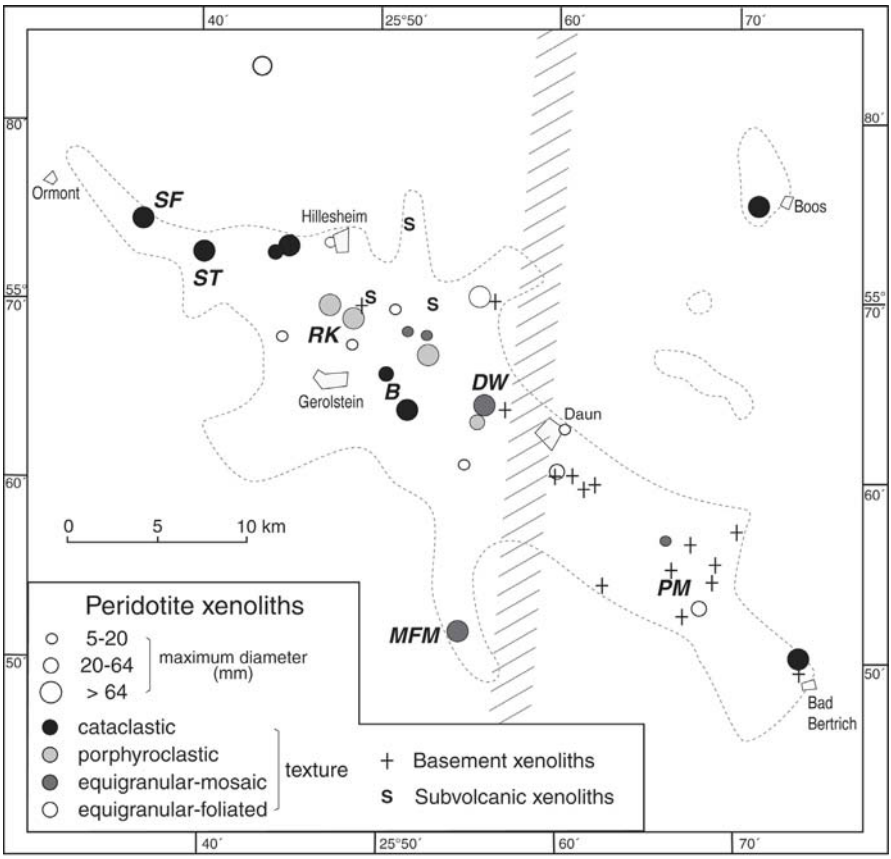

Fig. 12. Regional distribution of texturally contrasting peridotite xenoliths and their maximum diameters found in tephra (mostly maar) deposits. Also shown is the distribution of mostly syenitic subvolcanic rocks and metamorphic basement xenoliths. Major peridotite and ultramafic cumulate xenolith localities are, from NW to SE: Schönfeld (*SF*), Steffeln (*ST*), Rockeskyller Kopf (*RK*), Baarley (*B*), Dreiser Weiher (*DW*), Meerfelder Maar (*MFM*) and Pulvermaar (*PM*). The ruled vertical zone is the eastern boundary of the Eifel North-South Zone. Modified from Mertes (1983)

hornblendites and glimmerites. Ultramafic xenoliths occur in almost 90 % of all exposed WEVF volcanoes studied (Mertes and Schmincke 1985) and, contrary to common belief, most of the mafic volcanoes in the EEVF, where they are generally small and rare. Ultramafic xenoliths are especially abundant in some maar deposits, the two most famous localities being Dreiser Weiher in the eastern central WEVF and Meerfelder Maar (pit at Deudesfeld) in the southwestern WEVF. Peridotite xenoliths from the Westeifel have been studied in much detail especially during the past 25

years, mainly by Seck, Stosch and Witt-Eickschen and colleagues, more recently also by Edgar and Shaw and colleagues (e.g. Stosch and Seck (1980); Seck and Wedepohl 1983; Stosch 1987; Witt-Eickschen (this volume) and literature therein; Edgar et al. 1989, and Shaw et al. 2005) and are only briefly summarized below. The regional distribution of different types of xenoliths has been discussed by Mertes (1983) (Fig. 12).

6.2 Peridotites

The xenoliths are mainly spinel peridotites with 2 to 20 % modal clinopyroxene. Clinopyroxene-poor lherzolites and harzburgites predominate with dunites and lherzolites being less common. There are several types of websterites as well. The xenoliths are commonly subdivided into several groups (Seck and Wedepohl 1983; Witt-Eickschen et al. 2003). Highly deformed porphyroclastic peridotitic xenoliths similar to those found in many Tertiary volcanoes, recrystallized at about 750 to 900 ^{o}C, occur mainly around the periphery of the WEVF (Fig. 12). The xenolith suite in the more centrally located Dreiser Weiher Maar and in Meerfelder Maar contain high-temperature anhydrous coarse-grained LREE-depleted (Ib-type) spinel harzburgites, wehrlites and dunites characterized by lack of visible deformation, no visible amphibole and equilibrium temperatures of ca. 1100-1160 °C. Some of the anhydrous high-temperature xenoliths e.g. from Dreiser Weiher contain olivine clinopyroxenite as veins and as discrete xenoliths, interpreted as high pressure cumulates of Quaternary magmas based on cumulate textures and compositional resemblance to WEVF lavas (Witt-Eickschen and Kramm 1998, see below). Modally metasomatized hydrous xenoliths with texturally equilibrated amphibole (Ia - type, also called type II) (low-temperature average 950 ^{o}C, low pressure hydrous peridotite suite) contain pargasitic amphibole and variable amounts of phlogopite in addition to olivine, orthopyroxene, clinopyroxene, spinel or its breakdown products. They are strongly deformed, enriched in LREE over HREE and other incompatible elements and show higher radiogenic Sr and lower Nd isotope ratios. Type II xenoliths may have been derived from a metasomatized mantle domain of type I material. The metasomatized peridotites are unlikely to be the source for the basanite and nephelinite Eifel magmas (Stosch and Lugmair 1986). The low TiO_2-concentrations in pargasitic amphibole in porphyroclastic and recrystallized peridotite xenoliths is interpreted as reflecting reaction of peridotite (rising diapir?) with a low-density fluid (Witt and Seck 1989). These topics are discussed more fully in Witt-Eickschen (this volume). The fol-

lowing comments concern the relationship between veined xenoliths and Quaternary magmatism.

6.3 Age of mantle metasomatism and relationship to Quaternary magmatism

Witt-Eickschen et al. (2003) and Shaw et al. (2005) suggested that amphibole and clinopyroxene veins in peridotite xenoliths at Dreiser Weiher and Meerfelder Maar formed during two distinct events. An old Hercynian metasomatic event (e.g. Wörner et al. 1986; Wilson and Downes 1991) is thought to be reflected in widespread formation of secondary Ti-poor and Zr- and Hf-depleted amphibole, phlogopite and clinopyroxene in lherzolite xenoliths (Witt-Eickschen et al. 1998, 2003). Shaw et al. (2005) reached the same conclusion based on Ti-poor cores of clinopyroxenes studied in volcanic rocks to the west. The Hercynian metasomatic event is possibly related to fluids released from subducted lithosphere (e.g. Wilson and Downes 2006).

The second metasomatic event, characterized by Ti-rich amphibole-phlogopite-clinopyroxene veins hosted in lherzolite and harzburgite xenoliths, is thought by the above authors to have been associated with Quaternary magmatism. A young metasomatic event associated with Tertiary magmatism had also been suggested based both on isotope data (Wörner et al. 1986) as well as trace element arguments (Duda and Schmincke 1978; Mertes and Schmincke 1985).

Inasmuch as the isotopic signatures of the Eocene Hocheifel basalts (in the widest sense) are not very radiogenic (resembling many other Tertiary basalts of the CEVFs) (Wörner et al. 1986; Fekiacova et al. (a) this volume), it is difficult to understand how these magmas could have escaped being affected by a mantle metasomatically overprinted by major previous episodes of metasomatism unless they effectively bypassed such mantle domains. On the other hand, the area of Tertiary Eifel eruptive centers almost completely overlaps that of the Quaternary fields and covers a much wider area. Without discussing the arguments based on isotope signatures of mineral phases in the xenoliths, it seems likely (see also below) that metasomatism now reflected in most Quaternary lavas is basically associated with the Tertiary magmatism. This does not negate the possibility of several distinct metasomatic episodes in mantle domains not participating in the source of the released magmas as based e.g. on oxygen isotope studies one of which being due to release of H_2O-rich fluids possibly from subducted lithosphere (Kempton et al. 1988).

6.4 Host magma composition to the Dreiser Weiher and Meerfelder Maar xenolith suites

The correct identification of the composition of host magmas of xenoliths is of major interest with respect to (a) the postulated magma composition that may have resulted in very young metasomatic element transfer in the mantle pathways of ascending magmas and (b) whether or not veins (e.g. clinopyroxene and/or amphibole) or (c) glass in peridotite xenoliths formed from magma identical to the host magma of the xenoliths. The composition of the host magmas to the xenoliths has received surprisingly little attention, however. This may in part be due to the fact that the juvenile lapilli in the maar deposits are choked with small Devonian rock chips. This nasty type of contamination characteristic of lava lapilli formed during phreatomagmatic eruptions makes preparation of clean whole rock samples difficult. The host magma to the Dreiser Weiher xenolith suite is commonly referred to as basanite (Stosch and Lugmair 1986; Witt-Eickschen and Kramm 1998; Shaw et al. 2005) and that to the Meerfelder Maar xenolith suite as olivine nephelinite (Mertes and Schmincke 1985; Witt-Eickschen et al. 1998; Shaw et al. 2005) or basanite by other authors. In other words, the host magmas for both localities are commonly thought to belong to the young ONB magma group differing significantly in major and trace elements and isotopic signatures from the prevailing potassic foidites. Shaw et al. (2005) postulate that amphibole-phlogopite-pyroxene veins found in mantle xenoliths at both localities have crystallized from the passage of sodic host magmas contrasting with more potassic host magmas in similar veins in xenoliths found in volcanoes to the west. Witt-Eickschen et al. (1998) noted that the LREE-concentrations in clinopyroxene megacrysts from lavas as well as the Sr-Nd isotopic signatures of ONB magmas are close to those of amphibole in young metasomatic veins in peridotite xenoliths from Meerfelder Maar. This suggested to them that veins and the host magma had the same source.

Petrographic evidence and bulk rock compositions, however, clearly identify the host lavas at both major xenolith localities as melilite nephelinite and thus belong to the F-suite that prevails in the WEVF. The identification of one of two lavas (Ia/157, locality not given) as basanite (Stosch and Lugmair 1986) and discounted as parental to wehrlite xenoliths based on contrasting isotope signatures is also in doubt. If indeed the parental magmas to the veins at both localities had been sodic, and if the melt metasomatism associated with veinlets was an “extremely short (tens of years) and young (Quaternary) event” (Witt-Eickschen et al. 1998), then the xenolith-laden potassic melilite nephelinite magmas erupted were unrelated to the melt from which the veins in the peridotite xenoliths crystal-

lized. If the criteria for rapid and young vein formation can be relaxed while maintaining the compositional host magma criterion, the postulated sodic magmas might be related to the Eocene HEVF magmatism. There is clearly a need for a detailed study of the host magmas to the peridotite xenoliths at Dreiser Weiher and Meerfelder Maar.

6.5 Olivine-poor ultramafic xenoliths

A separate group of ultramafic xenoliths (wehrlites, clinopyroxenites, amphibolites and glimmerites) consisting dominantly of variable amounts of clinopyroxene, Ti-rich phlogopite, Ti-rich amphibole, glass and accessory apatite, titanite and rare hauyne are extremely common in foidite volcanoes in the eastern-southeastern part of the WEVF, especially Gemündener Maar, Weinfelder Maar and Pulvermaar. These xenoliths were interpreted by Lloyd and Bailey (1975) (see also Lloyd 1987) in a landmark paper introducing the model of mantle metasomatism as the final product of complete metasomatic alteration of mantle peridotite. Metasomatic processes are now widely accepted to occur in the upper mantle resulting from magma percolation, stagnation and crystallization as shown for type II peridotites (see above). Becker (1977) interpreted the cumulates chiefly as formed at low pressure but did not exclude that some formed at high pressure. Duda and Schmincke (1985) argued that the hornblende/phlogopite/pyroxene xenoliths in the Eifel are cumulates of liquidus phases crystallized from a magma compositionally resembling the present host magma having formed at the base of, or within, the lower crust. As main evidence they regarded the entirely undeformed constitution of the main mineral phases and the vuggy open texture of many of these xenoliths that is typical for cognate plutonic crystal aggregates. The relationship between potassic foiditic host magma and these cumulate xenoliths is further accentuated by the fact that WEVF basanites and olivine nephelinites lack such xenoliths. The same relationship holds for the EEVF where mineralogically and texturally similar cumulates are restricted to the foiditic Rieden subfield (Viereck 1984).

The moderate to high pressure cumulates such as those at Pulvermaar are thought to have been sampled from more extensive plutonic bodies underlying much of the southern WEVF, possibly mainly at lower midcrustal depths based on microthermometry of CO_2-dominated fluid inclusions in clinopyroxene and amphibole from xenoliths at Pulvermaar (Hansteen and Schmincke, unpubl.). Assuming a temperature of 1200 °C for the host magma, the secondary inclusions would have been trapped at a pressure of 620 ± 50 MPa. This corresponds to a depth range of magma holding stages

of 21 to 25 km, the likely depth of cumulate formation. A similar depth range (700 to 900 MPa) was inferred for wehrlite formation at Baarley (WEVF) (Shaw and Klügel 2002) as well as from fluid inclusion studies on cumulate and crustal xenoliths from the EEVF (Sachs and Hansteen 2000). *P*-wave velocities in the EEVF (6.1 to 6.4 km/s) in the depth interval 10 to 22 km) (Mechie et al. 1983) probably reflect the velocity structure of the Eifel crust prior to volcanism (see Fig. 3). The velocities most likely indicate the presence of amphibolite-facies gneisses of granodioritic and tonalitic composition (Mengel et al. 1991). The velocity increase to 6.7 km/s at a depth of 22 km defines the Conrad discontinuity. This ductile-brittle transition is probably the most efficient barrier against further magma ascent. Witt-Eickschen and Kramm (1998) inferred much higher pressures of formation for the clinopyroxenites from Dreiser Weiher (1.7-2.2 GPa, i.e. depth interval approximately 50-65 km). There is presently insufficient information on the range of clinopyroxenite types and compositions found in the three most prominent maar localities. It should be noted that peridotite xenoliths are practically lacking at Pulvermaar, further supporting the interpretation that this eruption has sampled mainly crustal magma storage levels.

Single xenocrystic deformed olivine or small aggregates, commonly embedded within some alkali pyroxenite and glimmerite nodules – informally named cuckoo olivines by us – are interpreted to represent remnants of peridotite xenoliths carried upward by earlier magma batches. They were deposited within a slowly cooling mafic potassic magma in lower/mid-crustal reservoirs where they were largely disintegrated and dissolved (see also Shaw et al. 2005). Lloyd and Bailey (1975) had found similar partly “digested” peridotite xenolith remnants in the clinopyroxene/amphibole/phlogopite nodules but interpreted this texture as reflecting metasomatism proceeding at mantle depths. The model of peridotite xenolith accumulation and partial to complete solution in lower crustal reservoirs was substantiated by studies on La Palma (Klügel et al. 1997; Klügel 1998). This evidence put to rest the general belief that ultramafic nodules in surface lavas are always powerful evidence for rapid rise of magma directly from the source region in the upper mantle. Recent work by Shaw (2004) and Shaw and Klügel (2002) has enhanced this reinterpretation. See also section on location of magma reservoirs.

6.6 Eruption of ultramafic xenoliths

Why are dense and sometimes large ultramafic xenoliths weighing several kilograms erupted in some volcanoes and not in others? To a first order,

there is a clear compositional control in the sense that, in the Eifel as elsewhere, practically only mafic magmas have carried such xenoliths to the surface. This is most easily explained by the rise of magmas from greater depth while more evolved magmas have formed in higher-level magma reservoirs, sites where dense mantle xenoliths have been removed by sinking and/or dissolution. For example, the 11,000 year-old Ulmener Maar deposits where the juvenile foidite magma is of intermediate composition, completely lacks peridotite xenoliths. When focusing on mafic volcanoes, the former interpretations of CO_2-rich explosive processes whereby massive exsolution of CO_2 has propelled a "fluidized" mixture of gases and magmatic particles at such high speeds that even blocks weighing several kg could be transported to the surface is not the only and sometimes not the major mechanism. Kimberlite diatremes have been classically explained in this way although magma-water encounter is likely to have played a major role in the emplacement of kimberlites (Lorenz 1985) although there may be a spectrum from entirely pyroclastic to dominantly phreatomagmatic eruptive processes. A few lava flows in the WEVF are choked with peridotite xenoliths and similar xenolith concentrations occur in erosional remnants (vent fillings) of basaltic volcanoes in the Tertiary Westerwald and Vogelsberg. Nevertheless, the fact that not only the two most famous xenolith occurrences in the Eifel (also Steffeln, Schönfeld etc) are maars cannot be explained away easily, especially since nearby large volcanic centers such as the very mafic Mosenberg lavas and scoria deposits practically lack peridotite xenoliths. The ability to erupt large amounts of peridotite xenoliths seems to depend mainly on transport energy. The high volatile concentrations characteristic for very alkalic magmas such as those of the WEVF are likely to have resulted in high ascent velocities carrying the mantle xenoliths to the upper crust (Schmincke 1977). In the Meerfeld and Dreiser Weiher maar deposits, the mass of peridotite xenoliths exceeds that of juvenile lapilli in some layers. The lava lapilli themselves are choked with Devonian slate/sandstone fragments and also contain small fragments of peridotite xenoliths. The intense mixing processes of highly fragmented country rock and a peridotite xenolith-laden magma must obviously have occurred within the Devonian basement where the rising magma encountered groundwater, the highly energetic steam explosions being able to propel mostly Devonian fragments and a smaller fraction of magma and xenoliths to the surface.

In summary, the most important boundary condition for eruption of abundant and large peridotite xenoliths in the Eifel fields is a characteristic magma composition typically mafic and highly alkaline. Such magmas may have risen upward from above the depth of massive CO_2 exsolution at high velocity owing to high volatile (CO_2) concentrations especially char-

acteristic of melilite nephelinites, all of which in the WEVF and EEVF show petrographic evidence for primary carbonate in the groundmass (Mertes and Schmincke 1985). At shallow depth, however, this transport mechanism is strongly enhanced due to intense mixing of rising magma and groundwater resulting in highly explosive eruptions. The fraction of external water/steam in most WEVF maar eruptions was not large enough to cause quenching of tephra to glass since ash and lapilli fractions of juvenile tephra of maar deposits in the Eifel are generally tachylitic, often with round peletal shapes and commonly agglutinated. This indicates that the cooling rate in the eruptive mixture was low enough to prevent the formation of glass while high enough to cause transport and deposition of the particle populations to have been cool and often wet. The ubiquitous partial melting of mica/amphibole-bearing igneous/metamorphic crustal xenoliths common in the Eifel maar deposits probably added to the volatile budgets of the ascending mafic magmas.

6.7 Lower/middle crustal xenoliths

A major motivation to study crustal xenoliths is to monitor crustal lithology, i.e. to compare the lithology inferred from seismic data (e.g. Mechie et al. 1983) with mineralogical and fluid inclusion geobarometers and to infer the levels at which magma reservoirs formed. Both mafic and felsic granulites representing lower/middle crustal lithologies occur as (partially melted) inclusions in lava and as separate xenoliths in the deposits of many volcanoes in both fields. They are especially common in the Kempenich-Engeln area in the EEVF where they have been studied in detail (e.g. Loock et al. 1990; Sachs and Hansteen 2000 and literature therein). Fragments of low- to intermediate-grade metamorphic rocks in deposits of highly explosive plinian eruptions (Wehr and LSV) in the EEVF have been extremely useful in estimating the depth of high-level magma reservoirs (e.g. Wörner et al. 1982). The depth of high-level magma reservoirs has been estimated as between ca. 5 and 7 km for the phonolitic magma reservoir Auf Dickel in the WEVF extending into the crystalline basement (Mertes and Schmincke 1983).

6.8 Upper crustal xenoliths

A very shallow depth of magma-water encounter is inferred from the dominance of Lower Devonian slates and sandstones representing different Devonian stages or formations in maar deposits and in initial tephra rings underlying many scoria cones. This is not surprising because the explosive

energy of phreatomagmatic eruptions is due to magma-water encounter at low pressure where the volume ratio steam/water exceeds 1000. Lower stratigraphic levels can be intersected as the explosive focus migrates downward following successive explosive removal of the overburden (Lorenz 1986) during the course of an eruption.

Middle Devonian limestones are restricted to the central WEVF as are lower Mesozoic Buntsandstein lithics because these formations are only preserved in the subsided Eifel NS zone (Mertes 1983). The fact that a broad spectrum of xenoliths from the metamorphic basement, a distinctive xenolith type in maar deposits, occurs exclusively in the eastern but not central part of the WEVF correlates with the fact that the seismic boundary between low velocity Devonian and higher density crystalline basement shallows from about 5 to 3 km east of Daun (Mertes, 1983). In other words, fragmentation of upper crustal rocks resulting from dominantly phreatomagmatic eruptive processes rarely propagated much deeper than about 3 km in the Eifel fields during successive deepening during an eruption.

7 Differentiation of Eifel magmas

7.1 Stage I (ca. 16 to ca. 8 wt% MgO)

At least 10 % of the WEVF volcanoes contain large (up to 50 cm) and some 20 % of the East Eifel volcanoes small (cm-sized) peridotite nodules, but only the ONBW and some of the FW magmas qualify as near-primary based on their chemical composition (high Mg-values etc), lavas with MgO >10 wt% being rare in the EEVF. The early stage of fractionation of primitive magmas is characterized in the Eifel as is common by a drastic decrease of Mg, Cr, Ni and by little change or only a slight increase in other elements. These trends can be explained mainly by olivine, or, at higher pressures, enstatite and spinel, as well as clinopyroxene and phlogopite fractionation, although disintegrated nodule debris – some likely redissolved in highly primitive WEVF magmas – makes exact calculation of fractionation uncertain.

Clinopyroxenes with several types of green cores, many with sharp boundaries to a normally zoned comagmatic titanaugite mantle, are common in mafic lavas not only in both Eifel fields but also worldwide in fields of alkali basalt volcanoes (Duda and Schmincke, 1985). Most cores are greenish pleochroic and moderately resorbed (acmitic augite). Cores of Al-augite composition and of Cr-diopside derived from peridotite xenoliths are rare. The acmitic augites are enriched in Na, Mn, Fe and depleted

in Al, Ti, Sr, Zr. Our model for polybaric fractionation assumes that green cores formed at high pressures, most likely in the uppermost mantle and in the transitional mantle/crust area. Primitive alkalic mafic magma is thought to rise through the upper mantle precipitating Al-augite en route. During stagnation near the crust/mantle boundary Fe-rich augites crystallize. Newly rising primitive magma is mixed with magmas differentiated at high pressure, greatly compromising attempts to define and reconstruct the original chemical character of the mixed magmas erupted at the surface. The more magnesian rims of erupted pyroxene phenocrysts are thought to have formed when new pulses of primitive magma mixed with the magma differentiated at high pressure.

7.2 Stage II (Intermediate magmas) (MgO 8 to <4 wt%)

Stage II is characterized mainly by a decrease in Mg and Ca, as well as by a further decrease in Cr and Ni, caused chiefly by clinopyroxene and lesser olivine fractionation. At MgO concentrations of <5-6 wt%, Fe, Ti, P and K decrease due to fractionation of phlogopite (which also fractionates in some more primitive lavas), titanomagnetite, amphibole, titanite and apatite. High-pressure fractionation of amphibole is suspected. The compositional range between about 2 and 4 weight percent MgO is almost devoid of rocks as in many other magmatic systems (Bunsen-Daly gap). The chemical composition of some such as those of Ettringer Bellerberg in the EEVF, which are especially rich in crustal xenoliths (see below), clearly reflects the local addition of SiO_2-rich crustal material while others such as the Niedermendig tephrite show no isotopic evidence for crustal assimilation (Wörner et al. 1986).

The common systematic compositional evolution of scoria cones from an early intermediate (e.g. tephritic) to a late more mafic stage is petrologically important because it reflects ubiquitous discontinuities in magma transfer from the melting anomaly to the surface. Compositional zonation is much more common than generally envisaged because traditional geochemistry is based on “grab” sampling. Similarly, the petrogenetic information based on average composition of lavas from several localities (e.g. Mertes and Schmincke 1985; Wedepohl et al. 1994) is of limited value as averages do not allow to trace the step-by-step evolution of magmas to reconstruct differentiation processes. This is particularly evident e.g. when comparing the average composition of LSV phonolites (Wedepohl et al. 1994) with the extreme ranges in composition reported by Wörner and Schmincke (1984) and Harms and Schmincke (2000). Where the base and top of a volcano are exposed to allow stratigraphically controlled sam-

pling, all our studies of Eifel volcanoes have revealed compositional zonation. This type of evolution is especially well-developed in practically all of the larger EEVF scoria cones studied in detail (Schmincke 1977 a; Duda and Schmincke 1978 and many later studies). The initial phase commonly begins with eruption of intermediate lavas (tephrites) that contain no or only small amounts of olivine and few and small phenocrysts of phlogopite and clinopyroxene, some with minor amounts of hauyne. The eruption generally ends with relatively primitive lavas, some late dikes being especially rich in larger clinopyroxene and olivine phenocrysts as well as fragments from lower crustal levels (granulites) and small peridotite xenoliths or other xenolith debris. Most probably, these mafic/intermediate compositionally zoned systems developed largely in magma reservoirs at mid-crustal levels, following earlier stages of differentiation at higher pressures. All volume calculations carried out so far show that a much larger volume of primitive parent magmas has not erupted. Even a basanitic volcanic complex such as the young Wartgesberg in the WEVF shows clear differences between the more evolved initial tephra, the main bulk of erupted lava and the terminal subplinian tephra that represents the most mafic material erupted (see above). Systematic sampling of individual lava flows in the EEVF such as the famous but relatively small Wingertsberg lava or the more voluminous Hochsimmer lava has shown that the last-erupted part of a lava flow is more mafic than the first erupted material (B Freundt 1988; Schulz 1992). Obviously, magma reservoirs at moderate to low pressures in which magma ponded, cooled and fractionated, were commonly of small dimensions, possibly finger- or dike-like with high aspect ratios (vertical versus lateral extent) to allow pronounced compositional changes to develop. Stress conditions in the EEVF were likely more favorable for such chambers to develop than in the WEVF.

The common assumption that vesiculation provides the final trigger for an eruption to commence is not supported by the field observations in the Eifel fields. The dominant trigger mechanism is most likely the positive buoyancy and the arrival from depth of new small batches of magmas pushing out the resident magmas. Volcanic juvenile particles erupted in the initial phreatomagmatic stages are generally nonvesicular or poorly vesicular. Highly explosive subplinian eruptions generally mark the terminal stages in the evolution of a scoria cone in the Eifel, possibly originating in a deeper level of a conduit system when slow magma supply does not keep pace with the evacuation of the conduit system.

7.3 Stage III (Highly evolved magmas <1.5 wt% MgO)

Stage III is characterized by a further decrease in Mg, Cr, Ti, P, Fe and related trace elements and by an enrichment in Si, Al, Na and trace elements such as LREE, Zr, Nb, Rb, Ba, U, and Th. Minor phonolite occurs locally in the WEVF but there are three large highly differentiated phonolitic volcanic complexes in the EEVF (Rieden, Wehr, Laacher See) and small local Dümpelmaar, the original size of the highly eroded Kempenich system being uncertain. Rieden, Laacher See and Wehr have been studied in detail (e.g. Wörner and Schmincke 1984 a, b; Bogaard and Schmincke 1984, 1985; Viereck 1984; Wörner et al. 1988; Bourdon et al. 1994; Harms and Schmincke 2000; Harms et al. 2004).

Plagioclase is completely lacking in the Rieden volcanic system (Fig. 8). This is reflected in high Sr concentrations even in highly differentiated phonolites derived from leucitites. The Rieden is also distinguished from the younger magmatic systems by many other chemical parameters (Fig. 7). The phonolitic magmas of the Wehr magma system, derived from basanite magmas and thus a forerunner of the LSV system, appear to have partially melted minor country rock around the magma reservoir, resulting in some uptake of SiO_2 (Wörner et al. 1982; 1988) leading to the formation of small amounts of trachytic magmas. Plagioclase was fractionated in the magmatic systems Wehr and Laacher See in addition to the mafic phases mentioned above. The terminal stage of differentiation is mostly governed by sanidine, as well as by smaller amounts of hauyne and nepheline. The Laacher See phonolite tephra deposits are strongly compositionally zoned from initial extremely phenocryst-poor, highly evolved hauyne phonolite (ca. 750 ^{o}C) to hotter very crystal-rich (up to 50 vol%) mafic phonolite. Several major and smaller compositional gaps occur in the deposits. A wide variety of cumulates was erupted chiefly during the terminal stages (Tait et al. 1989). The mostly phonolitic to trachytic Wehr magma system in the EEVF probably evolved in a metamorphic basement close to the Devonian upper basement rocks, i.e. below about 5 km depth (Wörner et al. 1982, 1988). The high-level magma reservoir of the strongly evolved LSV phonolites developed largely within Devonian slates and sandstones (Hunsrück and Siegen facies) at 5-8 km depth for the LSV (Wörner and Schmincke 1984b; Harms et al. 2004).

7.4 How much magma was erupted, where did the magmas differentiate and how much magma was supplied to the crust?

Quantification of the mass of magma supplied from a melting anomaly to the crust and surface is of some interest especially with respect to melt production calculated from a buoyantly rising plume (e.g. Ritter 2005). Magma volumes erupted in both fields are, unfortunately, impossible to determine quantitatively for all but the youngest volcanoes because of the advanced degree of erosion during glacial and interglacial periods and present cover by vegetation. Moreover, no quantitative estimate of juvenile clasts versus lithoclasts has yet been undertaken, e.g. for the many maar deposits. Judging from two well-exposed young maar deposits (Meerfeld and Ulmener Maars) I estimate that more than 80 % possibly 90 % by volume in these tephra rings consists of country rock fragments. An extremely rough estimate suggests about 1.7 km^3 magma DRE (dense rock equivalent) to have been erupted in the WEVF (Mertes and Schmincke 1985) but possibly as much as 15 km^3 in the EEVF. This is based on the most recent estimate of magma erupted at Laacher See (>6.3 km^3, Harms and Schmincke 2000), an estimate for the Rieden phonolitic system to have erupted magma around 4 km^3 (Viereck 1984) plus the smaller phonolitic Wehr system. To these volumes must be added the relatively large scoria cones and some very large lava flows, such as that erupted at Hochsimmer volcano in the EEVF. The amount of magma erupted in both Eifel fields together during the past ca. 0.7 Ma is thus estimated at roughly 20 km^3, possibly as much as 30 km^3.

Any attempt to assess the mass of magma supplied to the crust must, however, take into account the mass of magmas underplated and retained in magma reservoirs at several levels within the crust. For example, estimates of the amount of basanitic parent magma from which the highly evolved LSV phonolite magmas was derived range up to 60 km^3 depending on boundary assumptions (Wörner and Schmincke 1984 a, b). Judging from geobarometry, basement xenolith studies and experimental data, fractionation of the highly evolved LSV zoned phonolitic system took place at high crustal levels, the large magma columns probably having volumes approaching tens of km^3. The most recent estimates of the depth interval and temperature range of the erupted part of the LSV magma reservoir based on experimental data are 4.6–7.8 km and 750 ^oC and 880 ^oC (Harms et al. 2004; see also Berndt et al. 2001). Wörner and Schmincke (1984) preferred a model by which ca. 56 km^3 of basanite magma differentiated in the lower crust to form ca. 16 km^3 of mafic phonolite which, after ascending into the upper crust, evolved to form 5 km^3 of highly evolved phonolite magma. Further arguments in support of this model are based on U-Th

equilibria in minerals and glasses of pumice and cumulate nodules (Bourdon et al. 1994). Using the recently recalculated minimum volume of 6.3 km^3 for the erupted LS magma (Harms and Schmincke 2000), a total volume of some 100 km^3 for the basanite-mafic to evolved phonolite LS magma is assumed. Accepting a similar estimate for the Rieden system, a combined volume of 50 km^3 (mafic parent magma) for the smaller evolved systems Wehr, Glees and Dümpelmaar and a further 50 km^3 for the older phonolite systems Schellkopf, Olbrück, Perler Kopf and Engeln as well as basanite-tephrite systems, a total of some 200-300 km^3 of magma was supplied to the crust beneath the differentiated to intermediate and, locally, highly evolved volcanoes of the EEVF.

Because of intense erosion and poor exposures in the WEVF, especially of highly evolved pyroclastic centers such as Auf Dickel phonolite, estimates of magma volumes supplied to the crust in the western field are highly speculative but might be on the order of 50 km^3. The total volume of magma supplied to the base of, and into, the crust beneath both Quaternary fields was likely between roughly 300 and 500 km^3. Such very crude and highly speculative estimates are probably minimum volumes because they completely neglect the volumes of mafic magma underplated and having risen into the crust without ever reaching the surface. Ubiquitous magma storage, fractionation and mixing below the crust is reflected in the complex histories of the common green core clinopyroxenes which occur both as phenocrysts and as corroded crystals in cumulate nodules (Duda and Schmincke 1985). Further evidence is the fact that the crust/mantle boundary is highly complex and extends over a depth range of some 7 km (Mechie et al. 1983; Prodehl et al. 1992). The chemical similarity between veins in peridotite xenoliths and the Quaternary magmas (Witt-Eickschen et al. 2003; Shaw et al. 2005) further emphasizes that significant volumes of magmas have risen through the upper mantle without having erupted even though there is some doubt that the host magmas at Dreiser Weiher and Meerfelder Maar are of the same type from which the veins crystallized (see above). All this evidence combined suggests that the estimates given here are likely to be more realistic than the 70 to 100 km^3 volume of magma produced in the mantle beneath the Eifel fields and translated into an annual magma production rate of 100,000 to 150,000 m^3 suggested by Wörner (1998).

Since no active magma reservoirs have been detected beneath the Eifel volcanic fields so far, indirect evidence for size and depth of crustal magma reservoirs where magmas stagnated and differentiated to various degrees has been used to put constraints on the size (volume) and depth of magma reservoirs (Fig. 3). The criteria used include (a) a comparison of stratigraphic changes in crustal xenolith types in a volcano with known or

inferred lithology of the upper crust, (b) geobarometric estimates using mineral compositions and equilibria, (c) fluid inclusions and (d) seismic refraction data. Three types of evidence provide powerful arguments that underplating of magma has been – and probably still is – ubiquitous. This evidence includes (a) geothermometry and barometry derived from lower crustal granulites indicating very high temperatures thought to be due to underplating of magma and interaction with lower crustal material (Sachs and Hansteen 2000); (b) high pressure fractionation as inferred from green-core clinopyroxene (Duda and Schmincke 1985, see above), (c) seismic refraction data showing a prominent low velocity zone at the crust/mantle transition (Mechie et al. 1983) and (d) high flux of mantle-derived helium (see below). Approximate positions of inferred magma reservoirs as deduced from characteristic xenolith suites are shown diagrammatically in Fig. 3.

8 Volcano field analysis

The areal distribution of scoria cone volcanoes – as in the Eifel - has often been thought to be haphazard or random and referred to sometimes as „shot gun distribution“. Scoria cones – also called monogenetic volcanoes - are gregarious in the sense that they usually occur in clusters, however, forming distinct volcanic fields (Figs. 13 - 16).

The term volcanic field was introduced for the Quaternary Eifel volcanic areas to call attention to the systematic zonation of several parameters that help to understand the location and evolution of melting areas in the mantle and magma detachment zones (Schmincke 1977 a, 1982). Similar approaches to scoria cone fields using more elaborate statistics were applied by Connor (1990) to scoria cone clusters in the huge Transmexican Volcanic Belt. The size of most “monogenetic” volcanic fields appears to be independent of greatly contrasting crustal and lithospheric thicknesses. The dimensions of many such fields must thus reflect minimum areal extents and possibly orientation of melting anomalies and/or subcrustal magma collection zones. Volcano field analysis is thus the synopsis of several structural, volcanological and petrological parameters thought to reflect melting anomalies or magma collection zones. Parameters evaluated for both Eifel volcanic fields include: (a) volcano edifice spacing and volume/size; (b) spatial zonation of primitive and evolved magma compositions; (c) temporal evolution of eruptive centers and compositions; (d) zonation of type and degree of deformation of mantle and crustal xeno-

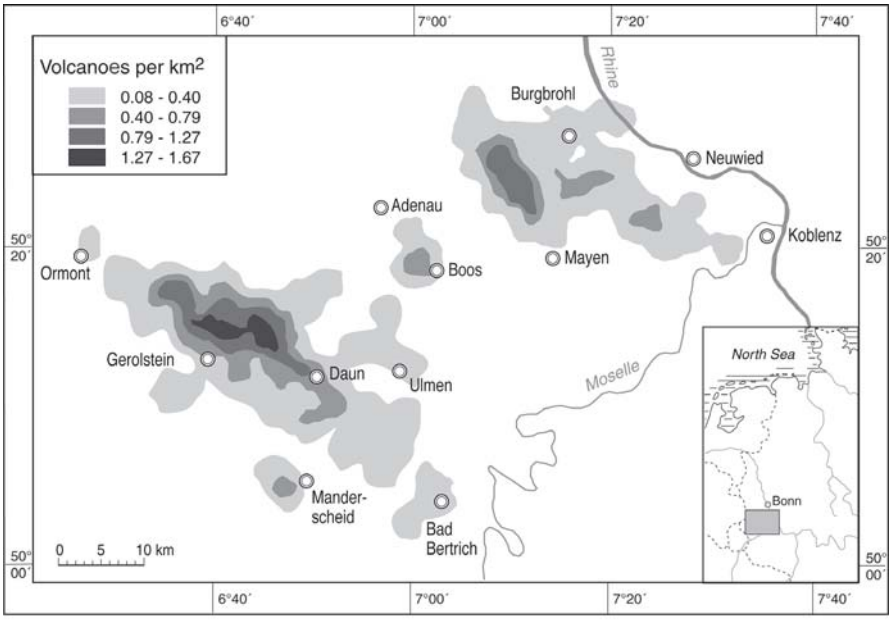

Fig. 13. Spacing of volcanoes of the West-Eifel and East-Eifel fields in each square kilometer of a quadrangle map. Modified from Schmincke (1982)

liths; (e) magma pathways (stress directions); (f) zonation of composition and discharge estimates of gas release.

(a) Volcano edifice spacing and volume/size distribution

The simplest operation in trying to view a field as a whole is to measure the distance between volcanoes or the number of volcanoes in a chosen standard area (Fig. 13). This is not trivial, however, because it must be preceded by careful mapping of as many volcanic edifices (or holes in the case of maars) as possible. Because many volcanic structures in the Eifel are highly eroded or covered by vegetation, detailed magnetic surveys have been carried out, a map of visible and inferred eruptive centers having been published by Büchel and Mertes (1982). The results of measuring volcano-spacing (Fig. 13) shows that the density of volcanic edifices per km^2 very clearly increases towards the center of the WEVF and is slightly more blurred in the EEVF where the two compositionally contrasting subfields show independent volcano density distributions. The closer spacing of volcanic centers in or near the center of a field by itself suggests, but does not prove, that the supply rate of magma through the lithosphere is

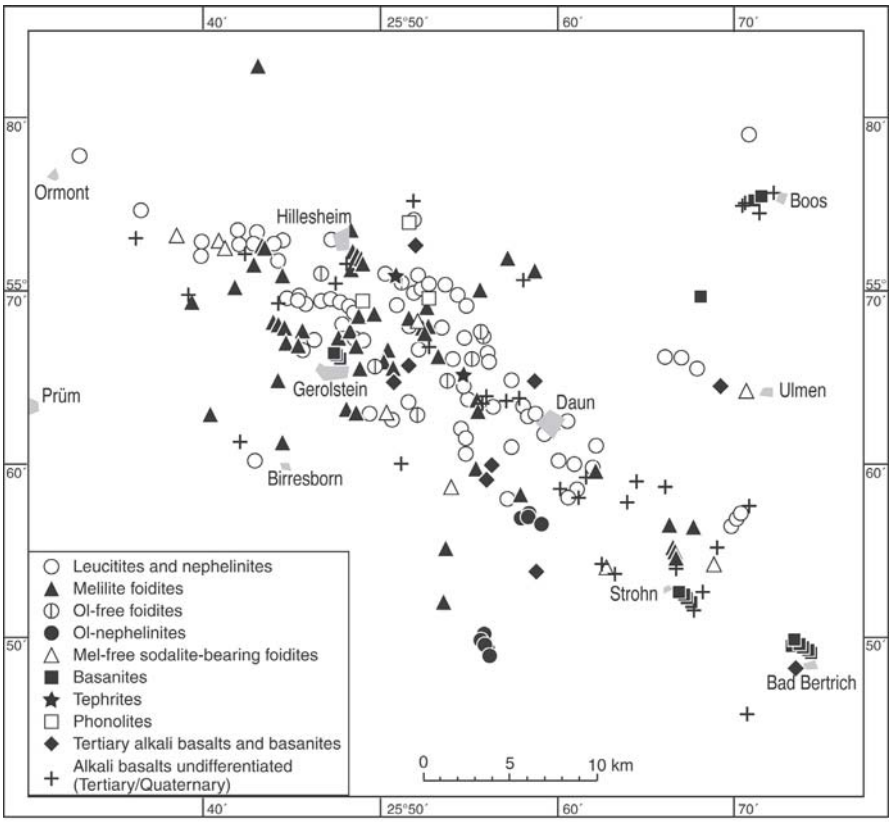

Fig. 14. Spatial distribution of lava compositions in the WEVF. Modified from Mertes and Schmincke (1985)

systematically zoned, the maximum roughly coinciding with the center of a field. The influence of crustal/fracture permeability on volcano clustering cannot entirely be ruled out, however (see below). Nevertheless, the fact that volcano density increases towards the center of many volcanic fields, the closest example being that of the Eocene Hocheifel field (Huckenholz 1983; Huckenholz and Büchel 1988; Fig. 1), strongly suggests that magma flux maxima toward a center of a field are controlled by a sub-crustal/sublithospheric anomaly.

(b) Spatial zonation of primitive and evolved magma compositions

Two compositional parameters are of special interest in terms of volcano field analysis: (1) spatial zonation of compositionally contrasting parent/primitive magmas representing different source characteristics

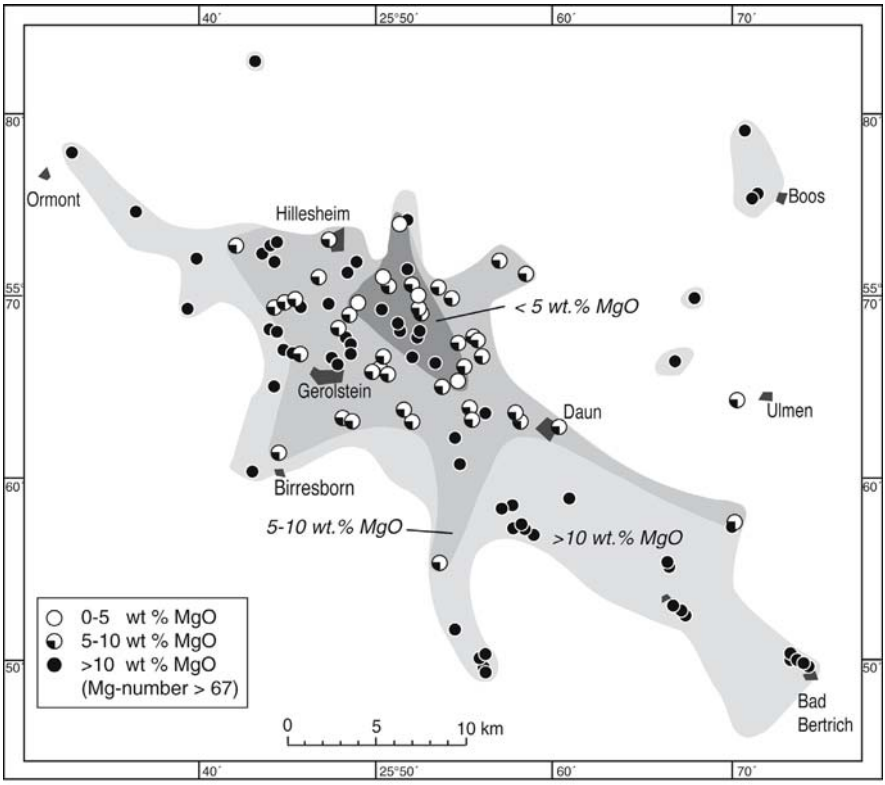

Fig. 15. Zonation of MgO concentrations in WEVF lavas. Primitive lavas with MgO >10 wt% occur only in an outer zone. Highly evolved compositions are restricted to the innermost zone. Modified from Mertes and Schmincke (1985)

(composition of source, degree of melting); (2) degree of differentiation of magmas and areal distribution of lavas differing in degree of differentiation.

(1) The five broad compositionally contrasting groups of primitive magmas distinguished occur in spatially distinct areas (Fig. 14). In the WEVF, the ONB group occurs exclusively in the southeastern/eastern subfield with one occurrence in the center. On the other hand, foidites also erupted in the same area side-by-side such as foiditic Meerfelder Maar next to olivine nephelinitic Mosenberg and melilite nephelinitic Pulvermaar next to basanitic Wartgesberg. In the EEVF, in contrast, the FE suite, concentrated in the western subfield and in a northern belt, shows almost no overlap in space with the BE lava suite to the east. This spatial distribution suggests that several types of magmas differing in major and trace

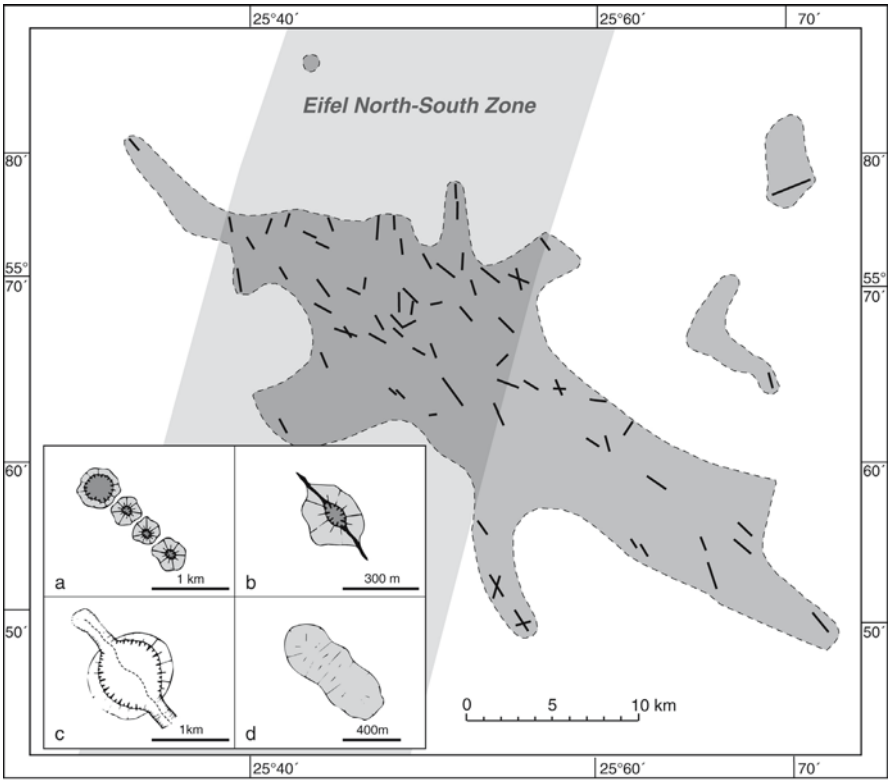

Fig. 16. Dominant dike directions and overall orientations of volcanic centers in the WEVF and criteria to determine the orientation of fissures beneath volcanoes. (a) linear rows of scoria cones and one maar; (b) dominant dike direction in a scoria cone; (c) zone of tectonic weakness (fracture), enlarged by erosion and a creek overprinted by a maar; (d) several overlapping scoria cones. Fissure directions deviate within the Paleozoic structural Eifel North South Zone (shaded gray) reflecting partial control by Paleozoic fractures. Modified from Mertes (1983)

element concentrations, mineralogy, type of ultramafic xenoliths and isotope and trace element ratios rose from several distinct mantle domains.

(2) Intermediate and minor highly evolved magmas occur only in the eastern center of the WEVF. In the EEVF, however, fractionation of primitive magmas has been highly efficient, especially in the younger Laacher See subfield. By far the largest evolved volcano (LSV) occurs in the western center of the younger subfield, the evolved Rieden phonolite complex in the older western subfield also occurring centrally. The significance of the outlying poorly constrained Kempenich volcanic complex is uncertain. Highly evolved magmas differentiated, at least during their final stage of

fractionation, in large high-level magma reservoirs, toward the center of a (sub)-field (see above) (Figs. 5, 6, 14, 15). The fact that the degree of differentiation increases towards the center of a (sub-) field is reasonably explained by a higher rate of magma generation and/or focused magma supply to the crust. More and larger magma reservoirs formed in the center are kept alive by sustained magma and thermal input from below allowing differentiation to proceed to extremely fractionated phonolite magmas. Such approximately concentric gradients in magma accumulation in a field are unlikely due to control by crustal filtering, especially as they are common features in other scoria cone fields such as the nearby Eocene Hocheifel (Huckenholz 1983, Huckenholz and Büchel 1988) and Westerwald (Haase et al. 2004).

(c) Temporal evolution of eruptive centers and compositions

The significance of the spatial zonation with respect to mantle dynamics is further strengthened by the temporal zonation of volcanic activity in space and composition. Firstly, both fields can be subdivided by age into older northwestern and younger southeastern subfields, the boundary between the age distributions of the subfields being rather sharp in the EEVF but not in the WEVF. In other words, in both fields volcanic activity migrated in time in a general way from the northwest to the southeast where the youngest eruptions occurred. Whether or not this spatial migration can be reconciled with the present mantle anomaly location is discussed below.

Volcanic activity periods in both fields seem to have roughly alternated during the past 700 ka. Foiditic magmas erupted in the WEVF between ca. 700-650 (?) and 450 ka while surface activity of chemically similar foiditic magmas is restricted to a brief period of <150 ka (<500 (?)-360 ka) in the older EE subfield (Rieden 430-360 ka). In the WEVF, sodic ONB lavas only appeared at the surface during the past 50 ka or less. The continuing eruption of foiditic magmas in part of the southeastern subfield – including the youngest volcano in the Eifel, Ulmener Maar -, indicates that the "older" magma type was still being generated - or released from magma storage reservoirs - until the present. In other words, two contrasting mantle domains were active simultaneously in the WEVF during the past few tens of thousands of years. In the EEVF, in contrast, the first surface manifestations of less silica-undersaturated but very potassic basanite-tephrite-phonolites suites (Wehr phonolite) occurred 215 ka ago, separated in time from the older Rieden subfield by a lull in surface activity lasting almost 150 ka. There was only minor surface activity following the formation of most basanitic scoria cones in the eastern EE subfield between ca. 215 and

190 ka, and none during the past 100 ka except for the comparatively huge LSV eruption 12,900 years ago.

(d) Mantle and crustal xenoliths

Xenoliths may reflect regional zonations in the rising melting domain (s), variable magma pressure related to magma production and/flux rates and regional differences in structure and lithology of the crust. Peridotite xenoliths occur as xenoliths and/or xenocrysts in more than 75 % of all mafic volcanoes in the WEVF. Highly deformed peridotite nodules, recording high temperatures of formation (1150–1250 ^{o}C) and depths of origin around 65 km (Witt-Eickschen et al. 2003), appear to be restricted to the northwestern periphery of the field (Fig. 12). In the most famous xenolith locality (Dreiser Weiher) sheared and recrystallized ones, recording high (~1150 °C) as well as low temperatures of formation (900-970 ^{O}C) (Sachtleben and Seck 1981) lower pressure (ca. 40 km) and intense metasomatism (Witt-Eickschen et al. 2003), reflect the center of the field, the area of highest magma production. Peridotites from the high-temperature suite may have been derived from the center of a melting domain with high geothermal gradients. The other main locality of both types of peridotite xenoliths (Meerfelder Maar) lies at the southwestern edge of the field. Both maar volcanoes are rather young, however, and the focus of volcanic activity has migrated to the south (see above). Shaw et al. (2005) also suggest that wehrlite xenoliths found mostly in the center of the WEVF north and south of Gerolstein formed by reaction of lherzolite-harzburgite during flow of potassic magma in the central area of the WEVF where supply of potassic magma was greatest. They also note that discrete peridotite xenoliths do not occur in a zone east of an axis Daun-Bad Bertrich. However, peridotite xenoliths do occur in the eastern zone such as at Bad Bertrich and Boos although they are smaller than those at Dreiser Weiher and Deudesfeld (Fig. 12). In my view, the abundance of ultramafic cumulate xenoliths in deposits e.g. of Gemündener Maar and Pulvermaar largely reflects the establishment of lower/middle crust magma reservoirs in which mantle peridotite xenoliths were largely dissolved and disintegrated, in short filtered out almost quantitatively. These centers are part of volcanic clusters that consist of several closely spaced but separate volcanoes that may reflect local focused magma flux. Peridotite and wehrlite xenoliths in the EEVF, generally of smaller diameter and minor abundance, occur mostly in the central areas such as Rieden (Viereck 1984), Engeln and the Eppelsberg-Jungebüsch volcanoes close to LSV.

(e) Lithosphere cracking

A classic problem in volcanotectonics and geodynamics is the question to what degree the orientation of feeder dikes beneath volcanoes – or entire volcanic fields – is influenced or controlled by the direction of structural discontinuities in (a) the upper/middle/lower crust, (b) the lithospheric mantle, (c) by sublithospheric anomalies or (d) by the present lithospheric stress field. With respect to the Eifel volcanic fields, three aspects are pertinent: (1) Is the overall NW-SE orientation of both fields controlled by ancient regional structures (lithospheric sutures) or by the present lithospheric stress field or both? (2) Are local dike and volcano row directions that deviate from the main directions controlled by older fracture directions in the brittle upper crust? (3) Do the shapes (directions) and dimensions of the surface fields in some way reflect the shape of the magma accumulation zones and/or partial melting domains?

(1) The simplest way to visualize the formation of volcanoes linearly aligned for tens of km, is by lithosphere cracking providing the pathways for magma to rise. The overall NW-SE orientation of both fields is mirrored on a smaller local scale in most directions of dikes, volcanic axes and rows of volcanoes (Figs. 13 - 16). The direction of largest horizontal normal principal stress of the lithosphere in Central Europe north of the Alps is presently NW-SE (σ_1 ca. 140^{o}–150^{o}) in central Europe (Baumann and Illies 1983) and interpreted as due to lateral motion of the lithosphere resulting from opening of the Mid-Atlantic Ridge which started in the Eocene (Müller et al. 1997). In a belt roughly parallel to Rhine River and partly covering the eastern part of the EEVF in the Neuwied Basin, the compressional stress field is transformed into a tensional field as also shown by the NW-SE oriented normal faults bordering the subsiding Lower Rhine Embayment. Cracks acting as magma pathways can thus form most easily perpendicular to the minimum compressional principal stress in a NW-SE direction with the maximum compressional principal stress being vertical. Fracture-controlled ascent of magmas through the lithosphere is likely determined by the same stress field. If this is correct, magma transport is focused even in the lower lithosphere in a NW-SE-oriented elongate belt characterized by episodically generated cracks that not only mimic but basically determine the direction of the surface fields. As it so happens, the Paleozoic stress field was practically identical to the present one. Fold axes in the Devonian basement strike NE-SW and faults at right angles (Meyer 1986). The depth extent of these faults is unknown. Several scoria cone/agglutinate cone/maar volcano clusters, each of homogeneous composition and emplaced very rapidly (weeks? months? years? as based on analogy with historic scoria cone formation) such as the young

volcano groups of Mosenberg, Bad Bertrich and Wartgesberg at the southeastern end of the WEVF, show strict NW-SE alignment. Most plausibly, these NW-SE directions are best explained by control of re-opened Paleozoic fault systems at least for upper crustal pathways or by an enhancement of the Paleozoic by the present stress field.

(2) There are a few significant deviations from the dominant directions (Fig. 16). Local N-S orientations of dikes and volcano alignments in the approximate central part of the WEVF occur in the roughly N-S trending Eifel North-South-Zone and are likely influenced by pre-existing zones of structural weakness in the brittle upper crust (Mertes 1983). Similarly, NE-SW to E-W directions in the EEVF, most pronounced in several groups of cones in the EEVF eastern subfield in the Neuwied basin (Fig. 5), mimic dominant NE-SW directions of normal faults in this Early/Middle Tertiary tectonic graben. Most likely, these fractures facilitated magma rise through the upper crust. Several voluminous nested volcano groups occur along roughly NE-SW to E-W directions that were repeatedly active. Finally, the Siegen thrust (see above) separates most of the eastern EEVF subfield from the older foiditic Kempenich/Rieden subfield, with the exception of Wehr and a few outlying scoria cones just W of Laacher See. Several dominantly or entirely tephritic cones (Nastberg, Krufter Ofen, Wingertsberg, Ettringer Bellerberg) erupted close to this thrust. Lavas of some (Wingertsberg and especially Bellerberg) are extremely rich in contact-metamorphosed and/or partially melted xenoliths of midcrustal crystalline rocks, the Bellerberg having been especially famous for over 100 years for its wealth of xenoliths and minerals formed during contact metamorphism (review in Sobczak 1985). Moreover, the cluster of scoria cones surrounding Laacher See basin at the western edge of this zone suggests that the Siegen thrust has not only facilitated enhanced magma flux. Magma reservoirs were apparently easier to develop along this zone than elsewhere in both volcanic fields. Most likely, repeated magma ascent may have been conditioned by this thrust that may have acted as a major lithosphere suture of Paleozoic age and may have provided some pre-fractured material from the lower upper crust (see below).

(3) The spatial resolution of the Eifel plume anomaly (Ritter this volume; Ritter et al. 2001; Keyser et al. 2002) is, unfortunately, insufficient to precisely define the orientation of the anomaly. The uppermost level of the anomaly between 30 and 100 km depth is subcircular and extends for more than 100 km, well beyond the outcrop limit of both volcanic fields. The reinvestigated mantle anomaly, first discovered by Raikes (1980) that extends for some 60 km depth beneath the Tertiary Vogelsberg volcanic complex, has a preferred NE-SW direction (Braun and Berckhemer 1993). In other words, anomalous linear belts of deeper-reaching anomalies re-

gionally closely associated with the Quaternary Eifel fields – and extending into the Westerwald area, also enclosed by the mantle anomaly of Ritter et al. (2001) and Keyser et al. (2002) - and mantle anomalies show strong preferred directions parallel to the Paleozoic b-axes and perpendicular to the overall orientation of the volcanic fields.

(f) Composition and rates of gas release

The Quaternary Eifel volcanic fields are typical of intraplate fields in that gases released from depth consist to more than 99 % of CO_2 providing huge resources for exploitation for carbonated mineral waters and other industrial use of CO_2. The total flux of magmatic CO_2 is estimated at ca. 1000 t/d in the EEVF and approximately 50-100 t/d in the WEVF and adjacent areas in the southwest (e.g. May 2001). The Laacher See alone releases about 5000 tons of CO_2 annually (Aeschbach-Hertig et al. 1996). Vigorous gas escape can be seen at the eastern shore of the lake, a site repeatedly sampled for detailed gas studies. Gases at LSV consist to more than 99 % of CO_2, with noble gas isotopes of He, Ne and Ar showing a clear mantle origin (Giggenbach et al. 1991; Aeschbach-Hertig et al. 1996). Further strong evidence for gas focusing beneath LSV – but not in maar lakes in the WEVF - is provided by the enormous helium flux, much higher than observed in the oceans (7.4×10^7 ^{3}He atoms $m^{-2}s^{-1}$ versus 4×10^4 ^{3}He atoms $m^{-2}s^{-1}$ (Aeschbach-Hertig et al. 1996)). CO_2 flux rates are highest in the center of both fields in the areas of highest volcano density and of eruption of more evolved magmas (May 2001). Mantle-influenced neon and argon contributions were also found at LSV (Aeschbach-Hertig et al. 1996) and SW of the WEVF close to the center of the *P*-wave velocity anomaly in the mantle. All present estimates of gas fluxes are only crude estimates when mass balances of total gas release from the mantle are to be estimated because no areally representative estimates of silent diffuse degassing have been published. Recent assessments of global total SO_2 gas release estimates, e.g., have shown that gas flux from nonexplosive degassing exceeds that released during explosive eruptions (Halmer and Schmincke 2004).

9 Synthesis of volcano field analysis

Volcano field analysis allows to define and, in part, quantify, important parameters that help shed light on the spatial and temporal evolution of the magma detachment areas underlying the volcanic fields. Many intraplate

volcanic fields, some developed on top of uplifted blocks, have diameters between 30 and 100 km, covering areas between 100 and 5,000 km^2 and generally consist of several tens to at most a few hundred scoria cones (unpubl data; see also Mertes 1983; Connor and Conway 2000; Spörli and Eastwood 1997). This similarity in field dimensions might suggest a control of physical properties of asthenospheric mantle (e.g. viscosity) that restricts finger-like diapirs to be of certain dimensions. Interestingly, the dimensions of nonvolcanic gaps between Central European volcanic fields resemble those of gaps between many large oceanic islands such as the Canary Islands suggesting a control by Raleigh-Taylor instabilities at the thermal boundary layer in governing the dimensions of rising asthenosphere. Small mantle diapirs or plumlets are nowadays sometimes called hot fingers (e.g. Tamura et al. 2002; Wilson and Downes 2006).

One of the complications in straightforward interpretation of volcano field parameters is the fact that two or more melting domains may overlap in space and time; a field may thus reflect more than one melting domain. The other complication is the possible control of volcano field parameters, especially prevailing directions, by ancient stress fields reflected in old sutures providing easy pathways for magma ascent independent of the size and geometry of a melting domain. Moreover, there are several stages of magma filtering with only a fraction of magma generated arriving at the surface.

Beneath a volcanic field, crustal magma reservoirs occur at several levels, ranging from a few km beneath the surface, such as the high-level LSV magma reservoir, through the middle crust to the uppermost mantle below the Moho, i.e. the vertical extent of magma fractionation suggested by mineral and fluid inclusion geobarometers, xenoliths and other evidence. Below the crustal reservoirs, where magmas stagnate and evolve in a low-temperature crustal environment, one may envision a broad zone of magma collection that is poorly defined but plausible for several reasons. It may be defined as the zone where magma, initially rising upwards by porous flow, starts to ascend more rapidly along fractures entraining mantle xenoliths on its way up, possibly due to voluminous CO_2 exsolution. This zone extends approximately from the actual zone of partial melting to the base of the crust that cannot be defined exactly below the Eifel fields (e.g. Mechie et al. 1983; Prodehl et al. 1992). No sharp boundaries are assumed between these levels but thinking in terms of such zones helps to visualize and understand the entire volcano-magma-melting domain system. The boundary zone at the Moho is viewed as a high-level magma accumulation and detachment zone. Many magmas previously interpreted as having risen directly from close to the melting areas on account of their erupted peridotite xenoliths can be interpreted as having picked up the

xenoliths at the Moho or from lower crustal reservoirs (Duda and Schmincke 1985; Shaw and Klügel 2002; Shaw 2004).

9.1 Magma focusing: mantle or crustal control?

The increase in volcano density, volcano volume, degree of differentiation and gas release from the periphery toward the center of the Eifel volcanic fields is difficult to explain by any type of crustal control, especially because other volcanic fields show similar patterns. A volcanic field systematically and concentrically zoned in many independent parameters thus represents to a first order a magma detachment field, in which the largest volume of magma rises in the center. In this central zone, more and larger magma reservoirs can develop at upper mantle/lower crustal levels and within the crust, where magma accumulates, cools and allows the primitive magmas to differentiate. Towards the periphery of a volcanic field, only a few highly mafic magmas are able to reach the surface most likely because of lower magma production rates at the margins of a melting domain, compounded by the lack of preheated pathways. The magma detachment and collection zones, whose vertical extents are unknown, may themselves reflect the systematic zonation of an underlying melting anomaly, the central zone in a volcanic field corresponding to the area of highest magma production in the melting anomaly, i.e. the center of the rising mantle diapir or the upper part of a deflected diapir. Here, the ascent velocity and, therefore, rate of decompression and thus magma production are likely to be at a maximum.

Volcanoes reflect a minimum amount of magma, generated at a melting anomaly in the mantle and transported into the crust. Most likely, magmas that do not reach this minimum volume - probably by far the largest volume generated - remain in the uppermost mantle and in the crust. The field dimensions of 30-50 km thus represent only a minimum area of magma generation because the magma collection zones – and even more so the melting anomalies – probably extend much farther laterally. In these hypothetical but plausible external zones outside the volcanic field boundaries, the magma generated is of such small volume that it is arrested in the subcrustal mantle and/or in crustal dikes/magma reservoirs and does not reach the surface.

Spörli and Eastwood (1997) suggested three models to explain the elliptical shape (28.9 km long and 16.5 km minor axis) of the late Quaternary intraplate Auckland volcanic field: (a) elliptical source area at depth in the lithospheric mantle; (b) depth contour on a very small mantle dome intruding into a neck of an extensional structure; or (c) boundary of a flat ellipti-

cal area where tensional stresses allow decompressional melting. The dimensions and shape of the young Auckland field resemble those of the Eifel fields and many others elsewhere, emphasizing the general nature of the underlying control mechanisms and processes. In view of the likelihood that many magmas generated in the mantle do not reach the surface especially along the periphery of a partially melting rising diapir, optimum dimensions of diapirically rising mantle material is suggested. This may also be roughly elliptical in shape but the actual downward projection of the surface field will more likely reflect a smaller ellipse of magma collection at lithospheric levels. Alternatively, the elliptical shape more strongly reflects that of a lithosphere crack system (extensional structure) that controls the actual ease of magma transfer to the surface but not necessarily the partial melting of the mantle.

9.2 Lifetime of melting anomalies

The compositional difference between mafic magmas of the older and younger subfields of the WEVF and EEVF as shown by the different major and trace element concentrations as well as trace element and isotopic ratios of the magmas and, partly, contrasting xenolith suites, reflects the limited lifetime of compositionally contrasting magma-producing mantle melting domains beneath both fields.

The lifetime (duration) of eruptive periods of compositionally distinct magmas and the development of one or more temporally restricted eruptive clusters with a specific composition can be defined from the age patterns in a volcanic field. The lifetime of a melting anomaly, however, is likely to last much longer. In other words, a field of surface volcanoes can only represent a portion, possibly a small fraction of the waxing and waning of a melting anomaly. The evolution and lifetime of distinct compositional domains within a melting anomaly as defined by contrasting major and trace element concentrations and isotope ratios of the magmas erupted can, however, be approximated.

The WEVF, the major leucitite and melilite nephelinite field, is relatively homogeneous in composition based on presently available data (although a significant difference between the magmas erupted prior to 400 ka and those erupted during the past 100 ka or so is suspected). This field appears to have spread with time to the southeast and possibly diminished in productivity between roughly 450 and 100 ka, its minimum lifetime being 0.7 million years. The younger ONB domain magmas have appeared during the past 50 ka and reflect the activation of a new compositional domain. Eruption of ONB magmas partly overlaps in time and space with

that of F-suite magmas. This is most easily explained in terms of vertical stacking of compositionally contrasting mantle reservoirs, the more enriched reservoirs (basal lithosphere?) possibly overlying the more depleted ones (see also below).

The lifetime of the surface expression of a compositional domain within a melting anomaly is more precisely defined in the EEVF. Eruptions in the strongly silica-undersaturated Rieden volcanic field lasted approximately 70 ka, separated by ca. 150 ka from the younger Wehr volcanic phase, this compositional domain remained active at least until 12.9 ka (LSV). Magma production was much higher and more focused in the EEVF judging from the development of three highly evolved larger central volcanic complexes. Their phonolite magmas require large volumes of mafic parent magmas stored in crustal reservoirs since the phonolite magmas cannot be explained as crustal melts.

In both fields, the more enriched magmas were erupted chiefly during the early phases of volcanism, possibly reflecting decompression of the fusible metasomatized base of the dynamically uplifted lithosphere above a rising mantle diapir (plume). Interestingly, some ONB suite volcanoes occur largely outside the areal distribution of Tertiary volcanic centers. The same holds for the EEVF where scattered local centers of Tertiary alkali basalts are only found close to, or within, the area of the highly alkalic lavas of the western subfield.

9.3 Activation of contrasting compositional domains at different times beneath the WEVF and EEVF

Several questions require answers: Do compositional changes of primitive magmas reflect a change in the degree of partial melting and/or activation of compositionally significantly different mantle domains? Why are changes so abrupt? Are the different domains vertically stacked or laterally juxtaposed? What type of mantle/plate tectonic processes caused the changes in activation of different mantle reservoirs and temporal migration of volcanism to the southeast in both fields?

The abrupt appearance of ONB magmas at <50 ka in the WEVF - while foiditic lavas continued to erupt - and the abrupt change (on the surface) in primitive magma composition at approximately 215 ka in the EEVF must be caused by major “geodynamic processes”. Could they represent increasing degrees of partial melting with time based simply on the much higher abundance of LILE and higher CaO/Al_2O_3-ratios in the older foiditic magmas? For the WEVF, such an explanation seems plausible at first sight because the simultaneous acceleration of volcanism would imply a higher

degree of partial melting or at least magma supply. Some young volcanoes such as Wartgesberg and the Mosenberg group are indeed unusually voluminous compared to older WEVF volcanoes. Nevertheless, a simple increase in the degree of partial melting from the same mantle source is ruled out because of significant differences in radiogenic isotopes and trace element ratios as discussed above. The same holds true for the EEVF. One has to bear in mind, however, that the abrupt change in composition is based only on surface lava compositions, the main uncertainty being the unknown compositional changes in magmas supplied to the lower crust without erupting.

Two additional observations in the Quaternary Eifel fields are pertinent. First, the more strongly alkalic and potassic magmas were erupted early in the history of both fields. This might reflect the updoming of the lithosphere as expressed by the accelerated uplift of the Rhenish Shield (Meyer and Stets this volume), coupled with decompression partial melting of the metasomatized base of the lithosphere. Many of the younger lavas in both fields reflect less strongly metasomatized sources and, in the WEVF, a strong component of asthenospheric mantle.

A consensus has presently been reached by many workers that highly alkalic silica-undersaturated magmas such as those erupted early in both Eifel fields may represent partial melting products of the metasomatically enriched base of the lithosphere (e.g. Wilson and Downes 1991). The most common problems discussed in this respect are the timing of such metasomatism as discussed briefly above, the number and nature of metasomatic events and their correlation with major plate tectonic events. Lloyd and Bailey (1975) postulated close affinities between lavas and nodules suggesting derivation of the magmas by partial melting of metasomatized mantle. Duda and Schmincke (1978) suggested that partial melting of a phlogopite-enriched mantle, previously metasomatized by the intense Tertiary magmatism, might help explain the potassic nature of the Quaternary Eifel magmas. Interestingly, the areas of the older highly alkalic foiditic volcanoes in both fields overlap spatially with that of Eocene volcanism that was on a much larger scale (Huckenholz and Büchel 1988). This suggests – but does not prove – that the lower lithosphere metasomatized during the Eocene became partially melted during the Quaternary uplift of the Rhenish shield mantle generating the most enriched foiditic magmas prevailing in the WEVF and erupting early in the EEVF. No Tertiary eruptive centers are known in the area where basanite magmas erupted in the EEVF and they seem to be relatively rare in the area where *ONB* lavas erupted in the southern – but not southeastern - WEVF. The amount of Tertiary magma that did not reach the surface is, of course, unknown and the area of Tertiary magma supply to the crust most likely ex-

tends significantly beyond the outcrops of Tertiary basalts. Indeed, the EEVF basanites comprise both potassic and a few sodic members but in general are much less LILE-enriched than the older FE lavas, perhaps because the degree of metasomatism of the lower lithosphere decreases away from the Tertiary volcanic field.

10 The Eifel plume model

Duncan et al. (1972), in one of the first papers applying plate tectonic principles to the CEVFs, postulated plate migration during the past 35 million years across a hypothetical fixed magma source called Eifel plume. They assumed an age progression of Cenozoic volcanic fields along a broad, 700 km-long band of volcano fields extending from Silesia (Poland, Tertiary volcanoes) in the east to the Quaternary Eifel volcanic fields (Germany) in the west, the present position of the postulated Eifel plume (Fig. 17).

Radiometric dates available at that time did not support the model of age progression, however (Duda and Schmincke 1978). For example, the Eifel area also encompasses not only Quaternary but also a relatively old Eocene volcanic field (Cantarel and Lippolt 1977) located mostly in between and north of the Quaternary volcanic fields with major areal overlap. All the available age data showed instead several distinct volcanic fields, volcanism in most having occurred roughly synchronously between about 40 and 15 million years. Finally, starting in the Pliocene, eruption of small volumes of strongly undersaturated magmas generated volcanic fields in the center and at the western end of the presumed plume "trace".

An alternative scenario for the origin of the CEVFs was proposed based on the observation that most of the CEVFs from Central France to Silesia form a peripheral belt roughly parallel to, and ca. 300-400 km north and northwest, to the curvature of the Alps. Volcanic activity in these fields coincided broadly in time most remarkably with major metamorphic, magmatic and deformational phases in the Alps as well as with uplift of some lithospheric blocks, rifting and subsidence e.g. of the Rhine Graben (Schmincke 1982) (Fig. 17). The Rhinegraben, the fundamental structure of the European Cenozoic Rift System, began to subside in the Eocene, peaked in the Oligocene, and terminated in the Miocene, graben formation being related to the collision of the African and Eurasian plates (Ziegler 1992). Most subsidence occurred between 20 and 15 Ma, maximum horizontal compressional stress directions changing from NNE-SSW to NNW-SSE at about 20 Ma, a temporal coincidence unlikely to be fortuitous.

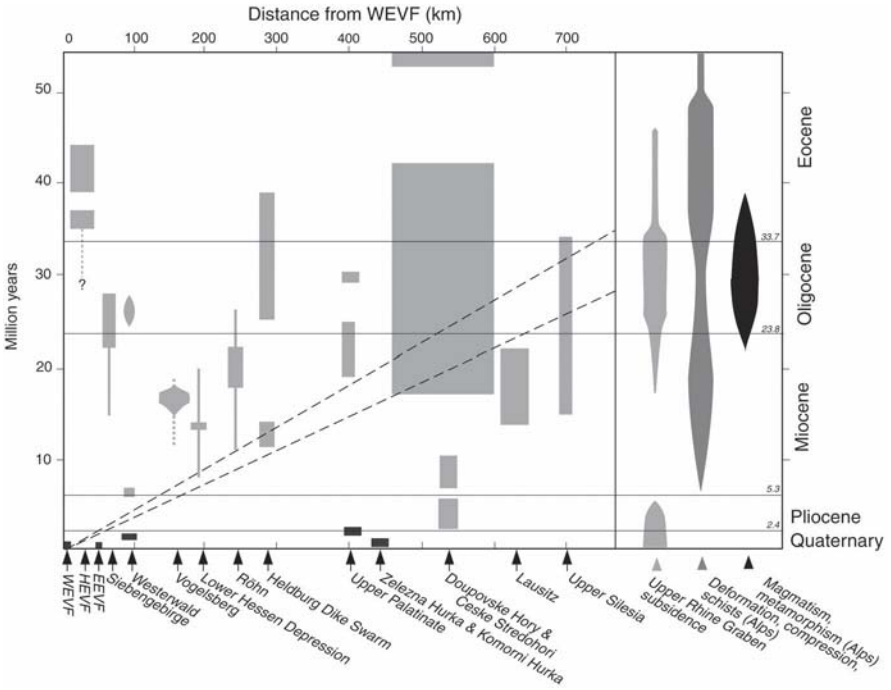

Fig. 17. Age and area occupied by Cenozoic volcanic fields in Central Europe. Dashed line = trace of age progression of the so-called Eifel plume postulated by Duncan et al. (1972). The main phases of subsidence of the Rhine Graben and folding and emplacement ages of magmas in the Alps for comparison. Ages of HEVF lavas based on Fekiacova (b, this volume), of Westerwald lavas on Haase et al. (2004), Vogelsberg lavas on Bogaard and Wörner (2003) and Rhön lavas on Jung and Hoernes (2000). High-precision dating is lacking for most fields and the age distributions shown are very approximate. Modified from Schmincke (1982), with modifications based on Becker (1993)

Apparently, plate tectonic processes ultimately driven by collision of the Eurasian and African plates were in some unknown manner responsible for triggering uplift and rift formation throughout central and western Europe with local rise of fertile mantle being dominantly passive (Duda and Schmincke 1978; Schmincke 1982). Volcanic activity in western and central Europe appeared to have been fed from a string of separate individual small melting anomalies – rather than one big plume - some of which were simultaneously active over a wide area and some erupting lavas of different composition at different times.

Convincing support for the model of spatially discrete melting areas (plumes) has come from teleseismic analyses especially in central France and in the Eifel (Granet et al. 1995; Ritter this volume; Ritter et al. 2001;

Keyser et al. 2002) (see below). Wilson and Downes (2006) in a recent review have extended the regional view to encompass Spain, the Balkans and northern Africa and have attempted to correlate magmatism of different composition to regional tectonic phases.

There is also recent geophysical evidence to better explain "mass movements in the mantle, associated with Alpine folding, resulting in uplift and magmatic activity some 300 km north of the Alpine chain" (Duda and Schmincke, 1978). A high *P*-wave velocity area in the mantle encompassing the Alps, Carpathians and Dinarids, is presently interpreted as a cold subducted slab at 500-600 km depth (Goes et al. 1999; Piromally et al. 2001). This slab is thought to have deflected mantle material rising from the lower mantle, part of a "superplume", leading to the uplift of some of the blocks and the generation of small finger-like plumes above about 400 km releasing magma during decompression. Work in the early nineties in the Eifel, Sicily and the Canaries and Madeira led to the postulate of a broad mantle source extending from the Canaries to Central Europe (Hoernle et al. 1995) and a similar model for a major mantle source was advanced by Cebria and Wilson (1995), a topic not discussed further in the present paper.

10.1 What is the spatial and temporal relationship between the plume anomaly of Ritter (this volume), Ritter et al. (2001) and Keyser et al. (2002) and the Quaternary Eifel volcanic fields?

Compressional and shear wave arrivals suggests a more than 100-km-wide low velocity structure covering the Eifel volcanic fields extending downward to at least 400 km into the upper mantle forming the deep roots of the volcanic surface fields (Ritter this volume; Keyser et al. 2002). The shear wave tomography model suggests a plume-like structure in the order of 100 km with a velocity contrast of –5 % between 40 and 170 km depth. This is interpreted as asthenospheric upwelling of hot peridotite (small plume) with an excess temperature of about 100 K plus about 1 % partial melt. The shear-wave velocity anomaly disappears between about 170 and 240 km depth but continues to about 400 km but with much lower velocity contrasts. The anomaly detected in *P*-velocity perturbations (Ritter et al. 2001) continues throughout the upper mantle down to 400 km depth and the central part lies some 20-40 km south of the WEVF.

Mantle anomalies defined by a reduction of seismic velocity and interpreted as areas of increased temperature and sometimes partial melting in the upper mantle (plume-like structures) are often cited as evidence that volcanism in a particular area is not extinct. The anomaly beneath the Eifel

(Raikes 1980; Raikes and Bonjer 1983; Ritter (this volume); Ritter et al. 2001; Keyser et al. (2002)) is of course highly suggestive of diapiric rise, decompression melting and magma rise mainly because the upper part is located near and partly underlies very young volcanic fields. Nevertheless, it is impossible to unequivocally infer presently rising melt from *P*-wave or shear-wave velocity reduction. It is similarly impossible to infer "ascending upper mantle-derived melt" in the Cheb basin (Czech Republic) (Bräuer et al. 2005, Kämpf et al. this volume) based only on high $^{3}He/^{4}He$ ratios in mofettes in an area that, while seismically quite active, lacks young volcanism, evidence for plume-like mantle anomalies having not yet been documented. Moreover, geophysical data, while allowing to describe, model and interpret the present dynamic state of the system cannot, of course, help to derive temporal changes in the system. This problem is well illustrated by anomalies east of the Quaternary fields (Westerwald, Vogelsberg). A tomographic anomaly beneath the Vogelsberg, where volcanic activity terminated in the middle Miocene (Bogaard and Wörner 2003) could not be clearly interpreted as indicating renewed diapiric rise of – partially melted - mantle or merely lingering anomalies following massive melting events 16–18 million years ago (Raikes and Bonjer 1983; Braun and Berckhemer 1993). Moreover, the large area of much more profuse Eocene volcanism in the Hocheifel also coincides spatially with the plume anomaly. Could the Eifel mantle anomaly be related also – or dominantly - to the Tertiary volcanism in the Eifel rather than to the volumetrically minor (until now) Quaternary volcanism? In other words, what is the age of the anomaly? Is it waxing or waning?

The long lifetimes - often >10 million years – postulated for many Tertiary volcanic fields (Lippolt 1983) likely reflect the slow waxing, high production peak and slow waning magma production rates but are probably commonly misleading. In other words, volcanic activity in these fields is likely to have occurred in distinct short episodes of compositionally contrasting magma batches rather than more or less continuously over long time periods. Quantifying the surface expression of a compositionally distinct melting anomaly in terms of spatial, temporal and compositional evolution is, however, beset with major problems in all Tertiary CEVFs because of limited exposures. An exception is the stratigraphically controlled dating and geochemical analysis of a 657 m deep borehole in the Tertiary Vogelsberg (Bogaard and Wörner 2003). The central part (450 m thick) of the section was erupted very rapidly between 16.6 and 17.2 Ma and consists of several compositionally distinct magma groups. Such temporal-compositional evolutionary patterns are similar to the episodic activation of compositionally distinct mantle reservoirs of the Quaternary Eifel fields and are likely to be the rule rather than the exception. High-resolution dat-

ing of the HEVF lavas (Fekiacova et al. (a, this volume)) has also shown that eruptive activity occurred mainly between 35-37 and 39-44 Ma.

Straightforward correlations of mantle anomalies, uplift and volcanism both in space and time are still ambiguous. The difficulties lie in the lack of spatial resolution of the seismic anomaly and the fact that its temporal evolution cannot be directly documented. For example, the Rhenish Massif as a whole is quite stable at present, the only exception being the Hohes Venn ca. 50 km NW of the WEVF where elevations exceed 600 m asl. This is the area showing the highest absolute uplift - some 400 m since the Oligocene - and also the highest present uplift rate (ca. 1.6 mm/a) (Mälzer et al. 1983). This nonvolcanic but presently seismically active (Ahorner 1983) area is underlain by the edge of the "Eifel Plume" mantle anomaly (Raikes and Bonjer 1983; Ritter et al. 2001) but far away from its center. Elevations of the base of most volcanoes in the WEVF are between 400 and 500 m asl, those in the western EEVF are generally below 400 m asl except for the Rieden-Hochsimmer area. In the eastern EEVF, in contrast, the base of most volcanoes is below 300 and for some below 200 m asl. This emphasizes that the driving force for uplift, possibly upwelling asthenosphere, is not reflected in the focus area of the present-day anomaly. The focus of the anomaly lies well south of the WEVF limiting attempts to explain e.g. the migration of WEVF volcanism to the southeast with the center of the anomaly, especially since a similarly-oriented migration in the EEVF is far away from the main surface projection of the mantle anomaly. A speculative way out of this dilemma might be lateral flow of both plume peridotite and melt generated by its decompression as modelled for mid-ocean ridges by Sleep (1996, 2002).

10.2 A three-tiered hierarchy of the dimensions of compositionally and spatially coherent melt-producing anomalies

If we take the documented mantle anomalies below the Eifel to represent a rising mantle diapir/plume/blob some 100 km in diameter, volcano field analysis suggests that there are two smaller-sized categories of mantle anomalies that can be defined by temporal, spatial and compositional parameters. In addition, adjacent volcanoes of the same magma type commonly show significant compositional differences reflecting small-scale heterogeneities in the melting area. The appearance of new magma compositions (ONB) in the WEVF and the abrupt temporal and spatial change in composition in the EEVF apparently reflect the limited productive lifetime of melting domains in the mantle of much smaller dimensions than the present plume anomaly, each producing – or erupting - a relatively small

volume of magma. These small mantle fingers are compositionally coherent and the dimensions of their volcanic surface expression are on the order of kilometers or at most a few tens of km. Such small rising "peridotite fingers" reflect not only significant compositional heterogeneities in the diapir but also temporal and spatial migration of "activation" of such subdomains, in the Eifel fields from northwest to southeast with time. There is no obvious explanation for the spatial shift in activity toward the southeast from highly alkalic to less alkalic or, in the WEVF, even sodic magmatism - nor is there any explanation why two Eifel volcanic fields developed in the first place. The lack of magma compositions transitional between the two major compositional groups in both Eifel fields does suggest that the small fingers are deeply rooted. Many volcanic fields as here understood represent the amalgamation of activation of two or more of such small-scale melting anomalies.

It is not clear whether or not such a hierarchy of melting anomalies (plume-volcanic field-small mantle/peridotite fingers) is common. In some fields, highly contrasting magma types (e.g. tholeiitic, alkali basalt, basanite) might erupt in adjacent volcanic centers during the lifetime of a scoria cone field (mostly ca. 0.1 - <5 million years) (Connor and Conway 2000) or even during eruptive periods lasting <5 years as during the famous 1730–1736 eruption on Lanzarote (Canary Islands) (unpubl data). There is clearly a need for more detailed studies of volcanic fields in order to allow a better understanding of the nature and evolution of melting anomalies of different dimensions.

11 Is volcanism in the Quaternary Eifel volcanic fields extinct?

As late as the 1980ies, opinion prevailed that volcanism in the Eifel is extinct (see review of arguments in Schmincke 2000). In my view, such an interpretation has never been based on convincing empirical data nor on scientific logic. The question of whether or not one can expect future volcanic eruptions in a volcanic field is obviously not only of scientific interest. There are several different parameters and criteria on which to base plausible arguments suggesting that volcanism in the Eifel is not extinct and might even increase in the future.

(a) Eruptive rates and episodicity

An evaluation of eruptive rates in both fields is beset with several problems. These include the high rate of erosion during alternating glacial and interglacial periods during the past 0.7 Ma, the general pervasive cover of vegetation and the small number of high precision $^{39}Ar/^{40}Ar$ ages available. Despite these shortcomings, it does appear that volcanic activity in the WEVF has increased during the past 100 ka to ca. 58 eruptions per 100 ka, mainly due to the appearance of two new magma types (ONB suite) on the surface (Mertes and Schmincke 1985). Nevertheless, the precise resolution of the temporal evolution in the WEVF is still in its infancy. Obviously, volcanism in the WEVF is not only not extinct but may be increasing in frequency. Some volcanoes in the southern part of the field are particularly voluminous (Mosenberg group) or have produced exceptionally long lava flows (e.g. Wartgesberg) indicating higher magma fluxes at least locally compared to fluxes prior to about 50 ka in the WEVF.

Volcanic eruption rates in the EEVF cannot be interpreted easily because of the clear difference between the two subfields separated in time, space and composition. Moreover, the incubation time of mafic parent magmas eventually evolving to highly differentiated phonolites is on the order of tens of thousands of years (see above). In other words, magma supply to the crust maybe as high or probably higher in the EEVF compared to the WEVF but instead of being erupted the magmas pooled and differentiated in crustal reservoirs. Most young prominent scoria cones in the Neuwied Basin formed roughly slightly less than 200 ka ago. Whether or not scoria cones other than Wingertsberg next to LSV are significantly younger or not is unknown. In any case, the largest volcanic eruption in the Eifel by erupted magma volume (>6.3 km^3) during the very late Quaternary (LSV) dwarfs all other eruptions in the past in this area. Nevertheless, volcanic activity in the EEVF is distinctly episodic with periods of high activity – a few tens of thousands of years – alternating with periods of quiescence lasting 100 to 150 ka (see above).

Strongly evolved rocks containing suitable material for dating (K-feldspar) are scarce in the WEVF and dating of mafic rocks has not been very thorough preventing a clear assessment of eruptive rates, although there is a hint of similar episodicity. Analysis of Virtual Geomagnetic Poles resulted in a highly focused group around 40^o N and 45^o E (SPGG: striking pole position group) which, when combined with $^{39}Ar/^{40}Ar$ determinations and previous dates, suggested that the anomalous low latitude pole geomagnetic field excursion formed during a relatively short time around 510 ka (Schnepp and Hradetzky 1994). Many of the volcanoes in the central part of the WEVF field appear to have formed around this time

and few if any in the age group 2 (400-100 ka) of Mertes and Schmincke (1983). If this is correct, volcanic activity – and possibly magma production – occurred, or at least peaked, alternating between the WEVF (<780 to 450 ka and <100 ka), EEVF (420 to 350 ka and <215 to 180 ka with few later - but in some cases very voluminous (LSV) - eruptions.

(b) Present signs of unrest

Volcanoes, unlike earthquakes, commonly show many different signs of unrest weeks or months prior to an eruption: earthquakes, increased degassing, surface deformation and rise in temperature. While there is no sign of an impending volcanic eruption, there is abundant evidence that the central and eastern parts of the EEVF are geodynamically active.

The Laacher See subfield shows several types of unrest: occasional increased microseismic activity beneath LSV, hypocenters that are several km closer to the surface than regionally suggesting an elevation of the brittle/ductile transition in the crust due to elevated temperatures (Ahorner 1983), the highest CO_2 flux in the entire Eifel and slightly higher temperatures of springs proximal to LSV (Langguth and Plum 1984). Moreover, the gases bubbling vigorously at the eastern shore of the lake are composed to more than 99 % of CO_2 but include noble gases, He, Ne and Ar of clear mantle origin (Giggenbach et al. 1991; Griesshaber et al. 1992; Aeschbach-Hertig et al. 1996). Further strong evidence for magma focusing beneath LSV – but not beneath maar lakes in the WEVF - is reflected in the enormous flux of primordial ^{3}He (Aeschbach-Hertig et al. 1996). The composition of gases presently emanating along the eastern shore of Laacher See show a strong mantle signature with $^3He/^4He$ ratios (relative to the ratio in air) of up to 5.5. Higher ratios (up to 6.2) in Central Europe were only measured in the Cheb basin (Czech Republic at Bubla´k), an area characterized by frequent earthquake swarms but lacking surface volcanism (Bräuer et al. 2005). Interpretation of these data is ambiguous since cooling of the complex diatreme area beneath the broad vent of LSV or emplacement of new magma at depth following the 12.9 ka BP eruption cannot be distinguished from each other. A seismically very active zone in the EEVF is the Ochtendung fault zone defined by a NW-SE alignment along a surface fault about 15 km long in the southeastern corner of the EEVF (Ahorner 1983) (Fig. 5). This active normal fault, dipping 60^o NE, is the most active microearthquake source in the entire Rhenish Massif and related to the seismically active Rhine Rift. Interestingly, this major fault and seismic zone is slightly offset to the north but has the same orientation as an impressive synvolcanic graben that formed as a system of growth

faults with a maximum displacement exceeding 10 m during eruption of the bulk of Laacher See Volcano, fractures continuing to the top of the deposit (Fig. 11.41 in Schmincke 2004). The graben has a minimum length of ca. 2 km and a width of ca. 250 m. These data show that the younger subfield of the EEVF is characterized by especially voluminous young volcanism and presently active tectonism and seismicity.

(c) Incubation time of mafic parent magmas

Taking the emplacement age of ca. 0.1 m.y. of mafic basanite magma parental to the LSV system (Bourdon et al. 1994; see also Bogaard 1995) at face value, several corollaries are apparent. For one, the "incubation" time for highly differentiated systems to fully evolve may be longer than some eruptive cycles. This could mean that only some of the magma reservoirs are successful in ever releasing magma to the surface. Secondly, the duration of eruptive intervals is probably significantly shorter than emplacement of mafic parent magmas in the lower crust. Further, parent magmas from which variably evolved magmas might evolve and ultimately erupt in the future are likely to have already been emplaced within or below the lower crust beneath the EEVF hundreds to thousands of years ago. These may be the source for the present vigorous release of magmatic gases.

d) The two youngest eruptions in the Eifel and type, place and composition of future eruptions

Conventionally, those volcanoes are called active that have erupted during the past 10,000 years – roughly the Holocene (e.g. Simkin and Siebert 1994). This is based on the simple observation that volcanoes that have erupted frequently in the recent past are most likely to erupt in the future. Nevertheless, the age limit is entirely arbitrary. In many volcanoes, intervals between eruptions last tens to many hundreds of thousands of years.

The space-time patterns for the two youngest eruptions in the Eifel are amenable to scientific analysis and speculations on the type, place and composition of future eruptions. LSV, extremely well-dated by several independent methods (see above) at ca. 12,900 a BP, developed in the center of the closest spacing of volcanoes in the entire EEVF inside and just outside Laacher See basin (Fig. 5). In other words, at least 15 eruptive centers have developed in a small area of some 25 km^2. This suggests that melt production below LSV has been at a maximum for more than 200,000 years. Long-term heating by repeated emplacement of a cluster of dikes may have greatly facilitated episodic rise of magma in a spot that may

have been controlled by both magma production and or release focusing below LSV and the surrounding cones as well as preheated pathways within the lithosphere.

Judging from the eruptive history of two older Rieden and Wehr phonolitic volcanic complexes in the EEVF, the eruption of LSV may indeed herald a new phase of volcanic activity based on the analogy to the preceding volcanic episodes. Recurrence of a major eruption of LSV within the lake basin would no doubt generate phreatomagmatic explosions more powerful than those that occurred 12.9 ka ago and would pose a major hazard and risk to the densely populated and highly industrialized lowland of the Neuwied Basin. Proximal to the eruptive center, major environmental impacts include highly destructive initial blasts up to ca. 5 km from vent. Fast deposition of huge tephra volumes especially in the form of pyroclastic flows may lead to renewed complete disruption of Rhine River within lower Neuwied Basin and the damming up of a lake. Sudden collapse of such a temporary tephra dam could generate destructive flood waves downstream for many tens of km. High eruption columns would strongly interfere with air traffic for many days. Whether or not LSV will erupt again remains to be seen, probably not before this book has come off the press.

The only volcanic eruption in the Eifel younger than that of Laacher See Volcano by roughly 2 ka is that of Ulmener Maar located ca. 30 km southwest of Laacher See Volcano. Tephra layers found in several maar lake deposits above those of the Laacher See eruption are correlated with the Ulmener Maar (Zolitschka et al. 1995). The location of Ulmener Maar confirms the trend of migration of volcanism in the WEVF to the southeast. It also shows that highly alkalic magmas are still available at depth in the WEVF. The fact that Ulmen volcano erupted 11 ka ago cannot be taken as evidence that volcanism is extinct in the area. Obviously, there is no reason to assume that volcanism in the WEVF has come to an end or slowed down. To the contrary, young Ulmener Maar shows that magma production beneath the WEVF is alive and well.

Partially melted areas in the mantle beneath the Eifel volcanic fields have been inferred by seismic wave velocity anomalies for more than 30 years, the degree of resolution presently achieved being remarkable (Ritter this volume; Ritter et al. 2001; Keyser et al. 2002). Nevertheless, compositionally contrasting mantle domains beneath both Eifel volcanic fields with different temporal patterns of evolution are unlikely to be detected in the near future by remote geophysical sensing of the root areas due to lack of resolution and present inability to interpret these anomalies in terms of composition, degree of melt production and temporal evolution. Detailed spatial/compositional analysis of volcanic fields such as discussed in this

paper thus allows conclusions that, in the foreseeable future, can only be derived from a study of volcanoes.

In summary, a scientifically sound statement can be made to the effect that, while volcanism in the Eifel is dormant at present, new volcanoes can form at any time. In analogy to other scoria type volcanoes (e.g. the two famous historic scoria cone/lava flow eruptions in Mexico of Paricutin (1943-52) (Luhr and Simkin 1993) and Jorullo (1759-74)) such eruptions are likely to be heralded months to years in advance by increased seismicity, deformation, increased gas flux and compositional changes in magmatic gases, and increased groundwater outflow rates. New volcanoes are most likely to grow in the southern to eastern areas of both fields, be maars/scoria cones of mafic/intermediate composition in both fields but possibly strongly explosive and of highly evolved composition in case LSV erupts again. Future eruptions in the WEVF are likely to be of ONB or highly alkalic and, in the EEVF, of moderately enriched but potassic basanite and/or tephrite and/or phonolite composition, predictions that are a safe bet in view of past eruption frequency.

12 Conclusions

1. Volcanically active periods in the EEVF and probably WEVF show a pronounced episodicity, eruptive intervals alternating with longer noneruptive pauses. Whether this episodicity is caused by episodes of enhanced melting and/or episodic changes in the lithospheric stress field facilitating rise of magma to the surface is unknown. The fact that clear temporally distinct episodes of volcanism are correlated with compositional jumps indicate lateral shifts in melting areas.
2. The lifetime of distinct mantle domains as expressed in at least 5 distinct compositional batches of magmas erupted unrelated to others by fractionation and/ differences in degree of partial melting is on the order of several 100,000 years.
3. The eruption of relatively large volumes of highly evolved magmas in the EEVF (Wehr and Laacher See eruptive centers) following noneruptive intervals lasting more than 100,000 years suggests long incubation times for larger magma reservoirs to develop to allow for thorough magma differentiation.
4. The enriched nature of the foiditic magmas dominating among the Quaternary lavas in the WEVF may have been due to derivation by partial

melting from the basal (?) lithosphere, metasomatically enriched mainly during Eocene magmatism.

5. The sodic young basanite and olivine nephelinite magmas in the WEVF may have been derived from a mantle source (asthenosphere?) resembling that from which the Tertiary magmas were derived but representing lower degrees of partial melting.

6. Magma focusing in the central part of both fields is expressed by closer volcano spacing, repeated eruptions in the same volcano cluster and higher abundance of intermediate and strongly evolved magmas.

7. Low degrees of magma leaking in the WEVF as expressed by more isolated volcano occurrences contrast with large-volume magma pooling in 3 major high-level reservoirs in the EEVF. This is also reflected in a concomitant scarcity of very primitive (MgO >10 wt%) and abundance of extremely evolved phonolitic magmas in the EEVF, the 12,900 a old Laacher See Volcano eruption with >6 km^3 erupted magma being most prominent.

8. There is a moderate correlation between degree of melting as expressed by CaO/Al_2O_3-ratios and volume of volcanic edifices, the basanite volcanoes in both fields being represented by especially large volcanic complexes.

9. Compositional zoning of scoria cones and lava flows is common, the first erupted lavas being generally more evolved. This reflects relatively continuous evacuation of compositionally zoned reservoirs even in the mafic magma spectrum.

10. Magma-water interaction was widespread during eruption on all scales from entirely phreatomagmatic eruptions to minor water influence on fragmentation mechanisms and eruptive processes. Several classical criteria for hydroclastic fragmentation mechanisms (glassy, angular, nonvesicular juvenile clasts) are lacking in many maar deposits where agglutinated, tachylitic and slightly vesicular clasts prevail.

11. The strong NW-SE orientation of fractures along which magmas rose and erupted appears to be due to reactivation of Paleozoic structural discontinuities by the present lithospheric stress field on broad and small scales.

12. The two Quaternary volcanic fields formed in the hinge area west and east of a NW-SE trending zone of highest Quaternary uplift (Kelberger Hoch) where Tertiary volcanism was concentrated.

13. Direct correlation of Quaternary volcanism with diffuse crust/mantle transitions (broad gradients and high density lamellae based on seismic reflection data) is spatially coherent but not unambiguous.

14. The Eifel volcanic fields show systematic changes with time
    - from lower to higher degrees of partial melting
    - from metasomatically enriched to more "depleted" mantle domains.
    - of volcanic activity from W/NW to E/SE
    - towards more mafic compositions in the WEVF

15. The accelerated uplift of the Rhenish Shield during the past ca. 0.8 m.y., inception of Quaternary volcanism and the ongoing substantial gas flux extending spatially beyond the volcanic fields, are all consistent with the model of a hot, rising, partially melting mantle diapir (Eifel plume). Other aspects such as time/space/compositional parameters of the volcanic fields cannot be correlated with the plume configuration because of lack of resolution. There is no overlap in space with the focus of compressional wave and shear-wave mantle anomalies with areas of maximum Quaternary or present uplift although much lateral overlap. Whether the plume is in a waxing or waning stage is unknown.

16. A three-tiered hierarchy in the dimensions of melt-producing anomalies appears to be reflected in the volcanic fields. The rising plume identified by seismic anomalies – and inferred higher temperature – is thought to be made up of smaller domains with dimensions on the order of a few km – or tens of km – that could reflect inherent compositional heterogeneities and/or variable ascent rates interacting with the lithosphere at different times or stages during the productive lifetime of plumes. The amalgamation of the surface products of several such small mantle fingers make up an entire volcanic field. The dimensions of a volcanic field are significantly smaller than the plume root that may feed more than one surface field as in the Eifel.

17. Volcanism in both fields is presently dormant but not extinct

Acknowledgments

Some of the work here summarized is the result of a group effort, carried out by my students, colleagues and myself between 1970 and 2005, work that is still ongoing. Some of our studies were supported by grants from the Deutsche Forschungsgemeinschaft – e.g. Schm 250/58-6 and 71-1- that

I gratefully acknowledge. Critical comments on the manuscript by Joachim Ritter, Cliff Shaw, H-G Stosch and Gerd Wörner are greatly appreciated. Mari Sumita did a great job in redoing the diagrams at the last minute. Many thanks to all of you.

References

Aeschbach-Hertig A, Kipfer R, Hofer M, Imboden DM, Wieler R, Signer P (1996) Quantification of gas fluxes from the subcontinental mantle: The example of Laacher See, a maar lake in Germany. Geochim Cosmochim Acta 60:31-41

Ahorner L (1983) Historical seismicity and present-day micro-earthquake activity of the Rhenish Massif, Central Europe. In: Fuchs K et al. (eds) Plateau Uplift. Springer Heidelberg, pp 198-221

Babuška V, Plomerová J (1992) The lithosphere in Central Europe - seismological and petrological aspects. Tectonophysics 207:101-163

Baumann H, Illies JH (1983) Stress field and strain release in the Rhenish Massif. In: Fuchs K et al. (eds) Plateau Uplift. Springer Heidelberg, pp 177-186

Becker A (1993) An attempt to define a "Neotectonic period" for central and northern Europe. Geol Rundsch 82:67-83

Becker HJ (1977) Pyroxenites and hornblendites from the maar-type volcanoes of the West Eifel, Federal Republic of Germany. Contrib Mineral Petrol 65:45-52

Bednarz U, Schmincke H-U (1990) Evolution of the Quaternary melilite-nephelinite Herchenberg volcano (East Eifel). Bull Volcanol 52:426-444

Bednarz U, Freundt A, Schmincke H-U (1983) Die Eignung von Lokationen in der E- und W-Eifel für ein deutsches HOT-DRY-ROCK Geothermik Projekt. BMFT Berichte, pp 1-100

Berndt J, Holtz F, Koepke J (2001) Experimental constraints on storage conditions in the chemically zoned phonolitic magma chamber of the Laacher See Volcano. Contrib Mineral Petrol 140:469-486

Bogaard PJF, Wörner G (2003) Petrogenesis of basanitic to tholeiitic volcanic rocks from the Miocene Vogelsberg, Central Germany. J Petrol 44: 569-602

Bogaard Pvd (1995) $^{40}Ar/^{39}Ar$ ages of sanidine phenocrysts from Laacher See Tephra (12,900 yr BP): Chronostratigraphic and petrological significance. Earth Planet Sci Lett 133:163-174

Bogaard Pvd, Schmincke H-U (1984) The eruptive center of the late Quaternary Laacher See tephra. Geol Rundsch 73:935-982

Bogaard Pvd, Schmincke H-U (1985) Laacher See Tephra: A widespread isochronous late Quaternary ash layer in Central and Northern Europe. Geol Soc Am Bull 96:1554-1571

Bogaard Pvd, Schmincke H-U (1990) Die Entwicklungsgeschichte des Mittelrheinraumes und die Eruptionsgeschichte des Osteifel-Vulkanfeldes. In: Schirmer W (ed) Rheingeschichte zwischen Mosel und Maas. DEUQUA-Führer 1, Düsseldorf, pp 1-30

Bogaard Pvd, Hall Ch, Schmincke H-U, York D (1989) Precise single-grain $^{40}Ar/^{39}Ar$ dating of a cold to warm climate transition in Central Europe. Nature 342:523-525

Böhnel H, Reismann N, Jäger G, Haverkamp U, Negendank JFW, Schmincke H-U (1987) Paleomagnetic investigation of Quaternary West Eifel volcanics (Germany): evidence for increased volcanic activity during geomagnetic excursion/event. J Geophys 62:50-61

Bosinski G (1981) Eiszeitjäger im Neuwieder Becken. Archäologie am Mittelrhein und Mosel 1:1-112

Bourdon B, Zindler A, Wörner G (1994) Evolution of the Laacher See magma chamber: Evidence from SIMS and TIMS measurements of U-Th disequilibria in minerals and glasses. Earth Planet Sci Lett 126:75-90

Brauer A, Endres C, Ganter C, Litt T, Stebich M, Negendank J (1999) High resolution sediment and vegetation responses to Younger Dryas climate change in varved lake sediments from Meerfelder Maar, Germany. Quat Sci Rev 18:321-329

Bräuer K, Kämpf H, Niedermanmn S, Strauch G (2005) Evidence for ascending upper mantle-derived melt beneath the Cheb basin, central Europe. Geophys Res Lett 32, LO8303, doi:10.1029/2004GL022205. 4 p

Braun T and Berckhemer H (1993) Investigation of the lithosphere beneath the Vogelsberg volcanic complex with *P*-wave travel time residuals. Geol Rundsch 82:20-29

Büchel G, Mertes H (1982) Die Eruptionszentren des Westeifeler Vulkanfeldes. Z Dt Geol Ges 133:409-429

Büchel G, Lorenz V (1982) Zum Alter des Maarvulkanismus der Westeifel. N. Jb Geol Paläont Abh 163:1-22

Cantarel P, Lippolt HJ (1977) Alter und Abfolge des Vulkanismus der Hocheifel. N Jb Geol Pal Mh 1977:600-612

Cebria JM, Wilson M (1995) Cenozoic mafic magmatism in central Europe: a common European asthenospheric reservoir? Terra Abstracts 7:162

Connor CB (1990) Cinder cone clustering in the Transmexican Volcanic Belt: implications for structural and petrologic models. J Geophys Res 95:19395-19405

Connor CB, Conway FM (2000) Basaltic volcanic fields. In: Sigurdsson et al. (eds) Encyclopedia of Volcanology. Academic Press, San Diego, pp 331-344

Duda A, Schmincke H-U (1978) Petrology of Quaternary basanites, nephelinites and tephrites from the Laacher See area (Eifel). N Jb Miner Abh 132:1-33

Duda A, Schmincke H-U (1985) Polybaric evolution of alkali basalts from the West Eifel: Evidence from green-core clinopyroxenes. Contrib Mineral Petrol 91:340-353

Duncan RA, Petersen N, Hargraves HB (1972) Mantle plumes, movement of the European plate and polar wandering. Nature 239:82-86

Edgar AD, Lloyd FE, Forsyth DM, Barnett RL (1989) Origin of glass in upper mantle xenoliths from the Quaternary volcanics of Gees, West Eifel, Germany. Contrib Mineral Petrol 103:277-286

Fekiacova Z, Mertz D, Hofmann AW (b) Geodynamic setting of the Tertiary Hocheifel volcanism (Germany), Part II: Geochemistry and Sr, Nd and Pb isotopic compositions. This volume

Fekiacova Z, Mertz DF, Renne PR (a) Geodynamic setting of the Tertiary Hocheifel volcanism (Germany), Part I: $^{40}Ar/^{39}Ar$ geochronology. This volume

Freundt A, Schmincke H-U (1985) Lithic-enriched segregation bodies in pyroclastic flow deposits of Laacher See Volcano (E-Eifel, Germany). J Volcanol Geotherm Res 25:193-224

Freundt A and Schmincke, H-U (1986). Emplacement of small-volume pyroclastic flows at Laacher See volcano (East Eifel, Germany). Bull Volcanol 48: 39-60

Freundt B (1986): Der leuzititische Hochsimmer Vulkan (Osteifel): vulkanologische, petrologische und geochemische Entwicklung und die Säulenbildung im Lavastrom. Diplomarbeit Ruhr-Universität Bochum, pp 1-251

Fuchs K, von Gehlen K, Mälzer H, Murawski H, Semmel A (eds) (1983) Plateau uplift, the Rhenish Shield - a case history. Springer, Heidelberg, pp 1-411

Fuhrmann U, Lippolt HJ (1987) Excess argon and dating of Quaternary Eifel volcanism: III. Alkalibasaltic rocks of the Central West Eifel/ FR Germany. N Jb Geol Pal Mh:213-236

Giggenbach W, Sano Y, Schmincke H-U (1991) CO_2 rich gases from lakes Nyos and Monoun (Cameroon), Laacher See (Germany), Dieng (Indonesia), and Mt. Gambier (Australia) - variations on a common theme. J Volcanol Geotherm Res 45:311-323

Goes S, Spakman W, Bijwaard H (1999) A lower mantle source for Central European volcanism. Science 286:1928-1932

Graf HF, Timmrick C (2001) A general climate model simulation of the aerosol radiative effects of the Laacher See eruption (10 900 BC). J Geophys Res 106:1474--14756

Granet M, Wilson M, Achauer U (1995) Imaging a mantle plume beneath the Massif Central (France). Earth Planet Sci Lett 136:281-296

Grapes RH (1986) Melting and thermal reconstitution of pelitic xenoliths, Wehr volcano, East Eifel, West Germany. J Petrol 27:343-396

Griesshaber E, O`Nions RK, Oxburgh ER (1992) Helium and carbon isotope systematics in crustal fluids from the Eifel, the Rhine Graben and Black Forest, FRG. Chem Geol 99:213-235

Haase KM, Goldschmidt B, Garbe-Schönberg CD (2004) Petrogenesis of Tertiary continental intra-plate lavas from the Westerwald region, Germany. J Petrol 45:883-905

Halmer MM, Schmincke H-U (2003) The impact of moderate-scale explosive eruptions on stratospheric gas injections. Bull Volcanol 65:433-440

Harms E, Schmincke H-U (2000) Volatile composition of the phonolitic Laacher See magma (12 900 yr BP): Implications for syneruptive degassing of S, F, Cl and H_2O. Contrib Mineral Petrol 138:84-98

Harms E, Gardner JE, Schmincke H-U (2004) Phase equilibria of the Lower Laacher See Tephra (East Eifel, Germany): constraints on pre-eruptive storage conditions of a phonolitic magma reservoir. J Volcanol Geotherm Res 134:125-138

Hoernle KA, Zhang YS, Graham D (1995) Seismic and geochemical evidence for large-scale mantle upwelling beneath the eastern Atlantic and western and central Europe. Nature 374:34-39

Houghton BF, Schmincke H-U (1986) Mixed deposits of simultaneous Strombolian and phreatomagmatic volcanism: Rothenberg Volcano, East Eifel Volcanic field. J Volcanol Geotherm Res 30:117-130

Houghton BF, Schmincke H-U (1989) Rothenberg scoria cone, East Eifel: a complex strombolian and phreatomagmatic volcano. Bull Volcanol 52:28-48

Huckenholz HG (1983) Tertiary volcanism of the Hocheifel area. In: Fuchs K et al (eds) Plateau Uplift - The Rhenish Shield - A Case History. Springer, Heidelberg, pp 121-128

Huckenholz HG, Büchel G (1988) Tertiärer Vulkanismus der Hocheifel. Fortschr Min 66, Beiheft 2:43-82

Jung S, Hoernes S (2000) The major and trace element and isotope (Sr, Nd, O) geochemistry of Cenozoic mafic volcanic rocks from the Rhön area (central Germany); constraints on the origin of continental alkaline and tholeiitic basalts and their mantle source. J Petrol 86:151-177

Keller J, Brey G, Lorenz V, Sachs P (1990) IAVCEI 1990 pre-conference excursion 2A: Volcanism and petrology of the Upper Rhinegraben (Urach-Hegau-Kaiserstuhl). IAVCEI Internat Volcanol Congress Mainz 1990, pp 1-60

Kempton PD, Harmon RS, Stosch H-G, Hoefs J, Hawkesworth CJ (1988) Open-system *O*-isotope behaviour and trace element enrichment in the sub-Eifel mantle. Earth Planet Sci Lett 89:273-287

Keyser M, Ritter JRR, Jordan M (2002) 3D shear-wave velocity structure of the Eifel plume, Germany. Earth Planet Sci Lett 203:59-82

Klügel A (1998) Reactions between mantle xenoliths and host magma beneath La Palma (Canary islands): constraints on magma ascent rates and crustal reservoirs. Contrib Mineral Petrol 131:237-257

Klügel A, Hansteen TH, Schmincke H-U (1997) Rates of magma ascent and depths of magma reservoirs beneath La Palma (Canary Islands). Terra Nova 9:117-121

Kramm U, Wedepohl KH (1990) Tertiary basalts and peridotite xenoliths from the Hessian depression (NW Germany), reflecting mantle compositions low in radiogenic Nd and Sr. Contrib Mineral Petrol 106:1-8

Langguth HR, Plum H (1984) Untersuchung der Mineral- und Thermalquellen der Eifel auf geothermische Indikationen. Forschungsber BMFT. T84-019: 1-196

Lippolt HJ (1983) Distribution of volcanic activity in space and time. In: Fuchs K et al (eds) Plateau Uplift - The Rhenish Shield - A Case History. Springer , Heidelberg, pp 112-120

Litt T, Schmincke H-U, Kromer B (2003) Environmental response to climatic and volcanic events in central Europe during the Weichselian Late glacial. Quat Sci Rev 22:7-32

Lloyd FE (1987) Characterization of mantle metasomatic fluids in spinel lherzolite and alkali clinopyroxenites from the West Eifel and Uganda. In: Menzies MA, Hawkesworth CJ (eds) Mantle Metasomatism. Academic Press, San Diego, pp 91-123

Lloyd FE, Bailey DK (1975) Light element metasomatism of the continental mantle: the evidence and the consequences. In: Ahrens LH, Dawson JB, Cunkan AR, Erlank AJ (eds) Physics Chemistry Earth 9. Pergamon, Oxford, pp 389-416

Lorenz V (1973) On the formation of maars. Bull Volcanol 37:183-204

Lorenz V (1985) Maars and diatremes of phreatomagmatic origin, a review. Trans Geol Soc South Africa 88:459-470

Lorenz V (1986) On the growth of maars and diatremes and its relevance to the formation of tuff rings. Bull Volcanol 48:265-274

Lorenz V, Büchel G (1980) Zur Vulkanologie der Maare und Schlackenkegel der Westeifel. Mitt Pollichia 68:29-100

Loock G, Stosch H-G, Seck HA (1990) Granulite facies lower crustal xenoliths from the Eifel, West Germany: petrological and geochemical aspects. Contrib Mineral Petrol 105:25-41

Luhr JF, Simkin T (eds) (1993) Paricutin, the volcano born in a Mexican cornfield. Geoscience Press, Phoenix, pp 1-427

Mälzer H, Hein G, Zippelt K (1983) Height changes in the Rhenish Massif: determination and analysis. In: Fuchs K et al (eds) Plateau Uplift - The Rhenish Shield - A Case History. Springer, Heidelberg, pp 164-176

May F (2001) CO_2-flux in a dormant intraplate volcanic field: the Westeifel, Germany. Water-rock interaction, Cidu (ed.) Swets and Zeitlinger. pp 883-886

Mechie J, Prodehl C, Fuchs K (1983) The long-range seismic refraction experiment in the Rhenish Massif. In: Fuchs K et al (eds) Plateau Uplift - The Rhenish Shield - A Case History. Springer Heidelberg, pp 260-275

Mengel K, Sachs PM, Stosch HG, Wörner G, Loock G (1991) Crustal xenoliths from Cenozoic volcanic fields of West Germany: implications for structure and composition of the continental crust. Tectonophysics 195:271-289

Mertes H (1983) Aufbau und Genese des Westeifeler Vulkanfeldes. Bochumer geol geotechn Arb 9, pp 1-415

Mertes H, Schmincke H-U (1983) Age distribution of volcanoes in the West-Eifel. N Jb Geol Paläont Abh 166:260-283

Mertes H, Schmincke H-U (1985) Mafic potassic lavas of the Quaternary West Eifel volcanic field. I. Major and trace elements. Contrib Mineral Petrol 89:330-345

Meyer W (1986) Geologie der Eifel. Schweizerbart´sche Verlagsbuchhdlg (Stuttgart), pp 1-615

Meyer W, Stets J (1981) Die Siegener Hauptaufschiebung im Laacher-See-Gebiet (Rheinisches Schiefergebirge). Z Dt Geol Ges 132:43-53

Meyer W, Stets J (1998) Junge Tektonik im Rheinischen Schiefergebirge und ihre Quantifizierung. Z Dt Geol Ges 149:359-379

Meyer W, Stets J. Quaternary uplift in the Eifel area. This volume

Müller B, Wehrle V, Zeyen H, Fuchs K (1997) Short scale variations of tectonic regimes in the western European stress province north of the Alps and Pyrenees. Tectonophysics 275:199-219

Panza GF, Müller ST, Calcagnile G (1980) The stress features of the lithosphere-asthenosphere system in Europe from seismic surface waves and body waves. Pure Appl Geophys 118:1209-1213

Park C and Schmincke H-U (1997). Lake formation and catastrophic dam burst during the late Pleistocene Laacher See eruption (Germany). Naturwiss 84:521-525

Piromallo C, Vincent AP, Yuen DA, Morelli A (2001) Dynamics of the transition zone under Europe inferred from wavelet cross-spectra of seismic tomography. Phys Earth Planet Int 125:125-139

Prodehl C, Müller St, Glahn A, Gutscher M, Haak V (1992) Lithospheric cross-section of the European Cenozoic rift system. In: Ziegler PA (ed), Geodynamics of rifting, Vol I. Case history studies on rifts: Europe and Asia. Tectonophysics 208, pp 113-138

Prodehl C, Müller St, Haak V (1995) The European Cenozoic rift system. In: Olsen KH (ed) Continental rifts: Evolution, structure, tectonics. Elsevier (Amsterdam), pp 133-212

Raikes SA (1980) Teleseismic evidence for velocity heterogeneity beneath the Rhenish Massif. J Geophys 48:80-83

Raikes SA, Bonjer K-P (1983) Large-scale mantle heterogeneity beneath the Rhenish Massif and its vicinity from teleseismic *p*-residuals measurements. In: Fuchs K et al (eds) Plateau Uplift - The Rhenish Shield - A Case History. Springer (Heidelberg), pp 315-331

Ritter JRR (2005) Small-scale mantle plumes: Imaging and geodynamic aspects. In: F Wenzel (ed) Perspectives in Modern Seismology. Lecture Notes Earth Sci, Springer, pp 69-94

Ritter JRR. The seismic signature of the Eifel plume. This volume

Ritter JRR, Jordan M, Christensen UR, Achauer U (2001) A mantle plume below the Eifel volcanic fields, Germany. Earth Planet Sci Lett 98:192-207

Sachs PM, Hansteen TH (2000) Pleistocene underplating and metasomatism in the lower continental crust: a xenolith study. J Petrol 41:331-356

Sachtleben T, Seck HA (1981) Chemical control of Al-solubility in orthopyroxene and its implications on pyroxene geothermometry. Contrib Mineral Petrol 78:157-165

Schmincke H-U (1977a) Eifel-Vulkanismus östlich des Gebietes Rieden-Mayen. Fortschr Miner 55, Beiheft 2:1-31

Schmincke H-U (1977b) Phreatomagmatische Phasen in quartären Vulkanen der Osteifel. Geol Jahrb 39:3-45

Schmincke H-U (1982) Vulkane und ihre Wurzeln. Rhein-Westf Akad Wissensch, Westd Verl (Opladen), Vorträge N 315:35-78

Schmincke H-U (2000) Vulkanismus. Wiss Buchges Darmstadt, 2nd ed, pp 1-264

Schmincke H-U (2004) Volcanism. Springer Heidelberg. pp 1-324

Schmincke H-U (2006) The Quaternary Eifel volcanic fields. Görres Verlag Koblenz, pp 1-125

Schmincke H-U, Fisher RV, Waters AC (1973) Antidune and chute and pool structures in base surge of the Laacher See area, (Germany). Sedimentology 20:1-24

Schmincke H-U, Bogaard Pvd, Freundt A (1990). Quaternary Eifel Volcanism. Excursion guide, workshop in explosive volcanism. IAVCEI Internat Volcanol Congr Mainz (Germany). Pluto Press Witten pp 1-188

Schmincke H-U, Lorenz V, Seck HA (1983) The Quaternary Eifel volcanic fields. In: Fuchs K et al (eds) Plateau Uplift - The Rhenish Shield - A Case History. Springer (Heidelberg), pp 139-151

Schmincke H-U, Park C, Harms E (2000) Evolution and environmental impacts of the eruption of Laacher See Volcano (Germany) 12,900 a BP. Quat Int 61:61-72

Schnepp E, Hradetzky H (1994) Combined paleointensity and $^{40}Ar/^{39}Ar$ age spectrum data from volcanic rocks of the East Eifel field (Germany): Evidence for an early Brunhes geomagnetic excursion. J Geophys Res 99:9061-9076

Schulz B (1992) Mineralogie und Geochemie des Niedermendiger Lavastroms. Diplomarbeit Ruhr Univ Bochum: pp 1-143

Schumacher ME (2002) Upper Rhine Graben: the role of pre-existing structures during rift evolution. Tectonics 21: doi: 10.1029/2001TC900022. 17 pp

Seck HA, Wedepohl KH (1983) Mantle xenoliths in the Rhenish Massif and the Northern Hessian Depression. In: Fuchs K et al (eds) Plateau Uplift - The Rhenish Shield - A Case History. Springer (Heidelberg), pp 343-351

Shaw CSJ (2004) The temporal evolution of three magmatic systems in the West Eifel volcanic field. J Volcanol Geotherm Res 131:213-240

Shaw CSJ, Klügel A (2002) The pressure and temperature conditions and timing of glass formation in mantle-derived xenoliths from Baarley, West Eifel, Germany: the case for amphibole breakdown, lava infiltration and mineral-melt reaction. Min Pet 74:163-187

Shaw CSJ, Eyzaguirre J, Fryer B, Gagnon J (2005) Regional variations in the mineralogy of metasomatic assemblages in mantle xenoliths from the West Eifel Volcanic Field, Germany. J Petrol 46:945-972

Simkin T, Siebert L (1994) Volcanoes of the World. 2nd ed. Geoscience Press, Missoula, pp 1-368

Sleep NH (1996) Lateral flow of hot plume material ponded at sublithospheric depths. J Geophys Res 101:28065-28084

Sleep NH (2002) Local lithospheric relief associated with fracture zones and ponded plume material. G3 3: 8506, doi:10.1029/2002GC000376

Sobczak G (1986) Vulkanologische und geochemische Entwicklung der spätquartären Bellerberg Vulkangruppe. Diplomarbeit (MA thesis) Ruhr Universität Bochum, pp 1-215

Spörli KB, Eastwood VR (1997) Elliptical boundary of an intraplate volcanic field, Auckland, New Zealand. J Volcanol Geotherm Res 79:169-179

Stosch HG (1987) Constitution and evolution of subcontinental upper mantle and lower crust in areas of young volcanism: differences and similarities between the Eifel (FR Germany) and Tariat Depression (central Mongolia) as evidenced by peridotite and granulite xenoliths. Fortschr Mineral 65:49-86

Stosch HG, Lugmair GW (1984) Evolution of the lower continental crust: granulite-facies xenoliths from the Eifel, West Germany. Nature 311:368-370

Stosch HG, Lugmair GW (1986) Trace element and Sr and Nd isotope geochemistry of peridotite xenoliths from the Eifel (West Germany) and their bearing on the evolution of the subcontinental lithosphere. Earth Planet Sci Lett 80:281-298

Stosch H-G, Seck HA (1980) Geochemistry and mineralogy of two spinel peridotite suites from Dreiser Weiher, West Germany. Geochim Cosmochim Acta 44:457-470

Tait SR, Wörner G, Bogaard Pvd, Schmincke H-U (1989) Cumulate nodules as evidence for convective fractionation in a phonolite magma chamber. J Volcanol Geotherm Res 37:21-37

Takada A (1994) The influence of regional stress and magmatic input on styles of monogenetic and polygenetic volcanism. J Geophys Res 99:13563-13573

Tamura Y, Tatsumi Y, Zhao D, Kido Y, Shukuno H (2002) Hot fingers in the mantle wedge: new insights into magma genesis in subduction zones. Earth Planet Sci Lett 197:105-116

Trieloff M, Altherr R. He-Ne-Ar isotope systematics in Eifel and Pannonian basin mantle xenoliths trace deep mantle plume-lithosphere interaction beneath the European continent. This volume

Viereck L (1984) Geologische und petrologische Entwicklung des pleistozänen Vulkankomplexes Rieden, Ost-Eifel. Bochumer geol geotechn Arb 17:1-337

Wedepohl KH, Gohn E, Hartmann G (1994) Cenozoic alkali basaltic magmas of western Germany and their products of differentiation. Contrib Mineral Petrol 115:253-278

Wilson M, Downes H (1991) Tertiary-Quaternary extension-related alkaline magmatism in western and central Europe. J Petrol 32:811-849

Wilson M, Downes H (1992) Mafic alkaline magmatism associated with the European Cenozoic rift system. Tectonophysics 208:173-182

Wilson M, Downes H (2006) Tertiary-Quaternary intra-plate magmatism in Europe and its relationship to mantle dynamics. In: Stephenson R, Gee D (eds) European Lithosphere Dynamics. Geol Soc London Mem (in press)

Wilson M, Patterson R (2002) Intraplate magmatism related to short-wavelength convective instabilities in the upper mantle: evidence from the Tertiary-Quaternary volcanic province of western and central Europe. Geol Soc Am Spec Paper 352:37-58

Wilson M, Rosenbaum JM, Dunworth EA (1995) Melilitites: partial melts of the thermal boundary layer? Contrib Min Pet 119:181-196

Witt-Eickschen G. Thermal and geochemical evolution of the shallow subcontinental lithospheric mantle beneath the Eifel: Constraints from mantle xenoliths: a review. This volume

Witt G, Seck HA (1989) Origin of amphibole in recrystallized and porphyroclastic mantle xenoliths from the Rhenish Massif: implications for the nature of mantle metasomatism. Earth Planet Sci Lett 91:327-340

Witt-Eickschen G, Kramm U (1998) Evidence for the multiple stage evolution of the subcontinental lithospheric mantle beneath the Eifel (Germany) from pyroxenite and composite pyroxenite/peridotite xenoliths. Contrib Mineral Petrol 131:258-272

Witt-Eickschen G, Kaminsky W, Kramm U, Harte B (1998) The nature of young vein metasomatism in the lithosphere of the West Eifel (Germany): geochemical and isotopic constraints from composite mantle xenoliths from the Meerfelder Maar. J Petrol 39:155-185

Witt-Eickschen G, Seck HA, Mezger K, Eggins SM (2003) Lithospheric mantle evolution beneath the Eifel (Germany): constraints from Sr-Nd-Pb isotopes and trace element abundances in spinel peridotite and pyroxenite xenoliths. J Petrol 44:1077-1095

Wörner G (1998) Quaternary Eifel volcanism, its mantle sources and effect on the crust of the Rhenish Shield. In: Neugebauer HJ (ed) Young tectonics – magmatism – fluids: a case study of the Rhenish Massif, University of Bonn, SFB 350 74:11-16

Wörner G, Schmincke H-U (1984a) Mineralogical and chemical zonation of the Laacher See tephra sequence. J Petrol 25:805-835

Wörner G, Schmincke H-U (1984b) Petrogenesis of the Laacher See tephra sequence (East Eifel, Germany). J Petrol 25:836-851

Wörner G, Viereck LG, Plaumann S, Pucher R, Bogaard Pvd, Schmincke H-U (1988) The Quaternary Wehr Volcano: A multiphase evolved eruption center in the East Eifel Volcanic field (FRG). N Jb Miner Abh 159:73-99

Wörner G, Wright TL (1984) Evidence for magma mixing within the Laacher See magma chamber. J Volcanol Geotherm Res 22:301-327

Wörner G, Zindler A, Staudigel H, Schmincke H-U (1986) The sources of continental basalts. Earth Planet Sci Lett 79:107-119

Wörner G, Schmincke H-U, Schreyer W (1982) Crustal xenoliths from the Quaternary Wehr volcano (East Eifel). N Jb Miner Abh 144:29-55

Wörner G, Staudigel H, Zindler A (1985) Isotopic constraints on open system evolution of the Laacher See magma chamber (Eifel, West Germany). Earth Planet Sci Lett 75:37-49

Ziegler PA (1992) European Cenozoic rift system. In: Ziegler PA (ed) Geodynamics of Rifting Volume I. Case History on rifts: Europe and Asia. Tectonophysics 208, pp 91-111

Zolitschka B, Negendank JFW, Lottermoser B G (1995) Sedimentological proof and dating of the early Holocene volcanic eruption of Ulmener Maar (Vulkaneifel, Germany). Geol Rdsch 84:213-219

Thermal and Geochemical Evolution of the Shallow Subcontinental Lithospheric Mantle Beneath the Eifel: Constraints from Mantle Xenoliths, a Review

Gudrun Witt-Eickschen

Institut für Geologie und Mineralogie der Universität Köln, Zülpicher Str. 49B, D-50674 Köln, Germany; E-mail: Gudrun.Witt-Eickschen@uni-koeln.de

1 Introduction

Seismic tomography studies provide clear evidence for a small-scale, finger-like body of low-velocity material extending from about 70 to 400 km depth (Ritter et al. 2001, Keyser et al. 2002, Ritter this volume) or to 650 km (Montelli et al. 2004) beneath the Eifel. The causes of such strong "upper mantle plumes" and their significance with respect to intra-plate volcanism are still a matter of controversial debate. The instabilities might either represent active thermal uplift driven by base heating of the 670 km discontinuity or a response to external tectonic developments, i.e. lithospheric stress might induce regions of decompression melting of fertile fusible patches within a heterogeneous upper mantle (e.g. Courtillot et al. 2003, Wilson 2003, Wilson and Patterson 2001). Thus the fundamental issue is whether elevated temperatures, the occurrence of partial melts, variations in modal composition, mineral anisotropy, or distinct combinations of these effects contribute to the upper mantle seismic anomalies.

Mantle fragments (xenoliths) hosted by the mafic alkaline magmas of the Quaternary West Eifel and East Eifel and the Tertiary Hocheifel (High Eifel) intra-plate volcanic fields represent samples of the shallow continental lithospheric mantle (SCLM). The xenoliths have been the subject of

extensive petrologic, geochemical and isotopic investigations since the early 1960's (Frechen 1963). Because of their rapid transport to the earth's surface, the mantle xenoliths retained evidence of the actual chemical composition and physical constitution of the Eifel SCLM and provide insights into its thermal and dynamic history. Specifically, the reconstruction of the geochemical evolution of the xenoliths places important constraints on metasomatic interaction between the SCLM and melts/fluids related to the asthenosphere and/or to slab dehydration during past subduction.

This article summarises a number of Eifel xenolith studies of the last twenty years. They are relevant to the thermal evolution of the Eifel SCLM and its geochemical modification through time by partial melting and subsequent metasomatic re-enrichment processes.

2 Modal Mineralogy of the Eifel SCLM

The SCLM xenoliths from the Eifel are mainly anhydrous and hydrous spinel peridotites covering a wide range of modal compositions from fertile lherzolite (21 wt% clinopyroxene) through harzburgite to dunite (Fig. 1). The hydrous xenoliths carry pargasitic amphibole (and/or its breakdown products) in textural and chemical equilibrium with the other phases olivine, clinopyroxene, orthopyroxene and spinel (Witt and Seck 1989; Witt-Eickschen and Harte 1994). Garnet, as an indicator of material coming from deeper mantle levels, is completely absent in the Eifel xenoliths.

In rare locations (Gees and Baarley/West Eifel) the xenolith population is dominated by phlogopite-bearing types (wehrlites, dunites, clinopyroxenites), whose origin has been attributed to pervasively metasomatic alteration processes (Lloyd et al. 1991; Zinngrebe and Foley 1995). Furthermore, Cr-rich anhydrous olivine-bearing clinopyroxenites and micaceous hornblendites occur as 0.2-5.0 cm broad veins crosscutting peridotite in composite xenoliths and as discrete xenoliths (Witt-Eickschen et al. 1993; Witt-Eickschen et al. 1998; Downes et al. 2004). These represent high-pressure precipitates of melts moving through a system of fractures within the Eifel SCLM (Witt-Eickschen and Kramm 1998; Witt-Eickschen et al. 2003b).

The spinel peridotites cover the entire range of microstructures described for mantle xenoliths from world-wide localities (e.g. Mercier and Nicolas 1975) and record different degrees of deformation and recrystallisation within the SCLM (see representative photomicrographs in Witt-Eickschen et al. 2003b). Equigranular xenoliths present in the West Eifel localities (Schmincke et al. 1983) reveal either coarse grained textures

(partly with local zones of recrystallisation) or mosaic and tabular recrystallised textures. The tabular texture, which is an unusual and rare texture in other regions of Europe, is considered to be the product of extensive shearing and recrystallisation and developed exclusively in amphibole-bearing xenoliths. Porphyroclastic xenoliths (with or without amphibole) occur in the Tertiary basalts of the High Eifel as well as in the Quaternary West Eifel and East Eifel volcanic fields (Huckenholz 1983; Witt and Seck 1987, Witt and Seck 1989). This texture is characterized by large (up to 1 cm), deformed, unmixed orthopyroxene relics surrounded by a fine-grained matrix of recrystallized olivine, pyroxene and spinel neoblasts.

Having been brought to the surface very rapidly by the rising host magma, the xenoliths preserve the mineral compositions of their last

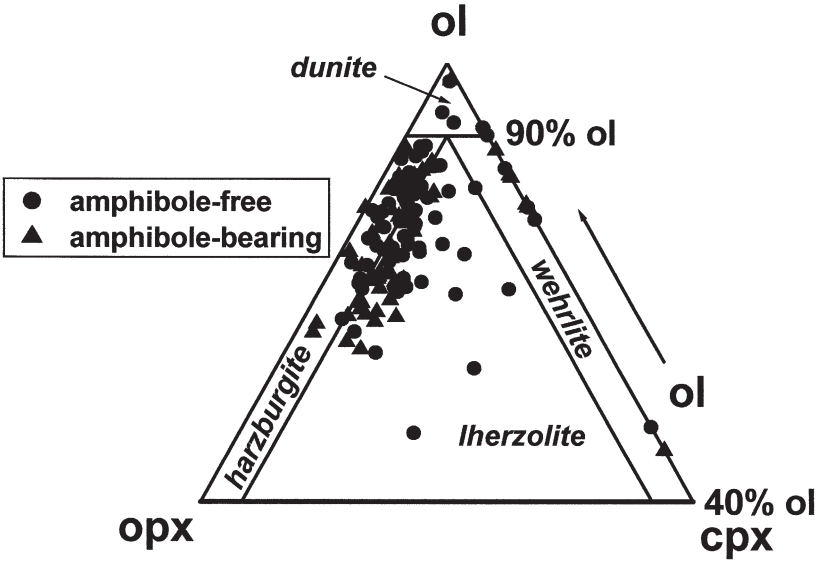

Fig. 1. Mineral modes of 150 spinel peridotite xenoliths from six localities in the West Eifel and East Eifel depicted in the IUGS classifications scheme (Lloyd et al. 1991, Sachtleben 1980, Stosch 1987, Witt and Seck 1987, Witt-Eickschen and Kramm 1998, Witt-Eickschen et al. 2003b, Witt-Eickschen and O'Neill 2005, Zinngrebe and Foley 1995, own data). The xenoliths are predominately clinopyroxene poor lherzolites and harzburgites.

equilibration state within the SCLM reflecting the temperature-pressure condition prior to their entrainment into the host lava. However, the estimate of pressure (corresponding to the depth level at which the xenoliths

resided in the SCLM) is only possible, if perfect chemical equilibrium is achieved within and between the mineral phases of the spinel peridotites. This is the case for some coarse-grained and tabular and mosaic equigranular recrystallised xenoliths from the West Eifel, whose mineral grains are chemically homogeneous with respect to both major element and trace element distribution (e.g. Witt-Eickschen and Harte 1994, Witt-Eickschen and O'Neill 2005).

The depths of origin for these equilibrated xenoliths derived from the iterative combination of the two-pyroxene geothermometer (Brey and Köhler 1990) with the Ca-olivine-clinopyroxene geothermobarometer (Köhler and Brey 1990) are shown in Fig. 2. At a depth interval of about 30 km to 70 km, both lherzolite and harzburgite occur excluding a large-scale systematic vertical zoning with respect to the degree of fertility in this part of the Eifel SCLM. However, a variation in modal composition with depth is in so far recognised as the amphibole-bearing equigranular recrystallised peridotites occur only in the upper part of the SCLM (<50 km). At depths of about 70 km to 80 km, the SCLM is exclusively composed of coarse-grained to recrystallized Cr-rich spinel harzburgites (<0.5 % to 5 % cpx). The porphyroclastic textured lherzolites and harzburgites are restricted to the shallowest depth (~30 km).

3 Thermal Evolution of the Eifel SCLM

In addition to the chemically equilibrated xenoliths mentioned above, xenoliths with significant intra-grain compositional variations indicative of chemical disequilibrium (exsolution lamellae, zoning patterns) are abundant. The chemical compositions of minerals in these un-equilibrated xenoliths provide information about changing thermal conditions in the Eifel SCLM due to cooling or re-heating events (e.g. Witt and Seck 1987, Witt-Eickschen et al. 1993). In summary three distinct thermal evolutions were reconstructed:

Equilibration along a 80-85 mWm^{-2} geotherm. The thermobarometric data of the chemically equilibrated xenoliths from the depth range of about 30 km to 80 km reflect a geothermal gradient within the Eifel SCLM (Fig. 2) consistent with the mean heat-flow density for Germany (about 80 mWm^{-2}). In contrast, local surface heat flow densities in the West Eifel volcanic field are lower than this average value (Haenel 1983). The high temperature harzburgites from depths of about 80 km approach the adiabatic upwelling curve of a normal temperature asthenosphere (McKenzie

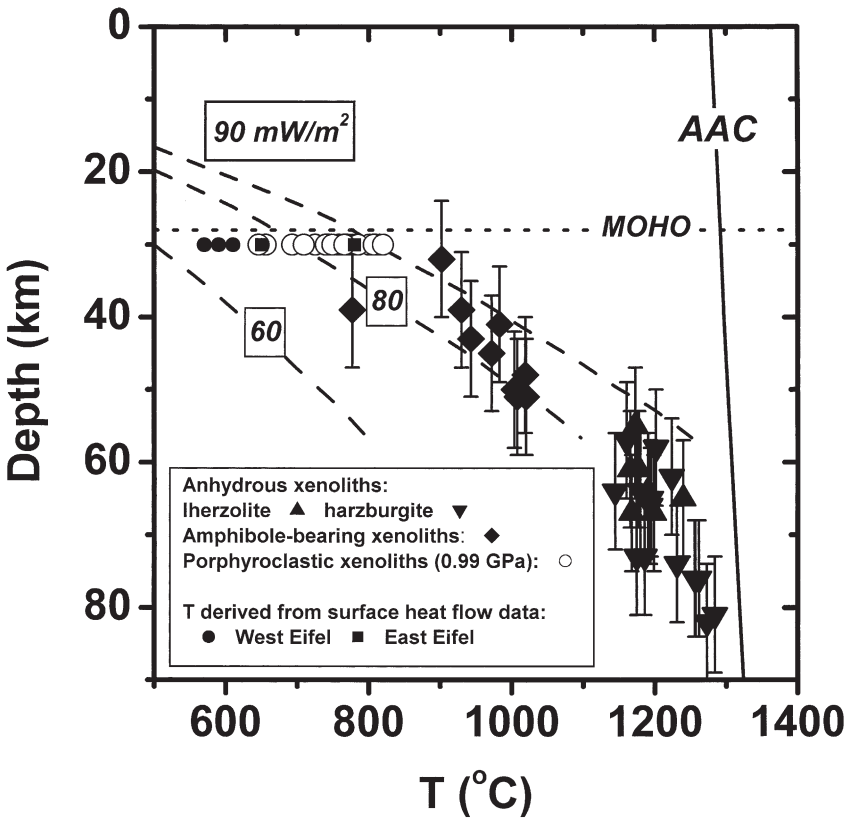

Fig. 2. *P-T* estimates for equilibrated West Eifel xenoliths (Köhler and Brey 1990, Witt-Eickschen and Kramm 1998, Witt-Eickschen and O'Neill 2005, own data). In addition, the temperatures of recrystallisation in porphyroclastic Eifel xenoliths are shown, which were calculated for a pressure of 0.99 GPa from the composition of the neoblast rims (Witt and Seck 1987, Witt-Eickschen and Harte 1994, own data) using the Ca-enstatite geothermometer of Brey and Köhler (1990). Steady-state conductive model geotherms (Chapman and Furlong 1992) and the temperature distribution at 30 km depth derived from surface heat-flow density data of West Eifel and East Eifel localities (Haenel 1983) are given for comparison. *AAC* is the adiabatic upwelling curve of a normal temperature asthenosphere (McKenzie and Bickle 1988).

and Bickle 1988). Assuming that the high temperatures (up to 1280 °C) result from thermal overprint, diffusion models imply a rapid re-equilibration of the pyroxene grains within maximal 2 Ma. Thus the achievement of chemical equilibrium in these deep-seated harzburgites does not neces-

sarily exclude a possibly young convective heat transport at the base of the lithosphere.

Cooling. The cores of the large deformed orthopyroxenes in the porphyroclastic xenoliths from shallow depths (~30 km) beneath the East Eifel, West Eifel, and High Eifel preserve evidence of an earlier high-temperature state (about 1100 °C) prior to unmixing. The rims of the porphyroclasts and the orthopyroxene neoblasts (Fig. 3) manifest a cooling event (<800 °C) that was in strong conjunction with a deformation process (Huckenholz 1983, Witt and Seck 1987, Witt-Eickschen and Harte 1994). As a result of temperature decrease, the neoblasts reveal marked zoning, with Al, Cr, Ca and Ti decreasing from core to rim (Fig. 3). Diffusion modelling of the chemical gradients in individual zoned grains from six xenoliths (example in Fig. 3) yields diffusion times between 50 to 130 Ma in order to produce the zoning patterns. Thus the porphyroclastic xenoliths reflect an old cooling event (at least since the Early Cretaceous), which might be even related to the major tectonic episode of this area, i.e. the Hercynian Orogeny. Consequently, a Tertiary to recent large-scale re-heating of the SCLM near to the crust/mantle boundary by conductive heat transport is excluded.

Local re-heating by young basalt intrusions. However, zoning patterns with Al, Cr and Ca increasing from core to grain margins, which developed in orthopyroxenes of a large number of Eifel xenoliths from mantle depths of less than 50 km, point to a rapid (<0.5 Ma) thermal overprint (Kramm-Glade and Seck 1981, Witt-Eickschen et al. 2003b). This final re-heating of the Eifel SCLM was a local event and took probably place adjacent to thermal aureoles around magma conduits of basaltic intrusions or small magma bodies as a consequence of the Cenozoic Eifel volcanism.

4 Geochemical Evolution of the Eifel SCLM

4.1 Old depletion of the SCLM by extraction of basaltic melts

Xenolith suites from distinct Eifel locations ranging in modal composition from spinel lherzolite to depleted harzburgites record well defined linear trends of bulk rock Mg or Ca versus moderately incompatible refractory lithophile elements (Al, Ca, Sc, Yb) (e.g. Sachtleben 1980, Stosch 1980, Witt 1981). In addition, the suites exhibit systematic variations between their modal composition (modal percentages of clinopyroxene) and the major element chemistry of minerals (e.g. Mg/(Mg + Fe) in olivine; Cr/(Cr + Al) in spinel), which are controlled by mineral/liquid equilibria. Thus the

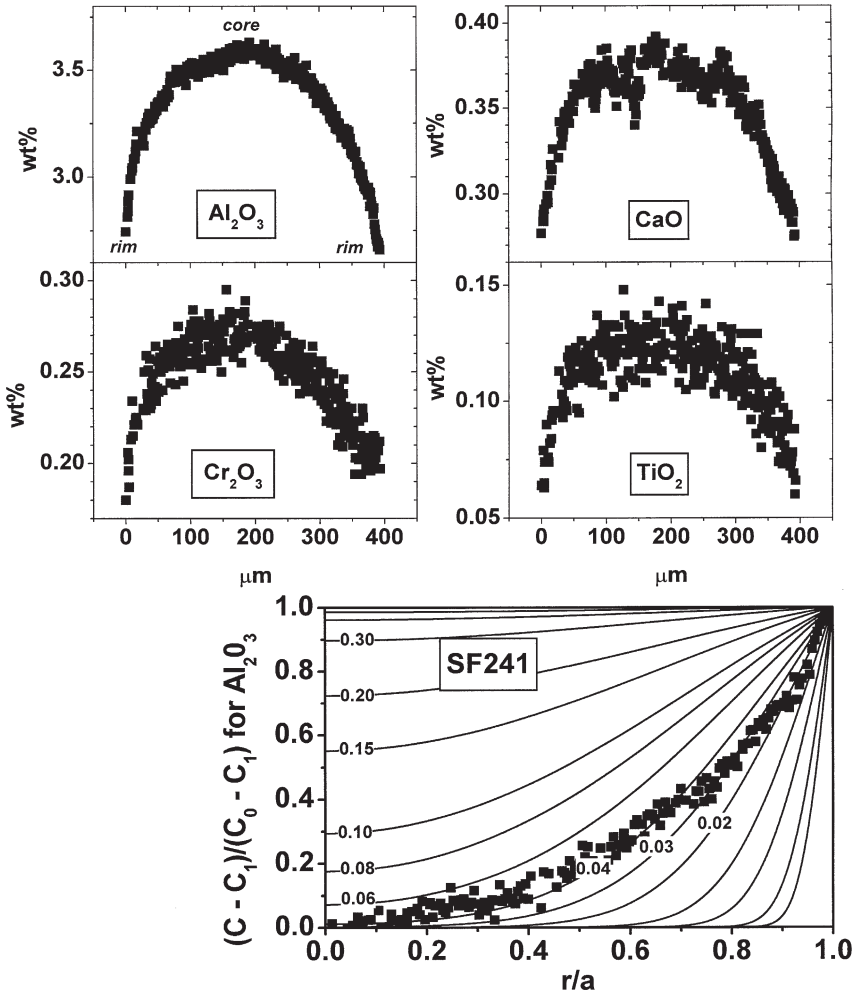

Fig. 3. Representative Al, Ca, Cr, and Ti zoning patterns of a polygonal orthopyroxene neoblast from a porphyroclastic xenolith (Schönfeld/West Eifel) with element concentrations decreasing from core to rim due to cooling. The lower diagram shows an example of element modelling of the Al zoning profiles (using the model of radial diffusion in a spherical grain by Crank (1975)). The curves in this diagram represent constant values of D^*t/a^2 (*t:* time; *D*: diffusion coefficient; *a*: radius of the grain; *r*: distance from the core; C_0: constant composition at the grain surface; C_1: initial composition; *C*: concentration at *r/a).* Because of the lack of diffusion data for Al in orthopyroxene, the diffusion coefficient for Al in clinopyroxene reported by Sautter et al. (1988) was applied (i.e. $D = 3.8\ 10^{-21}$ cm^2/s at 850 °C).

xenolith suites may represent coherent series of residues produced by various degrees of melt extraction from an assumed primitive mantle source.

The trace element and isotope compositions of high-temperature lherzolites support this melting scenario. Their bulk rocks and clinopyroxenes are slightly depleted in the light rare earth elements (LREE) (Fig. 4) and the Sr-Nd-Pb isotope signatures are similar to DMM (depleted MORB mantle) that defines the source region of mid-oceanic ridge basalts from the North Atlantic (Stosch 1987, Witt-Eickschen et al. 2003b). However, Stosch and Seck (1980) showed by trace element modelling that the observed geochemical array is not consistent with a single-stage partial melting event. It requires multistage depletion and enrichment processes. Nevertheless, the coincidence of Sm-Nd- and Rb-Sr model ages (that date the departure from the primitive mantle evolution path) established for some West Eifel xenoliths indicates that the Eifel SCLM suffered an ancient partial melting event about 2 Ga ago (Stosch and Lugmair 1986). The Re-Os isotope systematics of the West Eifel xenoliths yield a somewhat younger model age of ~1.6 Ga for the initial melt extraction (Schmidt and Snow 2002). Thereafter these mantle domains underwent a long-lived closed-system isotopic evolution without chemical processing since their last equilibration in the Proterozoic.

4.2 Re-enrichment of the depleted SCLM by mantle metasomatism

The majority of the xenoliths from the West Eifel and East Eifel volcanic fields provide strong evidence for multistage enrichment processes in the SCLM related to temporally distinct episodes of mantle metasomatism as described below. The activity of metasomatic agents related to a lower mantle plume has been clearly excluded by the noble gas (He, Ne, Ar) isotope compositions of the SCML xenoliths (Dunai and Baur 1995, Gautheron et al. 1999, Gautheron and Moreira 2002).

Metasomatic enrichment unrelated to Cenozoic volcanism

After Proterozoic melt extraction, metasomatic agents generated from an isotopically enriched mantle reservoir (i.e. EM-like) caused amphibole formation and enrichment in elements fairly soluble in aqueous fluids (e.g. Ba, Sr, Pb) in larger parts of the depleted uppermost SCLM (metasomatic episode 1). As the metasomatic hydrous fluids reveal hydrogen isotope values between those of upper mantle and seawater and the enrichment was temporally related to a phase of deformation and cooling, the fluids

have been interpreted to be subduction related and associated with the Hercynian orogeny (Kempton et al. 1988, Rosenbaum and Wilson 1996, Witt-Eickschen et al. 2003b).

During a second episode of mantle metasomatism the EM-like SCLM was affected by melts from a HIMU-like mantle source (i.e. high time- integrated $\mu = {}^{238}U/{}^{204}Pb$) that formed highly LREE-enriched clinopyroxenes (Fig. 4) and amphiboles in the tabular recrystallised xenoliths (Witt-Eickschen et al. 2003b). These metasomatic agents do not have their isotopic equivalent in the young alkaline Eifel lavas, because the HIMU-like component introduced by the fluids had a Pb isotope composition even

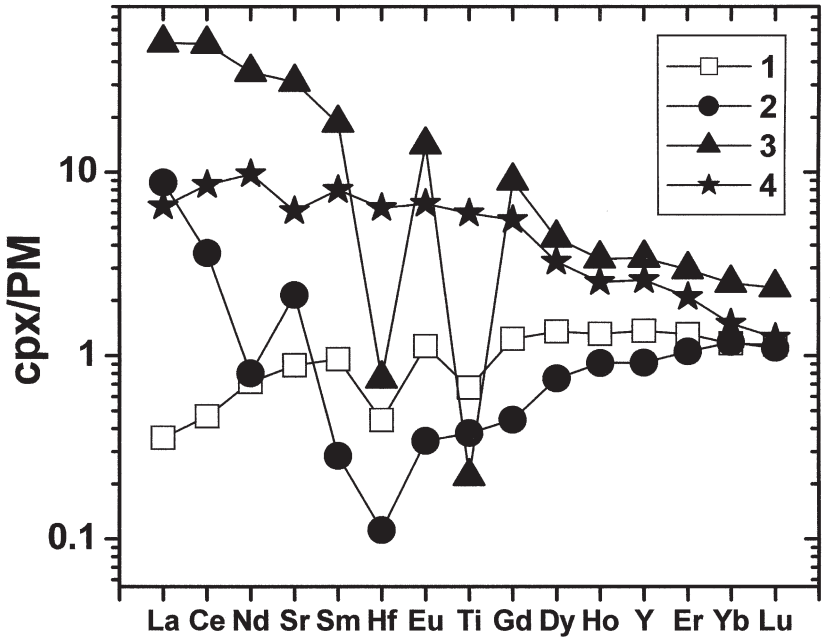

Fig. 4. Examples of primitive mantle-normalized (*PM*) incompatible trace element diagrams for clinopyroxenes (*cpx*) from different types of Eifel mantle xenoliths. 1: cpx from a LREE-depleted xenolith that suffered old partial melt extraction; 2: cpx with a V-shape pattern from an initially LREE-depleted xenolith that was re-enriched by aqueous subduction-related fluids (metasomatic episode 1); 3: cpx from a xenolith strongly enriched in both the LREE and the middle REE due to interaction with metasomatic melts from a HIMU-like mantle source (metasomatic episode 2); 4: cpx from a magmatic clinopyroxenite vein with convex-upward REE pattern and troughs for Sr and Hf (metasomatic episode 3). For more details and trace element modelling see Witt-Eickschen et al. (2003b).

more radiogenic than in the uniform asthenospheric source proposed for the Cenozoic European magmatism (Cebriá and Wilson 1995, Hoernle et al. 1995). The mantle source of the metasomatic melts is identical in Nd-Sr-Pb isotope composition to those of Cretaceous nephelinites intrusions in the Eifel (Witt-Eickschen et al. 2002). Therefore, the HIMU-like signature may be linked to reactivation of ancient subducted crustal domains during the early Cretaceous.

Vein metasomatism by Cenozoic basaltic melts

During a final episode of mantle metasomatism basaltic melts, migrating along fractures through the upper mantle, modified the heterogeneous enriched SCLM. This is manifested in composite xenoliths which are either composed of magmatic hornblendite veins crosscutting hydrous peridotite host xenoliths or magmatic anhydrous clinopyroxenite veins present in anhydrous host peridotites (Witt-Eickschen and Kramm 1998, Witt-Eickschen et al. 1998). Witt-Eickschen et al. (1998) showed by trace element modelling of compositional gradients within individual pre-existing amphibole grains that the interaction between the melts and the peridotite wall-rocks occurred within a time interval of only 10 to 1000 years before transport of the xenoliths to the surface. Furthermore, the magmatic veins, the peridotitic wall rocks and the Quaternary Eifel lavas share nearly the same diversity of Sr-Nd-Pb isotopic signatures. Thus vein metasomatism represents an extremely brief event, obviously as a consequence of the Cenozoic Eifel volcanism (Witt-Eickschen et al. 2003b).

Glasses in the SCLM

The interpretation of seismic data derived by the receiver function method points to the presence of a low-velocity zone that is locally restricted at a depth of about 60 km to 90 km within the West Eifel SCLM (Budweg 2003, Weber et al. this volume). This small-scale seismic anomaly might be explained by the presence of a small volume of liquid in this shallow part of the SCLM. In fact, glasses (melts) are abundant in the SCLM xenoliths from the West Eifel and occur in veins, along grain boundaries and in "melt-pockets", which replace partially or completely dissociated hydrous minerals (amphibole, phlogopite). The intra-xenolith glasses have been the subject of a large number of investigations (e.g. Edgar et al. 1989, Lloyd et al. 1991, Zinngrebe and Foley 1995, O'Connor et al. 1996, Shaw and Klügel 2002, Witt-Eickschen et al. 2003a, Ban et al. 2004). However, the studies provide contrasting conclusions with respect to melt origin, melt forming mechanisms and timing of melt production.

Ban et al. (2004) showed by mass balance calculations that melts in hydrous xenoliths formed by incongruent amphibole breakdown during entrainment of the xenoliths to the host magma. Shaw and Klügel (2002) attribute the occurrence of all intra-xenolith glasses in the Eifel to very late-stage processes taking place during transport of the xenoliths to the Earth's surface (decompression melting of hydrous phases, infiltration of early host melt). If this is correct, glass formation has not any effect on the seismic velocities in the SCLM source regions of the xenoliths.

On the other hand, small proportions of glass (1 %) present in anhydrous West Eifel xenoliths are associated with CO_2-rich fluid inclusions, which formed at depths greater than 47 km (Witt-Eickschen et al. 2003a). Glass formation in these deep-seated xenoliths is explained by infiltration of initially basaltic melts, which lost their Si-undersaturated character by reaction with orthopyroxene during their migration through the upper mantle. Thus, in this case glasses were present before the xenoliths were entrained by their host magmas.

Acknowledgements

I wish to thank all my colleagues with whom I have studied Eifel mantle xenoliths over the past years especially for their technical assistance, helpful suggestions and fruitful discussions. I am particularly grateful to my former teacher Hans Seck for help and advice in the xenolith work. Many thanks to Hilary Downes and Heinz-Günter Stosch for their reviews providing constructive comments and improving the manuscript. The Deutsche Forschungsgemeinschaft is gratefully acknowledged for funding the Eifel research projects.

References

Ban M, Witt-Eickschen G, Klein M, Seck HA (2004) The origin of glasses in hydrous mantle xenoliths from the West Eifel, Germany: incongruent break down of amphibole. Contribution to Mineralogy and Petrology, 10.1007/s00410-004-0623-x

Budweg M (2003) Der obere Mantel in der Eifel-Region untersucht mit der Receiver Function Methode. Dissertation, Universität Potsdam

Brey GP, Köhler T (1990) Geothermobarometry in four-phase lherzolites II. New thermobarometers and practical assessment of existing thermobarometers. Journal of Petrology 31:1353-1378

Cebriá JM, Wilson M (1995) Cenozoic mafic magmatism in Western/Central Europe: a common European asthenospheric reservoir? Terra Abstracts 7:162

Chapman DS, Furlong KP (1992) The thermal state of the lower crust. In: Fountain DM, Arculus RJ, Kay RM (eds) Continental lower crust. Development in Geotectonics Vol.23. Elsevier, Amsterdam, pp 179-199

Courtillot V, Davaille A, Besse J, Stock J (2003) Three distinct types of hotspots in the Earth's mantle. Earth and Planetary Science Letters 205:295-308

Crank J (1975) The mathematics of diffusion. 2nd ed., Oxford University Press, London, 414 pp.

Downes H, Beard A, Hinton R (2004) Natural experimental charges: an ion-microprobe study of trace element distribution coefficients in glass-rich hornblendite and clinopyroxenite xenoliths. Lithos 75:1-17

Dunai TJ, Baur H (1995) Helium, neon, and argon systematics of the European subcontinental mantle: implications for its geochemical evolution. Geochimica et Cosmochimica Acta 59:2767-2783

Edgar AD, Lloyd FE, Forsyth DM, Barnett RL (1989) Origin of glass in upper mantle xenoliths from the quaternary volcanics of Gees, West Eifel, Germany. Contributions to Mineralogy and Petrology 103:277-286

Frechen J (1963) Kristallisation, Mineralbestand, Mineralchemismus und Förderfolge der Mafitite vom Dreiser Weiher in der Eifel. Neues Jahrbuch Mineralogie Mh. 1963:205-225

Gautheron C, Moreira M (2002) Helium signature of the subcontinental lithospheric mantle. Earth and Planetary Science Letters 199:39-47

Gautheron C, Moreira M, Kunz J, Joron JL, Kurz M, Allègre CJ (1999) Subcontinental mantle below Eifel, Germany: constraints by noble gases. Ninth Annual V.M.Goldschmidt Conference, abstract 7281.pdf

Haenel R (1983) Geothermal investigations in the Rhenish Massif. In: Fuchs K, von Gehlen K, Mälzer H, Murawski H, Semmel A (eds.) Plateau uplift. Springer Verlag, Berlin, pp 228-246

Hoernle K, Zhang YS, Graham D (1995) Seismic and geochemical evidence for large-scale mantle upwelling beneath the eastern Atlantic and western and central Europe. Nature 374:34-39

Huckenholz HG (1983) Tertiary volcanism of the Hocheifel area. In: Fuchs K, von Gehlen K, Mälzer H, Murawski H, Semmel A (eds.) Plateau uplift. Springer Verlag, Berlin, pp 121-128

Kempton PD, Harmon RS, Stosch HG, Hoefs J, Hawkesworth CJ (1988) Open-system O-isotope behaviour and trace element enrichment in the sub-Eifel mantle. Earth and Planetary Science Letters 89:273-287

Keyser M, Ritter JRR, Jordan M (2002) 3D shear-wave velocity structure of the Eifel plume, Germany. Earth and Planetary Science Letters 203:59-82

Köhler T, Brey G (1990) Calcium exchange between olivine and clinopyroxene calibrated as a geothermobarometer for natural peridotites from 2 to 60 kbar with applications. Geochimica et Cosmochimica Acta 54:2375-2388

Kramm-Glade S, Seck HA (1981) Temperaturgeschichte von Mantelxenolithen abgeleitet aus der Elementzonierung von Orthopyroxenen. Fortschritte der Mineralogie 59, Beiheft 1:249-251

Lloyd FE, Edgar AD, Forsyth DM, Barnett RL (1991) The paragenesis of upper-mantle xenoliths from the quaternary volcanics south-east of Gees, West Eifel, Germany. Mineralogical Magazine 378:95-112

McKenzie D, Bickle MJ (1988) The volume and composition of melt generation by extension of the lithosphere. Journal of Petrology 29:625-679

Mercier JC, Nicolas A (1975) Textures and fabrics of upper mantle peridotites as illustrated by xenoliths from basalts. Journal of Petrology 16:454-487

Montelli R, Nolet G, Dahlen FA, Masters G, Engdahl ER, Hung SH (2004) Finite-frequency tomography reveals a variety of plumes in the mantle. Science 303:388-343

O'Connor TK, Edgar AD, Lloyd FE (1996) Origin of glass in Quaternary mantle xenoliths from Meerfeldermaar, West Eifel, Germany: Implications for enrichment in the lithospheric mantle. The Canadian Mineralogist 34:187-200

Ritter JRR, Jordan M, Christensen UR, Achauer U (2001) A mantle plume below the Eifel volcanic fields, Germany. Earth and Planetary Science Letters 186:7-14

Rosenbaum JM, Wilson M (1996) Two-stage enrichment of the Eifel mantle: new evidence. Journal of Conference Abstracts 1:523

Sachtleben T (1980) Petrologie ultrabasischer Auswürflinge aus der Westeifel. Dissertation, Universität Köln

Sautter V, Jaoul O, Abel F (1988) Aluminium diffusion in diopside using the $^{27}Al(p, \gamma)^{28}Si$ nuclear reaction: preliminary results. Earth and Planetary Science Letters 89:109-114

Schmidt G, Snow J (2002) Os isotopes in mantle xenoliths from the Eifel volcanic field and the Vogelsberg (Germany): age constraints on the lithospheric mantle. Contributions to Mineralogy and Petrology 143:694-705

Schmidt G, Witt-Eickschen G, Palme H, Seck H, Spettel B, Kratz KL (2003) Highly siderophile elements (PGE, Re and Au) in mantle xenoliths from the West Eifel volcanic field (Germany). Chemical Geology 196:77-105

Schmincke HU, Lorenz V, Seck HA (1983) The Quaternary Eifel volcanic fields. In: Fuchs K, von Gehlen K, Mälzer H, Murawski H, Semmel A (eds.) Plateau uplift. Springer Verlag, Berlin, pp 139-151

Shaw CSJ, Klügel A (2002) The pressure and temperature conditions and timing of glass formation in mantle-derived xenoliths from Baarley, West Eifel, Germany: the case for amphibole breakdown, lava infiltration and mineral – melt reaction. Mineralogy and Petrology 74:163-187

Stosch HG (1980) Zur Geochemie der ultrabasischen Auswürflinge des Dreiser Weihers in der Westeifel: Hinweise auf die Evolution des kontinentalen oberen Erdmantels. Dissertation, Köln

Stosch HG (1987) Constitution and evolution of subcontinental upper mantle and lower crust in areas of young volcanism: Differences and similarities between the Eifel (F.R.Germany) and Tariat Depression (central Mongolia) as evidenced by peridotite and granulite xenoliths. Fortschritte der Mineralogie 65:49-86

Stosch HG, Lugmair GW (1986) Trace element and Sr and Nd isotope geochemistry of peridotite xenoliths from the Eifel (West Germany) and their bearing

on the evolution of the subcontinental lithosphere. Germany. Earth and Planetary Science Letters 80:281-298
Stosch HG, Seck HA (1980) Geochemistry and mineralogy of two spinel peridotite suites from Dreiser Weiher, West Germany. Geochimica et Cosmochimica Acta 44:457-470
Wehrling F, Altherr R (1997) Thermal evolution of the lithosphere beneath the French Massif Central as deduced from geothermobarometry on mantle xenoliths. Tectonophysics 275:119-141
Wilson M (2003) The geodynamic setting of Tertiary-Quaternary intra-plate magmatism in Europe; the role of asthenospheric diapirs or mantle "hot fingers". Abstract of Penrose Plume IV Conference, Iceland
Wilson M, Patterson R (2001) Intraplate magmatism related to short-wavelength convective instabilities in the upper mantle: evidence from tertiary-Quaternary volcanic province of western and central Europe. Geological Society of America, Special Papers 352:37-58
Witt G (1981) Zur Temperaturgeschichte der porphyroklastischen Peridotitauswürflinge von Schönfeld, Westeifel. Diplomarbeit, Köln (unpublished)
Witt G, Seck HA (1987) Temperature history of sheared mantle xenoliths from the West Eifel, West Germany: evidence for mantle diapirism beneath the Rhenish Massif. Journal of Petrology 28:475-493
Witt G, Seck HA (1989) Origin of amphibole in recrystallized and porphyroclastic mantle xenoliths from the Rhenish Massif: implications for the nature of mantle metasomatism. Earth and Planetary Science Letters 91:327-340
Witt-Eickschen G, Harte B (1994) Distribution of trace elements between amphibole and clinopyroxene from mantle peridotites of the Eifel (western Germany): an ion-microprobe study. Chemical Geology 117:235-250
Witt-Eickschen G, Kramm U (1998) Evidence for the multiple stage evolution of the subcontinental lithospheric mantle beneath the Eifel (Germany) from pyroxenite and composite pyroxenite/peridotite xenoliths. Contributions to Mineralogy and Petrology 131:258-272
Witt-Eickschen G, O'Neill HStC (2005) The effect of temperature on the equilibrium distribution of trace elements between clinopyroxene, orthopyroxene, olivine and spinel in upper mantle peridotite. Chemical Geology 221:65-101
Witt-Eickschen G, Seck HA, Reys C (1993) Multiple enrichment processes and their relationships in the subcrustal lithosphere beneath the Eifel (Germany). Journal of Petrology 34:1-22
Witt-Eickschen G, Kaminsky W, Kramm U, Harte B (1998) The nature of young vein metasomatism in the lithosphere of the West Eifel (Germany): Geochemical and isotopic constraints from composite mantle xenoliths from the Meerfelder Maar. Journal of Petrology 39:155-185
Witt-Eickschen G, Mezger K, Seck HA (2002) Sr-Nd-Pb isotopes in mantle xenoliths and lavas from the Eifel (Germany): constraints for mantle components of the European Cenozoic alkaline magmatism. European Journal of Mineralogy 14, Beiheft 1:176
Witt-Eickschen G, Klemd R, Seck HA (2003a) Density contrast of fluid inclusions associated melt (glass) from two distinct suites of mantle peridotites from the

West Eifel, Germany: Implications for melt origin. European Journal of Mineralogy 15:95-102

Witt-Eickschen G, Seck HA, Mezger K, Eggins SM, Altherr R (2003b) Lithospheric mantle evolution beneath the Eifel (Germany): constraints from Sr-Nd-Pb isotopes and trace element abundances in spinel peridotite and pyroxenite xenoliths. Journal of Petrology 44:1077-1095

Zinngrebe E, Foley SF (1995) Metasomatism in mantle xenoliths from Gees, West Eifel, Germany: evidence for the genesis of calc-alkaline glasses and metasomatic Ca-enrichment. Contribution to Mineralogy and Petrology 122:79-96

He-Ne-Ar Isotope Systematics of Eifel and Pannonian Basin Mantle Xenoliths Trace Deep Mantle Plume-Lithosphere Interaction Beneath the European Continent

Mario Trieloff and Rainer Altherr

Mineralogisches Institut der Universität Heidelberg, Im Neuenheimer Feld 236, D-69120 Heidelberg, Germany

Abstract

Neogene to Quaternary mafic alkaline volcanism in the Eifel is part of the Central European volcanic province. Timing and geographical distribution suggest a common, plate-scale origin, either by passive or active mantle upwelling. Seismic tomography suggests confined, narrow plume-structures in the upper mantle below the Eifel and the Massif Central, but a lower mantle connection is not approved. Geochemical characteristics (trace elements and Nd, Sr, Pb, He isotopes) of European Cenozoic volcanics indicate locally varying contributions with enriched mantle character and a common "European Asthenospheric reservoir" (EAR) signature, but a lower mantle component cannot be identified unambiguously. Combined high-precision helium, neon and argon isotope data of mantle xenoliths from mafic alkaline volcanic formations from the Eifel region and the Pannonian Basin show the presence of variably fractionated atmosphere- and mantle-derived components. The xenoliths have different generations of fluid inclusions hosting two distinct noble gas components: one component most probably originated from the local lithospheric mantle source with $(^{21}Ne/^{22}Ne)_{mantle} = 0.07$ and $^{4}He/^{3}He \sim 120{,}000$ ($\sim 6\ R_A$), and dominates total helium and part of total neon. The second component is similar

to hot spot-type noble gases, as observed in volcanic rocks from Hawaii or Réunion. It markedly influences neon isotopes and dominates the argon isotopic composition. Its isotopic structure is inferred to $^{40}Ar/^{36}Ar = 15{,}000 \pm 1{,}200$, $(^{21}Ne/^{22}Ne)_{mantle} = 0.042 \pm 0.005$ and a model-dependent $^{4}He/^{3}He$ ratio of ~36,000 (~20 R_A). Elemental fractionation patterns of noble gases trapped in the xenolith inclusions indicate trapping of CO_2-rich fluids during extended episodes of mantle metasomatism: early fluids have higher proportions of the local lithospheric component, while later fluids increasingly contain plume-derived volatiles. Noble gas isotope systematics indicate that a common deep mantle component is involved in European intra-plate volcanism, probably from a rising super-swell that feeds narrow upper mantle plumes beneath Europe.

1 Igneous Activity in the Eifel and the Central European Volcanic Province

Neogene to Quaternary igneous activity within the Eifel is part of the Central European volcanic province that extends from Central Spain through France (Massif Central), Germany (Rhenish Massif) into the Czech Republic (Ohře Rift), Poland (Lower Silesia) and Hungary (western Pannonian Basin). The main volcanic areas are located on uplifted Variscan basement massifs (Wilson and Downes 1991, 1992), except for the Pannonian Basin where volcanism is associated with back-arc spreading (Dercourt et al. 1986). A prominent tectonic feature paralleling this volcanism in Western and Central Europe is the Cenozoic European Rift System that constitutes an almost continuous system of extensional structures (e.g. the Saône, Limagne, Bresse, Rhine, Ruhr and Leine grabens) more or less contemporaneously with the main and late orogenic phases in the Alps in a belt around the Alpine collision front (e.g. Ziegler 1982, 1992; Wedepohl 1985).

However, although localised volcanism (and possibly thermal doming) in the European volcanic province and Cenozoic rifting occurred to a certain degree related in space and time, only minor magmatic activity occurred directly in the main N-S trending graben systems, indicating no simple relationship to the Tertiary-Quaternary extensional thinning of the western European lithosphere. Generally, the bulk volcanic features are located on the adjoining horst blocks or near to the principal structural dislocations rather than within the grabens, suggesting structural control of the localised volcanic activities (Wilson and Downes 1991, 1992; Schmincke this volume).

The scale of the Cenozoic rift system and associated volcanic activity initiated a search for a common, plate-scale mechanism, driven by e.g. passive mantle upwelling due to indentation of the Adriatic block (Illies 1975), or by active mantle upwelling causing localised volcanic activity and possibly tectonic features. Active mantle upwelling was repeatedly advocated (Duncan et al. 1972; Hoernle et al. 1995; Granet et al. 1995), but due to the complex tectonic situation (plate collision and subduction) and implicitly complex upper mantle structure beneath Europe, a possible involvement of deep mantle plumes is not as easily recognizable as in oceanic areas: seismic tomography is more difficult to perform, no clear surface expressions such as hot spot tracks occur, due to the relatively thick continental lithosphere and intense plume-lithosphere interaction, plume material cannot as easily reach the surface, and geochemical signatures are additionally influenced by local lithospheric – possibly old – mantle components, simulating geochemical and isotopic characteristics of deep mantle material typical for oceanic island basalts (Hofmann 1997).

2 Evidence from Seismic Tomography

Granet et al. (1995) and Ritter et al. (2001) demonstrated the presence of geochemically and thermally anomalous, confined plume-like structures down to depths of several 100 km beneath the Massif Central (Barth et al. this volume) and the Eifel volcanic fields (Ritter this volume). Goes et al. (1999) reported to have identified broad lower mantle upwelling, similar to suggestions by Hoernle et al. (1995), but a definite connection of lower and upper mantle features could not be proved. Using improved seismic data processing, Montelli et al. (2004) could not find distinct narrow lower mantle features beneath the Eifel or other European localities. However, Montelli et al. (2004) also failed to identify compelling lower mantle structures for oceanic hot spots like Iceland or Galápagos that appeared only strong in the upper mantle. Contrary, for other ocean islands (e.g. Hawaii, Réunion, Kerguelen, Samoa) a deep mantle origin was confirmed, in cases tracked down to the core-mantle boundary. In general, a hot spot origin from the 660 km discontinuity seems problematic, as it hardly can be a thermal boundary layer, regarding increasing evidence of deep slab subduction and whole mantle convection (van der Hilst et al. 1997). Other explanations may apply: If the phase change at 660 km temporarily delays penetration of plumes rising from the lower mantle, this would feign an origin from the upper-lower mantle boundary (Montelli et al. 2004). Alternatively, the small upper mantle plumes could be fed by large-scale lower-

mantle upwellings as suggested by Hoernle et al. (1995), Granet et al. (1995), Goes et al. (1999) and recently discussed by Courtillot et al. (2003). In this case, a common geochemical or isotopic component could be expected in European volcanics, but its identification requires that the deep mantle component can be disentangled from more shallow components added within the upper asthenospheric or lithospheric mantle.

3 Geochemical Data (Sr, Nd and Pb isotopes): Identification of Enriched Mantle, (EM), HIMU and Depleted (DMM) Components

Indeed, a common geochemical component in European Neogene to Quaternary mafic alkaline volcanism was recognized by Wilson and Downes (1992), Hoernle et al. (1995), Granet et al. (1995) and ascribed to a common mantle plume endmember, possibly of deep origin (Wedepohl and Baumann 1999). In Nd-Sr-Pb isotope space, lavas display a range (partly along a line defined by Wilson and Downes 1991) between enriched mantle (EM1) composition and a second endmember that is intermediate between depleted MORB mantle (DMM) and HIMU (high μ, i.e. characterised by radiogenic Pb – for definitions of components, see Zindler and Hart 1986) and called European Asthenospheric Reservoir (EAR). It was reported that the EM1 component differs among various European locations, e.g. between Massif Central and Eifel, and therefore was attributed to local lithospheric contributions. These local lithospheric components were suggested to be related to the different Hercynian terrane blocks through which the magmas erupted (Wilson and Downes 1992): These geochemically different terrane blocks were welded together 360-325 Ma ago during the Hercynian orogeny, in the course of a major continental collision episode between Laurasia, Gondwana and a number of intervening microplates. Different terranes (from North to South) comprise the Rhenohercynian (with the Eifel and North Hessian Depression), the Saxothuringian (with the Eastern Eger Graben), and the Moldanubian (with Kaiserstuhl, Urach, Hegau). The Massif Central is mainly considered to be a part of a northern Gondwana foreland block, its northern part possibly an along-strike continuation of the Moldanubian terrane of Eastern Europe.

Contrary to the locally variable EM components, the HIMU-DMM endmember termed as European Asthenospheric Reservoir (EAR) seems to be present in all European volcanics, and was considered as indigenous plume composition (Granet et al. 1995; see also Hoernle et al. 1995). However, the origin of this component is highly debated, e.g. whether it

reflects contributions from an upper or lower mantle reservoir, or a lower lithospheric component. A major cause for these diverging interpretations is the ambiguity of the nature of enriched material in subcontinental areas: In oceanic areas, the lithosphere is generally young, so old oceanic crust causing a HIMU characteristic is only available as deeply subducted lithosphere rising in mantle plumes. In continental areas such as Europe, a HIMU signature may simply be derived from lithospheric remains of locally subducted slabs, e.g. from former consumption of oceanic lithosphere located between Laurasia and Africa during the closure of Tethys. Hence, a deep origin or even the identification of an indigenous sublithospheric mantle component is not ascertained.

4 Significance of Noble Gas Isotopes

Involvement of a HIMU component in the genesis of European volcanics would be consistent with the helium isotopic composition, as both European lavas and mantle xenoliths have $^3He/^4He$ ratios similar to HIMU island lavas characterised by a value of 6.8 ± 0.9 R_A (Hanyu and Kaneoka 1997) where 1 R_A corresponds to the atmospheric $^3He/^4He$ ratio (Ozima and Podosek 2002). However, this interpretation is ambiguous as well, as many data indicate that mantle rocks from different subcontinental areas (Europe, Australia, Africa) have a relatively uniform composition of similar values of 6 ± 1 R_A (Gautheron and Moreira 2002; Dunai and Porcelli 2002), indistinguishable from the HIMU composition.

Moreover, even if a HIMU component was present, an origin in the deep mantle is not implied for the following reason: hot spots with long-lived tracks or activities or pronounced buoyancy flux like Afar, Easter, Galápagos, Hawaii, Juan Fernandez, Kerguelen, Réunion, Samoa (see Courtillot et al. 2003) have been recently approved to have deep seismic roots within the lower mantle, in cases close to the core-mantle boundary (Montelli et al. 2004). Furthermore, they are high $^3He/^4He$ hotspots, with $^3He/^4He$ ratios up to 40 R_A. Although occasionally debated (e.g. Anderson 1998), the high $^3He/^4He$ signature is widely considered as a – probably deep (Kellogg et al. 1999) – less degassed mantle component (Ozima and Podosek 2002), as the proportion of primordial nuclides (^3He, and also ^{20}Ne, ^{22}Ne) is higher than in the degassed MORB mantle that has a relatively uniform value of 8 ± 1 R_A (Ozima and Podosek 2002; Trieloff and Kunz 2005). In this respect, mantle sources with $^3He/^4He$ ratios lower than MORB do not indicate contributions from less degassed or deep components. Contrary, if a contribution of a less degassed mantle source similar

to Hawaii or Réunion would be detected in European volcanics, this could be taken as a more substantial hint at a lower mantle component.

The principle significance of noble gas isotopes is related to the circumstance that the light rare gases helium and neon are solar-type in Earth´s mantle ($^{20}Ne/^{22}Ne \geq 12.5$ – Honda et al. 1991; Trieloff et al. 2000, 2002), contrary to the planetary-type signature of the terrestrial atmosphere ($^{20}Ne/^{22}Ne = 9.8$ – Ozima and Podosek 2002). The higher contributions of mantle-derived solar-type nuclides, i.e. $^{3}He/^{4}He$ ratios up to 40 R_A or a high $^{20}Ne/^{22}Ne$ component, can clearly be distinguished from (possibly recycled) atmospheric or crustal signatures with planetary-type low $^{20}Ne/^{22}Ne$ (≤ 9.8) and low $^{3}He/^{4}He$ ratios of ≤ 1 R_A. Hence, the less degassed hot spot signature can be unambiguously ascribed to nonrecycled – probably deep – mantle material, in contrast to the enriched signature of Sr, Nd and Pb: In oceanic areas, this signature may well be ascribed to deeply subducted and recycled material rising in a mantle plume, but in subcontinental areas, mixing of enriched lithospheric material and depleted mantle material can mimic "primitive" or "undifferentiated" mantle components. At this point, it seems to be important to note that the concomitant occurrence of a less degassed high $^{3}He/^{4}He$ signature and the enriched signature of Sr, Nd and Pb in oceanic areas requires entrainment of the high $^{3}He/^{4}He$ noble gas component into the deeply recycled protolith, from less degassed deep reservoirs, e.g. deep abyssal layers at the base of Earth´s mantle (Kellogg et al. 1999; Trieloff and Kunz 2005).

The circumstances outlined above make rare gases superior geochemical tracers of deep mantle contributions in subcontinental areas (Basu et al. 1995; Marty et al. 1998; Hopp et al. 2004; Buikin et al. 2005). However, in these subcontinental areas isotope measurements, in particular of the heavy noble gases neon, argon, xenon, are intrinsically difficult: magmas are seriously degassed, making these rocks highly susceptible for shallow-level contamination by crustal or atmospheric rare gases (Ballentine and Barfod 2000). In oceanic areas, this problem is circumvented by analysing the vesicle-rich, rapidly chilled glassy margins of submarine basalts that contain sufficient remains of undegassed mantle noble gases (Ozima and Podosek 2002; Moreira et al. 1998; Valbracht et al. 1997; Trieloff et al. 2003). Another solution is to analyse dunite xenoliths that incorporated magma chamber volatiles at greater depths (Trieloff et al. 2000, 2002). As in continental settings submarine basalt glasses are not available, the use of mantle xenoliths as suitable traps and carriers of mantle noble gases is mandatory. Further measures to reduce contaminant atmosphere-type rare gases are the analyses of pyroxene separates that are less affected by atmospheric contamination than olivine (Dunai and Baur 1995; Dunai and

Porcelli 2002; Hopp et al. 2004; Buikin et al. 2005) and using in vacuo stepwise crushing extraction techniques (Moreira et al. 1998; Trieloff et al. 2000, 2002; Hopp et al. 2004; Buikin et al. 2005).

Mantle xenoliths are not just principally promising bottles of unaltered mantle-derived noble gases, they also can potentially record fluids from different mantle sources varying in space and time. Indeed, some studies demonstrated that the fluid inclusion content directly correlates with the abundance of mantle-derived noble gases (Dunai and Baur 1995; Buikin et al. 2005), and that the mechanism incorporating noble gases was mantle metasomatism, most probably triggered by different epochs of interaction of mantle-derived magmas with the subcontinental lithospheric mantle (e.g. Török and de Vivo 1995; Buikin et al. 2005), although volatile incorporation from the host magma during xenolith uplift may certainly occur as well (Dunai and Porcelli 2002).

The above reasoning indicates that isotope analyses are more difficult for neon than for helium, and indeed only recent studies (Marty et al. 1998; Hopp et al. 2004; Buikin et al. 2005) succeeded in yielding high precision neon isotope measurements for subcontinental mantle rocks. However, in spite of the analytical problems, there is an important argument demonstrating the necessity of such precise neon measurements. Several noble gas studies of oceanic areas indicate that neon is less disturbed by admixture of MORB-type (shallow mantle or asthenospheric) noble gases (e.g. Moreira et al. 1995; Niedermann et al. 1997; Sarda et al. 2000). These effects will be discussed below in section 4.2. Hence, neon is a much more sensitive tracer for deep mantle plume contributions than helium, and future efforts can be expected to significantly improve our understanding of plume-lithosphere interactions.

4.1 Helium isotopes in the European subcontinental mantle

Mantle xenoliths from various European locations have a relatively uniform helium isotopic composition of ~6 R_A (Marty et al. 1994; Dunai and Baur 1995; Buikin et al. 2005), hardly distinguishable from other worldwide subcontinental mantle rocks that yielded helium isotopic compositions of about 6 ± 1 R_A (Gautheron and Moreira 2002; Dunai and Porcelli 2002). Nevertheless, some significant small-scale variations can be observed and are shown in Fig. 1A, where $^3He/^4He$ ratios are plotted versus ^4He concentrations. Only samples with $> 10^{-7}$ cc/g ^4He are shown, because at lower ^4He concentrations, the scatter is higher, due to possible additions of cosmogenic ^3He and in situ radiogenic ^4He. At high ^4He concentrations,

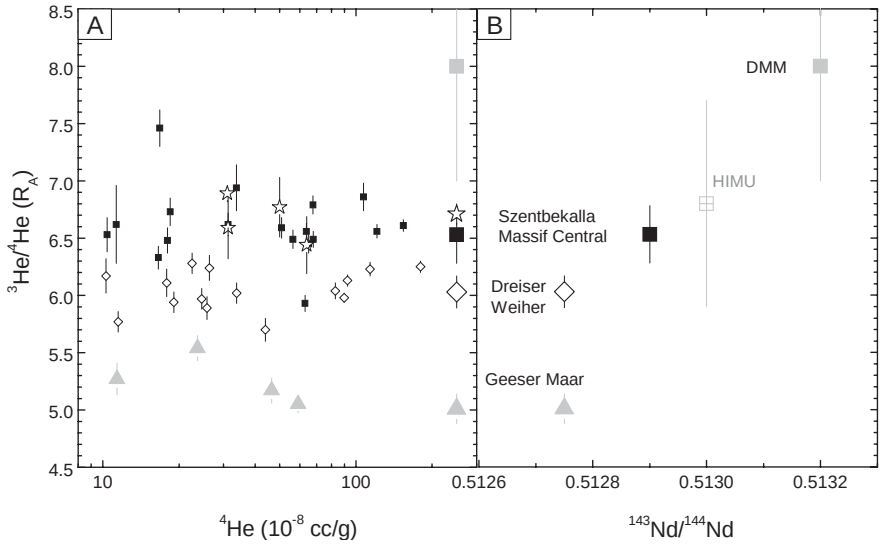

Fig. 1. He and Nd isotope systematics for different European localities and components **A)** Converging ^{3}He/^{4}He ratios at high ^{4}He concentrations show that at each locality, mantle xenoliths display specific helium isotope signatures **B)** These average values (large symbols) correlate with Nd isotopic compositions of the specific EM endmember (measured in lavas) and can be interpreted as reflecting mixing of local lithospheric and possibly asthenospheric components (EM, HIMU, DMM) earlier identified in Nd-Sr-Pb isotope space. Sample symbols: Pannonian basin xenoliths from Szentbekalla (open stars); Massif Central xenoliths (solid squares), Eifel xenoliths from Dreiser Weiher (open diamonds) and Geeser Maar (up grey triangles). Data sources see text

the ^{3}He/^{4}He ratios converge to values that are characteristic for each specific locality. For example, Massif Central xenoliths converge at 6.53 ± 0.25 (Dunai and Baur 1995), Dreiser Weiher and Meerfelder Maar (Eifel) xenoliths at 6.00 ± 0.15 R_A (Dunai and Baur 1995; Buikin et al. 2005), Geeser Maar (Eifel) xenoliths at 5.00 ± 0.15 R_A (Dunai and Baur 1995), Szentbekalla and Kapfenstein (Pannonian Basin) at 6.71 ± 0.10 R_A (Buikin et al. 2005) and 6.10 ± 0.70 R_A (Dunai and Baur 1995), respectively (uncertainties are mean standard errors).

In Fig. 1B, we furthermore plotted the average ^{3}He/^{4}He ratio versus the average Nd isotopic composition of the EM endmembers of these localities (e.g. Wilson and Downes 1992). Massif Central and Eifel data indicate a rough correlation of Nd and He isotopic compositions, varying between an enriched endmember with about 5-6 R_A and ^{143}Nd/^{144}Nd of 0.5127, and an endmember with either HIMU or DMM composition. This suggests that

the He isotope variation may be related to the locally variable EM components, and reflects similar mixing relationships as previously evaluated for solid isotope tracers (Wilson and Downes 1991, 1992; Granet et al. 1995, Hoernle et al. 1995, see also section 3.). Here it should be noted that we consider the xenolith´s He isotopic composition as proxy for the lava signature and compare it with the Nd isotopic composition of the enriched mantle endmember displayed by the lavas (Wilson and Downes 1991, 1992). If meaningful, this correlation implies that He isotopes are somewhat homogenized at certain localities before incorporation into xenoliths, while this does not seem to be the case for Nd isotopes, because the xenoliths have a larger compositional range than the host lavas (Rosenbaum et al. 1997, Dunai and Baur 1995). Note that a similar correlation between He and Nd isotopic compositions was found by Reid and Graham (1996) for southwestern U.S. basalts.

To summarise presently available He isotope data, there is no hint at a contribution of a "classical" high $^{3}He/^{4}He$ mantle plume to European Neogene to Quaternary mafic alkaline volcanism. However, while the above reasoning demonstrates that compelling evidence of geochemical plume signatures is not present, it does not a priori exclude that part of the isotope characteristics may be related to deep mantle material, particularly in the light of results by Witt-Eickschen et al. (2003 a). They performed a detailed Sr-Nd-Pb isotopic study on peridotitic and pyroxenitic xenoliths from the lithospheric mantle beneath the Eifel area. They found that this mantle is characterised by three distinct isotopic Sr-Nd-Pb compositions (see e.g. their Fig. 7): The first component has the well-known composition of the Quaternary Eifel magmas mentioned above: an EAR-EM1 mixture which is found in high Ti pyroxenite and hornblendite veins, which represent former magmas crystallised at intermediate depths. This means that both magmas, erupted subaerially and crystallised at depths, have similar isotopic signatures. The second component has nearly pure DMM isotope composition and is represented by high temperature anhydrous xenoliths equilibrated at great depth. The third component is a HIMU-EM1 ("loNd") array, present in low Ti amphibole-bearing low-temperature xenoliths derived from relatively shallow depths, and is clearly related to an older metasomatic overprint by subduction-related fluids/melts, possibly related to the Hercynian orogeny. To summarise, Eifel magmas that erupted subaerially and crystallised at depth surprisingly have a composition that was neither affected by shallow hydrous mantle composition nor the deep lithospheric DMM composition. In other words: the plume magmas have a composition that is neither found in shallower nor deeper lithospheric levels, thereby questioning significant interactions between the magma and shallow or deep lithospheric mantle. Hence, it cannot be guar-

anteed that the EM1 component in Eifel lavas is derived from the lithosphere. Instead, the possibility remains that the EAR-EM1 mixture observed in the lavas – which is actually similar to the PREMA (Prevalent mantle) value – could be an indigenous plume component, with a compositional variety observed also in oceanic areas.

4.2 Neon isotopes and Ne-He isotope mixing relations in the European subcontinental mantle

Although there are a number of studies that precisely measured He isotopes in subcontinental mantle rocks, only a few studies reported Ne isotopic compositions, and in some cases with insufficient precision to distinguish MORB- or plume-type contributions. Only two studies reported more precise results. Marty et al. (1998) obtained plume neon in carbonatitic rocks from the Kola peninsula, ascribed to a fossil plume. Matsumoto et al. (1997, 1998) reported few plume neon data on a metasomatic apatite from Australia, however, the significance of this result was debated (Dunai and Porcelli 2002).

Only two recent studies reported a larger number of high precision neon isotope analyses for peridotitic rocks: from the Red Sea region (Hopp et al. 2004) and Eifel and Pannonian Basin mantle xenoliths (Buikin et al. 2005). Some Eifel and Pannonian basin xenolith data are shown in Fig. 2, and some important observations can be made. For comparison, the plot also shows lines for plume-type (Hawaii, Réunion) and depleted MORB mantle reservoirs. The xenolith data scatter around straight mixing lines between mantle neon with $^{20}Ne/^{22}Ne$ ratios up to 12.5, and atmospheric neon that is a common contaminant in all samples (see above). The mixing lines for Pannonian Basin xenoliths (all lherzolites from Szentbekalla close to Lake Balaton) are indistinguishable from each other, having the highest slope, i.e. being closest to plume-type composition, and significantly different from the MORB line. The Eifel samples display a larger compositional range, from similarly steep lines (clinopyroxenite DW906) to MORB-like composition (clinopyroxenite DW918) and a line with a smaller slope than MORB samples (lherzolite DW1).

Obviously, the samples contain significant contributions of neon that is normally only found in rocks from high $^{3}He/^{4}He$ plumes like Hawaii or Réunion (Honda et al. 1991; Valbracht et al. 1997; Trieloff et al. 2000, 2002). However, the measured $^{3}He/^{4}He$ ratios are rather lower, not higher than MORB values. This apparent contradiction can be explained by a He-Ne isotope plot (Fig. 3). It displays $^{4}He/^{3}He$ ratios (note the use of the inverted ratio here) versus $(^{21}Ne/^{22}Ne)_{mantle}$ ratios, where the latter represent

the composition of the pure mantle neon component, i.e. corrected for atmospheric neon, contrary to the data in the neon 3 isotope plot in Fig. 2. The correction is simply done by connecting each single data point with a line through atmospheric composition and extrapolating the $^{21}Ne/^{22}Ne$ ratio to a mantle endmember value of $^{20}Ne/^{22}Ne$ = 12.5 (Trieloff et al. 2000, 2002) – note that extrapolation to the alternative solar value of $^{20}Ne/^{22}Ne$ = 13.8 (Benkert et al. 1993) does not affect the following discussion.

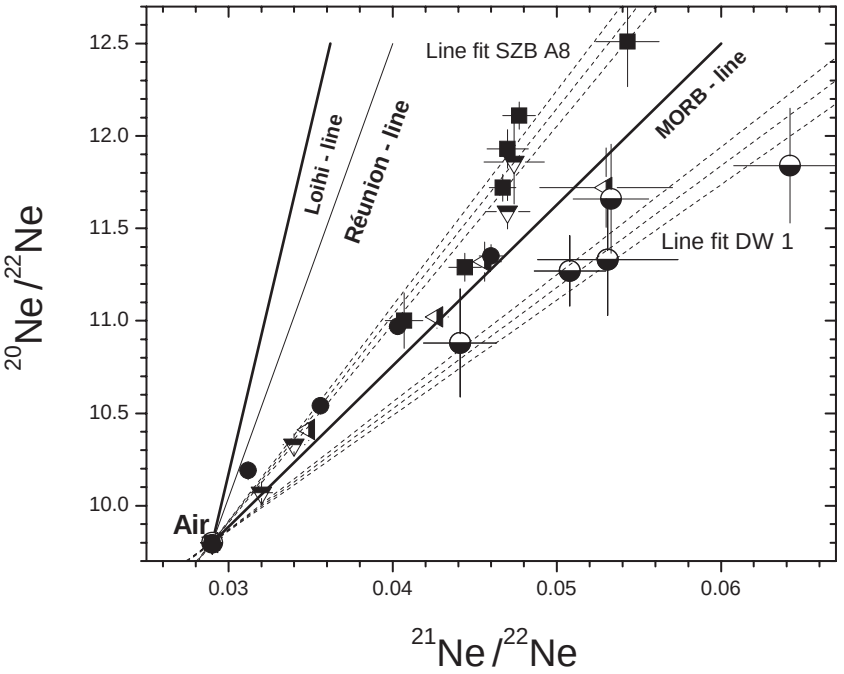

Fig. 2. Neon three isotope plot. Mixing lines of individual samples are different for Eifel samples, with DW1 having nucleogenic neon indistinguishable from the SCLM endmember, DW918 with MORB-like neon, and other samples with marked contributions of plume (i.e. Loihi, Réunion) type neon, most pronounced in Pannonian Basin xenoliths. Latter samples also exhibit slight intra sample variations. Error bars and confidence bands of line fits are 1σ, data from Buikin et al. (2005). Sample symbols: Pannonian Basin xenoliths (Buikin et al. 2005) from Szentbekalla (SZB): SZB A5 (solid circle), SZB A8 (solid square), SZB A20 (open diamond), SZB A9 (grey up triangle); Eifel xenoliths from Dreiser Weiher (Buikin et al. 2005): DW 906 (half filled down triangle), DW 918 (half filled left triangle), DW 1280 (half filled square), DW 1 (half filled circle)

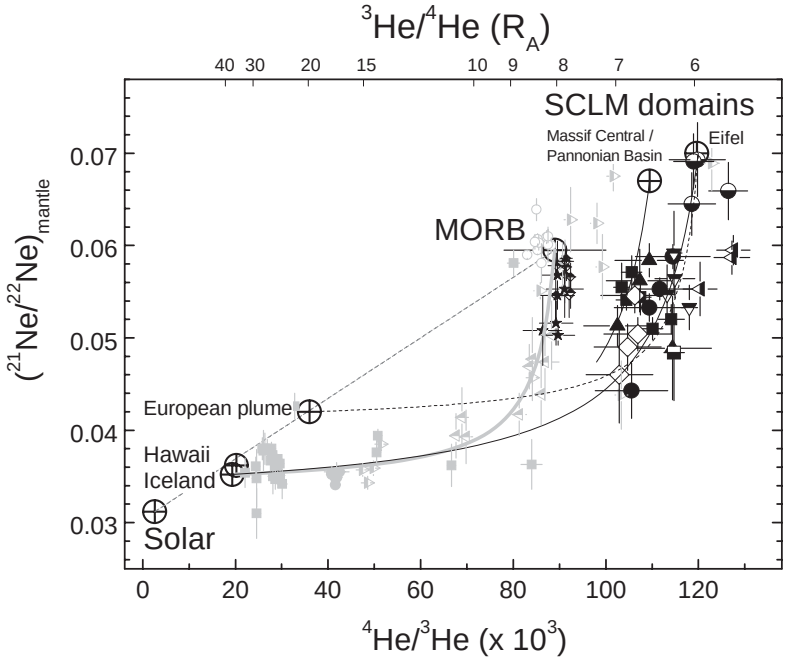

Fig. 3. Helium and neon isotope systematics. $(^{21}Ne/^{22}Ne)_{mantle}$ ratios extrapolated to a mantle endmember value of $^{20}Ne/^{22}Ne = 12.5$, versus $^{4}He/^{3}He$-ratios. Data of mid-oceanic ridge glasses influenced by local inter-plate hotspots and data from the Hawaiian intra-plate hotspot volcanics plot on hyperbolic mixing curves between MORB and deep mantle plume composition (all data in grey). Similarly, European SCLM xenolith data form a branch of a hyperbolic mixing curve between SCLM and deep mantle plume composition. While the helium composition is dominated by SCLM-type helium and nearly uniform (~6 R_A), the neon composition ranges between a pure SCLM signature and a composition similar to the Réunion deep mantle plume source. Only values with 1σ-uncertainties $\Delta(^{21}Ne/^{22}Ne)_{mantle}<0.005$ are used, and only data of crushed samples and total fusion data of heated samples. Sample symbols: Iceland basalt glass (grey circles; Trieloff et al. 2000; Dixon et al. 2000; Moreira et al. 2001), Hawaii: Loihi, Kilauea, Mauna Kea basalt glass or olivine phenocrysts (grey squares; Honda et al. 1991; Valbracht et al. 1997; Trieloff et al. 2000; Althaus et al. 2003); MORB popping rock 2ΠD43 (grey open circles; Moreira et al. 1998); East Pacific Rise (grey left triangles; Niedermann et al. 1997), South Atlantic Discovery anomaly (grey right triangles; Sarda et al. 2000). Zabargad Z13 (solid stars) and Harrat Al Birk SA87-2/12 (half filled diamond) data by Hopp et al. (2004). Other sample symbols see Fig. 2 caption

Plume and MORB mantle reservoirs (Fig. 3) contain specific proportions of primordial solar-type isotopes (^{3}He, ^{22}Ne) and radiogenic ^{4}He and

nucleogenic ^{21}Ne related to U and Th decay. The Hawaiian and Icelandic mantle plumes contain higher proportions of solar-type helium and neon when compared to the MORB and SCLM mantle reservoirs, attesting their less degassed character. Compositions of Hawaii, Iceland and MORB were evaluated by Trieloff and Kunz (2005), the SCLM composition by Hopp et al. (2004).

Obviously, mantle endmember compositions in Fig. 3 fit a linear trend which can be explained either by mixing of primordial (solar type) noble gases and radiogenic noble gases, or by radiogenic evolution in the various reservoirs with similar He/Ne ratios (see discussion in Trieloff and Kunz 2005). Grey symbols in Fig. 3 show data from oceanic areas: for plume-influenced ridge sections in the South Atlantic (Sarda et al. 2000) and the East Pacific Rise (Niedermann et al. 1997), Iceland (Trieloff et al. 2000) and Hawaii as intra-plate hotspot (Honda et al. 1991, Valbracht et al. 1997, Trieloff et al. 2000, Althaus et al. 2003). The data clearly indicate local mixing between rising mantle plumes and surrounding depleted mantle material. Remarkably, the mixing curve is a distinctly curved hyperbola (grey), indicating that plume gases have a He/Ne ratio of about 10 times lower than MORB gases, most probably due to elemental fractionation just prior to the mixing process. An important implication is that during admixing of surrounding asthenospheric or lithospheric mantle material, helium isotopes are readily affected when neon is hardly influenced. For example, when $^{4}He/^{3}He$ ratios approach the MORB lower range of 80,000, the neon composition is still much closer to Loihi than to MORB composition.

Fig. 3 also shows precise Ne data (with $\Delta^{21}Ne/^{22}Ne < 0.005$) of Eifel and Pannonian Basin mantle xenoliths. The most striking feature is that the data also plot on a mixing hyperbola: While helium in the xenoliths is largely dominated by a relatively uniform SCLM composition, $(^{21}Ne/^{22}Ne)_{mantle}$ ratios are less radiogenic, comparable to Réunion data (e.g. Trieloff et al. 2002). Another feature is that the radiogenic mixing endmember (termed SCLM and best approximated by Eifel lherzolite DW1) is different from MORB composition. It is defined by a more radiogenic composition with $^{4}He/^{3}He = 120{,}000$ (corresponding to the 6 R_A value identified by previous studies, see above) and with $(^{21}Ne/^{22}Ne)_{mantle} = 0.07$ (identified by Hopp et al. 2004). The other endmember has a plume-like composition, as indicated in Fig. 3: Its $(^{21}Ne/^{22}Ne)_{mantle}$ ratio must be at least as low as the lowest measured value of Eifel and Pannonian Basin samples in Fig. 3 (~0.042). Its $^{4}He/^{3}He$ ratio may then correspond to the composition denoted as “European plume” (~36,000), assuming that this mantle endmember fits the linear correlation defined by Hawaii, Iceland, MORB and SCLM domains. However, this needs verification, and other endmember compositions along the dashed

hyperbola with $^{4}He/^{3}He$ ratios significantly higher than 36,000 may also be possible.

It should be noted here that the SCLM endmember composition is perhaps not unique at different localities, but possibly varies slightly as indicated in Fig. 3 by the different SCLM domains (Eifel, Massif Central, possibly Pannonian basin) with varying, correlated He and Nd isotope compositions (Fig. 1B). This view is supported by data of lithospheric mantle rocks from the Red Sea region analysed by Hopp et al. (2004) that show a radiogenic endmember indistinguishable from MORB composition in Fig. 3. In any case, however, the plume neon component is an independent, different component and not related to local lithospheric variations or components.

4.3 Argon isotopes and Ne-Ar isotope mixing relations in the European subcontinental mantle

Recent studies on mantle noble gases have demonstrated that neon isotopes are not only essential to trace plume contributions more sensitive than helium, they have also shown that neon isotopes are important proxies to quantify and correct for contamination by atmospheric noble gases. For example - unlike neon - mantle argon cannot be distinguished from atmospheric argon by using the nonradiogenic argon isotopes ^{38}Ar and ^{36}Ar, because there are no measurable variations in the $^{38}Ar/^{36}Ar$ ratio indicating that solar argon contributions in mantle sources are very minor (< 5 %; Kunz 1999; Trieloff et al. 2002). Hence, correlations of neon and argon isotopes must be used to constrain a sample's proportion of atmospheric argon in order to evaluate the $^{40}Ar/^{36}Ar$ mantle composition.

Fig. 4 shows a plot of $^{40}Ar/^{36}Ar$ versus $^{20}Ne/^{22}Ne$. This plot displays sample-specific mixing curves between atmospheric and mantle-derived neon and argon for Eifel and Pannonian Basin mantle lherzolites. Buikin et al. (2005) recognized that crushing extraction data of certain individual samples plot along well defined individual mixing hyperbolae with different curvatures *r* that depend on the Ar/Ne ratios of the trapped mantle component and the trapped atmospheric contaminant. Hyperbola fits yielded curvatures that are consistent with the measured Ar/Ne ratios of the mantle and atmospheric components of individual samples. Remarkably, all hyperbolae of the Szentbekalla and Eifel samples intersect at $^{20}Ne/^{22}Ne = 12.5$ and $^{40}Ar/^{36}Ar = 15{,}000 \pm 1{,}200$ (Fig. 4), indicating that this value represents the indigenous composition of mantle argon, as well as mantle neon, because extrapolations to $^{20}Ne/^{22}Ne = 13.8$ yield inconsis-

tent values for both the $(^{40}Ar/^{36}Ar)_{mantle}$ and the $(Ar/Ne)_{mantle}$ ratios for the Szentbekalla samples that were all collected from one outcrop.

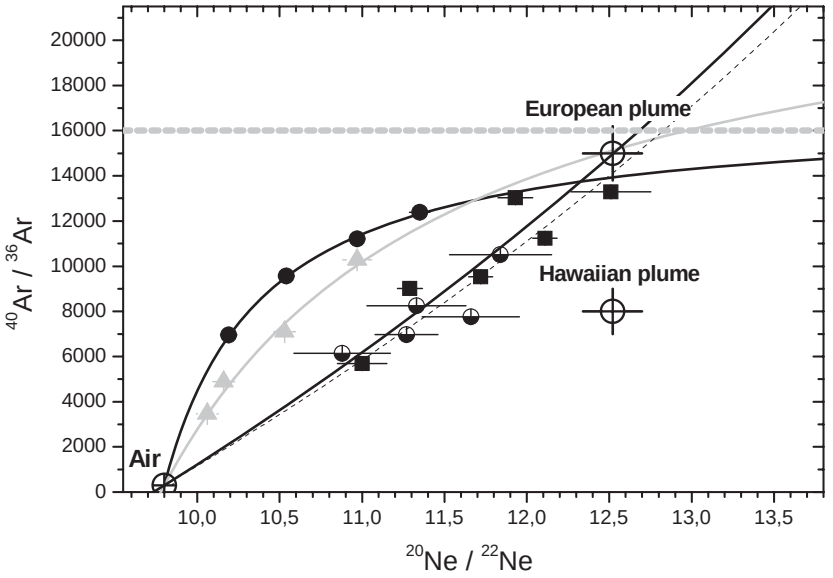

Fig. 4. $^{40}Ar/^{36}Ar$ versus $^{20}Ne/^{22}Ne$ isotope systematics. Crushing extraction data of xenolith pyroxene separates from Szentbekalla and Dreiser Weiher xenoliths reflect mixing between atmospheric and mantle derived neon and argon. Data of individual samples plot along individual mixing hyperbolae with different curvature *r*. All hyperbolae intersect at $^{20}Ne/^{22}Ne=12.5$ and $^{40}Ar/^{36}Ar=15{,}000 \pm 1{,}200$, indicating the preponderance of deep mantle plume type argon in these samples. The grey line corresponds to the highest $^{40}Ar/^{36}Ar$ values measured in European mantle xenoliths (Dunai and Baur, 1995; Buikin et al. 2005). Sample symbols see Fig. 2 and 3 captions

The mantle endmember composition of $^{40}Ar/^{36}Ar = 15{,}000 \pm 1{,}200$ is (i) intermediate between the Hawaiian and MORB sources (8,000 and 28,000-40,000, estimates see Trieloff and Kunz 2005; Burnard et al. 1997) and (ii) relatively uniform, though the $(^{21}Ne/^{22}Ne)_{mantle}$ ratios (Fig. 3) vary between SCLM- and Réunion-type. The latter circumstance is a hint that plume-type argon dominates these samples, due to the same mixing process that dominates He-Ne mixing relationships (Fig. 3).

Fig. 5 shows this possible mixing effect in Ne-Ar isotope space. As in Fig. 3, mantle endmember compositions are from Trieloff and Kunz (2005). The SCLM argon isotope composition is estimated to be more radiogenic than MORB composition, to fit on a line with similar Ar/Ne ratios as the other mantle reservoirs, in analogy with the He and Ne compo-

sitions in Fig. 3 that also plot on a single line. Similar to Fig. 3, the Eifel and Pannonian Basin data follow a mixing hyperbola that requires a depletion of the lighter noble gas nuclide in the plume source, i.e. lower $^{3}He/^{22}Ne$ and $^{22}Ne/^{36}Ar$ ratios. As a cautionary remark, we want to add, that the process causing these strong fractionations is still unclear (see below). While He/Ne fractionation is evident from the massive data body in Fig. 3, a similarly strong Ne/Ar fractionation is only inferred from the few reliable $^{40}Ar/^{36}Ar$ mantle endmember extrapolations in Figs. 4 and 5, and it is not clear, if processes fractionating He and Ne are also capable of fractionating Ne and Ar.

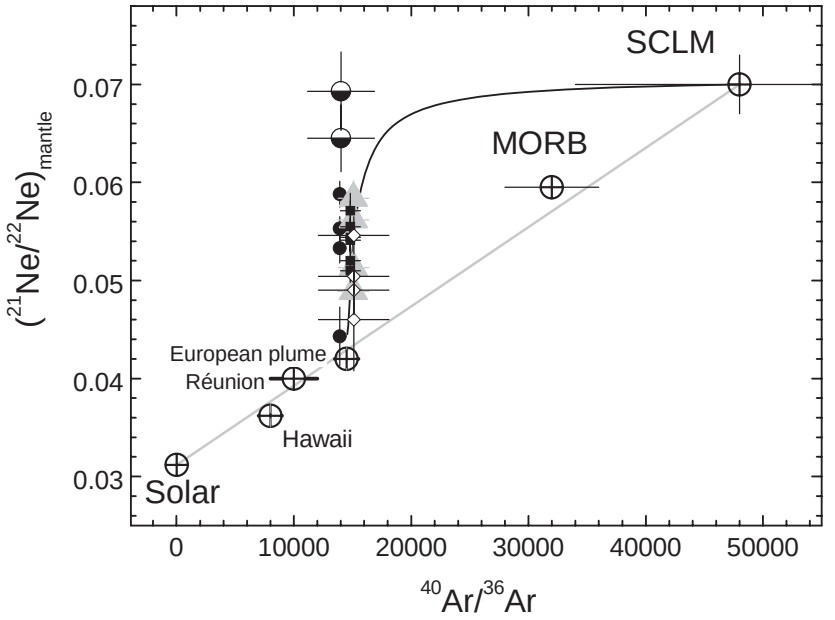

Fig. 5. Mantle argon and neon isotope systematics of subcontinental European and other mantle sources. Mantle endmember $(^{21}Ne/^{22}Ne)_{mantle}$ versus $^{40}Ar/^{36}Ar$ compositions. Deep mantle plumes have a less radiogenic composition than the shallow MORB or SCLM mantle sources. Pannonian Basin and Eifel xenolith data display a range in neon, but relatively constant argon isotopic composition. Similar to Fig. 3, the data indicate hyperbolic mixing of an SCLM and a European mantle plume component. Plume argon is dominating all samples, neon is influenced by both components. The SCLM argon isotopic composition is not yet confirmed and estimated to be more radiogenic than MORB, but its exact composition does not affect the hyperbolic mixing curve. Sample symbols see Fig. 2 and 3 captions

Nevertheless, the mixing systematics displayed in Figs. 3 and 5 match the overall result that noble gases in the Eifel and Pannonian Basin mantle xenoliths are a mixture of two distinct components dominating the isotopic signature of either heavy or light noble gases: (i) a Hawaii- or Réunion-like deep mantle noble gas component dominating argon, and (ii) a (possibly slightly heterogeneous) SCLM component dominating helium. Neon is influenced by both components to varying degrees. Plume-type argon most probably dominates all other Eifel samples from Dreiser Weiher, and ultramafic xenoliths from other European alkaline basalts, as out of a total of 240 argon isotope measurements, the maximum $^{40}Ar/^{36}Ar$ ratios are $17{,}000 \pm 1{,}000$ (Dunai and Baur 1995) and $16{,}200 \pm 200$ (Buikin et al. 2005), i.e. within uncertainties not significantly higher than the above estimate. Nevertheless, the latter conclusion remains to be verified, and certainly more samples should be analysed in the way described above, as there principally could be high $^{40}Ar/^{36}Ar$ samples that define the hyperbola branch at high $(^{21}Ne/^{22}Ne)_{mantle}$ ratios and high $^{40}Ar/^{36}Ar$ ratios in Fig. 5. Xenolith samples with such signatures have not yet been found, but such a component was reported by Wada and Matsuda (1998) for a cubic diamond from Zaire that yielded $^{4}He/^{3}He = 6.2 \pm 0.4\ R_A$, $^{20}Ne/^{22}Ne = 12.07$, $^{21}Ne/^{22}Ne = 0.069$ and $^{40}Ar/^{36}Ar = 34{,}200 \pm 235$, i.e. corresponding to a relatively pure SCLM composition in Figs. 3 and 5. However, unless such compositions are found in European mantle xenoliths, it seems to be advisable to explore alternative explanations, e.g. that the argon with $^{40}Ar/^{36}Ar = 15{,}000$ is a subducted component inherent to the European SCLM.

4.4 Element fractionation patterns of xenolith noble gases: differential source mixing and fluid evolution during magmatic evolution

Mantle xenoliths have long been known to contain fractionated mantle noble gases, most readily seen from $^{4}He/^{40}Ar^*$ ratios (where $^{40}Ar^*$ is mantle ^{40}Ar corrected for the atmospheric component) that differ significantly from expected production ratios of ^{4}He from U,Th-decay and ^{40}Ar from ^{40}K-decay. For typical mantle K/U ratios and accumulation times between 0 and 4.5 Ga, $^{4}He/^{40}Ar^*$ ratios between 1 and 5 are calculated (Ozima and Podosek 2002), but most ratios in ultramafic mantle rocks are significantly lower, and values as low as 0.1 are not unusual. Two major scenarios had been advocated to explain this observation: Either preferential ^{4}He loss at elevated mantle temperatures or solubility controlled fractionation in the parent magmas (Ozima and Podosek 2002). Dunai and Baur (1995) have

shown that $^{3}He/^{4}He$ ratios are not significantly fractionated in low $^{4}He/^{40}Ar^{*}$ ultramafic rocks, so diffusional loss can largely be excluded. Instead, solubility-controlled fractionation seems to be the more promising alternative (Jambon et al. 1985; Honda and Patterson 1999; Moreira and Sarda 2000; Sarda and Moreira 2002). As helium has a higher solubility than heavier noble gases in magmatic melts, heavy noble gases preferentially partition into the exsolving CO_2-dominated gas phase, while the melt contains the He-rich residual component (i.e. high $^{4}He/^{40}Ar^{*}$).

Loss of the gas phase during magmatic evolution results in continuous increase of bulk $^{4}He/^{40}Ar^{*}$, and progressively exsolving CO_2-dominated gas has increasingly higher (though still lower than the bulk) $^{4}He/^{40}Ar^{*}$ ratios (e.g. Jambon et al. 1985). This is exemplified by many studies of oceanic basalt glass with $^{4}He/^{40}Ar^{*}$ ratios of up to 100 (e.g. Sarda et al. 1988, 2000; Niedermann et al. 1997; Moreira et al. 1995; Valbracht et al. 1997).

Fig. 6 shows $^{4}He/^{40}Ar^{*}$ ratios versus $^{3}He/^{22}Ne_{mantle}$ ratios of Eifel and Pannonian Basin xenolith data. $^{4}He/^{40}Ar^{*}$ ratios have values between 0.1 and 2, $^{3}He/^{22}Ne_{mantle}$ ratios between 0.2 and 3. One endmember corresponds to a relatively unfractionated composition with a reasonable mantle-production $^{4}He/^{40}Ar^{*}$ ratio and a solar $^{3}He/^{22}Ne$ ratio. Lowest $^{4}He/^{40}Ar^{*}$ ratios can be interpreted to represent the first generation of CO_2-rich fluids exsolved from magmas and trapped in ultramafic mantle rocks. In the course of magmatic evolution, $^{4}He/^{40}Ar^{*}$ ratios of the bulk magma (as well as of the exsolving CO_2-phase) become progressively higher, closer to more “unfractionated” values. For the Eifel samples, variations are high. DW906 and DW1280 have nearly “unfractionated” elemental composition, while DW1 contains the most strongly fractionated, first generation CO_2-fluids with lowest $^{4}He/^{40}Ar^{*}$ ratios (Fig. 6A). Fig. 6B furthermore demonstrates that this variation is clearly reflected in neon isotopic composition: Early fluids (DW1) are composed of nearly pure SCLM neon, while late stage fluids (DW906, DW1280) have a marked plume signature with lower $(^{21}Ne/^{22}Ne)_{mantle}$ ratios, indicating an increasing admixture of plume-derived magma in the course of magmatic evolution. This correlation can even be traced (though not as compelling) on an intra-sample scale: DW918 and DW1 display highest plume contributions in first crushing steps with higher $^{4}He/^{40}Ar^{*}$ ratios (crush step numbers are indicated in Fig. 6B). For the Pannonian Basin xenoliths, inter-sample variations are not as pronounced, and if a correlation line with a slope similar to the Eifel samples would be present, its position/intercept would be different from the Eifel samples. Nevertheless, we observe at least the rough trend that the first crush extractions have generally higher plume-neon contributions, and higher $^{4}He/^{40}Ar^{*}$ ratios.

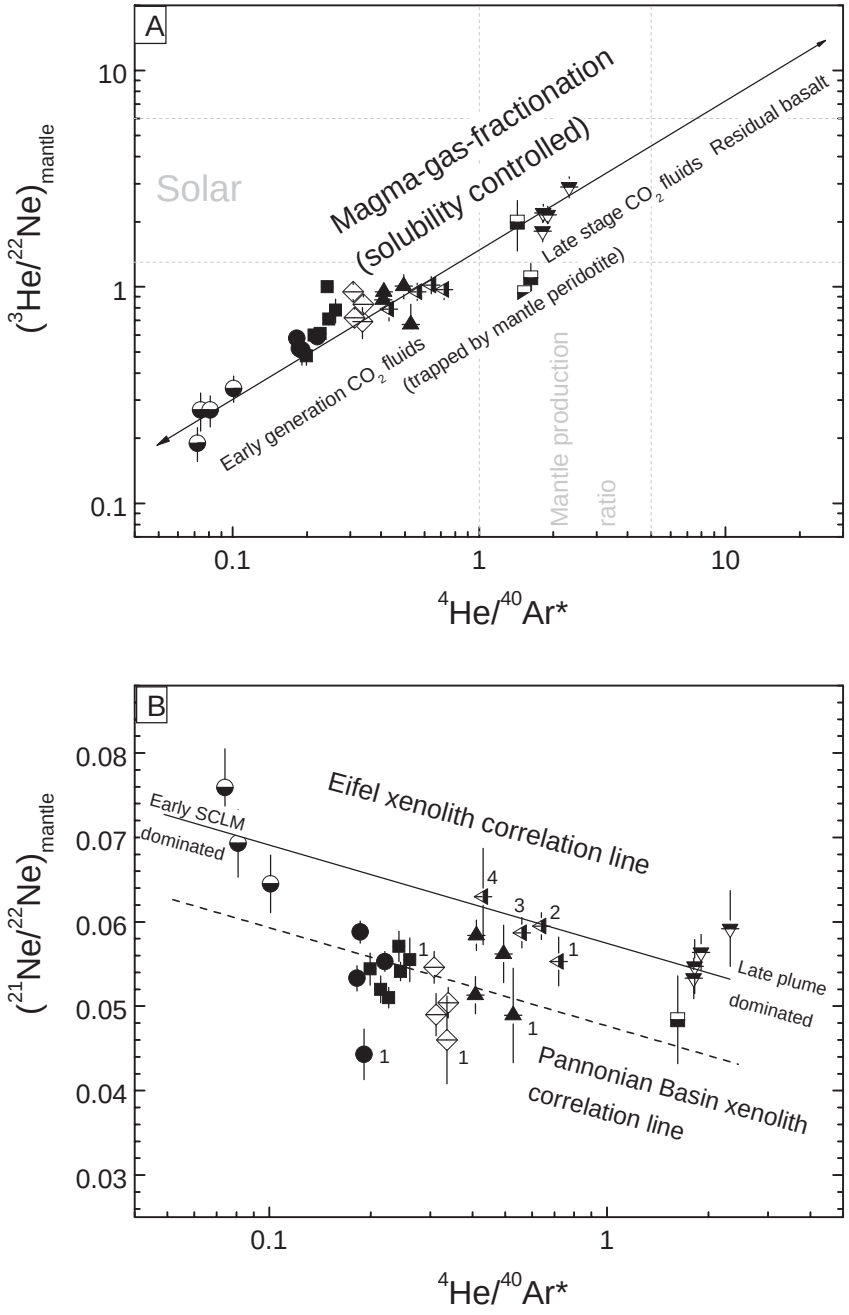
A
Solar
Magma-gas-fractionation
(solubility controlled)
Late stage CO2 fluids
Residual basalt
Early generation CO2 fluids
(trapped by mantle peridotite)
Mantle production
ratio
(3He/22Ne)mantle
4He/40Ar*
10
1
0.1
0.1
1
10
B
Eifel xenolith correlation line
Early SCLM
dominated
Late plume
dominated
Pannonian Basin xenolith
correlation line
(21Ne/22Ne)mantle
4He/40Ar*
0.08
0.07
0.06
0.05
0.04
0.03
0.1
1

Fig. 6. (previous page) Fractionation of mantle He, Ne, Ar in xenolith CO_2 inclusions **(A)** Plotting $^{3}He/^{22}Ne_{mantle}$ versus $^{4}He/^{40}Ar^{*}$ demonstrates fractionation of mantle noble gases in different generations of CO_2 fluid inclusions. This fractionation is controlled by different solubilities of He, Ne and Ar in magmas and different partitioning behaviour into exsolving CO_2. Low $^{4}He/^{40}Ar^{*}$ fluids represent the first generation of exsolving CO_2 dominated fluids **(B)** Early fluids have a higher contribution of SCLM type neon than late (more unfractionated) fluids with more plume type neon, indicating progressive admixture of plume type magmas with plume type neon in the course of magmatic evolution. Sample symbols see Fig. 2 and 3 captions

In any case, the ability of stepwise crushing to separate different types of fluid inclusions in individual samples with varying proportions of atmospheric and mantle-derived noble gases has been demonstrated in previous studies (Moreira et al. 1998, Trieloff et al. 2000, Hopp et al. 2004, Buikin et al. 2005). Higher proportions of atmospheric noble gases are generally released in the first crushing steps, indicating that this component is associated with less retentive or less stable inclusion types.

Most studies have shown that noble gases in ultramafic rocks are hosted by CO_2-rich fluid inclusions (Dunai and Baur 1995, Trieloff et al. 1997, Dunai and Porcelli 2002, Buikin et al. 2005). In Pannonian Basin xenoliths from Szentbekalla, mantle metasomatism is evidenced by both the presence of CO_2-rich fluid inclusions and SiO_2-rich glasses on grain boundaries. This indicates metasomatism by evolved magmas, associated with extended periods of deformation (Embey-Isztin et al. 2001) and most probably only minor input from the host magma (Buikin et al. 2005).

Most fluid inclusions in Szentbekalla xenoliths have maximum diameters of up to 30 μm, and are secondary, occurring along healed fractures. Orthopyroxene and clinopyroxene have much higher inclusion densities than olivine (Török and de Vivo 1995), in agreement with previous observations (Dunai and Porcelli 2002). Homogenization properties reveal two different groups: the majority is homogenizing to the liquid phase (corresponding to trapping depths between 40 and 8 km), very few inclusions homogenize to the vapour phase (3.8-3.1 km). Primary, solitary inclusions are very rare and most are decrepitated. In individual xenoliths, microthermometry indicates a range of equilibration pressures corresponding to maximum depths of 26-40 km and minimum depths of 3-10 km (Török and de Vivo 1995). This pressure variation is also observed among different inclusions within single crystals or single inclusion trails, and was mainly attributed to fluid redistribution during fast xenolith decompression, although some limited fluid influx from the rising and degassing magma was not excluded. Hence, most of the fluids were trapped within the upper mantle. Similar results were derived from a fluid inclusion study

of Eifel xenoliths, however, indicating even higher maximum trapping depths of up to 47 km for inclusions in anhydrous xenoliths (Witt-Eickschen et al. 2003 b) during multiple stages of mantle metasomatism (Witt-Eickschen et al. 1993, 1998).

Different generations of fluid inclusions, trapped or redistributed at different episodes of mantle metasomatism and possibly during transport to the surface can explain different proportions of plume- and lithosphere-derived noble gases. Moreover, it can also be explained why early incorporated (SCLM dominated) fluid inclusions are more resistant against laboratory crushing and are preferentially released in advanced crush extractions: Most fluid inclusions are secondary and occur as trails along planes, indicating that CO_2-fluids penetrate minerals in the course of shear processes. Inclusions form subsequently by fracture healing at elevated mantle temperatures. Incorporation of later CO_2-fluid generations requires repeated shear processes, during which earlier CO_2 inclusions are partially destroyed, and lost or redistributed. Only those first generation inclusions survive that are the most stable and resistant against shearing. The later the inclusions formed, the less shear processes they were subjected to, so correspondingly weaker inclusions can survive. This reasoning can explain why upon laboratory crushing, late generations dominate in first crush extractions. These late generations have higher $^4He/^{40}Ar^*$ ratios, and higher proportions of plume-derived neon and atmospheric noble gases.

5 Summary and Conclusions

The following major processes should be accommodated in a consistent scenario that describes the plume lithosphere interaction derived from noble gas systematics in Eifel and Pannonian Basin mantle xenoliths: (1) origin of the SCLM and plume noble gas components; (2) primary fractionation of noble gases causing the relative enrichment of light noble gases in the SCLM component and/or the enrichment of heavy noble gases in the plume component. This effect causes mixing hyperbolae in Figs. 3 and 5, and possible scenarios should principally apply to both continental and oceanic areas; (3) differential mixing of the two components in the course of magmatic evolution, and exsolution of different generations of CO_2-rich fluids from magmas, that are incorporated into SCLM rocks via fluid-rock interaction; (4) xenolith transport in magmas to the surface, late shallow-level interaction with atmosphere-derived noble gases.

The various processes outlined above are summarised in Fig. 7 and are discussed in detail here:

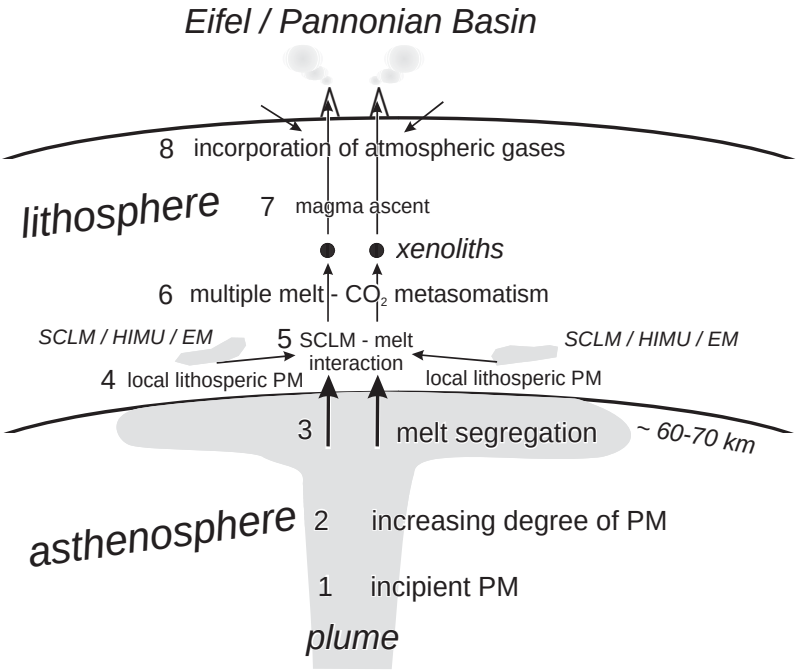

Fig. 7. Plume lithosphere interaction and noble gas incorporation into mantle rocks/xenoliths. Stages 1-3: Plume-type noble gases within plume-derived partial melts (PM) are mixed with SCLM noble gases carried by lithospheric melts (stages 4, 5). From these increasingly differentiated melts, CO2-rich, mostly low $^{4}He/^{40}Ar$ fluids exsolve that metasomatize ultramafic rocks (stage 6). These are brought up as xenoliths by magmas (stage 7), and incorporate atmosphere-derived, variably fractionated noble gases at shallow depths (stage 8). The processes are illustrated schematically, no attempt was made to provide all details or to cover all possible scenarios

1. As the evaluated noble gas isotope signature of the European plume is similar to mantle plumes like Hawaii, Iceland and Réunion, we suggest that the plume-type component is originating from the deeper mantle. This reasoning is based upon common models of a deep origin of these oceanic plumes but not completely ascertained. Although narrow seismic structures in the lower mantle were not confirmed below Europe (Montelli et al. 2004), broad structures were suggested (Hoernle et al. 1995, Goes et al. 1999) and not yet compellingly rejected. The lower mantle component – similar to the kind of superswells discussed by Courtillot et al. (2003) – could feed the identified narrow plumes below the Eifel (Ritter et al. 2001) and French Massif Central (Granet et al. 1995), but transport of geochemical tracers must also have occurred into

the subcontinental lithospheric mantle beneath the Pannonian Basin (Buikin et al. 2005). It should be noted that a common mantle endmember $^{40}Ar/^{36}Ar$ ratio in Eifel and Pannonian Basin samples is an important observation to be checked by future studies, as it is hard to imagine an independent origin of two separate plumes with similar $^{40}Ar/^{36}Ar$ within the shallow upper mantle. The origin of the SCLM noble gas component is not clear. From considerations outlined in sections 3 and 4.1, the low $^{3}He/^{4}He$ component seems to be correlated with the EM components that vary slightly among the Central European Volcanic Province. Hence, an origin in the local lithospheric mantle is possible, while the common EAR endmember could be a common mantle plume component. For the origin of the latter, Wilson and Downes (1992) proposed subduction of 500-400 Ma old oceanic lithosphere during the Hercynian orogeny, incompletely mixed into the asthenospheric upper mantle. Alternatively, if the compositional variations between EAR and EM are indigenous to the locally different (marble cake-like?) upper mantle plumes, the SCLM noble gas component may as well be carried by these variable plume compositions.

2. Another subsequent process fundamentally influencing noble gas systematics is mixing of fractionated plume and SCLM-type noble gases causing hyperbolic mixing in He-Ne isotope space (Fig. 3, stage 5 in Fig. 7). It most probably requires the presence of melts triggering fractionation via solubility properties, and occurs during plume-lithosphere interaction (stages 1-4 in Fig. 7). The processes are not known in detail, but it should be recognized that this kind of mixing is not restricted to subcontinental settings, but commonly observed in oceanic areas where plumes interact with the shallow lithospheric or asthenospheric mantle. One possible scenario involving crystal-melt partitioning is that a first generation of He-rich plume melts is lost in the lowermost lithosphere, and that 2nd generation He-poor plume melts penetrate the lithosphere and mix with locally derived SCLM melts (stage 3-5 in Fig. 7). It is, however, unclear if He and Ne crystal-melt partition coefficients are sufficiently different to cause large fractionations (Brooker et al. 2003). Other possibilities could consider gas-melt partitioning: the rise of the hot plume through the lithosphere induces melting of the lithospheric SCLM components. These melts then exsolve CO_2-rich fluids loaded with heavy noble gases that are lost to the surrounding SCLM, while the He-rich residual melt mixes with plume melts that did not loose their heavy noble gas inventory. One may ask why those “lost” noble gas components would not show up somewhere, but it should be kept in mind that the existence of heavy SCLM-type noble gases has not been excluded yet, while light plume-type noble gases – volumetrically minor

– probably do not manage to reach the surface without being diluted with SCLM-type gases. However, this issue is not yet solved, and other alternative scenarios and processes are certainly possible. The evaluation of the nature of this mixing process is an important future task that can potentially contribute to significantly elucidate plume-lithosphere interactions.

3. Mixing of the above-mentioned components occurs via magmas. From these magmas, CO_2-rich fluids exsolve and are trapped by peridotitic rocks that are later sampled as mantle xenoliths (stages 5 and 6 in Fig. 7). The preponderance of SCLM-type noble gases (high $^{21}Ne/^{22}Ne_{mantle}$) in early stage CO_2-rich fluids with low $^{4}He/^{40}Ar^*$ ratios, and plume-type noble gases (low $^{21}Ne/^{22}Ne_{mantle}$) in late stage CO_2-rich fluids with high $^{4}He/^{40}Ar^*$ ratios indicates that admixing of (or the proportion of) plume-type magmas increased in the course of magmatic evolution. This observation applies particularly to the Eifel (and less pronounced to Pannonian Basin) mantle xenoliths. Different degrees of fractionation of early- and late-stage fluids are caused by progressive exsolution and loss of CO_2-rich fluids with low $^{4}He/^{40}Ar^*$ ratios from magmas that metasomatize the peridotitic wall rocks. Magma evolution can also be recognized by former melts appearing as SiO_2-rich glasses in xenoliths. It should be noted that this fractionation process (after stage 5 in Fig. 7) may not be confused with the earlier fractionation (before stage 5 in Fig. 7) causing depletion of light noble gases in the plume component, as this secondary fractionation during gas-melt partitioning has a higher proportion of plume-type noble gases in CO_2 fluids with high $^{4}He/^{40}Ar^*$ ratios. Trapping of both early and late - more plume-like - fluids occurred at depths of up to 47 km. During ascent of the xenoliths to crustal magma chambers (stage 7 in Fig. 7), some initial fluids were redistributed into newly formed inclusions.
4. During residence in crustal magma chambers or later (stage 8 in Fig. 7) fractionated atmospheric noble gases are incorporated. A possible, but certainly not proven mechanism could involve water in volcanic magmas that is frequently found to have a significant meteoric component. Deeply circulating meteoric water systems are potential carriers of atmosphere-type noble gases, and could be assimilated by crustal magma chambers. Solution of Ne and Ar from meteoric fluids into magma could also explain the variably fractionated, low Ar/Ne ratio of the atmospheric component, causing mixing hyperbolae observed in Fig. 4.

Acknowledgements

We thank S. Niedermann and I. Kaneoka for helpful reviews and thoughtful comments. We thank the members of the Heidelberg noble gas group, A.I. Buikin, J. Hopp, T. Althaus, E.V. Korochantseva and W.H. Schwarz who contributed to the data on which this review is based. We acknowledge support by the Deutsche Forschungsgemeinschaft, grant no. TR333/4.

References

Althaus T, Niedermann S, Erzinger J (2003) Noble gases in olivine phenocrysts from drill core samples of the Hawaii Scientific Drilling Project (HSDP) pilot and main holes (Mauna Loa and Mauna Kea, Hawaii). Geochemistry, Geophysics, Geosystems 4:paper number 2001 GC 000275.

Anderson DL (1998) A model to explain the various paradoxes associated with mantle noble gas geochemistry. Proc Natl Acad Sci USA 95:9087-9092

Ballentine CJ, Barfod D (2000) The origin of air-like noble gases in MORB and OIB. Earth Planet Sci Lett 180:39-48

Basu AR, Poreda RJ, Renne PR, Teichmann F, Vasiliev YR, Sobolev NV, Turrin BD (1995) High ^{3}He plume origin and and temporal-spatial evolution of the Siberian flood basalts. Science 269 :822-825

Benkert JP, Baur H, Signer P, Wieler R (1993) He, Ne and Ar from the solar wind and solar energetic particles in lunar ilmenites and pyroxenes. J Geophys Res 98:13147-13162

Brooker RA, Du Z, Blundy J D, Kelley SP, Allan NL, Wood BJ, Chamorro E M, Wartho JA, Purton JA (2003) The 'zero charge' partitioning behaviour of noble gases during mantle melting. Nature 423:738-741

Buikin AI, Trieloff M, Hopp J, Althaus T, Korochantseva EV, Schwarz WH, Altherr R (2005) Noble gas isotopes suggest deep mantle plume source of late Cenozoic mafic alkaline volcanism in Europe. Earth Plan Sci Lett 230:143-162

Burnard PG, Graham D, Turner G (1997) Vesicle-specific noble gas analyses of „popping rock“: Implications for primordial noble gases in Earth. Science 276:568-571

Courtillot V, Davaille A, Besse J, Stock J (2003) Three distinct types of hotspots in the Earth´s mantle. Earth Planet Sci Lett 205:295-308

Dercourt J et al. (1986) Geological evolution of the Tethys Belt from the Atlantic to the Pamirs since the Lias. Tectonophysics 123:241-315

Dixon ET, Honda M, McDougall I, Campbell IH, Sigurdsson I (2000) Preservation of near-solar neon isotopic ratios in Icelandic basalts, Earth Planet Sci Lett 180:309-324

Dunai T, Porcelli D (2002) Storage and transport of noble gases in the subcontinental lithosphere. In: Porcelli D, Ballentine CJ, Wieler R (eds) Noble gases

in geochemistry and cosmochemistry - Reviews in Mineralogy and Geochemistry vol. 47 pp. 371-410
Dunai T, Baur H (1995) Helium, neon, and argon systematics of the European subcontinental mantle: Implications for its geochemical evolution. Geochim Cosmochim Acta 59:2767-2783
Duncan RA, Petersen N, Hargraves RB (1972) Mantle plumes, movement of the European plate, and polar wandering. Nature 239:82-86
Embey-Isztin A, Dobosi G, Altherr R, Meyer H-P (2001) Thermal evolution of the lithosphere beneath the western Pannonian basin: evidence from deep-seated xenoliths. Tectonophysics 331:285-306
Gautheron C, Moreira M (2002) Helium signature of the subcontinental lithospheric mantle. Earth Plan Sci Lett 199:39-47
Goes S, Spakman W, Bijwaard H (1999) A lower mantle source for Central European volcanism. Science 286:1928-1931
Granet M, Wilson M, Achauer U (1995) Imaging a mantle plume beneath the French Massif Central, Earth Planet Sci Lett 136:281-296
Hanyu T, Kaneoka I (1997) The uniform and low $^{3}He/^{4}He$ ratios of HIMU basalts as evidence for their origin as recycled materials. Nature 390:273-276
Hoernle K, Zhang Y, Graham D (1995) Seismic and geochemical evidence for large-scale mantle upwelling beneath the eastern Atlantic and western and central Europe. Nature 374:34-39
Hofmann AW (1997) Mantle geochemistry: the message from oceanic volcanism. Nature 385:219-229
Honda M, Patterson DB (1999) Systematic elemental fractionation of mantle-derived helium, neon, and argon in mid-oceanic ridge glasses. Geochim Cosmochim Acta 63:2863-2874
Honda M, McDougall I, Patterson DB, Doulgeris A, Clague DA (1991) Possible solar noble-gas component in Hawaiian basalts. Nature 349:149-151
Hopp J, Trieloff M, Altherr R (2004) Neon isotopes in mantle rocks from the Red Sea region reveal large-scale plume–lithosphere interaction. Earth Planet Sci Lett 219:61-76
Illies JH (1975) Recent and paleo-intraplate tectonics in stable Europe and the Rhinegraben rift system. Tectonophysics 29:251-264
Jambon A, Weber HW, Begemann F (1985) Helium and argon from an Atlantic MORB glass: Concentration, distribution and isotopic composition. Earth Planet Sci Lett 73:255-267
Kellogg LH, Hager BH, van der Hilst RD (1999) Compositional stratification in the deep mantle. Science 283:1881-1884
Kunz J (1999) Is there solar argon in the Earth's mantle? Nature 399:649-650
Marty B, Trull T, Luissiez P, Basile B, Tanguy J (1994) He, Ar, O, Sr and Nd isotope constraints on the origin and evolution of Mount Etna. Earth Planet Sci Lett 126:23-39
Marty B, Tolstikhin I, Kamensky IL, Nivin V, Balaganskaya E, Zimmermann JL (1998) Plume-derived rare gases in 380 Ma carbonatites from the Kola region (Russia) and the argon isotopic composition of the deep mantle. Earth Planet Sci Lett 164:179-192

Matsumoto T, Honda M, McDougall I, Yatsevich I, O'Reilly S (1997) Plume-like neon in a metasomatic apatite from Australian lithospheric mantle. Nature 388:162-164

Matsumoto T, Honda M, McDougall I, O'Reilly S (1998) Noble gases in anhydrous lherzolites from the Newer Volcanics, southeastern Australia: A MORB-like reservoir in the subcontinental mantle. Geochim Cosmochim Acta 62:2521-2533

Montelli R, Nolet G, Dahlen FA, Masters G, Engdahl ER, Hung SH (2004) Finite-Frequency Tomography Reveals a Variety of Plumes in the Mantle. Science 303:338-343

Moreira M, Sarda P (2000) Noble gas constraints on degassing processes. Earth Planet Sci Lett 176:375-386

Moreira M, Staudacher Th, Sarda P, Schilling JG, Allègre CJ (1995) A primitive plume neon component in MORB: The Shona ridge-anomaly, South Atlantic (51-52°S). Earth Planet Sci Lett 133:367-377

Moreira M, Kunz J, Allègre CJ (1998) Rare gas systematics in Popping Rock: Isotopic and elemental compositions in the upper mantle. Science 279:1178-1181

Moreira M, Breddam K, Curtice J, Kurz MD (2001) Solar neon in the Icelandic mantle: new evidence for an undegassed lower mantle. Earth Plan Sci Lett 185:15-23

Niedermann S, Bach W, Erzinger J (1997) Noble gas evidence for a lower mantle component in MORBs from the southern East Pacific Rise: Decoupling of helium and neon isotope systematics. Geochim Cosmochim Acta 61:2697-2715

Ozima M, Podosek FA (2002) Noble Gas Geochemistry (2nd ed) Cambridge Univ Press, Cambridge

Reid MR, Graham DW (1996) Resolving lithospheric and sub-lithosperic contributions to helium isotope variations in basalts from the southwestern US. Earth Planet Sci Lett 144:213-222

Ritter JRR, Jordan M, Christensen UR, Achauer U (2001) A mantle plume below the Eifel volcanic fields, Germany. Earth Planet Sci Lett 186:7-14

Rosenbaum JM, Wilson M, Downes H (1997) Multiple enrichment of the Carpathian-Pannonian mantle: Pb-Sr-Nd isotope and trace element constraints. J Geophys Res 102:14947-14961

Sarda P, Moreira M (2002) Vesiculation and vesicle loss in mid-ocean ridge basalt glasses: He, Ne, Ar elemental fractionation and pressure influence. Geochim Cosmochim Acta 66:1449-1458

Sarda P, Staudacher Th, Allegre CJ (1988) Ne-isotopes in submarine basalts. Earth Planet Sci Lett 91:73-88

Sarda P, Moreira M, Staudacher Th (2000) Rare gas systematics on the southernmost Mid-Atlantic Ridge: Constraints on the lower mantle and the Dupal source. J Geophys Res 105:5973-5996

Schmincke HU. The Quaternary volcanic fields of the East and West Eifel (Germany). This volume.

Török K, De Vivo B (1995) Fluid inclusions in upper mantle xenoliths from the Balaton Highland, Western Hungary. Acta Vulcanologica 7:277-284

Trieloff M, Kunz J (2005) Isotope systematics of noble gases in the Earth´s mantle: Possible sources of primordial isotopes and implications for mantle structure. Phys Earth Planet Int 148:13-38

Trieloff M, Weber HW, Kurat G, Jessberger EK, Janicke J (1997) Noble gases, their carrier phases, and argon chronology of upper mantle rocks from Zabargad Island, Red Sea. Geochim Cosmochim Acta 61:5065-5088

Trieloff M, Kunz J, Clague DA, Harrison D, Allègre CJ (2000) The nature of pristine noble gases in mantle plumes. Science 288:1036-1038

Trieloff M, Kunz J, Allègre CJ (2002) Noble gas systematics of the Réunion mantle plume source and the origin of primordial noble gases in Earth´s mantle. Earth Planet Sci Lett 200:297-313

Trieloff M, Falter M, Jessberger EK (2003) The distribution of mantle and atmospheric argon in oceanic basalt glasses. Geochim Cosmochim Acta 67:1229-1245

Valbracht PJ, Staudacher Th, Malahoff A, Allègre CJ (1997) Noble gas systematics of deep rift zone glasses from Loihi Seamount, Hawaii. Earth Planet Sci Lett 150:399-411

van der Hilst RD, Widiyantoro S, Engdahl ER (1997) Evidence for deep mantle circulation from global tomography. Nature 386:578-584

Wada N, Matsuda JI (1998) A noble gas study of cubic diamonds from Zaire: Constraints on their mantle source. Geochim Cosmochim Acta 62:2335-2345

Wedepohl KH (1985) Origin of the Tertiary basaltic volcanism in the Northern Hessian depression. Contrib Mineral Petrol 89 :122-143

Wedepohl KH, Baumann A (1999) Central European Cenozoic plume volcanism with OIB characteristics and indications of a lower mantle source. Contrib Mineral Petrol 136:225- 239

Wilson M, Downes H (1991) Tertiary-Quaternary extension-related alkaline magmatism in Western and Central Europe. J Petrol 32:1811-1849

Wilson M, Downes H (1992) Mafic alkaline magmatism associated with the European Cenozoic rift system. Tectonophysics 208:173-182

Witt-Eickschen G, Kramm U (1998) Evidence for the multiple stage evolution of the subcontinental lithospheric mantle beneath the Eifel (Germany) from pyroxenite and composite pyroxenite/peridotite xenoliths. Contrib Min Petr 131:258-272

Witt-Eickschen G, Seck HA, Reys C (1993) Multiple enrichment processes and their relationships in the subcrustal lithosphere beneath the Eifel (Germany). J Pet 34:1-22

Witt-Eickschen G, Seck HA, Mezger K, Eggins SM, Altherr R (2003a) Lithospheric mantle evolution beneath the Eifel (Germany): constraints from Sr-Nd-Pb isotopes and trace element abundances in spinel peridotite and pyroxenite xenoliths, J Petrol 44:1077-1095

Witt-Eickschen G, Klemd R, Seck HA (2003b) Density contrast of fluid inclusions associated with melt (glass) from two distinct suites of mantle peridotites from the West Eifel, Germany: Implications for melt origin. Eur J Min 15:95-102

Ziegler P (1982) Geological Atlas of Western and Central Europe. Elsevier, Amsterdam.
Ziegler P (1992) European Cenozoic rift system. Tectonophysics 208:91-111
Zindler A, Hart SR (1986) Chemical geodynamics. Ann Rev Earth Planet Sci 14:493-571

Quaternary Uplift in the Eifel Area

Wilhelm Meyer and Johannes Stets

Geologisches Institut, Universität Bonn, Nussallee 8 D-53115 Bonn, Germany

Abstract

The Rhenish Massif was affected by uplift since the Early Tertiary. The uplift velocity increased abruptly during the Pleistocene, just after the paleomagnetic Brunhes/Matuyama boundary, i.e. about 0.8 Ma BP. Since that time the rivers were forced to cut deep valleys into the uprising crustal block. The height difference (δh) between an 0.8 Ma old valley floor, the Younger "Hauptterrasse" (Main Terrace), and the bottoms of the recent valleys allows us to quantify the amount of the young strong uplift. While in the central and eastern part of the Rhenish Massif the amount of uplift is between 50 and 100 m on average, the Eifel and the north-eastern part of the Hunsrück area show uplift of more than 200 m. This area of intense uplift contains a distinct anomaly with nearly 300 m uplift, situated just east of the Quaternary West Eifel volcanic field. The strong uplift in the Rhenish Massif is synchronous with the young volcanism of the Eifel region.

1 Introduction

The Rhenish Massif (Fig. 1), which is part of the Rhenohercynian fold and thrust belt of the Variscan orogene, was covered in parts by the Mesozoic seas. Since the Early Tertiary, i.e. since about 50 Ma, this region rose up in relation to the neighbouring areas. So, step by step, rivers could develop with the well-known "valley-in-valley" fluvial terrace system (Fig. 2). These river terraces demonstrate different evolutionary stages of the ancient erosional regime. During Pliocene, i.e. at the end of the first stage of

uplift with estimated elevation rates of 1.7 cm ka^{-1} (near St. Goar at the Upper Middle Rhine), broad-floored, up to 10 km wide flat valleys (so called trough valleys) developed.

During the Older Pleistocene, the velocity of uplift may have increased. According to the height differences of the then developed terraces one can

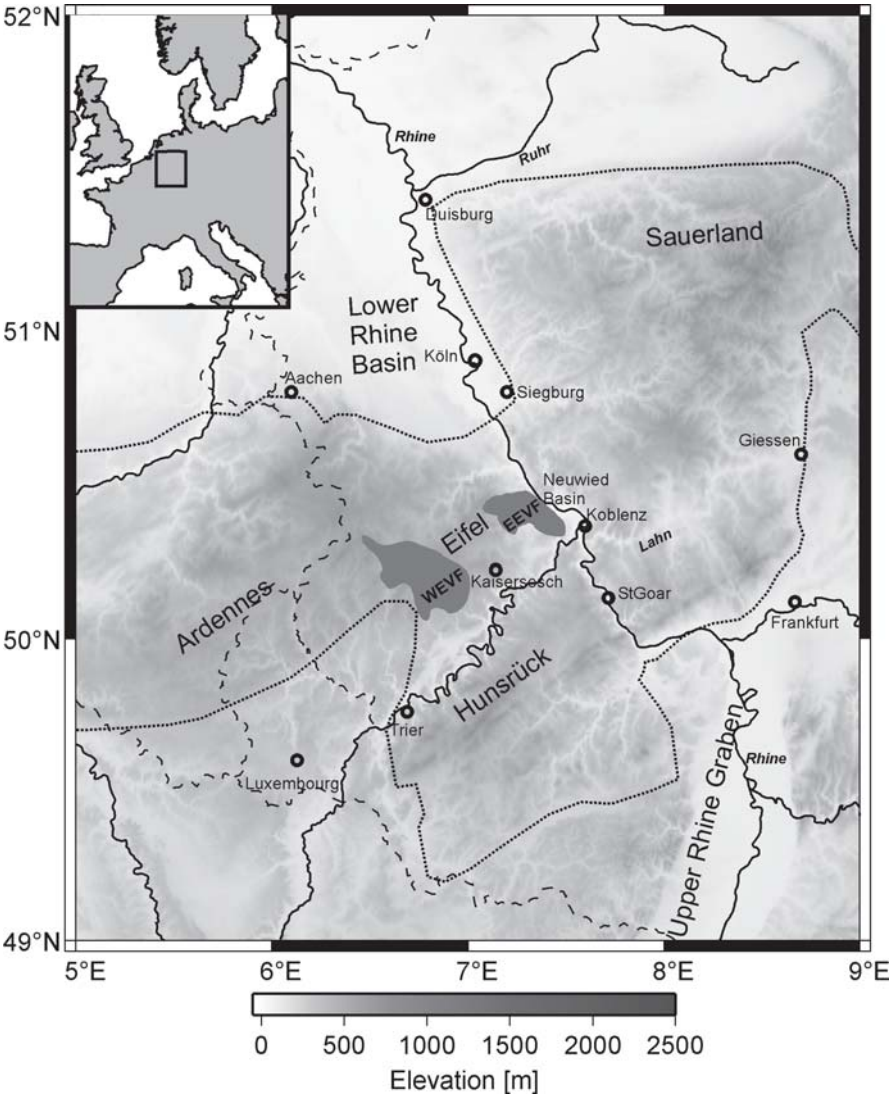

Fig. 1. Overview of study area. The border of the Rhenish Massif is indicated by the dotted line, the Quaternary West (*WEVF*) and East (*EEVF*) Eifel volcanic fields are displayed in dark grey

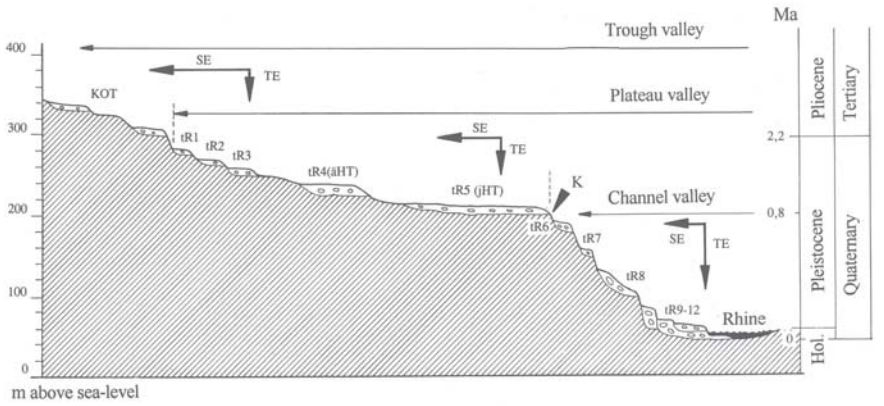

Fig. 2. Diagram of the terrace system in the Rhenish Massif as developed along the Rhine (after Meyer and Stets 1998). Abbreviations: *SE* lateral erosion, *TE* downcutting erosion, *K* morphological edge between Plateau Valley and Inner Canyon, *KOT* Kieseloolith Terraces (Pliocene), tR_{1-3} Older Pleistocene terraces, tR_4 Older Hauptterrasse (Main Terrace, *äHT*), tR_5 Younger Hauptterrasse (*jHT*), tR_6 youngest unit of Hauptterrasse complex, tR_{7-12} suite of Middle and Lower Terraces

assume elevation rates of 7 cm ka^{-1}. Still broad and flat valleys were formed, so called plateau valleys, which of course are narrower than the Tertiary trough valleys.

The last and deepest valley bottom of this period is the kilometer-wide so called Younger Hauptterrasse (Younger Main Terrace) which is a dominant feature not only of Rhine (Rhein) and Mosel, but also in nearly all smaller valleys within the Rhenish Massif (so, the term “Main Terrace” may be explained). After the development of this terrace system, the velocity of uplift abruptly increased up to amounts of 16.5 cm ka^{-1} on average in the reference region near St. Goar (Fig. 1). Due to this strong uplift the rivers were forced to cut deep valleys into the rising block, and the morphology changed from wide trough and plateau valleys to deeply incised narrow channels or canyons (Fig. 2). The sediments of the Younger Hauptterrasse contain the change from reverse to normal magnetic polarity (Fromm 1987). This corresponds to the Brunhes/Matuyama boundary which has been dated with 780 ka (Spell and McDougall 1992). Therefore, we can assume that the phase of strong uplift started about 800 ka ago. First studies demonstrated that the rise of the Rhenish Massif was not homogeneous but occurred at different uplift rates. This pattern of variation in uplift rates in the Rhenish Massif is the subject of the present paper, which will be of interest in the discussion of the Eifel Plume (Ritter this volume).

2 Methods

The height difference between the floor of the Younger Hauptterrasse and that of the recent corresponding river (δh) shows the amount of downcutting erosion to compensate the uplift during the last 0.8 Ma. As the Younger Hauptterrasse could be identified not only in the main valleys, but also in most of the tributaries, we got a tool to quantify uplift rates in the whole Rhenish Massif. A characteristic feature is the morphological sharp edge between the plateau valley of the Younger Hauptterrasse and the steep walls of the incised canyon (Fig. 2). Of course, the development of the river profiles will also be influenced by eustatic sea level changes and by the change of climatic conditions. But there is no doubt that for uplift values up to several hundreds of meters endogeneous processes play the most important role. The most relevant studies on this terrace type within the Rhenish Massif were conducted by Bibus (1980), Birkenhauer (1971), Hoselmann (1994), Kremer (1954), Quitzow (1982), Schnütgen (1974) and Semmel (1983).

For our recent approach the main difficulty was to find out and to map the exact position of the floor of the plateau valley of the Younger Hauptterrasse which is covered by sand and gravel deposits of different thicknesses. It was necessary to follow the floor of this terrace system in the field along the whole course of the valley to recognize dislocations by uplift and younger faults. This was important especially in the area around the Neuwied Basin north of Koblenz, where several faults cut the terrace niveaus and prevented the correlation of the terrace systems of Rhine, Mosel and Lahn in former morphological studies. We succeeded in correlating these systems in a step by step mapping of the terrace niveaus across the basin, and with this systematic approach we were able to compile a map of the distribution of δh in the western, southern and central Rhenish Massif as well as neighbouring areas (Fig. 3). Beside our own observations, we used data from Lafrenz (1933), Richter (1962), Gebhardt (1963), Bibus (1980), Zöller (1983), Ploschenz (1994), Hoffmann (1996), Zapp (2003), and unpublished data from I. Stritzke (southern part of the Lower Rhine Basin).

The determination of the uplift rates in the tributaries caused a special difficulty: The height difference between the floor of the 0.8 Ma old terrace and the floor of the recent valleys can be determined directly along all the rivers that have their sources outside the Rhenish Massif such as Rhine, Mosel, Saar and Lahn (downstream of Giessen). In contrast the source areas of the smaller tributaries suffered uplift too. Thus comprehensive mapping of all terraces has to be corrected by reconstruction of the long river

profiles contemporaneous with the Younger Hauptterrasse. From this compilation δh data can be deduced. For detailed information see Meyer and Stets (1998).

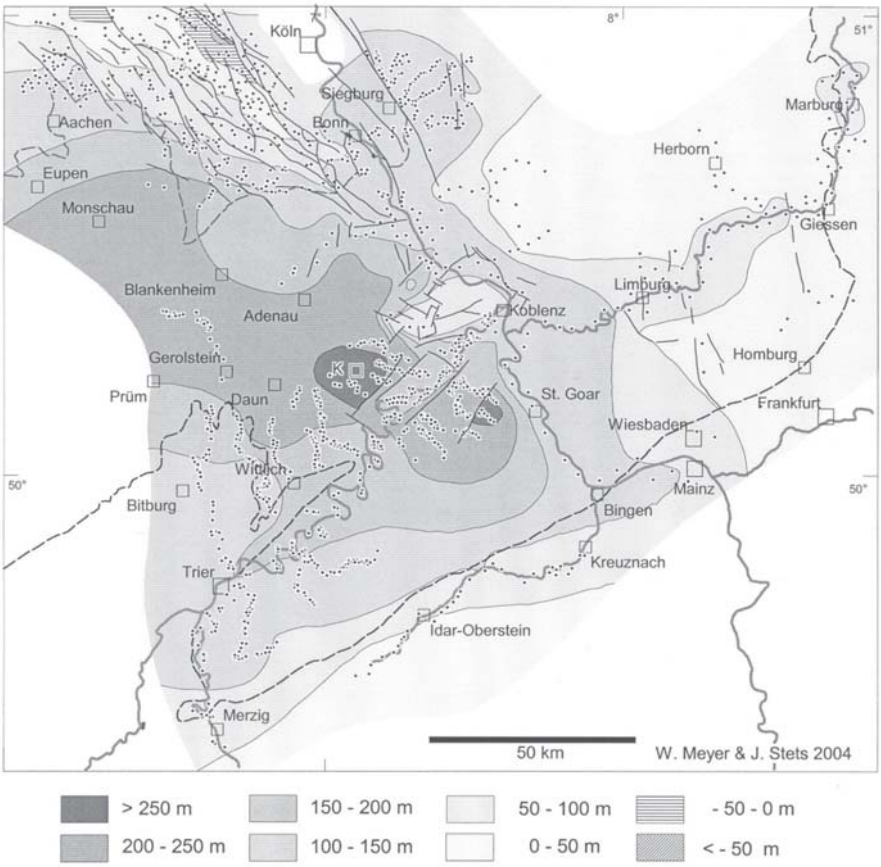

Fig. 3. Map showing the uplift of the Rhenish Massif during the last 0.8 Ma; contour lines illustrate 50 m in height difference of Younger Hauptterrasse level relative to the recent bottoms of the river systems. Observational data points are small dots, lines mark young faults, the outer boundary of the Massif is outlined by the dash line. Abbreviation: *K* Kaisersesch

3 Results

The map (Fig. 3) and the cross-sections (Fig. 4) show the amount of the young uplift during the last 0.8 Ma with contour lines of 50 m in height

difference between the floor of the Younger Hauptterrasse valley and the recent corresponding river floor. Observational data points are marked by dots. A first version was published by Meyer and Stets (2002), which is slightly modified in this paper.

In the eastern part of the Rhenish Massif the contour lines (Fig. 3) show uplift of about 50 to 100 m during the last 0.8 Ma, respectively uplift rates between 6 and 12 cm ka^{-1}. In contrast, west of the Rhine, there is a northwest–southeast extended area with uplift amounting more than 200 m. It covers the central and western part of the Eifel region and seems to continue into the eastern part of the Ardennes. There it cannot be resolved due to the absence of Younger Hauptterrasse data. In southeastern direction, this zone is elongated into the northeastern Hunsrück area, but is interrupted by the graben/depression of the Lower Mosel valley. In the centre of this zone of stronger uplift there is an area where uplift exceeds 250 m in the southeastern Eifel region and in a small area in the Hunsrück west of St. Goar. This anomaly contains a small zone with the maximum uplift, which reaches nearly 300 m, respectively uplift rates exceeding 35 cm ka^{-1}. This maximum uplift is situated west of Kaisersesch north of the Mosel valley, just between the Pleistocene West Eifel and East Eifel volcanic fields. It is the source area of the valleys of Uessbach, Elzbach, Endertbach and Pommerbach, for details see Gebhardt (1963) and Hoffmann (1996). Thus the influence on morphological processes is evident and well documented in this area.

The huge domal uplift is affected by normal faulting in the Neuwied Basin northwest of Koblenz, in the Lower Mosel area, and in the Lower Rhine Basin (Aachen, Köln, Siegburg). The Lower Rhine Basin shows fault-related subsidence. In the zones of maximum subsidence the reference niveau of the Younger Hauptterrasse has a position deeper than 50 m below sea level (Fig. 4, sect. I).

According to Zapp (2003), there exists another zone of strong uplift in the northeastern part of the Rhenish Massif (Sauerland area, outside the map in Fig. 3). Here the gradients are much smoother than in the Eifel anomaly, but the amount of uplift also exceeds 200 m.

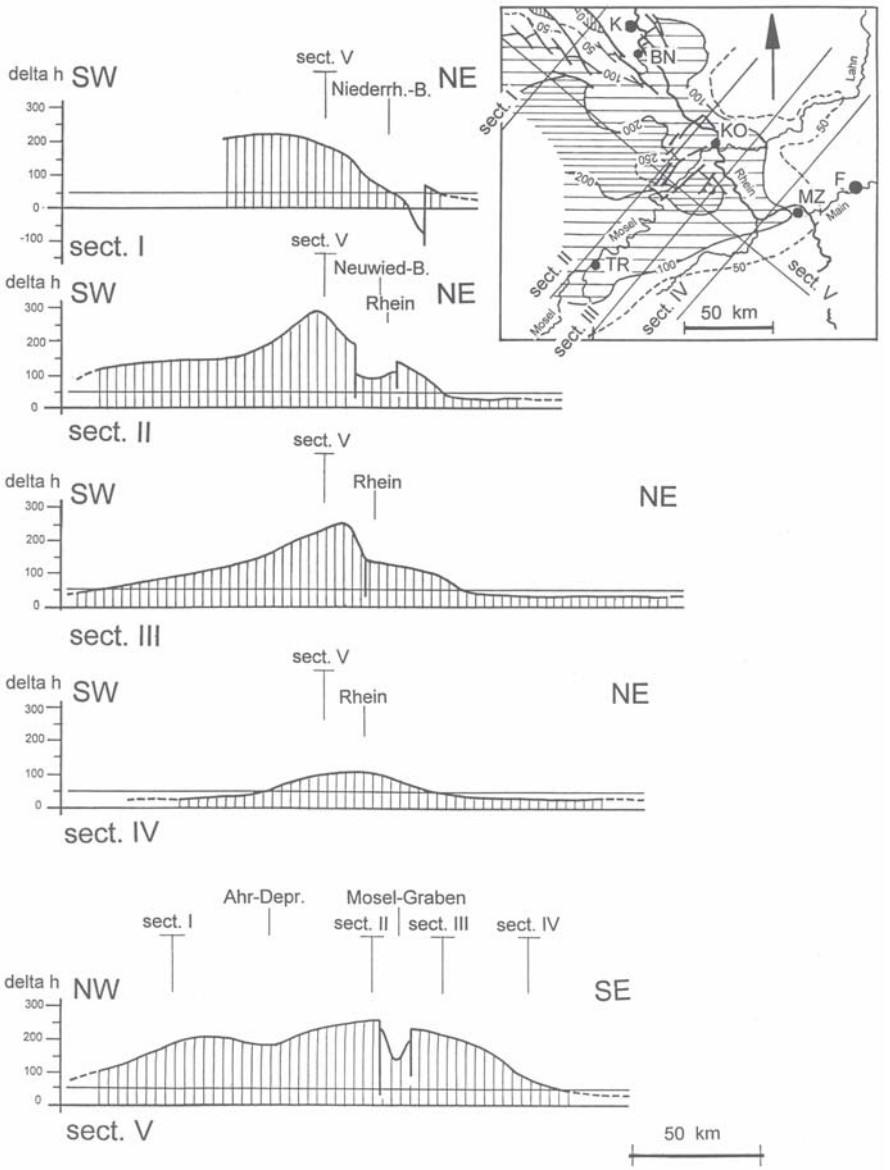

Fig. 4. Five sections crossing the Quaternary domal uplift in the Eifel and eastern Hunsrück region. Contour lines and δh represent uplift in meters. Abbreviations: *BN* Bonn, *F* Frankfurt/Main, *K* Köln (Cologne), *KO* Koblenz, *MZ* Mainz, *TR* Trier

4 Discussion

Concerning the processes, which caused the movements described above, one has to distinguish between the general uplift of the Rhenish Massif as a whole and the zones of distinct strong uplift. In general, the Rhenish Massif is part of a large region of uplift on both sides of the Rhine between Basel (Switzerland) in the south and Duisburg in the north; Cloos (1939) called it therefore "Rheinischer Schild" (Rhenish Shield). Its southern part contains the Upper Rhine Graben. In its northwestern continuation a fracture zone crosses the Rhenish Massif. The Neuwied Basin is part of this fracture system which opens into the Lower Rhine Basin. We don't discuss here the cause of this long-term crustal movements.

We are also not able to give a satisfying explanation for the mentioned zone of stronger uplift in the northeastern part of the Rhenish Massif (Sauerland) yet. This anomaly seems to be elongated parallel to the eastern margin of the Rhenish Massif, where it is accompanied by the graben-like Hessian depression. So, the stronger elevation may be a shoulder uplift at the margins of the Hessian graben system analogous to Schwarzwald and Vosges mountains on both flanks of the Upper Rhine Graben.

The area of strong uplift in the Eifel and Lower Mosel region in the centre of the Rhenish Massif needs another explanation. It is situated in the area where a deep-reaching temperature anomaly (the Eifel plume) was detected in the mantle (Ritter et al. 2001 and Ritter this volume). A connection to the young volcanism in this area is given by the published age relations: In the West Eifel volcanic field, according to radiometric age determinations, the first volcanoes seem to have ages of 970±100 ka (Beuel near Zilsdorf, K/Ar, Cantarel and Lippolt 1977), 620±110 ka (Dietzenley south of Gerolstein, K/Ar, Fuhrmann 1983) and 710±150 ka (Hohenfels east of Gerolstein, K/Ar, Fuhrmann 1983). In the East Eifel volcanic field, the oldest known age is 618±13 ka (phonolithic tephra layer in the Kärlich clay pit north of Koblenz, $^{40}Ar/^{39}Ar$, van den Bogaard et al. 1989). Thus, we consider the strong young uplift and the Quaternary volcanism as synchronous, and we connect the uplift anomaly in the western part of the Rhenish Massif with the heat anomaly beneath the region, i.e. the Eifel plume. The cause of domal uplift in the crust here may be induced by a volume increase in the mantle, due to the excess temperature of the plume.

Acknowledgements

We thank the Deutsche Forschungsgemeinschaft, Bonn, for financial support in the framework of "Sonderforschungsbereich 350", and M. Valdivia-Manchego, Bonn for assistance along with the preparation of our map.

References

Bibus E (1980) Zur Relief-, Boden- und Sedimententwicklung am unteren Mittelrhein. Frankfurter Geowiss Arb D1:1-296

Birkenhauer J (1971) Vergleichende Betrachtung der Hauptterrassen in der rheinischen Hochscholle. Kölner geogr Arb Festschrift K Kaiser:99-140

Bogaard vdC, Bogaard P, Schmincke HU (1989) Quartärgeologisch-tephrostratigraphische Neuaufnahme und Interpretation des Pleistozänprofils Kärlich. Eiszeitalter u Gegenwart 39:62-86

Cantarel P, Lippolt HJ (1977) Alter und Abfolge des Vulkanismus der Hocheifel. Neues Jahrb Geol Paläont Monatshefte 1977:600-612

Cloos H (1939) Hebung – Spaltung – Vulkanismus; Elemente einer geometrischen Analyse irdischer Großformen. Geolog Rundschau 30:401-527

Fromm K (1987) Paläomagnetische Bestimmungen zur Korrelierung altpleistozäner Terrassen am Mittelrhein. Mainzer geowiss Mitt 16:7-29

Fuhrmann U (1983) Kalium-Argon-Untersuchungen an neogenen Vulkaniten des Rheinischen Schildes. Diss Univ Heidelberg:158 + 22 pp

Gebhardt I (1963) Die Talbildung der Eifel im Ablauf der Klimate, des Vulkanismus und der periglazialen Bodenbildung im Quartär erläutert am Beispiel der Nette, der Kyll und an einigen kleineren Tälern. Decheniana 115:143-214

Hoffmann R (1996) Die quartäre Tektonik des südwestlichen Schiefergebirges begründet mit der Höhenlage der jüngeren Hauptterrasse der Mosel und ihrer Nebenflüsse. Bonner geowiss Schriften 19:1-156

Hoselmann C (1994) Stratigraphie des Hauptterrassenbereichs am unteren Mittelrhein. Sonderveröff Geol Inst Univ Köln 96:1-235

Kremer E (1954) Die Terrassenlandschaft der mittleren Mosel als Beitrag zur Quartärgeschichte. Arb Rhein Landeskunde 6:1-100

Lafrenz G (1933) Das Ahrtal und seine Terrassen. Beitr Landeskunde Rheinlande 2:1-76

Meyer W, Stets J (1998) Junge Tektonik im Rheinischen Schiefergebirge und ihre Quantifizierung. Z dt geol Ges 149:359-379

Meyer W, Stets J (2002) Pleistocene to recent tectonics in the Rhenish Massif (Germany). Geologie en Mijnbouw 81:217-221

Ploschenz C (1994) Quartäre Vertikaltektonik im südöstlichen Rheinischen Schiefergebirge begründet mit der Lage der Jüngeren Hauptterrasse. Bonner geowiss Schriften 12:1-185

Quitzow HW (1982) Die Hochflächenlandschaft der zentralen Eifel und der angrenzenden Teile des Rhein-Troges und Neuwieder Beckens. Mainzer geowiss Mitt 11:173-206

Richter D (1962) Die Hochflächen-Treppe der Nordeifel und ihre Beziehungen zum Tertiär und Quartär der Niederrheinischen Bucht. Geolog Rundschau 52:376-404

Ritter JRR, Jordan M, Christensen UR, Achauer U (2001) A mantle plume below the Eifel volcanic fields, Germany. Earth Planet Sci Lett 186:7-14

Schnütgen A (1974) Die Hauptterrassenfolge am linken Niederrhein aufgrund der Schotterpetrographie. Forsch-Ber Land Nordrhein-Westf 2399:1-150

Semmel A (1983) The Early Pleistocene terraces of the Upper Middle Rhine and its southern foreland – Questions concerning their tectonic interpretation. In: Fuchs K et al (eds): Plateau Uplift, Springer, Heidelberg, pp 49-54

Spell TL, McDougall I (1992) Revisions to the age of the Brunhes-Matuyama Boundary and the Pleistocene geomagnetic polarity timescale. Geophys Res Lett 19:1181-1184

Zapp R (2003) Analyse und Bilanzierung der quartären Tektonik des nordöstlichen Rheinischen Schiefergebirges unter Bezug auf die Raumlage der jüngeren Hauptterrasse. Bonner geowiss Schriften 30:1-207

Zöller L (1983) Geomorphologische und quartärmorphologische Untersuchungen im Hunsrück – Saar – Nahe – Raum. Forsch deutsch Landeskunde 225:1-240

The Seismic Signature of the Eifel Plume

Joachim R.R. Ritter

Geophysical Institute, University of Karlsruhe, Hertzstr. 16, 76187 Karlsruhe, Germany

Abstract

In 1997/98 the seismological Eifel Plume experiment was conducted in Belgium, France, Germany and Luxembourg to record a comprehensive dataset for several analysis techniques. Here we summarise the main points about the field experiment, the 3D tomography studies using compressional (*P*) and shear (*S*) waves and the analysis of the *P*-coda for scattering characteristics. Our seismic models are compared with results from surface wave dispersion studies, teleseismic shear-wave splitting and receiver functions. The models contain as a common feature a low-velocity anomaly in the upper mantle. This anomaly starts at about 50-60 km depth and reaches down to at least 410 km depth. The velocity reduction reaches up to 2% for compressional waves and 5% for shear waves in its upper part (50-100 km depth). In the lower part of the upper mantle the reduction is about 1% for both wave types. The diameter of this anomaly is about 100-120 km. As cause for the velocity reduction we infer increased ambient temperatures of about 100-150 °C. At 50-100 km depth there may be also about 1% of partial melt. We interprete this seismic anomaly as small upper-mantle plume that buoyantly upwells from the transition zone and starts to melt just below the continental lithosphere and possibly also at greater depth. At the surface the plume activity is documented by the Quaternary Eifel volcanic fields. Solidified magma chambers and dykes in the lithosphere are inferred to cause strong scattering of seismic waves as discovered by coda analyses.

1 Introduction

The Eifel region is located in the western part of the Rhenish Massif in the triangle between the cities of Trier, Koblenz and Aachen (Fig. 1). In the last 800 ka, a domal uplift of more than 250 m occurred in the region and two Quaternary volcanic fields evolved where the uplift was strongest (Meyer and Stets, 2002 and this volume). The Quaternary volcanic activity is documented by about 250 eruption centers in the West Eifel and 100 eruption centers in the East Eifel volcanic fields. Most eruptions built small tuff rings or the famous maars. Only in the East Eifel did voluminous crustal magma chambers evolve with associated strong explosive eruptions, e.g., at the Laacher See volcano about 12.9 ka BP. Altogether less than 20 km^3 of material was erupted, making the Eifel volcanic fields a smaller piece of the Central European volcanic belt. More details on the volcanology of the Eifel can be found in Schmincke (this volume). A review of the uplift and the Earth's structure and geodynamic processes of the region is given in Fuchs et al. (1983).

The recent intraplate volcanism in the Eifel region and its possible relationship to the Central European volcanic belt led Duncan et al. (1972) to the hypothesis that there is a hotspot track over an 'Eifel plume'. Although the concept of this hotspot track is no longer accepted, several seismic anomalies in the upper mantle underneath the Eifel may argue in favour of the existence of a mantle plume. Raikes and Bonjer (1983) revealed a low *P*-wave velocity (v_p) anomaly (~ -3%) at 50 km to 200 km depth beneath the Eifel region using teleseismic tomography with recordings from permanent stations supplemented by a regional temporary field experiment. In a European-wide v_p tomography model Spakman et al. (1993) also identified a low-velocity zone in the upper 200 km of the mantle, and Goes et al. (1999) proposed a deep magma source in the lower mantle based on a global v_p tomography model by Bijwaard et al. (1998). Studying surface waves, Passier and Snieder (1996) determined a low shear wave velocity (v_s) anomaly in the upper 200 km south of the Eifel which they interpreted as Eifel plume.

To obtain detailed seismological models of the crust and upper mantle beneath the Eifel region an European, interdisciplinary initiative was started in 1997. The scientific aim was to apply all available modern techniques, such as high-resolution velocity and attenuation tomography, receiver functions (Weber et al. this volume), shear-wave splitting analysis (Walker et al. this volume), surface-wave analysis (Mathar et al. this volume) and crustal studies, to image the crust and upper mantle. The Eifel plume team wanted to use compressional, shear and surface waves, to in-

vestigate traveltime and amplitude properties including seismic velocity, attenuation and scattering techniques. In order to measure the required high-quality dataset, ten institutions from Belgium, France, Germany, Luxembourg and the Netherlands shared their facilities during an eight months field experiment (Fig. 2). Additionally, seismic recordings from 84 permanent stations were included from these countries.

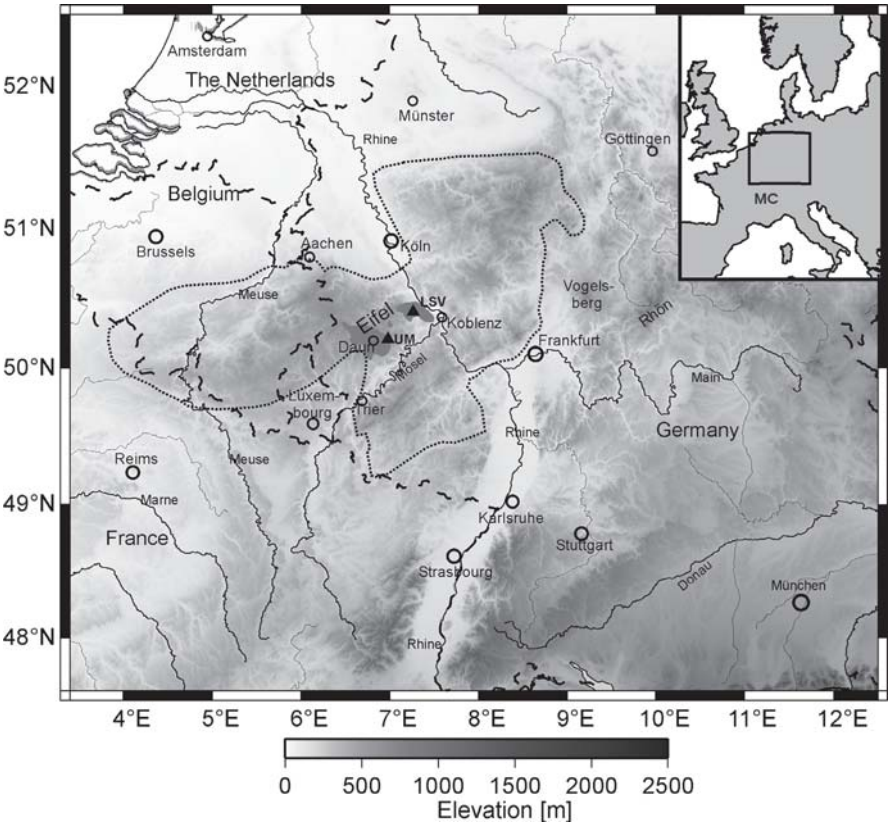

Fig. 1. Study region of the Eifel Plume Project. The Quaternary West and East Eifel volcanic fields are shown in dark gray. At the Ulmener Maar (*UM*) and the Laacher See volcano (*LSV*) the latest eruptions occurred at 11,700 and 12,900 years before present (Brauer et al. 1999). The dotted line gives the border of the Rhenish Massif. The inset shows the regional context within Europe and the location of the French Massif Central (*MC*)

2 Eifel Plume Experiment

The configuration of the Eifel Plume network (Fig. 2) was planned in consideration of the following conditions:

- Filling of gaps between the 84 permanent stations with 158 mobile stations, including 32 portable broadband instruments.
- High signal-to-noise ratio within a densely populated area.
- Availability of electricity and a time signal (mostly GPS).
- Safety of stations and accessibility during winter conditions.
- Dense-ray coverage in a tomographic inversion volume down to at least 400 km depth. This requires that the aperture of the network must be at least 400 km wide.
- Reasonable configuration of a broadband subarray to obtain a sufficient slowness and backazimuth resolution of seismic wavefronts with array processing.
- Dense station coverage in the inner Eifel region for crustal studies and high spatial resolution of lithospheric structures.
- A connection and overlap with previous mobile networks to obtain a dense station coverage across Central Europe.

The final network configuration comprised a 500 km by 500 km aperture (Fig. 2) including a broadband array in the form of a cross with its long axis aligned SW-NE aiming at the seismicity of South America and the NW Pacific. Seven permanent seismic networks (the national networks of Belgium, France, Germany and Luxembourg, the networks of the states of Baden-Württemberg and Nordrhein-Westfalen, as well as the network of the University of Köln) were incorporated into the project.

The mobile stations were deployed between 3 November 1997 and 23 June 1998 and recorded between 4 and 8 months. The recording equipment was provided by the GeoForschungsZentrum Potsdam (126 stations), the French Lithoscope Pool (17), the Royal Observatory of Belgium (2) and the University of Potsdam (13). Additionally 10 broadband Streckeisen STS-2 sensors were provided by the University of Utrecht.

To the present (2005) the following studies have been conducted using the Eifel data set:

- 3D teleseismic v_p tomography of the upper mantle using a linear inversion (Ritter et al. 2000) and a non-linear inversion (Ritter et al. 2001).
- 3D teleseismic v_p tomography of the upper mantle using a linear inversion, crustal traveltime corrections and data from previous tem-

porary networks in the Rhine Graben area and the Massif Central (Barth 2002).

- 3D teleseismic v_s tomography of the upper mantle using crustal traveltime corrections and a linear inversion (Keyser 2001) as well as a non-linear inversion (Keyser et al. 2002).
- Teleseismic shear-wave splitting (preliminary results in Budweg et al. 1999) and enhanced studies of the shear-wave splitting including a model for mantle flow (Walker 2003, Walker et al. 2005a, 2005b and this volume).
- Imaging of seismic discontinuities with receiver functions (Budweg 2003, Budweg et al. 2006, Weber et al. this volume).
- Attenuation of teleseismic *P*-waves including a 3D tomography (Meyer 2001).
- Dispersion of surface waves (Mathar 2005, Mathar et al. 2006 and this volume).
- Estimation of the random fine-scale structure of the lithosphere using *P*-coda analysis and scattering properties (Hock et al. 2004).
- Estimation of geodynamic plume properties (Ritter 2005, Wüllner et al. 2006).
- A core study using the Eifel network as large-scale array (Garcia et al. 2004).

This range of studies demonstrates that the Eifel plume is one of the best studied mantle anomalies on Earth. The combination of the different modelling techniques, using different properties of the recorded seismic waves, allowed the detailed imaging of the lithosphere-asthenosphere systems, even down into the mantle transition zone. The models further benefit from accompanying other geophysical and especially petrological studies (e.g. Witt-Eickschen this volume). The Eifel plume dataset is now available via the Internet through the Seismological Data Archive at the GeoForschungsZentrum Potsdam (www.gfz-potsdam.de).

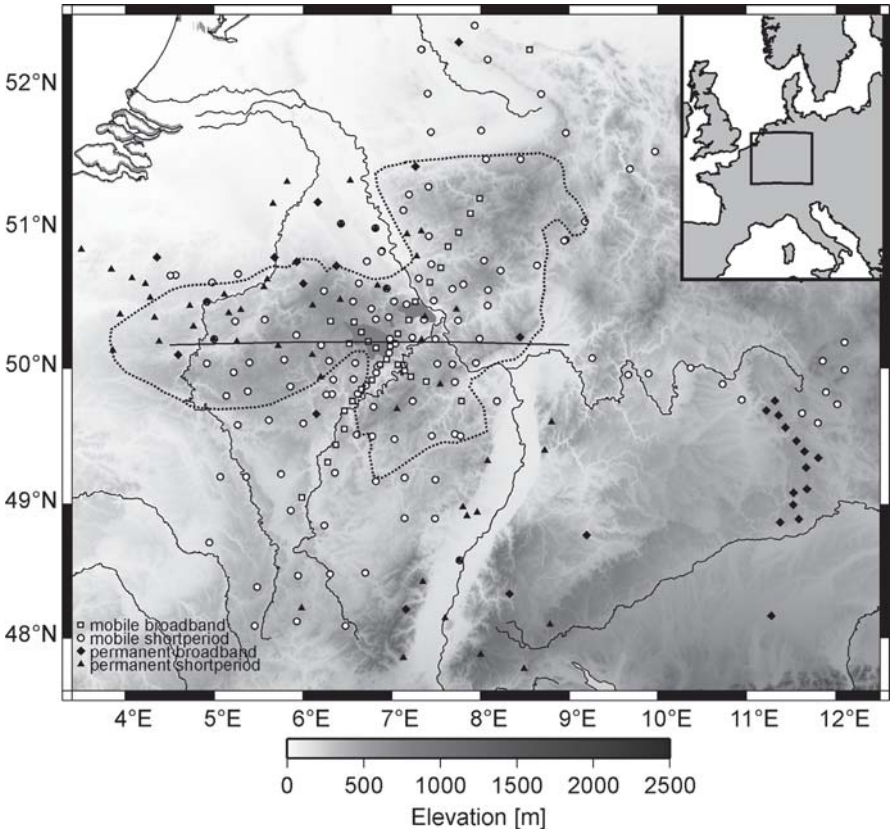

Fig. 2. Distribution of the mobile stations (open squares and dots) during the Eifel Plume experiment from November 1997 to June 1998 and the used permanent stations (black diamonds and triangles) in the region (for geographical orientation see also Fig. 1). The dashed east-west oriented line indicates the location of the tomographic cross-sections in Fig. 3-5

3 Mantle Tomography

To determine the 3D v_p structure of the upper mantle underneath the Eifel and surrounding regions, travel time residuals (r_{ij}) of teleseismic phases (j) were calculated for each recording station (i). As reference Earth model, iasp91 (Kennett and Engdahl 1991) was chosen:

$$r_{ij} = t_{ij,obs} - t_{ij,iasp91} \quad (1)$$

where $t_{ij,obs}$ is observed the travel time. To eliminate effects due to the source and source-side path, the average residual of each wavefront was subtracted to obtain relative travel residuals *rr*:

$$rr_{ij} = r_{ij} - \frac{1}{n}\sum_{i=1}^{n} r_{ij} \quad (2)$$

n is the number of observation per wavefront. Additionally a weighting factor was used to account for the quality of the individual data points (Evans and Achauer 1993). These relative weighted *P*-wave residuals range from -0.8 s to + 0.8 s and outline a region of delayed arrivals centered approximately on the southern West Eifel volcanic field. Within a radius of about 60-80 km, seismic waves that traverse the mantle below the western Eifel are delayed, while seismic waves that do not cross the upper mantle underneath the Eifel are relatively fast. Note that these delays are only relative with respect to the seismic network in Fig. 2.

We use the JI-3D program (Jordan 2003 and Barth et al. this volume) for the inversion of the residuals into velocity perturbations relative to the background model iasp91 (Kennett and Engdahl 1991). JI-3D uses a Bayes inversion algorithm, and it can incorporate a priori information such as crustal delay times. The model is parameterised into horizontal layers which are subdivided into blocks according to the ray distribution.

3.1 *P*-wave Model

For our *P*-wave model we use 7319 residuals and reach a variance reduction of 88.8%, for further details see Ritter et al. (2001). In Fig. 3 and Colour Plates 6-7 cross-sections through the 3D model of velocity perturbations (Δv_p) are shown. Fig. 3 is along the E-W profile in Fig. 2. There is a clear negative Δv_p anomaly centered below the West Eifel volcanic field. The anomaly reaches –2% v_p at 60-150 km depth. Above about 50 km depth the resolution of the model is low due to hardly crossing, steep ray paths. This ray geometry may cause smearing effects (Evans and Achauer 1993), and therefore, we do not interprete the Δv_p at depths shallower than 50 km. As resolution problems can also distort the bottom part of the model, we do not show the result of the deepest layer. Vertical smearing was also found in resolution tests, but it was demonstrated that deep-seated low-velocity structure can be reliably resolved with our dataset (Ritter at al. 2001) and that structures of about 80 km diameter can be recovered down to 400 km depth (Ritter 2005).

Colour Plate 6: *P*-wave velocity anomalies after Ritter et al. (2001). The centre of the co-ordinate system is at 7.33 °E and 49.75 °N. Only the well-resolved layers are displayed, checker-board resolution tests for these layers are given in Ritter (2005). The grid size for the inversion parameterisation (black rectangles) varies with ray density and azimuthal ray distribution. The inversion is based on relative travel-time residuals with a mean value of zero, therefore only velocity contrasts should be interpreted, not absolute *P*-wave velocity perturbations.

a) Depth range from 31-70 km: There is a clear negative *P*-wave velocity anomaly (Δv_p) below the West Eifel which is found in several blocks. In the NW and SW negative *P*-wave velocity anomalies appear within single blocks which are poorly resolved and may be due to crustal smearing.
b) Depth range from 70-120 km: There is clear negative Δv_p below the West Eifel which is found in several blocks. At the edges of the model negative *P*-wave velocity anomalies appear within single blocks which are poorly resolved and may be artefacts.
c) Depth range from 120-170 km: There is clear negative Δv_p below the West Eifel which is found in several blocks. Isolated negative Δv_p patches appear within single blocks which are poorly resolved and may be artefacts. In the south there is a broad region with positive Δv_p which presumably indicates a high-velocity region associated with the Alpine lithospheric root.
d) Depth range from 170-220 km: There is clear negative Δv_p below the Eifel which is found in several blocks. Another negative anomaly is found further east, below the Vogelsberg area. However, the model resolution there is low. In the south there is a broad region with positive Δv_p which presumably indicates a high-velocity region associated with the Alpine lithospheric root.

Colour Plate 7: *P*-wave velocity anomalies after Ritter et al. (2001), for details see caption of Colour Plate 6.

a) Depth range from 220-270 km: There is clear negative Δv_p below the Eifel and towards south (western Hunsrück) which is found in several blocks. Another negative anomaly is found further east, below the Vogelsberg area. However, the model resolution there is low. In the south there is a broad region with a positive anomaly which presumably indicates a high-velocity region associated with the Alpine lithospheric root.
b) Depth range from 270-340 km: There is clear negative Δv_p below the Eifel which is found in several blocks. Another negative anomaly is found further east, below the Vogelsberg area and below the Rhön. However, the resolution there is low, and the size of the anomalies may be overestimated due to the coarse parameterisation.
c) Depth range from 270-340 km: There is clear negative Δv_p below the Eifel and stretching to the west which is found in several blocks. The negative anomalies further east, below the Vogelsberg and Rhön area are poorly resolved and should be explored in more detail in the future.

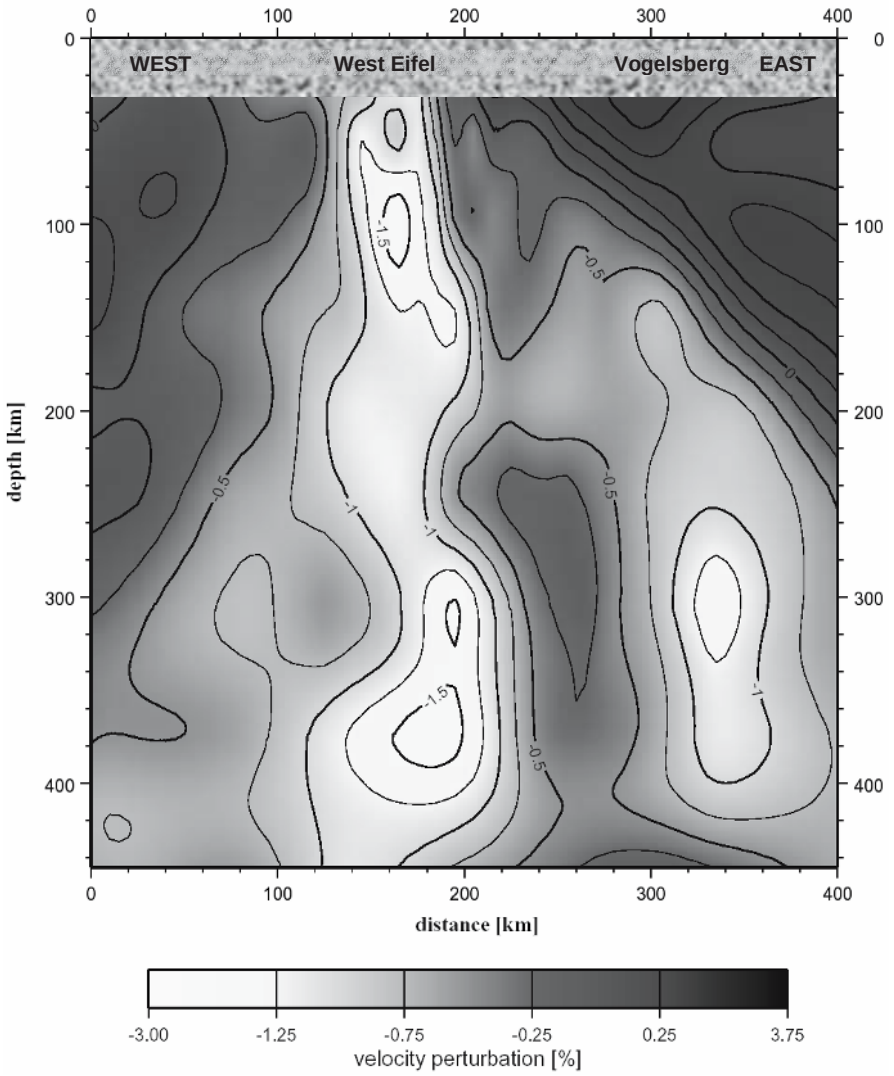

Fig. 3. East-west depth section through the compressional-wave tomography model, showing perturbations (Δv_p) relative to the iasp91 background model. The crustal part (0-35 km depth) is not interpreted due to low resolution. There is a clear, deep-seated low-velocity anomaly at 100-200 km along the profile which coincides with the western part of the Eifel region. To the east, at 300 to 400 km along the profile (Vogelsberg region), there is another anomaly below 200 km depth which is probably exaggerated in size due to the coarse parameterisation and weaker resolution in this part of the model. Horizontal slices are given in the Colour Plates 6 and 7

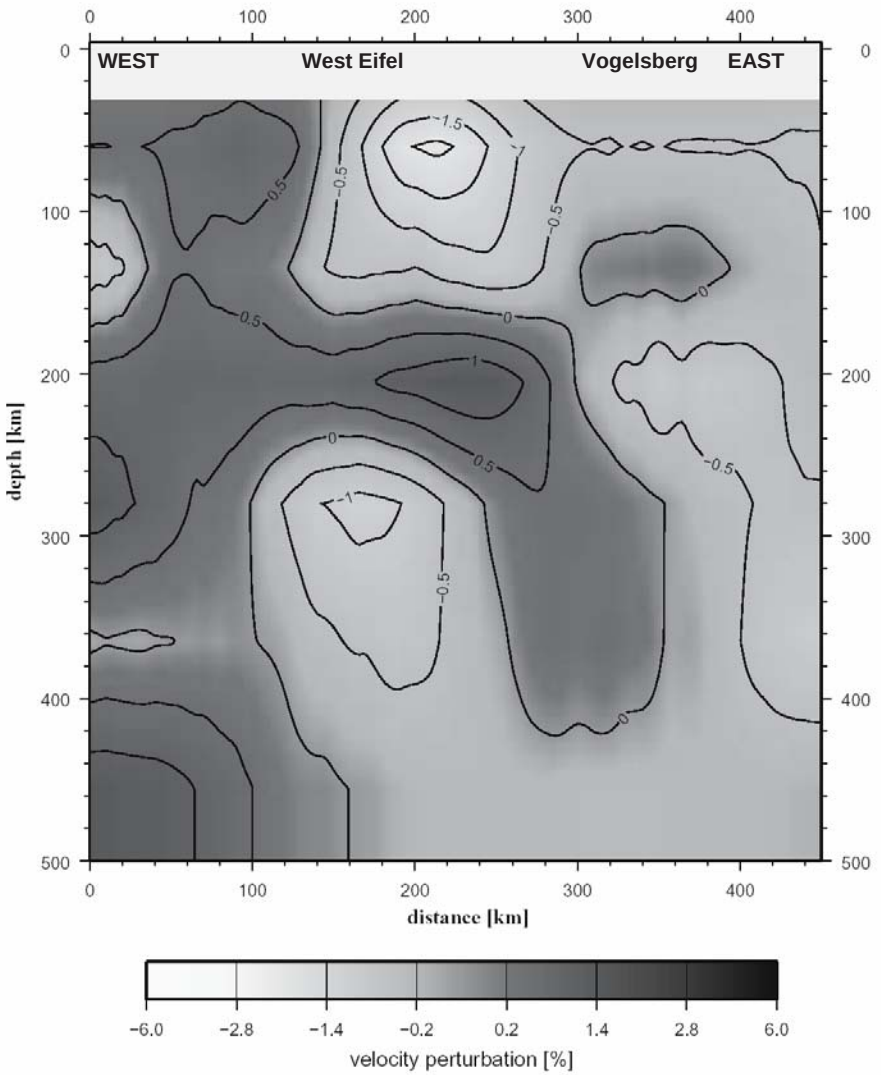

Fig. 4. East-west depth section through the shear-wave tomography model, showing perturbations (Δv_s) relative to the iasp91 background model. The crustal part (0-35 km depth) is not shown, because station corrections were used and smearing occurs. There is a low-velocity anomaly at 30-150 km depth and another deep-seated low-velocity anomaly at 250-400 km depth below the Eifel. At about 170-240 km depth there is no negative shear-velocity anomaly. To the east the shear-wave velocities are generally slower than to the west

3.2 *S*-wave Model

In the same way as the *P*-wave residuals we determined teleseismic *S*-wave residuals to achieve a 3D Δv_s model. We determined 2994 relative residuals on the radial (*R*) component and 2044 residuals on the transverse (*T*) component. Keyser (2001) and Keyser et al. (2002) demonstrate that first-order travel-time effects due to seismic anisotropy do not occur in the *S*-wave residual data. Therefore, a combined set of 3773 radial and transverse *S*-wave residuals were inverted using JI-3D to determine a 3D Δv_s model (Keyser et al. 2002). In Fig. 4 a cross-section through this Δv_s model is presented along the same profile as Fig. 3. There is a low Δv_s anomaly from the uppermost mantle down to at least 410 km depth. Again anomalies above about 40-50 km depth are not interpreted due to low resolution and smearing and the deepest layer is excluded in Fig. 4. Several resolution tests (Keyser et al. 2002) confirmed that the main anomalies in the upper mantle down to the transition zone are well resolved. At 40-100 km depth the biggest lateral velocity contrast occurs reaching up to –5% below the West and East Eifel volcanic fields. At about 170-240 km depth this low Δv_s anomaly disappears, and below 250 km depth it reappears with Δv_s about –1%. The "hole" in the anomaly at 170-240 km depth is not an artifact of the inversion as shown by the resolution tests (Keyser et al. 2002) and it will be explained below.

The shear-wave velocity anomaly in the upper mantle is consistent with other models (see above Introduction). A recent Rayleigh wave tomography study finds low v_s down to 410 km depth (Pilidou et al. 2005). However, their model does not contain a hole at 170-240 km depth, instead they find a slight increase in negative v_s perturbation.

3.3 Attenuation model

To image the seismic attenuation structure below the Eifel, Meyer (2001) determined δt^* operators which are proportional to variations of the quality factor *Q* and which are relative over the station network in a manner similar to the relative travel residuals above. *Q* describes the loss of energy (ΔE) per wave cycle:

$$Q \equiv \frac{2\pi E}{\Delta E} \tag{3}$$

Low *Q* values characterise increased attenuation. The operator t^* gives the integrated attenuation along a ray path *s* through a seismic velocity (*v*) structure and is defined as:

$$t^* = \int_s \frac{1}{Q v} ds \tag{4}.$$

t^* values are determined from spectral amplitudes $A_i(f)$, and we used the mean spectral amplitude $A_{ref}(f)$ of each analysed wavefront to calculate relative attenuation parameters (δt^*) across the network (for details see Meyer 2001):

$$\frac{A_i(f)}{A_{ref}(f)} = e^{-\pi f \, \delta t^*} \tag{5}.$$

The δt^* value can be determined from logarithmic spectra by a linear fit, assuming frequency-independent attenuation (more details on this method can be found in Evans and Zucca 1993). The δt^* values reveal a region of increased damping in the Eifel area, and a linear (one-step) inversion using JI-3D (Jordan 2003) was applied to calculated an image of the 3D attenuation structure. The ray path for the projection along the attenuation parameters were calculated in the 3D v_p model described above. In Fig. 5 we show a vertical slice through this model along a shorter line as in Fig. 3 and Fig. 4.

The most prominent anomaly occurs close to the East Eifel volcanic field, however, it is found in the poorly resolved crust by the inversion and therefore it is not shown in Fig. 5. In the upper mantle a high-attenuation anomaly is visible at 80-120 km depth below the West Eifel volcanic field, roughly at the same position as the low-velocity anomalies in the *P*- (Fig. 3 and Colour Plate 6) and *S*-wave (Fig. 4) models. At around 200 km depth the attenuation anomaly is vanishing (comparably with the location of the "hole" in the *S*-wave model). Below 250 km depth the anomaly of increased attenuation reoccurs but with a low amplitude. Because the resolution of the inversion is poor below 300 km depth (the deepest layer is not shown in Fig. 5), we cannot trace this anomaly down to the transition zone.

In the following the low-velocity, increased-attenuation anomaly below the Eifel is called "Eifel Plume", because several arguments will lead to an upwelling of upper mantle material.

4 Scattering of Teleseismic Waves

Small-scale heterogeneities (<20 km diameter in our case) are not recovered by seismic travel-time tomography but produce scattered arrivals in the coda of the main seismic phases. The waveforms measured during the Eifel Plume network were used to analyse the coda of the direct *P*-wave with the teleseismic fluctuation wavefield method (TFWM, Ritter et al.

1998) and the energy flux modelling technique (Korn 1993 and 1997). Hock et al. (2004) derived models with statistical parameters (size of the heterogeneities, velocity fluctuations and type of statistical distribution) to describe the average fine-scale heterogeneity pattern of the lithosphere below the network as a random medium.

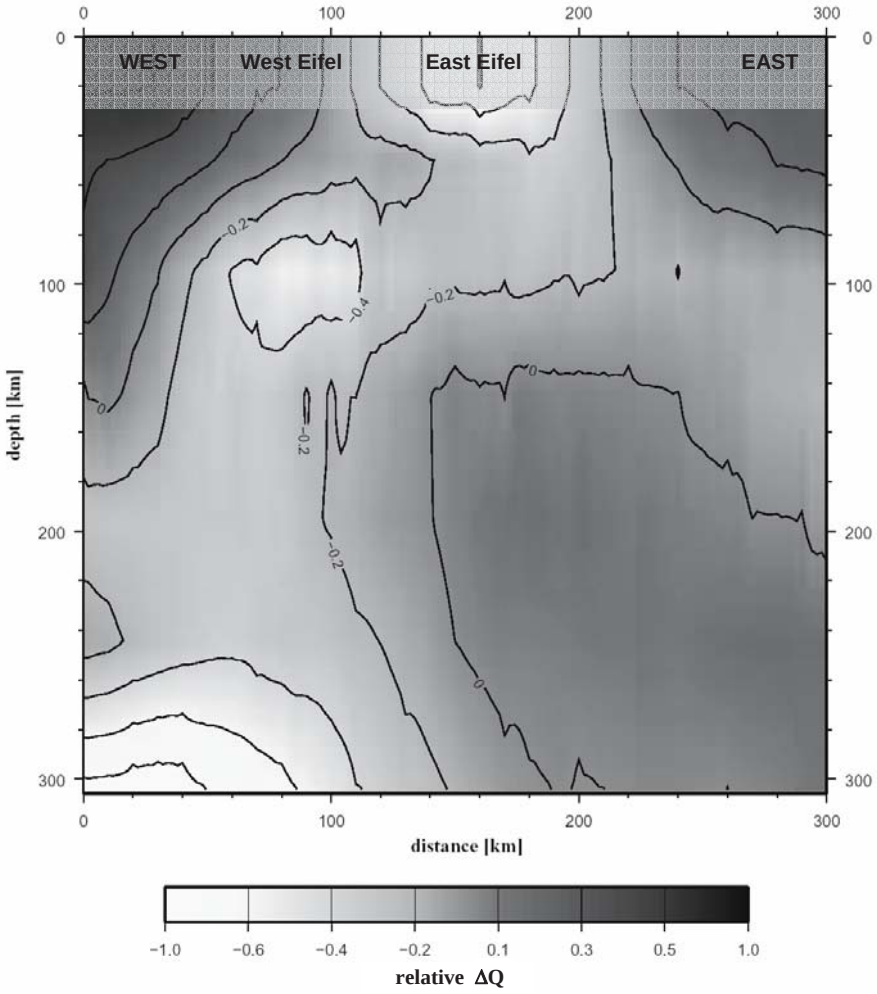

Fig. 5. East-west depth section through the attenuation tomography model. The modelled 3D attenuation variations are normalised to maximum (+1) and minimum (-1) relative attenuation. In the upper lithosphere the strongest attenuation is found underneath the East Eifel volcanic field at ~160 km distance. Deeper in the asthenosphere, attenuation is increased below the West Eifel (at ~60-100 km distance)

Compared to 10 other regions in Europe (e.g., Baltic Shield, North Germany, Frankonian Jura) the TFWM revealed that the most intense scattering occurs in the Eifel and Massif Central regions (Hock et al. 2004). The size of the heterogeneities is estimated to range between 1 km and 4 km, the velocity fluctuations reach 5-6 % and their distribution is Gaußian or exponential. As for the Massif Central (Ritter and Rothert 2000, Barth et al. this volume) we explain the strong seismic scattering underneath the Eifel volcanic fields by wavefield interaction with magmatic intrusions related to the mantle plume activity. For example, solidified gabbroic intrusions in a mafic granulite lower crust have a +4-5% velocity contrast relative to the host rocks. Thus cooled magma chambers with dense cumulates in the lower or upper crust are potential seismic heterogeneities below the West and East Eifel volcanic fields.

5 Geometry of the Eifel Plume

The tomography models in Figs. 2-5 and Colour Plate 6-7 outline a roughly 100 km wide low-velocity, high-attenuation structure in the upper mantle below the West Eifel. Due to smearing effects along the ray paths and also to uneven ray sampling (for examples few sources in the south) as well as the large wavelength of about 10 km for teleseismic *P*-waves and 40-60 km for teleseismic *S*-waves, there are uncertainties of 20-60 km in lateral resolution depending on the type of seismic wave. Vertical resolution is low in the upper 50 km depth of the *P*- and *S*-wave velocity models due to few crossing and subvertical rays. Below about 300 km depth the recovered anomalies are underestimated in perturbation amplitude, as shown by several resolution tests (Ritter et al. 2001, Keyser et al. 2002, Ritter 2005). Thus the geometrical size of the Eifel Plume should be determined by a combined interpretation of the tomography results with receiver function as and surface-wave inversion models, which better resolve the depth of seismic discontinuities.

The top of the Eifel Plume is seen as low-velocity anomaly (LVA) at about 50 km depth in v_s models derived with Rayleigh waves ($\Delta v_s \sim -2.5\%$) by Mathar et al. (this volume). At a similar depth of about 60 km, the top of a LVA is determined by Weber et al. (this volume) using teleseismic receiver functions. These two complementary models and our tomography results allow us to well constrain the depth of the top of the Eifel Plume at 50-60 km depth. This depth range is also in accordance with gravity modelling results for the Eifel region (Ritter et al. this volume).

In the traveltime tomography models (Figs. 3 and 4 and Colour Plate 7) the bottom of the Eifel plume seems reach into the mantle transition zone, because the LVA extends downwards at least to the 410 km discontinuity. Below 250 km depth the v_p and v_s perturbations are about -1%, however, the above cited resolution tests indicate an underestimation of the perturbation amplitude at this depth range. The depth-migrated receiver function model by Weber et al. (this volume) contains a 410 km discontinuity depressed about 20 km. A lowering of the 410 km phase boundary is expected for an anomalously hot mantle domain (Bina and Hellfrich 1994) such as a buoyant upper mantle plume (Shen et al. 1998). On the contrary, the 660 km discontinuity is at its expected depth below the Eifel (Weber et al. this volume), ruling out a thermal perturbation at the bottom of the transition zone. This receiver function model is consistent with the result by Grunewald et al. (2001) who also find a lowered 410 km discontinuity and an average 660 km discontinuity. The global finite-frequency *P*-wave tomography model by Montelli et al. (2004) also contains a LVA in the upper mantle below the Eifel region but none in the lower mantle. Therefore, we infer that the thermal upwelling of the Eifel plume either

- originates within the mantle transition zone, or
- rose from the lower mantle in the past but did not leave behind a thermal seismic signature that is still visible at 600-700 km depth, or
- rises or rose from the lower mantle offset from the Eifel region, and that the material flows or flew laterally in the transition zone, before penetrating across the 410 km discontinuity underneath the Eifel for its final ascent.

An origin in the transition zone is an option with regard to recent numerical geodynamic models (Davies 2005, Farnetani and Samule 2005). The second and the third assumptions may be in accordance with the global tomography model by Bijwaard et al. (1998) which contains a LVA in the lower mantle underneath Central Europe that is interpreted as lower mantle plume (Goes et al. 1999). However, the resolution of presently available global tomography models is still too coarse to get a clear answer about a possible lower mantle origin of the Eifel Plume.

6 Physical properties of the Eifel Plume in the upper mantle

6.1 Temperature and partial melt

Our modelled seismic velocity and damping perturbations (Fig. 3-5 and Colour Tables 6 and 7) can be interpreted physically in several ways. The lateral changes in seismic velocity may be due to variations in mineral composition, temperature, anisotropy, melt fraction or fluid content. Damping can be due to anelastic attenuation, which varies with changes in temperature or fluid content (Karato and Spetzler 1990), or scattering attenuation, which results from interactions of the seismic wavefield with structural heterogeneities of different sizes (Sato and Fehler 1998).

In the upper mantle velocity variations due to changes in anhydrous mineral composition are small (Sobolev et al. 1997, Cammarano et al. 2003), whereas temperature, partial melt and fluid-content changes produce significant velocity variations at ambient mantle conditions (Jackson and Ridgen 1998, Goes et al. 2004). The average mineral composition of the uppermost mantle underneath the Eifel can be assessed from numerous mantle xenoliths which are contained in the Quaternary volcanic rocks (see Witt-Eickschen this volume and references therein). Using published anharmonic temperature ($\partial v/\partial T$) and pressure ($\partial v/\partial p$) derivatives for upper mantle minerals and the anelastic correction terms from Karato (1993), we estimate what temperature anomalies would be required to produce the seismic perturbations in the tomography models. Calculations for composite mantle rocks are based on the Voigt-Reuss-Hill averaging algorithm, for further details see Ritter (2005).

As rock in the shallow mantle a spinel lherzolite is taken with a mineral composition of 75% olivine (Ol), 17% orthopyroxen (OPx), 7% clinopyroxene (CPx) and 1% spinel (Sp) (Witt-Eickschen pers. comm.). At ambient *p*-*T*-conditions in the uppermost mantle a 1% v_p or v_s reduction corresponds to about 90 K or 60 K increase in temperature, respectively. These values are nearly identical to the relationships given by Cammarano et al. (2003) or Goes et al. (2004). A linear extrapolation of these values implies in up to 150 K (for –1.5% to –2% Δv_p) and 300 K (for –5% Δv_s) excess temperature in the mantle anomaly at 60-100 km depth relative to the adjacent mantle. At high temperature these relationships are non-linear with increasing temperature sensitivity of v_s (Jackson et al. 2002). Thus smaller temperature variations may explain the Δv_s anomaly and the discrepancy between temperatures estimated from the perturbation amplitude of the *P*- and *S*-wave anomalies. A temperature increase of 100-150 K also can ex-

plain the ΔQ in the upper mantle by solid-state relaxation processes (Tan et al. 2001). These elevated temperatures inside the anomaly compared to the surrounding mantle are reasonable, because the solidus temperature of the mantle peridotites must have been exceeded in the recent past to account for the Quaternary magmatism.

Another likely option is the presence of partial melt in the uppermost mantle, because the Quaternary volcanism requires melting of mantle material. Small amounts of partial melt, distributed in penny-shaped melt inclusions in the rock fabric, reduce v_p and v_s by up to 1.8% and 3.3% per 1% melt (Faul et al. 1994). Thus the combined effect of about 1% partial melt plus 100 K excess temperature can explain the observed velocity contrasts, especially the discrepancy between the Δv_p and Δv_s anomalies in the upper mantle.

The temperature anomalies may be superimposed by compositional variations, such as changes in partitions of mineral phases, partial melt and fluids. In the shallow mantle, reasonable variations in Ol, OPx and CPx have little influence on the seismic velocities. However, Sp, garnet (Gt), amphibole (Amph) and phlogopit (Phl) may be important. Hydrous peridotite xenoliths with Amph and Phl are abundant in the Eifel region. Phl is characterised by quite slow seismic velocities (about 60% of olivine) and may contribute to the velocity reduction in the mantle (exact p and T derivatives of the elastic moduli for Phl are not available and prevent presently the calculation of ambient velocities).

To estimate the temperature anomaly in the lower asthenosphere (300-400 km depth) an anhydrous garnet peridotite is used (60% Ol, 25% CPx and 15% garnet (Gt)), as proposed for a global petrology model (Agee 1993). The anharmonic and anelastic temperature-velocity relations at ambient p-T-conditions predict 70 K increase in temperature for the modelled 1% v_p and 1% v_s reduction (Fig. 3 and 4). This small temperature anomaly may be quite underestimated, because of the underestimation of the velocity perturbation amplitudes as revealed by the resolution tests. The temperature anomaly related to the ~20 km lowering of the 410 km discontinuity revealed by the receiver function study (Weber et al. this volume) is about 150-200 K.

6.2 Fluids

Volatiles or fluids such as H_2O or CO_2 are present in the upper mantle (Thompson 1992) and may explain some physical and geodynamical aspects of mantle convection including plumes (Bercovici and Karato 2003). Volatiles and fluid phases have a significant influence on the elastic prop-

erties of mantle material, especially on the shear modulus which controls seismic velocities and attenuation. In the uppermost mantle water is bonded e.g. in mineral phases such as Phl. In the lower asthenosphere water may be bonded in minerals as hydrogen or hydroxyl (Kohlstedt et al. 1996). Increased water content in plume material can occur, if it rises from the transition zone as we infer for the Eifel plume. Although the minerals in the transition zone may not be completely saturated with water, at least some amount of water can be carried upwards by a mantle upwelling. E.g. Poreda et al. (1986) report that such 'primary' mantle water may occur in ocean-ridge basalts near the Iceland hotspot.

The solubility of hydrous components in upper mantle minerals such as (α-)Ol, OPx, CPx and Gt increases with pressure. Thus the physical influence of the hydrous components, namely reducing the elastic moduli and the solidus temperature, should increase with depth.

The properties of hydrous components may support a speculation concerning the 'hole' that is found at 200 km depth in the *S*-wave and attenuation models (Figure 5). Two scenarios are possible: First, the plume carries a small amount of water (< 1 wt%) out of the transition zone. The water concentration in the minerals decreases due to the pressure-dependent solubility of the hydrous components while the mantle material is rising. At around 200 km depth most of the water has left the minerals and forms a fluid phase. Thus the shear strength of the solid phases increases. Below, the excess temperature and the hydrous components in the solid phases cause the observed low-velocity and high-attenuation anomaly. Second, the solidus temperature of the rising mantle material is lowered by the hydrous components. At around 200 km depth fractional melting starts and preferentially removes water from the hydrous mantle rock (e.g. Hirth and Kohlstedt 1995) by moving melts. Ito et al. (1999) proposed a similar melting scenario of water-enriched rock as deep as 180 km for the Iceland hot spot. This implies that the location of the hydrous melting zone would be an important boundary region where the shear strength of the mantle material changes considerably (Karato and Jung 1998). Below, increased excess temperature and water produce the velocity reduction and the increased attenuation. Above, the influence of water diminishes and mainly the temperature conditions plus possible partial melt control the velocity and attenuation perturbations.

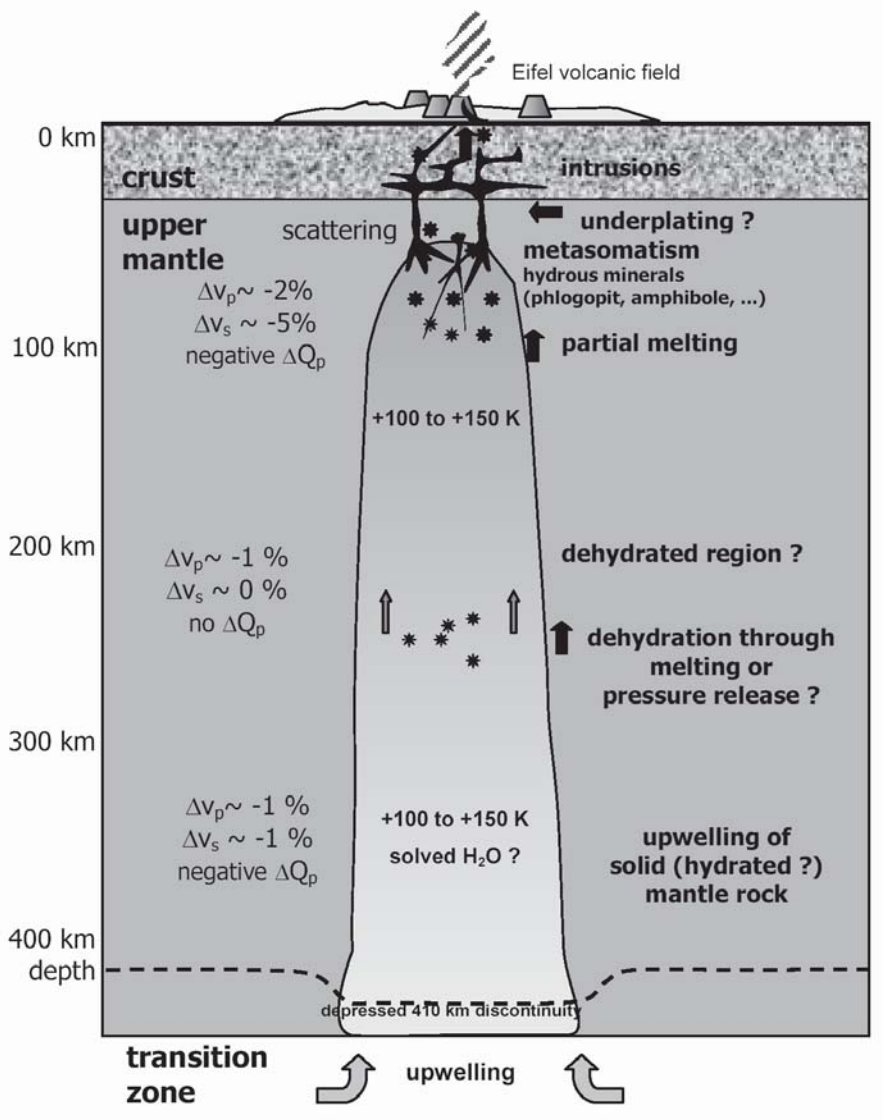

Fig. 6. Schematic model of the Eifel plume summarising the interpretations (right) of different seismological results (left) as described in the text

6.3 Integrated model

The tomography models and their interpretation together with the other cited results of the Eifel Plume project are summarised in Fig. 6. We pro-

pose that there is a small-scale upper mantle plume below the Quaternary Eifel volcanic fields at 50-60 km depth and reaching downwards at least to the 410 km mantle transition zone. The values on the left side in Fig. 6 indicate the seismological properties, on the right side the petrophysical interpretation is given. It is assumed that heated, buoyant material flows upwards across the upper boundary of the transition zone at 410 km depth. This upflow is 100-200 K hotter than the surrounding mantle, and it may bear volatiles in the form of water which are dissolved in the minerals. The combined effects of elevated temperature and hydrated minerals cause a decrease in seismic velocities and a reduction of the quality factor. At around 200 km depth the combined effect of excess heat, decompression and hydrous components may induce the onset of a first melting stage (< 1% partial melt). The melts preferentially extract the hydrous components from the solid phases and leave anhydrous minerals. This hydrous-anhydrous transformation causes a mechanical stiffening of the minerals, mainly an increase in the shear modulus. This stiffening in turn increases the shear-wave velocity and the quality factor. Thus the "hole" in the v_s anomaly (Fig. 4) and a high-velocity discontinuity at ~200 km depth (Weber et al. this volume) may be explained.

The further upwelling of the plume leads to a second melting zone in the shallow asthenosphere (above 100 km depth) due to more decompression of the hot material. The seismic models can be explained with a partial melt fraction of about 1% between 50-60 km and 90-100 km depth. We assume that this LVA is the small head of the Eifel plume. A lateral spread of this head is not found in our seismological models, even not in surface wave data (Mathar et al. this volume). Farnetani and Samuel (2005) show numerical geodynamic simulations that can explain upper mantle plumes without a spreading plume head. However, Walker et al. (this volume) identified a more broad-scale anomaly in the asthenosphere below the Rhenish Massif using *SKS*-splitting analyses.

The partial melt in the uppermost mantle further rises towards the crust-mantle boundary (Moho) where it possibly stops due to a loss of buoyancy. Such an underplating at the bottom of the crust is found under the Rhenish Massif in the seismic refraction model by Mechie et al. (1983). Furthermore, petrological data point to a high-pressure differentiation at this depth level (Schmincke this volume). From time to time, magma batches penetrate into the crust where they form magma chambers and reach the surface (Shaw 2004, Schmincke this volume). A portion of the magmas solidifies in the upper mantle and crust, forming dykes and sills. These intrusions and magmatic residues have a marked velocity and often density contrast relative to the surrounding rock material and thus they can act as scatterers.

The radius of the Eifel plume (50-60 km) and its excess temperature of 100-150 K can be used to estimated the related buoyancy flux using Poiseuille's equations (Sleep 1990, Ritter 2005) and mean upper mantle viscosity. Such a calculation gives a buoyancy flux of 0.05±0.04 Mg/s or a volume flux of 0.03-0.18 km^3/a which can be roughly balanced with the erupted volcanics (Ritter 2005).

7 Conclusions

The Eifel plume experiment provides a high-quality data set that is well-suited to study the upper mantle underneath the western Rhenish Massif and adjacent regions. The combined interpretation of different seismological models (tomography, receiver functions, surface-wave dispersion, SKS-splitting, attenuation) allows us to physically describe the state of the upper mantle underneath the Eifel volcanic fields. As a result we infer that there is a region of about 100 km diameter between 50-60 km and at least 410 km depth with elevated temperature (100-150 °C) that is buoyant and the main source for the Quaternary volcanism in the region.

Acknowledgements

A. Barth, M. Jordan, M. Keyser, J. Mathar, R. Meyer and M. Portmann helped with the data analysis and visualisation of results. J. Evans gave very valuable comments on an earlier version of the manuscript.

The fieldwork was done by the following people: U. Achauer, C. Auth, O. Barckhausen, A. Barth, G. Bissing, G. Bock, G. Bokelmann, S. Bourguignon, B. Bukasa, T. Camelbeeck, G. Celli, U. Christensen, F. Collin, J. Cruse, N. d`Oreye, H. Erlenhorst, I. Eschghi, C. Förster, A. Goertz, A. Häussermann, K.-G. Hinzen, J. Höhne, Y. Igel, K.-H. Jäckel, M. Jordan, T. Kaspar, D. Kossakowski, L. Kühne, C. Kutzner, F. Lange, F. Lorenz, M. Martin, J. Mathar, F. Müller, T. Münch, R. Pelzing, M. Pohl, M. Portmann, S. Rau, S. Reamer, J. Ritter, E. Rothert, H. Rudolf, H.-M. Rumpel, B. Schechinger, K. Schiffbauer, J. Schmalholz, J. Schütte, M. Snissaert, Y.-F. Temme, C. Thomas, D. Vollmer, J. Wassermann and F. Zetsche. Further support came from G. Asch, J. Bribach, S. Grunewald, W. Hanka, S. Hock, G. Jahnke, F. Krüger, M. Leven, M. Ohrnberger, F. Scherbaum, J. Schliebe, W. Steinhoff, R. Verbeiren, M. Weber and A. van Wettum.

Special thanks to the county administration of Daun/Vulkaneifel and the GeoZentrum Vulkaneifel (Dr. Eschghi and Mrs. Rudolf) for providing lo-

gistical help. Mr. J. Brauer (Manderscheid) and Mr. J. Mathar (Hillesheim) helped with the site surveys. Numerous officals and private individuals provided space for installing instruments.

The field equipment was supplied by the following institutions: Geophysical Instrument Pool at the GeoForschungsZentrum Potsdam, Germany; Institute for Geosciences, University of Potsdam, Germany; Lithoscope Pool, France; University of Utrecht, the Netherlands; University of Karlsruhe, Germany; Free University of Berlin, Germany; Royal Observatoire of Belgium. Data from permanent stations were supplied by: Bundesanstalt für Geowissenschaften und Rohstoffe (BRG) Hannover, Germany (GRSN & GRF); GeoForschungsZentrum Potsdam, (GEOFON); Geological Survey Nordrhein Westfalen; Geological Survey Baden-Württemberg; ORFEUS Data Center; Réseau National de Surveillance Sismique, France; Royal Observatory of Belgium (Belgian and Luxembourgish National Networks); Seismological Division KMNI, Netherlands; Seismological Station Bensberg, University of Cologne.

Funding was provided by the Deutsche Forschungsgemeinschaft (Ch77/9-1); European Center for Geodynamics and Seismology - Musee National d'Histoire Naturelle, Luxembourg; Ecole et Observatoire des Sciences de la Terre, Strasbourg, France; Royal Observatory of Belgium, Brussels, Belgium.

References

Agee CB (1993) Petrology of the mantle transition zone. Annu Rev Earth Planet Sci 21:19-41

Barth A (2002) *P*-Wellen-Tomographie des oberen Mantels und der Übergangszone unter Eifel und Zentralmassiv. Diplomarbeit, Institut für Geophysik, Universität Göttingen 96 pp

Bercovici D, Karato S-I (2003) Whole mantle convection and the transition-zone water filter. Nature 425 39-44

Bijwaard H, Spakman W, Engdahl ER (1998) Closing the gap between regional and global travel time tomography. J Geophys Res 103: 30055-30078

Bina CR, Helffrich G (1994) Phase transition Clapeyron slopes and transition zone seismic discontinuity topography. J Geophys Res 99:15853-15860

Brauer A, Endres C, Günter C, Litt T, Stebich M, Negendank FJW (1999) High resolution sediment and vegetation responses to Younger Dryas climate change in varved lake sediments from Meerfelder Maar, Germany. Quaternary Sci Rev 18:321-329

Budweg M (2003) Der obere Mantel in der Eifel-Region untersucht mit der Receiver Function Methode. Dissertationsschrift, Universität Potsdam, 117 pp, also as Scientific Technical Report STR03/04, GFZ Potsdam

Budweg M, Weber M, Bock G, Ritter J, Christensen U, Eifel Plume Team (1999) A 400 km long broadband antenna in the Eifel Region. ORFEUS electronic newsletter 1: 23 @ http://www.orfeus-eu.org/newsletter/vol1no3/eifel.html

Budweg M, Weber M, Bock G (2006) Receiver functions image the Eifel plume. Geophys J Int 166:579-589, doi:10.1111/j.1365-246X2005.02778.x

Cammarano F, Goes S, Vacher P, Giardini D (2003) Inferring upper-mantle temperatures from seismic velocities. Phys Earth Planet Inter 138:197-222

Davies JH (2005) Mantle convection – plumes rooted in mid-mantle. AGU Chapman Conference, The great plume debate: The origin and impact of LIPs and hot spots, abstract volume 24

Duncan RA, Petersen N, Hargraves RB (1972) Mantle plumes, movement of the European plate, and polar wandering. Nature 239:82-85

Evans JR, Achauer U (1993) Teleseismic velocity tomography using the ACH method: Theory and application to continental-scale studies. In: Iyer HM, Hirahara K (Eds.) Seismic tomography: Theory and practice, Chapman & Hall, London, pp 319-360

Evans JR, Zucca JJ (1993) Active source, high-resolution (NeHT) tomography: velocity and Q. In: Iyer HM, Hirahara K (Eds.) Seismic tomography: Theory and practice, Chapman & Hall, London, pp 695-732

Farnetani CG, Samuel H (2005) Beyond the thermal plume paradigm. Geophys Res Lett 32:L07311, doi:10.1029/2005GL022360

Faul UR, Toomey DR, Waff HS (1994) Intergranular basaltic melt is distributed in thin, elongated inclusions. Geophys Res Lett 21:29-32

Faul UH, Fitz Gerald JD, Jackson I (2004) Shear wave attenuation and dispersion in melt-bearing olivine polycrystals: 2. Microstructural interpretation and seismological implications. J Geophys Res 109:B06202, doi:10.1029/2003JB002407

Fuchs K, von Gehlen K, Mälzer H, Murawski H, Semmel A (eds) (1983) Plateau uplift, the Rhenish shield - a case history. Springer-Verlag, Berlin

Garcia R, Chevrot S, Weber M (2004) Non-linear waveform and delay time analysis of triplicated core phases. J Geophys Res 109:B01306, doi:10.1029/2003JB002429

Goes S, Spakman W, Bijwaard H (1999) A lower mantle source for Central European volcanism. Science 286:1928-1931

Goes S, Govers R, Vacher P (2000) Shallow mantle temperatures under Europe from *P* and *S* wave tomography. J Geophys Res 105:11153-11169

Goes S, Cammarano F, Hansen U (2004) Synthetic seismic signature of thermal plumes. Earth Planet Sci Lett 218:403-419.

Grunewald S, Kind R, Weber M (2001) The upper mantle under Central Europe - indications for the Eifel plume. Geophys J Int 147:590-601

Hirth G, Kohlstedt DL (1995) Experimental constrains on the dynamics of the partially molten upper mantle: Deformation in the diffusion creep regime. J Geophys Res 100:1981-2001

Hock S, Korn M, Ritter JRR, Rothert E (2004) Mapping random lithospheric heterogeneities in northern and central Europe. Geophys. J. Int. 157:251-264

Ito G, Shen Y, Hirth G, Wolfe CJ (1999) Mantle flow, melting, and dehydration of the Iceland mantle plume. Earth Planet Sci Lett 165:81-96

Jackson I, Ridgen S (1998) Composition and temperature of the Earth's mantle: Seismological models interpreted through experimental studies of Earth materials. In: Jackson I (ed) The Earth's Mantle, Cambridge University Press, Cambridge, pp 405-460

Jackson I, Fitz Gerald JD, Faul UR, Tan BH (2002) Grain-size sensitive seismic wave attenuation in polycrystalline olivine. J Geophys Res 107:2360 doi:10.1029/2001JB001225

Jordan M (2003) JI-3D a new approach to high resolution regional seismic tomography: theory and applications. PhD Thesis, Institute for Geophysics, University of Göttingen

Karato S-i (1993) Importance of anelasticity in the interpretation of seismic tomography. Geophys Res Lett 20:1623-1626

Karato S, Spetzler HA (1990) Defect microdynamics in minerals and solid-state mechanisms of seismic wave attenuation and velocity dispersion in the mantle. Rev Geophys 28:399-421

Karato S-i, Jung H (1998) Water, partial melting and the origin of the seismic low velocity and high attenuation zone in the upper mantle, Earth Planet Sci Lett 157:93-207

Kennett BLN, Engdahl ER (1991) Traveltimes for global earthquake location and phase identification. Geophys J Int 105:429-465

Keyser M (2001) Dreidimensionale Scherwellen-Geschwindigkeitsstruktur des Lithosphären/Astehosphären-Systems unter der Eifel. Diplomarbeit, Institut für Geophysik, Universität Göttingen, 105 pp

Keyser M, Ritter JRR, Jordan M (2002) 3D shear-wave velocity structure of the Eifel plume, Germany. Earth Planet Sci Lett 203:59-82

Kohlstedt DL, Keppler H, Rubie DC (1996) Solubility of water in the α, β and γ phases of $(Mg,Fe)_2SiO_4$. Contrib Mineral Petrol 123:345-357

Korn M (1993) Determination of site-dependent scattering *Q* from *P*-wave coda analysis with an energy-flux model. Geophys J Int 113:54-72

Korn M (1997) Modelling the teleseismic *P* coda envelope: depth dependent scattering and deterministic structure. Phys Earth Planet Inter 104:23-36

Mathar JP (2005) Oberflächentomographie in der Eifel-Region. Diplomarbeit, Geophysikalisches Institut, Universität Karlsruhe, 97 pp

Mathar JP, Ritter JRR, Friederich W (2006) Surface waves image the top of the Eifel Plume. Geophys J Int 164:377-382, doi: 10.1111/j.1365-246X.2006.02835.x

Mechie J, Prodehl C, Fuchs K (1983) The long-range seismic refraction experiment in the Rhenish Massif. In Fuchs K, von Gehlen K, Mälzer H, Murawski H, Semmel A (eds) Plateau uplift, the Rhenish shield - a case history. Springer-Verlag, Berlin, pp 260-275

Meyer R (2001) Teleseismische *P*-Wellendämpfung in der Eifel: Analyse und Tomographie. Diplomarbeit, Institut für Geophysik, Universität Göttingen, 87 pp

Meyer W, Stets J (2002) Pleistocene to recent tectonics in the Rhenish Massif (Germany). Netherlands J Geosc / Geologie en Mjinbouw 81:217-221

Montelli R, Nolet G, Dahlen FA, Masters G, Engdahl ER, Huang S-H (2004) Finite-frequency tomography reveals a variety of plumes in the mantle. Science 303:338-343

Passier ML, Snieder RK (1996) Correlation between shear wave upper mantle structure and tectonic surface expressions: Application to central and southern Germany. J Geophys Res 101:25293-25304

Pilidou S, Priestley K, Debayle E, Gudmundsson Ó (2005) Rayleigh wave tomography in the North Atlantic: high resolution images of the Iceland, Azores and Eifel mantle plumes. Lithos 79:453-474

Poreda R, Schilling JG, Craig H (1986) Helium and hydrogen isotopes in ocean-ridge basalts north and south of Iceland. Earth Planet Sci Lett 78:1-17

Raikes S, Bonjer K-P (1983) In: Fuchs K, von Gehlen K, Mälzer H, Murawski H, Semmel A (eds) Plateau uplift, the Rhenish shield - a case history. Springer-Verlag, Berlin, pp 315-331

Ritter JRR (2005) Small-scale mantle plumes: Imaging and geodynamic aspects. In: Wenzel F (ed) Perspectives in Modern Seismology, Lecture Notes in Earth Sciences, Springer-Verlag, Heidelberg, 105:69-94

Ritter JRR, Shapiro SA, Schechinger B (1998) Scattering parameters in the lithosphere below the Massif Central, France, from teleseismic *P*-wavefield records. Geophys J Int 134:187-198

Ritter JRR, Achauer U, Christensen UR, the Eifel Plume Team (2000) The teleseismic tomography experiment in the Eifel region, Central Europe: Design and first results. Seism Res Lett 71:437-443

Ritter JRR, Rothert E (2000) Variations of the lithospheric seismic scattering strength below the Massiv Central, France and the Frankonian Jura, SE Germany. Tectonophysics 328:297-305

Ritter JRR, Jordan M, Christensen UR, Achauer U (2001) A mantle plume below the Eifel volcanic fields, Germany. Earth Planet Sci Lett 186:7-14

Sato H, Fehler MC (1998) Seismic wave propagation and scattering in the heterogeneous Earth. Springer-Verlag, Heidelberg

Shaw CSJ (2004) The temporal evolution of three magmatic systems in the West Eifel volcanic field, Germany. J Volc Geotherm Res 131:213-240

Shen Y, Solomon SC, Bjarnason IT, Wolfe CJ (1998) Seismic evidence for a lower-mantle origin of the Iceland plume. Nature 395:62-65

Sleep NH (1990) Hotspots and mantle plumes: Some phenomenology. J Geophys Res 95:6715-6736

Sobolev SV, Zeyen H, Granet M, Achauer U, Bauer C, Werling F, Altherr R, Fuchs K (1997) Upper mantle temperatures and lithosphere-asthenosphere system beneath the French Massif Central constrained by seismic, gravity, petrologic and thermal observations. In: Fuchs K, Altherr R, Müller B, Prodehl C (eds) Stress and stress release in the lithosphere – structure and dynamic processes in the rifts of Western Europe, Tectonophysics 275:143-164

Spakman W, van der Lee S, van der Hilst R (1993) Travel-time tomography of the European-Mediterranean mantle down to 1400 km. Phys Earth Planet Inter 79:3-74

Tan BH, Jackson I, Fitz Gerald JD (2001) High-temperature viscoelasticity of fine-grained polycrystalline olivine. Phys Chem Min 28:641-664

Thompson AB (1992) Water in the Earth's upper mantle. Nature 358:295-302

Walker K (2003) Exploring problems in tectonics and geodynamics with seismology. PhD thesis, Stanford University, 273 pp.

Walker KT, Bokelmann GHR, Klemperer SL, Bock G (2005a) Shear-wave splitting around the Eifel hotspot: evidence for a mantle upwelling. Geophys J Int 163:962-980, doi:10.1111/j.1365-246X.2005.02636.x

Walker KT, Bokelmann GHR, Klemperer SL, Nyblade A (2005b) Shear wave splitting around hot spots: Evidence for up-welling related mantle flow? In Foulger GR, Natland JH, Presnall DC, Anderson DL (eds.) Plates, plumes, and paradigms, Geol Soc Am Spec Pap 388:171-192, doi:10.1130/2005.2388(11)

Wessel P, Smith WHF (1998) New, improved version of Generic Mapping Tools released. Eos Trans. American Geophys Union 79:579

Wüllner U, Christensen U, Jordan M (2006) Joint geodynamical and seismic modelling of the Eifel plume. Geophys J Int, 165:357-372, doi:10.1111/j.1365-246X.2006.02906.x

Zeyen H, Pous J (1993) 3-D joint inversion of magnetic and gravimetric data with a priori information. Geophys J Int 112:244-256

Upper Mantle Structure Beneath the Eifel from Receiver Functions

Michael Weber [1, 2], Günter Bock[†] and Martin Budweg[1,*]

[1]GeoForschungsZentrum Potsdam, Telegrafenberg, D-14473-Potsdam, Germany
[2]Universität Potsdam, D-14471-Potsdam, Germany

* Now at Texas Instruments Deutschland GmbH, Berlin, Germany
[†]Günter Bock died tragically in a plane crash on November 6th, 2002

Abstract

The average Moho depth in the Eifel is approximately 30 km, thinning to ca. 28 km under the Eifel volcanic fields. Receiver function (RF) images suggest the existence of a low velocity zone at about 60 to 90 km depth underneath the West Eifel. This observation is supported by *P*- and *S*-wave tomographic results and absorption (Ritter this volume). Indications for a zone of increased velocity near 200 km depth, again agree with *S*-wave and absorption tomographic results. This anomaly, surprisingly not visible in *P*-wave tomography, could be due to an area of *S*-wave anisotropy that compensates for elevated plume temperatures. All three RF anomalies – at the Moho, at 60 to 90 km and near 200 km depth – have a lateral extent of about 100 km. The aperture of the Eifel network limits the resolution of tomographic methods to the upper 400 km. The RF method does not suffer from this limitation and can resolve deeper structures. The 410 km discontinuity under the Eifel is depressed by 15 to 25 km. Lowering of the 410 km discontinuity could be explained by a maximum temperature increase of +200 to +300 °C. The second surprising feature in the 3-D RF image of the Eifel Plume is the occurrence of two additional, currently unexplained conversions between 410 and 550 km depth. They could represent remnants of previous subduction or anomalies due to delayed phase changes.

The lateral extent of the two additional conversions and the depression of the 410 km discontinuity is about 200 km. The 660 km discontinuity, in contrast to the 410 km discontinuity, does not show any depth deviation from its expected value, a scenario also encountered in the western US. Based on these observations we present the following scenario for the Eifel plume. The Eifel plume is a plume with temperature excess relative to the surrounding mantle of about +200 to +300 °C. The plume is imaged in the upper mantle and might be fed by regions imaged as low velocity anomalies in the lower mantle under Central Europe. Seismological methods provide only a blurred present day snap-shot. Thus we can not exclude the possibility that ascent of plume material, possibly coming even from the lower mantle, is intermittent and we see only the present day effects and configuration of the plume.

1 Data Acquisition and Processing

1.1 Initial data processing

From the nearly 200 recorded teleseismic events we chose the 96 earthquakes with magnitude $m_b > 5.2$ in the distance range from 30 to 95 degrees. A list of the 96 events is found in Budweg (2003). Since the data were recorded by different broadband and short-period seismic stations the recorded traces were first low-pass filtered with 8 Hz and resampled to 20 Hz. Then the traces were restituted to true ground motion (displacement) and band-pass filtered between 0.05 to 5 Hz.

We applied the Receiver function (RF) method, which uses three-component recordings to derive the Earth's structure. For overviews and applications that emphasise imaging plume structures, see e.g. Vinnik (1977), Langston (1979), Ammon (1997), Li et al. (2000, 2003, 2004), Ryberg and Weber (2000), Grunewald et al. (2001), Fee and Dueker (2004) and Yuan et al. (this volume). The basic idea of the RF method is to use *P* to *S* converted seismic waves from first-order discontinuities that arrive after the direct *P*-wave, most strongly on the horizontal components (Fig. 1). Rotation to ray co-ordinates *L*, *Q*, *T* and subsequent deconvolution of the *L* with the *Q* component gives the conversion operator, these are the RFs, for each source-receiver combination. The time traces are then migrated to map the 3-D subsurface under the Eifel network following an approach suggested by Yuan et al. (1997).

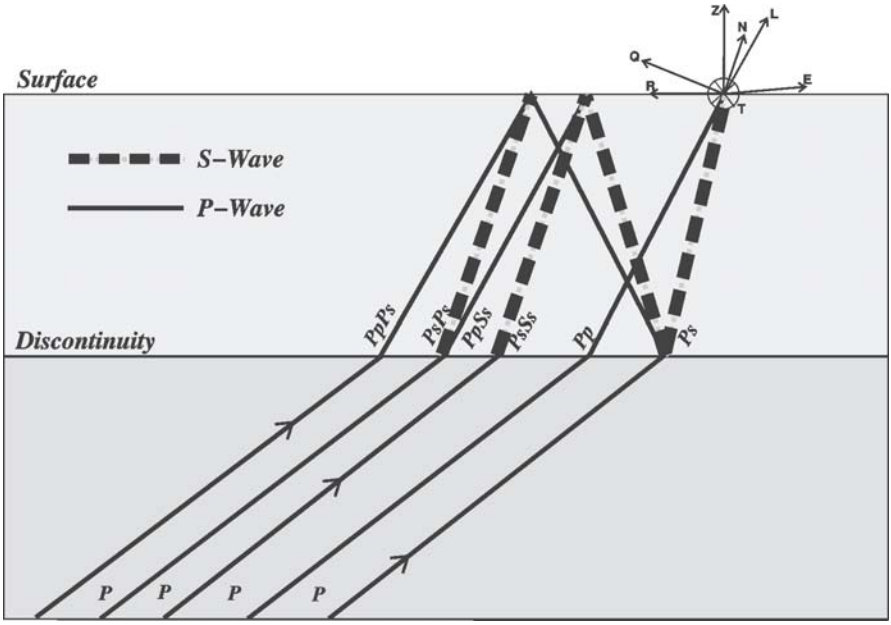

Fig. 1. Sketch showing the ray path geometry used. The direct *P*-wave, the converted *Ps*-wave and multiples, e.g. crustal multiples, if the discontinuity is the Moho, are observed at the seismometer. Rotation to ray co-ordinates *L*, *Q*, *T* divides the wave motion into *P*, *SV* and *SH* components, respectively

1.2 Comparison of tomographic and RF imaging results

Fig. 2 (Colour Plate 8) shows 1-D depth sections for a high velocity shear wave velocity lid, a low velocity zone and a high velocity zone tapering off with depth, respectively to illustrate the resulting RF images and to compare them with tomographic images. The high velocity lid (Fig. 2a) is imaged in tomography, under ideal conditions, as a solid blue depth range. The RF method, in contrast, shows the first order jump at the top of the lid (with increasing depth: slow to fast = red) and the bottom (fast to slow = blue) of the lid. A reversed, but otherwise unchanged image is obtained for the low velocity zone in Fig. 2b. For a high velocity lid with a gradual decrease of the velocity anomaly with depth, tomography images the tapering of the anomaly, whereas the RF method can only detect the first-order contrast at the top of the lid (Fig. 2c). This shows that the two seismic methods, tomography and RF, are complementary.

Figures 2-9 appear as Colour Plates 8-13

Fig. 2 (Colour Plate 8). Images produced by teleseismic tomography (*Tomo*) and Receiver functions (*RF*) for three types of velocity anomalies. **(a)** High velocity zone **(b)** Low velocity zone **(c)** Positive velocity jump with gradual decrease of velocity below. Red (blue) in the RFs indicates a positive (negative) velocity jump with increasing depth. The same colour code is used throughout the paper

Fig. 3 (Colour Plate 8). Horizontal slices at four depth ranges with their normalised average number of hits per 5 x 5 x 2 km^3 volume element (voxel). A value of 1 indicates the maximum of 928 hits. Areas with less than 20 hits are shown in grey. The centre of the temporary network and the Tertiary volcano Vogelsberg northeast of it are indicated by crosses. The East and West Eifel volcanic fields (solid lines) and political boundaries (dashed lines) are also indicated for orientation

Fig. 4 (Colour Plate 9). Sum over a 2 degree wide strip (N to S **(A)** and E to W **(B)**) of depth migrated RF, for location see small inserts. Bright colours indicate better coverage (see also Fig. 3). The labels *HVZ* (*LVZ*) indicate a high velocity zone (low velocity zone), respectively. The dashed lines give the centre of each anomaly. The thin black horizontal lines correspond to the depth of 35 km (Moho depth according to the iasp91-model), the 210, the 410 and the 660 km discontinuities. The triangle at the top indicates the location of the Eifel volcanic fields and the black triangles outline the Eifel volcanic area

Fig. 5 (Colour Plate 9). Moho depth as colour code and contour lines under the Eifel volcanic fields (solid lines) determined from migrated RF. Stars indicate seismic stations and dashed lines are the political borders

Fig. 6 (Colour Plate 10). Horizontal slices averaged over 10 km thickness from the volume of migrated RF for six depth ranges between 40 and 100 km depth. The volcanic fields of the Eifel are outlined (solid closed lines). The left cross is the centre of the Eifel network, the right cross shows the location of the Tertiary volcano Vogelsberg. A low velocity zone (LVZ) is observed between ca. 60 km depth (dark blue colours) and ca. 90 km depth (red colour; see also Fig. 2b). The bright red spots in the depth range between 90 to 100 km are first Moho multiples

Fig. 7 (Colour Plate 11). As Fig. 6 but for eight depth ranges between 150 and 230 km depth. The bright red colours from 160 to 210 km depth indicate a conversion at a high velocity contrast (see Fig. 2c)

Fig. 8 (Colour Plate 12). (Top) Topography of the 410 km discontinuity. South of the Eifel volcanic fields (solid lines and left cross) the 410 km discontinuity is depressed by about 15 to 25 km. **(Bottom)** Topography of the 660 km discontinuity. No deviation from the expected 660 km value is observed

Fig. 9 (Colour Plate 13). (Left) *P*-wave tomography results (Ritter et al. 2001). **(Centre)** *S*-wave tomography results (Keyser et al. 2000, 2002). Deviations in *P*- and *S*-wave velocity are in percent relative to IASP91. **(Right)** Migrated RF data (Fig. 4b) on an E-W slice through the Eifel plume. The triangle at the top indicates the location of the Eifel volcanic fields

1.3 Processing and resolution

The depth migration follows closely the technique developed by Grunewald et al. (2001), where the sub-surface is divided in 5 x 5 x 2 km^3 volume elements ("voxels") in which the different contributions from the migrated traces are binned. Fig. 3 (Colour Plate 8) shows the average number of the hits for four depth intervals to indicate areas where station and receiver combinations provide a good coverage and resolution. With increasing depth more rays intersect, and therefore the area of good coverage (blue and green colours with a maximum of 928 hits) increases. Areas with less then 20 hits per voxel are shown in grey and are muted in the following slices. The area of good resolution migrates north with increasing depth since most events occurred NE of the Eifel network.

2 Receiver Function Migration Results

2.1 Vertical slices through the 3-D migration volume

Fig. 4 (Colour Table 9) shows a north-south and an east-west slice through the migrated 3-D volume (sum over the 45 voxels in a 2 degree wide strip). The colour convention of Fig. 2 (Colour Table 8) was used. We used a sliding window of 30 km width with 2 km step size to enhance dominant features. Areas with reduced coverage are muted. Here we give a first interpretation of the major features followed by a more detailed interpretation and comparison with tomography results.

At about 30 km depth in Fig. 4, the red feature (positive velocity jump with increasing depth) can be associated with the Moho, that is elevated with respect to the iasp91-model value of 35 km (Kennett and Engdahl 1991), indicated by the thin black line. The succession of blue and red at ca. 60 and 90 km depth is interpreted as a low velocity zone, see also Fig. 2b. The red and blue features labelled 1. Mul and 2. Mul are the expected crustal multiples (*P*- and *S*-multiples shown in Fig. 1). At ca. 200 km depth the red anomaly (HVZ) in Fig. 4 (Colour Plate 9) can be associated with the top of a high velocity anomaly. The 410 km discontinuity is deflected

15 to 25 km downward, followed at larger depth by two red anomalies indicative of positive velocity jumps, labelled with a question mark. In the following several of these features are discussed in more detail.

2.2 Moho

Fig. 5 (Colour Plate 9) shows the Moho depth map derived from the 3-D volume of migrated data, see also Fig. 4. The map is centred on the Eifel, the area with the best resolution (Fig. 3, top left). A thinning of the Moho just south of the two Eifel volcanic fields to about 28 km depth can be seen. This observation agrees with previous wide-angle refraction seismic studies, that show a variation of the crustal thickness in the Rhenish Massif between 29 and 33 km (see e.g. Mechie et al. 1983). Due to the limited resolution of the RF method we cannot exclude that these variations could also be partially due to the variation in crustal velocity reported e.g. by the DEKORP Research Group (1991). The most straightforward interpretation for this crustal thinning is to link it to lateral displacement and stretching due to a plume. Note that the area east of 8 °E is not well resolved at this depth (see Fig. 3, top left).

2.3 Low velocity zone from 60 to 90 km depth

To ensure that the sequence of blue (at ca. 60 km depth) to red (at ca. 90 km depth) in Fig. 6 (Colour Table 10) are indeed the top and bottom of a low velocity zone (see Fig. 6b) and not crustal multiples, inversions at several stations for velocity structures down to 150 km were computed (for details see Budweg 2003). The inversions indicate that a low velocity zone is required to explain the blue to red sequence in Fig. 6. The low velocity zone is most strongly observed under the West Eifel and Quaternary volcanism. It coincides with the area of strongest uplift that reaches more than 250 m (Meyer and Stets 1998, this volume).

Beginning at a depth of about 100 km (Fig. 6, bottom right and even better visible in Fig. 4) strong crustal multiples (red) appear over a large area. The identification of these arrivals as the first crustal multiple (red, 1. Mul in Fig. 4) and second crustal multiple at ca. 150 km depth (blue, 2. Mul in Fig. 4) was confirmed by forward modelling (Budweg et al. 2006).

2.4 High velocity contrast at about 200 km depth

At about 200 km depth a strong (red) signal is visible in Fig. 7 (Colour Plate 11) and Fig. 4. The large amplitude of this converted phase rules out, that it is the third crustal multiple. Our preferred interpretation of this feature is a velocity structure similar to the one shown in Fig. 2c, i.e. a positive velocity contrast, tapering off with depth. Such an interpretation is supported by Keyser et al. (2002) in the *S*-wave tomography and will be discussed together with the *P*-wave tomography results of Ritter et al. (2000, 2001, this volume).

2.5 The 410 km discontinuity

The endothermic character of the 410 km phase transition depresses the phase boundary for a temperature increase. Such lowering of the 410 km discontinuity is visible in Fig. 4. Figure 8 (Colour Plate 12) provides an estimate of the lateral extent of the depression; the figure shows a map view of the effective conversion depths from 400 to 450 km averaged horizontally over 50 x 50 km^2 cells, similar to Grunewald et al. (2001). The 410 km discontinuity is depressed under and south of the Eifel by 15 to 25 km. A similar depression in this region, but with much reduced lateral resolution due to the larger station spacing, was reported in Grunewald et al. (2001). With the Eifel Plume project data the lateral extent of the 15 km depression can now be determined to be about 250 km centred slightly south of the Eifel. Within this area two regions of about 100 km diameter, one under Luxembourg and one south-east of it, seem to be depressed by up to 25 km.

The depth values given are almost independent from the velocity anomalies above the 410 km discontinuity, since *P*- and *S*-waves are both affected simultaneously, resulting in a potential bias in the conversion depth of less then 2 km. The same argument also holds for the 660 km discontinuity.

2.6 The 660 km discontinuity

The effective conversion depth of the 660 km discontinuity, averaged horizontally over 50 x 50 km^2 cells, is given in map view in Fig. 8 (bottom). Over the whole well resolved area, see Fig. 3 (bottom right), the 660 km discontinuity appears unperturbed in Fig. 8 (bottom).

3 Discussion and Conclusions

Analysis of Eifel Plume data with the RF method confirms the model that a mantle plume feeds the Eifel volcanism. Both, *P*- and *S*-velocity tomography models in Fig. 9 (Colour Plate 13), show an extension of reduced seismic velocities down to about 400 km depth, interpreted as the effect due to the Eifel plume.

The most convincing evidence supporting the assumption of a plume under the Eifel are:

(1) Thinning of the crust under the Eifel by at least 2 km (slightly south of the volcanic fields, diameter ca. 100 km, Fig. 5).
(2) Detection of a low *S*-velocity zone between roughly 60 to 90 km depth under the West Eifel (diameter ca. 100 km, Fig. 6).
(3) A region of about 100 km thickness (100 to 200 km depth) with reduced *S*-velocities (roughly under the Eifel, diameter about 100 km, Fig 9; Keyser 2000, 2002; Ritter this volume).
(4) Occurrence of an area with slightly elevated *S*-velocities at about 200 km depth (under the West Eifel, diameter ca. 150 km, Fig. 7). This unusual feature could be due to *S*-wave anisotropy (see also Walker et al. 2005a,b, this volume) which compensates for elevated temperatures.
(5) From 250 km to about 400 km depth, *P*- and *S*-wave tomography both show a plume-like structure (under the Eifel, diameter about 150 km, Fig. 9).
(6) The 410 km discontinuity is depressed by 15 to 25 km (south of the Eifel, diameter of about 200 km, Fig. 8, top) due to increased temperatures of +200 to +300 °C relative to the surrounding upper mantle (Bina and Helffrich 1994).
(7) Below the depressed 410 km discontinuity two additional positive *S*-velocity jumps can be identified in the depth range between 450 and 500 km (roughly under the Eifel, diameter ca. 200 km; Fig. 4 and Fig. 9 right). This could possibly be the (present day) source of the plume, but the lack of tomographic images and mineralogical/petrological data precludes further speculation at the moment.
(8) The 660 km discontinuity seems unaffected by the plume (Fig. 8, bottom).

The most likely scenario for the Eifel plume is therefore a plume with temperature increase of about +200 to +300 °C. To decide, whether the Eifel Plume, now residing in the upper mantle, was originally connected to a larger plume in the lower mantle (see e.g. Goes et al. 1999, 2000) and was sheared from its deep root, e.g., by closing of the Tethys ocean, re-

quires the inversion of larger tomographic data sets combining data from several field experiments like Eifel, Massif Central (Sobolev et al. 1997, Barth et al. this volume), TOR (Hossein Shomali et al. 2002, Wilde-Piorko et al. 2002, Alinaghi et al. 2003) and SVEKALAPKO (Bruneton et al. 2002, Alinaghi et al. 2003, Sandoval et al. 2004).

References

Alinaghi A, Bock G, Kind R, Hanka W, Wylegalla K, TOR & SVEKALAPKO Groups (2003) Receiver function analysis of the crust and upper mantle from the North German Basin to the Archean Baltic Shield. Geophys J Int 155:641–652

Ammon CJ (1997) An overview of Receiver Function Analysis. http//www.eas.slu.edu/People/CJAmmon/HTML/RftnDocs/rftn01.html, Saint Louis University, St. Louis, MO

Bina C, Helffrich G (1994) Phase transitions, Clapeyron slopes and transition zone seismic discontinuity topography. J Geophys Res 99:15,858-15,860

Bruneton M, Farra V, Pedersen HA, the SVEKALAPKO Seismic Tomography Working Group (2002) Non-linear surface wave phase velocity inversion based on ray theory. Geophys J Int 151:583-596

Budweg M (2003) The upper mantle in the Eifel region studied with the Receiver Function method. Scientific Technical Report GFZ, STR03/04, 117 pp

Budweg M, Bock G, Weber M (2006) The Eifel plume – imaged with converted seismic waves. Geophys J Int 166:579-589, doi:10.1111/j.1365-246X2005.02778.x

DEKORP Research Group (1991) Results from the DEKORP 1 (BELCORP-DEKORP) deep seismic reflection studies in the western part of the Rhenish Massif. Geophys J Int 106:203-227

Fee D, Dueker K (2004) Mantle transition zone topography and structure beneath the Yellowstone hotspot. Geophys Res Lett 31:doi:10.1029/2004GL02063

Goes S, Spakman W, Bijwaard H (1999) A lower mantle source for Central European volcanism. Science 286:1928-1931

Goes S, Govers R, Vacher P (2000) Shallow mantle temperatures under Europe from *P* and *S* wave tomography. J Geophys Res 105:11.153-11.169

Grunewald S, Kind R, Weber M (2001) The upper mantle under Central Europe - Indications for the Eifel plume. Geophys J Int 147:590-601

Hossein Shomali Z, Roberts R, TOR Working Group (2002) Non-linear body wave teleseismic tomography along the TOR array. Geophys J Int 148:562–574

Kennett BLN, Engdahl E (1991) Travel times for global earthquake location and phase identification. Geophys J Int 105:429-465

Keyser M, Meyer R, Ritter JRR (2000) Teleseismic *S*-wave and Q_p recordings at the Eifel plume project. In Bonatz, M. (ed) Comptes-Rendus Journées Luxembourgeoises de Géodynamique 87:72-77

Keyser M, Ritter JRR, Jordan M (2002) 3-D shear wave velocity structure of the Eifel plume, Germany. Earth Planet Sci Lett 203:58-82

Langston CA (1979) Structure under Mount Rainer, Washington, inferred from teleseismic body waves. J Geophys Res 84:4749-4762

Li X, Kind R, Priestley K, Sobolev SV, Tillman F, Yuan X, Weber M (2000) Mapping the Hawaiian plume conduit with converted seismic waves. Nature, 405:938-941

Li X, Kind R, Yuan X, Sobolev SV, Hanka W, Ramesh DS, Gu Y, Dziewonski AM (2003) Seismic observation of narrow plumes in the oceanic upper mantle. Geophy Res Lett 30:10.1029/2002GL015411

Li X, Kind R, Yuan X, Wölbern I, Hanka W (2004) Rejuvenation of the lithosphere by the Hawaiian plume. Nature 427:827-829

Mechie J, Prodehl C, Fuchs K (1983) The long-range seismic refraction experiment in the Rhenish Massif. In Fuchs K, von Gehlen K, Mälzer H, Murawski H, Semmel A (eds) Plateau uplift, the Rhenish shield - a case history. Springer-Verlag, Berlin, pp 260-275

Meyer W, Stets J (1998) Junge Tektonik im Rheinischen Schiefergebirge und ihre Quantifizierung. Z dt geol Ges 149:359-379

Ritter JRR, Achauer U, Christensen UR, the Eifel Plume Team (2000) The teleseismic tomography experiment in the Eifel region, Central Europe: Design and first results. Seism Res Lett 71:437-443

Ritter JRR, Jordan M, Christensen UR, Achauer U (2001) A mantle plume below the Eifel volcanic fields, Germany. Earth Planet Sci Lett 186:7-14

Ryberg T, Weber M (2000) Receiver function arrays, a reflection seismic approach. Geophys J Int 141:1-11

Sandoval S, Kissling E, Ansorge J, SVEKALAPKO Seismic Tomography Working Group (2004) High-resolution body wave tomography beneath the SVEKALAPKO array – II. Anomalous upper mantle structure beneath the central Baltic Shield. Geophys J Int 157:200–214, doi: 10.1111/j1365-246X.2004.02131.x

Sobolev S, Zeyen H, Granet M, Achauer U, Bauer C, Werling F, Altherr R, Fuchs K (1997) Upper mantle temperatures and lithosphere-asthenosphere system beneath the French Massif Central constrained by seismic, gravity, petrologic and thermal observations. Tectonophysics 275:143-164

Vinnik LP (1977) Detection of waves converted from *P* to *SV* in the mantle. Phys Earth Planet Inter 15:39-45

Walker KT, Bokelmann GHR, Klemperer SL, Nyblade A (2005a) Shear wave splitting around hot spots: Evidence for up-welling related mantle flow? In Foulger GR, Natland JH, Presnall DC, Anderson DL (eds.) Plates, plumes, and paradigms, Geol Soc Am Spec Pap 388:171-192, doi:10.1130/2005.2388(11)

Walker KT, Bokelmann GHR, Klemperer SL, Bock G (2005b) Shear-wave splitting around the Eifel hotspot: evidence for a mantle upwelling. Geophys J Int 163:962-980, doi:10.1111/j.1365-246X.2005.02636.x

Wilde-Piorko M, Grad M, TOR Working Group (2002) Crustal structure variation from the Precambrian to Paleozoic platforms in Europe imaged by the inversion of teleseismic receiver functions-project TOR. Geophys J Int 150:261-270

Yuan X, Kind R, Mechie J, Sandvol E (1997) Lithospheric and upper mantle structure of southern Tibet from seismological passive source experiments. J Geophys Res 102:27,491-27,500

Rayleigh Wave Dispersion in the Eifel Region

Jan P. Mathar[1], Wolfgang Friederich[2] and Joachim R.R. Ritter[1]

[1]Geophysical Institute, University of Karlsruhe, Hertzstr. 16, 76187 Karlsruhe, Germany
[2]Institute for Geology, Mineralogy and Geophysics, Ruhr-University Bochum, Universitätsstr. 150, 44801 Bochum, Germany

Abstract

We obtain Rayleigh wave dispersion curves and 1D models of the shear wave velocity v_s underneath the Eifel region, Germany from teleseismic recordings. Using 31 broadband mobile stations and 10 permanent stations distributed across a nearly 400 km × 400 km wide area centred on the Eifel, an average regional model is obtained which shows a clear low v_s anomaly (LVA) at 70 to 200 km depth with a maximum velocity reduction of 2.3 % at 135 km depth. To enhance the resolution below the volcanic Eifel region we calculated a local v_s model based on a reduced data set with stations only from that area. This local model contains a more pronounced LVA starting at 45-50 km depth with a minimum v_s at around 85 km depth (-2.5 % v_s). The upper boundary of this local LVA is interpreted as the uppermost portion of the Eifel plume, and its location is in accordance with receiver function results (see Weber et al., this volume).

1 Introduction

Several seismological projects provide evidence for a low shear wave velocity (v_s) anomaly beneath the Eifel (Fig. 1). Passier and Snieder (1996) derived a 3D v_s model for southern and central Germany from the inver-

sion of fundamental mode Rayleigh waveforms. Their model contains a low velocity zone below the western Rhenish Massif reaching from about 50 km depth down to at least 200 km depth with velocities varying from 4.0 to 4.3 km/s approximately (Fig. 2). Their maximum of the relative velocity perturbation varies between -4 % and -7 %. The anomaly is centred south-east of the actual Eifel region below the Saarland and is terminated to the east by the river Rhine.

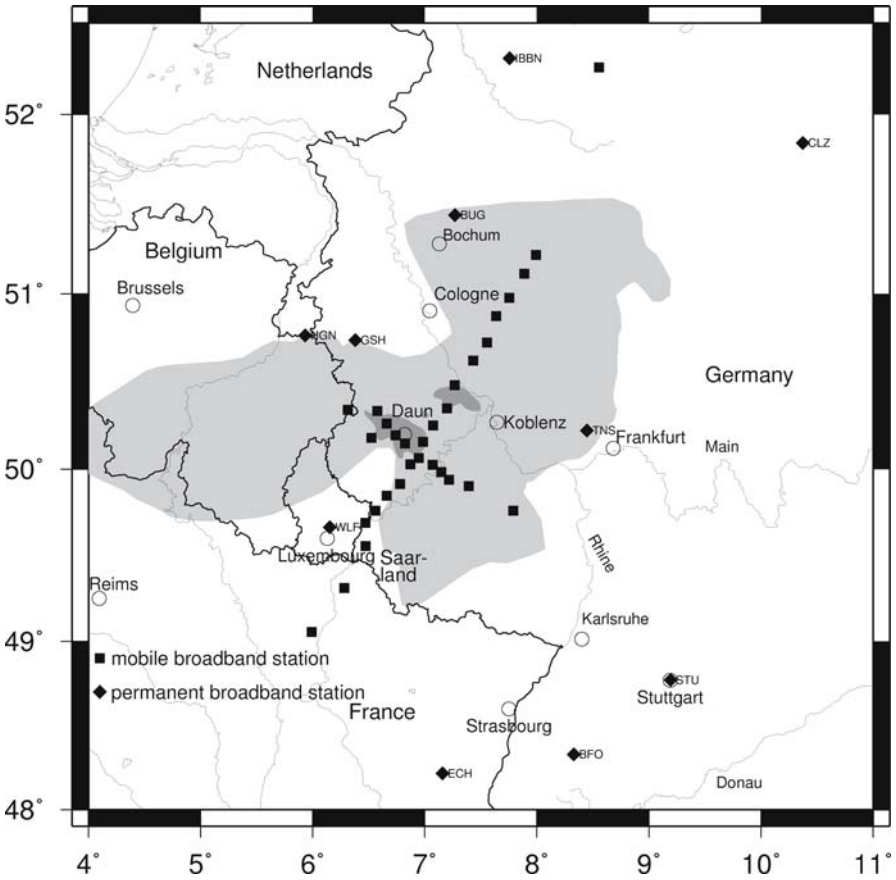

Fig. 1. Network of used mobile (squares) and permanent (diamonds) broadband stations. Light grey shaded area marks the Rhenish Massif and dark grey areas the Quaternary volcanic fields of the Eifel

Research by Keyser et al. (2002) led to similar results using the Eifel Plume network and permanent stations (Ritter et al. 2000). By inverting 3773 teleseismic shear wave travel time residuals they found a zone with a –2 to –5 percent perturbation in v_s directly underneath the Eifel volcanic

fields. Their anomaly starts at about 30 km depth and reaches down to at-least 400 km (see also Ritter this volume). However, due to vertical smearing they were not able to properly resolve the upper 50 km. Below ~170 km depth the negative velocity perturbation is intersected by a positive one ($\leq$ +1 % v_s) which continues to about 240 km depth. The v_s perturbation at this depth and down to at least the transition zone decreases to less than -1 % being less in amplitude than above 150 km depth (Fig. 2), what might be due to loss of resolution at depth.

Budweg (2003), Budweg et al. (2006) and Weber et al. (this volume) analysed receiver functions at the Eifel Plume network. They found evidence for a seismic discontinuity at about 50 km depth with reduced seismic velocities below the discontinuity. Positive phases of the receiver functions at a depth of 80-100 km indicate a possible limitation in depth of the observed anomaly. However, the anomaly found by Keyser et al. (2002) shows a drop in velocity perturbation from -5 to -3 % below 100 km depth. So the positive phases observed by Budweg (2003) may be due to a change in the seismic velocity gradient. The anomaly at about 50 km depth can be interpreted as the top of the Eifel plume.

Apart from the work that has been done to determine the distribution of v_s below the Eifel region, there have also been studies on the *P*-wave velocity v_p structure in this region. Mechie et al. (1983) found a low velocity zone at the Moho (30–35 km depth) below the Eifel with v_p dropping to 6.3-7.0 km/s at the base of the lower crust and then rising to upper mantle velocities of 8.1 km/s. To explain the v_p anomaly Mechie et al. (1983) postulate a possible magmatic underplating at the crust-mantle boundary in this area due to uprising melted rock.

Raikes and Bonjer (1983) determined an anomaly in v_p in the mantle below the Eifel volcanic fields from teleseismic *P*-wave travel time residuals. Their model has perturbations in v_p of -3 to -5 % and reaches from 50 to 200 km depth. Below 200 km however, the v_p perturbations do not exceed ±1 %. A recent *P*-wave tomography revealed that the LVA reaches down to at least 400 km depth (Ritter et al. 2001, Ritter this volume), however the resolution above 50-60 km depth was insufficient to map the top of the Eifel plume due to the used subvertical ray paths.

The results of the mentioned experiments motivated our research: Using surface waves we want to test and improve the existing v_s models. We analyse part of the data acquired during the Eifel Plume Project (Ritter et al. 2000). As our inversion is based on the fundamental mode of the recorded Rayleigh wavetrains we only use data from the broadband (BB) stations. The available BB instrumentation consists of 10 permanent stations (STS-1 with eigenperiod T_0=360 s and STS-2 with T_0=120 s) from the German Regional Seismic Network (7), the Geofon network (1), Reseau National

de surveillance sismique, France (1) and the network of the Koninklijk Nederlands Meteorologisch Instituut (1) as well as 31 mobile stations (Güralp 40T with eigenperiod T_0=30 s, Güralp 3T with T_0=100 s and STS 2 with T_0=120 s).

Fig. 1 shows the distribution of these stations. Our station coverage is much better than that of previous surface wave tomography studies performed in the Eifel or adjacent regions like e.g. by Passier and Snieder (1996) or Stange and Friederich (1993) who could only use permanent stations. The mobile BB stations were deployed along two axes which provide an excellent coverage in the region of interest. Data acquisition took place from November 1997 to June 1998. The NE-SW station axis was deployed in January 1998. This causes a resolution limitation for waveforms collected in November and December 1997, especially for events with wavevectors perpendicular to the NW-SE axis.

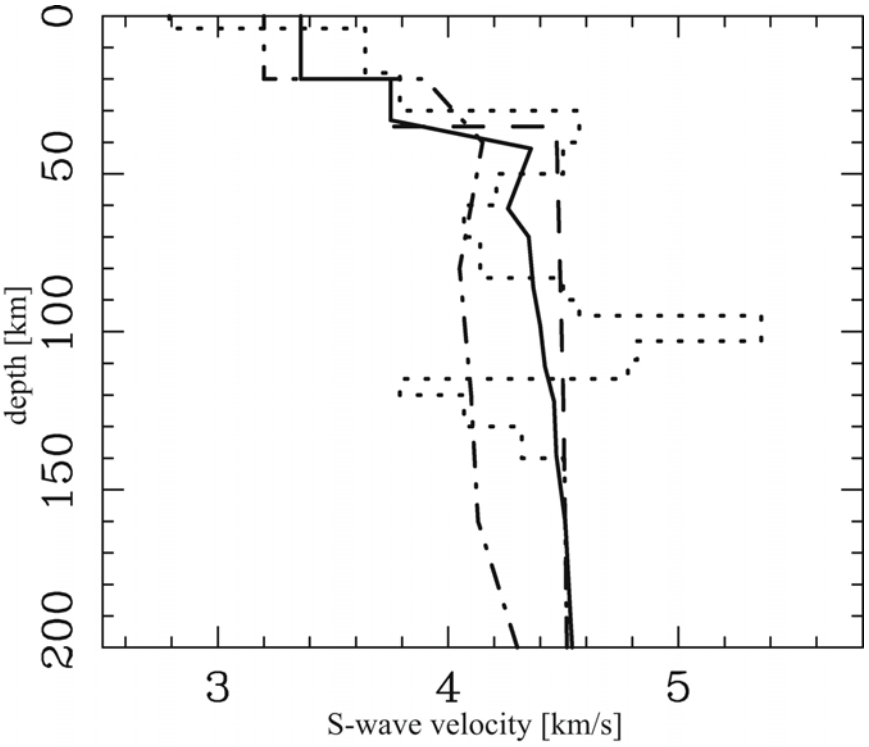

Fig. 2. Average shear wave velocity models for the Eifel area: Passier and Snieder (1996): dashed and dotted line, Keyser et al. (2002): solid line and Budweg (2003): dotted line as well as the iasp91 reference model (Kennett and Engdahl 1991): dashed line

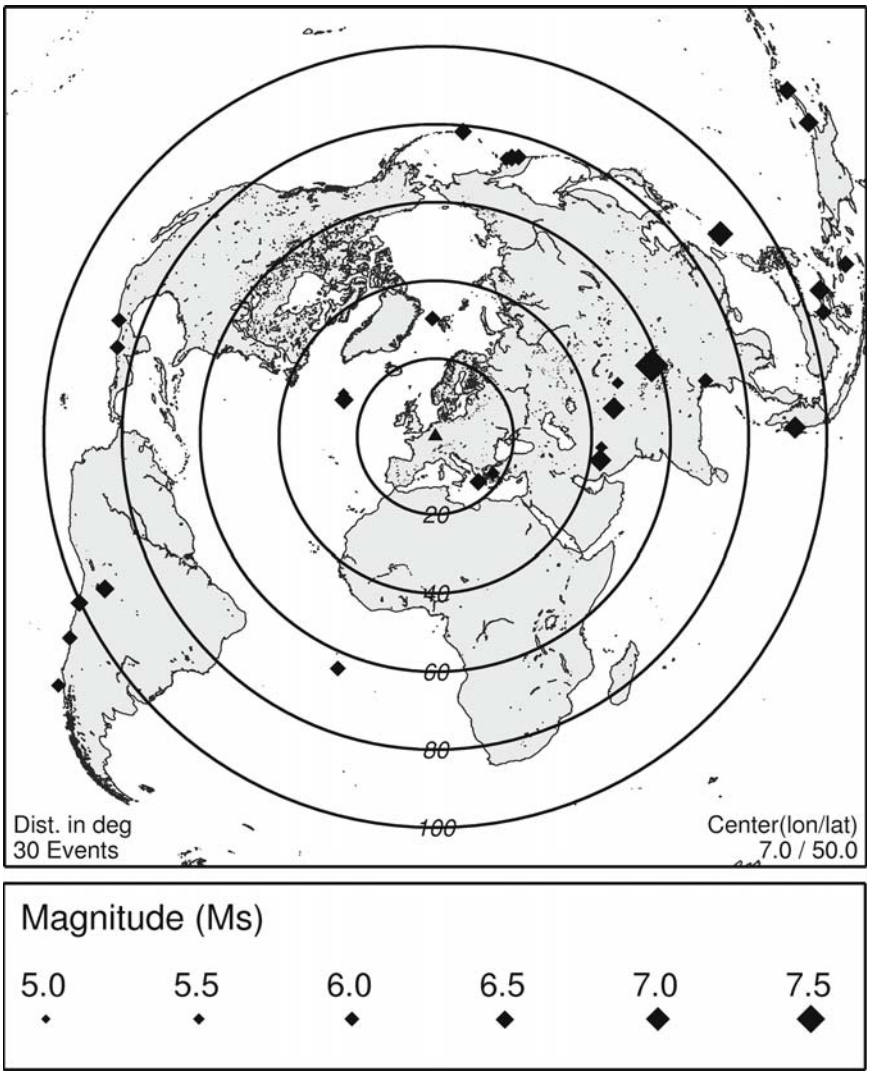

Fig. 3. Azimuthal distribution of used events, distances are given in degree from the center of the station network (triangle)

2 Data selection and processing

From the data set of the Eifel Plume Project we chose 30 events as basis for our inversion which had to fulfil the following quality criteria:

1. The Rayleigh wavetrain has to be completely recorded on the majority of the stations.
2. The Rayleigh wavetrain must be clearly identifiable, so it should not be too strongly dispersed or influenced by higher modes.
3. The epicentral distance must not exceed 130°, as we want to prevent interference between the minor arc and the major arc wavetrains. This restriction also keeps attenuation below an acceptable limit to achieve a favourable signal-to-noise ratio.
4. Surface wave magnitude M_S should be above 5.5 to achieve a good signal to noise ratio.

In addition to these selection criteria we also tried to achieve a good azimuthal coverage. The epicentres of the events taken for the inversion are displayed in Fig. 3. The azimuthal coverage is quite good except for a gap to the southern direction.

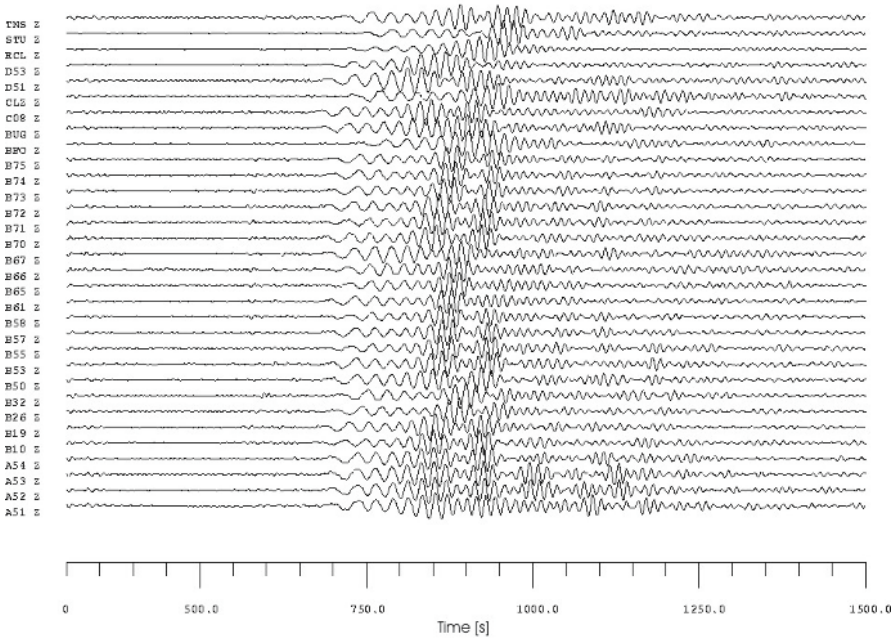

Fig. 4. True-amplitude record section of vertical velocity seismograms of an event below the North Atlantic Ocean at February 25th 1998. The waveforms are low-pass filtered at 0.1 Hz and the fundamental mode of the Rayleigh wavetrain is clearly visible and well dispersed. The signal-to-noise ratio is well above 10

The seismic waveforms were recorded with sampling frequencies of 20 or 50 Hz and archived in miniSEED format. A waveform example that displays clearly dispersed Rayleigh waves is given in Fig. 4.

For pre-processing of the dataset we used the Seismic Handler software by Stammler (1993). Seismograms were cleaned of spikes and afterwards filtered using a Butterworth lowpass filter of fourth order and a corner frequency of 0.1 Hz. After filtering the seismograms were decimated to a sampling frequency of 1 Hz.

To eliminate the influence of the different types of used instruments, we performed a restitution to true ground motion for every seismogram. Along with the restitution we also applied a highpass filter of fourth order and a corner frequency of 0.003 Hz. This filter was necessary due to an artificial signal with a period of 200 s created during the restitution.

3 Analysis

We apply a method developed by Friederich, Wielandt and Stange (1994). The method is based on the fitting of plane waves to a given dataset of spectral amplitudes, thereby obtaining an average dispersion curve underneath the station network. This dispersion curve is then inverted for a 1D v_s-model. Our actual dataset consists of spatial amplitude spectra recorded at discrete locations. Plane waves are then fitted to this spectral dataset by describing them in terms of spectral amplitude A_q, wavenumber k_0 and azimuth α_q per event q. The plane wavefield is described by these parameters as:

$$P_q(x,y) = A_q e^{-ik_0(x\cos\alpha_q + y\sin\alpha_q)} \tag{1}$$

with x and y being Cartesian coordinates. A_q, k_0 and α_q are obtained by minimising the term

$$E_{N,q} = \sum_{n=1}^{N} \left| D_{n,q} - P_q(x_x, y_n) \right| \tag{2}$$

for every event q. $D_{n,q}$ represents the actual wavefield belonging to event q as it has been recorded at station n. Note that k_0 is the same for all events, as we are working with the plane wave assumption. As a result of the minimisation process we obtain the dispersion curve which can then be inverted for a 1D v_s-model.

To obtain a usable dataset we determine spectral amplitudes within a certain frequency band for every station and event. We first deconvolve each seismogram using phase velocity curves for the spherical standard earth model ak135q (Kennett et al. 1995). We then compute Gabor matri-

ces for all records to evaluate the signal-to-noise ratio (S/N) of the spectral amplitudes used for the actual inversion. An example Gabor matrix exhibiting the high S/N of the waveforms in Fig. 4 is displayed in Fig. 5. The deconvolved Rayleigh wavetrain is shifted to an arbitrary arrival time at 2000 s. The amplitude maxima (from 7 to 60 mHz) all occur in a narrow time window around 2000 s, displaying the efficiency of the performed deconvolution as well as the high quality of the data. The signal-to-noise ratio is also remarkably low in the mentioned frequency range. Low black diamond symbols at the bottom of Fig. 5 indicate frequencies which have passed all quality checks. Only these spectral values are used for the later inversion.

The fundamental mode of the Rayleigh wavetrain is cut out of the deconvolved sections with a Gaußian window. Spectral amplitudes, which pass the quality check, are determined at frequencies between 0.005 Hz and 0.08 Hz. An example for spectral amplitudes obtained by this method is given in Fig. 6. The variation in amplitude (due to non-plane geometries of the wavefield) between the different stations decreases strongly for periods longer than 30 s, and it is well below 20 percent above 50 s period.

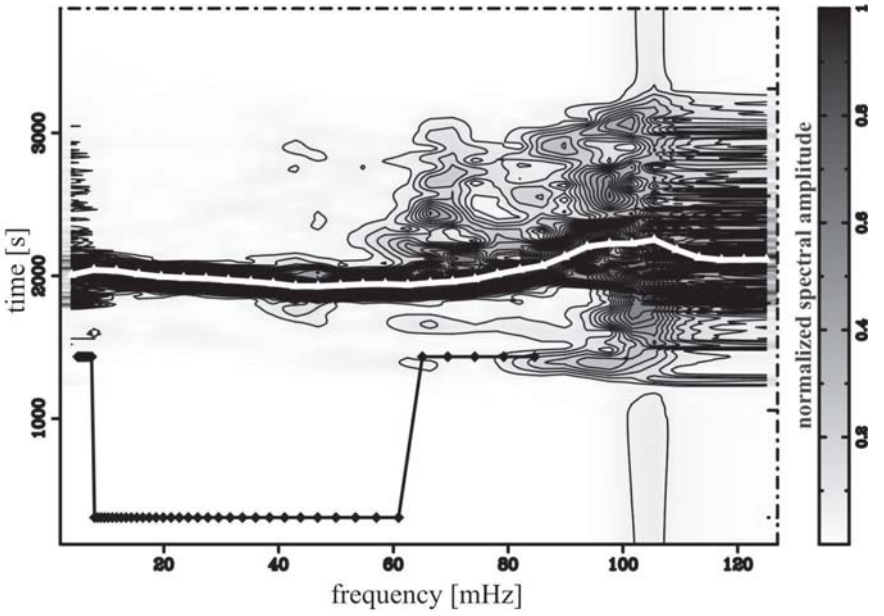

Fig. 5. Gabor matrix of the North Atlantic Ocean event (Fig. 4) recorded at station B57. Spectral amplitudes are normalized according to their maximum. The white line indicates the maximum amplitude as a function of frequency. Low black diamond symbols indicate a high S/N of the spectral amplitudes

Finally, we perform the plane wave fit as described above which results in the dispersion curve displayed in Fig. 7. The error bars have been determined using a bootstrap method (Efron and Gong 1983). The large standard deviation for periods below 30 s is due to strong crustal heterogeneities that scatter the Rayleigh waves. For periods longer than 80 s the acquired velocities also contain increased deviations due to long period noise.

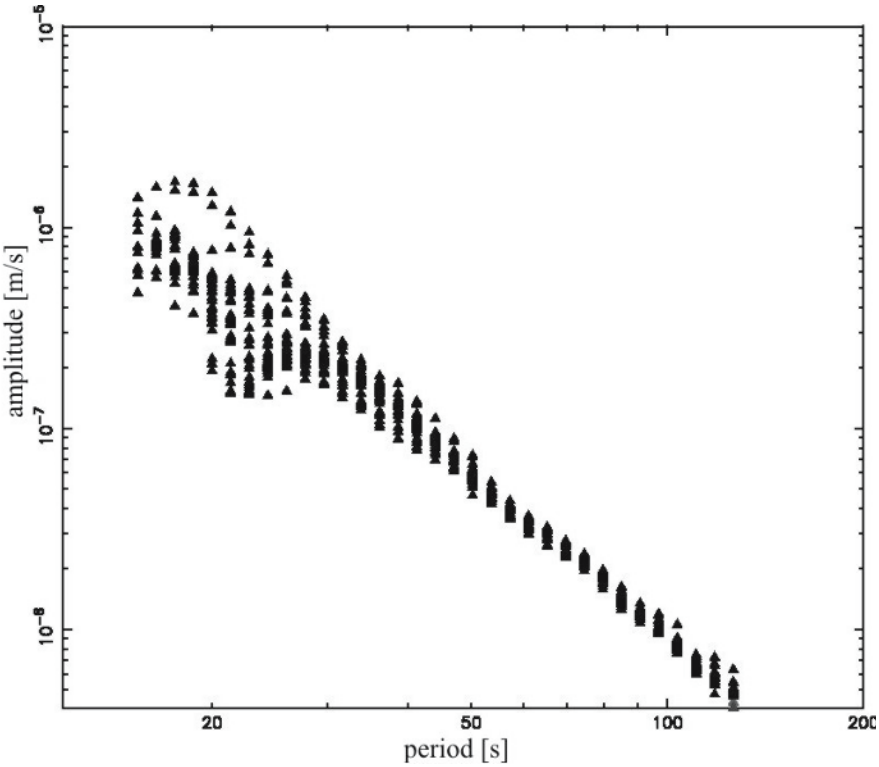

Fig. 6. Spectral amplitudes for the North Atlantic Ocean event (Fig. 4). Every triangle represents the spectral amplitude recorded at a station for a given frequency. The increased amplitude variation below 30 s period results mainly from scattering in the crust

4 Modelling

The inversion of the dispersion curves is performed assuming an isotropic background model. After choosing an initial model, the inversion process is performed iteratively. Synthetic dispersion curves are computed for the

inverted model and compared to the measured curve. When the misfit of the inverted model converges the iteration is stopped. The misfit is calculated as follows:

$$\Delta = \frac{1}{N}\sum_{l=1}^{N}\frac{c_l - c_{inv,l}}{\sigma_l} \tag{3}$$

c_l represents the measured phase velocity for period l and $c_{inv,l}$ the phase velocity as obtained from the inversion. σ_l is the standard deviation of c_l. A misfit of Δ<1 indicates that most phase velocities obtained from the inversion lie within the error bars of the measured velocities at N periods.

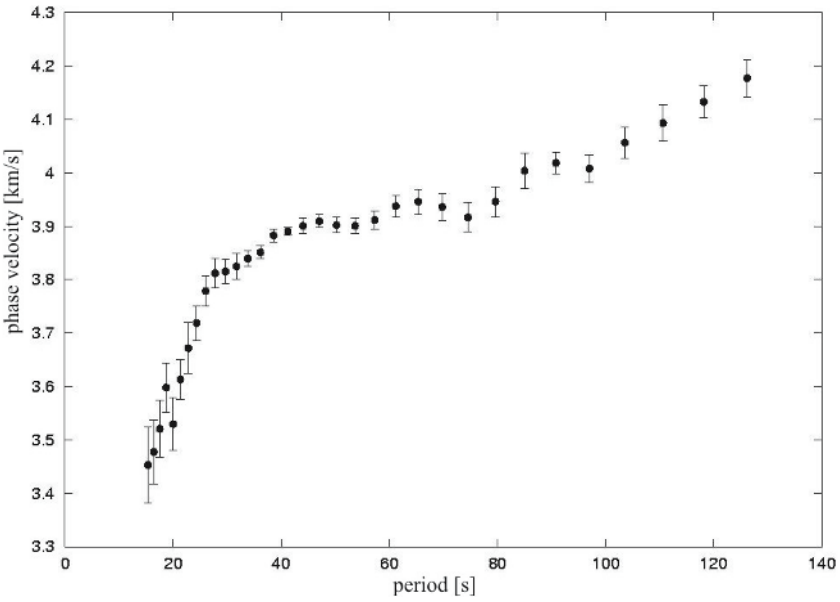

Fig. 7. Average dispersion curve for all stations obtained from the fundamental mode Rayleigh wavetrains. Error bars were determined with a bootstrap analysis

4.1 Starting model iasp91

As a first starting model M1 (Fig. 8a) for the inversion the iasp91 model (Kennett and Engdahl 1991) together with densities from PREM (Dziewonski and Anderson 1981) is taken. The Moho for M1 is fixed at 35 km depth. The a priori variance of the given crustal velocities is 0.05 km/s. The inversion is performed to a maximum depth of 400 km with moderate smoothing in the mantle.

For periods longer than 30 s the dispersion curve of M1 lies well above the one obtained from our data (Fig. 8a). This is a clear indication for a low-velocity zone below the Eifel region. The misfit according to equation (3) of M1 is 12 and thus the iasp91 model obviously does not explain our data. After 5 modelling iterations the misfit decreases to 0.5 and the dispersion curve of the resulting shear wave velocity (v_s) model E1 (Fig. 8a) is within the error bars for the different measured frequencies (Fig. 8b).

The v_s model E1 exhibits a pronounced low v_s zone starting below the Moho and reaching down to ~220 km depth. While the crust shows no significant variations from the standard earth model iasp91, v_s decreases from 4.42 km/s at 50 km depth to 4.29 km/s at 135 km depth. This is a relative velocity anomaly of about -3 percent which correlates well with the anomaly that Keyser et al. (2002) discovered using teleseismic body-wave tomography.

To check the stability of model E1, the inversion is performed several times, varying the following parameters:

- The maximum depth to which the starting model could be altered.
- A priori variance of the crustal velocities of the starting model.
- The smoothing weight for v_s in the mantle.
- The range in which the algorithm is allowed to alter the Moho depth.
- The total number of iterations that the algorithm has to perform.

The inversion result in model E2 (Fig. 9) is obtained with a strong smoothing constraint for the mantle v_s. To obtain a misfit comparable to model E1 we had to perform a total of 15 iterations. The Moho was fixed to 35 km depth and the lower boundary of the lithosphere was set to 60 km depth. The resulting model E2 shows no significant variation compared to model E1. The low v_s anomaly starts at about 50 km depth with v_s = 4.42 km/s and reaches down to 220 km depth. The maximum v_s perturbation is situated at a depth of 135 km with v_s = 4.3 km/s. Thus the relative v_s perturbation is the same as for model E1. Too low smoothing increases the perturbation amplitude with an unlikely anomaly (E3, Fig. 9) and also changes the depth of the v_s anomaly.

Fig. 8. (next page) a) M1 (dotted) and E1 (solid) shear wave velocity models. b) Measured dispersion values with error bars and dispersion curves calculated for models M1 (dotted) and E1 (solid)

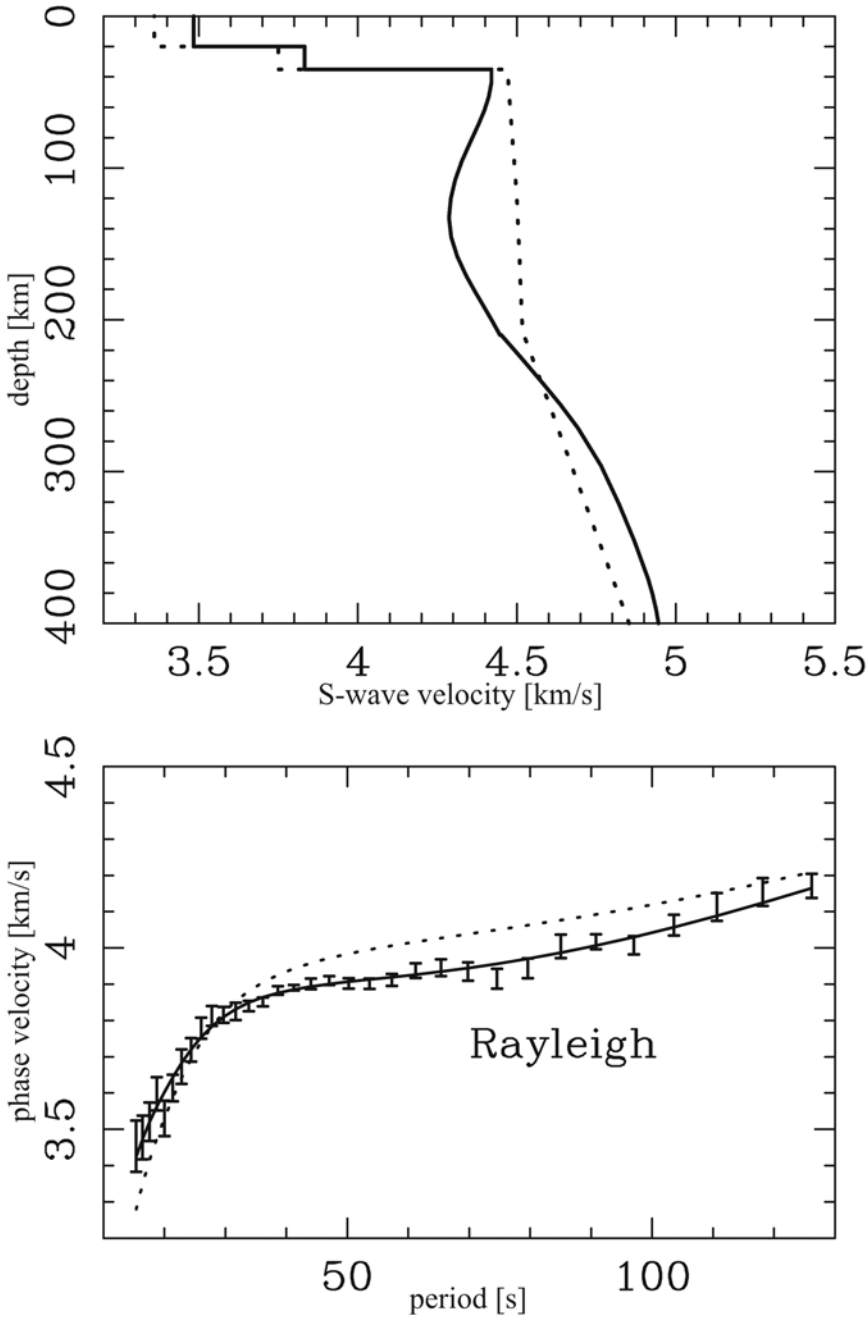
depth [km]
0
100
200
300
400
3.5
4
4.5
5
5.5
S-wave velocity [km/s]
phase velocity [km/s]
4.5
4
3.5
Rayleigh
50
100
period [s]

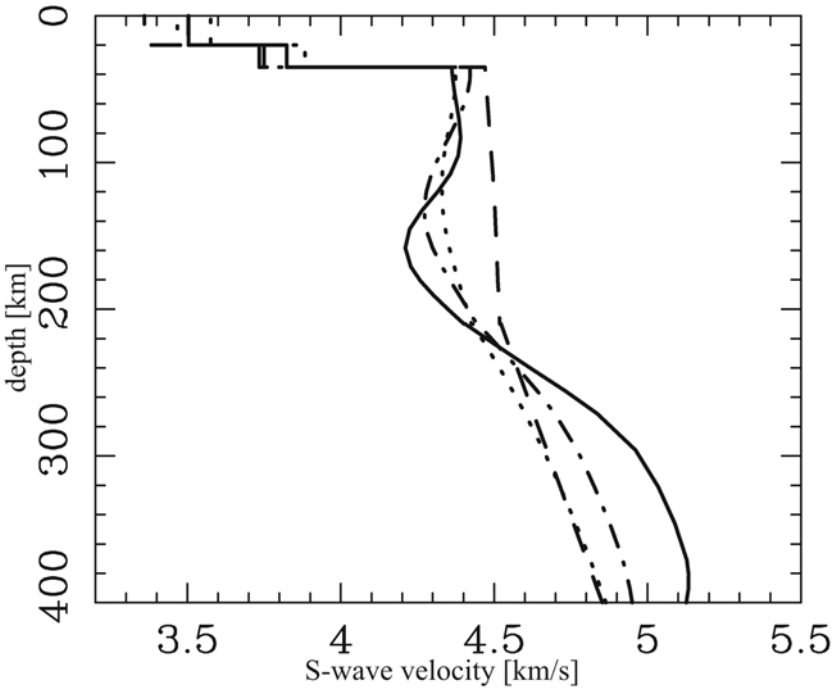

Fig. 9. Seismic shear wave velocity models: iasp91 (dashed), E2 (dotted), E3 (solid) and E4 (dotted and dashed). Modelling details are given in the text

To determine the influence of the crustal velocities in the starting model on the mantle velocities in the inversion model, we set the a priori variance of the crustal v_s to 1 km/s. The resulting inversion model E4 is given in Fig. 9. While the depth of the anomaly does not vary from model E1, we observe a slight drop of the maximum v_s decrease from 4.29 km/s (E1) to 4.27 km/s (E4) at ~130 km depth. As the a priori variance of the crustal v_s for model E4 is 20 times the one for model E1, we find that fixing the crustal velocity has no significant influence on the inversion model in the mantle.

As can be observed from these examples, the low v_s anomaly is very stable against variations of the mentioned input parameters. However, it significantly depends on the a priori variance of the Moho depth in the starting model. This is demonstrated by inversion model E5 shown in Fig. 10. The starting model was again M1, but the a priori variance was set to 10 km. As can be seen the inversion tends to push the Moho upwards (about +3 km), if it is not fixed. Together with the shallowing of the Moho, the upper boundary of the mantle low v_s anomaly is pushed downwards to

a depth of about 60-70 km. The minimum value of v_s is about 4.3 km/s in this case. Compared to v_s = 4.39 km/s at the upper boundary this is a relative perturbation of -2.1 % which is less than in model E1. The misfit (eq. 3) for all inversion results (E1-E5) is almost equally small (about 0.5).

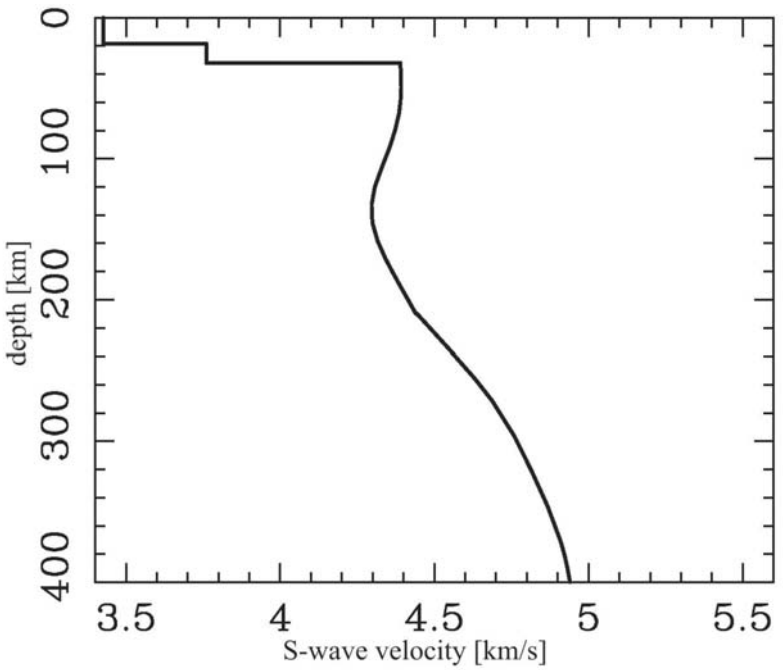

Fig. 10. Seismic shear wave velocity model E5 (starting model iasp91 with a priori variance of Moho depth set to 10 km)

4.2 Starting model iasp91 with local crustal model

To determine which inversion model (E1 or E5) is more realistic we choose to alter the crustal part of the starting model according to the results from the long-range seismic refraction project by Mechie et al. (1983). The starting model for the mantle is again taken from iasp91 and PREM. The detailed crustal model by Mechie et al. (1983) is smoothed and averaged over the region of interest with a spline function to get a continuous model (Fig. 11a). As result the average crustal v_s in the starting model M2 is slightly higher than in the model by Mechie et al. (1983).

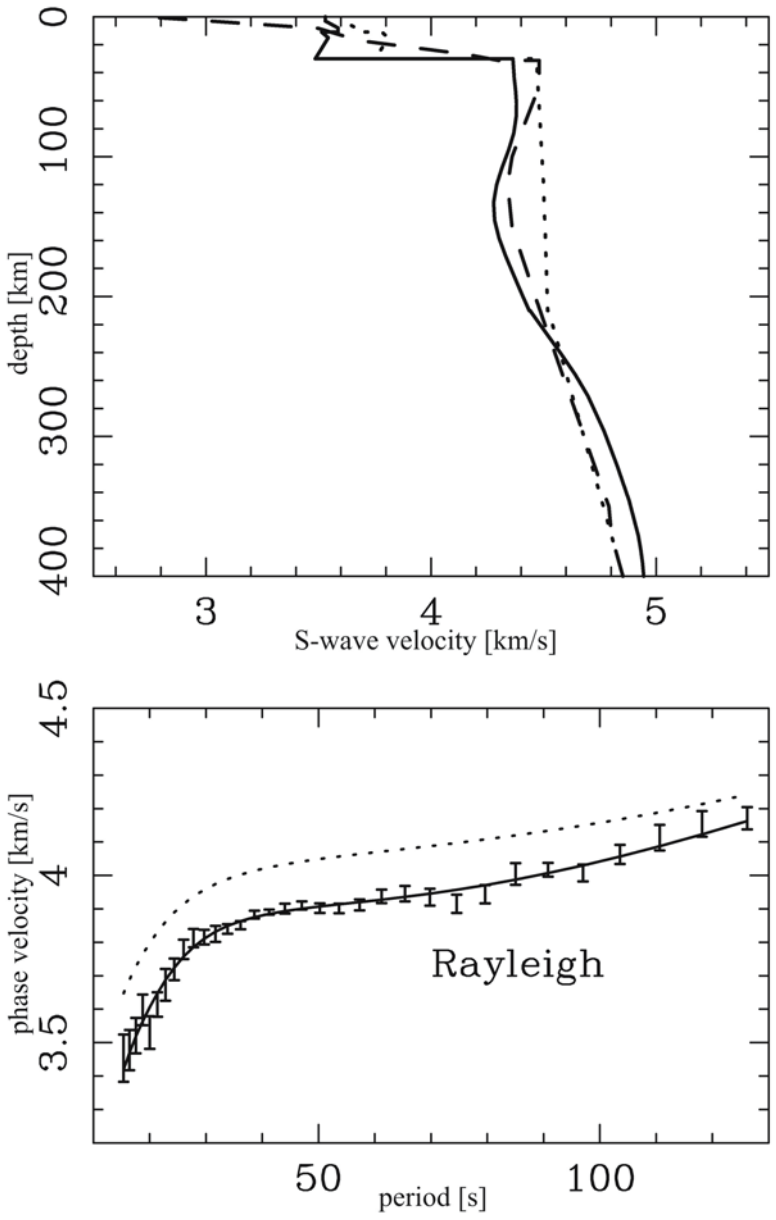

Fig. 11. a) Seismic shear wave velocity models M2 (dotted), E6 (solid) and mantle model (dashed) by Friederich and Huang (1996). Mantle v_s is taken from iasp91 and density from PREM, crustal v_s from Mechie et al. (1983). b) Dispersion curves from M2 (dotted) and E6 (solid) compared to measured dispersion values with their error bars

The Moho depth is fixed at 30 km depth. The initial misfit of 46 is remarkably higher than the one retrieved from iasp91 but decreases after 5 iterations to 0.5. The resulting model E6 (Fig. 11) varies significantly from E1 concerning the velocity structure in the mantle. The low v_s anomaly shows the same maximum perturbation and the same v_s distribution below 100 km depth as E1. However, the anomaly in E6 starts at a depth of 70 km which is 20 km deeper than the anomaly found with the iasp91 starting model M1 and fixed Moho depth. E6 has lower v_s at Moho depth together with a slight increase of v_s between the Moho and the anomaly. The minimum v_s value is 4.27 km/s at a depth of 135 km. The upper boundary of the low v_s anomaly at 70 km depth has v_s = 4.37 km/s, thus the maximum v_s perturbation reaches -2.3 %.

Compared to model E5, which we obtained from the inversion of the iasp91 model and allowing a standard deviation of Moho depth of 10 km, we find only few differences in the obtained results for E6. The upper boundary of the low velocity zone varies from 50-60 km to 60-70 km depth, and the difference in the maximum v_s perturbation is below 1 %. The relative perturbation in v_s is almost equal to E5. This indicates that the models E5 and E6 can be considered more realistic than those obtained from the iasp91 model with Moho depth fixed to 35 km (e.g. E1), especially as we know from other observations, that the Moho below the Eifel region is at 30 km depth and that there is a trade-off between the Moho depth and our resulting v_s mantle model.

4.3 Local Eifel model

Friederich and Huang (1996) found a low v_s anomaly (LVA) starting at 50 km depth, reaching down to about 200 km depth in southern Germany (Fig. 11a, dashed line). Their LVA is situated below a thin lid with v_s = 4.47-4.48 km/s. The minimum v_s of the LVA is found at 120-130 km depth with v_s = 4.35-4.37 km/s. This is a relative perturbation of –2 % to -3 %. Although the total minimum of the anomaly observed in model E6 is about 0.1 km/s less than the one described by Friederich and Huang (1996) below southern Germany, the v_s distribution at depth as well as the relative perturbation are very similar.

Friederich and Huang (1996) interpreted their result in terms of a shallow asthenosphere combined with a *S*-wave anisotropy of 4 % and a small *P*-wave anisotropy in the mantle between 70 km and 200 km depth. To check if we actually see the same structure as found in this earlier study or if our observation indeed is an indication for the existence of the Eifel plume, we redo the inversion without data from stations A03, BFO, CLZ,

ECH, IBBN and STU. This smaller network of 200 km by 200 km is used to rule out the influence of heterogeneities from outside the area of interest.

The obtained dispersion curve for the actual Eifel area is shown in Fig. 12. The error bars for short periods decrease due to the reduced aperture of the network. As a result of the smaller network we can only analyse Rayleigh wave periods up to 80 s. This also limits the maximum depth of our inversion to 200 km due to a loss of sensitivity. A key feature of the dispersion curve is the negative step in phase velocity at a period of 30-35 s. According to sensitivity kernels of Rayleigh waves this corresponds to a low v_s zone at a depth of about 50-60 km. The drop in phase velocity can also be observed in Fig. 7, however, it is far less pronounced as a result of averaging across a much larger area.

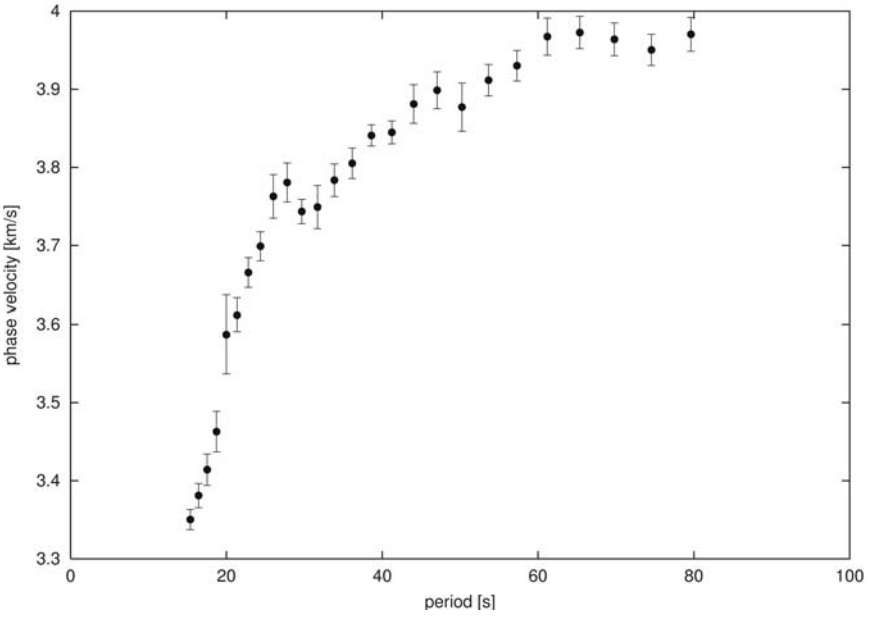

Fig. 12. Dispersion curve of data collected only from stations in the Eifel area. Error bars are determined by a bootstrap analysis

The inversion of the reduced data set is performed with starting model M2 and the Moho is fixed at 30 km depth. The obtained inversion model E7 (Fig. 13) contains a thin lid beneath the Moho with v_s = 4.38 km/s at 45-50 km depth. Below 45-50 km depth we find a low v_s zone with minimum v_s = 4.27 km/s at 85 km depth. This is a relative perturbation of -2.5 %. It is terminated by a zone of slightly higher v_s at a depth of 130 km.

This is in agreement with earlier observations by Budweg (2003), Budweg et al. (2006) and Keyser et al. (2002). However, due to the lack of data with periods above 80 s the resolution decays strongly below 150 km depth. The misfit of E7 is 1.3 which is due to the smaller error bars for low periods (see equation 3). The anomaly in Fig. 13 is very stable against all parameter variations mentioned earlier. Choosing iasp91 as a starting model with the Moho fixed at 35 km results in a very similar model E8 (Fig. 13). The lid below the Moho is less pronounced and the minimum v_s of the anomaly is situated at a depth of 70 km. However, the relative velocity perturbation and absolute values of v_s are equivalent to E7 which is our preferred local model, because the starting model contains a locally determined crustal structure.

5 Discussion

From the inversion of teleseismic Rayleigh waves a regional v_s model E6 and a local Eifel v_s model E7 are determined. Both models contain a low velocity anomaly (LVA) in the upper mantle which may represent two different features. The regional model has a stable LVA with its velocity minimum at about 135 km depth. This LVA starts at 70 km depth and reaches down to about 200 km depth. We interpret this LVA as the average effect of the asthenosphere in the region (NE France, Belgium, Luxembourg and SW Germany, see Fig. 1). This anomaly is similar to the LVA determined by Friederich and Huang (1996).

The local model E7 has a much shallower LVA starting at 45-50 km depth with its minimum v_s at 85 km depth. Below 150-200 km depth the resolution is low, because only Rayleigh wave periods up to 80 s could be used for E7. The v_s anomaly reaches as much as -2.5 % at relatively shallow depth, and thus we interpret it as local asthenospheric upwelling. Such an upwelling is compatible with other seismological models for the Eifel area and can be due to a mantle plume. Our models correspond very well with the receiver function results obtained by Budweg et al. (2006) and Weber et al. (this volume). The LVA also agrees with the teleseismic v_s tomography model by Keyser et al. (2002), however, the upper boundary of the low v_s anomaly observed here is situated about 20 km shallower. This discrepancy is a result of the blurred tomography image due to its subvertical rays which limit the vertical resolution of teleseismic *S*-wave tomography at a depth of less than 60-70 km. Therefore, together with the receiver function results of Budweg et al. (2006) or Weber et al. (this volume), we can state from our model E7 that the upper boundary of the low

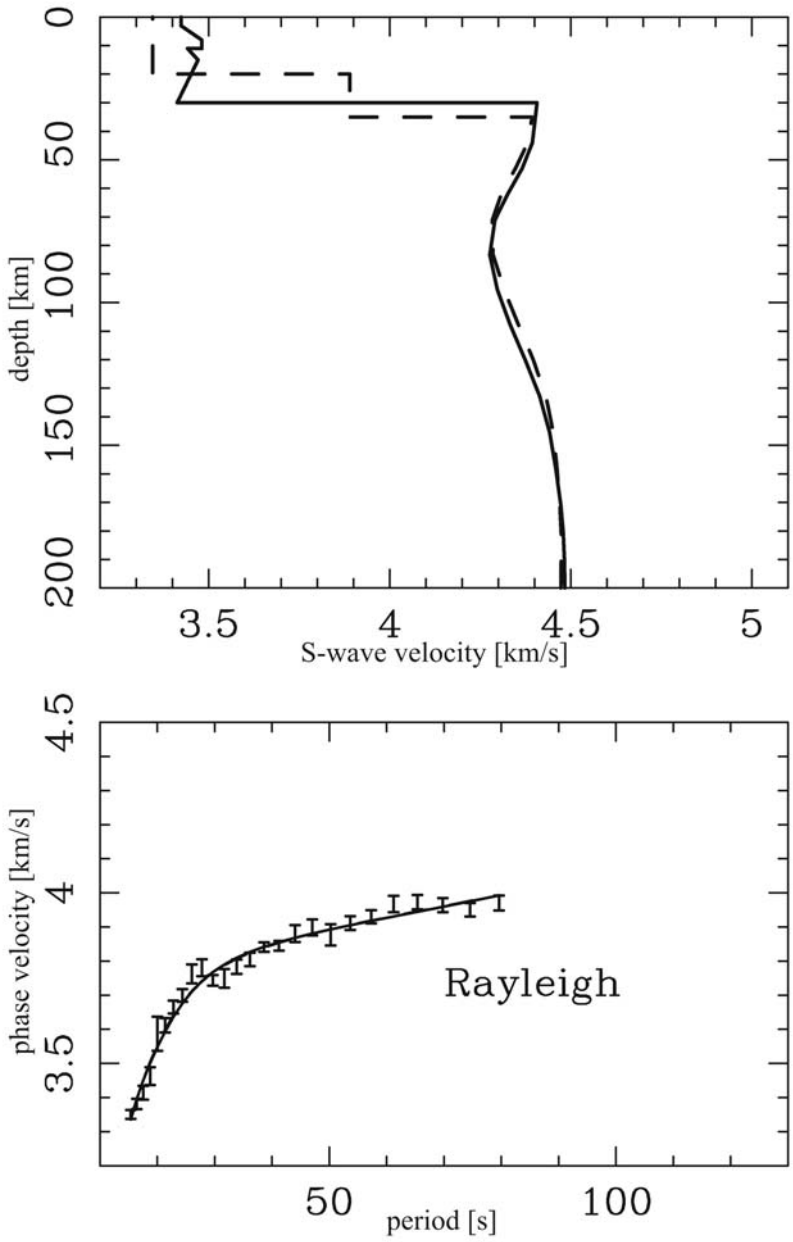

Fig. 13. (previous page) a) Seismic shear wave velocity models E7 (solid) and E8 (dashed). b) Dispersion curve for E7 and measured dispersion values with error bars

v_s anomaly underneath the Quaternary Eifel volcanic fields can be interpreted as the head of the Eifel Plume and is situated at a depth of 45-50 km.

Acknowledgements

We thank the Eifel Plume Team for the data collection and processing. S. Funke and S. Lebedev provided useful reviews and comments. Mobile broadband instruments for this study were provided by the Geophysical Instrument Pool at the GeoForschungsZentrum Potsdam and the Network of Autonomously Recording Stations (NARS) at the University of Utrecht. Data from permanent stations were gathered from the German Regional Seismic Network (GRSN), the Geofon network, the network of the Koninklijk Nederlands Meteorologisch Instituut and Reseau National de surveillance sismique, France. GMT (Wessel and Smith, 1998) was used for plotting the maps. Funding was provided by the Deutsche Forschungsgemeinschaft (Ch77/9); European Center for Geodynamics and seismology - Musee National d'Histoire Naturelle; Institut de Physique du Globe, Strasbourg, France; Royal Observatoire of Belgium.

References

Budweg M (2003) Der obere Mantel in der Eifel-Region untersucht mit der Receiver Function Methode. PhD thesis, University of Potsdam

Budweg M, Bock G, Weber M (2006) The Eifel Plume – Imaged with converted seismic waves, Geophys J Int, 166:579-589, doi:10.1111/j.1365-246X2005.02778.x

Dziewonski AM, Anderson DL (1981) Preliminary reference Earth model. Phys Earth Planet Int 25:297-356

Efron B, Gong G (1983) A leisurely look at the bootstrap, the jackknife and cross-validation. The American Statistician 37:36-48

Friederich W, Wielandt E, Stange S (1994) Non-plane geometries of seismic surface wavefields and their implications for regional surface-wave tomography. Geophys J Int 119:931-948

Friederich W, Huang Z-X (1996) Evidence for upper mantle anisotropy beneath southern Germany from Love and Rayleigh wave dispersion. Geophys Res Lett 23:1135-1138

Kennett BLN, Engdahl ER (1991) Traveltimes for global earthquake location and phase identification. Geophys J Int 105:429-465

Kennett BLN, Engdahl ER, Buland R (1995) Constraints on seismic velocities in the Earth from traveltimes. Geophys J Int 122:108-124

Keyser M, Ritter JRR, Jordan M (2002) 3D shear wave velocity structure of the Eifel plume, Germany. Earth and Plan Science Let 203:59-82

Mechie J, Prodehl C, Fuchs K (1983) The long-range seismic refraction experiment in the Rhenish massif. In: Fuchs K, von Gehlen K, Mälzer H, Murawski H, Semmel A (eds) (1983) Plateau uplift, the Rhenish shield - a case history. Springer-Verlag, Berlin, pp 260-275

Passier ML, Snieder RK (1996) Correlation between shear wave upper mantle structure and tectonic surface expressions: Application to central and southern Germany. J Geophys Res 101:25293-25304

Raikes S, Bonjer KP (1983) Large-scale mantle heterogeneity beneath the Renish Massif and its vicinity from teleseismic *P*-residuals measurements. In: Fuchs K, von Gehlen K, Mälzer H, Murawski H, Semmel A (eds) (1983) Plateau uplift, the Rhenish shield - a case history. Springer-Verlag, Berlin, pp 315-331

Ritter JRR, Achauer U, Christensen UR, the Eifel Plume Team (2000) The teleseismic tomography experiment in the Eifel region, Central Europe: Design and first results. Seism Res Lett 71:437-443

Ritter JRR, Jordan M, Christensen UR, Achauer U (2001) A mantle plume below the Eifel volcanic fields, Germany. Earth Planet Sci Lett 186:7-14

Stammler K (1993) SeismicHandler: programmable multichannel data handler for interactive and automatic processing of seismological analyses. Comp Geosci 19:135-140

Stange S, Friederich W (1993) Surface wave dispersion and upper mantle structure beneath southern Germany from joint inversion of network recorded teleseismic events. Geophys Res Lett 20:2375-2378

Wessel P, Smith WHF (1998) New, improved version of Generic Mapping Tools released. Eos Trans. American Geophys Union 79:579

Seismic Anisotropy in the Asthenosphere Beneath the Eifel Region, Western Germany

Kristoffer T. Walker[1], Götz H.R. Bokelmann[2], Simon L. Klemperer[3], Günter Bock[4] and The Eifel Plume Team[5]

[1]Institute of Geophysics and Planetary Physics, Scripps Institution of Oceanography, University of California, San Diego
[2]Laboratoire de Tectonophysique, Université Montpellier II, Montpellier, France
[3]Department of Geophysics, Stanford University
[4]GeoForschungsZentrum Potsdam
[5]U. Achauer, M. Budweg, T. Camelbeeck, U. Christensen, F. Collin, N. d'Oreye, I. Eschghi, H. Gaensicke, K.-G. Hinzen, M. Jordan, T. Kaspar, M. Keyser, R. Pelzing, J.R.R. Ritter, F. Scherbaum, Y.-F. Temme, M. Weber, and U. Wüllner

Abstract

We provide evidence for a plume-like upwelling beneath the Eifel hotspot, Western Germany, by using teleseismic shear-wave splitting to resolve the anisotropy associated with upwelling flow that is spreading laterally into the asthenosphere. The variation in fast–polarization azimuth we find across the Eifel hotspot is explained by a model of slowly upwelling material that is horizontally being deflected or sheared in a parabolic asthenospheric flow (PAF) pattern toward west-southwest, a direction that correlates with Eurasian absolute plate motion. We suggest that the lack of an age progression for Eifel volcanism, which is expected for a fixed-upwelling model, is a result of (1) sporadic volcanism due to a low excess plume temperature and/or varying crustal stresses that periodically relax and facilitate eruption, and (2) complex upwelling flow pathways and/or Late Tertiary changes in the slow Eurasian plate motion. The success of the PAF model in fitting the data is remarkable given the small number of parameters (four) and the consistency with the plate motion direction determined from geology and/or geodesy. This suggests that a predictable mantle-anisotropy pattern may exist also for other hotspots driven by plume-like upwellings, and that splitting can be a useful diagnostic to differentiate between plume-like and alternative sources for mantle hotspots.

1 Introduction

The plate-tectonic hypothesis, that rigid plates move over the Earth's surface above a fluid-like mantle, is used to explain most of Earth's geological and geophysical features (Dietz 1961, Hess 1962). The plume hypothesis, that cylindrical conduits of hot upwelling mantle material are responsible for up to 10 % of Earth's heat flow, has been used to explain "hotspots", anomalous volcanic regions far from plate boundaries (e.g., Hawaii and Yellowstone) that are often associated with some combination of rapid and voluminous eruptions of basaltic lava, broad topographic swells and geoid highs, and linear age progressions of volcanic centres (Morgan 1971, Sleep 1990, Davies and Richards 1992). Recently the plume hypothesis has been challenged, and complex plate-tectonic models have been proposed instead to explain such regions (e.g., Anderson 1994, King and Anderson 1998, Smith and Lewis 1999).

Plumes are elusive targets of seismological investigation due to their hypothesised geometry and depth. Regional tomographic inversions of teleseismic body-wave data, which suffer from the inherent trade-off between misfit reduction and model complexity, tend to smear anomalies vertically in regions penetrated by mostly subvertical rays. Consequently applications of this technique around hotspots (e.g., Bijwaard and Spakman 1999, Foulger et al. 2001, Wolfe et al. 2002) have led to intriguing, but sometimes controversial image interpretations. In addition, resolution constraints and choice of reference velocity in past global and regional inversions have limited reliable detailed imaging of the deep lower mantle beneath hotspots (Ritsema and Allen 2003).

Although there has been recent success in detecting some plumes with surface-wave anisotropy tomography (Montagner 2002), finite-frequency body-wave tomography (Montelli et al. 2004), and *SS* precursor modelling and receiver functions (Li et al. 2003), and the debate for some may be shifting from "whether plumes exist" to "where and at what depth they exist," new approaches for detecting plumes will help resolve the controversy. For example, seismic velocity anisotropy in the upper mantle that is detected by teleseismic shear-wave splitting (separation of the shear-wave in an anisotropic rock into two polarised waves travelling at different speeds) can be explained by a lattice preferred orientation (LPO) of olivine fast axes due to either past or present mantle deformation. This interpretation has been made to explain correlations of fast polarisation directions with absolute plate motion (Vinnik et al. 1992, Bormann et al. 1996, Schutt and Humphreys 2001), although many other interpretations have been proposed to explain other correlations (e.g., Savage 1999). An essen-

tial part of the plume hypothesis, the deflection of plume material by a moving plate, can be tested by analysing shear-wave splitting of shear phases generated from teleseismic earthquakes (Walker 2004). Although, because mantle anisotropy from a plume would be mostly confined to the upper 300 km of the Earth's mantle, a positive result only suggests a "plume-like" upwelling - the depth of origin not being constrained.

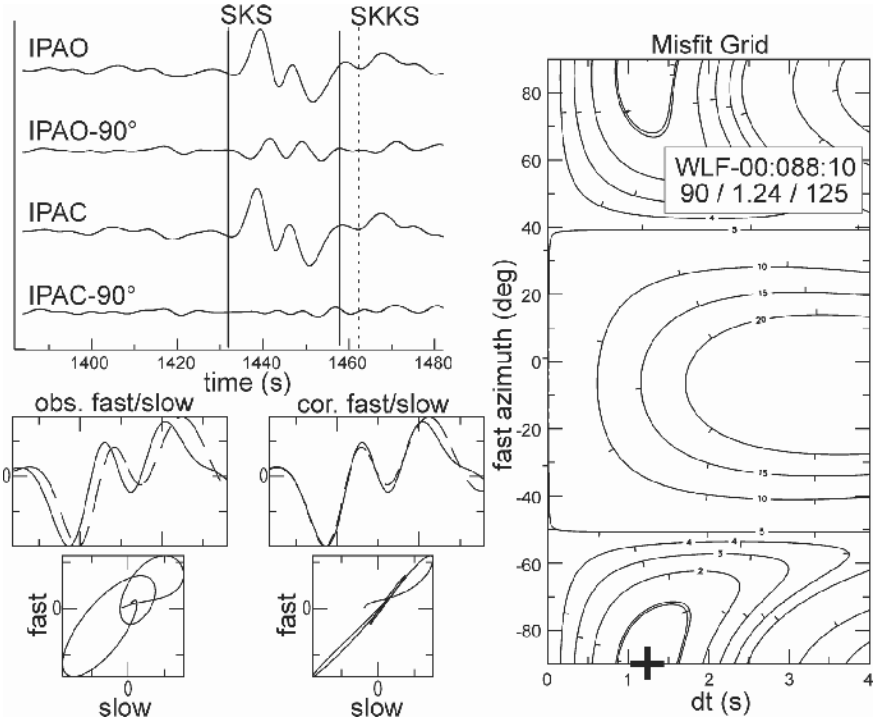

Fig. 1. Shear-wave splitting example for station WLF (for location, see Figure 6). We use the method of Silver and Chan (1991) as modified by Walker (2004) to find the optimum fast polarisation azimuth (ϕ) and delay time (*dt*) by performing a grid search over ϕ and *dt* to minimise coherent energy on the IPAC-90° (transverse) component, energy that is a diagnostic signal of anisotropy. In the upper left we show the observed horizontal-component waveforms parallel and perpendicular to the initial polarisation azimuth (*IPAO/IPAO-90°*). After correcting for the splitting using ϕ and *dt*, the energies on the corresponding waveforms *IPAC* and *IPAC-90°* are maximised and minimised, respectively. The box in the upper right indicates the date and UTC time of the analysed event (year:julday:hour), the measured ϕ and *dt*, and the energy signal-to-noise ratio (*SNR*)

A vertically oriented low *P*- and *S*-seismic velocity anomaly was imaged in the mantle (Ritter et al. 2001, Keyser et al. 2002, Ritter this volume) down to the 400 km depth limit of resolution beneath the 1997-98 Eifel Plume Project seismic network, a dense network of 158 mobile seismic stations centred on the Eifel hotspot in west-central Europe (Ritter et al. 2000). Receiver functions also resolve a depression of the 410 km discontinuity and thinning of the transition zone beneath the Eifel (Grunewald et al. 2001, M. Budweg personal communication 2003, Weber et al. this volume). We test an upwelling model for the Eifel hotspot by analysing shear-wave splitting in seismograms recorded during the seven-month operation of the Eifel network, and comparing the fast directions to those predicted for a simple upwelling.

2 New Data

During the seven-month deployment of the Eifel network, several core-refracted teleseismic shear phases (*SKS*) were recorded. However, only two of these events are analysed because they were of high quality, with energy signal-to-noise ratio (SNR) greater than 20 (Table A1 of Appendix). We used the method of Silver and Chan (1991) as modified by Walker et al. (2004a) to measure the apparent fast polarisation azimuth (ϕ) and delay time between the fast and slow waves (dt) and associated errors (Table A2 of Appendix). We also analysed up to 15 years of recorded data on permanent seismic stations throughout western and central Europe. Figure 1 shows an example of splitting at station WLF (see location in Figure 2). These permanent stations afforded us the possibility of testing between different models of mantle anisotropy: single-layer with a horizontal fast axis, single-layer with a dipping fast axis, and two-layer with horizontal fast axes. In general, we found that the best-fit models for both the dipping-layer and two-layer case fit the data at each station marginally better than the single-layer models, but the minor improvement in fit does not justify the inclusion of extra model parameters (see Walker 2004 for details of the statistics). In addition, these best-fit models for stations that are relatively close together are very different, and the misfit functions used to find them have many local minima. Because the single-layer model only has one local minimum, because these models are very similar for stations that are relatively close together, and because there are only two seismic events for which significant splitting was measured across the Eifel network, we cautiously prefer the single-layer model to estimate the

first-order anisotropy signal beneath the study area (Table A3 of Appendix).

Fig. 2 shows the single-layer splitting ϕ in the Eifel region of west-central Europe (white bars). Numerous stations did not demonstrate any splitting (white crosses), which suggests that no anisotropy exists beneath them or that the fast axis of anisotropy (assuming single layer) is parallel or perpendicular to the backazimuth. The backazimuths of the two Eifel *SKS* events (~70° and ~250°) are ~180° apart. Because some of these "null stations" occur between nearby constrained stations that have ϕ subparallel to the backazimuths, we interpret the lack of splitting to indicate there is anisotropy beneath those stations with a $\phi \approx 70°$.

Fig. 2. (next page) Shear-wave splitting measurements for study area and Eifel region. Short lines indicate the station splitting estimates, with orientation parallel to fast polarisation azimuth (ϕ) and length proportional to delay time (*dt*). Black crosses indicate stations for which no splitting was observed (null stations). Measurements at stations (a-f) are presented in Fig. 3. The thick black line marks the boundary of anomalous topography associated with the uplifted Rhenish Massif. Black lines with hatch marks delineate the Cenozoic rift system: Rhine Graben in the south, the Rur Graben in the northwest, and the Leine Graben in the northeast. Thick lines are deep-seated reverse and wrench faults that separate terranes that formed during the Hercynian orogeny (Edel and Fluck 1989); *RH*-Rhenohercynian and *S*-Saxothuringian sutures. White bodies are volcanic centers with their ages in Ma before present (Illies et al. 1979; Jung and Hoernes 2000). Double-headed arrow in the south indicates *Pn*-velocity fast direction (Smith and Ekström 1999). Double-headed arrow in the north is the regional average least horizontal compressive stress direction (σ_3) (Müller et al. 1997). Black vectors in the upper right indicate the absolute plate motion (and 2σ error bars) in a fixed hotspot reference frame (Gripp and Gordon 2002). Analyses for stations (a-f) are shown in detail in Fig. 3

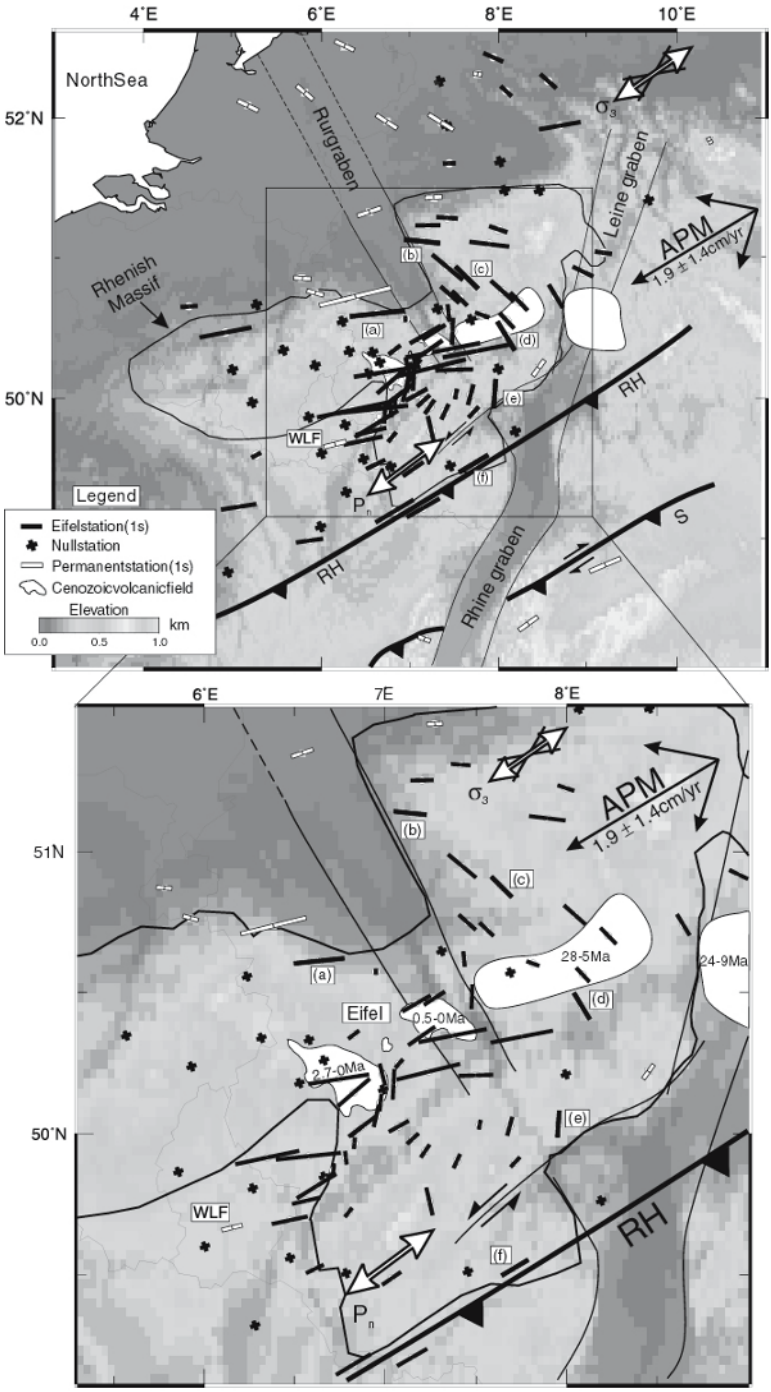
4°E
6°E
8°E
10°E
52°N
50°N
NorthSea
Rurgraben
Leine graben
Rhenish Massif
APM
1.9 ± 1.4cm/yr
σ3
(a)
(b)
(c)
(d)
(e)
(f)
WLF
RH
S
Pn
Rhine graben
Legend
Eifelstation(1s)
Nullstation
Permanentstation(1s)
Cenozoicvolcanicfield
Elevation
km
0.0
0.5
1.0
6°E
7E
8°E
51N
50°N
28-5Ma
24-9Ma
Eifel
0.5-0Ma
2.7-0Ma

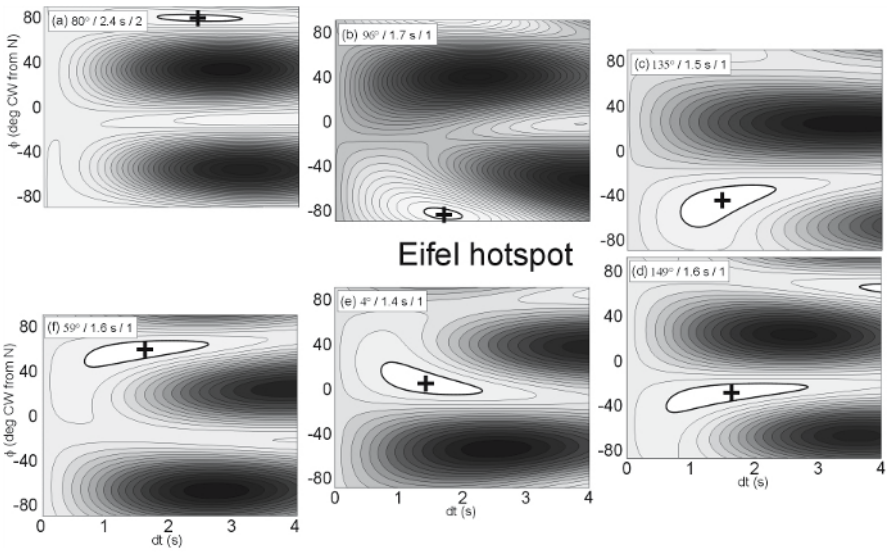

Fig. 3. Examples of station splitting estimates for stations (a-f) showing clockwise rotation of ϕ around the Eifel hotspot. White boxes give the splitting parameters, and number of events analysed. The optimum splitting parameters are indicated by the global minima (pluses) of the misfit grids. The 95% confidence region is indicated in white. See Figure 2 for station locations

3 Tectonic/Geodynamic Interpretation

The general trend of ϕ, for the non-null stations, radially rotates clockwise around the Quaternary volcanic fields from the northwest Eifel to northeast Eifel to southeast Eifel to southwest Eifel (Figures 2 and 3). The high SNR of the waveforms analysed, the small 95 % error bars (average < 20°) on these models, and the gradual nature of the rotation argue against this rotation being a result of noise. This general rotation cannot be explained by a single-layer of fossilised LPO anisotropy within the lithosphere that is parallel to the 70° strike of the Hercynian orogeny, an interpretation that explains many, but not all, of the fast directions beneath Europe's permanent broadband stations (Babuška and Plomerová 1993, Bormann et al. 1993, Silver 1996). The long *dt* close to the hotspot associated with the ENE ϕ could be explained by magma-filled lenses in the lithosphere and/or asthenosphere. However, whereas the northwest-oriented ϕ to the northeast of the Eifel could be explained by vertically oriented lenses (Crampin 1991, Kendall 1994, Gao et al. 1997) that have formed in the lithosphere and asthenosphere perpendicular to the northeast minimum horizontal

compressive stress direction, it is difficult to explain the range of other directions with such a model when the minimum stress direction remains relatively constant throughout the area (Müller et al. 1997). Hence our main interpretation is that the splitting data resolve LPO associated with active mantle deformation of the lower lithosphere/asthenosphere.

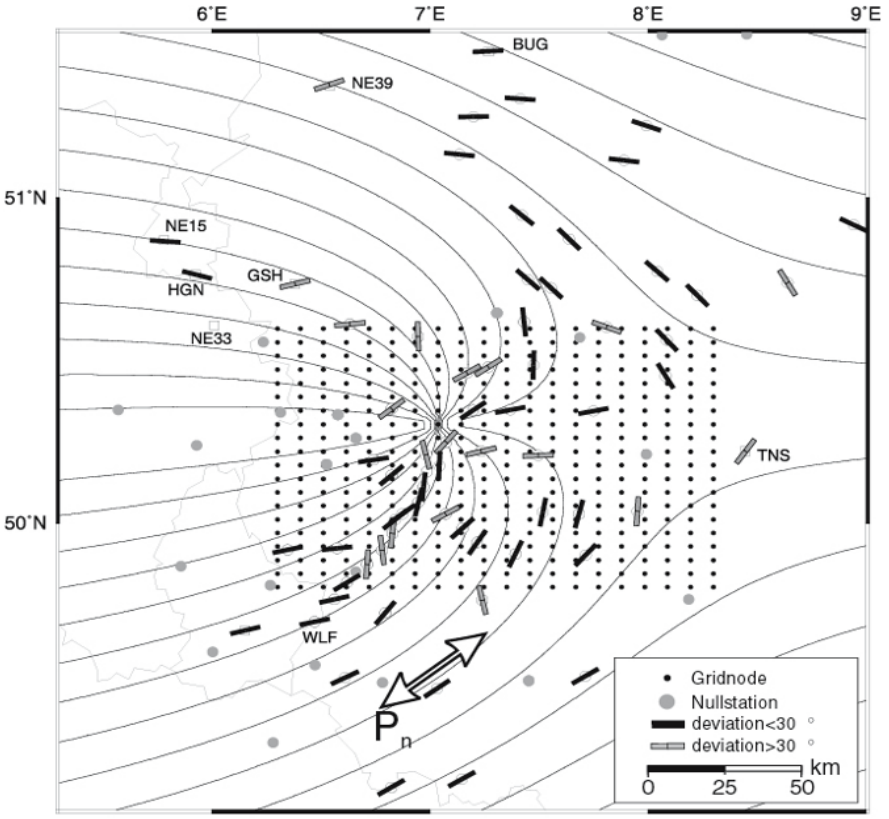

Fig. 4. Testing the parabolic asthenospheric flow (PAF) model for the Eifel hotspot. Lines indicate the station splitting estimates normalised to a uniform *dt* because the PAF model we test is only kinematic. Black dots show the plume-center search grid, which was chosen to cover the *P*-wave and *S*-wave slow velocity anomalies (Ritter et al. 2001, Keyser et al. 2002) while maintaining a 20-node sampling in both X and Y directions for computational reasons. The black curves are the asthenospheric horizontal flow lines of the optimum PAF model, which predict 61 % of the spatial variations in ϕ. This suggests there is a plume-like upwelling beneath the Eifel hotspot and that the flow lines are, for the most part, parallel to the LPO fast directions in the asthenosphere

We test the plume hypothesis by using a hydrodynamical streaming potential function (Milne-Thomson 1968) to estimate the orientations of the flow lines expected for a vertical plume conduit feeding plume material into a tabular horizontal stream (top of asthenosphere). We refer to this model as the parabolic asthenospheric flow (PAF) model. It is assumed that the deformation occurs partly via dislocation creep, and that the ϕ are approximately parallel to the flow directions. A grid search is performed using the ϕ from constrained station estimates over the four model parameters: plume center latitude/longitude, the background asthenospheric flow direction (relative to fixed hotspot reference frame), and the stagnation distance. The latter is the on-axis distance between plume center and the stagnation point of the flow. Our best-fit PAF model has a 61% variance reduction relative to the 70° mean ϕ (Fig. 4). Approximately the same model is recovered if we include the null stations in our grid search and use several different grid-search optimisation techniques (Table 1). In addition, an incremental F-test demonstrates that the more complicated PAF model (four model parameters) explains the data statistically better than a unidirectional model with a fast direction of 70°. Finally, inspection of the marginal misfit functions, random sampling of the misfit space (4-D histogram projections), and trade-off plots (2-D projections) all confirm that the PAF model is well constrained (Fig. 5).

Table 1. Optimum PAF model parameters and associated uncertainties estimated via different techniques (1D-Projection, Bootstrap, stacking). *CLAT/CLON* is the plume center latitude (°N)/longitude (°E). *R* is the stagnation distance (km). *APM* is the direction (degrees clockwise from north) of absolute plate motion relative to the Eifel hotspot. The model is well-constrained by the data, as all techniques yield very similar models and small uncertainty estimates (*YNULLS/NNULLS*=with/without null measurements).

TYPE	CLAT	CLON	R	APM
NNULLS	[50.20 50.31 50.37]	[6.88 7.04 7.09]	[43 59 77]	[254 267 270]
YNULLS	[50.24 50.31 50.33]	[6.88 7.04 7.09]	[43 53 77]	[259 262 270]
NNULLS 1Dproj	[50.21 50.29 50.37]	[6.87 6.98 7.09]	[45 59 83]	[258 266 274]
NNULLS stack	[50.24 50.31 50.37]	[6.88 7.04 7.09]	[43 59 77]	[259 267 270]
NNULLS btstrp	[50.14 50.31 50.48]	[6.60 7.05 7.50]	[48 59 77]	[239 262 285]

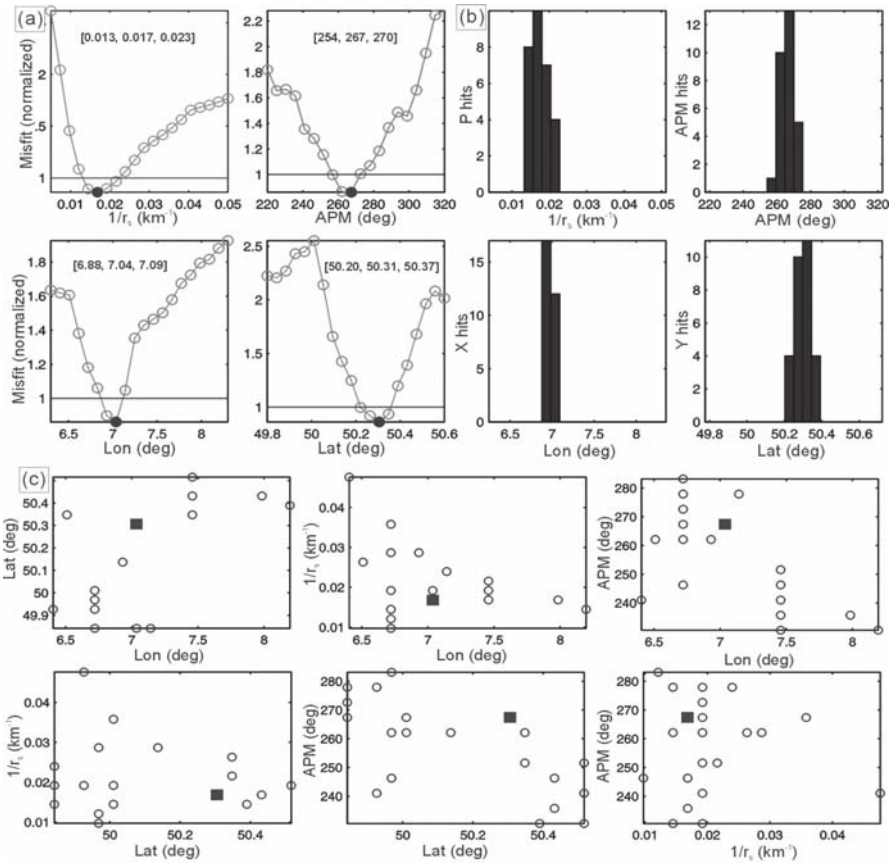

Fig. 5. The resolution of the optimum parabolic asthenospheric flow (PAF) model. We assumed that the local flow direction would be parallel to ϕ, and searched for the optimum PAF model parameters that explained best the observed ϕ. The model parameters are the latitude/longitude of the plume center, the stagnation distance (r_s), and the absolute plate motion direction (*APM*). (a) The marginal misfit curves showing the optimum model (solid circle) and 95 % confidence region as defined by the region beneath the horizontal line. The numbers in brackets are minimum, optimum and maximum values for each parameter. (b) The histograms of the results of randomly targeting nodes in the misfit grid and testing if they are below the 95 % confidence contour. (c) 2-D projections of the locations of local minima that are not possible solutions at the 2σ confidence level (circles) showing the optimum solution (square). These plots indicate that the optimum model, which explains 61 % of the variation in ϕ, is well-resolved

The second order variation (39 % not fit by the PAF model) is interpreted to be due to a combination of data error and model error. The data error will decrease in time after more splitting data have been collected and

analysed around the Eifel hotspot; however, we interpret the model error to be due to several possible factors. Many lines of evidence suggest that the lithosphere beneath the Eifel region is only 50-70 km thick (e.g., Babuška and Plomerová 1993). Fresnel zone calculations can be used to quantify the minimum lateral extent of a homogeneous anisotropic region as a function of depth for two adjacent stations (e.g., Alsina and Snieder 1995). In theory, this could allow one to calculate the maximum depth of the anisotropy, above which the Fresnel zones at adjacent stations do not significantly overlap. However, this approach requires the restrictive assumption of a single anisotropic layer and horizontal symmetry axis, and also requires one to specify what constitutes a "significant overlap". Rümpker and Ryberg (2000) found that for an abrupt lateral change in the parameters of an anisotropic layer at a depth of 100-250 km for a signal period of 8 s, the variation in ϕ/dt that occurs over 30 km could be at least 30°/1.0 s. However, only some of the lateral variations we observe can be explained by such a model, and other lateral variations might be explained better by stronger contrasts in anisotropy and/or anisotropy at shallower depths (Rümpker and Ryberg 2000). For a typical two-layer model, the splitting that occurs in the upper layer has the most effect on the total apparent splitting (e.g., Rümpker and Silver 1998, Saltzer et al. 2000). It is therefore possible to explain lateral variations in apparent splitting by a combination of slowly varying anisotropy below and varying anisotropy above some depth (the depth depending on the rapidity of change in observed splitting). We interpret the remaining 39 % variation not fit by the PAF model as due to additional lithosphere/asthenosphere anisotropy associated with fossilised olivine fabrics, magma-filled lenses, and/or strong active deformation associated with flow complexities or small-scale convection.

For most of the data, the *dt* are around ~1.0-1.5 s. However, the constrained *dt* in and close to the Quaternary Eifel volcanic fields are anomalously long (~2-3.5 s) (Fig. 2). These long *dt* of the predicted plume center may suggest strong anisotropy in the asthenosphere; i.e., the large splitting values just downwind of the plume conduit may be due to the development of LPO associated with the deflection of upwelling plume material by a moving plate (Kaminski and Ribe 2002). However, because the modelled LPO varies dramatically in three dimensions, one must forward model the observed splitting before a valid comparison can be made (e.g., Tommasi 1998, Rümpker et al. 1999, 2003). Nonetheless, if splitting above the hotspot is due to anisotropy in the conduit itself, the olivine fast a-axes are probably not vertical (Rümpker and Silver 2000), which would produce small values of splitting unless there are considerable amounts of water in the conduit (Jung and Karato 2001, Karato 2003).

The large *dt* may also be a result of a poor ability to resolve splitting because ϕ is approximately parallel to the back azimuth (*BAZ*) of the *SKS* phase. The threshold of splitting resolution (deviation between ϕ and *BAZ* below which splitting is not reliably detected) depends on two factors: the signal bandwidth and the signal-to-noise ratio. The higher these two factors are, the lower the threshold. The data have a high SNR, but the bandwidth is only fair (between 0.05-0.2 Hz). However, although the null measurements clearly do not have significant energy on their transverse components, the measurements with large splitting have a significant amount of transverse energy that is highly attenuated after correction using the optimum splitting parameters. Given that these large *dt* are some of the largest observed anywhere in the world for *SKS* phases, and that in some places, our splitting parameters change significantly over short spatial distances, we prefer to present the PAF model as a simple first-order model for the study region. Additional data gathered in the future may perhaps more adequately constrain any additional complexity.

Fig. 6 (Colour Plate 14). Shear-wave splitting measurements across the Eifel hotspot in west-central Europe. Background tomographic map indicates relative seismic *S*-velocity between 100-170 km depth (Keyser et al. 2002). White curves are flow lines of our optimum PAF model, which has a stagnation distance of ~50 km (see text)

Our model has interesting consistencies with other results. Fig. 6 (Colour Plate 14) shows the optimum PAF model superimposed upon an *S*-velocity tomographic image between 100-170 km depth (Keyser et al. 2002). The most obvious consistency is that our optimum conduit location from the grid search is at the center of the slow velocity anomaly and between the two most recently active Eifel volcanic fields, roughly forming a line as expected for a hotspot axis. Our optimum plate motion direction of ~265° also correlates well with both the HS3-NUVEL1A absolute plate motion direction of 239°±44° (Gripp and Gordon 2002), and the average direction (~270°) of fast olivine a-axes inferred from a magnetotelluric investigation that documents a directional dependence of conductivity for depths below 70-90 km (Leibecker et al. 2002). The good correlation with plate motion suggests that asthenospheric flow beneath the Eifel is a passive response to plate motion. Furthermore, a 410-km discontinuity deflection (Grunewald et al. 2001, Weber et al. this volume) and the depth extent of the *P*- and *S*-slow anomalies (Ritter et al. 2001, Keyser et al. 2002, Ritter this volume) suggest the upwelling originates from at least 400 km beneath the Eifel. In fact, a large part of the slow *P*-anomaly beneath the Eifel, which is not as well-resolved as the main anomaly beneath the center

of the Eifel network, plunges towards the northeast as would be expected for a plate dragging upwelling material toward the west-southwest.

4 Eurasian Plate Speed Estimation

Resolving the plate motion of Eurasia with respect to a fixed lower-mantle/hotspot reference frame has been challenging. The success of the PAF model in explaining the data allows us to put constraints on absolute plate motion (APM). If we assume that the vertical extent of the zone where plume material spreads beneath the plate is the same beneath Eifel and Hawaii, and that the ratio of volcanic eruption to plume volumetric flow rates between hotspots remains constant, we can use the stagnation distances for the Hawaiian (Walker et al. 2001) and Eifel models, and the known Pacific plate motion (103 km/Ma) to calculate a 1.6 km/Ma Eurasian absolute plate motion. This estimate is much slower than the 19±5 km/Ma HS3-NUVEL1A Eurasian plate speed (Gripp and Gordon 2002), and if correct, it would suggest an extremely small buoyancy flux. Such a buoyancy flux would not be unreasonable given the necessity for subduction-related return flow in the mantle, but perhaps unlikely given the flow pathways provided by other upwellings with much higher buoyancies. If the ratio of Eifel to Hawaii volcanic eruption rates is instead about an order of magnitude less than the ratio of Eifel to Hawaii plume-flow rates, the calculated speed would be faster and consistent with the HS3-NUVEL1A speed. This is probably the case, because the Eifel excess plume temperature, which partly controls the melt production rate (White and McKenzie 1989), is about one-third that beneath Hawaii.

We calculate a Eurasian plate speed of 12 km/Ma by taking a different approach using the Eifel excess plume temperature of 100-150 K and the plume radius of 50-60 km estimated from the tomographic data (Ritter 2005), standard mantle rheological parameters (Karato and Wu 1993), and geodynamic plume parameters for Hawaii (Ribe and Christensen 1999, Walker et al. 2001). This latter estimate is nearly compatible with the 19±5 km/Ma HS3-NUVEL1A estimate. Using the upper bound of 24 km/Ma, the Eurasian plate would have moved toward the west-southwest a total distance of 65 km over the Eifel hotspot during the last 2.7 Ma of Eifel volcanism, which is the distance between the recently active East and West Eifel volcanic fields (Fig. 6).

5 Conclusions

Our data and modelling imply that a plume-like upwelling exists beneath the Eifel region, and that the upwelling material is being horizontally deflected or sheared by the Eurasian plate toward the west-southwest relative to the fixed lower-mantle hotspot reference frame. This suggests that while the opening of the Rhine Graben provides a pathway for partial melt to erupt at the surface, it is not the driving mechanism responsible for Late Tertiary Eifel magmatism and Rhenish Massif uplift.

The wider implication of our results is that upper-mantle upwellings exhibit simple plume-like characteristics. Furthermore, splitting in the Great Basin of the U.S. (Savage and Sheehan 2000, Walker et al. 2004b) and around the Hawaiian hotspot (Walker et al. 2001, 2003) also suggest simple mantle flow associated with the lateral spreading of upwelling material beneath an active hotspot. Careful observations around these hotspots where additional anisotropy does not overly complicate the signal are making it clear that splitting can be a useful tool to help distinguish between plume-like and alternative sources for hotspots.

Acknowledgments

We thank the Eifel Plume Team and all the other people who helped acquire the Eifel network seismological data set. The following institutions were involved in the operation of the seismic network: GeoForschungsZentrum Potsdam, GeoZentrum Vulkaneifel, European Institute for Geodynamics and Seismology, Geological Survey of Nordrhein-Westfalen, Royal Observatory of Belgium and the Universities of Bochum, Cologne, Göttingen, Potsdam, and Strasbourg. Regional permanent-station broadband data were provided by the ORFEUS, IRIS, and GEOFON data centres. We also thank Jaroslava Plomerová and Thomas Plenefisch for thoughtful reviews. SAC2000 and GMT were used to generate figures. This work was supported by the National Science Foundation.

References

Alsina D, Snieder R (1995) Small-scale sublithospheric continental mantle deformation: Constraints from *SKS* splitting observations. Geophys J Int 123:431-448

Anderson DL (1994) The sublithospheric mantle as the source of continental flood basalts: The case against the continental lithosphere and plume head reservoirs. Earth Planet Sci Lett 123:269-280

Babuška V, Plomerová J (1993) Lithospheric thickness and velocity anisotropy - seismological and geothermal aspects. Tectonophysics 225:79-89

Bijwaard H, Spakman W (1999) Tomographic evidence for a narrow whole mantle plume below Iceland. Earth Planet Sci Lett 166:121-126

Bormann P, Burghardt P-T, Makeyeva LI, Vinnik LP (1993) Teleseismic shear-wave splitting and deformations in Central Europe. Phys Earth Planet Inter 78:157-166

Bormann P, Grunthal G, Kind R, Montag H (1996) Upper mantle anisotropy beneath Central Europe from *SKS* wave splitting: Effects of absolute plate motion and lithosphere-asthenosphere boundary topography. J Geodyn 22:11-32

Crampin S (1991) Wave propagation through fluid-filled inclusions of various shapes: Interpretation of extensive-dilatancy anisotropy. Geophys J Int 104:611-623

Davies GF, Richards MA (1992) Mantle convection. J Geology 100:151-206

Dietz RS (1961) Continent and ocean basin evolution by spreading of the sea floor: Nature 190:854-857

Edel JB, Fluck P (1989) The upper Rhenish Shield basement (Vosges, Upper Rhinegraben and Schwarzwald): main structural features deduced from magnetic, gravimetric and geological data. Tectonophysics 169:303-316

Foulger GR, Pritchard MJ, Julian BR, Evans JR, Allen RM, Nolet G, Morgan WJ, Bergsson BH, Erlendsson P, Jakobsdottir S, Ragnarsson S, Stefansson R, Vogfjord K (2001) Seismic tomography shows that upwelling beneath Iceland is confined to the upper mantle. Geophys J Int 146:504-530

Gao S, Davis PM, Liu H, Slack PD, Rigor AW, Zorin YA, Mordvinova VV, Kozhevnikov VM, Logatchev NA (1997) *SKS* splitting beneath continental rift zones. J Geophys Res 102:22,781-22,797

Gripp AE, Gordon RG (2002) Young tracks of hotspots and current plate velocities. Geophys J Int. 150:321-361

Grunewald S, Weber M, Kind R (2001) The upper mantle under Central Europe: Indications for the Eifel plume. Geophys J Int 147:590-601

Hess H (1962) The history of ocean basins. In Engel, AEJ and others (eds) Petrologic studies: A volume to honor AF Buddington, Boulder CO, Geological Society of America pp 599-620

Illies JH, Prodehl, C, Schmincke H-U, Semmel A (1979) The Quaternary uplift of the Rhenish shield in Germany, Tectonophysics, 61:197-225

Jung S, Hoernes S (2000) The major- and trace element and isotope (Sr, Nd, O) geochemistry of Cenozoic alkaline rift-type volcanic rocks from the Rhön area (central Germany): Petrology, mantle source characteristics and implications for asthenosphere-lithosphere interactions Journal of Volcanology and Geothermal Research 99:27-53

Jung H, Karato S-I (2001) Water-induced fabric transitions in olivine. Science 293:1460-1463

Kaminski E, Ribe E (2002) Timescales for the evolution of seismic anisotropy in mantle flow. G-cubed 3:101029/2001GC000222

Karato S-I, Wu P (1993) Rheology of the upper mantle: A synthesis. Science 260:771-777

Karato S-I (2003) Mapping water content in the upper mantle. In Eiler J (ed) Inside the Subduction Factory. Geophys Monograph 138, American Geophys Union pp 135-152

Kendall J-M (1994) Teleseismic arrivals at a mid-ocean ridge: Effects of mantle melt and anisotropy. Geophys Res Lett 21:301-304

Keyser M, Ritter JRR, Jordan M (2002) 3D shear-wave velocity structure of the Eifel plume, Germany. Earth Planet Sci Lett 203:59-82

King SD, Anderson DL (1998) Edge-driven convection. Earth Planet Sci Lett 160:289-296

Leibecker J, Gatzemeier A, Honig M, Kuras O, Soyer W (2002) Evidence of electrical anisotropic structures in the lower crust and upper mantle beneath the Rhenish Shield. Earth Planet Sci Lett 202:289-302

Li X, Kind R, Yuan X, Sobolev SV, Hanka W, Ramesh DS, Gu Y, Dziewonski AM (2003) Seismic observation of narrow plumes in the oceanic upper mantle. Geophys Res Lett 30:1334, doi:101029/2002GL015411

Milne-Thomson LM (1968) Theoretical Hydrodynamics. Macmillan, New York, ed 5, pp211-213

Minster JB, Jordan TH (1978) Present-day plate motions. J Geophys Res 83:5331-5354

Montagner JP (2002) Upper mantle low anisotropy channels below the Pacific Plate. Earth Planet Sci Lett 202:263-274

Montelli R, Nolet G, Dahlen FA, Masters G, Engdahl ER, Huang SH (2004) Finite-frequency tomography reveals a variety of plumes in the mantle. Science 303:338-343

Morgan WJ (1971) Convection plumes in the lower mantle. Nature 230:42-43

Müller B, Wehrle V, Fuchs K (1997) The 1997 release of the world stress map. http://wwwworld-stress-map.org/

Ribe N, Christensen U (1999) The dynamical origin of Hawaiian volcanism. Earth Planet Sci Lett 171:517-531

Ritsema J, Allen RM (2003) The elusive mantle plume. Earth Planet Sci Lett 207:1-12

Ritter JRR (2005) Small-scale mantle plumes: Imaging and geodynamic aspects. In Wenzel, F (ed) Modern perspectives in seismology, Springer, Heidelberg, 69-94

Ritter JRR, Achauer U, Christensen UR, The Eifel Plume Team (2000) The teleseismic tomography experiment in the Eifel Region, Central Europe: Design and First Results. Seism Res Lett 71:437-443

Ritter JRR, Jordan M, Christensen UR, Achauer U (2001) A mantle plume below the Eifel volcanic fields, Germany. Earth Planet Sci Lett 186:7-14

Rümpker G, Ryberg T (2000) New Fresnel-zone estimates for shear-wave splitting observations from finite-difference modeling. Geophys Res Lett 27:2005-2008

Rümpker G, Ryberg T, Bock G, DESERT Seismology Group (2003) Boundary-layer mantle flow under the Dead Sea transform fault inferred from seismic anisotropy. Nature 425:497-501

Rümpker G, Silver PG (1998) Apparent shear-wave splitting parameters in the presence of vertically varying anisotropy. Geophys J Int 135:790-800

Rümpker G, Silver PG (2000) Calculating splitting parameters for plume-type anisotropic structures of the upper mantle. Geophys J Int 143:507-520

Rümpker G, Tommasi A, Kendall J-M (1999) Numerical simulations of depth-dependent anisotropy and frequency-dependent wave propagation effects, J. Geophys. Res. 104: 23141-23153

Saltzer R, Gaherty J, Jordan TH (2000) How are vertical shear wave splitting measurements affected by variations in the orientation of azimuthal anisotropy with depth? Geophys J Int 141:374-390

Savage MK (1999) Seismic anisotropy and mantle deformation: What have we learned from shear wave splitting? Rev Geophys 103:65-106

Savage MK, Sheehan AF (2000) Seismic anisotropy and mantle flow from the Great Basin to the Great Plains, western United States. J Geophys Res 105:13,715-13,734

Schutt D, Humphreys ED (2001) Evidence for a deep asthenosphere beneath North America from western United States *SKS* splits. Geology 29:291-294

Silver P (1996) Seismic anisotropy beneath the continents: Probing the depths of geology. Ann Rev Earth Planet Sci 24:385-432

Silver PG, Chan WW (1991) Shear-wave splitting and subcontinental mantle deformation. J Geophys Res 96:16,429-16,454

Sleep N (1990) Hotspots and mantle plumes: Some phenomenology. J Geophys Res 95:6715-6736

Smith AD, Lewis C (1999) The planet beyond the plume hypothesis. Earth Science Rev 48:135-182

Smith GP, Ekström G (1999) A global study of *Pn* anisotropy beneath continents J Geophys Res 104:963-980

Tommasi A (1998) Forward modeling of the development of seismic anisotropy in the upper mantle. Earth Planet Sci Lett 160:1-18

Vinnik LP, Makeyeva LI, Milev A, Usenko AYu (1992) Global patterns of azimuthal anisotropy and deformations in the continental mantle. Geophys J Int 111:433-447

Walker KT (2004) Exploring problems in tectonics and geodynamics with seismology. PhD thesis, Stanford University, 273 pp

Walker KT, Bokelmann GHR, Klemperer SL (2001) Shear-wave splitting to test mantle deformation models around Hawaii. Geophys Res Lett 28:4319-4322

Walker KT, Bokelmann GHR, Klemperer SL (2003) Shear-wave splitting to test mantle deformation models around Hawaii, Reply. Geophys Res Lett 30:1676, doi:101029/2002GL016712

Walker KT, Nyblade AA, Bokelmann GHR, Klemperer SL, Owens, TJ (2004a) On the relationship between extension and anisotropy: Constraints from shear-wave splitting across the East African Plateau. J Geophys Res 109:B0802, 101029/2003JB002866

Walker KT, Bokelmann GHR, Klemperer SL (2004b) Shear-wave splitting reveals mantle upwelling beneath eastern Nevada, USA. Earth Planet Sci Lett, 222:529-542

White RS, McKenzie DP (1989) Magmatism at rift zones: the generation of volcanic continental margins and flood basalts. J Geophys Res 94:7685-7729

Wolfe CJ, Bjarnason GC, VanDecar JC, Solomon SC (2002) Assessing the depth resolution of tomographic models of upper mantle structure beneath Iceland. Geophys Res Lett 29:101029/2001GL013657

Wolfe CJ, Silver PG (1998) Seismic anisotropy of oceanic upper mantle: Shear-wave splitting methodologies and observations. J Geophys Res 103:749-771

Appendix

Table A1. List of teleseismic events analysed for apparent shear-wave splitting. The first 106 "*RNE*" events were analysed on the regional network throughout West-central Europe. Because of the large dimensions of the study region, sometimes several phases were analysed for a single event. For these events, only the dominant phase is indicated. The last two "*E*" events were analysed across the temporary seven-month Eifel Network. These data are from the ANSS earthquake catalogue.

NUM	DATE	ELAT	ELON	DEP	MAG	PHASE
RNE1	90:197:70	15.679	121.172	25	6.5	SKS
RNE2	90:217:70	29.551	137.630	496	6.5	SKS
RNE3	90:290:01	-10.970	-70.776	598	6.8	SKS
RNE4	91:040:01	-9.929	159.139	10	6.9	PKS
RNE5	91:095:50	-5.982	-77.094	19	6.5	SKS
RNE6	91:139:90	1.156	122.957	33	6.8	SKS
RNE7	91:187:71	-13.108	-72.187	104	6.5	SKS
RNE8	91:287:71	-9.094	158.442	23	7.1	PKS
RNE9	92:270:02	1.289	129.118	27	6.5	SKS
RNE10	92:326:62	-56.665	-26.405	20	6.6	SKKS
RNE11	93:019:91	38.649	133.465	448	6.6	S
RNE12	93:065:50	-10.972	164.181	20	7.1	PKS
RNE13	93:109:92	4.015	128.204	23	6.7	SKS
RNE14	93:131:11	7.219	126.570	58	6.6	SKS
RNE15	93:138:81	19.914	122.450	168	6.8	SKS
RNE16	93:145:50	-22.671	-66.543	221	7.0	SKS
RNE17	93:157:71	15.823	146.595	13	6.6	SKS
RNE18	93:220:00	12.982	144.801	59	7.1	SKS
RNE19	93:249:90	-4.641	153.231	49	6.6	SKS
RNE20	93:284:41	32.020	137.832	350	6.9	SKS
RNE21	94:010:01	-13.339	-69.446	596	6.9	SKS
RNE22	94:021:10	1.015	127.733	19	7.2	SKS
RNE23	94:046:61	-4.967	104.302	23	7.0	SKS
RNE24	94:108:81	-6.470	154.934	26	6.7	PKS
RNE25	94:119:90	-28.299	-63.252	561	6.9	SKS
RNE26	94:130:00	-28.501	-63.096	600	6.9	SKS
RNE27	94:153:31	-10.477	112.835	18	7.2	SKS
RNE28	94:160:00	-13.841	-67.553	631	8.2	SKS
RNE29	94:202:21	42.340	132.865	471	7.3	S
RNE30	94:206:62	-56.362	-27.365	81	6.6	SKKS
RNE31	94:231:11	-26.642	-63.421	563	6.5	SKS
RNE32	95:098:81	21.833	142.691	267	6.7	SKS
RNE33	95:110:00	6.279	126.777	94	6.6	SKS
RNE34	95:111:10	12.047	125.920	27	6.9	SKS
RNE35	95:113:30	12.390	125.396	24	6.6	SKS

Table A1. (cont.)

NUM	DATE	ELAT	ELON	DEP	MAG	PHASE
RNE36	95:122:20	-3.792	-76.917	97	6.7	SKS
RNE37	95:125:50	12.626	125.297	16	7.0	SKS
RNE38	95:175:50	-3.959	153.930	386	6.8	PKS
RNE39	95:207:72	2.534	127.681	65	6.7	SKS
RNE40	95:211:10	-23.340	-70.294	45	6.6	SKS
RNE41	95:228:81	-5.429	153.773	18	6.6	PKS
RNE42	95:235:50	18.856	145.218	594	7.1	SKKS
RNE43	95:266:62	-10.680	-78.581	59	6.5	SKS
RNE44	95:276:60	-2.750	-77.881	24	7.0	SKS
RNE45	95:279:91	-2.045	101.436	33	6.8	SKS
RNE46	95:291:11	27.929	130.175	28	7.1	SKS
RNE47	95:305:50	-28.906	-71.417	19	6.7	SKS
RNE48	95:359:90	-6.903	129.151	141	7.1	SKS
RNE49	96:001:10	0.729	119.931	24	7.9	SKS
RNE50	96:052:21	-9.593	-79.587	10	7.5	SKS
RNE51	96:065:51	24.092	122.215	29	6.5	SKS
RNE52	96:076:62	28.983	138.944	477	6.6	SKS
RNE53	96:110:00	-23.944	-70.093	49	6.6	SKS
RNE54	96:161:10	17.444	145.458	149	6.5	SKS
RNE55	96:163:31	12.614	125.154	33	7.1	SKS
RNE56	96:198:81	1.016	120.254	33	6.6	SKS
RNE57	96:204:41	1.000	120.450	33	7.0	SKS
RNE58	96:215:51	-10.769	161.445	33	6.9	PKS
RNE59	96:264:40	9.454	126.334	33	6.6	SKS
RNE60	96:264:40	9.463	126.284	33	6.6	SKS
RNE61	96:317:71	-14.993	-75.675	33	7.7	SKS
RNE62	97:023:30	-21.999	-65.719	276	7.1	SKS
RNE63	97:070:01	7.742	127.647	10	6.9	SKS
RNE64	97:111:11	-12.584	166.676	33	7.8	PKS
RNE65	97:113:31	13.986	144.901	100	6.5	SKS
RNE66	97:142:20	18.684	-101.604	70	6.5	SKS
RNE67	97:149:91	-35.964	-102.511	10	6.5	PKS
RNE68	97:187:71	-30.058	-71.872	19	6.8	SKS
RNE69	97:288:80	-30.933	-71.220	58	7.1	SKS
RNE70	97:301:10	-4.368	-76.681	112	7.2	SKKS
RNE71	97:329:91	1.241	122.536	24	7.0	SKS
RNE72	97:332:22	-13.740	-68.788	586	6.7	SKS
RNE73	98:010:00	14.374	-91.473	33	6.6	SKS
RNE74	98:030:01	-23.913	-70.207	42	7.1	SKS
RNE75	98:093:32	-8.148	-74.238	164	6.6	SKS
RNE76	98:141:10	0.207	119.584	33	6.7	SKS
RNE77	98:142:20	-17.731	-65.431	24	6.6	SKS
RNE78	98:197:71	-11.040	166.160	110	7.0	PKS

Table A1. (cont.)

NUM	DATE	ELAT	ELON	DEP	MAG	PHASE
RNE79	98:210:01	-2.693	138.901	33	6.7	SKKS
RNE80	98:232:20	28.932	139.329	440	7.1	SKS
RNE81	98:245:50	5.410	126.764	50	6.8	SKS
RNE82	98:246:61	-29.450	-71.715	27	6.6	SKS
RNE83	98:271:11	-8.194	112.413	151	6.6	SKS
RNE84	98:333:31	-2.071	124.891	33	7.7	SKS
RNE85	99:093:30	-16.660	-72.662	87	6.8	SKS
RNE86	99:098:81	43.607	130.350	565	7.1	S
RNE87	99:319:90	-1.339	88.976	10	7.0	SKS
RNE88	99:334:40	-18.901	-69.171	128	6.6	SKS
RNE89	99:345:51	15.766	119.740	33	7.3	SKS
RNE90	00:088:81	22.338	143.730	126	7.6	SKS
RNE91	00:114:40	-28.307	-62.990	608	7.0	SKS
RNE92	00:125:50	-1.105	123.573	26	7.6	SKS
RNE93	00:133:31	-23.548	-66.452	225	7.2	SKS
RNE94	00:156:61	-4.721	102.087	33	7.9	SKS
RNE95	00:159:92	-4.612	101.905	33	6.7	SKS
RNE96	00:219:90	28.856	139.556	394	7.4	SKS
RNE97	00:222:21	18.198	-102.480	45	6.5	SKS
RNE98	00:312:20	-55.627	-29.876	10	6.8	SKS
RNE99	01:055:50	1.271	126.249	35	7.1	SKS
RNE100	01:099:90	-32.668	-73.109	11	6.7	SKKS
RNE101	01:177:70	-17.745	-71.649	24	6.8	SKS
RNE102	01:184:41	21.641	142.984	290	6.5	SKS
RNE103	01:186:61	-16.086	-73.987	62	6.6	SKS
RNE104	01:188:80	-17.543	-72.077	33	7.6	SKS
RNE105	01:285:51	12.686	144.980	37	7.0	SKS
RNE106	01:352:20	23.917	122.774	14	6.9	SKS
E1	97:332:22	-13.740	-68.788	586	6.7	SKS
E2	97:141:05	0.207	119.584	33	6.7	SKS

Table A2. (next page) Apparent *SKS* splitting measurements for stations of the 1997-98 Eifel Plume Experiment. The asterisks indicate null measurements, which were determined manually (see text for more details). Events 1 and 2 are the Nov. 28, 1997 and May 21, 1998 events, respectively (Table 1). *SNR* is the ratio of the radial signal to the transverse energy, which is >20 except for phases with very large time windows (to analyse *SKS* and *SKKS* simultaneously) or where the noise window contained an event phase. *FPA* and *DT* are the fast polarisation azimuth and delay time (and 2σ error bars). *NDF* is the number of degrees of freedom calculated directly from the data via the method of Silver and Chan (1991).

Table A2.

STAT	STLA	STLO	EVTE	VLA	EVLO	MAG	DEP	DEL	BAZ	SNR	IPA	FPA	-2S	+2S	DT	-2S	+2S	NDF
A02	52.422	7.935	2	0.21	119.58	6.7	33	102	72	24.2	72	-66	-11	14	1.04	-0.24	0.28	13
A03	52.258	8.556	2	0.21	119.58	6.7	33	102	73	151.8	73	132	-19	14	0.96	-0.32	0.40	10
A04	52.188	8.081	2	0.21	119.58	6.7	33	102	72	121.7	72	-47	-35	19	0.72	-0.34	0.62	9
A05	51.949	8.684	2	0.21	119.58	6.7	33	102	73	91.6	73	80	-2	5	2.00	-0.76	0.84	12
A06	51.683	7.441	2	0.21	119.58	6.7	33	103	72	70.9	72	89	-10	60	0.62	-0.40	0.72	11
*A07	51.696	8.010	2	0.21	119.58	6.7	33	103	72	62.7	72	80	-5	15	2.04	-1.66	1.96	7
*A09	51.492	8.064	2	0.21	119.58	6.7	33	103	72	48.0	72	-13	-180	180	4.00	-4.00	0.00	8
*A10	51.494	8.453	2	0.21	119.58	6.7	33	102	73	49.1	73	76	-180	180	4.00	-4.00	0.00	10
A11	51.300	7.414	2	0.21	119.58	6.7	33	103	72	129.0	72	-86	-8	18	0.96	-0.38	0.52	9
A12	51.245	7.199	2	0.21	119.58	6.7	33	103	72	244.1	72	89	-5	12	1.16	-0.42	0.50	12
A13	51.131	7.135	2	0.21	119.58	6.7	33	103	72	34.3	72	-84	-4	7	1.70	-0.30	0.32	13
A14	50.947	7.421	2	0.21	119.58	6.7	33	103	72	15.6	72	-50	-5	8	1.92	-0.30	0.36	21
A15	50.750	7.449	2	0.21	119.58	6.7	33	103	72	32.9	72	-48	-7	7	1.24	-0.20	0.26	29
A18	50.564	8.086	2	0.21	119.58	6.7	33	103	73	100.4	73	-43	-25	15	0.98	-0.42	0.64	9
A19	50.605	7.810	2	0.21	119.58	6.7	33	103	72	35.9	72	-70	-24	38	0.68	-0.32	0.64	11
A20	50.702	8.226	2	0.21	119.58	6.7	33	103	73	36.4	73	-44	-14	12	1.22	-0.40	0.50	9
A21	50.776	8.040	2	0.21	119.58	6.7	33	103	72	30.2	72	-48	-16	14	1.52	-0.54	0.64	9
*A31	52.258	7.332	2	0.21	119.58	6.7	33	103	72	159.1	72	-20	-2	3	2.46	-1.26	1.50	14
*A33	51.951	7.407	2	0.21	119.58	6.7	33	103	72	37.9	72	83	-7	11	2.08	-1.30	1.92	7
A50	51.218	7.993	2	0.21	119.58	6.7	33	103	72	76.9	72	-71	-26	44	0.92	-0.54	1.02	10
A51	51.113	7.889	2	0.21	119.58	6.7	33	103	72	160.1	72	-83	-11	20	1.86	-0.80	1.04	9
A53	50.874	7.638	2	0.21	119.58	6.7	33	103	72	92.2	72	135	-24	15	1.48	-0.68	0.84	10
A54	50.724	7.555	2	0.21	119.58	6.7	33	103	72	37.6	72	-46	-37	19	1.00	-0.50	0.88	9
A80	50.740	8.639	2	0.21	119.58	6.7	33	103	73	104.2	73	-31	-24	11	1.28	-0.86	1.08	9
A82	51.051	9.176	2	0.21	119.58	6.7	33	102	73	52.2	73	-82	-13	36	0.84	-0.44	0.72	9
*A83	51.426	9.684	2	0.21	119.58	6.7	33	102	74	155.3	74	-17	-180	180	2.32	-2.32	1.64	11
A85	50.917	8.943	2	0.21	119.58	6.7	33	102	73	46.7	73	-64	-21	25	1.12	-0.48	0.52	9
B01	50.614	6.632	2	0.21	119.58	6.7	33	104	71	45.4	71	84	-4	8	2.56	-0.84	0.90	14
*B01	50.614	6.632	1	-13.74	-68.79	6.7	586	91	250	56.5	70	78	-3	6	2.38	-0.94	1.58	8
*B02	50.576	6.945	2	0.21	119.58	6.7	33	104	72	65.8	72	74	-180	180	1.64	-5.52	2.36	14
B02	50.576	6.945	1	-13.74	-68.79	6.7	586	91	250	68.1	70	-2	-14	70	0.32	-0.24	0.90	15
*B03	50.648	7.307	2	0.21	119.58	6.7	33	103	72	96.5	72	156	-81	7	1.08	-1.08	2.92	9
*B03	50.648	7.307	1	-13.74	-68.79	6.7	586	91	250	29.9	70	58	-75	13	0.70	-0.66	1.94	10
*B04	50.572	7.686	2	0.21	119.58	6.7	33	103	72	11.8	72	-33	-71	16	0.62	-0.56	1.70	24
*B08	50.463	7.168	2	0.21	119.58	6.7	33	103	72	87.2	72	-9	-3	6	2.18	-0.76	0.82	13
B08	50.463	7.168	1	-13.74	-68.79	6.7	586	91	250	132.7	70	60	-1	3	1.70	-0.28	0.26	21
B09	50.488	7.475	1	-13.74	-68.79	6.7	586	92	250	54.7	70	2	-8	15	1.28	-0.52	0.66	12
*B10	50.335	6.577	2	0.21	119.58	6.7	33	104	71	46.6	71	169	-180	180	1.74	-5.62	2.26	7
*B10	50.335	6.577	1	-13.74	-68.79	6.7	586	91	250	45.8	70	-21	-180	180	3.66	-3.66	0.32	13
B11	50.353	6.823	2	0.21	119.58	6.7	33	104	72	39.1	72	52	-44	14	0.74	-0.44	0.74	14
*B11	50.353	6.823	1	-13.74	-68.79	6.7	586	91	250	22.2	70	-13	-180	180	2.08	-2.08	1.88	8
B13	50.350	7.368	1	-13.74	-68.79	6.7	586	91	250	70.9	70	79	-2	3	3.56	-0.54	0.44	14
B14	50.346	7.749	2	0.21	119.58	6.7	33	103	72	126.8	72	79	-2	4	3.26	-0.80	0.70	22
B15	50.212	6.981	1	-13.74	-68.79	6.7	586	91	250	327.3	70	-14	-2	6	1.16	-0.52	0.78	11
*B16	50.222	7.235	2	0.21	119.58	6.7	33	104	72	48.3	72	-10	-6	74	1.10	-1.00	2.84	10
B16	50.222	7.235	1	-13.74	-68.79	6.7	586	91	250	30.8	70	76	-1	3	3.40	-0.60	0.50	14
B17	50.209	7.495	2	0.21	119.58	6.7	33	103	72	48.9	72	88	-2	5	1.78	-0.32	0.34	24
*B19	50.181	6.524	2	0.21	119.58	6.7	33	104	71	93.2	71	58	-180	180	1.36	-5.24	2.64	7
*B19	50.181	6.524	1	-13.74	-68.79	6.7	586	91	250	50.5	70	74	-180	180	3.76	-7.60	0.24	8
B22	50.033	7.518	1	-13.74	-68.79	6.7	586	91	250	80.8	70	11	-21	48	0.48	-0.24	0.70	10
*B23	49.916	6.346	2	0.21	119.58	6.7	33	104	71	31.0	71	-3	-14	81	0.42	-0.40	2.22	26
B23	49.916	6.346	1	-13.74	-68.79	6.7	586	91	249	66.0	69	78	-3	4	3.40	-0.72	0.58	12
*B24	49.921	6.574	2	0.21	119.58	6.7	33	104	71	31.9	71	15	-180	180	0.40	-4.30	3.60	16
B24	49.921	6.574	1	-13.74	-68.79	6.7	586	91	250	78.0	70	84	-2	4	3.44	-0.34	0.28	11
B26	49.903	7.392	2	0.21	119.58	6.7	33	104	72	106.5	72	36	-15	14	1.26	-0.36	0.36	10
B26	49.903	7.392	1	-13.74	-68.79	6.7	586	91	250	181.6	70	172	-9	71	1.12	-1.04	1.80	8
B27	49.900	7.713	2	0.21	119.58	6.7	33	103	72	39.6	72	43	-45	22	0.68	-0.36	0.78	10
B29	49.719	6.794	2	0.21	119.58	6.7	33	104	72	67.9	72	39	-36	22	0.64	-0.28	0.58	22
*B29	49.719	6.794	1	-13.74	-68.79	6.7	586	91	250	40.8	70	73	-180	180	3.90	-3.90	0.08	8
B30	49.759	7.240	2	0.21	119.58	6.7	33	104	72	137.6	72	1	-12	51	0.88	-0.58	1.12	8
B30	49.759	7.240	1	-13.74	-68.79	6.7	586	91	250	154.6	70	165	-1	5	1.86	-0.84	0.70	16
*B33	49.761	8.186	2	0.21	119.58	6.7	33	103	73	63.5	73	-7	-180	180	0.50	-0.50	3.42	9
B34	49.521	7.712	2	0.21	119.58	6.7	33	103	72	26.7	72	59	-15	10	1.60	-0.94	1.04	9
B35	49.516	6.609	2	0.21	119.58	6.7	33	104	72	24.7	72	64	-56	8	1.02	-0.88	1.32	14
*B36	49.501	6.782	1	-13.74	-68.79	6.7	586	91	250	20.1	70	-22	-180	180	1.76	-1.76	2.18	10
B37	49.482	7.032	1	-13.74	-68.79	6.7	586	91	250	28.8	70	55	-35	12	1.20	-0.90	0.98	13
*B38	49.507	7.453	2	0.21	119.58	6.7	33	104	72	17.0	72	-12	-180	180	1.22	-1.22	2.72	13
*B38	49.507	7.453	1	-13.74	-68.79	6.7	586	91	250	35.7	70	67	-180	180	1.86	-1.86	2.08	12
B40	49.171	6.822	2	0.21	119.58	6.7	33	104	72	25.1	72	59	-6	6	2.10	-0.76	0.74	9
B41	49.197	7.145	2	0.21	119.58	6.7	33	104	72	27.5	72	60	-33	11	1.80	-1.46	2.14	13
B43	50.027	7.683	2	0.21	119.58	6.7	33	103	72	114.7	72	17	-12	18	1.18	-0.42	0.42	8
B43	50.027	7.683	1	-13.74	-68.79	6.7	586	91	251	65.7	71	9	-20	46	0.74	-0.52	0.90	10
B44	50.036	7.950	2	0.21	119.58	6.7	33	103	73	65.9	73	4	-10	20	1.42	-0.72	0.90	10

Table A2. (cont.)

STAT	STLA	STLO	EVTE	VLA	EVLO	MAG	DEP	DEL	BAZ	SNR	IPA	FPA	-2S	+2S	DT	-2S	+2S	NDF
*B46	50.213	7.992	2	0.21	119.58	6.7	33	103	73	65.0	73	-13	-180	180	1.68	-1.68	2.26	9
B49	50.454	8.081	2	0.21	119.58	6.7	33	103	73	106.9	73	-31	-17	10	1.64	-1.00	1.24	9
*B50	50.621	7.431	2	0.21	119.58	6.7	33	103	72	128.4	72	80	-5	28	2.10	-1.78	1.86	7
B50	50.621	7.431	1	-13.74	-68.79	6.7	586	92	250	113.0	70	-6	-7	21	0.82	-0.50	0.70	10
*B51	50.482	7.267	2	0.21	119.58	6.7	33	103	72	126.1	72	160	-180	180	4.00	-7.84	0.00	6
B51	50.482	7.267	1	-13.74	-68.79	6.7	586	91	250	76.1	70	57	-10	7	1.34	-0.64	0.66	11
*B52	50.349	7.197	2	0.21	119.58	6.7	33	104	72	82.3	72	75	-180	180	3.48	-3.48	0.50	13
B52	50.349	7.197	1	-13.74	-68.79	6.7	586	91	250	42.5	70	55	-8	7	1.66	-0.60	0.66	12
B53	50.251	7.074	2	0.21	119.58	6.7	33	104	72	67.2	72	-8	-5	9	2.42	-1.20	1.48	13
B53	50.251	7.074	1	-13.74	-68.79	6.7	586	91	250	20.1	70	56	-27	10	1.18	-0.76	0.96	10
B54	50.177	7.043	1	-13.74	-68.79	6.7	586	91	250	13.9	70	3	-6	9	1.62	-0.42	0.48	11
*B55	50.158	6.985	2	0.21	119.58	6.7	33	104	72	91.2	72	8	-25	65	1.50	-1.46	2.44	6
*B55	50.158	6.985	1	-13.74	-68.79	6.7	586	91	250	39.9	70	-3	-180	180	0.96	-0.96	2.98	5
B56	50.112	6.971	2	0.21	119.58	6.7	33	104	72	12.3	72	48	-56	21	1.14	-0.88	1.84	18
B56	50.112	6.971	1	-13.74	-68.79	6.7	586	91	250	19.1	70	4	-10	20	1.00	-0.40	0.52	10
B57	50.065	6.947	2	0.21	119.58	6.7	33	104	72	68.7	72	13	-26	55	1.22	-0.98	2.10	8
*B57	50.065	6.947	1	-13.74	-68.79	6.7	586	91	250	47.0	70	78	-5	7	4.00	-3.76	0.00	12
B58	50.028	6.872	2	0.21	119.58	6.7	33	104	72	44.0	72	53	-13	10	1.82	-0.78	0.98	18
B59	50.010	6.839	1	-13.74	-68.79	6.7	586	91	250	34.7	70	50	-27	11	0.82	-0.40	0.56	17
B60	49.967	6.827	2	0.21	119.58	6.7	33	104	72	53.4	72	11	-21	54	0.48	-0.26	0.72	19
B60	49.967	6.827	1	-13.74	-68.79	6.7	586	91	250	57.0	70	4	-15	48	0.62	-0.36	0.78	14
B61	49.915	6.780	2	0.21	119.58	6.7	33	104	72	323.4	72	-7	-10	79	0.74	-0.68	2.50	11
*B61	49.915	6.780	1	-13.74	-68.79	6.7	586	91	250	59.7	70	48	-180	180	0.46	-0.46	3.46	4
B62	49.871	6.711	2	0.21	119.58	6.7	33	104	72	222.4	72	4	-17	61	0.68	-0.48	1.30	9
*B62	49.871	6.711	1	-13.74	-68.79	6.7	586	91	250	52.5	70	167	-1	3	2.04	-0.44	0.32	18
*B63	49.848	6.659	1	-13.74	-68.79	6.7	586	91	250	45.5	70	75	-1	4	3.26	-0.94	0.72	14
B64	49.814	6.618	2	0.21	119.58	6.7	33	104	72	53.8	72	58	-4	6	2.44	-0.62	0.68	13
*B64	49.814	6.618	1	-13.74	-68.79	6.7	586	91	250	19.8	70	153	-9	7	2.40	-1.90	1.60	10
*B65	49.761	6.560	2	0.21	119.58	6.7	33	104	71	132.2	71	65	-180	180	1.86	-1.86	2.08	5
B65	49.761	6.560	1	-13.74	-68.79	6.7	586	91	250	80.5	70	77	-4	38	1.52	-1.30	1.66	7
*B66	49.691	6.470	2	0.21	119.58	6.7	33	104	71	32.5	71	74	-180	180	4.00	-4.00	0.00	13
B66	49.691	6.470	1	-13.74	-68.79	6.7	586	91	250	56.0	70	78	-4	13	1.88	-1.20	1.10	11
*B67	49.556	6.472	2	0.21	119.58	6.7	33	104	71	74.9	71	170	-180	180	0.84	-4.74	3.16	11
*B70	50.262	6.660	2	0.21	119.58	6.7	33	104	71	141.9	71	62	-31	10	3.20	-2.84	0.78	10
*B70	50.262	6.660	1	-13.74	-68.79	6.7	586	91	250	130.4	70	73	-2	5	3.40	-2.44	0.58	8
*B71	50.195	6.740	2	0.21	119.58	6.7	33	104	72	80.4	72	41	-180	180	0.66	-0.66	3.26	8
B71	50.195	6.740	1	-13.74	-68.79	6.7	586	91	250	23.8	70	81	-4	7	3.20	-1.04	0.78	10
B72	50.148	6.824	2	0.21	119.58	6.7	33	104	72	83.3	72	49	-16	12	2.22	-0.94	1.08	8
*B72	50.148	6.824	1	-13.74	-68.79	6.7	586	91	250	36.5	70	52	-180	180	0.66	-4.56	3.34	4
B73	50.027	7.071	2	0.21	119.58	6.7	33	104	72	7.3	72	56	-9	8	2.04	-0.86	0.88	17
B73	50.027	7.071	1	-13.74	-68.79	6.7	586	91	250	67.7	70	58	-68	11	0.70	-0.60	1.12	12
B74	49.984	7.149	2	0.21	119.58	6.7	33	104	72	54.6	72	53	-9	9	1.90	-0.68	0.76	18
B74	49.984	7.149	1	-13.74	-68.79	6.7	586	91	250	123.9	70	0	-14	59	0.78	-0.58	1.24	12
B75	49.939	7.217	2	0.21	119.58	6.7	33	104	72	64.8	72	42	-23	15	0.96	-0.36	0.48	13
B75	49.939	7.217	1	-13.74	-68.79	6.7	586	91	250	44.8	70	1	-16	57	1.30	-1.04	1.88	9
*B82	50.559	6.236	2	0.21	119.58	6.7	33	104	71	76.1	71	-12	-4	6	2.12	-1.18	1.34	18
*C03	50.680	5.270	2	0.21	119.58	6.7	33	105	70	45.1	70	-3	-180	180	0.52	-0.52	3.40	9
*C04	50.210	5.000	2	0.21	119.58	6.7	33	105	70	189.5	70	-24	-42	5	0.72	-0.64	1.34	9
C05	50.480	4.920	2	0.21	119.58	6.7	33	105	70	72.8	70	79	-3	5	2.46	-0.72	0.82	17
*C06	50.350	5.570	2	0.21	119.58	6.7	33	104	71	159.9	71	73	-180	180	1.12	-1.12	2.82	9
*C07	50.240	5.930	2	0.21	119.58	6.7	33	104	71	52.8	71	-10	-4	8	1.64	-0.80	0.92	22
*C08	50.342	6.314	2	0.21	119.58	6.7	33	104	71	121.9	71	55	-180	180	1.00	-1.00	2.94	11
*C13	49.970	5.220	2	0.21	119.58	6.7	33	105	70	148.4	70	66	-180	180	1.68	-1.68	2.26	15
C18	50.667	4.508	2	0.21	119.58	6.7	33	105	70	34.5	70	86	-13	69	0.76	-0.68	1.26	18
*C20	49.865	5.858	2	0.21	119.58	6.7	33	104	71	29.9	71	164	-1	4	3.38	-2.36	0.62	15
*C22	49.806	6.267	2	0.21	119.58	6.7	33	104	71	77.9	71	156	-180	180	1.04	-4.94	2.96	9
*C23	49.597	6.004	2	0.21	119.58	6.7	33	104	71	32.1	71	67	-2	5	4.00	-3.44	0.00	20
D01	49.585	5.267	2	0.21	119.58	6.7	33	105	70	221.6	70	62	-80	10	0.46	-0.46	1.40	9
D02	49.204	5.070	1	-13.74	-68.79	6.7	586	90	249	69.3	69	81	-4	9	1.72	-0.68	0.74	9
*D06	48.717	4.948	1	-13.74	-68.79	6.7	586	89	248	37.0	68	150	-79	9	0.48	-0.48	1.28	13
*D51	49.312	6.281	2	0.21	119.58	6.7	33	104	71	49.0	71	-11	-180	180	1.66	-1.66	2.28	10
*D53	49.055	5.991	2	0.21	119.58	6.7	33	105	71	214.5	71	-20	-180	180	3.06	-3.06	0.92	15
D54	48.954	5.865	1	-13.74	-68.79	6.7	586	90	249	113.3	69	82	-3	9	1.34	-0.48	0.48	13

Table A3. Station splitting estimates and 2σ error bars. N is the number of measurements analysed. For stations with one null measurement and one constrained measurement, the null measurement was discarded. For stations with two constrained measurements, the measurements were stacked via the method of Wolfe and Silver (1998) to estimate the station splitting parameters. Stations for which only null measurements were recorded are indicated by "*N/A*".

STAT	N	MODEL	PARAMETERS		(GLOBAL MIN)		
		MIN	FA	MAX	MIN	DT	MAX
A02	1	103	114	126	0.8	1.0	1.3
A04	1	98	133	150	0.4	0.7	1.3
A06	1	79	89	147	0.2	0.6	1.3
A09	1	N/A	N/A	N/A	N/A	N/A	N/A
A11	1	86	94	110	0.6	1.0	1.4
A13	1	92	96	101	1.4	1.7	2.0
A15	1	125	132	137	1.0	1.2	1.5
A19	1	86	110	146	0.4	0.7	1.3
A21	1	116	132	144	1.0	1.5	2.1
A33	1	N/A	N/A	N/A	N/A	N/A	N/A
A51	1	86	97	115	1.1	1.9	2.9
A54	1	97	134	151	0.5	1.0	1.8
A82	1	85	98	132	0.4	0.8	1.5
A85	1	95	116	139	0.6	1.1	1.6
B02	1	164	178	246	0.1	0.3	1.2
B04	1	N/A	N/A	N/A	N/A	N/A	N/A
B09	1	-6	2	15	0.8	1.3	1.9
B11	1	8	52	64	0.3	0.7	1.4
B14	1	77	79	81	2.5	3.3	4.0
B16	1	75	76	77	2.8	3.4	3.9
B19	1	N/A	N/A	N/A	N/A	N/A	N/A
B23	1	75	78	80	2.7	3.4	4.0
B26	2	-5	25	58	0.4	0.8	1.5
B29	1	3	39	59	0.4	0.6	1.2
B33	1	N/A	N/A	N/A	N/A	N/A	N/A
B35	1	8	64	70	0.1	1.0	2.3
B37	1	20	55	65	0.3	1.2	2.2
B40	1	53	59	63	1.4	2.1	2.8
B43	2	3	15	32	0.7	1.0	1.4
B46	1	N/A	N/A	N/A	N/A	N/A	N/A
B50	1	167	174	193	0.3	0.8	1.5
B52	1	47	55	60	1.1	1.7	2.3
B54	1	-3	3	10	1.2	1.6	2.1
B56	2	-3	6	20	0.7	0.9	1.3
B58	1	40	53	61	1.0	1.8	2.8
B60	2	-7	6	42	0.3	0.6	1.0
B62	1	-13	4	63	0.2	0.7	1.9

Table A3. (cont.)

STAT	N	MODEL	PARAMETERS		(GLOBAL MIN)		
		MIN	FA	MAX	MIN	DT	MAX
B66	1	74	78	89	0.7	1.9	3.0
B70	2	N/A	N/A	N/A	N/A	N/A	N/A
B72	1	33	49	59	1.3	2.2	3.3
B74	2	0	47	63	0.3	0.8	1.7
B82	1	N/A	N/A	N/A	N/A	N/A	N/A
C04	1	N/A	N/A	N/A	N/A	N/A	N/A
C06	1	N/A	N/A	N/A	N/A	N/A	N/A
C08	1	N/A	N/A	N/A	N/A	N/A	N/A
C18	1	73	86	153	0.1	0.8	2.0
C22	1	N/A	N/A	N/A	N/A	N/A	N/A
D01	1	-18	62	70	0.0	0.5	1.9
A03	1	113	132	144	0.7	1.0	1.4
A05	1	78	80	83	1.3	2.0	2.8
A07	1	N/A	N/A	N/A	N/A	N/A	N/A
A10	1	N/A	N/A	N/A	N/A	N/A	N/A
A12	1	84	89	99	0.7	1.2	1.6
A14	1	125	130	136	1.6	1.9	2.2
A18	1	112	137	150	0.6	1.0	1.6
A20	1	122	136	146	0.8	1.2	1.7
A31	1	N/A	N/A	N/A	N/A	N/A	N/A
A50	1	83	109	151	0.4	0.9	1.9
A53	1	111	135	148	0.8	1.5	2.3
A80	1	125	149	158	0.4	1.3	2.3
A83	1	N/A	N/A	N/A	N/A	N/A	N/A
B01	1	80	84	90	1.7	2.6	3.4
B03	2	N/A	N/A	N/A	N/A	N/A	N/A
B08	1	59	60	61	1.5	1.7	2.0
B10	2	N/A	N/A	N/A	N/A	N/A	N/A
B13	1	77	79	80	3.1	3.6	4.0
B15	1	164	166	170	0.6	1.2	1.9
B17	1	86	88	91	1.5	1.8	2.1
B22	1	-10	11	57	0.2	0.5	1.1
B24	1	82	84	86	3.1	3.4	3.7
B27	1	-2	43	63	0.3	0.7	1.4
B30	2	165	167	174	0.6	1.5	2.4
B34	1	44	59	67	0.7	1.6	2.6
B36	1	N/A	N/A	N/A	N/A	N/A	N/A
B38	2	N/A	N/A	N/A	N/A	N/A	N/A
B41	1	27	60	69	0.3	1.8	4.0
B44	1	-6	4	22	0.7	1.4	2.3
B49	1	132	149	157	0.6	1.6	2.8
B51	1	47	57	62	0.7	1.3	2.0

Table A3. (cont.)

STAT	N	MODEL	PARAMETERS		(GLOBAL MIN)		
		MIN	FA	MAX	MIN	DT	MAX
B55	1	N/A	N/A	N/A	N/A	N/A	N/A
B57	1	-13	13	66	0.2	1.2	3.3
B59	1	23	50	59	0.4	0.8	1.3
B61	1	163	173	250	0.1	0.7	3.2
B63	1	N/A	N/A	N/A	N/A	N/A	N/A
B65	1	73	77	113	0.2	1.5	3.1
B67	1	N/A	N/A	N/A	N/A	N/A	N/A
B71	1	77	81	86	2.2	3.2	4.0
B73	2	32	61	66	0.3	1.2	2.1
B75	2	10	34	52	0.6	0.8	1.2
C03	1	N/A	N/A	N/A	N/A	N/A	N/A
C05	1	76	79	82	1.7	2.5	3.2
C07	1	N/A	N/A	N/A	N/A	N/A	N/A
C13	1	N/A	N/A	N/A	N/A	N/A	N/A
C20	1	N/A	N/A	N/A	N/A	N/A	N/A
C23	1	N/A	N/A	N/A	N/A	N/A	N/A
D02	1	77	81	88	1.0	1.7	2.4

Gravity Observations in the Western Rhenish Massif and Forward Modelling of the Eifel Plume Bouguer Anomaly

Joachim R.R. Ritter[1], Jan P. Mathar[1], Michael Jordan[2] and Gerald Gabriel[3]

[1]Geophysical Institute, University of Karlsruhe, Hertzstr. 16, 76187 Karlsruhe, Germany
[2]College of Mines and Earth Sciences, Salt Lake City, USA
[3]Leibniz Institute for Applied Geosciences, Hannover, Germany

Abstract

We study the gravity field of the western Rhenish Massif, Germany, to search for relationships to the mantle source of the recent Eifel volcanism. First we compile the available gravity data from the region and present them as Bouguer gravity map. This map does hardly show any anomaly univocally related to the Eifel plume, even after careful wavelength filtering the data. Forward modelling of the Bouguer gravity field with the seismological low-velocity anomaly in the upper mantle as input anomaly finds that the seismological model corresponds to an approximately –10 mGal anomaly (1 mGal is 10^{-5} m s^{-2}). Such a tiny signal can be hardly recognized in the real data: Intrusions of magmatic high-density dykes and sills may even hide or reverse the expected negative mantle gravity signal which makes the situation even worse. As conclusion we find that a gravity signal of the Eifel plume cannot be seen in the available Bouguer data, but that this negative result is at least consistent with the seismological mantle models. Furthermore the forward modelling results suggest that small-scale upper mantle plumes may not be recognized as a Bouguer anomaly underneath a typical heterogeneous continental lithosphere.

1 Introduction

The Eifel region and its Tertiary and Quaternary volcanic fields are located in the western part of the Rhenish Massif (Fig. 1). Although the Quaternary activity at the surface is relatively sparse (<20 km^3 erupted material, Wörner 1998), there is a broad mantle root: Recent seismological tomography and receiver function models contain a voluminous seismic low-velocity body in the upper mantle below the western Eifel region. This roughly cylindrical body has a radius of 50-60 km and extends from about 50-60 km depth (Mathar et al. this volume; Weber et al. this volume) down to the top of the transition zone (Budweg 2003, Grunewald et al. 2001, Ritter this volume, Weber et al. this volume). The seismological anomaly is interpreted as a small-scale upper mantle plume. The seismic velocity reduction varies with depth. However -1% to -2% *P*-wave velocity and -1% to -5% *S*-wave velocity can be regarded as average values (Ritter this volume). Based on petrophysical relations the excess temperature of the plume is estimated to reach 100-150 K (Ritter 2005).

In this contribution we present an updated Bouguer gravity map of the western Rhenish Massif and its surroundings. It serves as basis for a regional gravity study of the Eifel volcanism and possible test of the seismic tomography model: We determine the expected gravity signal of the seismic tomography model and compare it with the observed Bouguer gravity.

Previously, a Bouguer gravity map for the Rhenish Massif and its surroundings was published by Jacoby et al. (1983). This map was based on Gerke's (1957) gravity map plus added new data acquired by then, however the western part of the Rhenish Massif (western Eifel, Hunsrück) was still poorly covered and only a general correlation of major tectonic features with the gravity field was possible (Jacoby et al. 1983). Drisler and Jacoby (1983) tried to extract deep crustal and even upper mantle information from the Bouguer anomalies determined by Jacoby et al. (1983) combined with further geophysical models, mainly from seismology. For the Eifel region they proposed that a low-density body is not required in the upper mantle to explain the observed (coarse) Bouguer anomaly in this region. Such a low-density body could have been expected, because Raikes and Bonjer (1983) had found a low-velocity body with a 3-5% *P*-wave velocity decrease from 50 to about 200 km depth. Drisler and Jacoby (1983) estimated that a possible high-temperature, low-density anomaly in the mantle below the Rhenish Massif, consistent with the low-velocity body, should produce a density anomaly of 10 kg m^{-3} which may produce a Bouguer gravity signal of less than -20 mGal. Such a small anomaly could not be resolved by the then available Bouguer map.

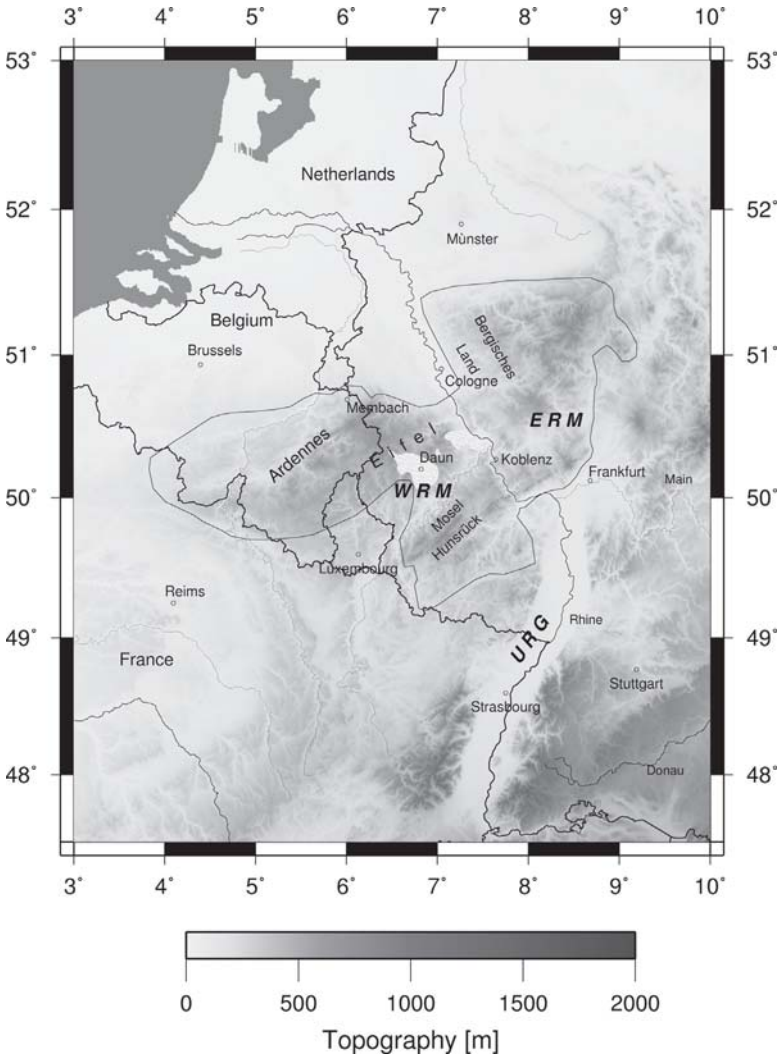

Fig. 1. Map of the study region including the outline of the Rhenish Massif. The locations of the Quaternary West Eifel (around Daun) and East Eifel (NW of Koblenz) volcanic fields are indicated in grey

Later gravity work in the Eifel region was concentrated on local volcanic structures (e.g. Büchel et al. 1988, Büchel 1992, Wörner et al. 1988). Büchel (1994) contributed a gravity map of the state of Rheinland-Pfalz where most of the Eifel region belongs to. He discusses the gravity anomalies with regard to the tectonic units. Repeated absolute gravity measurements along a SW-NE profile across the NW Rhenish Massif (Ardenne

mountains - Roer Graben - Bergisches Land) are currently underway (Van Camp et al. 2002) to constrain the present geodynamic motions in the region. First results from the permanent observatory Membach (eastern Belgium) are interpreted as about 3 mm/yr uplift which may be caused by post-glacial rebound or even the upwelling Eifel plume (Francis et al. 2004).

2 Data

The basis of our research is a compilation of gravity data provided mainly by the Leibniz Institute for Applied Geosciences (Hannover), the Royal Observatory of Belgium (Brussels), Cadastre Administration de Luxembourg and the Bureau Gravimetrique International (Toulouse). It is composed of about 37400 data points in the region of interest. The Bouguer anomaly is calculated with a reduction density of 2670 kg m^{-3}. Fig. 2 (Colour Plate 15) displays the Bouguer anomaly (BA) map which is characterized by the following main features: The Upper Rhine Graben with a low BA is clearly visible. The eastern Rhenish Massif (east of the Rhine river) has a higher BA (about +8 to +15 mGal) than the western Rhenish Massif (mostly negative BA). At the West and East Eifel volcanic fields no distinct BA relative to the surrounding areas can be found.

To enhance gravity anomalies that are of deep origin, we use 2D spatial bandpass filtering with cosinus-type flanks. The filter routines have been checked carefully with synthetic data to avoid artifacts such as strong sidelobes. The dominant wavelength λ of the gravity signal in km is approximately sensitive to density anomalies at $\lambda/3$ km depth (Telford et al. 1978).

In Fig. 3 a-e (Colour Plate 16) the contributions to the total BA (Fig. 2, Colour Plate 15) at different wavelengths are presented which may correspond to density anomalies at different depth ranges. At small wavelengths ($30<\lambda<90$ km) the BA (Fig. 3a) reflects the well-known tectonic structures which are blurred at $100<\lambda<180$ km (Fig. 3b). For $150<\lambda<250$ km the difference between the western (negative BA) and eastern (positive BA) Rhenish Massif is clearly observed. This indicates a possible general difference in the upper mantle density between both parts (~50-80 km depth). Such a distinction is also found in the shear wave velocity (v_s) structure in the upper 100 km depth with relatively decreased v_s in the western part (Keyser et al. 2002). A positive BA in Belgium, SE of Brussels, corresponds to the western margin of the Rhenish Massif.

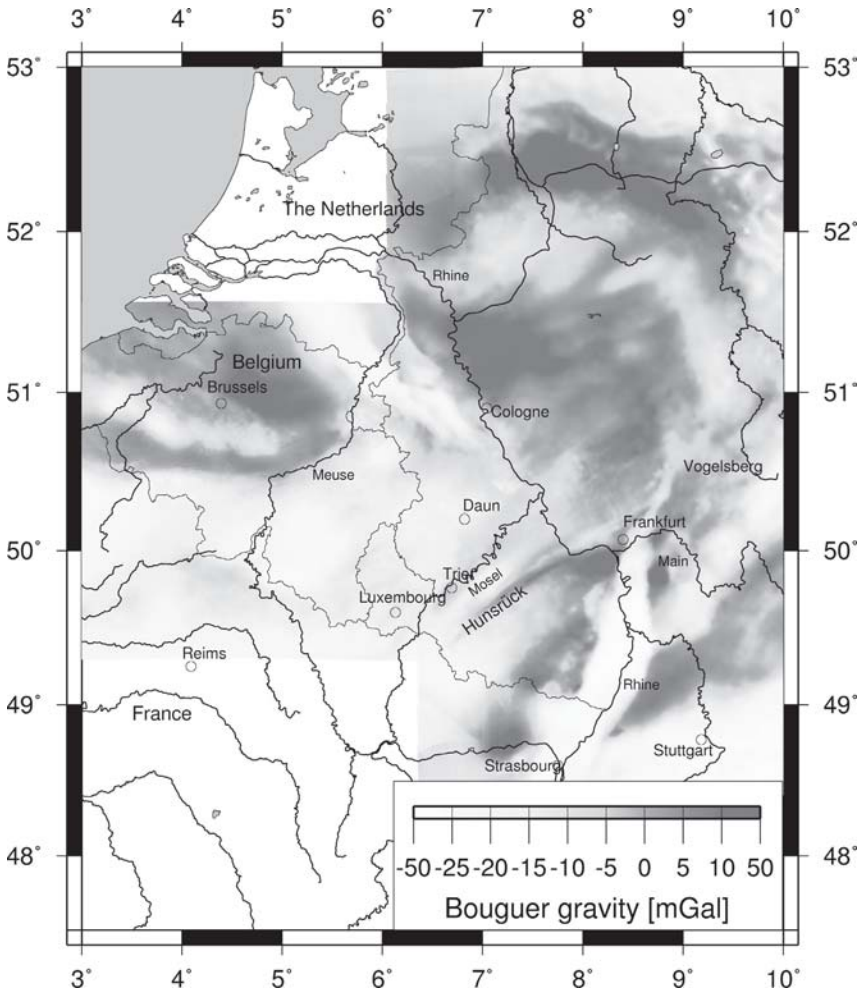

Fig. 2 (Colour Plate 15). Bouguer anomaly map of the Rhenish Massif and surrounding regions. Regions in the NW and SW without a high density of data points are blanked

For wavelengths between 210 km and 270 km (depth range between 70 and 90 km, Fig. 3d) the contrast between the western and eastern Rhenish Massif can still be seen. Additionally, a negative Bouguer signal is found in the area of the western Eifel region and Luxembourg which correlates spatially with the low-velocity anomaly found in teleseismic tomography. However, this BA is very low (about –8 mGal) and similar signals can be found also at other regions. For wavelengths between 300 and 400 km (depth 100 to 130 km) a negative, long-wavelength BA is seen further to

the west (NE France and S Belgium, Fig. 3e) which is possibly a broad shallow (crustal) feature (see Fig. 2). A clear signature of the Eifel plume is absent in the Bouguer data at all wavelength intervals in Fig. 3 (Colour Plate 16).

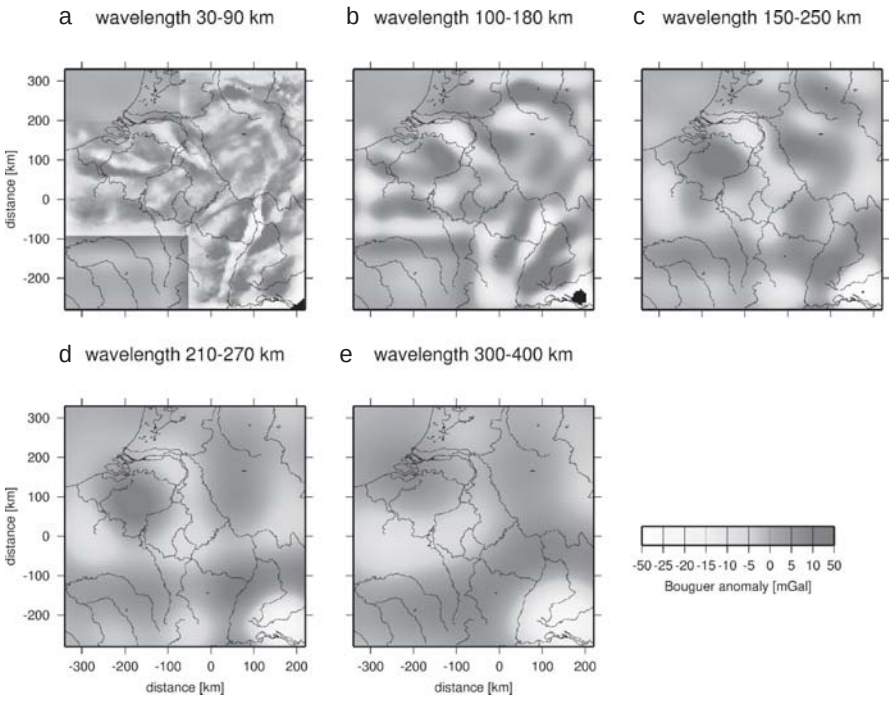

Fig. 3 (Colour Plate 16). Various wavelength bands of the Bouguer anomaly in the Rhenish Massif and surrounding areas: a) bandpass $30<\lambda<90$ km, b) $100<\lambda<80$ km, c) $150<\lambda<250$ km, d) $210<\lambda<270$ km, e) $300<\lambda<400$ km

3 Forward Modelling

To estimate quantitatively the Bouguer anomaly produced by the seismic low-velocity body found in teleseismic tomography (Ritter et al. 2001, Ritter this volume) synthetic BA data are calculated. We use the JI-3D program (Jordan 2003) for the forward modelling which is based on the algorithm of Zeyen and Pous (1993). Fig. 4 shows a sketch of the input models which have a homogeneous background density in the crust (2750 kg m^{-3}) and mantle (3400 kg m^{-3}) comparable to standard Earth models. The density anomaly represents an idealised mantle plume as a vertical cy-

lindrical body. The following parameters are systematically varied for a parameter search: radius (r=50-65 km), depth to the top edge of the anomaly (d=50-80 km) and the density contrast ($\Delta\rho$ from –14 kg m^{-3} to -27 kg m^{-3}) corresponding to differently assumed excess temperatures (ΔT=100-200 K). These physical parameters exceed the range of possible models of the Eifel plume (Ritter 2005) and should represent the expected Bouguer gravity response as well as larger BA values.

In Figs. 5-8 the BA for different parameters and their density anomalies are presented as map views. The BA increases in amplitude and diameter with temperature (~density decrease, Fig. 5), radius (Fig. 6) and position to the top edge of the anomaly (Fig. 8). Only input anomalies with parameters exceeding the reasonably interpretations of the seismic tomography models produce a BA greater than -15 mGal (e.g. ΔT>150 K, r>60 km or d<60 km). The preferred seismological model with a radius below 60 km, an excess temperature below 150 K and a top edge at 50-60 km depth causes a synthetic BA of maximum about –10 mGal.

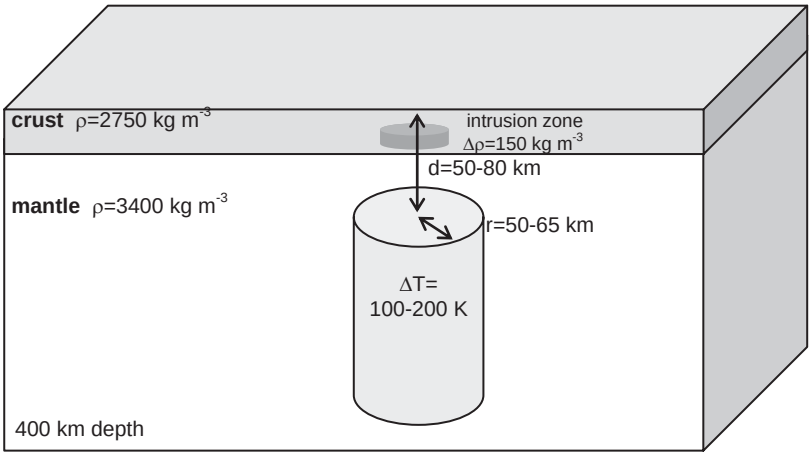

Fig. 4. Sketch of the input density model (plume-like cylinder) for the forward calculations of the Bouguer gravity. For some input models a high-density intrusion anomaly is assumed in the crust

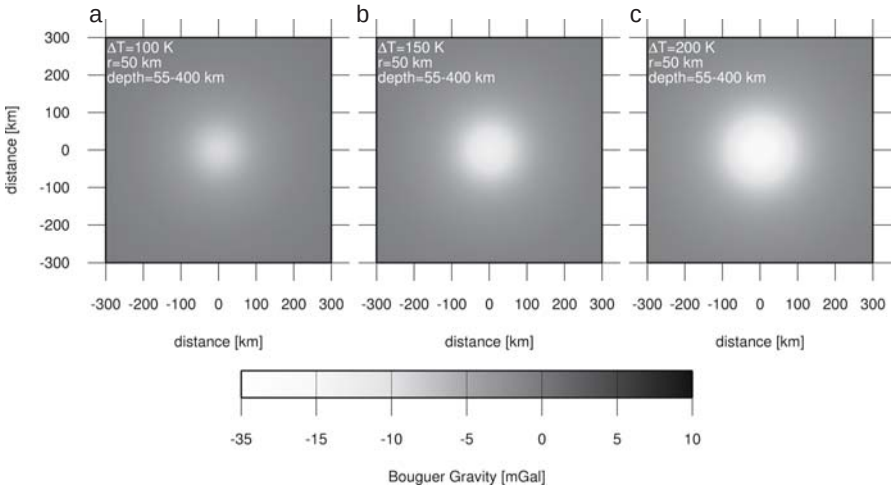

Fig. 5. Bouguer anomaly of the density structure in Fig. 4 for different excess temperatures ΔT: a) ΔT=100 K, b) ΔT=150 K, c) ΔT=200 K

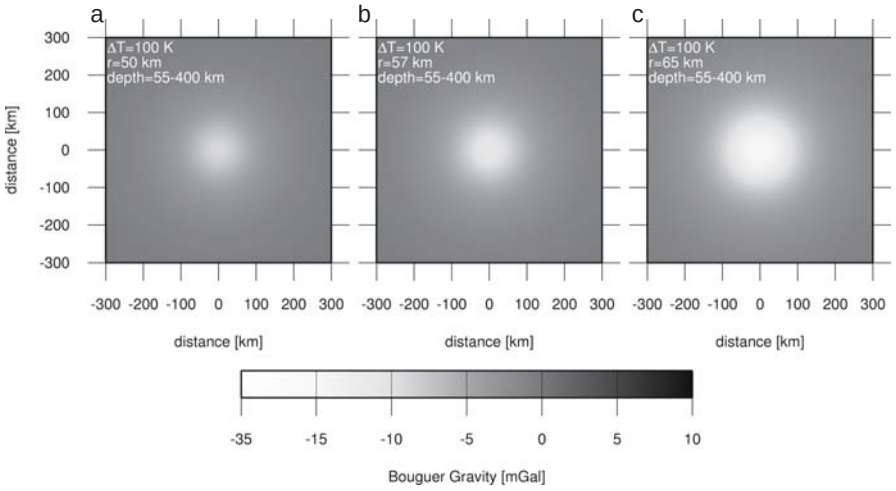

Fig. 6. Bouguer anomaly of the density structure in Fig. 4 for different plume radii r: a) r=50 km, b) r=57 km, c) r=65 km

The increased scattering of teleseismic *P*-waves in the Eifel region (Hock et al. 2004) may be explained by solidified magmatic intrusions in the crust. The incorporation of a high-density intrusion zone ($\Delta\rho$=+150 kg m^{-3}) in our input model with a radius of 20 km at 20-25 km depth can even overcompensate the BA of the small mantle anomaly (Fig. 7a, ΔT=100 K, r=50 km, d=55 km). Only for a large excess temperature such as ΔT=200

K the mantle BA dominates (Fig. 7c), but this case is a rather unrealistic scenario for the Eifel plume.

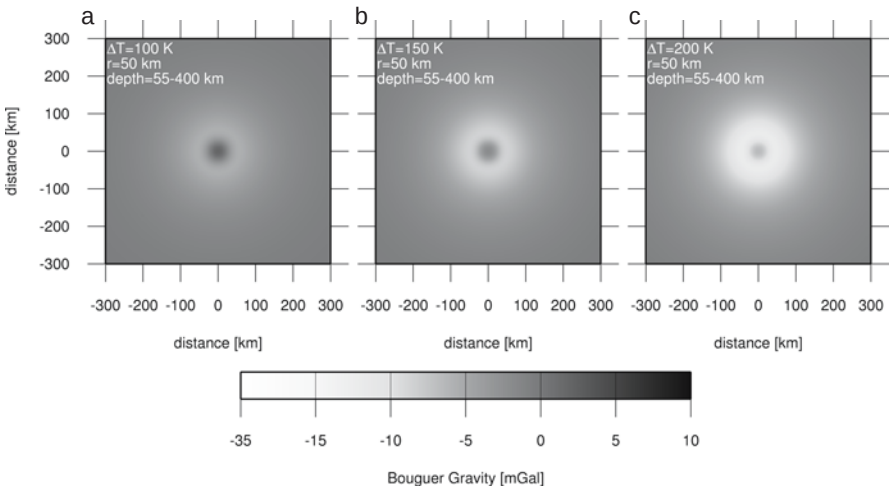

Fig. 7. Bouguer anomaly of the density structure in Fig. 4 including a crustal high-density intrusion zone (+150 kg m^{-3}). The mantle anomaly has different excess temperatures ΔT: a) ΔT=100 K, b) ΔT=150 K, c) ΔT=200 K

The top edge of the Eifel plume is presumably at 50-60 km depth, where Budweg (2003), Weber et al. (this volume) and Mathar et al. (this volume) find the upper boundary of a seismic low-velocity zone. The teleseismic tomography results (Ritter et al. 2001, Ritter this volume) have a low resolution at this shallow depth level; however such a depth is within the range of the reasonable parameters of the seismic tomography models. In Fig. 8 we compare the BA for d=50-80 km as well as reasonable r (50 km) and ΔT (150 K). Only the density anomaly with the low value d=50 km produces a BA of more than -15 mGal (Fig. 8a) that exceeds the observed BA. The deeper density anomalies (d=60-80 km) have a smaller BA (Fig. 8b-d). This result indicates that a low-density anomaly (ΔT=150 K; r=50 km) should be below 50 km depth in the Eifel region.

The parameter search with different input density anomalies is summarised in Fig. 9 for three models with different depths to the top edge of the low density anomaly. For d=80 km (Fig. 9a) a –10 mGal BA (maximum reasonable BA for the Eifel plume) is obtained for r=50 km and ΔT=180 K or r=63 km and ΔT=100 K. For larger anomalies (r=65 km, ΔT=200 K) the –10 mGal BA is quickly exceeded. For d=50 km (Fig. 9c) the parameter limits for a –10 mGal BA are 50 km / 140 K and 55 km / 100 K. Bouguer anomalies exceeding –10 mGal are also visible in Fig. 9, but such plume-

related anomalies are not observed in the Rhenish Massif (Fig. 2), and therefore we exclude corresponding combinations of r, ΔT and d for the Eifel plume.

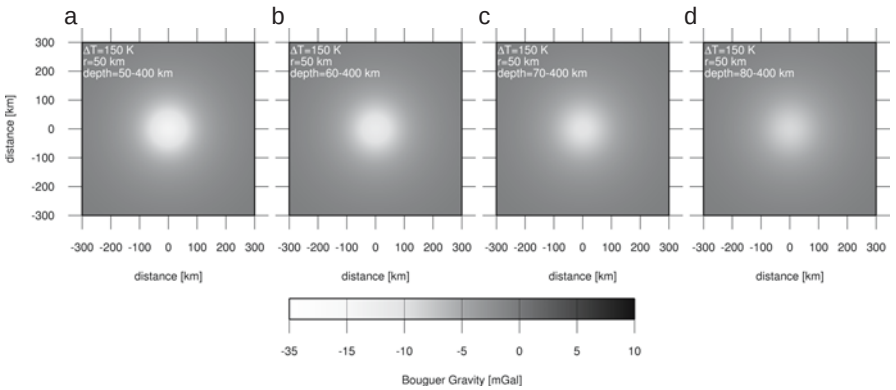

Fig. 8. Bouguer anomaly of the density structure in Fig. 4 for different depth d to the top edge of the anomaly: a) d=50 km, b) d=60 km, c) d=70 km, d) d=80 km

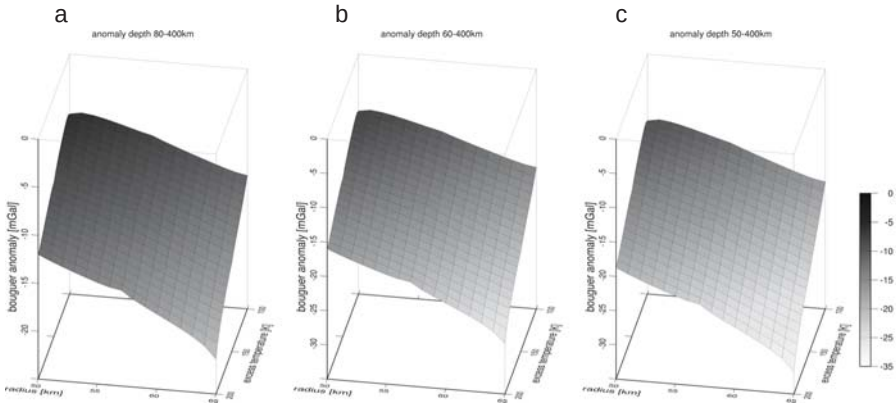

Fig. 9. Results of the parameter search for the expected Bouguer anomaly from a small upper mantle plume with varying radius and excess temperature as well as three different depths to the top edge of the anomaly: a) d=80 km b) d=60 km, c) d=50 km

4 Interpretation and Conclusions

A comparison of the measured Bouguer anomaly (BA) in the western Rhenish Massif with the synthetic BA derived from the seismological Eifel plume models shows that the related density anomaly is too small that it

could identified in the available BA maps (Figs. 2, 3 and Colour Plates 15, 16). Thus the gravity and seismological models are indeed compatible but cannot fully confirm each other.

Small-scale upper mantle plumes, as the Eifel plume, underneath a structurally complicated continental lithospheric plate can hardly be identified in Bouguer data. Because such mantle anomalies have a small volume and moderate density contrast and because they are situated underneath a heterogeneous lithospheric plate, the Bouguer gravity signal is less than minus 10-15 mGal. This small negative mantle signal may be further masked by high-density intrusions in the lithosphere related to the magmatic processes. Because of their shallow depth the high-density bodies can even cause a local positive Bouguer signal (Fig. 7).

Provided a high-resolution density model for the lithosphere is available, gravity stripping methods can enhance the resolution of asthenospheric density anomalies. Such a methodology may be more efficient than spatial filtering, but in our case cannot be applied due to the lack of an appropriate 3D lithospheric density model.

Acknowledgements

We thank U. Achauer, M. Bonatz, M. Everaerts and B. Reisch for providing data and advice. B. Meurers and M. Van Camp helped to clarify some points in the manuscript. The Generic Mapping Tool GMT (Wessel and Smith 1998) was used for plotting. The Eifel plume project is financed by the Deutsche Forschungsgemeinschaft through grant Ch77/9.

References

Büchel G (1992) Das Kehlberger Hoch. Die Geowissenschaften 10:132-142

Büchel G (1994) Schwereanomalien von Rheinland-Pfalz 1:250 000 mit Erläuterungen. Landesvermessungsamt Rheinland Pfalz (Ed)

Büchel G, Christensen U, Jacoby W, Ritzert M, Wolters B (1988) Gravimetrische Untersuchungen im Bereich des Kelberger Hochs (Hocheifel). Mainzer geowiss Mitt 17:377-387

Budweg M (2003) Der obere Mantel in der Eifel-Region untersucht mit der Receiver Function Methode. PhD Thesis, University of Potsdam and GeoForschungsZentrum Potsdam, scientific technical report STR03/04

Drisler J, Jacoby WR (1983) Gravity anomaly and density distribution of the Rhenish Massif. In: Fuchs K, von Gehlen K, Mälzer H, Murawski H, Semmel

A (eds) (1983) Plateau uplift, the Rhenish shield - a case history. Springer-Verlag, Berlin, pp 366-380

Francis O, Van Camp M, van Dam T, Warnant R, Hendrickx M (2004) Indication of the uplift of the Ardenne in long-term gravity variations in Membach (Belgium). Geophys J Int 158:346-352

Gerke K (1957) Die Karte der Bouguer-Isoanomalen 1:1000000 von Westdeutschland. Dtsch Geodät Komm 46

Grunewald S, Kind R, Weber M (2001) The upper mantle under Central Europe - indications for the Eifel plume. Geophys J Int 147:590-601

Hock S, Korn M, Ritter JRR, Rothert E (2004) Mapping random lithospheric heterogeneities in northern and central Europe. Geophys J Int 157:251-264

Jacoby WR, Joachimi H, Gerstenecker C (1983) The gravity field of the Rhenish Massif. In: Fuchs K, von Gehlen K, Mälzer H, Murawski H, Semmel A (eds) (1983) Plateau uplift, the Rhenish shield - a case history. Springer-Verlag, Berlin, pp 247-258

Jordan M (2003) JI-3D a new approach to high resolution regional seismic tomography: theory and applications. PhD Thesis, Institute for Geophysics, University of Göttingen

Keyser M, Ritter JRR, Jordan M (2002) 3D shear-wave velocity structure of the Eifel plume, Germany. Earth Planet Sci Lett 203:59-82

Raikes S, Bonjer K-P (1983) Large-scale mantle heterogeneity beneath the Rhenish Massif and its vicinity from teleseismic *P*-residuals measurement. In: Fuchs K, von Gehlen K, Mälzer H, Murawski H, Semmel A (eds) (1983) Plateau uplift, the Rhenish shield - a case history. Springer-Verlag, Berlin, pp 315-331

Ritter JRR (2005) Small-scale mantle plumes: Imaging and geodynamic aspects. In: Wenzel F, Perspectives in Modern Seismology, Lecture Notes in Earth Sciences 105, Springer Verlag, Heidelberg, pp 69-94

Ritter JRR, Jordan M, Christensen UR, Achauer U (2001) A mantle plume below the Eifel volcanic fields, Germany. Earth Planet Sci Lett 186:7-14

Telford WM, Geldart LP, Sheriff RE, Keys DA (1978) Applied geophysics. Cambridge University Press, Cambridge

Van Camp M, Camelbeeck T, Francis O (2002) Experiment to evaluate crustal motions across the Ardenne and Roer Graben (north-western Europe) using absolute gravity measurements. Metrologia 39:503-508

Wessel P, Smith WHF (1998) New, improved version of Generic Mapping Tool released. Eos Trans AGU 79:579

Wörner G (1998) Quaternary Eifel volcanism, its mantle sources and effect on the crust of the Rhenish Shield. In: Neugebauer HJ (ed) Young tectonics – magmatism – fluids: a case study of the Rhenish Massif, University of Bonn, SFB 350 74:11-16

Wörner G, Viereck L, Plaumann S, Pucher R, v.d.Bogaard P, Schmincke HU (1988) The Quaternary Wehr volcano: a multiphase evolved eruption center in the east Eifel volcanic field (FRG). Neues Jahrbuch Miner Abh 159:73-99

Zeyen H, Pous J (1993) 3-D joint inversion of magnetic and gravimetric data with a priori information. Geophys J Int 112:244-256

Colour Plates

Colour Plate 1:
Top: Topography and bathymetry from GTOPO30 of Iceland and its surroundings.
Bottom: Free-air gravity from Sandwell and Smith (1997) of Iceland and its surroundings; the colour scale for gravity is clipped at ±80 mgal.
(Fig. 2 in Ruedas et al.)

Colour Plate 2:
Top: Map of the Mohorovičić discontinuity of Iceland (Reprinted from Earth Planet. Sci. Lett. 181(3), Darbyshire FA, White RS, Priestley, KF, Structure of the crust and uppermost mantle of Iceland from a combined seismic and gravity study, pp. 409-428, © 2000 with permission from Elsevier).
(Fig. 4 in Ruedas et al.)
Bottom: Calculated crustal thickness (in km) of a convection model of the Iceland plume with 136 K excess temperature and 1% melt extraction threshold (Ruedas et al. 2004) at 21 Ma model time. The ridge axis is located at x=800 km and is 60 km wide; plate drift has not yet transported crust further than about 210 km from it.
(Fig. 5 in Ruedas et al.)

Colour Plate 3:
Horizontal and vertical cross sections of the P-wave (left) and S-wave (right) seismic velocity anomaly models of the ICEMELT experiment (Reprinted from Wolfe CJ, Bjarnson IP, Van Decar JD, Solomon SC, Seismic structure of the Iceland mantle plume, Nature 385(5727), pp 245-247, © 1997 with permission from Nature Publishing Group).
(Fig. 6 in Ruedas et al.)

Colour Plate 4:
Top: Global P-wave seismic tomography images of the mantle beneath Iceland. Left: Roughly ridge-perpendicular vertical cross-section (slightly modified , reprinted from Earth Planet. Sci. Lett. 166(3-4), Bijwaard H, Spakman W, Tomographic evidence for a narrow whole mantle plume below Iceland, pp. 121-126, © 1999 with permission from Elsevier). Right: Horizontal cross sections (Montelli R, Nolet G, Dahlen FA, Masters G, Engdahl ER, Hung S-H, Finite-frequency tomography reveals a variety of plumes in the mantle; Science 303 (5656), 338-343, © 2004 reprinted with

permission from AAAS). Note that the colour scales are clipped at ±0.5 % in the left image and at ±1.5 % in the right image.
(Fig. 7 in Ruedas et al.)
Bottom: Non-adiabatic temperature field in the mantle below the North Atlantic based on the Bijwaard and Spakman (1999) tomography model at 290 and 1200 km depth (left) and resulting mantle flow field (right).
(Fig. 12 in Ruedas et al.)

Colour Plate 5:
Horizontal cross-section through the inversion model (layers 2-7). Shown are *P*-wave velocity perturbations with respect to the background model (compare Table 1 in Barth et al.).
(Fig. 10 in Barth et al)

Colour Plate 6:
P-wave velocity anomalies after Ritter et al. (2001). The centre of the coordinate system is at 7.33 °E and 49.75 °N. Only the well-resolved layers are displayed, checker-board resolution tests for these layers are given in Ritter (2005). The grid size for the inversion parameterisation (black rectangles) varies with ray density and azimuthal ray distribution. The inversion is based on relative travel-time residuals with a mean value of zero, therefore only velocity contrasts should be interpreted, not absolute *P*-wave velocity perturbations.
Depth range from 31-70 km: There is a clear negative *P*-wave velocity anomaly (Δv_p) below the West Eifel which is found in several blocks. In the NW and SW negative *P*-wave velocity anomalies appear within single blocks which are poorly resolved and may be due to crustal smearing.
Depth range from 70-120 km: There is clear negative Δv_p below the West Eifel which is found in several blocks. At the edges of the model negative *P*-wave velocity anomalies appear within single blocks which are poorly resolved and may be artefacts.
Depth range from 120-170 km: There is clear negative Δv_p below the West Eifel which is found in several blocks. Isolated negative Δv_p patches appear within single blocks which are poorly resolved and may be artefacts. In the south there is a broad region with positive Δv_p which presumably indicates a high-velocity region associated with the Alpine lithospheric root.
Depth range from 170-220 km: There is clear negative Δv_p below the Eifel which is found in several blocks. Another negative anomaly is found further east, below the Vogelsberg area. However, the model resolution there is low. In the south there is a broad region with positive Δv_p which pre-

sumably indicates a high-velocity region associated with the Alpine lithospheric root.
(Ritter)

Colour Plate 7:
P-wave velocity anomalies after Ritter et al. (2001), for details see caption of Colour Plate 6.
Depth range from 220-270 km: There is clear negative Δv_p below the Eifel and towards south (western Hunsrück) which is found in several blocks. Another negative anomaly is found further east, below the Vogelsberg area. However, the model resolution there is low. In the south there is a broad region with a positive anomaly which presumably indicates a high-velocity region associated with the Alpine lithospheric root.
Depth range from 270-340 km: There is clear negative Δv_p below the Eifel which is found in several blocks. Another negative anomaly is found further east, below the Vogelsberg area and below the Rhön. However, the resolution there is low, and the size of the anomalies may be overestimated due to the coarse parameterisation.
Depth range from 270-340 km: There is clear negative Δv_p below the Eifel and stretching to the west which is found in several blocks. The negative anomalies further east, below the Vogelsberg and Rhön area are poorly resolved and should be explored in more detail in the future.
(Ritter)

Colour Plate 8:
Top: Images produced by teleseismic tomography (*Tomo*) and Receiver functions (*RF*) for three types of velocity anomalies. (a) High velocity zone (b) Low velocity zone (c) Positive velocity jump with gradual decrease of velocity below. Red (blue) in the RFs indicates a positive (negative) velocity jump with increasing depth. The same colour code is used throughout the chapter.
(Fig. 2 in Weber et al.)
Bottom: Horizontal slices at four depth ranges with their normalised average number of hits per 5 x 5 x 2 km^3 volume element (voxel). A value of 1 indicates the maximum of 928 hits. Areas with less than 20 hits are shown in grey. The centre of the temporary network and the Tertiary volcano Vogelsberg northeast of it are indicated by crosses. The East and West Eifel volcanic fields (solid lines) and political boundaries (dashed lines) are also indicated for orientation.
(Fig. 3 in Weber et al.)

Colour Plate 9:
Top: Sum over a 2 degree wide strip (N to S (A) and E to W (B)) of depth migrated RF, for location see small inserts. Bright colours indicate better coverage (see also Fig. 3 on Colour Plate 8). The labels *HVZ* (*LVZ*) indicate a high velocity zone (low velocity zone), respectively. The dashed lines give the centre of each anomaly. The thin black horizontal lines correspond to the depth of 35 km (Moho depth according to the iasp91-model), the 210, the 410 and the 660 km discontinuities. The triangle at the top indicates the location of the Eifel volcanic fields and the black triangles outline the Eifel volcanic area.
(Fig. 4 in Weber et al.)
Bottom: Moho depth as colour code and contour lines under the Eifel volcanic fields (solid lines) determined from migrated RF. Stars indicate seismic stations and dashed lines are the political borders.
(Fig. 5 in Weber et al.)

Colour Plate 10:
Horizontal slices averaged over 10 km thickness from the volume of migrated RF for six depth ranges between 40 and 100 km depth. The volcanic fields of the Eifel are outlined (solid closed lines). The left cross is the centre of the Eifel network, the right cross shows the location of the Tertiary volcano Vogelsberg. A low velocity zone (LVZ) is observed between ca. 60 km depth (dark blue colours) and ca. 90 km depth (red colour; see also Fig. 2b). The bright red spots in the depth range between 90 to 100 km are first Moho multiples.
(Fig. 6 in Weber et al.)

Colour Plate 11:
As Fig. 6 (Colour Plate 10) but for eight depth ranges between 150 and 230 km depth. The bright red colours from 160 to 210 km depth indicate a conversion at a high velocity contrast (see Fig. 2c in Weber et al., Colour Plate 8).
(Fig. 7 in Weber et al.)

Colour Plate 12:
Top: Topography of the 410 km discontinuity. South of the Eifel volcanic fields (solid lines and left cross) the 410 km discontinuity is depressed by about 15 to 25 km.
Bottom: Topography of the 660 km discontinuity. No deviation from the expected 660 km value is observed.
(Fig. 8 in Weber et al.)

Colour Plate 13:
(Left) *P*-wave tomography results (Ritter et al. 2001). (Centre) *S*-wave tomography results (Keyser et al. 2000, 2002). Deviations in *P*- and *S*-wave velocity are in percent relative to IASP91. (Right) Migrated RF data (Fig. 4b in Weber et al., Colour Plate 9) on an E-W slice through the Eifel plume. The triangle at the top indicates the location of the Eifel volcanic fields.
(Fig. 9 in Weber et al.)

Colour Plate 14:
Shear-wave splitting measurements across the Eifel hotspot in west-central Europe. Background tomographic map indicates relative seismic *S*-velocity between 100-170 km depth (Keyser et al. 2002). White curves are flow lines of our optimum PAF model, which has a stagnation distance of ~50 km (see text).
(Fig. 6 in Walker et al.)

Colour Plate 15:
Bouguer anomaly map of the Rhenish Massif and surrounding regions. Regions in the NW and SW without a high density of data points are blanked.
(Fig. 2 in Ritter et al.)

Colour Plate 16:
Various wavelength bands of the Bouguer anomaly in the Rhenish Massif and surrounding areas: a) bandpass $30<\lambda<90$ km, b) $100<\lambda<80$ km, c) $150<\lambda<250$ km, d) $210<\lambda<270$ km, e) $300<\lambda<400$ km.
(Fig. 3 in Ritter et al.)

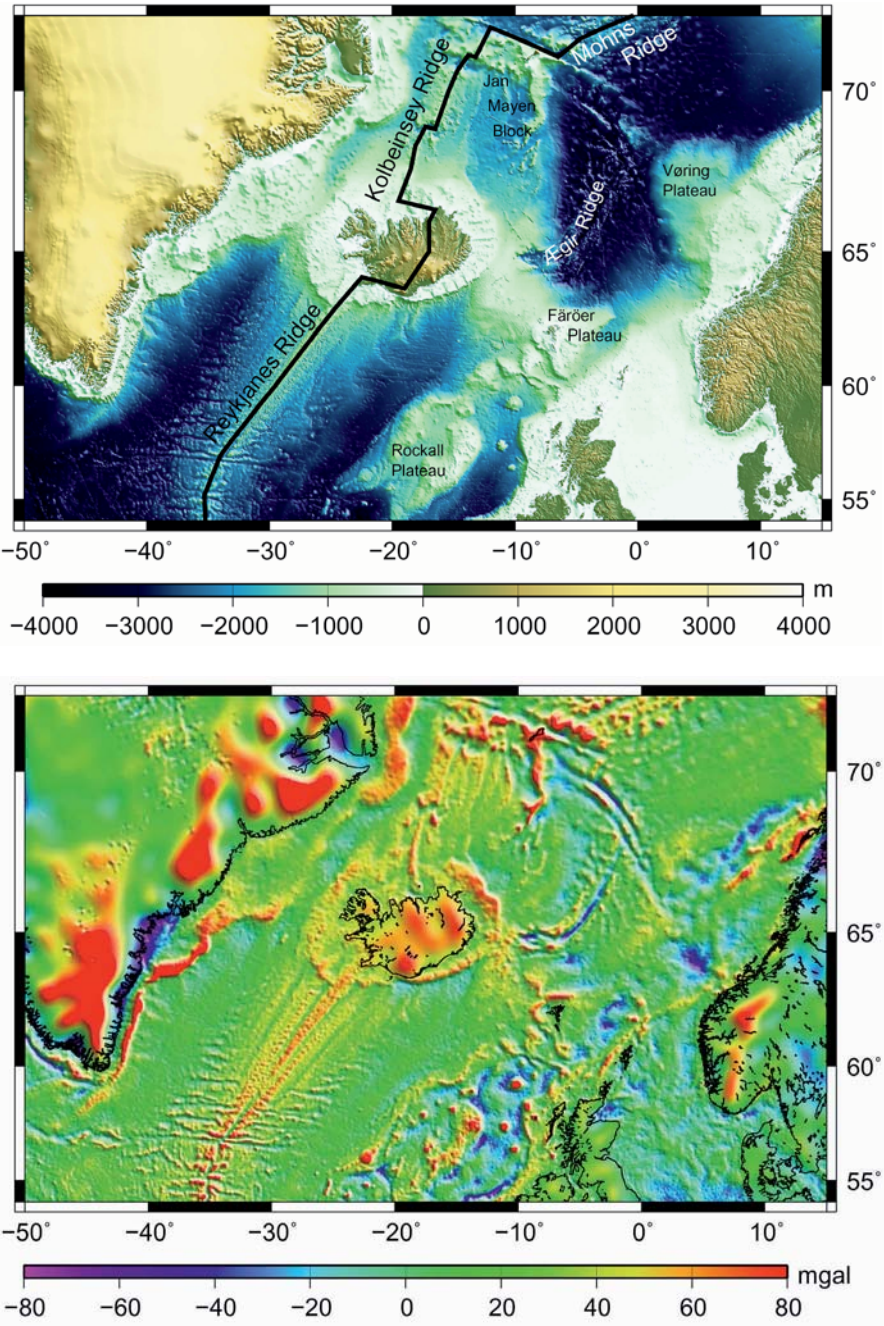

Fig. 2 (Ruedas et al.)

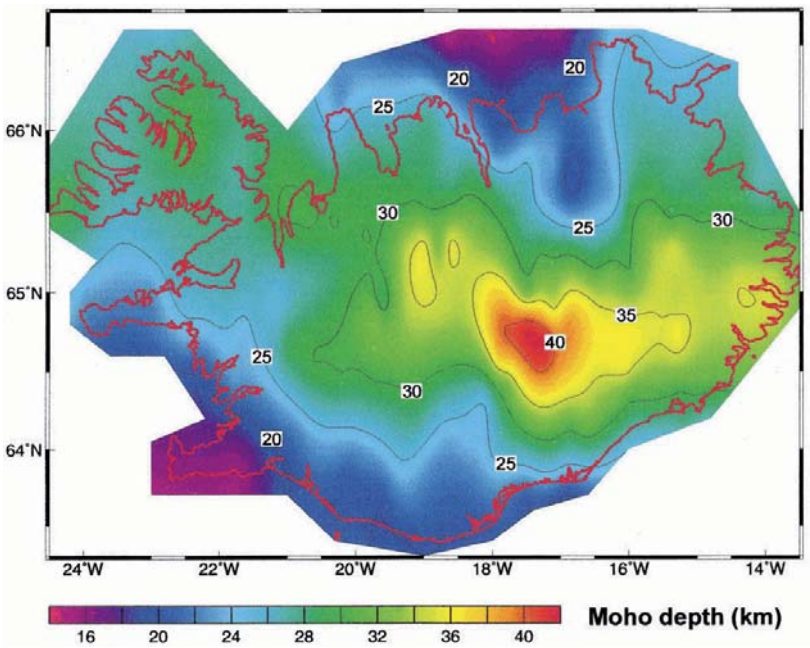

Fig. 4 (Ruedas et al.)

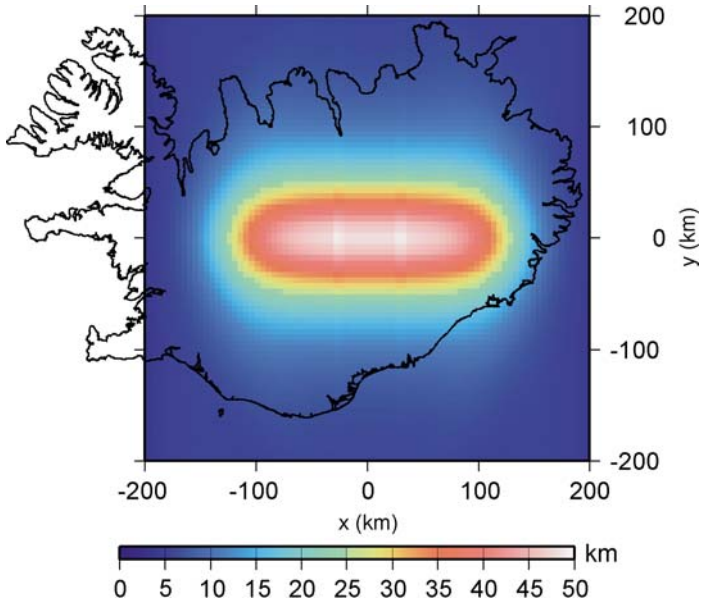

Fig. 5 (Ruedas et al.)

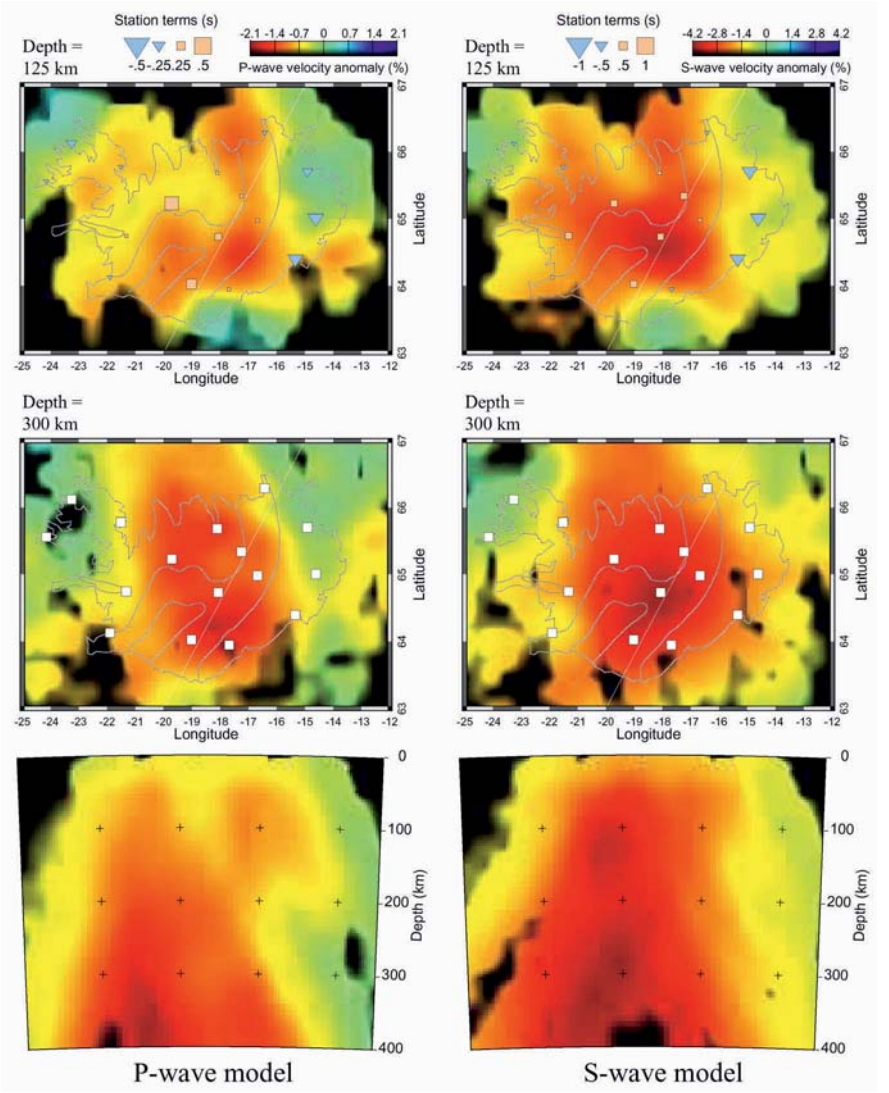

Fig. 6 (Ruedas et al.)

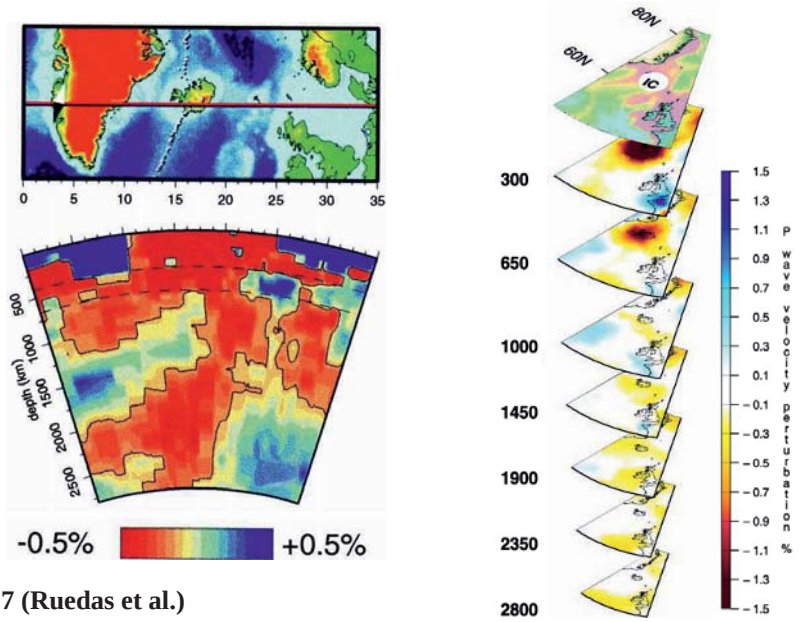

Fig. 7 (Ruedas et al.)

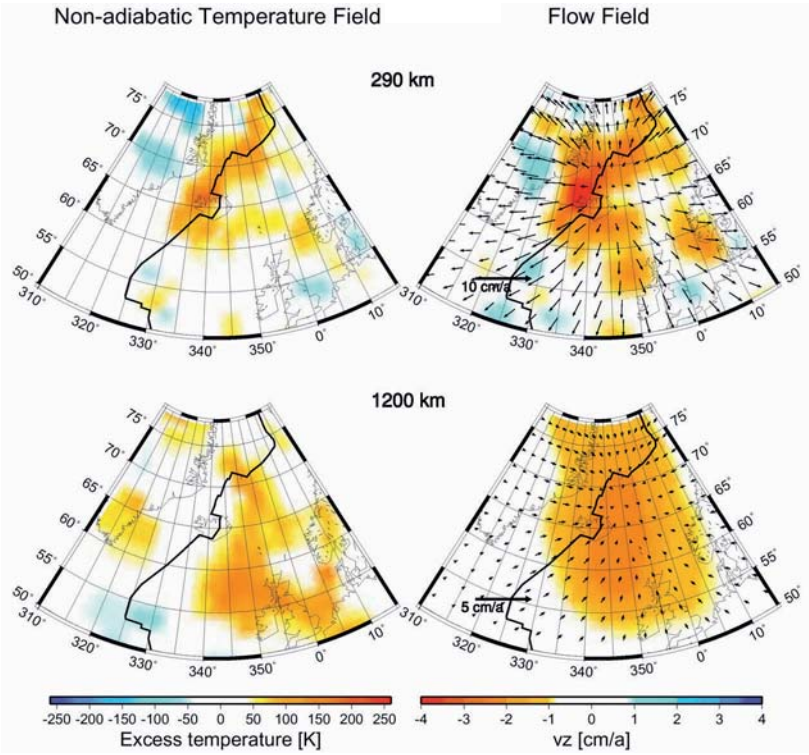

Fig. 12 (Ruedas et al.)

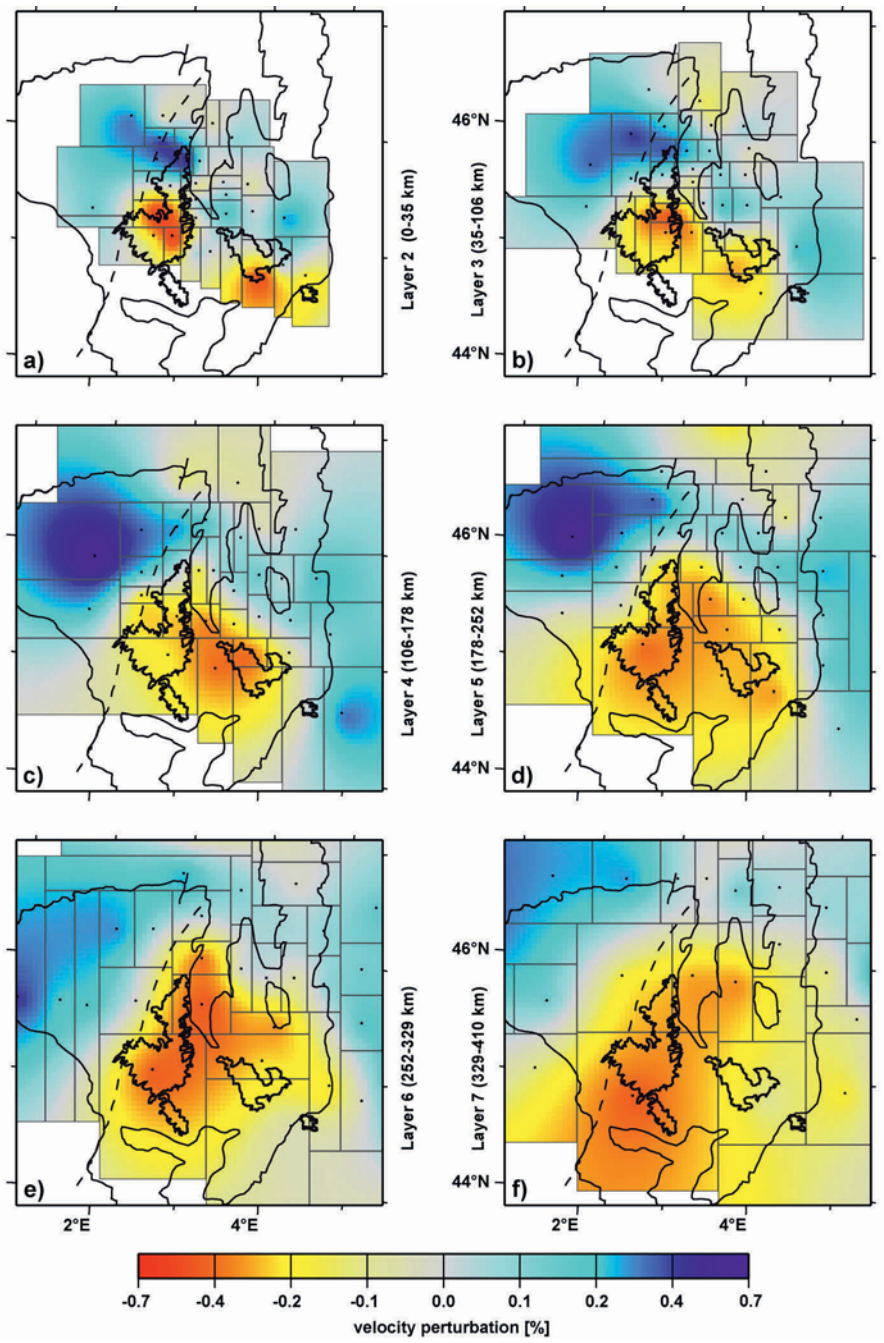

Fig. 10 (Barth et al.)

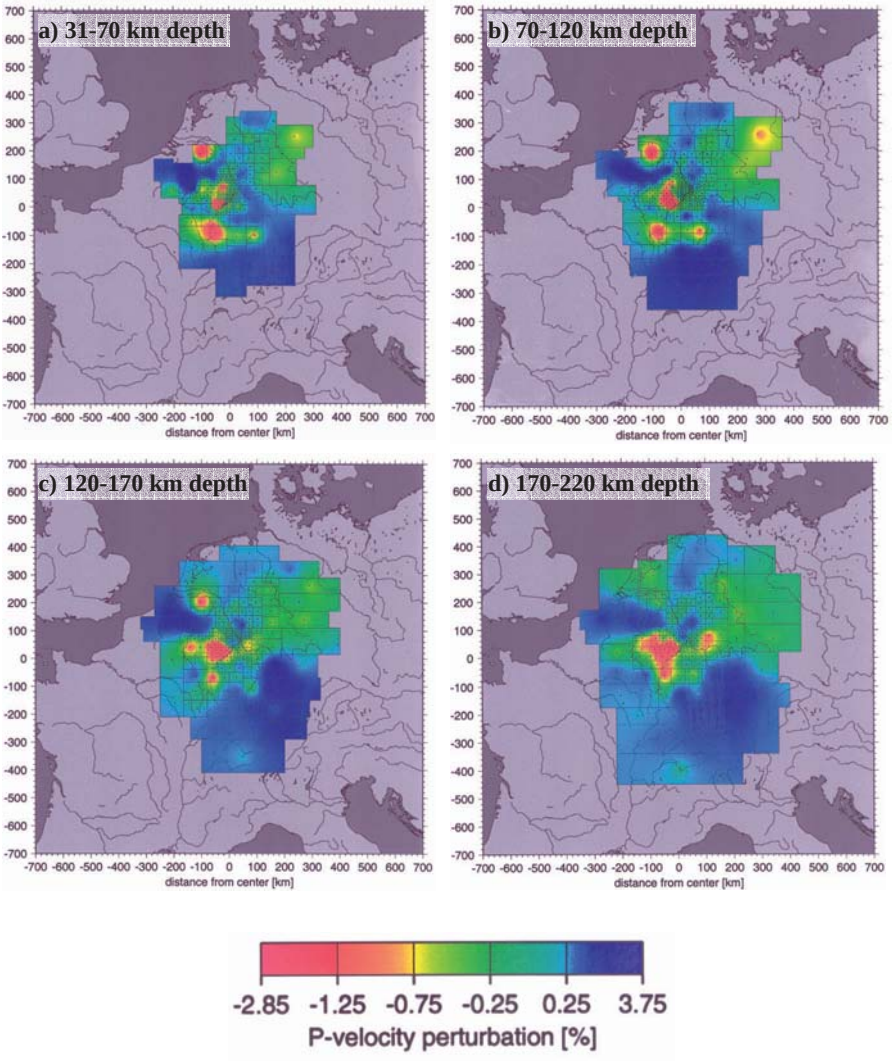

Colour Plate (Ritter)

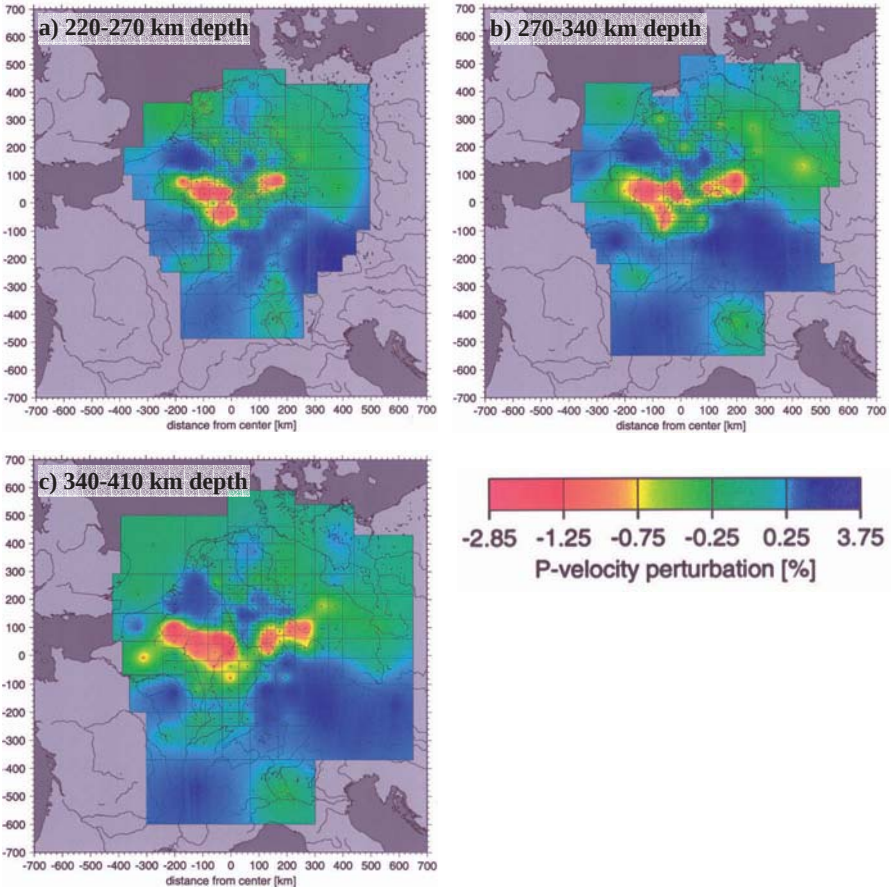

Colour Plate (Ritter)

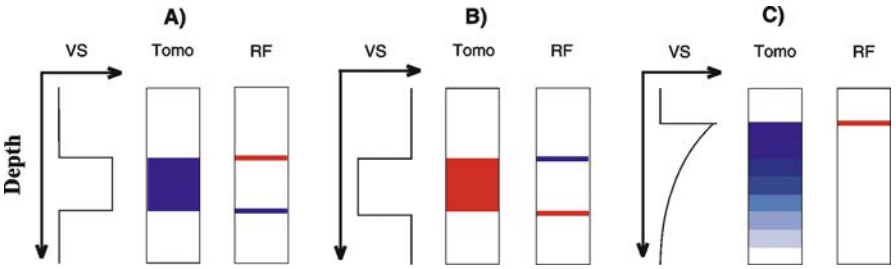

Fig. 2 (Weber et al.)

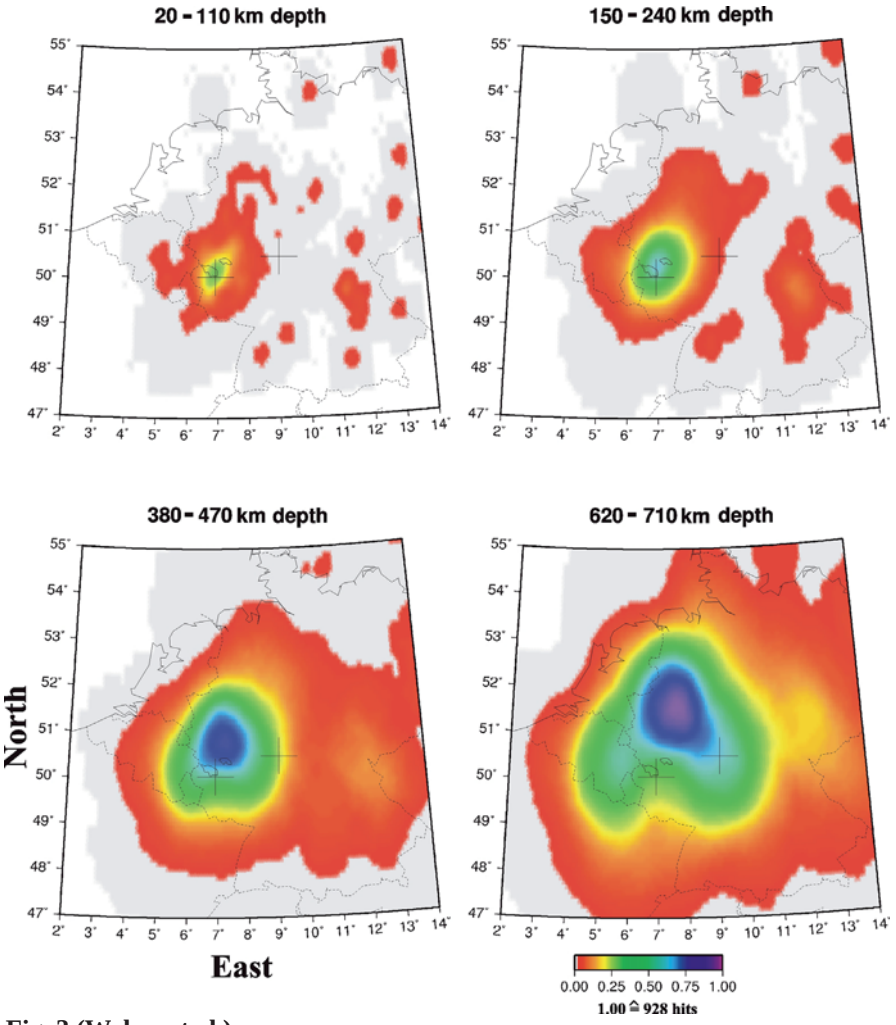

Fig. 3 (Weber et al.)

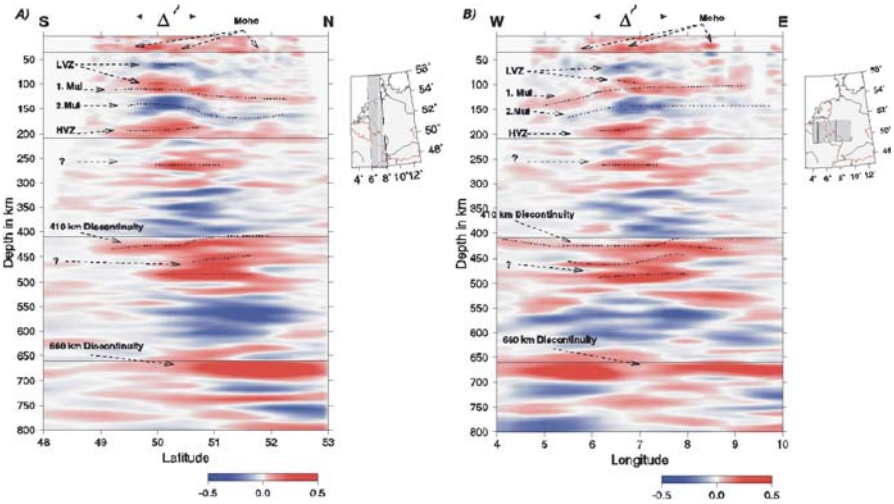

Fig. 4 (Weber et al.)

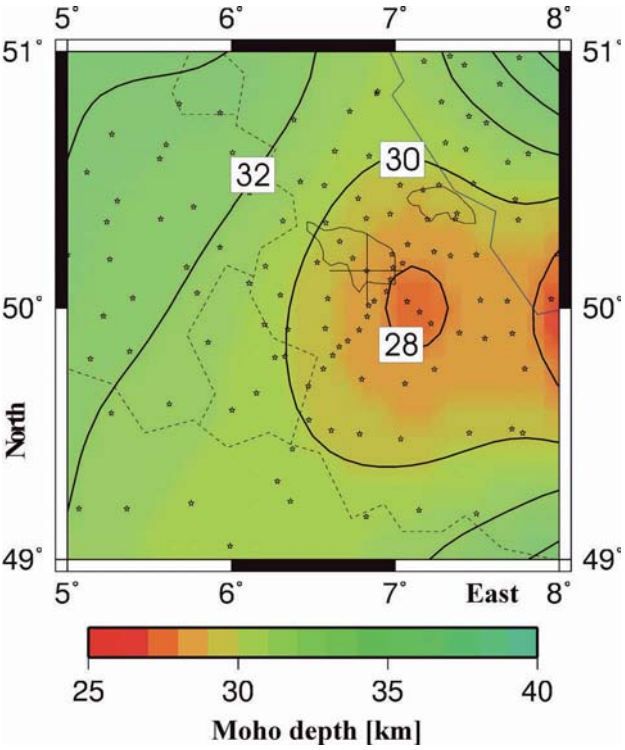

Fig. 5 (Weber et al.)

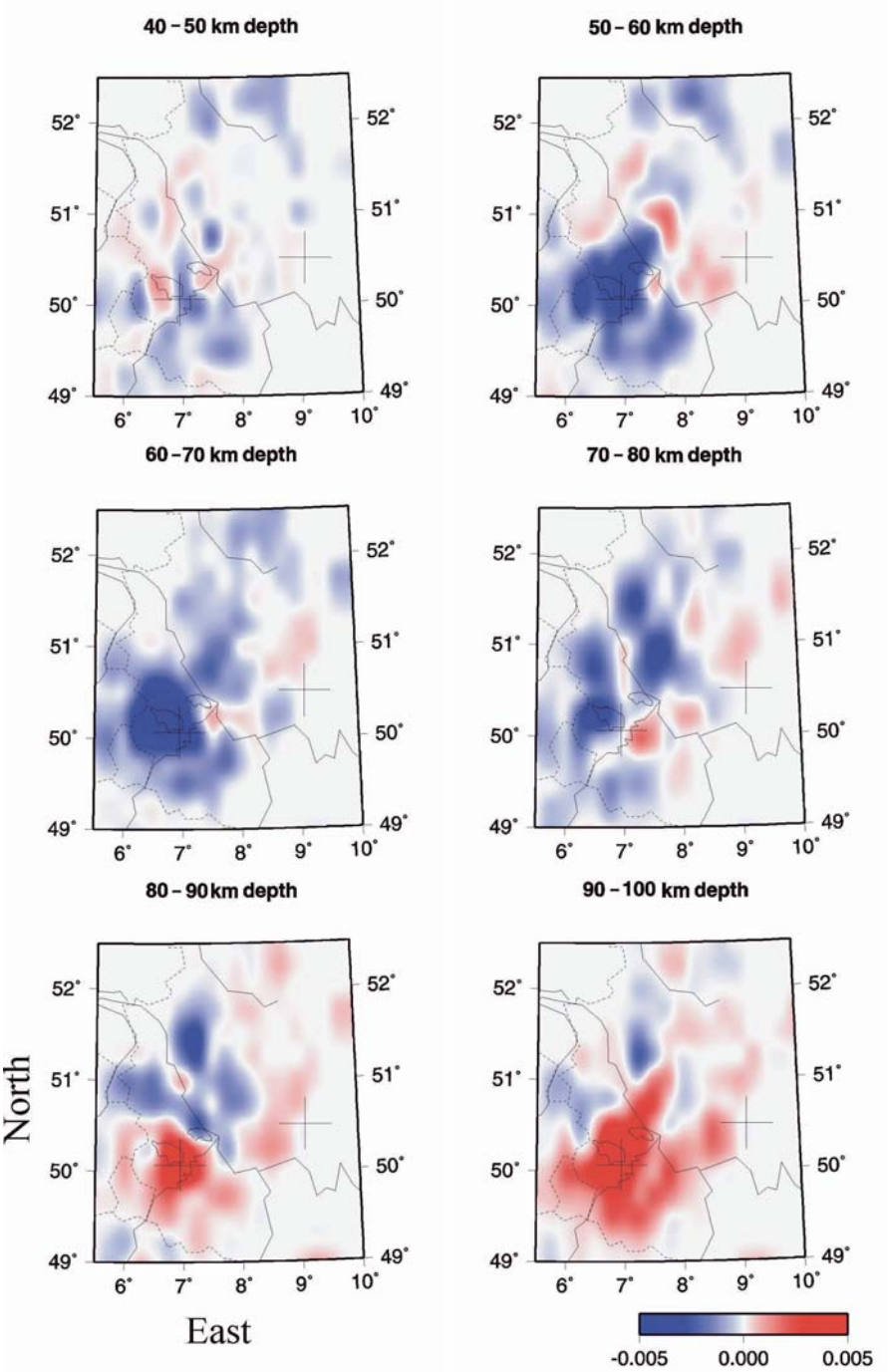

Fig. 6 (Weber et al.)

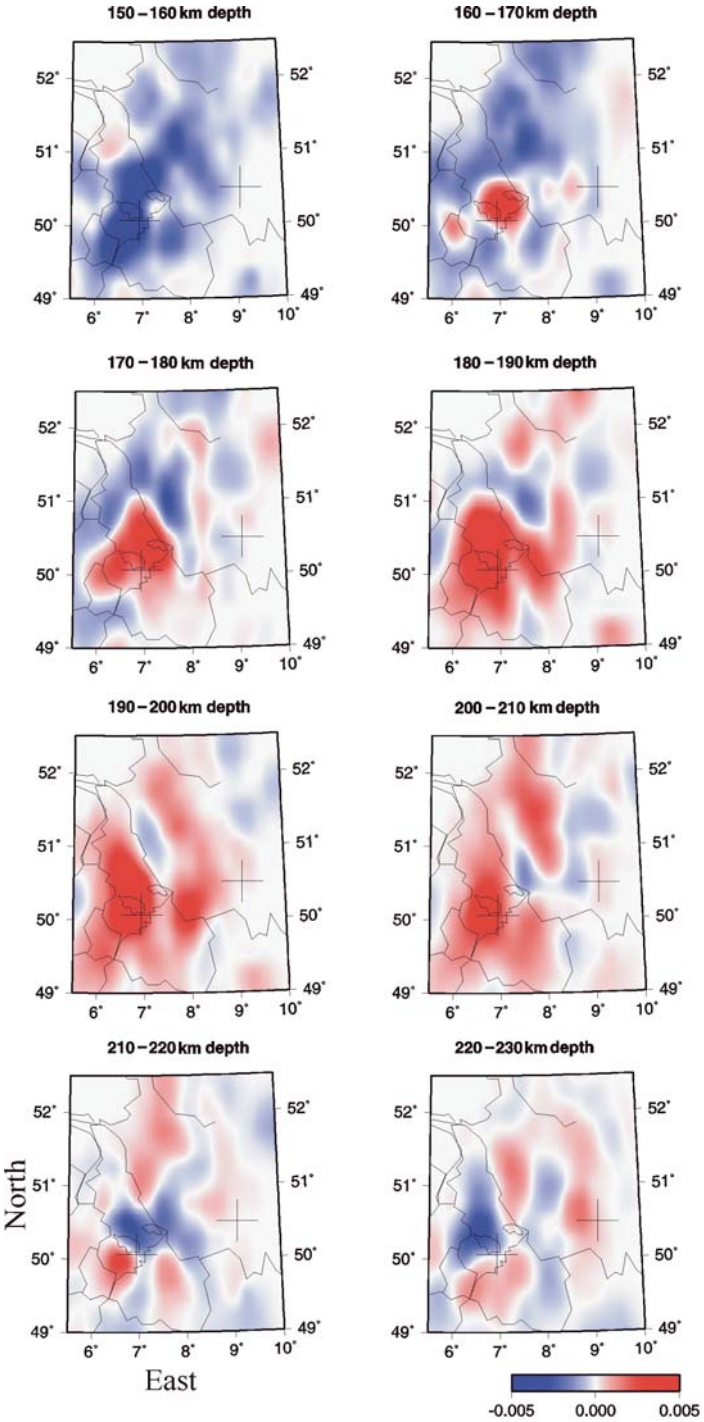

Fig. 7 (Weber et al.)

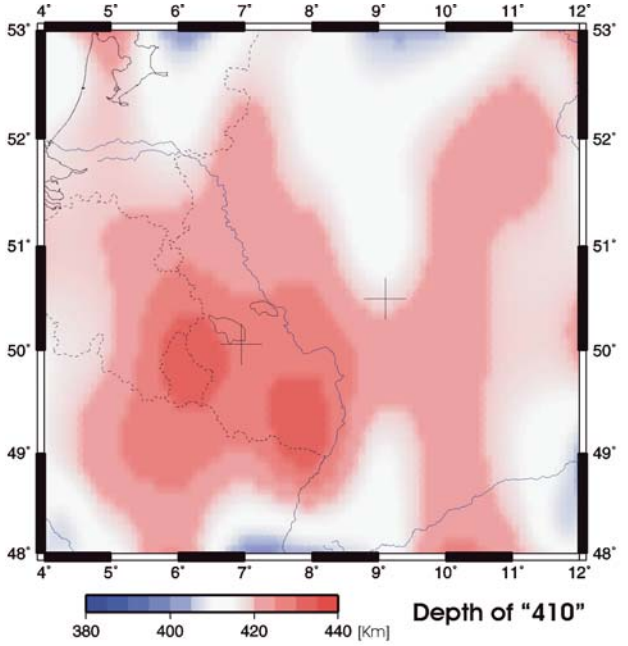

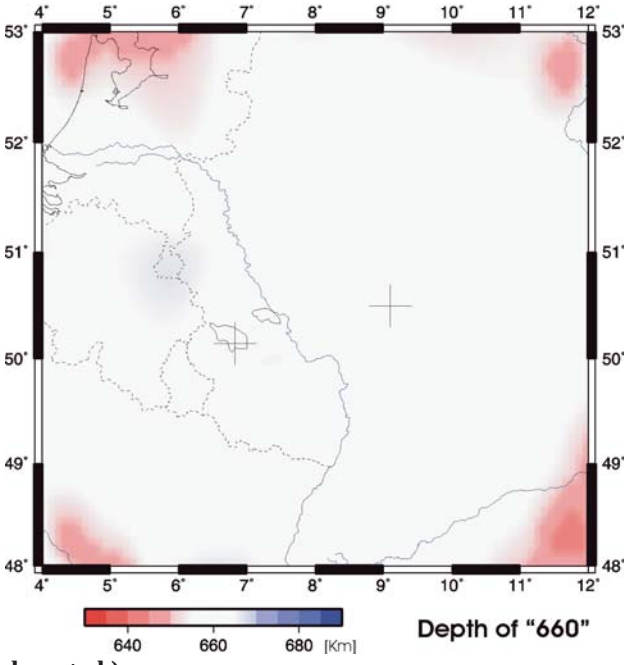

Fig. 8 (Weber et al.)

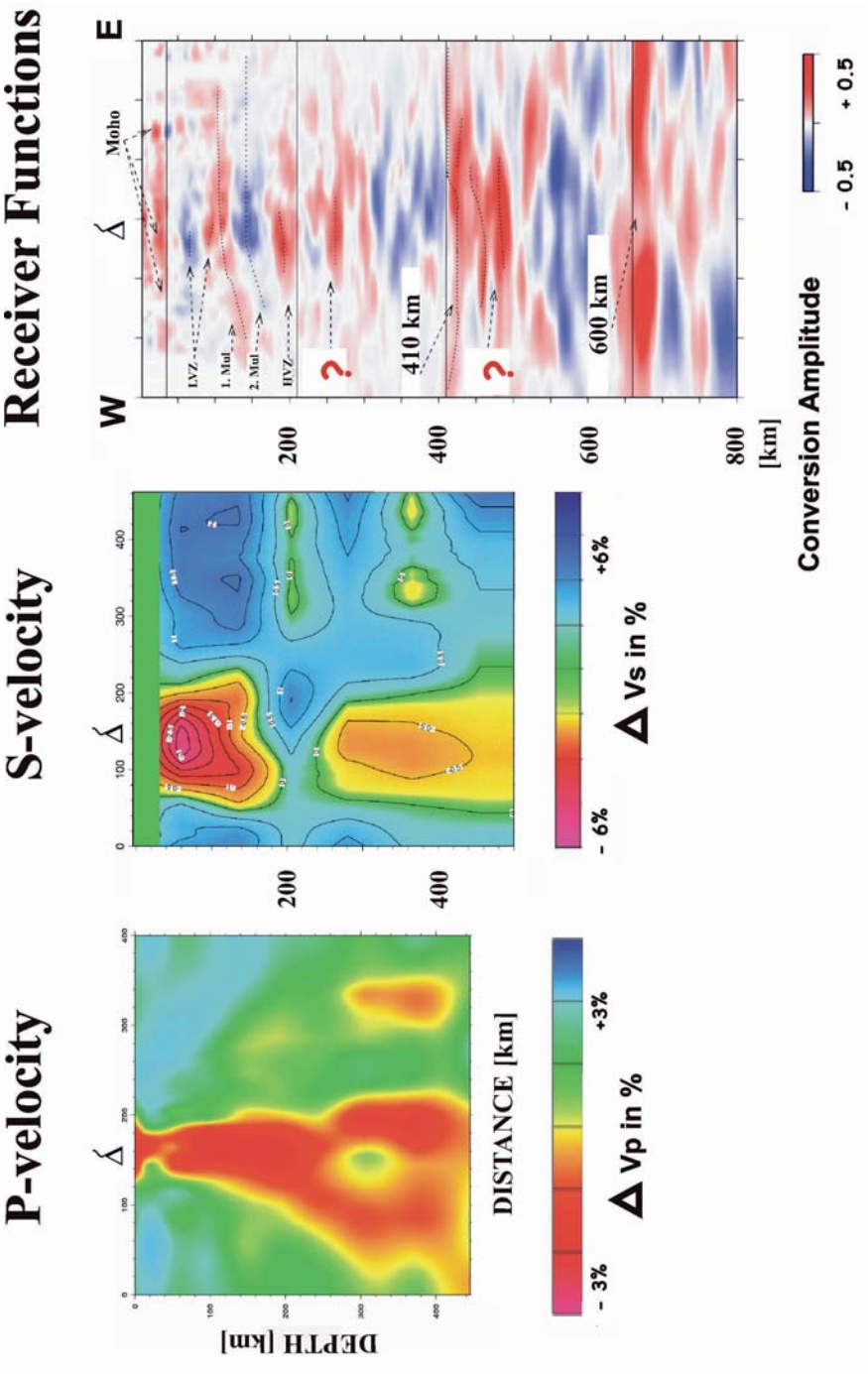

Fig. 9 (Weber et al.)

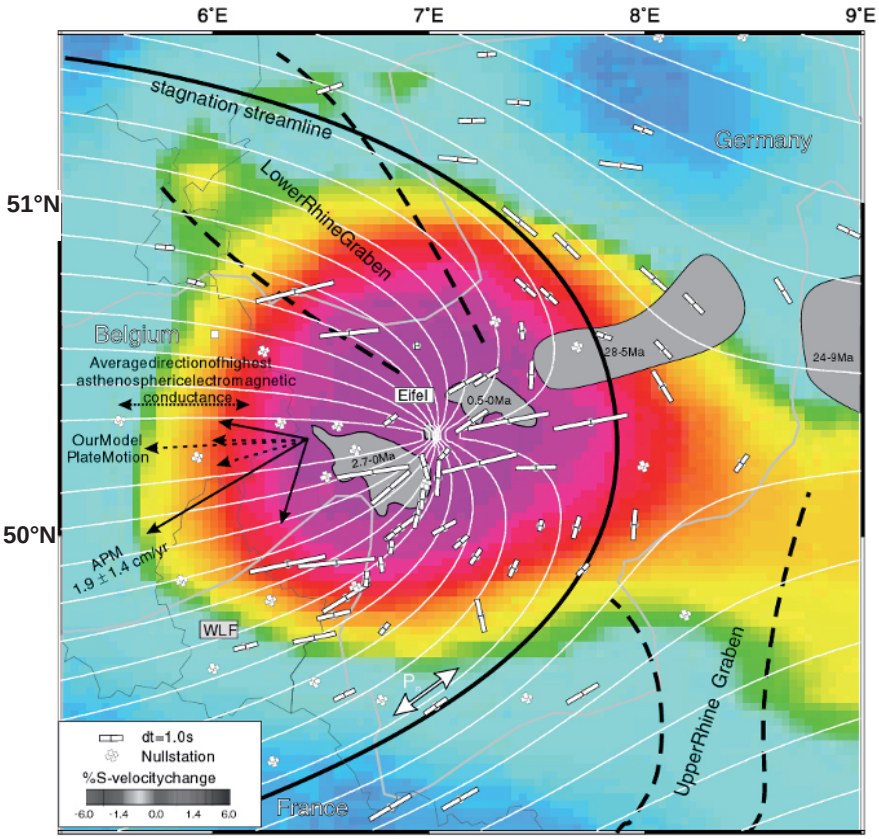

Fig. 6 (Walker et al.)

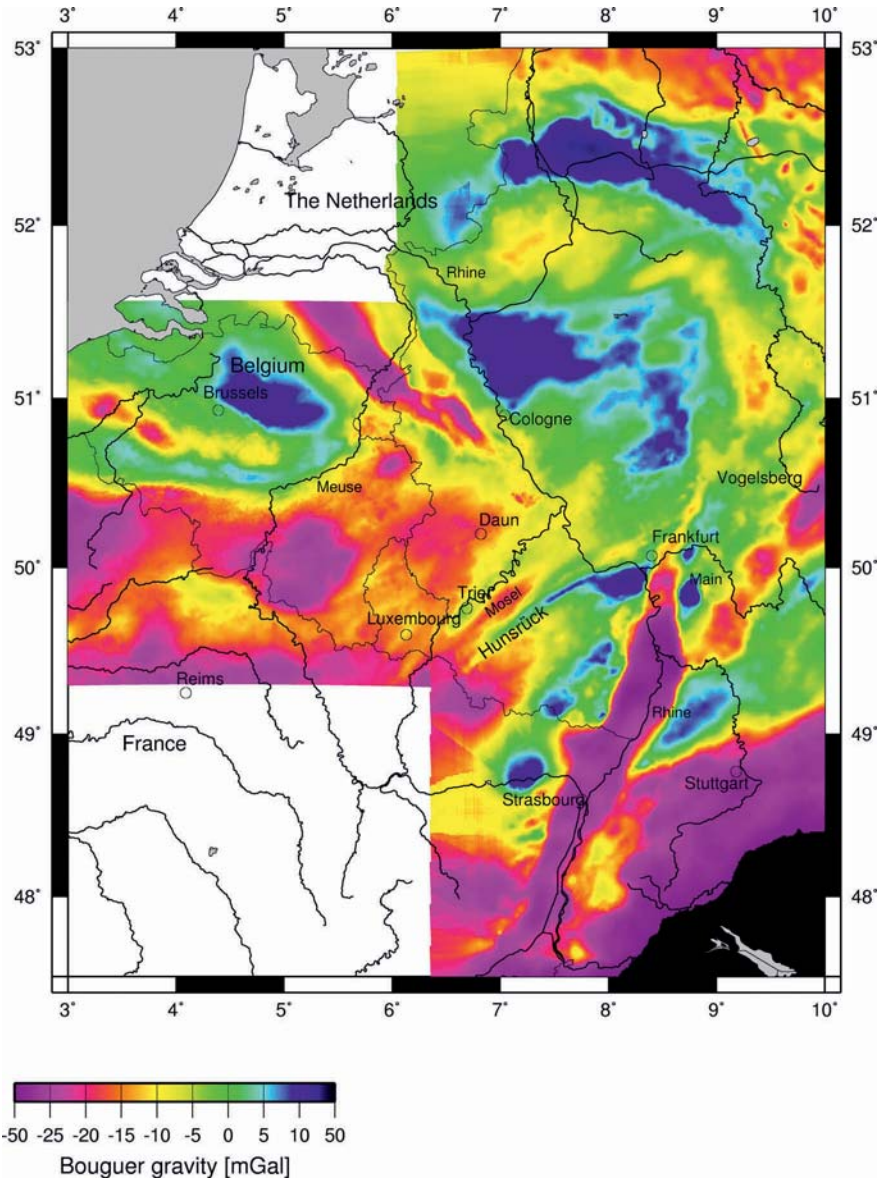

Fig. 2 (Ritter et al.)

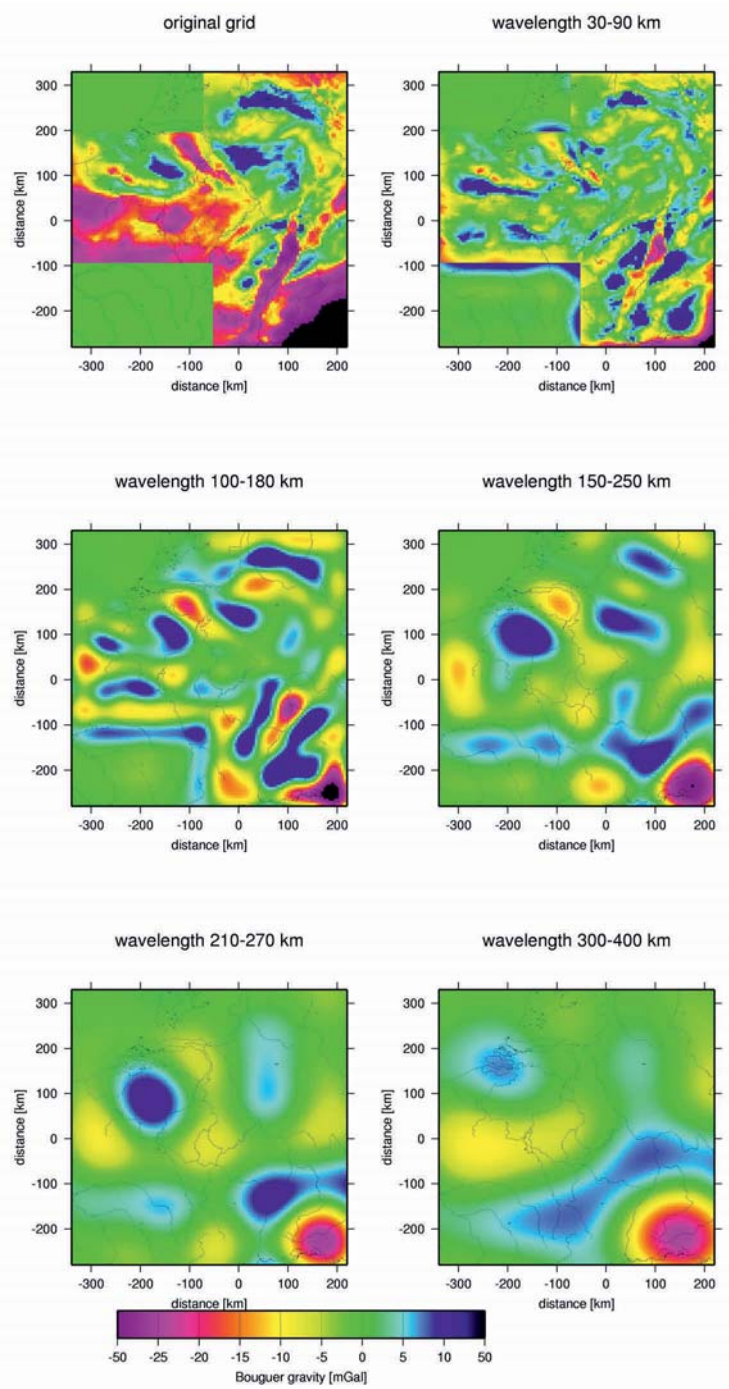

Fig. 3 (Ritter et al.)

Index